UNIVERSITÀ DI PARMA

UNIVERSITA' DEGLI STUDI DI PARMA

DOTTORATO DI RICERCA IN

"Scienze Chimiche"

CICLO XXXVII

Lignin-based hybrid materials for agrochemical applications and Cr(VI) water remediation

Coordinatore:

Chiar.mo Prof. Giovanni Maestri

Tutore:

Chiar.ma Prof. Dominga Rogolino

Dottoranda: MariannaVescovi

Anni Accademici 2021/2022 – 2023/2024

Table of contents

Abstract 7

List of abbreviations used in this study 11

Lignin: a promising renewable resource 15

Lignin extraction 18
Lignin in circular economy 21
Characterization of Lignin 25
Lignin Analysis in Wood 25
Nuclear Magnetic Resonance (NMR) 25
Ultraviolet Spectrophotometry 26
Infrared Spectroscopy 26
Pyrolysis-GC/MS 26
Size exclusion Chromatography (SEC) 26
Thermal Analyses 27
Lignin materials used in the PhD project 28
References 30

Chapter 1: Lignin and lignin-based materials in Cr(VI) water remediation 37

EXPERIMENTAL SECTION 43
Materials and methods 43
Materials preparation 43
RESULTS AND DISCUSSION 46
Conclusions 64
Supporting information 65
Procedures 65
Tables 67
Figures 68
References 77

Chapter 2: Lignin@ZnO 83

EXPERIMENTAL SECTION 93
Materials and methods 93
Materials preparation 93
RESULTS AND DISCUSSION 96
Seed germination and *in vivo* preliminary studies 116
EXPERIMENTAL SECTION 116
Materials and methods 116

RESULTS AND DISCUSSION 118
Antimicrobial activity: *in vitro* tests **122**
EXPERIMENTAL SECTION 122
Materials and Methods 122
RESULTS AND DISCUSSION 124
Solargo@ZnO **127**
EXPERIMENTAL SECTION 127
Materials and Methods 127
Materials preparation 127
RESULTS AND DISCUSSION 128
Conclusions **133**
Supporting information **134**
Procedures 134
Tables 135
Figures 140
References **152**

Chapter 3 Lignin@metal oxides: mechanochemical synthesis **161**

EXPERIMENTAL SECTION 171
Materials and Methods 171
Materials preparation 171
RESULTS AND DISCUSSION 174
HMW@Cu_2O mechanochemical synthesis **182**
HMW@ZnO_Cu_2O mechanochemical synthesis **189**
Conclusions **196**
Supporting information **197**
Procedures 197
Tables 198
Figures 203
References **220**

Chapter 4: Lignin@molybdate hybrid materials **225**

Wet synthesis of HMW@molybdate materials **233**
EXPERIMENTAL SECTION 233
Materials and methods 233
RESULTS AND DISCUSSION 238
Solargo@molybdate **260**
EXPERIMENTAL SECTION 260
Materials and methods 260
Materials preparation 260
RESULTS and DISCUSSION 261
HMW@molybdate mechanochemical synthesis **269**

EXPERIMENTAL SECTION 269
Materials and methods 269
Materials preparation 269
RESULTS AND DISCUSSION 271
Conclusions 276
Supporting information 277
Tables 277
Figures 278
References 291

Characterization techniques 297

Powder X-ray Diffraction (PXRD) 298
Inductively Coupled Plasma - Atomic Emission Spectroscopy (ICP-AES) 298
ICP-AES analysis on root and shoot samples after *in vivo* studies conducted on tomato plants 298
UV-Visible measurements 299
Transmission Electron Microscopy (TEM) and Energy Dispersive X-ray Spectrometry (EDX) 300
Scanning Electron Microscopy (SEM) and Energy Dispersive X-ray Spectrometry (EDX) 300
Dynamic Light Scattering (DLS) 300
Infrared Spectroscopy (IR) 301
Size exclusion chromatography (SEC) 301
Pyrolysis-GC/MS (Py-GC/MS) 301
Thermogravimetric Analysis (TGA) 301
Differential Scanning Calorimetry (DSC) 301
Company Partners 302
UPM-Kymmene Oyj 302
Green Innovation GmbH 303

Acknowledgments 305

Abstract

Lignin holds significant promise as a sustainable material being a widely available byproduct of the paper-pulp and bioethanol industries, holding potential for conversion into valuable materials with applications in water remediation and agrochemical production. With around 100 million tons of technical lignin produced annually worldwide, there is a growing need for sustainable and innovative uses for this underexploited resource. Its polyphenolic structure gives it promising antimicrobial and antioxidant properties, making it an attractive candidate for various eco-friendly applications. Its natural abundance, biodegradability, interesting polyphenolic and versatile chemical structure make it an ideal candidate for various applications that can reduce environmental impact and promote resource efficiency within a circular economy framework. All these aspects are outlined in the Introduction of this work, followed by four chapters describing the studies carried out to obtain innovative products and strategies by harnessing lignin properties, such as its antimicrobial, plant-stimulant and metal-reducing and adsorbing capabilities, particularly in the fields of agriculture and heavy metals-polluted water remediation.

Chapter 1 explores the issue of water contaminated by a variety of pollutants, including viruses, bacteria, organic matter, dyes, and in particular heavy metals. Unlike organic toxins, heavy metals persist in the environment and can accumulate in living organisms, causing severe health issues such as skin disorders, neurological damage, and organ failure. Additionally, they can contaminate soil and crops, which further threat to human health. Common adsorbents, such as synthetic ion exchange and chelating resins, are highly resistant to mechanical and chemical stress but pose significant environmental concerns due to their disposal challenges. As a result, there has been increasing interest in developing more sustainable and cost-effective alternatives, often derived from waste or by-products. We have assessed the effectiveness of a Kraft softwood lignin (named HMW in this thesis) and a hardwood enzymatic lignin (EH) in reducing Cr(VI) to the less toxic Cr(III) and lowering chromium concentrations by adsorption mechanisms in contaminated water. The lignin-based materials used in this study are provided by UPM-Kymmene Oyj and Green Innovation GmbH, the companies supporting this study: the provided lignin is used without further purification and has already been characterized to ensure reproducible properties, given the intrinsic structural complexity of the biopolymer. The work also investigates the role of lignin functionalization on Cr(VI) remediation, testing acetylated (Ac_Lig) and phosphorylated (P_Lig) lignin derivatives. When comparing the performance of HMW with the functionalized lignin, it becomes evident that the hydroxyl phenolic groups present in lignin play a pivotal role in the adsorption and reduction of metal ions. Additionally, the hybrid material HMW@Fe_3O_4, combining lignin with magnetite inorganic phase, demonstrates very promising performance in reducing Cr(VI) to Cr(III). The study also highlights the exceptional chromium adsorption capacity of EH lignin, with up to 60% adsorption, attributed to its higher surface area and major syringyl unit content. These results demonstrate the potential of lignin as a sustainable biosorbent for environmental remediation.

The subsequent chapters explore sustainable, scalable synthetic approaches for hybrid organic-inorganic materials, combining lignin with inorganic crystalline phases. Chapter 2 explores the possibility to synthetize hybrid materials containing lignin (HMW) and zinc

oxide, named HMW@ZnO, that shows promise for agricultural applications, particularly in stimulating plant growth. We have successfully synthesized hybrid materials containing zinc oxide (ZnO) crystals, demonstrating their versatility for agrochemical applications. The synthesis employed is a scalable, environmentally friendly process, producing materials with tunable metal contents. The materials have been studied from both inorganic and organic perspectives by several techniques, ensuring a comprehensive understanding of their properties and behaviours. *In vivo* trials on tomato seedlings treated with HMW@ZnO has shown reduced germination times and increased dry weight. Zinc distribution analysis has highlighted a correlation between effects on plants and zinc accumulation. *In vitro* studies have demonstrated superior antibacterial activity of HMW@ZnO against *Bacillus subtilis*, a Gram-positive bacterium commonly found in the rhizosphere, outperforming controls, including ZnO alone. Therefore, integrating ZnO into a lignin matrix not only leads to functional materials but also increases the value of lignin, a renewable biopolymer, aligning with sustainable agricultural practices. We have also explored the use of commercial liquid lignin formulation, Solargo™, provided by UPM Kymmene Oyj, that offers advantages for potential foliar applications. The findings deriving from this research establish a foundation for further studies, exploring these hybrid materials as sustainable fertilizers and pesticides, reducing reliance on harmful agricultural chemicals.

Furthermore, Chapter 3 explores the use of a mechanochemical approach to provide an alternative synthetic method for the preparation of the studied hybrid materials. This approach offers several benefits, including potentially lower energy consumption and no or little solvent employment, which could further enhance the sustainability of the material synthetic process. Mechanochemistry is a versatile technique applicable to a broad spectrum of chemical reactions and materials, and it simplifies the scaling up process. Initially, the mechanochemical synthesis of HMW@ZnO has been explored, with results comparable to those obtained by wet conditions. The materials have been synthesized with different zinc contents, and successful mechanochemical scale-up has been achieved. Similarly, HMW@Cu_2O has been synthesized based on previous studies of our research group, that highlighted its promising properties for agrochemical applications, making it valuable to investigate the mechanochemical reduction of Cu(II) to Cu(I). Finally, a material containing both zincite (ZnO) and cuprite (Cu_2O) crystals in the same biopolymeric matrix has been synthesized under simple and sustainable conditions, HMW@ZnO_Cu_2O.

Chapter 4 explores the possibility of obtaining lignin-based hybrid materials containing molybdate phases, combined with zinc or copper. These materials hold promise for improving plant health through two main pathways. First, they could provide essential micronutrients, like Mo, Zn and Cu, that support plant growth and well-being. The presence of lignin may play a critical role in enabling a slow-release mechanism for these nutrients, ensuring a gradual supply over time. This slow-release function is particularly important, as without it, heavy metals could accumulate in soil and plants, potentially leading to toxicity and negative environmental consequences. A second promising application of these hybrid materials lies in their use as potential pesticides for crop protection. Studies exploring the antifungal properties of molybdate inorganic phases in

the literature have shown encouraging results, indicating the potential for these materials to offer an environmentally friendly alternative to traditional chemical pesticides, also given the synergistic activity with lignin. The inorganic phases have been synthesized using a sustainable and easy procedure, making it suitable for in-field applications and ensuring that the materials are not only effective but also environmentally friendly, in line with the increasing demand for green chemistry in industrial applications. This research demonstrates that it is possible to obtain crystalline molybdate phases within the lignin matrix under mild, scalable and environmentally friendly conditions.

All the hybrid materials have been analysed by means of various techniques: Powder X-Ray Diffraction (PXRD) has been chosen to confirm the nature of the synthesized inorganic phase, together with Energy-Dispersive X-Ray Spectroscopy (EDX) and with Selected Area Electron Diffraction (SAED). Inductively Coupled Plasma-Atomic Emission Spectroscopy (ICP-AES) has been used to determine the metal loadings in the final materials. Transmission electron microscopy (TEM) studies have been conducted to evaluate the shape and morphology of the inorganic crystals formed and compare the results obtained with different synthetic strategies, together with dynamic light scattering (DLS). Scanning Electron Microscopy-Energy Dispersive X-Ray Spectroscopy mapping (SEM-EDX) has been useful to demonstrate the homogeneous distribution of the metal-containing nanocrystals into the organic matrix. Thermal analyses, such as Thermogravimetric Analysis (TGA), Differential Scanning Calorimetry (DSC), Pyrolysis GC-MS have been conducted for all the hybrid materials to ensure that the synthetic conditions can not negatively affect the organic component of the composite, together with size exclusion chromatography (SEC).

To conclude, this study opens new opportunities for developing sustainable, efficient, and cost-effective materials for agricultural applications, contributing to the future of sustainable practices. Furthermore, this work highlights the promising potential of lignin and its modified forms as sustainable materials for addressing critical environmental challenges, such as the removal of toxic chromium from water. It also underscores the importance of further exploring the functionalization of lignin and the use of hybrid organic-inorganic materials to enhance its adsorption and reduction capabilities, paving the way for the development of greener, more effective remediation strategies.

List of abbreviations used in this study

In this Section a list of the acronyms used in this work is reported, to specify the lignin reagents and the synthesized hybrid materials used, divided accordingly to the chapters where they first appear.

Chapter 1:

HMW: softwood Kraft lignin isolated from *Pinus taeda;* provided by UPM-Kymmene Oyj and Green Innovation.

EH: enzymatically hydrolysed hardwood lignin isolated from *Fagus sylvatica;* provided by UPM-Kymmene Oyj and Green Innovation.

Ac_Lig: acetylated HMW.

P_Lig: phopshorylated HMW.

HMW@Fe_3O_4: hybrid material where magnetite was synthesized embedded in HWM lignin matrix.

Fe_3O_4_ref: magnetite synthesized with the same conditions of HMW@Fe_3O_4, but in absence of lignin.

Chapter 2:

HMW@ZnO_X% (with X= 5, 10, 20 %, 30%): hybrid material where zinc oxide is synthesized embedded in HWM lignin matrix, where X refers to zinc content.

ZnO_ref: zinc oxide synthesized with the same conditions of HMW@ZnO_5%, but in absence of lignin.

HMW@ZnO_HCl: HMW after removal of zinc by acidic treatment starting from HMW@ZnO_10%

HMW_HCl: HMW after acidic treatment, using the same conditions adopted for HMW@ZnO_HCl.

HMW_NaOH: HMW after treatment with NaOH 0.07 M, ratios among lignin and NaOH were chosen accordingly to HMW@ZnO 10% experimental synthetic conditions.

Solargo™ is a liquid formulate, where lignin is suspended with propylene glycol, KOH and water (Composition: lignin (100 g), water (325 g), potassium hydroxide 50% (75 g) and propylene glycol (500 g)).

Solargo@ZnO_X% (with X= 5, 10, 20 %): hybrid material where zinc oxide is synthesized embedded in Solargo™, where X refers to zinc content.

Chapter 3:

HMW@ZnO_X%_m (X=5, 10, 20, 30% of Zn): hybrid material where zinc oxide is synthesized embedded in HWM lignin matrix and X refers to zinc content.

HMW@Cu_2O_X%_m (X=5, 10, 15, 20% of Cu): hybrid material where copper-deriving phase is synthesized embedded in HWM lignin matrix and X refers to copper content.

HMW@ZnO_X%_Cu_2O_Y%_m (X=4, 8, 12 % of Zn; Y= 4, 8, 12 % of Cu): hybrid material where zinc oxide and cuprite are synthesized embedded in HWM lignin matrix, where X refers to zinc content and Y to copper content.

Chapter 4:

HMW@$Cu_3(MoO_4)_2(OH)_2$_X%: hybrid material where lindgrenite phase is synthesized embedded in HWM lignin matrix, where X% refers to molybdenum content.

HMW@$NH_4Cu_2(MoO_4)_2(OH)(H_2O)$_X%: hybrid material where $NH_4Cu_2(MoO_4)_2(OH)(H_2O)$ phase is synthesized embedded in HWM lignin matrix, where X% refers to molybdenum content.

HMW@$NH_4Zn_2(MoO_4)_2(OH)(H_2O)$_X%: hybrid material where $NH_4Zn_2(MoO_4)_2(OH)(H_2O)$ phase is synthesized embedded in HWM lignin matrix, where X% refers to molybdenum content.

HMW@$NaZn_2(MoO_4)_2(OH)(H_2O)$: hybrid material where $NaZn_2(MoO_4)_2(OH)(H_2O)$ phase is synthesized embedded in HWM lignin matrix, where X refers to molybdenum content.

HMW@$KZn_2(MoO_4)_2(OH)(H_2O)$ hybrid material where $KZn_2(MoO_4)_2(OH)(H_2O)$ phases are synthesized embedded in HWM lignin matrix, where X% refers to molybdenum content.

$Cu_3(MoO_4)_2(OH)_2$_ref: $Cu_3(MoO_4)_2(OH)_2$ synthesised with the same conditions of HMW@$Cu_3(MoO_4)_2(OH)_2$_13% in absence of lignin.

$NH_4Cu_2(MoO_4)_2(OH)(H_2O)$_ref: $NH_4Cu_2(MoO_4)_2(OH)(H_2O)$ synthesised with the same conditions of $NH_4Cu_2(MoO_4)_2(OH)(H_2O)$_12%, in absence of lignin.

$NH_4Zn_2(MoO_4)_2(OH)(H_2O)$_ref: $NH_4Zn_2(MoO_4)_2(OH)(H_2O)$ synthesised with the same conditions of HMW@$NH_4Zn_2(MoO_4)_2(OH)(H_2O)$_14% in absence of lignin.

$NaZn_2(MoO_4)_2(OH)(H_2O)$_ref: $NaZn_2(MoO_4)_2(OH)(H_2O)$ synthesised with the same conditions of HMW@$NaZn_2(MoO_4)_2(OH)(H_2O)$_14% in absence of lignin.

Solargo@$Cu_3(MoO_4)_2(OH)_2$: hybrid material where lindgrenite is synthesized embedded in Solargo™

Solargo@$KCu_2(MoO_4)_2(OH)(H_2O)$: hybrid material where $KCu_2(MoO_4)_2(OH)(H_2O)$ is synthesized embedded in Solargo™

Solargo@$KZn_2(MoO_4)_2(OH)(H_2O)$: hybrid material where $KZn_2(MoO_4)_2(OH)(H_2O)$ is synthesized embedded in Solargo™

HMW@$NH_4Zn_2(MoO_4)_2(OH)(H_2O)$_MM400: hybrid material where $NH_4Zn_2(MoO_4)_2(OH)(H_2O)$ phase is synthesized by mechanochemistry with MM440

HMW@$NH_4Zn_2(MoO_4)_2(OH)(H_2O)$_PM100: hybrid material where $NH_4Zn_2(MoO_4)_2(OH)(H_2O)$ phase is synthesized by mechanochemistry with PM100

HMW@$Cu_3(MoO_4)_2(OH)_2$_PM100: hybrid material where lindgrenite phase is synthesized by mechanochemistry with PM100

Lignin: a promising renewable resource

Lignin is a natural polymer found in the cell walls of plants, and it is a major component of lignocellulosic biomass, which consists of three primary fractions: cellulose, hemicellulose, and lignin. Lignocellulose is organized in microfibrils, consisting of about 30–50% cellulose, 20–35% hemicellulose and 20–35% lignin,[1] which results the second most abundant natural polymer on earth, after cellulose. During the formation of the cell wall, the microfibrils, constituted by cellulose crystallites surrounded by hemicelluloses, are embedded in an amorphous matrix of lignin (Figure I.1). Multiple microfibrils align and wrap around each other, creating a thicker and stronger bundle forming macrofibrils, that are essential for the structure and strength of the plant cell wall.

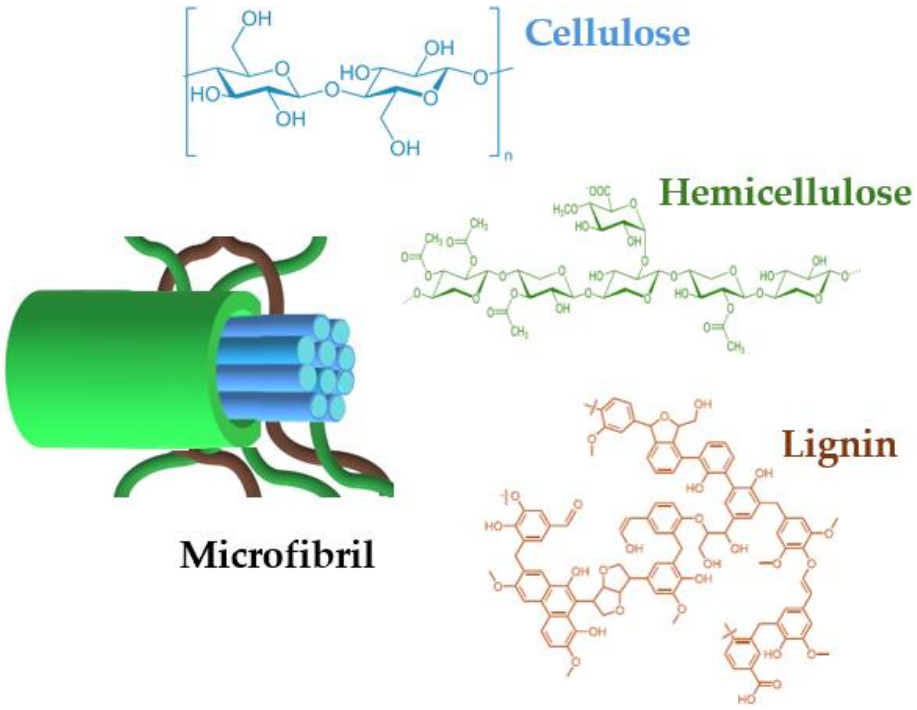

Figure I.1. Microfibril constituted by cellulose, hemicellulose and lignin[2]

Lignin is a complex and water-insoluble aromatic polymer: its composition and content in plants vary depending on the botanical species. In softwoods, lignin makes up approximately 30% of the total mass, whereas in hardwoods, this proportion decreases to 20–25%. Herbaceous plants exhibit variable and generally lower lignin content.[3] Lignin structure is primarily derived from methoxylated hydroxycinnamyl alcohol building blocks, called monolignols. In gymnosperms it predominantly consists of guaiacyl residues, while in angiosperms, it is a blend of guaiacyl and syringyl residues. Grass lignin contains a mixture of all three aromatic units. These contents are reported in Table I.1. Different types of lignin are categorized as type-G, type-G-S, type-H-G-S, and type-H-G, depending on the relative abundance of the core phenolic units—guaiacyl (G), syringyl (S), and p-hydroxyphenyl (H)—in the polymer.[4] Enzymes are directly involved in the biosynthesis of these typical lignin monomers. These monolignols—p-coumaryl alcohol, coniferyl alcohol, and sinapyl alcohol—play a key role in lignification, the polymerization process that forms the lignin polymer through an oxidative coupling process, resulting in the so-called respectively "H," "G," and "S" units[5] (Table I.1).

Table I.1. Proportions of basic structural units of lignin in different plant species. Table taken from Ralph et al.[6] The representation of the three monolignols and their related phenyl propanoic units that build the structure of lignin are reported below.

Units	Hardwood	Softwood	Grass
S	50–75 %	0–1 %	25–50 %
G	25–50 %	90–95 %	25–50 %
H	Trace	0.5–3.4 %	10–25 %

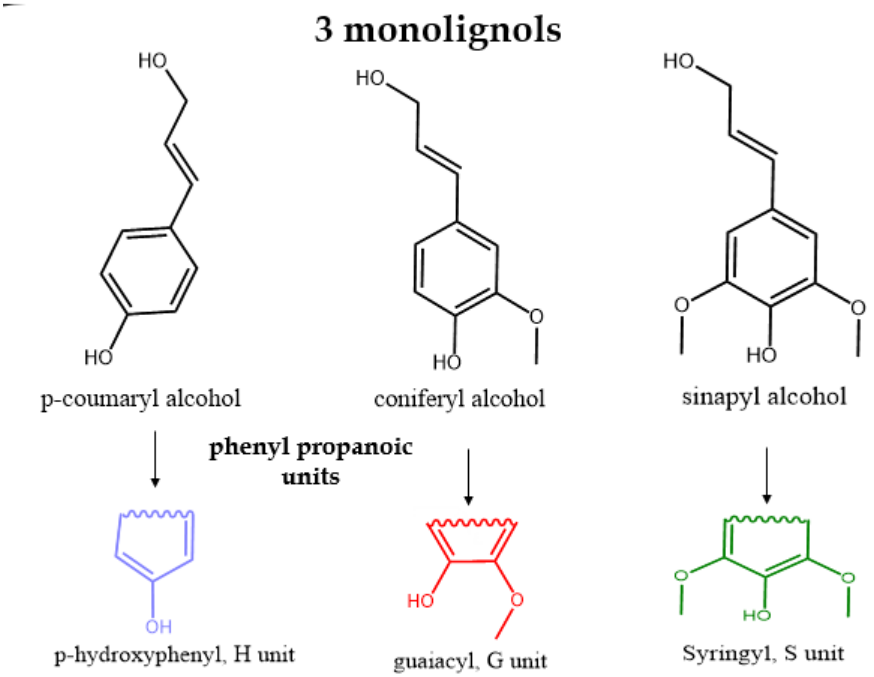

Variations in the ratio of monolignols lead to differences in the number of functional groups, which in turn influences the reactivity of the various lignin types. Table I.2 compares the content of the functional groups for softwood and hardwood lignin.

Table I.2. Amount of main functional groups in softwood and hardwood lignin. Table taken from Alèn et al.[7]

Functional groups	Native lignin (per 100 monolignoids)	
	Softwood lignin	Hardwood lignin
Phenolic hydroxyl	20-30	10-20
Aliphatic hydroxyl	115-120	110-115
Methoxyl	90-95	140-160
Carbonyl	20	15

Unlike cellulose, which has a well-defined sequence of monomeric units linked by regular β-1,4-glycosidic bonds, lignin is characterized by a variety of distinct and chemically different bonding motifs, each requiring specific conditions for cleavage during selective depolymerization, resulting in a structure that is composed of a cross-linked network of

polyphenolic units. The biopolymer variable molecular masses result from the random cross-linking polymerization of phenolic groups, which arise from radical-coupling reactions between phenolic radicals,[8] connected by C−C bonds and aryl–ether linkages, including aryl–glycerol and β-aryl ether bonds[9] (Figure I.2). The botanical source also influences the types of interunit linkages. While the β-O-4 ether bond is consistently the most abundant, comprising approximately 50-80% of all interunit bonds, the presence of monolignols with ortho-methoxy groups in the structure tends to reduce the occurrence of 5-5 and β-5 carbon-carbon linkages. The types of chemical linkages are reported in Figure I.2. As a result, hardwood lignin contains fewer of these bonds compared to softwood lignin. In addition, monolignols can also form bonds with other cell wall polymers, such as cross-linking polysaccharides and proteins, resulting in the creation of complex three-dimensional networks. This process is catalysed by the enzyme peroxidase. The resulting lignin structure is highly resistant to enzymatic degradation, which is why it plays such a significant role in plant cell wall rigidity.

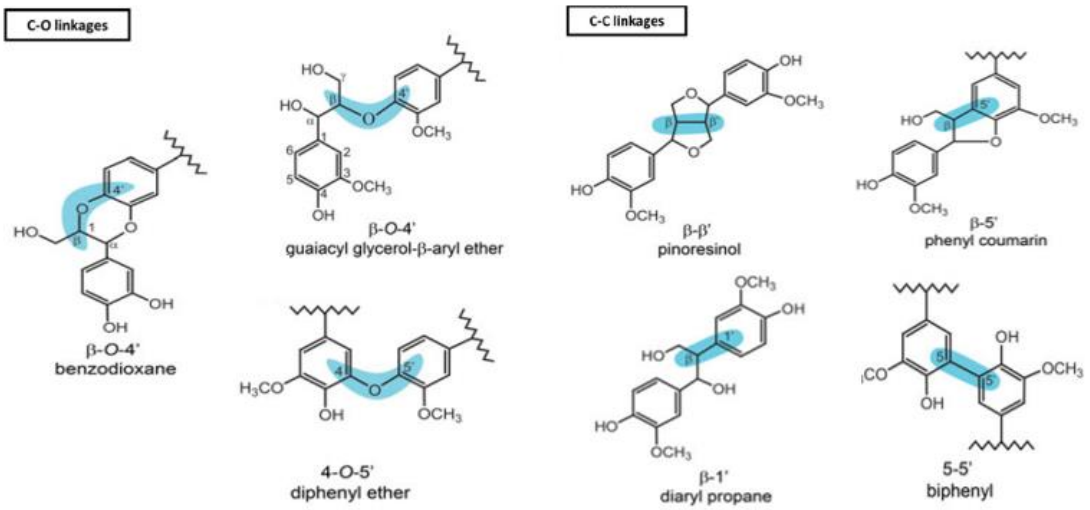

Figure I.2. Major ether and C-C bonds in lignin**.** The figure is derived from Hao et al.[10]

Lignin extraction

A variety of different kinds of lignin, derived from different extraction and isolation methods, are commercially available. Depending on the type of plant and the extraction method employed, they exhibit diverse chemical functionalization, physical characteristics and molecular mass distributions, making them suitable for a wide range of applications. Lignin extraction methods from lignocellulosic biomass are closely associated with those used in the paper industry and they could be categorized into chemical and mechanical extraction, depending on the intended application of lignin and other by-products (cellulose and hemicellulose). Mechanical methods are typically used for ethanol production through fermentation, while chemical extraction techniques are already employed in the paper industry.[11] Chemical lignin extraction methods are divided into three main categories: sulfur-based, sulfur-free processes and other alternative methods have been employed to perform the function of fractionating lignocellulosic biomass to extract lignin. Mechanical extraction methods are further divided into two essential processes:

refining and grinding.[12] A schematic representation of the lignin extraction techniques is reported in Figure I.3 and a brief description of the chemical methods is provided below.

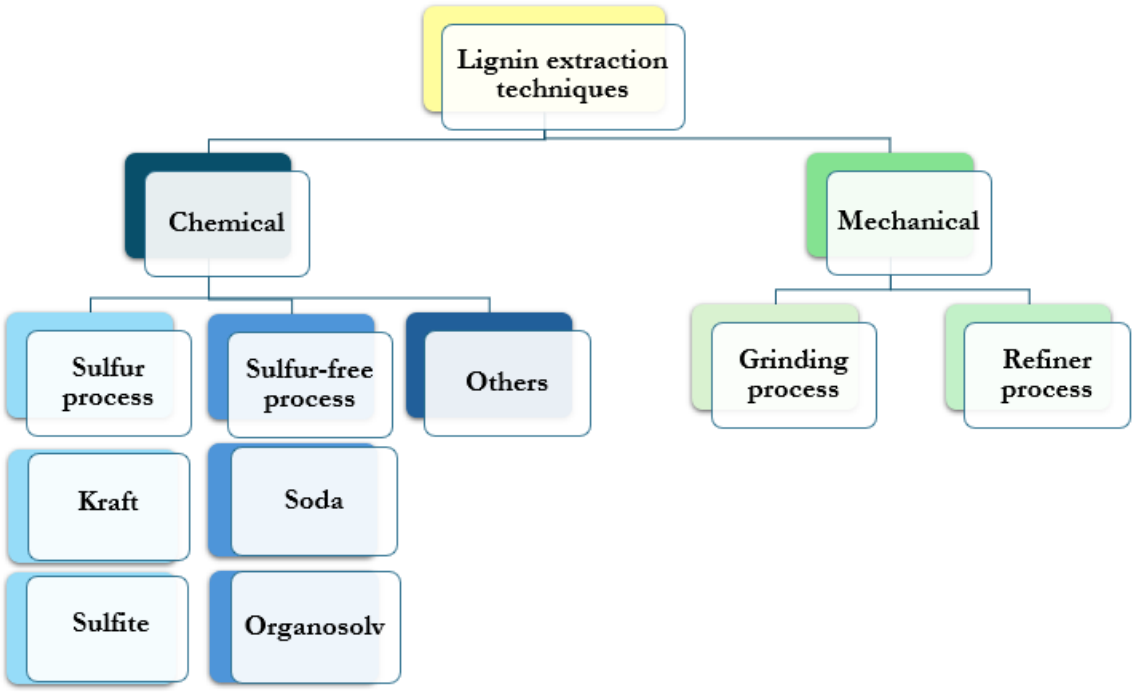

Figure I.3. Lignin extraction methods: the scheme is derived from Lobato-Peralta et al.[13]

The majority of global paper pulp is produced using the Kraft process, which transforms wood into pulp. According to this method, wood is treated with a Na_2S/NaOH solution at temperatures ranging from 155–175 °C for several hours, separating solid (cellulose) and liquid (black liquor) components. **Kraft lignin**[14] is produced through a delignification process, where the black liquor is precipitated, neutralized with an acidic solution (pH 1–2), and then dried to obtain a brown powder. Kraft lignin is hydrophobic and has a lower molecular weight compared to the original lignin. A large portion of commercial Kraft lignin exists in a water-soluble sulfomethylated form, resulting from the reaction between alkaline lignin, sodium sulphite, and formaldehyde.

Lignosulfonates[15] are obtained from the **sulfite process**, where softwood is treated with sulphurous acid salts (such as sulfites or bisulfites) to separate lignin from cellulose, extracting lignin via the sulfite-pulping process. Lignosulfonates are water-soluble and chemically altered with sulfonate groups, and contain carbohydrates, minor amounts of wood extractives and inorganic compounds. They are typically prepared as salts of calcium, magnesium, or ammonium. Compared to the Kraft pulping process, this method is milder and produces lignosulfonates with a higher molecular mass, preserving a structure that more closely resembles the original lignin.

The **soda process**[16] is commonly used to extract lignin from materials other than wood, such as annual plants and bagasse. The process involves alkaline hydrolysis with sodium hydroxide (NaOH 13–16 wt%) at temperatures between 140°C and 170°C in pressurized reactors, which breaks the bonds in lignin phenolic units. After extraction, lignin is recovered using centrifugation, filtration, or precipitation, although silica may co-precipitate with lignin in some cases. Several studies have explored variations of the soda

process for different feedstocks. The soda process is advantageous because it preserves the lignin structure, making it suitable for applications like phenolic resins, dispersants, and animal feed.

Organosolv lignins[17] are produced through different organic solvent-based techniques, collectively known as the organosolv process. In these processes, lignin is extracted from biomass using a mixture of organic solvents and water, under high temperature and pressure. Alcohols are the most commonly used solvents, often combined with other solvent mixtures and reagents. The lignin is then isolated by acidic precipitation. However, only organosolv lignins, named Alcell and Organocell lignin are commercially available. Considering Kraft lignin, organosolv lignins are less modified compared to pristine lignin and typically free of sulphur.

When wood undergoes treatment with steam at high temperature and pressure (approximately 180–200°C), followed by rapid decompression in the presence of chemicals, partial hydrolysis of the lignin takes place, resulting in **steam-exploded lignin**.[18] This process results in a water-insoluble lignin material with reduced levels of carbohydrates and wood extractives. The lignin produced has a low molecular weight due to acidic hydrolysis reactions.

Enzymatically hydrolysed lignin[19] is produced through the action of enzymes such as cellulases, hemicellulases, laccases, and microorganisms. To enhance the accessibility of the biomass to these enzymes, various chemical and physical pre-treatment methods are employed before enzymatic degradation. These include milling, dilute acid or steam treatments, ammonia fiber explosion, and alkaline or organosolv processes. This type of lignin is highly chemically reactive due to the large number of active functional groups present. One key advantage of enzymatic hydrolysis is the absence of toxic and corrosive by-products. However, even after purification, the resulting lignin still contains impurities (some residual carbohydrates, for instance) and has a high-water retention capacity, which limits its use as a fuel.

Lignin in circular economy

As a polyphenol, lignin plays a critical role in the structural integrity of trees and plants. By providing mechanical strength and rigidity, lignin enables trees to grow tall and withstand environmental stresses, such as wind, physical damage, and microbial attacks. Its cross-linked polyphenolic structure not only supports the plant cell walls but also serves as a defence mechanism against chemical and physical stresses. In addition to its role in plants, lignin contributes has environmental significance and its distinctive chemical properties make it an attractive alternative to fossil-based materials. Its structure offers numerous opportunities for chemical conversions, thanks to its abundance and adaptability, making it suitable for a wide range of applications. However, its complex nature has historically made challenging its efficient use. The irregular and strong C−C and C−O bonds in its structure contribute to this difficulty. Despite these challenges, significant progress has been made in the valorization of lignin, but with its higher carbon and lower oxygen content, compared to polysaccharides or cellulose, lignin is an attractive feedstock for producing biofuels and chemicals. It stands out as a remarkable and versatile natural polymer with many beneficial properties: the Ecologic Institute (www.ecologic.eu) ranked seven lignin-based products among the top 20 emerging biobased products in 2018, highlighting the growing interest towards lignin as a versatile and sustainable resource.[20] This waste material, from both paper pulp manufacturing and bioethanol production, is often underutilized: the data on chemical pulp production indicates that the annual amount of lignin passing through industrial processes is currently between 70 to 80 million tons.[21] However, only an estimated 1.65 million tons per year of isolated technical lignin are being utilized for material applications, representing less than 2% of the worldwide processed lignin. The remaining lignin is typically combusted for energy recovery, due to its high calorific value.[22] In addition, the increasing demand for bioethanol, particularly second-generation bioethanol derived from lignocellulosic biomass, has led to an even larger production of lignin waste.[23] While this combustion provides energy, it results in the release of carbon dioxide into the atmosphere, which is a concern from a sustainability perspective. Therefore, there is the growing need for more sustainable and economically viable ways to use lignin, transforming it into a valuable resource in a circular economy perspective.[24] The growing demand for cellulosic packaging products, driven by the need for more sustainable packaging materials, aligns with global efforts to reduce plastic waste and carbon footprints. As a result, the amount of lignin processed during chemical pulping is expected to increase, making the exploration of its potential applications a highly active area of research. As already mentioned, due to its properties, lignin has potential applications in a wide range of industries. Key areas of lignin utilization include vanillin production, as well as polymeric materials and composites.[25] The unique characteristics of polyphenolic compounds, including metal chelation, hydrogen bonding, pH sensitivity, redox potential, radical scavenging, polymerization, and light absorption, have established them as ideal structural motifs for creating functional materials.[5] Materials derived from phenolic compounds frequently preserve these valuable properties, often with synergistic effects, in applications spanning from catalysis to biomedicine. Lignin has been identified as a potential precursor to produce carbon fibers, which are used in lightweight, high-strength applications such as automotive parts, aerospace components, and sporting goods and it can also be used in biofuel production, thanks to its conversion

into bio-oils or other energy-dense materials.[18,26,27] Further applications include the production of biobased filler and functional additives in composites. In addition, due to the presence of phenolic hydroxyl and methoxy functional groups, lignin could remove heavy metal ions from contaminated wastewater through chemical adsorption, that is recognized as an effective and affordable approach. Water can be contaminated by various substances, including viruses, bacteria, organic particles, dyes, and heavy metal ions, such as Cu^{2+}, Cr^{6+}, Pb^{2+}, Co^{2+}, Cd^{2+}, Zn^{2+}, As^{3+}, Ni^{2+}, and Hg^{2+}. Unlike other toxins, heavy metals are non-biodegradable and can accumulate in living tissues, entering the food chain. This accumulation can lead to serious health issues, such as skin diseases, brain damage, anemia, liver and kidney failure, ulcers, and cancer.[28] Heavy metals can also contaminate soil and crops, affecting agricultural products and human health.[29] Their sources include industrial waste from battery, fertilizer, pesticide, petrochemical, pharmaceutical, metallurgical, mining, and paper industries.[30] This pollution threatens public health, reduces drinking water availability, and increases the risk of disease. Commonly used adsorbents, such as synthetic ion exchange and chelating resins, are known for their high mechanical and chemical resistance. However, their disposal after use is challenging and environmentally unfriendly. Recently, there has been growing interest in developing new, eco-friendly sorbents, with a focus on replacing expensive traditional materials with cheaper alternatives, often derived from waste or by-products. As reviewed by Miros-Kudra et al.,[31] lignin has emerged as a promising sorbent due to its low cost and biodegradability. Studies have shown that lignin can effectively bind various contaminants, including radionuclides and estrogens.[32] Furthermore, lignin-based adsorbents offer significant environmental advantages, such as stability, biocompatibility, and wide availability. The extensive structure of lignin provides a large number of functional groups on its surface, enabling efficient capture of harmful metal ions and their removal from polluted environments.[33, 34, 35, 36] Nasrullah et al.[37] found that bio-sorbent lignin efficiency in removing heavy metals from contaminated water could be achieved by chemical modification of the structure. Several research teams have proposed that chemical modifications of lignin can enhance its ability to eliminate heavy metals from aqueous solutions.[32,38] These modifications can be achieved through thermal or chemical processes, with chemical modifications typically involving the functionalization of hydroxyl groups, the introduction of new active chemical sites, and fragmentation. Indeed, its three-dimensional amorphous structure and the functional groups previously mentioned make it easily modifiable.[39,40] A more detailed discussion about its use as adsorbent and the role of functionalization is discussed in the introduction of Chapter 1, comparing the system used with other studies reported in the literature. Circular economy and potential applications of lignin are illustrated in the Figure I.4.

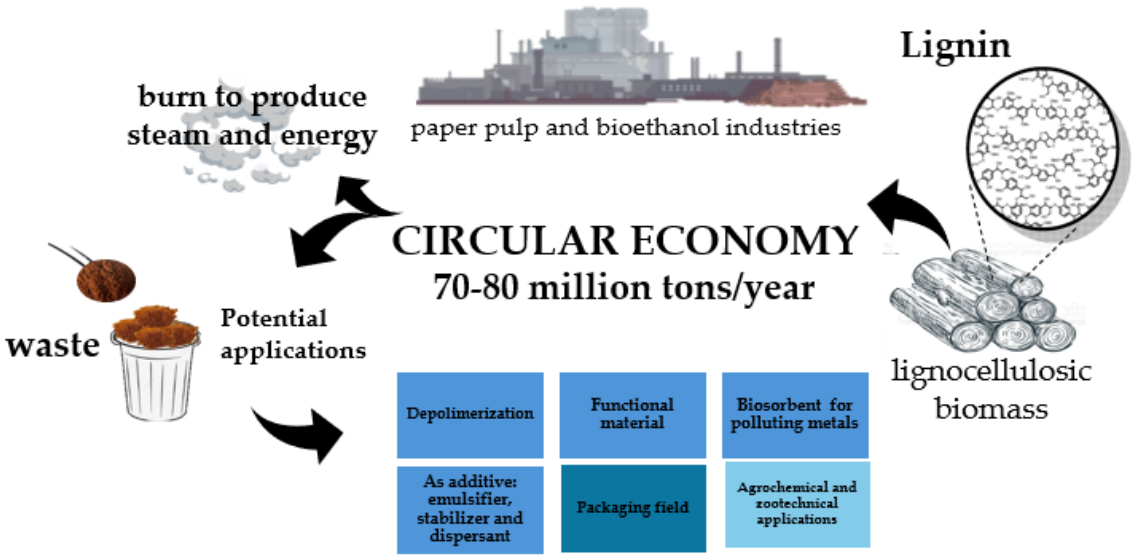

Figure I.4. A schematic representation of the methods valorising lignin in a circular economy perspective.

Beyond its mechanical properties, lignin also plays a crucial protective role for plants, acting as a defense mechanism against physical damage, chemical exposure, and attacks from pests or pathogens. Lignin and its derivatives show significant potential in healthcare, particularly as antimicrobial agents. Thanks to its natural antibacterial properties, in fact, lignin can be used in medical devices, wound dressings and other healthcare products. In the food industry, the phenolic hydroxyl groups of lignin provide antioxidant properties, making it valuable for preserving color, flavor, and vitamin content, as well as stabilizing the molecules responsible for these qualities. Additionally, Kraft lignin, derived from the pulp industry, has been found to protect corn oil from oxidation, with an efficacy comparable to that of vitamin E.[41] Lignin antioxidant properties make it an effective neutralizer or inhibitor of reactions triggered by oxygen radicals during oxidation processes. According to Li et al.,[42] lignin can neutralize harmful free radicals by reacting with them, thus preventing further oxidative damage and reducing cellular harm. However, unlike synthetic antioxidants or other polyphenolic compounds (such as flavonoids and tannins), connecting lignin antioxidant effectiveness to a specific chemical structure is challenging, due to its complex and variable composition.[43] In biological systems, the polyphenolic structure of lignin exerts its antioxidant effects by modulating reactive oxygen species (ROS).[44] This process helps in mitigating oxidative stress by converting highly reactive radicals into less harmful or inactive forms.[45]

Lignin bactericidal, insecticidal and antifungal properties derive from direct contact with bacteria.[46] This contact leads to the disruption of bacterial cell membranes and the accumulation of ROS on the bacterial surface, which effectively prevents microbial growth.[47] ROS refers to oxygen derivatives more reactive than oxygen itself, typically including O_2^-, ·OH, H_2O_2.[48] These species are produced during normal physiological processes and play crucial roles in cell signalling and maintaining tissue balance. The antibacterial action of lignin is linked to an increase in intracellular oxidative stress and the breakdown of bacterial membranes.[49] When lignin interacts with bacteria, its polyphenolic structure also penetrates the cell wall, causing mechanical damage to the membrane and leading cell death. These characteristics make lignin a key factor in plant resilience,

contributing to protecting plants from a range of external threats.[50] These features could be used for agrochemical applications, as reviewed by Ahmad et al.[51] A study by Singh et al.[52] has showed that lignin-based pesticides can reduce soil leaching, soil pollution, and groundwater contamination. With advantages like slow-release characteristics, abundant availability, and a harmless chemical nature, lignin-based pesticides hold practical significance and warrant further research and development. Sinisi et al.[53] have introduced a hybrid organic-inorganic material by incorporating copper (II) salts (cuprite or brochantite) into lignin, showing that these materials can impair the diffusion and intensity of plant diseases. A more in-depth analysis of its antimicrobial activity in combination with inorganic phases is provided in the introductions of Chapters 2, 3 and 4, where the systems employed are compared with other studies available in the literature. Recent studies on the biostimulant potential of lignin have demonstrated that this macromolecule and some of its derivatives can positively impact the growth and development of certain crops. Specifically, lignin has been shown to enhance seed germination, promote root elongation and stimulate early developmental stages.[54] These studies suggest that these benefits are linked to lignin ability to influence the hormone balance in treated species, with the effect being dose dependent. Lower doses have been found to be more effective, while higher doses tend to lose efficacy due to the potential formation of aggregates or have phytotoxic effects on the plants.[55] The slow degradation process of lignin and the gradual release of its nutrients make it an ideal raw material for new fertilizers. In addition, the complex three-dimensional polymer structure of lignin has a similar effect to plant hormones in promoting plant growth and development.[56] Savy et al.[57] have showed that water-soluble lignin, extracted from biomass sources like mango and giant reed, can promote the germination and early growth of maize seedlings. These aspects will be outlined in Chapter 2.

In conclusion, lignin is a sustainable biopolymer with significant potential for various applications within a circular economy perspective. Its biodegradability, antimicrobial properties, and ability to adsorb heavy metals make it a promising candidate for environmental remediation and agrochemical applications. A comparison with lignin-based materials previously studied in our and other laboratories has been presented in the introduction of each subsequent chapter, based on the specific application.

Characterization of Lignin

Lignin complex structure presents significant challenges for its characterization and due to its complexity, several techniques must be combined. This section outlines the key techniques commonly used for lignin characterization, based on methodologies from *Methods in Lignin Chemistry*.[58]

Lignin Analysis in Wood

For lignin analysis in wood, techniques like Raman spectroscopy and microscopy are commonly used. Raman spectroscopy, particularly in the region around 1600 cm^{-1}, identifies lignin aromatic rings and is effective for quantifying lignin in lignocellulosic materials.[59] Ultraviolet and interference microscopy can provide both qualitative and quantitative information about lignin distribution and orientation in the wood cell wall structure, offering insights into how lignin is integrated within the plant matrix.[60] Solid-state NMR spectroscopy has been extensively used for the structural characterization of the key components of wood, including carbohydrates and lignin.[61] Goring et al.[62] have studied the distribution of lignin in the cell walls of spruce and beech wood using high-voltage transmission electron microscopy (TEM) on sections stained with potassium permanganate, as well as field-emission scanning electron microscopy (FE-SEM) combined with a back-scattered electron detector on mercurized specimens. The latter technique, which involves the mercurization of lignin and the visualization of mercury via back-scattered electron microscopy (BSE), is a novel approach. This combination has allowed for a comprehensive visual overview of lignin distribution across the various layers of the cell wall. Each of these techniques contributes a unique perspective, collectively providing a comprehensive toolkit for understanding the complex structure and potential diverse applications of lignin.

Nuclear Magnetic Resonance (NMR)

NMR spectroscopy is essential for both qualitative and quantitative analyses of lignin structure: ^{1}H-NMR and ^{13}C{^{1}H} NMR spectroscopy can provide detailed information about the nature of all the carbon atoms in lignin, offering insight into its chemical structure. Solid-state NMR spectroscopy could be a helpful technique in analysing insoluble lignin. However, interpreting the NMR spectra of lignin presents challenges, due to the significant overlap of signals, which exist in similar but non-identical chemical environments. Some of these challenges can be addressed by using more advanced ^{13}C NMR pulse sequences, such as the attached proton test experiment and the DEPT sequence[63] (Distortionless Enhancement by Polarization Transfer). Also, HSQC (Heteronuclear Single Quantum Coherence) could be particularly useful, and quantitative ^{1}H-^{13}C HSQC measurements have recently greatly facilitated lignin analyses.[64] NMR techniques can also be fundamental in understanding the effectiveness of polymer functionalization strategies. Acetylation is typically employed in ^{1}H-NMR to prevent exchange phenomena: the hydroxyl groups in lignin are substituted with acetyl groups, greatly enhancing its solubility in organic solvents. Phosphitylation is used in ^{31}P-NMR to enhance sensitivity and it is particularly effective for the quantification of different hydroxyl groups in lignin, providing insight into the relative abundance of H, G, and S units.

Ultraviolet Spectrophotometry

Ultraviolet (UV) spectrophotometry is an essential technique for characterizing lignin, primarily due to its aromatic nature. Lignin typically exhibits absorption bands between 200 nm and 380 nm, with softwood lignin showing a peak at 280 nm, accompanied by a shoulder at 230 nm and a sharp peak between 200-210 nm. In contrast, hardwood lignin display shifts toward shorter wavelengths (268-277 nm). UV spectrophotometry is also effective for distinguishing between Kraft lignin and lignosulfonates, with the former typically showing a higher degree of conjugation, though both types have a maximum absorption at 280 nm.[65] This technique offers several advantages, including ease of sample preparation and the ability to perform both qualitative and quantitative analyses. Traditional lignin solvents include dimethyl sulfoxide (DMSO), dimethyl formamide (DMF), and 2-methoxyethanol. Other solvents used for lignin solubilisation include diethylene glycol monobutyl ether (butyl carbitol) and 1-methoxy-2-propanol.[66]

Infrared Spectroscopy

Infrared (IR) spectroscopy,[67] particularly in the mid-infrared range (4000-500 cm^{-1}), is crucial for identifying functional groups within lignin. The complex nature of lignin structure makes interpretation challenging, yet certain bands can be confidently assigned. For example, stretching vibrations corresponding to OH groups appear between 3412-3460 cm^{-1}, while C-H stretching of methylene and methyl groups is observed from 3000-2842 cm^{-1}. Carbonyl groups, including those in esters and non-conjugated ketones, show absorption between 1738-1709 cm^{-1}. IR spectroscopy is particularly useful for semi-quantitative analysis of the H, G, and S units present in lignin, with the aromatic skeleton vibrations around 1510 cm^{-1} providing critical information.

Pyrolysis-GC/MS

Pyrolysis coupled with Gas Chromatography/Mass Spectrometry (Pyrolysis-GC/MS) is an effective technique for identifying lignin types and analysing lignocellulosic materials.[68,69] This method involves heating lignin in the absence of oxidants to decompose it into smaller fragments, which are then analysed using gas chromatography and mass spectrometry. By normalizing peak areas and employing internal standards, Pyrolysis-GC/MS facilitates both qualitative and quantitative analyses based on phenylpropanoid unit ratios. Lignin pyrolysis products have been identified in various studies, proving that hydroxyphenyl, guaiacyl, and syringyl components of lignin can be distinguished by this technique. The similarity index (SI) is often used to compare pyrograms from different lignin samples. This index quantifies the degree of similarity between unknown and known lignin samples, helping to assess the reproducibility of the pyrolysis process and providing a useful tool for lignin identification.

Size exclusion Chromatography (SEC)

Size Exclusion Chromatography (SEC) is crucial for assessing the molecular weight distribution of lignin, which greatly influences its properties.[70] In SEC, lignin is separated based on its size using a porous stationary phase, with larger molecules eluting more quickly than smaller ones. This technique provides important data on the number-average molecular weight (M_n), weight-average molecular weight (M_w), and the polydispersity index

(M_w/M_n), which are vital for understanding lignin structure and behaviour. The number average molecular weight M_n is the statistical average molecular weight of all the polymer chains in the sample and is defined as:

$$M_n = \frac{\sum N_i M_i}{\sum N_i}$$

where M_i is the molecular weight of a chain and N_i is the number of chains with that molecular weight. M_n estimates the effect on the molecular weight of the polymer resulting from the number of chains having that molecular weight.

The weight average molecular weight M_w is defined as:

$$M_w = \frac{\sum N_i M_i^2}{\sum N_i M_i}$$

Unlike M_n, M_w considers the molecular weight of a chain when determining its contribution to the molecular weight average. The heavier the chain, the greater its contribution to M_w. M_w is determined using methods that are sensitive to the molecular size rather than just their number.

The polydispersity index is used to measure the breadth of a polymer's molecular weight distribution and is defined as:

$$Polydispersity\ index = \frac{M_w}{M_n}$$

The larger the polydispersity index, the broader the molecular weight distribution. A monodisperse polymer, where all the chain lengths are equal (such as a protein), has an M_w/M_n ratio of 1. The most well-controlled synthetic polymers (narrow polymers used for calibrations) typically have an M_w/M_n ratio between 1.02 and 1.10. Step polymerization reactions usually yield M_w/M_n values around 2.0, while chain polymerization reactions result in M_w/M_n values ranging from 1.5 to 20.

Thermal Analyses

Thermal analysis techniques, including Thermogravimetric Analysis (TGA), Differential Scanning Calorimetry (DSC), and Differential Thermal Analysis (DTA), offer critical insights into lignin thermal properties. TGA measures weight loss as a function of temperature, revealing residual water content and degradation temperatures. DSC and DTA provide information on phase transitions and heat capacity.[71]

Lignin materials used in the PhD project

The lignin materials used in this study, provided by UPM-Kymmene Oyj (Finland) and Green Innovation GmbH (Austria), are named HMW and EH. HMW is a Kraft softwood lignin derived from *Pinus taeda* (southern yellow pine). This lignin is studied in this work as potential biosorbent in water bioremediation processes and for the synthesis of hybrid organic-inorganic materials with agronomical applications. EH is an enzymatically processed lignin from *Fagus sylvatica* and it contains a higher proportion of syringyl moieties with respect to HMW due to its hardwood origin. Detailed characteristics of HMW used in this study are collected in Table I.3 and a comparison of HMW and EH features is collected in Table I.4. The rather constant composition of the two kinds of lignin is assured by the use of a unique type of plant and by the standardized production process applied. HMW and EH have been used without any further purification and without additional characterization beyond that provided by the supplier, except for the morphological analysis, surface area determination and thermal behaviour in the case of Cr (VI) removal studies (Chapter 1). Thermal and SEC characterizations have been carried out on the biopolymeric component of the hybrid materials, to verify that the synthetic conditions required for the formation of the metal oxides do not affect the lignin structure (Chapter 2, 3 and 4).

Table I.3. Characteristics of HMW used in the PhD project.

Characteristics	
pH (10 % slurry)	2.5-4.5
Particle size, μm	< 25
Dry matter content	95%
Ash, %	< 2
Sulphur, %	< 3
Carbohydrates, %	< 5
Cellulose, %	0
Purity, %	> 95
M_w, g/mol	4400 – 5000
	5950 – 6000
M_n, g/mol	1200 – 1300
	1560 – 1565
Functional groups (mmol/g)	
Aliphatic OH	1.8
Carboxylic acid	0.5
p-OH-phenyl	0.3
Guaiacyl	1.9
Syringyl	1.7
Phenolic OH	3.9
Total OH	6.1
Property	
Antioxidant capacity, DPPH method TEAC	18.2
Lethal Dose 50%, LD_{50} mg/Kg	>2000

Table I.4. Comparison of HWM and EH used in the PhD project.

Production	HMW Kraft lignin	EH Biorefinery lignin
Wood feedstock	Pine	Beech
Odour	Strong	Very mild
Lignin content	~ 95% dry	~ 82% dry
Ash content	<2 %	<0.3 %
Sulphur	<2.5 %	<0.1 %
Residual sugars/Fibers	<2.5 %	~ 8-12% dry
pH	2.5-4	6-8
M_w, g/mol	~ 4500-5000	~ 7000 (NaOH soluble)
Phenolic OH	4.3 mmol/g	4.5 mmol/g
Aliphatic OH	1.8 mmol/g	5.9 mmol/g

HMW has been subjected to acetylation and phosphorylation, obtaining functionalized lignin (named respectively Ac_Lig and P_Lig). HMW, EH, Ac_Lig and P_Lig have been evaluated and compared as potential biosorbents for Cr(VI) in Chapter 1; for the synthesis of the hybrid materials HMW has been selected. Furthermore, HMW has been employed for the synthesis of hybrid materials in Chapters 2, 3 and 4.

A commercial liquid formulation of HMW, named UPM Solargo™, has been also employed in this work. UPM Solargo™, kindly provided by UPM-Kymmene Oij and Green Innovation GmbH, is a formulation containing lignin (HMW, 100 g), water (325 g), potassium hydroxide 50% (75 g) and propylene glycol (500 g) for 1 L of Solargo™. UPM Solargo™ has been employed for the synthesis of hybrid materials in Chapters 2 and 4.

References

[1] Zakzeski J, Bruijnincx PC, Jongerius AL, Weckhuysen BM. The Catalytic Valorization of Lignin for the Production of Renewable Chemicals, *Chem Rev.,* **110**(6), 3552-99, 2010. DOI: 10.1021/cr900354u.

[2] S. Z. A. Hakimi Saadon, N. B. Osman, S. Yusup, Pretreatment of Fiber-based Biomass Material for Lignin Extraction. *Value-Chain of Biofuels: Fundamentals, Technology, and Standardization*, ***5,*** 105-135. 2022. DOI:10.1016/B978-0-12-824388-6.00024-5.

[3] K. V. Sarkanen, C. H. Ludwig, Lignins: Occurrence, Formation, Structure, and Reactions. Wiley-Interscience. *Journal of Polymer Science Part B: Polymer Letters,* ***10***(3), 228-230, 1971. doi: 10.1002/pol.1972.110100315.

[4] M. Lewin, I. S. Goldstein, Wood Structure and Composition, *International Fiber Science and Technology*, CRC Press, 183-261, 1991.

[5] R. Rinaldi, R. Jastrzebski, M. T. Clough, J. Ralph, M. Kennema, P. C. A. Bruijnincx, B. M. Weckhuysen, Paving the Way for Lignin Valorisation: Recent Advances in Bioengineering, Biorefining and Catalysis. *Angewandte Chemie International Edition,* ***55***(47), 14422-14443, 2016. DOI: 10.1002/anie.201510351.

[6] J. Ralph, K. Lundquist, G. Brunow, F. Lu, H. Kim, P. F. Schatz, J. M. Marita, R. D. Hatfield, S. A. Ralph, J. H. Christensen, W. Boerjan, Lignins: Natural Polymers from Oxidative Coupling of 4-hydroxyphenylpropanoids. *Phytochemistry Reviews,* **3**(1-2), 29-60, 2004. DOI: 10.1023/B:PHYT.0000047471.58297.45.

[7] R. Alén, Chapter 1: Structure and Chemical Composition of Wood. in Forest Products Chemistry Fapet Oy, 2000.

[8] W. Boerjan, J. Ralph, M. Baucher, Lignin Biosynthesis. *Annual Review of Plant Biology,* **54**, 519-546, 2003. DOI:10.1146/annurev.arplant.54.031902.134938.

[9] H. S. Abreu, A. M. Nascimento, M. A. Maria, Lignin Structure and Wood Properties. *Wood and Fiber Science,* **31**(4), 426-433, 1999.

[10] Z. Hao, D. Mohnen, A Review of Xylan and Lignin Biosynthesis: Foundation for Studying Arabidopsis Irregular Xylem Mutants with Pleiotropic Phenotypes. *Crit Rev Biochem Mol Biol.*, **49**(3):212-41, 2014. DOI: 10.3109/10409238.2014.889651.

[11] P.Bajpai, Pulp and Paper Industry, *Nanotechnology in Forest Industry* book, 2017

[12] H. Sixta, Handbook of Pulp, 2006, DOI:10.1002/9783527619887.fmatter

[13] D. R. Lobato-Peralta, E. Duque-Brito, H. I. Villafán-Vidales, A. Longoria, P. J. Sebastian, A. K. Cuentas-Gallegos, C. A. Arancibia-Bulnes, P. U. Okoye, A Review on Trends in Lignin Extraction and Valorization of Lignocellulosic Biomass for Energy Applications. *Journal of Cleaner Production,* **293**, 126123, 2021.DOI: 10.1016/j.jclepro.2021.126123

[14] D. D. S. Argyropoulos, C., Crestini, C. Dahlstrand, E. Furusjö, C. Gioia, K. Jedvert, G. Henriksson, C. Hulteberg, M. Lawoko, C. Pierrou, J. S. M. Samec, E. Subbotina, H. Wallmo, M. Wimby, Kraft Lignin: A Valuable, Sustainable Resource, Opportunities and Challenges. *ChemSusChem*, **16**(23), 2023. DOI: 10.1002/cssc.202300492.

[15] T. Aro, P. Fatehi, Production and Application of Lignosulfonates and Sulfonated Lignin. *ChemSusChem,* **10**(9), 1831-1841, 2017. DOI: 10.1002/cssc.201700082.

[16] A. Vishtal, A. Kraslawski, Challenges in Industrial Applications of Technical Lignins, *BioResources*, **6**, 3547-3568, 2011, 10.15376/biores.6.3.3547-3568

[17] G. Tofani, E. Jasiukaitytė-Grojzdek, M. Grilc, B. Likozar, Organosolv Biorefinery: Resource-based Process Optimisation, Pilot Technology Scale-up and Economics. *Green Chemistry*, **25**(24), 7220-7238, 2023. DOI: 10.1039/D3GC02834J.

[18] I. Ziegler-Devin, L. Chrusciel, N. Brosse, Steam Explosion Pretreatment of Lignocellulosic Biomass: A Mini-Review of Theoretical and Experimental Approaches. *Frontiers in Chemistry,* **9**, 705358, 2021 DOI: 10.3389/fchem.2021.705358.

[19] Y. Sheng, S. S. Lam, Y. Wu, S. Ge, J. Wu, L. Cai, Z. Huang, Q.V. Le, C. Sonne, C. Xia, Enzymatic Conversion of Pretreated Lignocellulosic Biomass: A Review on Influence of Structural Changes of Lignin, *Bioresour Technol.,* 324:124631, 2021. DOI: 10.1016/j.biortech.2020.124631.

[20] Ecologic Institute, Top Emerging Bio-based Products, their Properties and Industrial Applications, Berlin 2018.

[21] Production of chemical wood pulp worldwide from 1961 to 2021, Statista. 2023, from https://www.statista.com/statistics/1178289/production-of-chemical-pulpworldwide/

[22] D. Kai, M. J. Tan, P. L. Chee, Y. K. Chua, Y. L. Yap, X. J. Loh, Towards Lignin-based Functional Materials in a Sustainable World. *Green Chemistry,* **18**(5), 1175-1200, 2016. DOI: 10.1039/C5GC02616D.

[23] M. Gavahian, P. E. S. Munekata, Ismail Eş, J. M. Lorenzo, A. M. Khaneghah, and F. J. Barba, Emerging Techniques in Bioethanol Production: from Distillation to Waste Valorization, *Green Chem.,* 2019, **21**, 1171-1185, DOI:10.1039/C8GC02698J

[24] B. L. Tardy, E. Lizundia, C. Guizani, M. Hakkarainen, M. H. Sipponen, Prospects for the Integration of Lignin Materials into the Circular Economy. *Materials Today, **61,*** 142-160, 2023. DOI: 10.1016/j.mattod.2023.04.001.

[25] F. García Calvo-Flores, J. A. Dobado, Lignin as Renewable Raw Material. *ChemSusChem,* **3**(12), 1301-1315, 2010, DOI:10.1002/cssc.201000157.

[26] M. Fache, B. Boutevin, S. Caillol, Vanillin Production from Lignin and its Use as a Renewable Chemical. *ACS Sustainable Chemistry & Engineering,* ***4***(1), 35–46, 2016, DOI:10.1021/acssuschemeng.5b01344.

[27] W. G. Glasser, About Making Lignin Great Again—some Lessons from the Past. *Frontiers in Chemistry,* **7**, 565, 2019, DOI: 10.3389/fchem.2019.00565.

[28] C. Ezeabara, O. Okanume, A. Emeka, C. Okeke, E. Mbaekwe, Heavy Metal Contamination of Herbal Drugs: Implication for human health—a review. *International Journal of Tropical Disease & Health,* ***4***(10), 1044–1058, 2014. DOI: 10.9734/IJTDH/2014/11481.

[29] R. Baby, B. Saifullah, M. Z. Hussein, Palm Kernel Shell as an Effective Adsorbent for the Treatment of Heavy Metal Contaminated Water. *Scientific Reports,* ***9***(1), 2019. DOI: 10.1038/s41598-019-55099-6.

[30] P. B. Tchounwou, C. G. Yedjou, A. K. Patlolla, D. J. Sutton, Heavy Metal Toxicity and the Environment. *Experimental Suppl.*, **101**, 133–164, 2012, DOI: 10.1007/978-3-7643-8340-4_6.

[31] P. Miros-Kudra, P. Sobczak, E. Kopania, Removal of Heavy Metals from Aqueous Solutions with the Use of Lignins and Biomass. *Fibres & Textiles in Eastern Europe,* **30**(2), 99–111, 2022. DOI: 10.2478/ftee-2022-0013.

[32] S. K. Singh, Solubility of Lignin and Chitin in Ionic Liquids and their Biomedical Applications. *International Journal of Biological Macromolecules,* **132**, 265–277, 2019. DOI: 10.1016/j.ijbiomac.2019.03.182.

[33] L. Bulgariu, D. Bulgariu, T. Malutan, M. Macoveanu, Adsorption of Lead(II) Ions from Aqueous Solution onto Lignin. *Adsorption Science & Technology,* ***27***(4), 435–445, 2009. DOI: 10.1260/026361709790252623.

[34] F. Pagnanelli, S. Mainelli, F. Vegliò, L. Toro, L., Heavy Metal Removal by Olive Pomace: Biosorbent Characterisation and Equilibrium Modelling. *Chemical Engineering,* **58**(20), 4709–4717, 2003. DOI: 10.1016/j.ces.2003.08.001.

[35] B. Strzemiecka, L. Klapiszewski, A. Jamrozik, T. Szalaty, D. Matykiewicz, T. Sterzyński, A. Voelkel, T. Jesionowski, Physicochemical Characterization of Functional Lignin–Silica Hybrid Fillers for Potential Application in Abrasive Tools. *Materials,* **9**(7), 517, 2016. DOI: 10.3390/ma9070517.

[36] Y. Ge, Z. Li, Application of Lignin and its Derivatives in Adsorption of Heavy Metal Ions in Water: A Review. *ACS Sustainable Chemistry & Engineering,* **6**(5), 7181–7192, 2018. DOI: 10.1021/acssuschemeng.8b01345.

[37] A. Nasrullah, A. H. Bhat, M. H. Isa, Lignin: a Sustainable Biosorbent for Heavy Metal Adsorption from Wastewater, a Review. *AIP Conference Proceedings,* **1787**, 040001, 2016. DOI: 10.1063/1.4968080.

[38] F. Kong, K. Parhiala, S. Wang, P. Fatehi, Preparation of Cationic Softwood Kraft Lignin and its Application in Dye Removal, *European Polymer Journal,* ***67,*** 335-345, 2015. DOI: 10.1016/j.eurpolymj.2015.04.004

[39] B. Prieur, M. Meub, M. Wittemann, R. Klein, S. Bellayer, G. Fontainea e S. Bourbigot, Phosphorylation of Lignin: Characterization and Investigation of the Thermal Decomposition, *RSC Adv.*, **7**, 16866, 2017, DOI: 10.1039/c7ra00295e

[40] P. Buono, A. Duval, P. Verge, L. Averous e Y. Habibi, New Insights on the Chemical Modification of Lignin: Acetylation versus Silylation, *ACS Sustainable Chem. Eng.*, **4**, 5212, 2016. DOI: 10.1021/acssuschemeng.6b00903.

[41] G. L. Catignani, M. E. Carter, Antioxidant Properties of Lignin. *Journal of Food Science,* **47**(5), 1745, 2006. DOI: 10.1111/j.1365-2621.1982.tb05029.x.

[42] K. Li, W. Zhong, P. Li, J. Ren, K. Jiang, W. Wu, Recent Advances in Lignin Antioxidant: Antioxidant Mechanism, Evaluation Methods, Influence Factors, and Various Applications. *International Journal of Biological Macromolecules,* ***240***, 125992, 2023. DOI:10.1016/j.ijbiomac.2023.125992.

[43] H.A. Ariyanta, F. P. Sari, A. Sohail, W. K. Restu, M. Septiyanti, N. Aryana, W. Fatriasari, A. Kumar, Current Roles of Lignin for the Agroindustry: Applications, Challenges, and Opportunities., *Int J Biol Macromol.,* **240**, 124523, 2023. DOI: 10.1016/j.ijbiomac.2023.124523.

[44] L. M. Guedes, S. Torres, K. Sáez-Carillo, J. Becerra, C. I. Pérez, N. Aguilera, High Antioxidant Activity of Phenolic Compounds Dampens Oxidative Stress in *Espinosa Nothofagi* Galls Induced on *Nothofagus Obliqua* Buds., *Plant Sci.*, **314**, 111114, 2022. DOI: 10.1016/j.plantsci.2021.111114.

[45] B. Kim, Y. Kim, Y. Lee, J. Oh, Y. Jung, W. G. Koh, J. J. Chung, Reactive Oxygen Species Suppressive Kraft Lignin-Gelatin Antioxidant Hydrogels for Chronic Wound Repair, *Macromol Biosci.*, **22**(11):e2200234, 2022. DOI: 10.1002/mabi.202200234.

[46] K. Li, W. Zhong, P. Li, J. Ren, K. Jiang, K., W. Wu, Antibacterial Mechanism of Lignin and Lignin-based Antimicrobial Materials in Different Fields. *International Journal of Biological Macromolecules, **243***, 126281, 2023. DOI: 10.1016/j.ijbiomac.2023.126281.

[47] C. H. Tay, B. T. Pugh, S. R. Clough, Dermal Irritation Assessment of Three Benzene Sulfonate Compounds. *International Journal of Toxicology, **23***(1), 11–16, 2004. DOI: 10.1080/10915810490252899.

[48] B. Jiang, Y. Zhang, H. Zhao, H., et al., Structure-Antioxidant Activity Relationship of Active Oxygen Catalytic Lignin and Lignin-carbohydrate Complex. *International Journal of Biological Macromolecules, **139***, 21–29, 2019. DOI: 10.1016/j.ijbiomac.2019.07.080.

[49] L. Wang, C. Hu, L. Shao, L., The Antimicrobial Activity of Nanoparticles: Present Situation and Prospects for the Future. *International Journal of Nanomedicine, **12,*** 1227–1249, 2017. DOI: 10.2147/IJN.S121036.

[50] C. P. Vance, T. K. Kirk, R. T. Sherwood, Lignification as a Mechanism of Disease Resistance. *Annual Review of Phytopathology*, **18,** 259-288, 1980. DOI:10.1146/annurev.py.18.090180.001355

[51] M. Ahmad, N. Ji, H. Li, Q. Wu, C. Song, Q. Liu, D. Ma, X. Lu, Can Lignin be Transformed into Agrochemicals? Recent Advances in the Agricultural Applications of Lignin. *Industrial Crops and Products, **170***, 113646, 2021. DOI: 10.1016/j.indcrop.2021.113646.

[52] A. Singh, N. Dhiman, A. K. Kar, D. Singh, M. P. Purohit, D. Ghosh, S. Patnaik, Advances in Controlled Release Pesticide Formulations: Prospects to Safer Integrated Pest Management and Sustainable Agriculture, *J Hazard Mater.,* 2020. DOI: 10.1016/j.jhazmat.2019.121525.

[53] V. Sinisi, P. Pelagatti, M. Carcelli, A. Migliori, L. Mantovani, L. Righi, G. Leonardi, S. Pietarinen, C. Hubsch and D. Rogolino, A Green Approach to Copper-Containing Pesticides: Antimicrobial and Antifungal Activity of Brochantite Supported on Lignin for the Development of Biobased Plant Protection Products, *ACS Sustainable Chem. Eng.,* **7**, 3213, 2019. DOI: 10.1021/acssuschemeng.8b05135.

[54] R. Spaccini, V. Cozzolino, V. Di Meo, D. Savy, M. Drosos, A. Piccolo, Bioactivity of Humic Substances and Water Extracts from Compost Made by Ligno-cellulose Wastes from Biorefinery. *Science of the Total Environment, **646***, 792-800, 2019. DOI: 10.1016/j.scitotenv.2018.07.334.

[55] D. Savy, V. Cozzolino, Novel Fertilising Products from Lignin and its Derivatives to Enhance Plant Development and Increase the Sustainability of Crop Production. *Journal of Cleaner Production,* **366**, 132832, 2022. DOI: 10.1016/j.jclepro.2022.132832.

[56] T. Ma, H. Zhan, D. Wang, Research Progress on the Application of Black-papermaking-liquor Lignin in Agriculture. *Guangdong Paper Industry,* ***128***, 130-139, 1997.

[57] D. Savy, V. Cozzolino, A. Nebbioso, M. Drosos, A. Nuzzo, P. Mazzei, A. Piccolo, Humic-like Bioactivity on Emergence and Early Growth of Maize (*Zea mays, L.)* of Water-soluble Lignins Isolated from Biomass for Energy. *Plant and Soil,* **402**, 221-233, 2016. DOI: 10.1007/s11104-015-2780-2.

[58] S. Y. Lin, C. W. Dence, Methods in Lignin Chemistry. Springer-Verlag, 1992.

[59] V. A. Gerasimov, A. M. Gurovich, D. K. Kostrin, L. M. Selivanov, V. A. Simon, A. B. Stuchenkov, A. V. Paltcev and A. A. Uhov, Raman Spectroscopy for Identification of Wood Species. *Journal of Physics: Conference Series,* **741**, 012131, 2016. DOI: 10.1088/1742-6596/741/1/012131.

[60] J. A. N Scott., A. Procter, D. A. I. Goring, The Application of Ultraviolet Microscopy to the Distribution of Lignin in Wood: Description and Validity of the Technique. *Wood Science and Technology,* **3**(1), 13-21, 1969. DOI: 10.1007/BF00355477.

[61] A. M. Gil, C. Pascoal Neto, Solid-State NMR Studies of Wood and Other Lignocellulosic Materials. *Wood Science and Technology,* **31**(6), 423-445, 1997. DOI: 10.1007/BF00769849.

[62] D. A. I. Goring, A. J. N. Scott, Lignin Distribution in Wood Cell Walls Determined by TEM and Backscattered SEM Techniques. *Journal of Structural Biology,* **143**(1), 77-84, 2003. DOI: 10.1016/S1047-8477(03)00119-9.

[63] Chen, Chen-Loung, D. Robert. Characterization of Lignin by ^{1}H and ^{13}C NMR Spectroscopy, *Methods in Enzymology*, **161**, 137-174, 1998. DOI: 10.1016/0076-6879(88)61017-2.474

[64] M. Sette, H. Lange, C. Crestini, Quantitative HSQC Analyses of Lignin: A Practical Comparison. *Comput Struct Biotechnol J.*, 2013. DOI: 10.5936/csbj.201303016.

[65] N. Smyk, J. Sjöström, G. Henriksson, O. Sevastyanova, UV–Vis Spectroscopy as a Rapid Method for Evaluation of Total Phenolic Hydroxyl Structures in Lignin. *Nordic Pulp & Paper Research Journal*, ***38***(3), 95, 2023. DOI: 10.1515/npprj-2023-0095.

[66] A. Dastpak, T. V. Lourencon, M. Balakshin, S. F. Hashmi, M. Lundstrom, B. P. Wilson, Solubility Study of Lignin in Industrial Organic Solvents and Investigation of Electrochemical Properties of Spray-coated Solutions. *Industrial Crops and Products*, **148**, 112310, 2020. DOI: 10.1016/j.indcrop.2020.112310.4

[67] C.G. Boeriu, D. Bravo, R.J.A. Gosselink, J.E.G. van Dam, Characterisation of Structure-Dependent Functional Properties of Lignin with Infrared Spectroscopy. Industrial Crops and Products, **20**(2), 205-218, 2004. DOI:10.1016/j.indcrop.2004.04.022

[68] J. J. Lucejko, D. Tamburini, F. Modugno, E. Ribechini, M. P. Colombini, Analytical Pyrolysis and Mass Spectrometry to Characterise Lignin in Archaeological Wood. *Applied Sciences*, **11**(1), 240, 2021. DOI: 10.3390/app11010240.

[69] T. J. Fullerton, R. A. Franich, Lignin Analysis by Pyrolysis-GC-MS: Characterisation of Ethanol Lignin Pyrolysates and Identification of Syringyl Units in *Pinus radiata* Milled Wood Lignin. *Holzforschung*, **37**(5), 267-269, 1983.

[70] A. A. Andrianova, N. A. Yeudakimenka, S. L. Lilak, E. I. Kozliak, A. Ugrinov, M. P. Sibi, A. Kubátová, Size Exclusion Chromatography of Lignin: The Mechanistic Aspects and Elimination of Undesired Secondary Interactions, *J Chromatogr A.,* **1534**, 101-110, 2018. DOI: 10.1016/j.chroma.2017.12.051.

[71] M. El Moustaqim, A. El Kaihal, M. El Marouani, S. Men-La-Yakhaf, M. Taibi, S. Sebbahi, S. El Hajjaji, F. Kifani-Sahban, Thermal and Thermomechanical Analyses of Lignin. *Bioresource Technology*, **314,** 122882, 2020. DOI:10.1016/j.biortech.2020.122882.

Chapter 1: Lignin and lignin-based materials in Cr(VI) water remediation

The contamination of water sources by a broad spectrum of pollutants such as heavy metals, pesticides, dyes, pharmaceuticals, microplastics and it has become an increasingly alarming environmental issue. In particular, the presence of heavy metals in aquatic environments poses significant threats to living organisms and contribute to environmental pollution. Inorganic discharges introduce toxic metals like Cr, Cd, Hg, Ni, Pb, and Zn into wastewater.[1,2] These contaminants are notorious for their long-lasting and often irreversible effects on aquatic ecosystems, biodiversity, and human health.[3] Particularly, heavy metals are highly toxic, non-biodegradable, and can accumulate along the food chain, even in trace amounts. As a result, industries like electroplating, aerospace, and metal finishing are considered some of the most dangerous in terms of wastewater contamination. The presence of such pollutants in water represents a threat to the environment and public well-being, making it a critical area of research and concern. As the global demand for fresh, clean water grows, the need to develop effective methods for water purification and contamination removal has never been more urgent. Numerous scientific studies have therefore been dedicated to the identification and development of sustainable, efficient, and cost-effective techniques for managing and treating contaminated water.[4,5,6] Among the various pollutants, chromium compounds have emerged as particularly concerning, due to their widespread use in industrial processes. These compounds are commonly found in industries such as leather tanning, metallurgy, textile dyeing, painting, and electroplating.[7,8] Chromium is the seventh most abundant element on earth and it exists in two primary oxidation states in nature: Cr(III) and Cr(VI).[9] Cr(III) is an essential trace element in many biological systems, playing a role in processes like glucose metabolism and nucleic acid synthesis.[10] The presence of Cr(VI) in the environment is mainly due to human activities. Cr(VI) is particularly hazardous, being 100 times more toxic than Cr(III), due to its high solubility in water, greater mobility, and ease of reduction.[11] Cr(VI) is highly soluble in water across a broad range of pH levels, which, combined with its high mobility in aquatic systems, makes it a significant environmental and public health risk. Cr(VI) is highly toxic, carcinogenic, mutagenic[12] and its toxicity stems from its strong oxidizing properties, which enable Cr(VI) causing extensive cellular damage, gene mutations, and even cancer. Studies on the carcinogenicity of Cr(VI) have highlighted that chromate ions (CrO_4^{2-}) rapidly cross cellular and nuclear membranes, often through anion transport pathways (such as those used for sulphate). Once inside the cytoplasm, chromate ions can either pass through the nuclear membrane and be reduced to Cr(III), or undergo reduction within the cytoplasm. Unlike Cr(III), Cr(VI) reacts strongly with DNA, and it is believed that the reduction of Cr(VI) to Cr(III), whether in the cytoplasm, nucleus, or bloodstream, generates free radicals that can bind to DNA.[13] In contrast, Cr(III) easily hydrolyses at physiological pH to form insoluble hydroxide. Moreover, due to its d^3 electronic configuration, Cr(III) is kinetically stable, and ligand exchange reactions occur very slowly. In soil, Cr(VI) is only weakly adsorbed, making it easily accessible for plant absorption and prone to leaching into groundwater. Thus, the maximum contaminant level (MCL) for Cr(VI) in drinking water is set at 0.05 mg/L, while the discharge of total chromium, including Cr(III), Cr(VI), and other chromium species, is regulated to be less than 2 mg/L.[14] The solubility and chemical forms of Cr(VI) are highly dependent on the pH of the environment. In conditions of 6–8 pH, Cr(VI) is predominantly present as yellow chromate ions (CrO_4^{2-}). When the pH is lower (between

1 and 6), Cr(VI) exists in equilibrium between the dichromate ion ($Cr_2O_7^{2-}$) and the hydrogen chromate ion ($HCrO_4^-$). In very acidic environments (pH below 1), other chromium species, such as di-, tri-, and tetra-chromates, can form. This complexity in chromium chemistry makes the removal of Cr(VI) from contaminated water quite challenging. However, the effective removal of Cr(VI) is crucial to protecting both human health and the environment. Several techniques have been proposed and employed for the removal of chromium from contaminated water. These include chemical treatments such as coagulation, flocculation, precipitation, and oxidation/reduction reactions, as well as biological methods involving microorganisms. Additionally, advanced filtration technologies, such as ultrafiltration and nanofiltration, have been investigated, along with adsorption techniques using materials like ion exchange resins, activated carbon, or biosorbents.[15, 16, 17] In many cases, these methods are used in combination to enhance the overall effectiveness of chromium removal.[18] However, despite their usefulness, these conventional techniques often fail to achieve complete remediation, particularly referring to reduction of Cr(VI) to its less toxic form, Cr(III). Among the available methods, adsorption is one of the most widely used due to its simplicity, efficiency, and versatility. However, the high costs of commercial adsorbents have led researchers to search for more affordable alternatives.[19] Over the past few years, there has been an increasing focus on using adsorption materials that offer a large specific surface area, easy recyclability, and high reusability. Various types of adsorbents have been created for treatment purposes, including activated carbon, activated alumina, coated silica gel, and modified sawdust.[20,21,22,23] In recent years, a growing interest has emerged in the use of biosorbents, materials derived from natural sources such as agricultural waste and biomass.[24, 25, 26] These biosorbents offer several advantages, including low cost, sustainability, and minimal environmental impact. They provide an attractive and effective solution for the removal of various pollutants, including chromium, from water. Lignocellulosic materials, which consist mainly of cellulose, hemicellulose, and lignin, have been identified as promising biosorbents for heavy metal removal.[27] Among these, lignin has gained significant attention due to its abundance, low cost, and high adsorption capacity. Lignin is the second most abundant natural polymer after cellulose and is produced in large quantities as a byproduct in industries like paper manufacturing and bioethanol production, as outlined in the Introductive Section. Despite its abundance, lignin is often underutilized, being discarded or burned. This presents a unique opportunity to repurpose lignin as a valuable resource for water remediation, promoting a circular economy approach that emphasizes sustainability and waste reduction. Lignin is a complex, branched polymer composed of phenylpropanoid units such as coniferyl, p-coumaryl, and synapyl monomers. These structural components, along with the presence of functional groups like phenolic hydroxyl, aliphatic hydroxyl, and carboxyl groups, give lignin the ability to effectively adsorb chromium and other heavy metals.[28, 29, 30, 31] Additionally, lignin can act as a reducing agent, allowing to reduce toxic Cr(VI) to the less harmful Cr(III). This dual function of lignin—both as an adsorbent and a reducing agent—makes it an ideal material for water treatment applications, particularly in the context of chromium remediation.[32,33] Various mechanisms have been proposed to explain the chromium removal process when using lignin and other biomass-based adsorbents. One mechanism is anionic adsorption,[34, 35] in which negatively charged chromium species are attracted to the positively charged

functional groups on the surface of the biosorbent, particularly under acidic conditions. Another mechanism, known as adsorption-coupled reduction,[36] involves the reduction of Cr(VI) to Cr(III) through interaction with the electron-donating groups of lignin, such as phenolic and carbonyl groups. This reduction process is most effective at low pH values, resulting in the formation of Cr(III) species that are less toxic than their Cr(VI) counterparts. These reduced chromium species can either remain bound to the biosorbent or be released into the surrounding solution. The adsorption-coupled reduction mechanism takes into account the reduction of Cr(VI), which is promoted under acidic pH conditions, as shown in equation (1):

$$Cr_2O_7^{2-} + 14\,H^+ + 6e^- = 2Cr^{3+} + 7H_2O, E_0 = 1.33\,V \qquad (1)$$

The Cr(VI) remediation process is schematized in Figure 1.1.

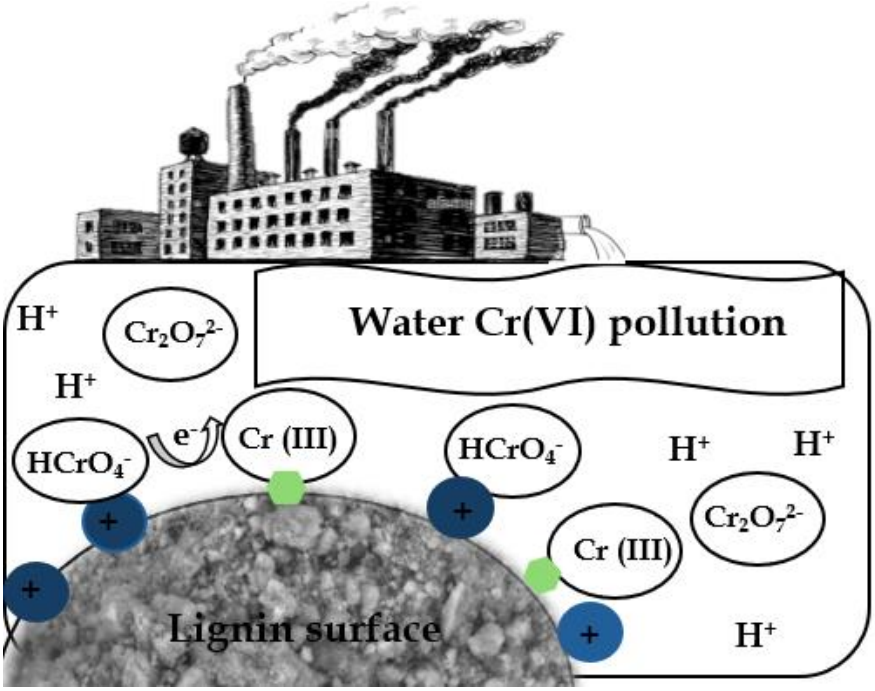

Figure 1.1. Schematic represantion of Cr(VI) bioremediation performed by lignin.

Numerous studies have investigated the potential of different lignocellulosic materials for chromium removal. The efficiency of chromium adsorption and reduction can vary depending on the source of lignin and the specific industrial processes used to extract it. For instance, Wu et al. have studied the use of lignin derived from black liquor, a byproduct of the paper industry: this material has maximum Cr(III) adsorption capacity of about 18 mg/g.[37] Other types of lignin, such as alkali lignin and enzymatic hydrolysis lignin, studied by Jin et al., have demonstrated higher capacities for Cr(VI) adsorption, with values reaching up to 270 mg/g and 135 mg/g, respectively.[38] Some types of lignin, particularly

those obtained from pulping black liquor or enzymolysis processes, have shown even higher adsorption capacities, up to 800-860 mg/g, as reported by Zhang et al.[39]

To further enhance the performance of lignin-based adsorbents, researchers have explored various functionalization techniques. The appropriate functionalization of the lignin structure, or the development of hybrid materials by combining lignin with crystalline inorganic phases, could result in materials with improved adsorption properties.[40, 41] By modifying the lignin structure through processes such as acetylation and phosphorylation, it is possible to introduce additional functional groups that improve the material ability to coordinate metal ions. As part of our ongoing research on potential high-value applications of lignin[42, 43,44], we have investigated the Cr(VI) remediation capability of two types of industrial lignin: a high molecular weight (HMW) lignin, which is derived from softwood, and an enzymatic hydrolysis (EH) lignin, which comes from hardwood. These two types of lignin differ in their chemical structure and functional group content, leading to variations in their chromium adsorption properties thanks to the presence of large number of functional groups, including methoxy groups, hydroxyl groups and carboxylic acid groups. We have also functionalized the HMW lignin by acetylation and phosphorylation reactions, creating modified types of lignin (P_Lig and Ac_Lig), in order to compare their performances with the unmodified HMW lignin. The ability of organophosphates to coordinate chromium ions is well-documented in the literature, which makes the phosphorylation of lignin an appealing approach to improve its capacity of removing Cr(VI).[45] Several experimental parameters can be studied, since they are able to affect Cr(VI) removal, such as pH, initial chromium concentration, biosorbent amount, contact time and temperature. We have also investigated the use of magnetic sorbents. By incorporating magnetic iron oxide nanoparticles into lignin-based materials, it is possible to enhance their adsorption capacity and overcome challenges related to adsorbent separation. Magnetic sorbents can be easily recovered from the treated water using an external magnetic field, making them a convenient and effective solution for large-scale water treatment applications.[46,47,48,49] Magnetic separation has emerged as an highly effective technique for separating solid and liquid phases.[50] Superparamagnetic iron oxide (Fe_3O_4) nanoparticles have found applications across diverse fields, including physics, medicine, biology, environmental science, and materials engineering. Their small size and superparamagnetic properties allow for easy recovery using an external magnetic field, while also being minimally toxic.[51] In our study, we have developed and characterized a novel hybrid material, HMW@Fe_3O_4, which combines lignin with magnetite (Fe_3O_4) nanoparticles. This hybrid material has been designed to improve both the adsorption capacity for chromium and the ease of sorbent recovery. We have compared the performance of HMW@Fe_3O_4 with that of unmodified lignin, as well as with the acetylated and phosphorylated lignin derivatives. The primary objective of our research is to investigate the various factors that influence the removal and reduction of Cr(VI) from water using these different lignin-based adsorbents. Key factors such as pH, sorbent dosage, initial chromium concentration, contact time, and ionic strength have been carefully analysed to determine the optimal conditions for effective chromium removal. By optimizing these parameters, we aim to contribute to the development of sustainable and cost-effective solutions for the remediation of chromium-contaminated water,

ultimately advancing the field of water treatment and pollution control. A schematic representation of the materials studied as potential biosorbents is reported in Figure 1.2.

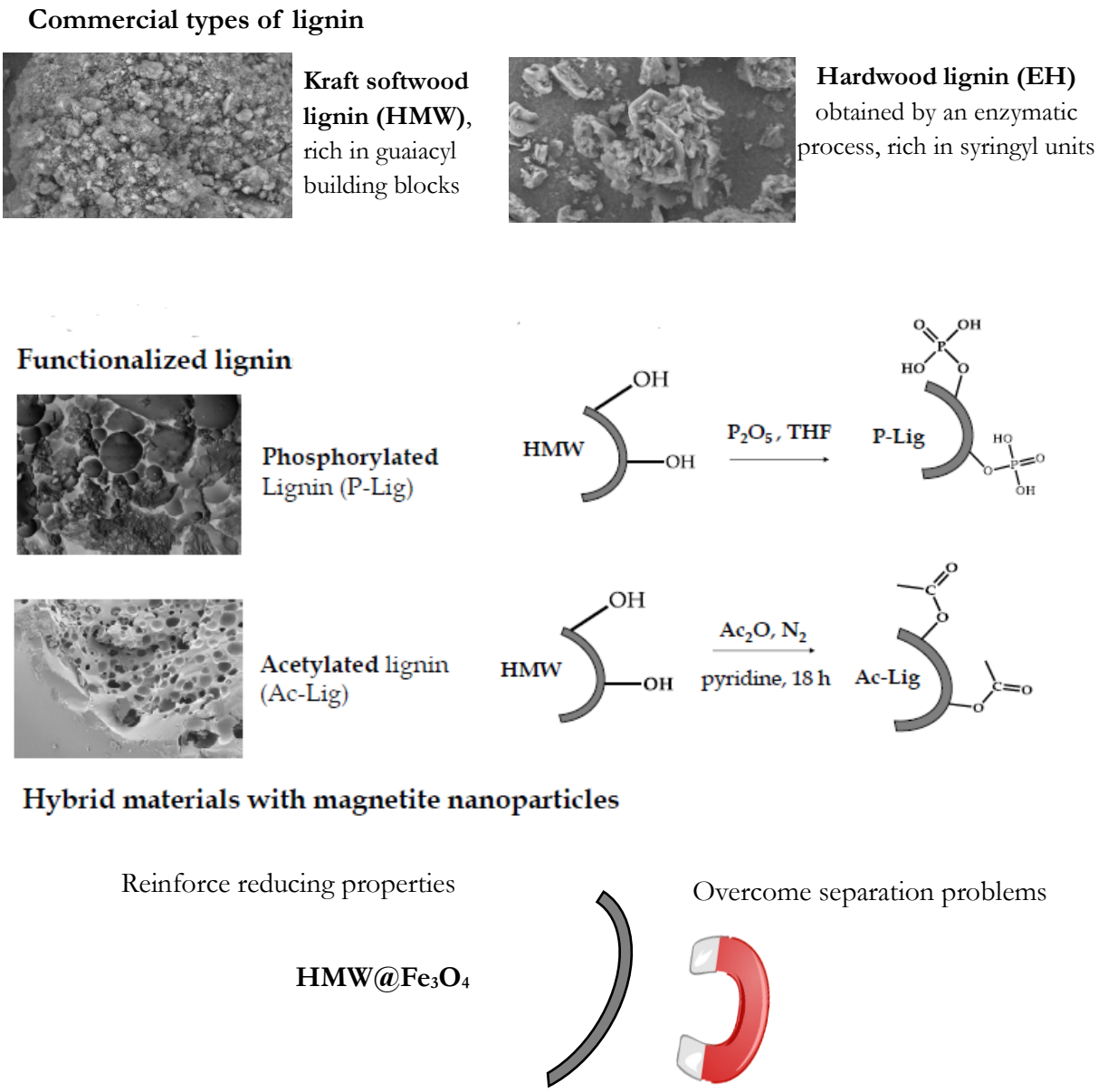

Figure 1.2. Schematic representantion of the material studied as potential biosorbents.

EXPERIMENTAL SECTION

Materials and methods

All reagents and solvents are purchased from Sigma Aldrich (Saint Louis, MO 63103, USA) and used without further purification. HMW (BioPiva395; Pinus taeda) and EH lignin (Fagus sylvatica) are kindly provided by UPM-Kymmene Oyi (Helsinki, Finland) and Green Innovation GmbH (Innsbruk, Austria). $K_2Cr_2O_7$ (minimum purity 99.5%, Sigma-Aldrich) is used to prepare a 1000 mg L^{-1} Cr(VI) stock solution, which has been diluted to final concentrations of 5, 20, 50 and 80 mg L^{-1}. $FeSO_4 \cdot 7H_2O$ and $FeCl_3 \cdot 6H_2O$ (Sigma-Aldrich) are used as sources of Fe(II) and Fe(III), respectively. Fuming HNO_3 has been purchased by Fluka (≥65%) and sodium hydroxide has been purchased by AnalaR NORMAPUR®ACS (99.5-100%).

Materials preparation

Preparation of HMW@Fe_3O_4: HMW@Fe_3O_4 composite material has been synthesized using a coprecipitation technique.[52] Initially, 585 mg of HMW lignin has been suspended in 50 mL of distilled water. Separately, 968 mg of $FeCl_3 \cdot 6H_2O$ (3.60 mmol) and 498 mg of $FeSO_4 \cdot 7H_2O$ (1.80 mmol) have been dissolved in 50 mL of distilled water. The lignin suspension has been then combined with the salt solution, and 3.6 mL of 4 M NaOH (14.4 mmol) have been slowly added dropwise to the mixture. The reaction has been stirred at room temperature for 3 hours. After this time, the resulting mixture has been centrifuged to isolate the solid material, which has been washed with distilled water.

Synthesis of Fe_3O_4_ref: Pure magnetite nanoparticles have been synthesized using a method adapted from existing literature procedures.[52] 324 mg of $FeCl_3 \cdot 6H_2O$ (1.20 mmol) and 167 mg of $FeSO_4 \cdot 7H_2O$ (0.60 mmol) have been dissolved in 100 mL of distilled, degassed water. A 4 M NaOH solution (1.20 mL; 4.8 mmol) has been then added dropwise to the solution. The reaction mixture has been stirred at room temperature for 3 hours. After this period, the resulting magnetite has been separated from the solution using an external magnet, followed by three washings with distilled water.

Effect of pH on Cr(VI) removal: To study the influence of pH on Cr(VI) removal, solutions containing 20 mg/L of Cr(VI) have been adjusted to pH values of 2, 3, 4, 5, 6, 7, 8, and 10, by using 2 M HNO_3 or 2 M NaOH. Each 50 mL sample has been treated with 50 mg of HMW lignin (1 g/L) and stirred for 24 hours at room temperature. After the treatment, the mixtures have been centrifuged to separate the solid lignin, and the solutions have been filtered through a 0.45 μm Nylon filter for further analysis. To explore the reduction of Cr(VI) to Cr(III), a more limited pH range (2, 3, and 4) has been tested with a lower initial Cr(VI) concentration of 5 mg/L. In these experiments, the samples have been treated for 2 hours.

Effect of contact time: Cr(VI) solutions at two concentrations (5 ppm and 20 ppm) have been treated with HMW lignin (1 g/L) at pH 2. The contact time has been varied as 2, 6, 10, 18, and 24 hours. After the treatment, the mixtures have been centrifuged to recover the solid lignin, and the solutions have been filtered through a 0.45 μm Nylon filter.

Influence of competing ions: Under the reference conditions, the impact of various ions in solution has been assessed. The pH has been adjusted using different 2 M acid solutions (HCl, HNO_3, and H_3PO_4), and two types of Cr(VI) solutions have been prepared: one using tap water and the other with a 0.1 M $NaNO_3$ solution. The tap water used has the following characteristics: hardness of 31 °F, pH 7.4, HCO_3^- 227.0 mg/L, Na^+ 16.9 mg/L, K^+ 2.1 mg/L, Ca^{2+} 117.0 mg/L, and Mg^{2+} 11.9 mg/L. After treatment, the solid lignin has been recovered by centrifugation, and the solutions have been filtered through a 0.45 μm Nylon filter.

Evaluation of different initial Cr(VI) concentrations: The initial concentration of $K_2Cr_2O_7$ has been varied from 5 to 80 ppm. The pH of each 50 mL solution has been adjusted to 2 with 2 M HNO_3, and then treated with 1 g/L of HMW lignin for 24 hours under magnetic stirring. After the treatment, the mixtures have been centrifuged to recover the solid lignin, and the solutions have been filtered through a 0.45 μm Nylon filter.

Variation of lignin quantity: Using the reference conditions, the effect of increasing lignin concentration has been evaluated by testing 1, 2, and 4 g/L of HMW lignin. The test with 4 g/L has been repeated with a reduced contact time of 1 hour. After the treatment, the mixtures have been centrifuged to recover the solid lignin, and the solutions filtered through a 0.45 μm Nylon filter.

Regeneration of HMW lignin: Lignin, recovered by centrifugation from the Cr(VI) removal experiments, has been washed three times with distilled water and dried at 80 °C overnight. Approximately 150 mg of this lignin has been dispersed in 10 mL of distilled water, and the pH has been adjusted to 13, using 1 M NaOH. The mixture has been centrifuged, and the supernatant has been separated. It has been then acidified with 2 M HCl to regenerate HMW. The regenerated lignin has been collected by centrifugation, washed three times with distilled water, and dried at 80 °C overnight. The regenerated lignin has been tested for its ability to remove/reduce Cr(VI) under the reference conditions with initial Cr(VI) concentrations of 5 and 80 mg/L. The aliquots of Cr(VI) solution and regenerated lignin used are of 15–20 mL and 15–20 mg, respectively. After the treatment, the mixtures have been centrifuged, and the solutions have been filtered through a 0.45 μm Nylon filter.

Use of different types of lignin: Different types of lignin (HMW, EH, P_Lig, and Ac_Lig) have been tested under the reference conditions to assess their reduction and adsorption behaviour for Cr(VI) removal. pH values of 2, 3, and 4 have been evaluated. After treatment, the solid lignin has been recovered by centrifugation, and the solutions have been filtered through a 0.45 μm Nylon filter.

Adsorption isotherm for EH lignin: The concentration of $K_2Cr_2O_7$ has been varied from 5 to 900 mg/L. The pH of each 25 mL solution has been adjusted to 2 using 1 M HNO_3. The samples have been treated with 1 g/L of EH lignin at 30 °C for 24 hours under magnetic stirring. After the treatment, the solid lignin has been recovered by centrifugation, and the solutions have been filtered through a 0.45 μm Nylon filter.

Evaluation of HMW@Fe_3O_4: HMW@Fe_3O_4 has been evaluated for its ability to adsorb and reduce Cr(VI) and compared with pure magnetite as a reference. Three pH values (2,

5, and 7) have been tested, with a contact time of 2 hours, an initial Cr(VI) concentration of 5 mg/L, and 1 g/L of lignin used as the biosorbent. For the pure magnetite test, only two pH values (2 and 5) have been tested, using the same amount of magnetite as in the HMW@Fe_3O_4 sample (20.5 mg/L). After treatment, the solid has been recovered either by centrifugation or with a magnet, and the solutions have been filtered through a 0.45 µm Nylon filter.

RESULTS AND DISCUSSION

As outlined in the introduction, lignin can be a valid candidate for the removal of hexavalent chromium from contaminated water, offering a low-cost alternative derived from a waste material. Various experimental parameters influencing the removal of Cr(VI) can be investigated, including pH, initial chromium concentration, type of biosorbent, biosorbent quantity, contact time, and temperature. We have begun this study by exploring the capabilities of a Kraft lignin derived from a softwood type, named HMW, to both absorb and/or reduce Cr(VI). The removal of Cr(VI) from aqueous solutions using HMW lignin depends on several key factors, with pH playing a particularly important role in both the reduction and adsorption process. One possible lignin action mechanism could be the adsorption of anions, where negatively charged chromium species are drawn to the positively charged functional groups on the biosorbent surface, especially in acidic environments. Another process, called adsorption-assisted reduction, can occur when Cr(VI) is reduced to Cr(III) by the electron-donating groups in lignin, such as phenolic and carbonyl groups. This reduction is most efficient at low pH, leading to the formation of Cr(III) species, which are less toxic compared to Cr(VI). To confirm this, the first step is to optimize the Cr(VI) removal process involved, determining the ideal pH conditions under which lignin would be most effective at reducing hexavalent chromium to its trivalent form and adsorbing it from solution. A stock solution of chromium at 1000 ppm has been prepared by dissolving $K_2Cr_2O_7$ in deionized water; treated samples have been obtained by dilution of the stock solution. To investigate the effect of pH, we have conducted a series of experiments using 1 g/L HMW lignin as the sorbent towards a 20 mg L^{-1} Cr(VI) solutions, maintaining a contact time of 24 hours at room temperature and setting the pH at different values. Although the nominal concentration of chromium has been set at 20 mg L^{-1}, the actual concentrations have been measured using ICP-AES to ensure accuracy in the results. The concentration of Cr(VI) in the solution has been determined through UV-visible analysis, as described in the Supporting Information section, named as Procedure S1.1. The total chromium content has been measured by ICP-AES (further details can be found in the Supporting Information section, named as Procedure S1.2). The difference between the total chromium and Cr(VI) concentrations corresponds to the amount of Cr(III) present in the solution. All experiments have been conducted in triplicate. The optimal pH for Cr(VI) removal has been confirmed to be 2, which is consistent with the stronger oxidizing potential of Cr(VI) in acidic environments (Figure 1.3). At this pH, the lignin carboxylic and hydroxyl groups facilitate interaction with Cr(VI) anions, allowing them to either be adsorbed onto the lignin surface or be reduced to Cr(III) through electron transfer from the lignin functional groups.[39] At low pH, the dominant mechanism for Cr(VI) removal is electrostatic attraction between the protonated hydroxyl groups on the lignin surface and the Cr(VI) ions, primarily in the form of $HCrO_4^-$ and $Cr_2O_7^{2-}$.[15] As the pH increases, however, the adsorption capacity decreases due to the competition for available adsorption sites from hydroxide ions (OH^-) present in solution. At pH 2, the reduction of Cr(VI) to Cr(III) is particularly effective, driven by the oxidation of the hydroxyl and carbonyl groups on the lignin surface. According to Elovitz and Fish,[53] the oxidation of phenols produces quinones and carboxylate anions.[54] These carboxyl and carbonyl groups can subsequently serve as binding sites for Cr(III) generated through the reduction of Cr(VI). In contrast, at higher

pH values (above 4), the reduction capacity drops significantly,[39] with a decrease in the chromium reduction efficiency from near 100% at pH 2 to just 4–10% at pH 5 or higher (Table 1.1). At pH 2, the residual chromium in solution is almost entirely in its reduced Cr(III) form, with a concentration of 12.8 mg L^{-1}, representing 36% removal of total chromium. In contrast, at pH 5–7, most of the chromium remains in the hexavalent Cr(VI) form (Figure 1.3 and Table 1.1).

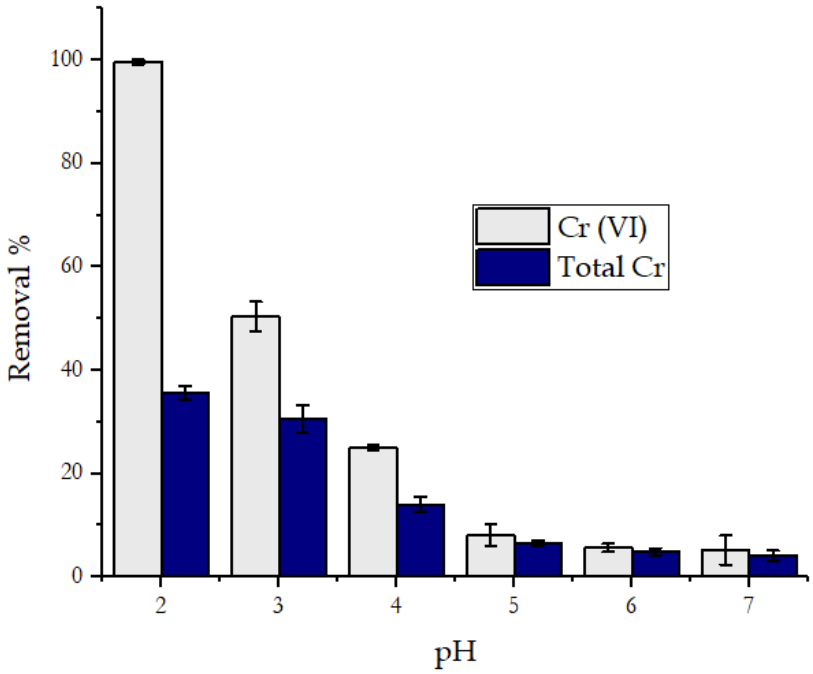

Figure 1.3. Removal percentages of Cr(VI) and total chromium that remains in solution for experiments performed with an initial Cr(VI) concentration of 20 ppm; contact time: 24 hours; 1 g/L of HMW.[55]

The percentage of removed exavalent chromium has been calculated using equation 2:

$$Removal\ \%: \frac{C_i - C_f}{C_i}\ x\ 100 \qquad Eq\ (2)$$

Where C_i and C_f are the initial and final Cr(VI) concentration in aqueous solution, respectively (mg/L).

Table 1.1. Total chromium that remains in solution and removal percentages of Cr(VI) for experiments performed with an initial Cr(VI) concentration of 20 ppm; contact time: 24 hours; 1 g/L of HMW.

pH	Cr (VI)		Cr (tot)		Cr(III)/Cr(VI) (ppm)
	Concentration (ppm)	Removal (%)	Concentration (ppm)	Removal (%)	
2	<0.02	>99	12.8 (±0.2)	36 (±1)	Cr(III) only
3	10.0 (±0.6)	50 (±3)	13.7 (±0.2)	30.6 (±3)	0.37
4	10.7 (±0.6)	24.5 (±0.4)	15.3 (±0.3)	14 (±1.4)	0.43
5	16.2 (±0.4)	8.1 (±2)	16.5 (±0.3)	6.5 (±0.5)	0.018
6	16.9 (±0.1)	5.6 (±0.8)	16.9 (±0.3)	4.9 (±0.3)	Cr(VI) only
7	16.7 (±0.5)	5.2 (±2.8)	16.7 (±0.3)	4.1 (±1)	Cr(VI) only

It could be concluded that the removal of chromium is attributable both to adsorption and reduction of Cr(VI).

We have also explored the effect of contact time on the reduction efficiency by reducing the reaction time from 24 hours to just 2 hours within a narrower pH range. An initial Cr(VI) concentration of 5 mg L^{-1} has been used for this experiment and a further evidence has been provided that the highest reduction rate occurs at pH 2 (Figure 1.4 and Table 1.2).

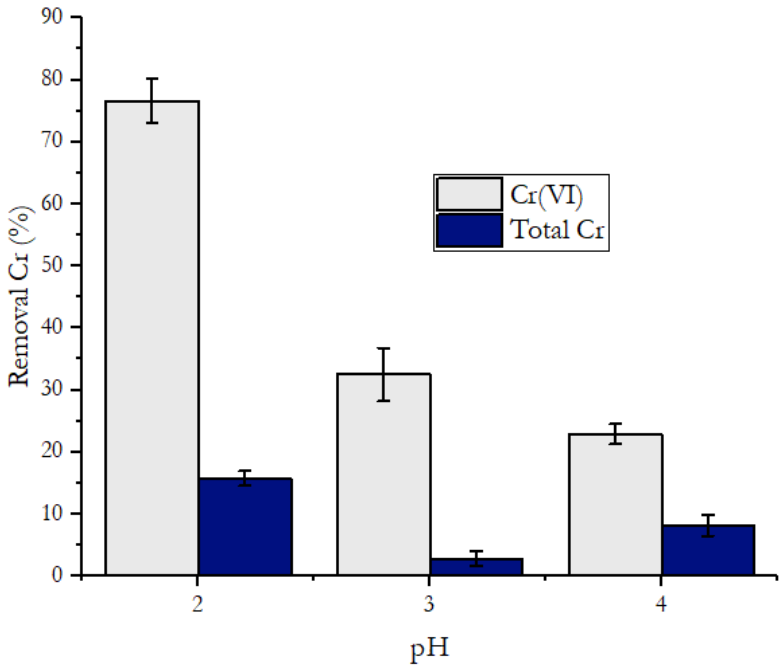

Figure 1.4. Removal percentage of Cr(VI) and total chromium for experiments performed at 5 mg/L of initial Cr(VI) concentration, 2 h contact time and 1 g/L of HMW. [55]

Table 1.2. Removal percentage of Cr(VI) and total chromium for experiments performed at 5 ppm initial Cr(VI) concentration with 2 h contact time and 1 g/L of HMW.

pH	Cr (VI)		Cr (tot)	
	Concentration (ppm)	Removal (%)	Concentration (ppm)	Removal (%)
2	1.2 (±0.2)	77 (±4)	2.7 (±0.05)	38.3 (±1)
3	3.4 (±0.2)	33 (±4)	4.9 (±0.1)	3 (±1)
4	3.9 (±0.1)	23 (±2)	4.6 (±0.1)	8 (±2)

It can be observed that already with 2 h of contact time, the removal of total chromium is comparable with that observed at 24 hours (Tables 1.1 and 1.2), while the reduction of Cr(VI) to Cr(III) is higher at 24 h.

The effect of contact time on the reduction of Cr(VI) has been further investigated on solution with different initial concentration of Cr(VI), keeping the pH constant. The results have revealed that the extent of Cr(VI) reduction increases with contact time. For solutions with initial Cr(VI) concentrations of 5 mg L^{-1} or 20 mg L^{-1}, complete reduction to Cr(III) has been achieved after 6 and 24 hours, respectively (Figure 1.5). These findings emphasize the importance of allowing sufficient contact time for the Cr(VI) reduction process to proceed efficiently, especially when dealing with higher concentrations of chromium. Furthermore, these results suggest that higher chromium concentrations require longer contact times, to effectively reduce Cr(VI).

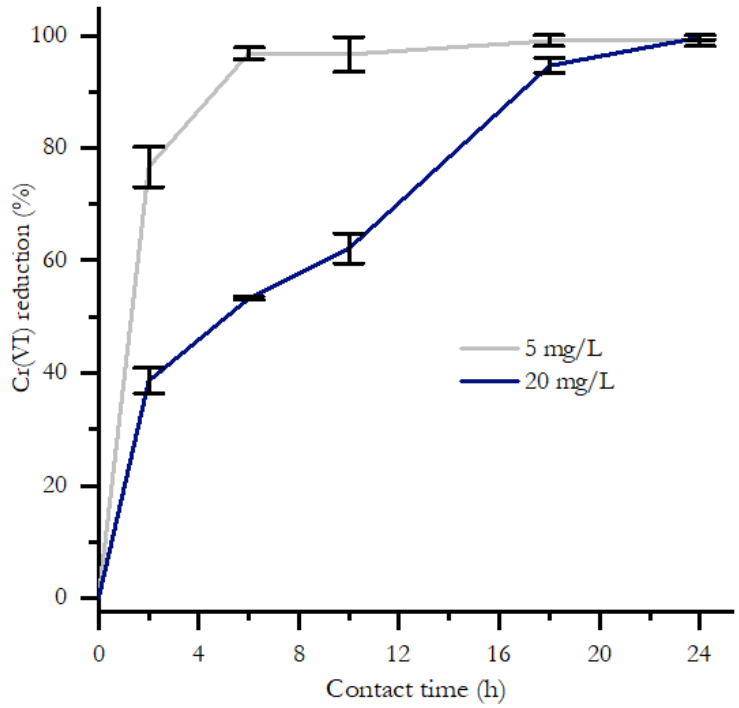

Figure 1.5. Influence of contact time on the Cr(VI) reduction. The grey line refers to experiments with an initial Cr(VI) concentration of 5 mg/L, and the blue line refers to experiments with an initial Cr(VI) concentration of 20 mg/L (pH = 2, 1 g/L of HMW).[55]

In addition to pH, the nature of the acid used to adjust the solution pH can also influence the Cr(VI) reduction performance, since industrial wastewater may contain ions other than chromium. The impact of ionic strength on the biosorption of Cr(VI) by lignin has been also evaluated. Donmez and Asku[56] have demonstrated that chromium uptake typically decreases with increasing ionic strength in aqueous solutions. At higher ionic strength, the biosorption of chromium may be reduced due to competition between the anions and chromate ions for the active biosorption sites. To examine this, we have tested the effect of various acids (HNO_3, H_3PO_4, and HCl) on the removal of Cr(VI), maintaining the pH at 2 (Figure 1.6). This has allowed us to evaluate how different anions, with varying coordination abilities, affect the interaction between Cr(VI) and lignin. We have also investigated the impact of more complex solutions by preparing the Cr(VI) stock solution using tap water instead of distilled water. Tap water contains additional ions, such as calcium, sodium, and carbonates, which might influence the sorption behaviour. Furthermore, to assess the effect of ionic strength on the process, we have used a 0.1 M $NaNO_3$ solution to prepare the chromium stock solution and again adjusted the pH to 2 with HNO_3. The results have showed that Cr(VI) reduction has been largely consistent across all the tested conditions, with the exception of experiments involving HCl and $NaNO_3$. In these cases, Cr(VI) reduction has been observed to be 10–15% lower, likely due to competitive interactions between the chloride and nitrate anions and the chromate ions for binding sites on the lignin surface. Additionally, the increased ionic strength due to the presence of $NaNO_3$ in solution may lead to smaller hydrodynamic radii of the lignin macromolecules caused by stronger interchain electrostatic interactions, which could reduce the number of available active sites for chromium binding.

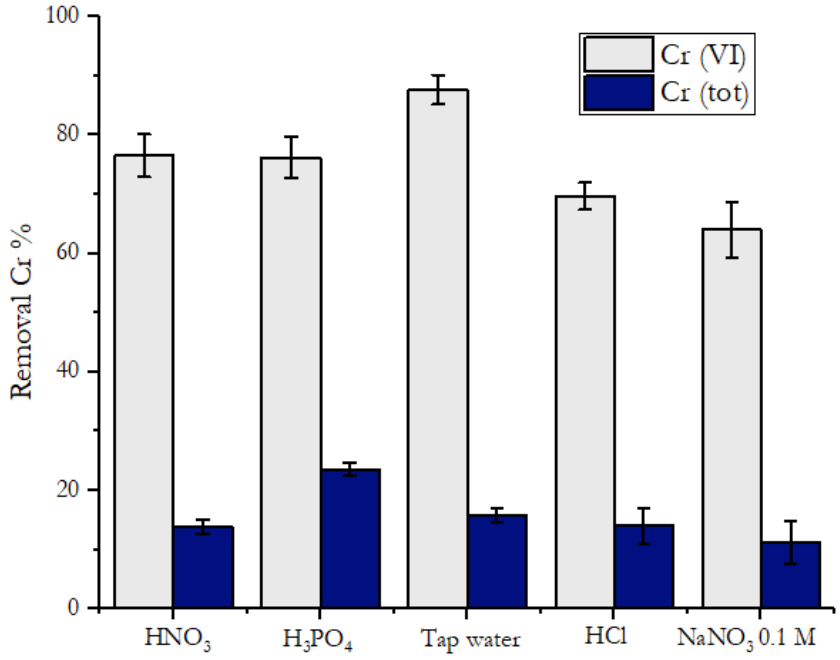

Figure 1.6. Effect of the use of different acids to adjust the pH of the solutions. The effect of the use of a 0.1 M solution of $NaNO_3$ and of tap water instead of distilled water in the preparation of the initial Cr(VI) solution is also reported. Blue bars refer to the removal of Cr(tot) whereas the grey bars refer to the reduction of Cr(VI). pH = 2; 1 g/L of HMW, 5 mg/L of initial Cr(VI) concentration, 2h contact time.[55]

We have further explored the effect of initial Cr(VI) concentration on the adsorption and reduction efficiency of HMW lignin by testing solutions with varying Cr(VI) concentrations ranging from 5 to 80 mg L^{-1}. As shown in Figure 1.7 and Table 1.3, for lower concentrations of Cr(VI) (5 and 20 mg L^{-1}), complete reduction to Cr(III) has occurred within 24 h, with more than 35% of the total chromium removed by adsorption. However, as the initial concentration of Cr(VI) has been increased, the reduction efficiency decreases, with no more than 84% reduction achieved for concentrations higher than 20 mg L^{-1}. This decrease can be attributed to the surface modification of the lignin polymer, as the oxidation of the hydroxyl groups reduces the number of active sites available for further adsorption. Consequently, the adsorption capacity of lignin diminishes as the surface becomes saturated with oxidized groups. This observation aligns with the poor remediation performance of acetylated lignin (Ac_Lig), which will be discussed further below.

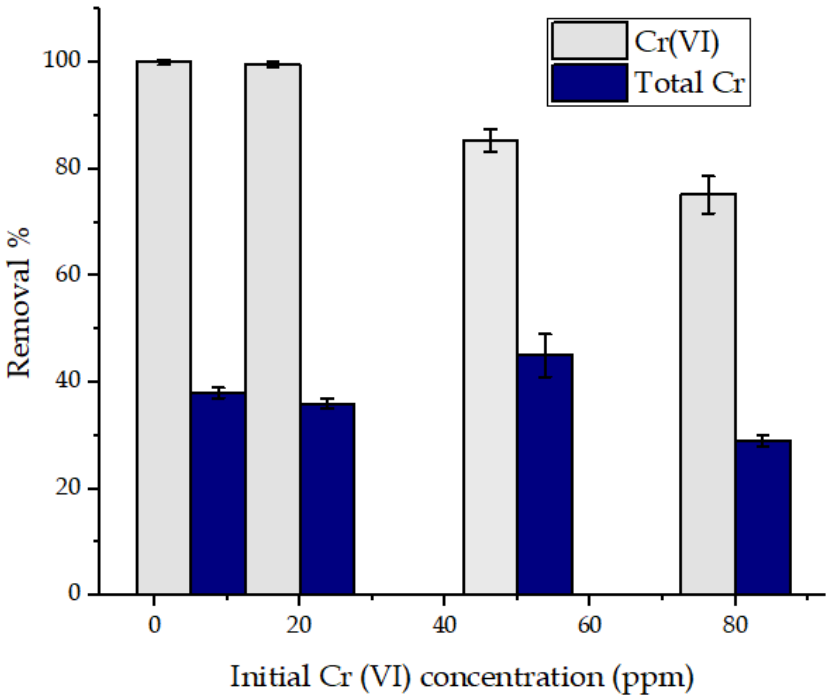

Figure 1.7. Removal of chromium (VI) and total chromium after the treatment with 1 g/L of HMW of solutions at different initial concentrations of Cr(VI), and 24 hours contact time at pH 2.[55]

Table 1.3. Removal of chromium (VI) and total chromium after the treatment with 1 g/L of HMW of solutions at different initial concentrations of Cr(VI), and 24 hours contact time at pH 2.

Initial Cr (VI) concentration (ppm)	Cr (VI)		Cr (tot)		Cr(III)/Cr(VI) (ppm)
	Concentration (ppm)	Removal (%)	Concentration (ppm)	Removal (%)	
5	<0.02	>99	3.10 (±0.05)	38 (±1)	Cr(III) only
20	<0.02	>99	12.8 (±0.2)	36 (±1)	Cr(III) only
50	8 (±2)	84 (±4)	27.5 (±2)	45 (±4)	2.44
80	14 (±3)	77 (±4)	56.8 (±0.8)	29 (±1)	3.06

In summary, the adsorption and reduction of Cr(VI) by HMW lignin are strongly influenced by factors such as pH, initial chromium concentration and contact time. The optimal pH for maximum Cr(VI) removal is 2, where both adsorption and reduction occur efficiently. However, the presence of competing ions and the oxidation of lignin functional groups at high concentrations can significantly reduce the material effectiveness, highlighting the importance of controlling experimental conditions to achieve the best results.

In the context of sustainable practices and circular economy principles, it is vital to explore the regeneration of biosorbents, allowing them to be reused in subsequent cycles of environmental remediation. To investigate this issue, we have subjected HMW lignin (at a concentration of 1 g L^{-1}) to a series of regeneration steps following its interaction with Cr(VI)-contaminated solutions. Initially, HMW has been exposed to Cr(VI) solutions at two different concentrations (5 mg L^{-1} and 80 mg L^{-1}) at pH 2 under stirring for 24 hours. After this initial contact, the lignin has been separated from the solution and treated with aqueous NaOH to dissolve the adsorbed chromium and leading to $Cr(OH)_3$ formation, which has been subsequently removed by centrifugation. To regenerate the lignin, HCl has been added to the mixture, causing precipitation of lignin and allowing the recovery of the biosorbent. The regenerated lignin has been referred to as HMW_reg_5 (from the 5 mg L^{-1} Cr(VI) solution) and HMW_reg_80 (from the 80 mg L^{-1} Cr(VI) solution). These regenerated biosorbents have been then tested by exposing them to a second batch of 5 mg L^{-1} Cr(VI) solution under the same reference conditions as the initial experiments. Results are shown in Figure 1.8 and they have demonstrated that the regenerated sorbent HMW_reg_5 retained a slightly lower reducing ability compared to the original HMW lignin, indicating some loss in functionality. This reduction in performance can be attributed to the partial oxidation of the lignin hydroxyl (OH) groups by Cr(VI) during the first adsorption cycle, which diminishes its capacity to reduce Cr(VI) in subsequent cycles. In contrast, the sorbent regenerated from the 80 mg L^{-1} Cr(VI) solution (HMW_reg_80) exhibits a notably lower reducing capability, demonstrating a more substantial degradation in its ability to facilitate Cr(VI) reduction. Despite this, both kinds of regenerated lignin (HMW_reg_5 and HMW_reg_80) show improved total chromium removal compared to the unmodified HMW lignin. Specifically, under the same experimental conditions, the removal efficiency reaches up to 50%, suggesting that the

regeneration process enhances the biosorbent overall performance. This improvement can be attributed to a decrease in polymer chain aggregation during the dissolution-precipitation steps, which likely increases the surface area available for adsorption. The regeneration process, therefore, not only allows to recover lignin, but appears to slightly enhance its adsorption capacity, which is a promising result for its reusability in continuous remediation cycles.

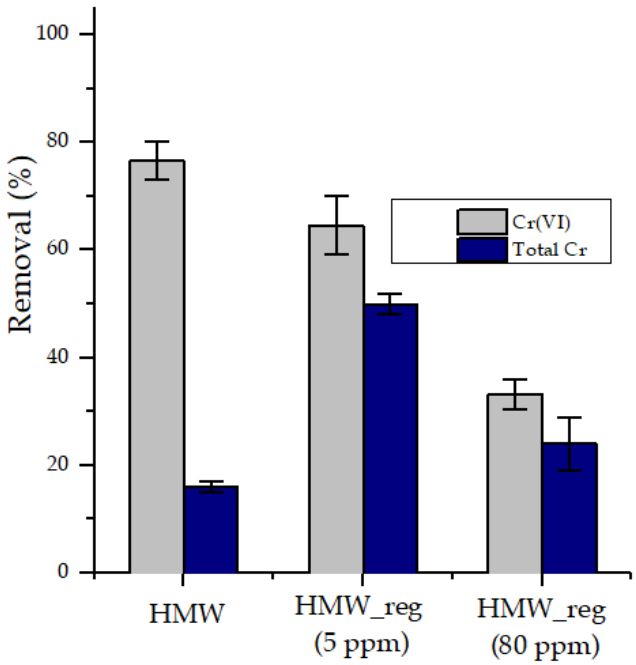

Figure 1.8. Reduction of Cr(VI) by HMW and two different regenerated lignin, HMW_reg_5 and HMW_reg_80. pH 2 obtained with 2M HNO3; 1 g/L of lignin; initial Cr(VI) concentration: 5 mg/L; contact time: 2 h.[55]

The study has revealed important insights into the role of functional groups in determining the adsorption and reduction abilities of different kinds of lignin. Functionalized kinds of lignin are emerging as promising materials with improved capabilities for the removal of Cr(VI), particularly when coordinating groups are incorporated into the biopolymer backbone. To explore this potential, we have focused on the phosphorylation of HMW lignin, aiming to compare the Cr(VI) remediation performance of the phosphorylated derivative (referred to as P_Lig) with that of the native biosorbent. The potential of organophosphates to coordinate chromium ions is well-established in the literature, making lignin phosphorylation an attractive method for enhancing its ability to remove Cr(VI). Previous study on lignin phosphorylation of our research group[57] has been carried out using an excess of phosphorus pentoxide as phosphorylating agent, after dissolving lignin in tetrahydrofuran. The procedure is described in the Supporting Information section as Procedure S1.3. The reaction has been performed under reflux for 8 hours, during which the phosphorylated lignin precipitates as an insoluble solid. After the reaction, the mixture has been quenched with water, and the product has been isolated by filtration and thoroughly washed with the same solvent to remove any traces of phosphoric acid or other soluble phosphorus-containing species. The absence of free phosphoric acid or low-molecular-weight phosphorus species has

been confirmed in previous work[57] by the lack of corresponding signals in the $^{31}P\{^{1}H\}$-NMR spectrum of the product, which has been suspended in DMSO-d_6, where P_Lig is completely insoluble. The solid-state $^{31}P\{1H\}$-MAS-NMR spectrum[57] of P_Lig reveales the presence of phosphate groups in the polymer, as indicated by a prominent peak around 0 ppm, which is characteristic of organic orthophosphate groups.[58] (Figure S1.1). The $^{13}C\{^{1}H\}$-MAS-NMR spectra[57] of both pristine and phosphorylated lignin (P_Lig) show minimal differences, suggesting that the polymeric chains remain structurally intact after functionalization.[59] The aromatic signals are concentrated in the 150–110 ppm region, while the methoxy groups show a distinct signal around 55 ppm, and aliphatic carbons give rise to signals in the 75–61 ppm region (Figure S1.2). Scanning electron microscopy (SEM) images of both pristine lignin and P_Lig show significant differences in their surface morphology (Figure 1.9) and elemental analysis is reported in Table S1.1.[55,57] EDX analysis and EDX mapping are shown in Figure S1.3. [55,57]

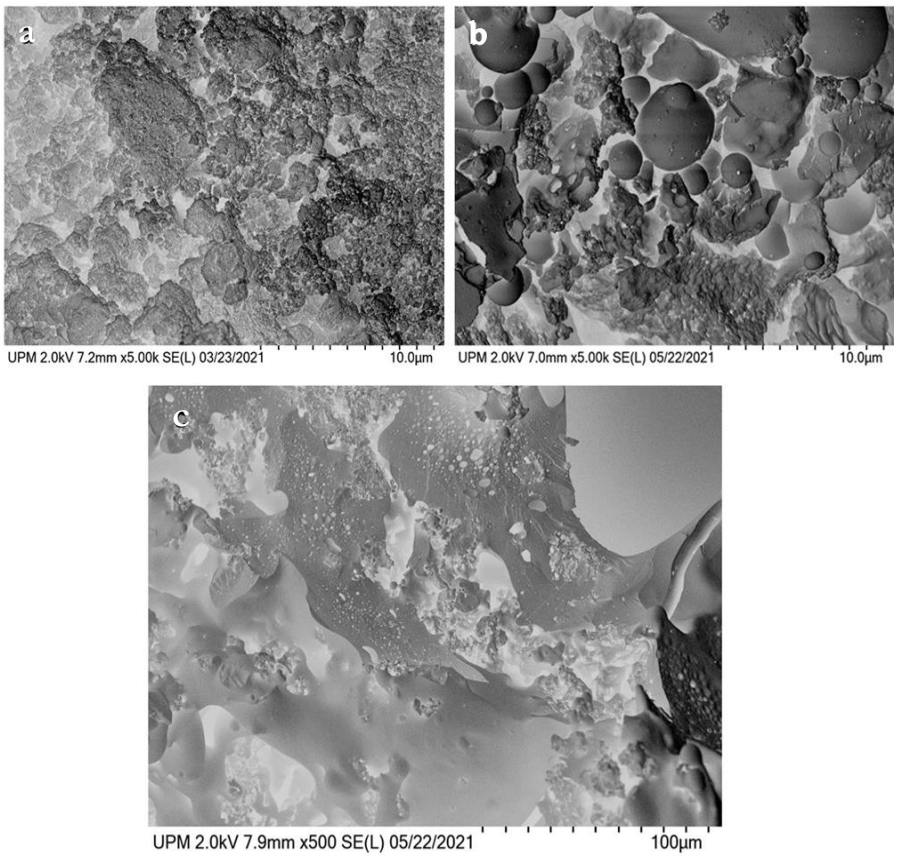

Figure 1.9. SEM images of HMW (a) and P_Lig (b and c).

The surface of P_Lig appears to contain larger particles with more pronounced pores compared to the native lignin. This change in surface morphology can be attributed to the presence of phosphate groups, which likely promote aggregation and trigger precipitation during the synthesis process. Energy-dispersive X-ray spectroscopy (EDX) analysis reveals a rough phosphorus-to-sulphur ratio of approximately 1.4 (Table S.1.1 and Figure S.1.3),[55,57] suggesting a phosphorus content of about 2%, which aligns well with the expected value for P_Lig.[60] Thermogravimetric analysis (TGA) further confirms the successful functionalization of lignin, as the thermal stability of P_Lig has been significantly improved, compared to the precursor HMW lignin. The TGA data show a

higher residual mass, indicating a reduction in the overall weight loss percentage during heating, which is consistent with the incorporation of phosphate groups. (Figure S1.4).[57,60] Additionally, acetylation of lignin has been previously carried out by our research group[57] using a procedure described by Buono et al.,[61] which also contributed to improving the material performance. The procedure is described in the Supporting Information section as Procedure S1.4. The acetylation process has been confirmed through spectroscopic characterization using FTIR and NMR techniques, which showed the complete transformation of hydroxyl groups into acetyl groups. In the FTIR spectrum, the stretching band corresponding to OH groups disappears, and a new band appears around 1760 cm^{-1}, characteristic of C=O stretching (Figure S1.5).[55, 57] In the $^{13}C\{^{1}H\}$-NMR spectrum (Figure S1.6), [55, 57] the presence of acetyl groups is evident, with signals at 170 ppm and 20 ppm, corresponding to the carbonyl and methyl carbons, respectively. SEM analysis of acetylated lignin (Ac_Lig) shows a distinct surface morphology compared to HMW lignin, further indicating that chemical modifications occur (Figure 1.10).

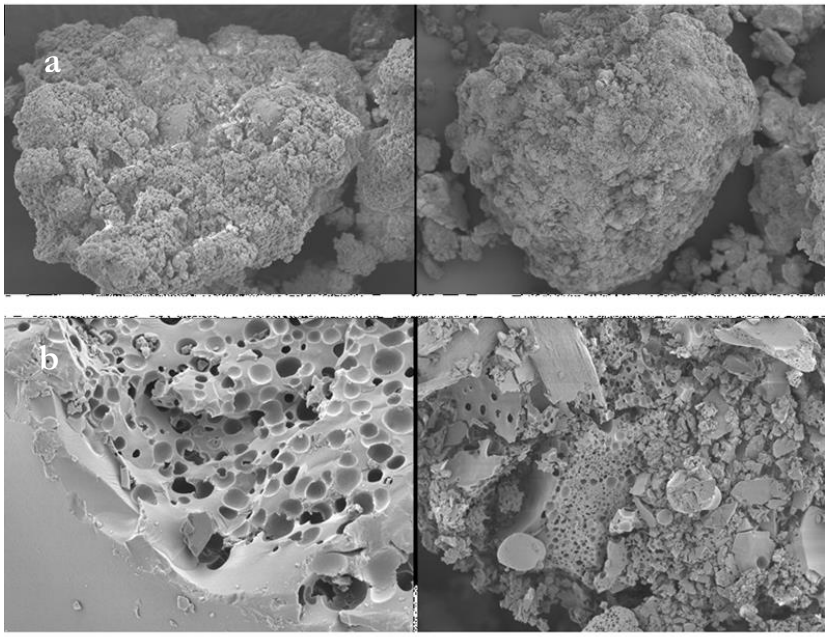

Figure 1.10. SEM images of A) HMW, and B) Ac_Lig

We have evaluated the different sorption ability of P_Lig, Ac_Lig, and the enzymatic lignin EH, in order to relate their performance to their different structures and available functional groups. To note also that P_Lig and Ac_Lig are derived from softwood lignin with molecular weights of 5,000 g mol^{-1} and 10,000 g mol^{-1}, respectively, while EH is a hardwood lignin characterized by a higher molecular weight and a distinct chemical structure.

For this comparison, we have treated the separate solutions, each containing 5 mg L^{-1} of Cr(VI), with 1 g L^{-1} of the respective lignin at pH 2 for 2 hours (Figure 1.11)Table. The results of Cr(VI) reduction and total chromium removal have been assessed, as illustrated in Fig. 1.11. Ac_Lig, which has been chemically modified through acetylation, exhibits a significantly lower adsorption and reducing capacity compared to the other kinds of lignin.

The acetylation process replaces the hydroxyl groups with ester moieties, which are inactive in both the reduction and adsorption processes, leading to poor performance in Cr(VI) remediation.[62] As expected, Ac_Lig doesn't show any measurable reduction or adsorption of Cr(VI) under the experimental conditions, highlighting the crucial role of phenolic hydroxyl groups in the effectiveness of lignin-based biosorbents. P_Lig, which retains its hydroxyl groups, demonstrates a lower reducing capability than HMW lignin. This reduction in efficiency is attributed to the partial substitution of hydroxyl groups with phosphate groups, which may impair the reduction process. However, P_Lig still achieves a significant total chromium removal (up to 30%) due to the phosphate groups providing strong binding sites for Cr(III) ions, which remain after the reduction of Cr(VI). In contrast, EH lignin shows remarkable performance, with complete reduction of Cr(VI) to Cr(III). This biosorbent also exhibits the highest adsorption capacity, removing up to 60% of the total chromium from the solution, which is significantly higher than that observed for HMW. EH has a higher content of syringyl units, which are known for their stronger chelation properties. This structural feature likely plays a key role in EH superior ability to chelate and remove chromium ions, in contrast to HMW lignin, which is mainly composed of guaiacyl units.

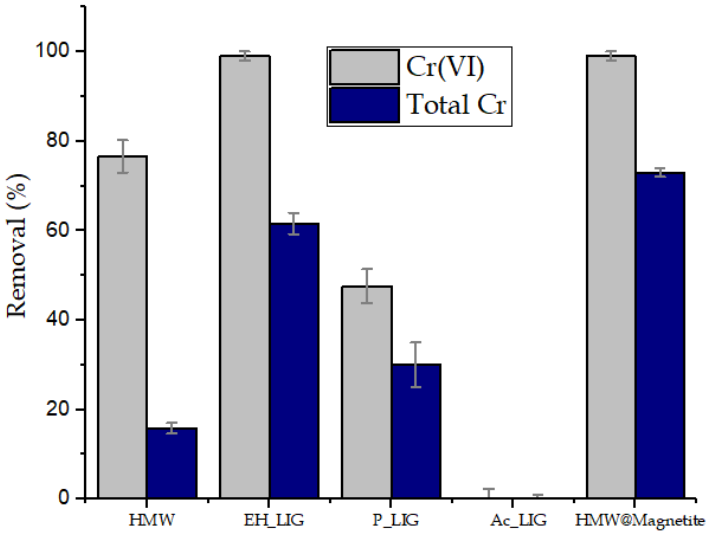

Figure 1.11. Cr(tot) removal and Cr(VI) reduction by using different types of lignin at pH 2 (2M HNO_3). 1 g/L of lignin; initial Cr(VI) concentration: 5 mg/L; contact time: 2 h.[55]

Figure 1.12 illustrates the adsorption behaviour of both EH and HMW lignin as a function of the amount of adsorbent used, with concentrations reaching up to 4 g L^{-1}. For EH lignin, a complete reduction of Cr(VI) has been achieved with just 1 g L^{-1} of the material, indicating its high efficiency even at low concentrations. In contrast, HMW lignin requires a higher concentration (2 g L^{-1}) to fully reduce Cr(VI) under the same experimental conditions, demonstrating that EH outperforms HMW in terms of its reducing ability. Regarding the overall chromium removal, EH shows a superior performance compared to HMW. Specifically, a plateau in chromium removal has been reached at approximately 75% when the adsorbent concentration has been increased to 2 g L^{-1} or higher. On the other hand, the maximum chromium removal achieved with HMW is around 35%, and this has

been only observed when the adsorbent concentration has been raised to 4 g L^{-1}. This indicates that while EH is more efficient at lower adsorbent concentrations, HMW requires a much higher amount to achieve comparable removal levels.

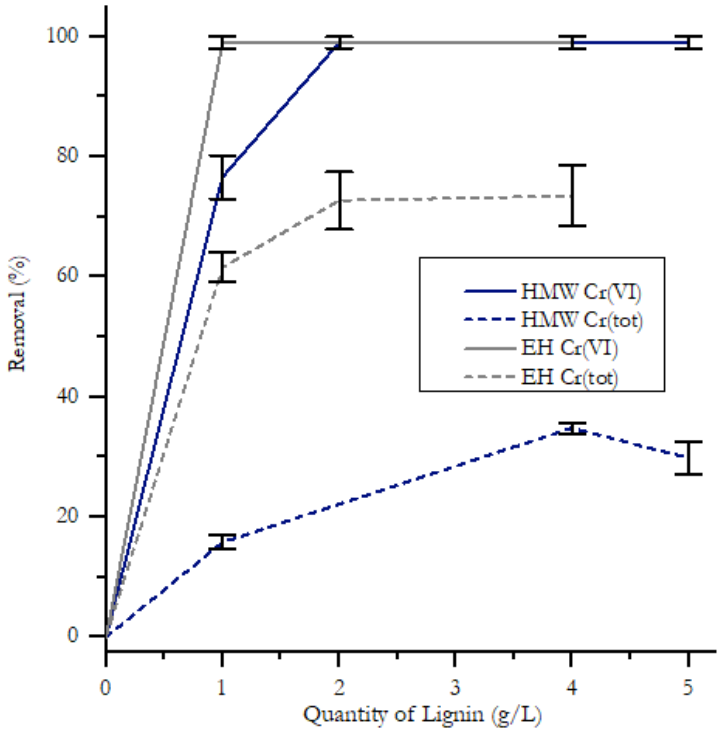

Figure 1.12. Reduction and removal of Cr(VI) and Cr(tot) using different quantities of EH and HMW at reference conditions.

To assess the role of available surface area on sorption capability of the materials, they have been evaluated through nitrogen adsorption isotherms collected at 77 K. These isotherms have provided valuable information on the specific surface area and porosity of the lignin-based biosorbents and how these characteristics influence their ability to capture and reduce chromium (Figure S1.7 and Figure S1.8). The data have revealed that the highest surface area values are observed for EH lignin (Figure 1.13 and Table 1.4), which correlates well with its enhanced adsorption capacity. Following chemical functionalization, a notable decrease in nitrogen uptake has been observed, with a reduction of approximately 53% for P_Lig (4.2 m^2/g) and 82% for Ac_Lig (1.6 m^2/g), compared to the pristine HMW lignin (8.9 m^2/g). This reduction in surface area is likely due to the insertion of phosphate and acetyl groups onto the pore walls, which partially block the available pore space and decrease the overall free volume within the material.

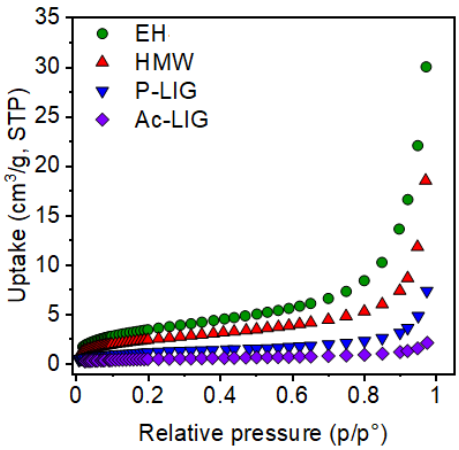

Figure 1.13. Comparison between nitrogen adsorption isotherms collected at 77 K of HMW, EH, P_LIG and Ac_Lig.

Table 1.4. Surface area for different lignin-based materials according to BET and Langmuir models.

Sample	BET surface area (m^2/g)	Langmuir surface area (m^2/g)
HMW	8.9	12.0
EH	12.8	18.2
Ac_Lig	1.6	2.4
P_Lig	4.2	6.2

In summary, the adsorption and reduction capabilities of different lignin types vary significantly depending on their chemical composition, functional groups and surface area. While HMW lignin performs well in Cr(VI) reduction and removal, the superior performance of EH suggests that lignin with higher surface area and specific functional groups may offer even greater potential for environmental remediation. The superior performance of EH can therefore be related to its higher BET surface area, as this increased surface area likely provides more active sites for Cr(VI) binding; additionally, EH contains a higher proportion of syringyl moieties, which have been associated with stronger chelation properties. This structural characteristic likely contributes to EH enhanced ability of removing chromium ions compared to HMW lignin, which primarily contains guaiacyl units, as shown by pyrolysis GC-MS (Figure 1.14). The thermal behaviour of EH has been investigated by means of TGA and DSC and no significant difference can be found with the respect to the one of HMW (Figure S1.9, TGA and DSC profile of HMW are reported in Chapter 2).

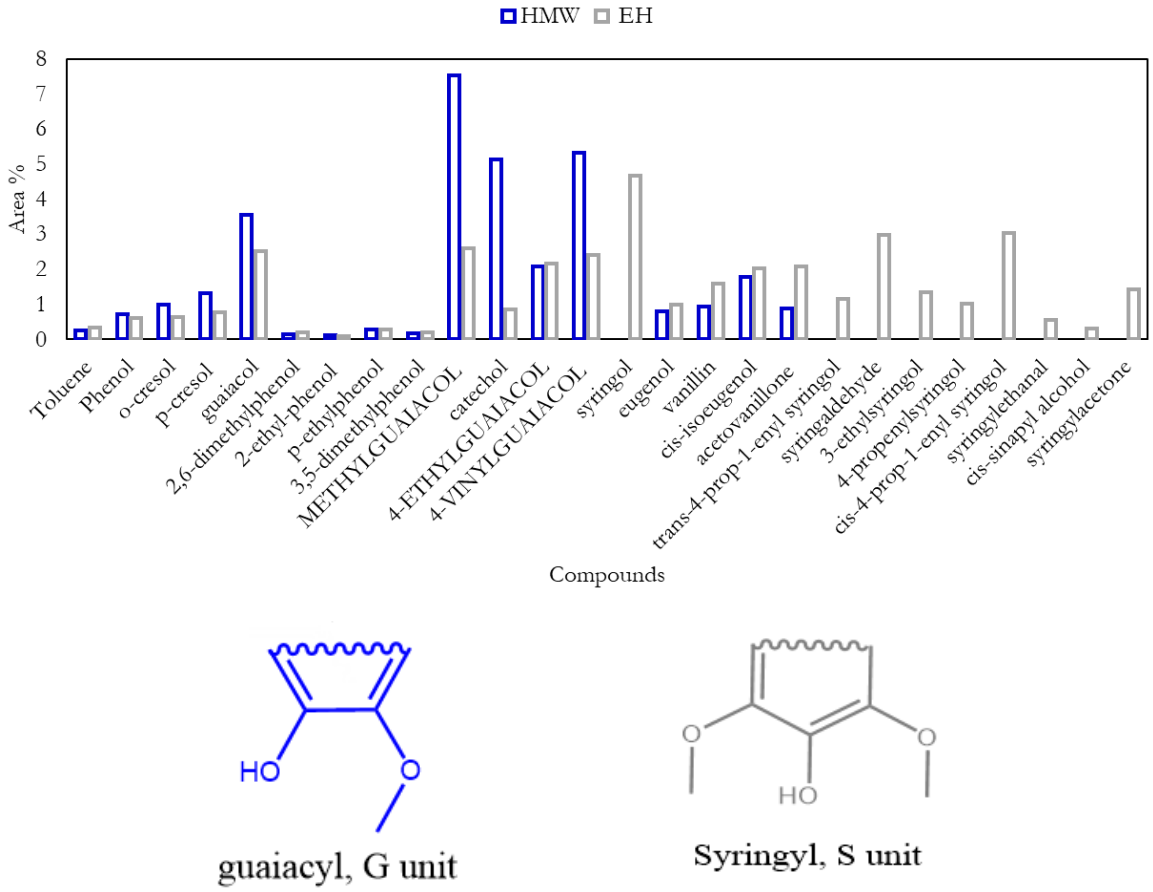

Figure 1.14. Comparison of pyrolysis GC-MS results of HMW and EH lignin. A schematic representation of the guaiacyl and syringyl units, highlighting the differences between the two types of lignin, is provided.

For the development of a magnetic lignin-based material (HMW@Fe_3O_4), we have explored the synthesis of magnetite (Fe_3O_4) crystals embedded in lignin as matrix. This functionalization not only enhances the lignin ability to adsorb and reduce Cr(VI), but also enables the use of magnetic separation techniques for efficient biosorbent recovery. A co-precipitation method has been employed, which is well-documented in the literature.[52] In this process, iron salts ($FeCl_3 \cdot 6H_2O$ and $FeSO_4 \cdot 7H_2O$) have been added to a lignin slurry in the presence of NaOH to induce the precipitation of magnetite. The reaction has been conducted under basic conditions and under nitrogen atmosphere, but for the following tests as potential sorbents the experiments have been conducted in normal atmosphere, mimicking the applicative conditions. The first attempt, using a lignin/iron sulphate weight ratio of 1.7, resulted in HMW@Fe_3O_4 material containing 10% iron by weight. However, PXRD, FT-IR and TEM-EDX analyses (Figure S1.10, S 1.11 and S1.12)[57] reveal the formation of goethite (FeO(OH)) instead of magnetite, likely due to the oxidation of Fe(II) in the presence of oxygen, since the reactions have been not conducted under nitrogen environment. In subsequent experiments, a higher iron content has been used, resulting in a final iron loading of 30%. This modification successfully leads to the formation of magnetite with only trace amounts of goethite, as confirmed by PXRD analysis. The final product, a dark powder, has been then further analysed using ICP-AES and FT-IR. The ICP analysis shows that the iron content in the composite material has

been calculated to be 30%, with an experimental value of 28.6 ± 0.3%. The FT-IR spectrum displays the following peaks: ν(OH) 3600–3100 cm^{-1}, n(CHalif) 2930 cm^{-1}, ν(CHring) 1633 cm^{-1}, ν(C–C, C–O) 1090 cm^{-1}, 1120 cm^{-1}, and ν(Fe–O) 540, 400 cm^{-1}. PXRD and FT-IR analyses are provided in the SI (Figure S1.13 and S1.14). The retention of the metal low oxidation state can likely be attributed to the fast formation kinetic, which prevent oxygen-induced oxidation and inhibits the formation of the more thermodynamically stable goethite.[63] PXRD of Fe_2O_3_ref is also reported for comparison (Figure S1.15).

The performance of HMW@Fe_3O_4 in Cr(VI) remediation has been investigated, in comparison to HMW and to magnetite alone as a reference. The hybrid HMW@Fe_3O_4 has been anticipated to enhance the reducing properties of the material, while also providing the added advantage of easy removal from the treated solution using an external magnet. As shown in Figure 1.15, HMW@Fe_3O_4 exhibits almost complete Cr(VI) reduction under acidic conditions (pH 2), outperforming both HMW and pure magnetite, which only achieved about 80% reduction. Interestingly, as the pH has been increased, a significant decrease in reduction efficiency has been observed for HMW, whereas the HMW@Fe_3O_4 composite maintains a substantial reducing ability, although still lower than that of pure magnetite. This suggests that the inclusion of lignin in the hybrid material helps in maintaining some level of reducing power at higher pH values. An additional advantage of using HMW@Fe_3O_4 is the simplicity of sorbent recovery. Since the material is magnetically responsive, it can be easily removed from the solution by applying an external magnetic field, offering a convenient solution for post-treatment handling.

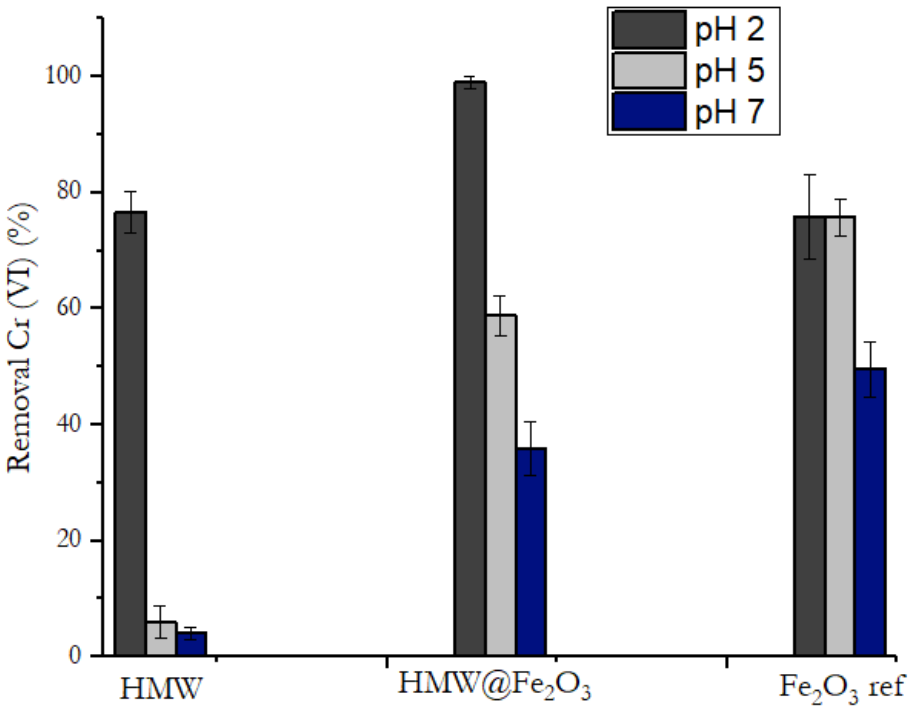

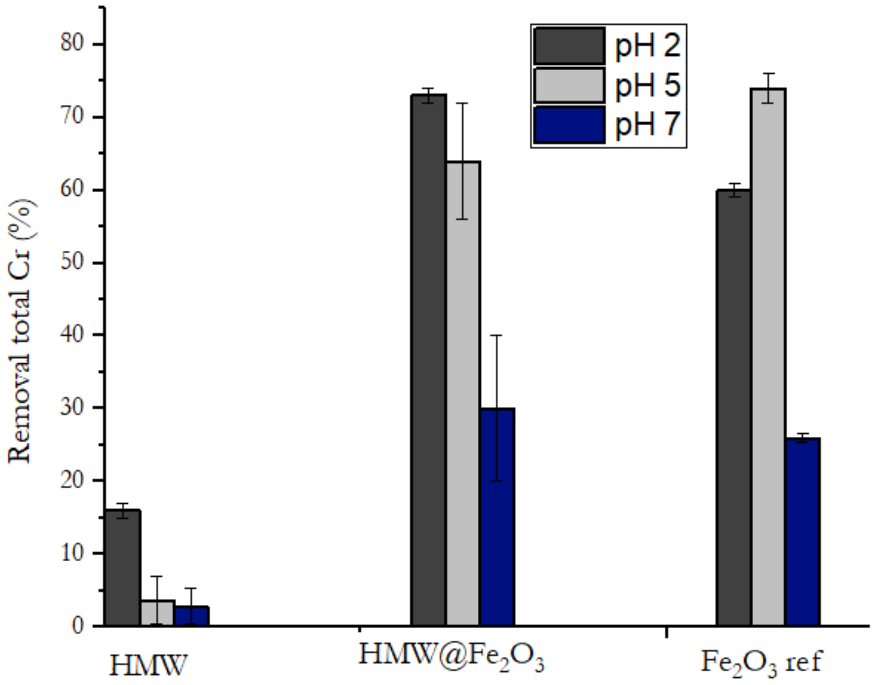

Figure 1.15. Cr(VI) reduction (top) and total Cr removal (bottom) percentages for the experiments with HMW, magnetite and HMW@Fe_2O_3 at three different pHs. pH controlled with 2M HNO_3 or NaOH, 1 g/L of lignin or HMW@Fe_2O_3 and 0.43 g/L of Fe_2O_3_ref, 5 mg/L of initial Cr(VI) concentration, contact time of 2 h.[55]

The potential leaching of iron from the magnetic materials during the Cr(VI) reduction process has been assessed by analysing the supernatants for Fe content using ICP-AES analysis. The results show that iron leaching is negligible at pH values of 5 or higher, with less than 1.5% of iron being released into the solution. However, at pH 2, iron leaching increases, though it doesn't exceed 4.5%, which is still within acceptable limits for many applications. Furthermore, the HMW@Fe_2O_3 composite demonstrates better resistance to acidic conditions than Fe_2O_3_ref, as shown in Figure S1.16, indicating that the lignin component contributes to enhancing the stability of the material under acidic conditions.

In conclusion, the functionalization of lignin with phosphoryl, acetyl groups and presence of magnetite significantly impacts the material performance in Cr(VI) removal, as well as its structural and thermal stability. These modifications enhance the potential of lignin-based biosorbents for environmental remediation applications, especially when coupled with advanced recovery techniques like magnetic separation. Furthermore, the performance of lignin as a biosorbent for Cr(VI) removal is largely influenced by the structure and availability of functional groups on its surface and this has been investigated with further studies. In fact, to better understand the interactions between the adsorbent and the chromium ions in solution, adsorption isotherms have been constructed. These isotherms provide valuable insights into the relationship between the concentration of Cr(VI) in the solution and the amount of chromium adsorbed onto the solid phase when equilibrium is reached. Adsorption isotherms are useful to determine the nature of the adsorption process, whether it is single-layered or multilayered, and whether interactions between adsorbed molecules or between the adsorbate and adsorbent are significant. Two

widely used models to describe adsorption isotherms are the Langmuir and Freundlich models.[26]

Langmuir model assumes that adsorption occurs on a homogeneous surface with no interactions between adsorbed molecules. It describes the adsorption process as single-layer adsorption.[39] The Langmuir isotherm can be expressed with equation (3)[26]:

$$q_e = \frac{q_m C_e K}{1 + K C_e} \qquad (3)$$

where C_e (mg L^{-1}) is the metal residual concentration in solution at the equilibrium, q_e (mg g^{-1}) is the metal concentration adsorbed at equilibrium, q_m (mg g^{-1}) is the maximum adsorption capacity of the solid sorbent, and K is the Langmuir isotherm constant. Unlike the Langmuir model, the Freundlich model assumes that adsorption occurs on a heterogeneous surface and allows for multilayer adsorption. It also takes into account the interactions between the adsorbed molecules and between the adsorbate and adsorbent. The Freundlich isotherm can be described by the equation (4) [26]:

$$q_e = K C_e^{1/n} \qquad (4)$$

n indicating the adsorption intensity. This model is often used when adsorption sites have unequal energies and are not uniformly distributed across the surface. Both the models provide insights into the efficiency and nature of the adsorption process, allowing for a better understanding of how different materials interact with chromium ions in solution, guiding the optimization of biosorbents for environmental clean-up applications.

In the context of adsorption studies, the parameters K and n play significant roles in describing the adsorption behaviour of a material. The constant K represents the distribution coefficient, which quantifies the affinity between the adsorbent and the adsorbate, while n serves as a correction factor that accounts for deviations from ideal adsorption behaviour, indicating the intensity and heterogeneity of the adsorption process. These two parameters are critical for understanding how efficiently a given material adsorbs metal ions from a solution.

Given the superior adsorption capacity of EH lignin, we have aimed to characterize its adsorption isotherm at 30°C. To do so, we have varied the initial concentration of Cr(VI) in the solution, spanning a range from 5 mg L^{-1} to 900 mg L^{-1}, and we have applied a adsorbent concentration of 1 g L^{-1} of EH at pH 2. The system has been allowed to equilibrate over a 24-hours period, after which the concentration of chromium in the solution has been measured using ICP-AES. The experimental data have been subsequently fitted to both the Langmuir and Freundlich adsorption models in order to determine which one can more accurately describe the adsorption behaviour of Cr(VI) onto EH. The results, shown in Figure 1.16, indicate that the Langmuir model provide the best fit to the experimental data, with a very high coefficient of determination (R^2 = 0.998). The Langmuir model, which assumes monolayer adsorption on a surface with homogeneous adsorption sites, yields a maximum adsorption capacity (q_m) of 208.65 ± 2.98 mg g^{-1} and a constant K of $1.33 \times 10^{-2} \pm 5.7 \times 10^{-4}$. The value of K falling between 0 and 1 suggests that the adsorption process occurs favourably under the given conditions,

meaning that as the concentration of Cr(VI) in the solution increases, the adsorption of chromium onto EH lignin becomes more efficient. In contrast, when the experimental data have been fitted to the Freundlich model, which accounts for multilayer adsorption on a heterogeneous surface, the fit is not as good, with a lower R^2 value of 0.97. This suggests that the adsorption of Cr(VI) onto EH lignin is more accurately described by a monolayer model, where the metal ions primarily occupy the available, homogeneous active sites on the lignin surface, rather than forming multiple layers or undergoing complex interactions between adsorbed molecules. These findings underscore the importance of the Langmuir model in describing the adsorption of Cr(VI) by EH lignin, highlighting its potential for effective chromium removal under the conditions tested. The high adsorption capacity and favourable adsorption conditions make EH lignin an attractive material for applications in environmental remediation, particularly for the removal of toxic metal ions from aqueous solutions.

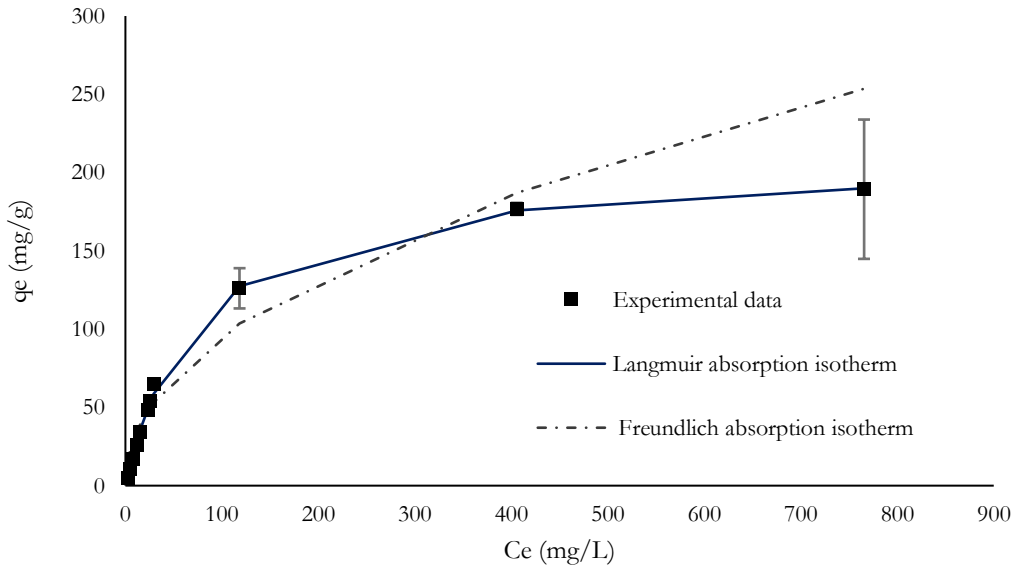

Figure 1.16. Isotherm model fitting of Cr(VI) adsorption on EH lignin as adsorbent.

Conclusions

This study is part of a larger initiative with the aim of developing novel, sustainable applications that transform lignin—an abundant byproduct of the paper-pulp and bioethanol industries—into a valuable resource. Approximately 100 million tons of technical lignin are produced globally each year, highlighting the pressing need to find innovative and environmentally friendly uses for this abundant, yet underutilized, material. Over recent years, there has been a growing interest from both academic researchers and industries in exploring ways to valorise lignin. A key focus has been its potential to address environmental issues, particularly in the remediation of toxic contaminants such as hexavalent chromium (Cr(VI)), which poses serious threats to human health and ecosystems. In this study, we have investigated the effectiveness of two distinct technical lignin—softwood lignin (HMW, derived from the Kraft pulping process) and hardwood enzymatic lignin (EH)—in their ability to reduce Cr(VI) to the less toxic Cr(III) and to lower the overall chromium concentration in contaminated water. Additionally, we have prepared and characterized two functionalized kinds of lignin: acetylated (Ac_Lig) and phosphorylated lignin (P_Lig), in order to assess how modifications of lignin scaffold might impact its performance in water treatment. We have also explored the potential of HMW@Fe_3O_4 hybrid material, combining lignin with magnetite to enhance the efficiency of the removal process. Under standard testing conditions, HMW lignin has demonstrated very good Cr(VI) reduction rate of approximately 80%, completing the reduction process within just 6 hours. When comparing the performance of HMW with the functionalized kinds of lignin (Ac_Lig and P_Lig), it becomes evident that the hydroxyl phenolic groups present in lignin play a pivotal role in the adsorption and reduction of metal ions. The comparison further emphasizes the significance of these functional groups in facilitating the reduction of Cr(VI) and the removal of chromium from the water. The HMW@Fe_3O_4 hybrid material exhibits exceptional performance as a reducing agent, outperforming both HMW and pure magnetite. Under the same conditions, the HMW@Fe_3O_4 composite achieves complete Cr(VI) reduction in just 2 hours, making it a highly efficient material for this application. Interestingly, when tested under the same conditions, the hardwood lignin (EH) demonstrates a remarkable ability to reduce Cr(VI) to Cr(III) quantitatively, showcasing its potential as a highly effective biosorbent. The hardwood lignin (EH) exhibites a remarkable four-fold increase in its ability to adsorb total chromium compared to HMW, achieving up to 60% adsorption. This enhanced chromium reduction and uptake by EH is consistent with its higher surface area and superior coordinating capacity, which is attributed to greater content of syringyl units. This work highlights the promising potential of lignin and its modified forms as sustainable materials for addressing critical environmental challenges, such as the removal of toxic chromium from water. It also underscores the importance of further exploring the functionalization of lignin to enhance its adsorption and reduction capabilities, paving the way for the development of greener, more effective remediation strategies.

Supporting information

Procedures

Procedure S1.1. **UV-Visible measurements.** UV–visible spectra of the Cr(VI)-DPC solutions systems have been collected with a Lambda 465 (PerkinElmer) Diode Array spectrophotometer, equipped with a Peltier Control (PerkinElmer) using the 8-position cell changer as sample holder. 1 cm path length quartz cuvettes have been used in all experiments. The analysed solutions have been prepared by dilution of the Cr(VI) containing supernatants of the lignin reduction tests. The 1,5-diphenyl carbazide (DPC, minimum purity 98 %) solution has been prepared as follows: 20 mg of 1,5-diphhenylcarbazide have been dissolved in 20 ml of ethanol (95 %) (solution A). In a 250 ml flask, 75 mL of 85% H_3PO_4 have been added, and the volume has been brought to 250 mL with distilled water (solution B). The final solution (C) has been obtained by slow addition of 20 mL of the DPC solution to 80 mL of the H_3PO_4 solution. This solution stored at 4°C can be used within 3-4 days. The spectra have been collected in the 200–800 nm range and the calculations for the Cr(VI) concentrations have been done taking in consideration only the intensity at λ = 540 nm (maximum absorption of the Cr(VI)-DPC adduct). To prepare the solutions for the analysis, 1:10 of the total volume of the final solution has been composed by solution C. The rest has been composed by the diluted Cr(VI) solution (dilution factors 1:2.5, 1:20 and 1:100) to reach a final concentration of Cr(VI) in the range of 0.02 and 0.4 ppm (linearity interval of the technique). Calibration lines have been prepared each time the sample solutions were analysed. Those solutions have been obtained in the same way as the samples, but using a 5-ppm stock solution of $K_2Cr_2O_7$ obtaining final samples with concentrations of 0.02, 0.05, 0.10, 0.20, 0.30 and 0.40 ppm. Linear regressions of the point of the calibration lines have been performed using the Origin program.

Procedure S1.2. **Inductively Coupled Plasma Atomic Emission Spectroscopy (ICP-AES).** For solid samples, 5 - 15 mg have been suspended in 5 mL of HNO_3 65% and 1 mL of H_2O_2 30%, then digested in a Milestone microwave MLS-1200 MEGA (digestion sequence: 1 min at 250-Watt, 1 min at 0-Watt, 5 min at 250-Watt, 5 min at 400-Watt, 5 min at 650-Watt, 5 min of cooling). Those solutions have been diluted to 50 mL with bi-distilled water. For liquid samples, the solutions have been either analysed as they were or diluted 1:2 with bi-distilled water and 1:100 with 10% HNO_3 and analysed using an emission spectrometer JY 2501 with coupled plasma induction in radial configuration HORIBA Jobin Yvon (Kyoto, Japan), ULTIMA2 model. Instrumental features: monochromator Model JY 2501; focal length 1 m; resolution 5 pm; nitrogen flow 2 L/min. ICP source: nebulizer Meinhard, cyclonic spraying chamber; argon flow 12 L/min; wavelengths range 160-785 nm; optical bench temperature 32 °C. The wavelength used for quantitative analysis has been chosen by examining the emission line with greater relative intensity, ensuring that there has been no spectral interference with the Argon emission lines. Acquisition parameters: wavelength Fe(nm); Cr (nm): 267.716. Voltage (V): 580; gain: 100. The quantitative analysis has been performed after the acquisition of a calibration line using standard solutions in HNO_3 10% for the solid samples and water for

solutions to simulate the final acidity of the samples. The concentration range of the standards has been varied from 0.05 mg/L to 50 mg/L of Fe and 0.05 mg/L to 70 mg/L of Cr. Data acquisitions and processing have been performed using the ICP JY v 5.2 software (Jobin Yvon). Measurements have been performed in triplicate.

Procedure S1.3. **Synthesis of P_Lig (Phosphorylated HMW Lignin)[57,60]**

The phosphorylation of HMW lignin has been carried out, according to the method outlined by Prieur et al.[60] First, 2.00 g of HMW has been dissolved in 20 mL of THF. After a few minutes, 2.13 g (7.5 mmol) of P_2O_5 has been added to the mixture. The reaction has been then heated under reflux for 8 hours. Following the reaction, the mixture has been quenched by adding cold water in an ice bath. The resulting solid product has been filtered and washed thoroughly with water. The product has been dried at 60 °C overnight and characterized using a variety of techniques, including FT-IR spectroscopy, SEM-EDX, $^{13}C\{^1H\}$-MAS-NMR, and $31P\{^1H\}$-MAS-NMR. The FT-IR (ATR, cm^{-1}) spectrum showed peaks at: n(OH) 3364, n(CH_{alif}) 2936, 2843, n(C–C) 1596, 1512, 1427, and n(C–O) 1266, 1125, 1031. The $^{31}P\{^1H\}$-MAS-NMR (δ, ppm) showed a signal at δ 0.09 ppm, while the $^{13}C\{^1H\}$-MAS-NMR (δ, ppm) displayed signals at δ 146 (C_{Ar}–O), 130–114 (C_{Ar}–C and C_{Ar}–H), 69.7 (C_g), and 55 (CH_3O).

Procedure S1.4. **Synthesis of Ac_Lig (Acetylated HMW Lignin)[57,61]**

According to Buono et al. [61] for the acetylation of HMW lignin, 20.48 g of HMW lignin, which had been dried overnight at 60 °C, have been dissolved in 80 mL of pyridine at 26 °C. The solution has been stirred at 4 Hz under an inert atmosphere. After 10 minutes, 32.2 mL of acetic anhydride has been slowly added in increments of 10 mL each, ensuring the inert atmosphere can be maintained. The reaction has been allowed to proceed at room temperature for 18 hours in a 2 L reactor. Following the reaction, the mixture has been quenched by adding cold 0.4 M HCl, which lead to the precipitation of the product. The precipitate has been filtered and washed with water until the pH became neutral. The product has been then dried at 40 °C in a vacuum oven overnight. Characterization of the acetylated product has been carried out using FT-IR, ^1H-NMR, and $^{13}C\{^1H\}$-NMR spectroscopy. The FT-IR (ATR, cm^{-1}) spectrum showed the following peaks: n(C=O) 1762, 1764; n(C–C) 1592, 1508, 1427; and n(C–O) 1192, 1033. The ^1H-NMR (δ, ppm) spectrum exhibited signals at 8–6 (Ar-H), 3.83–3.41 (CH_3 and OCH_3), 2.24 (acetyl groups bound to aromatic rings), and 1.92 (acetyl groups linked to the aliphatic chain). The $^{13}C\{^1H\}$-NMR (δ, ppm) spectrum displayed signals at 170 (C=O of acetyl groups), 151.53–110.76 (aromatic carbons), 56.26 (OCH_3), and 20.02 (CH_3, acetyl groups).

Tables

Table S1.1. Elemental analysis results for P_Lig samples (triplicate).[57]

	N	C	H	S
P_Lig1	0.14	60.44	5.65	1.56
P_Lig2	0.14	58.57	5.83	1.45
P_Lig3	0.14	60.78	5.69	1.54
HMW	0.13	63.28	6.66	1.91

Figures

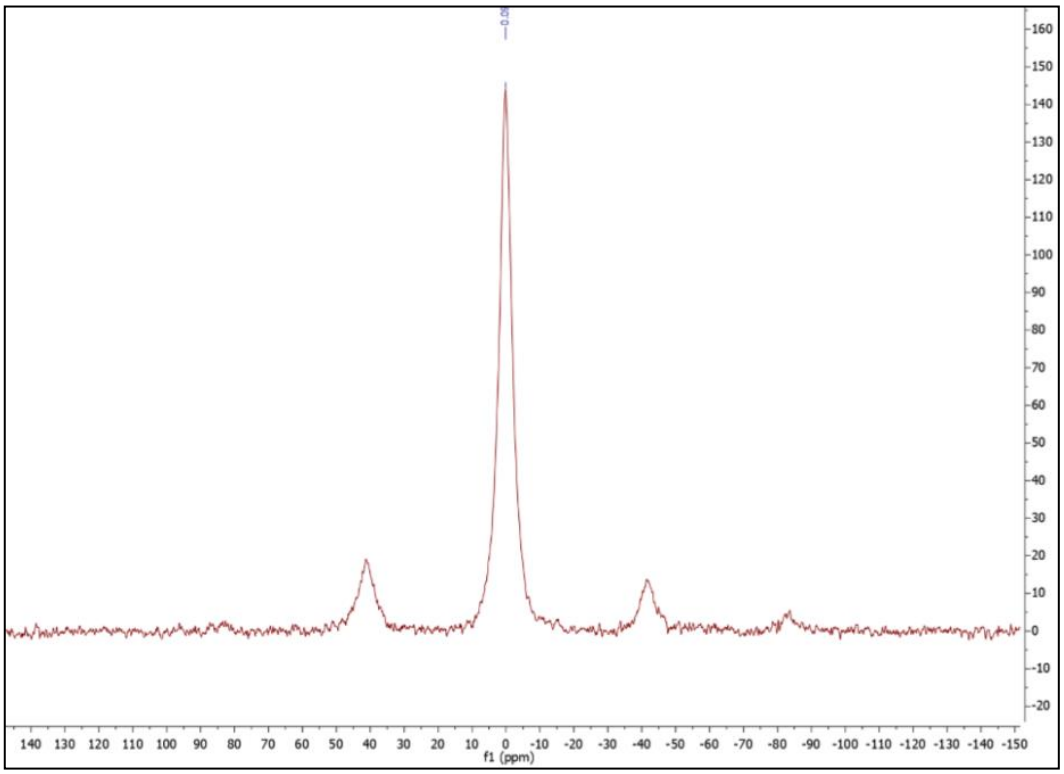

Figure S1.1. $^{31}P\{^{1}H\}$-MAS-NMR spectrum of P_Lig. [55,57]

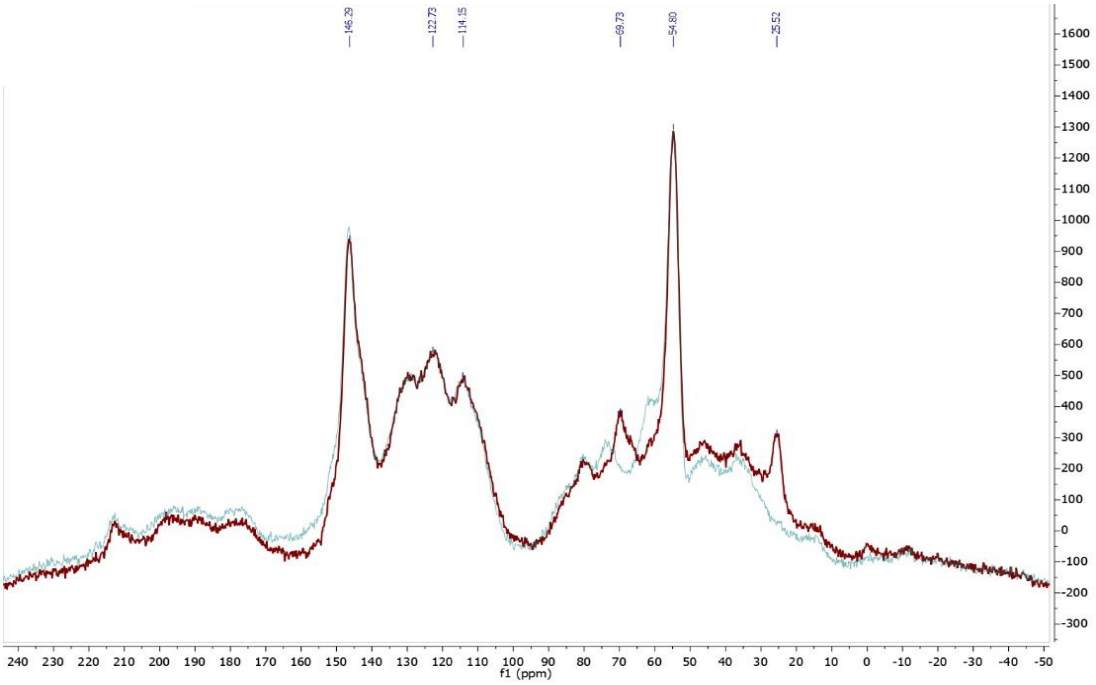

Figure S1.2. Solid state $^{13}C\{^{1}H\}$-NMR of HMW (green) and P_Lig (red). [55,57]

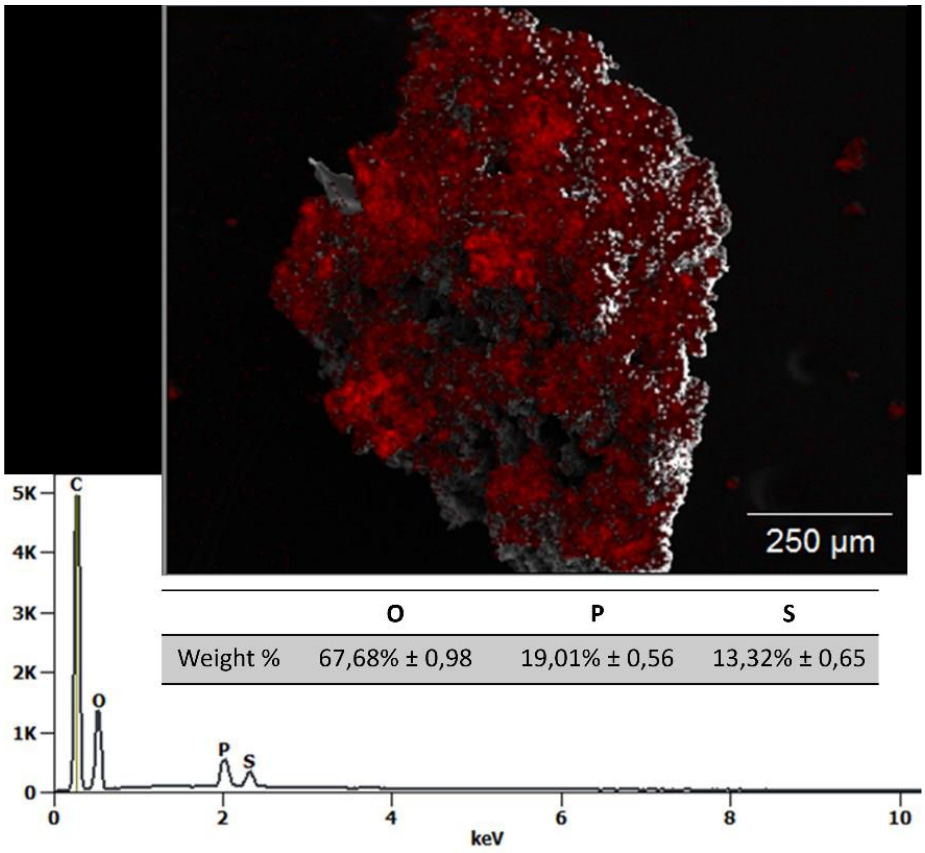

Figure S1.3. EDX analysis and EDX mapping for P_Lig, phosphorous is represented in red.[55,57]

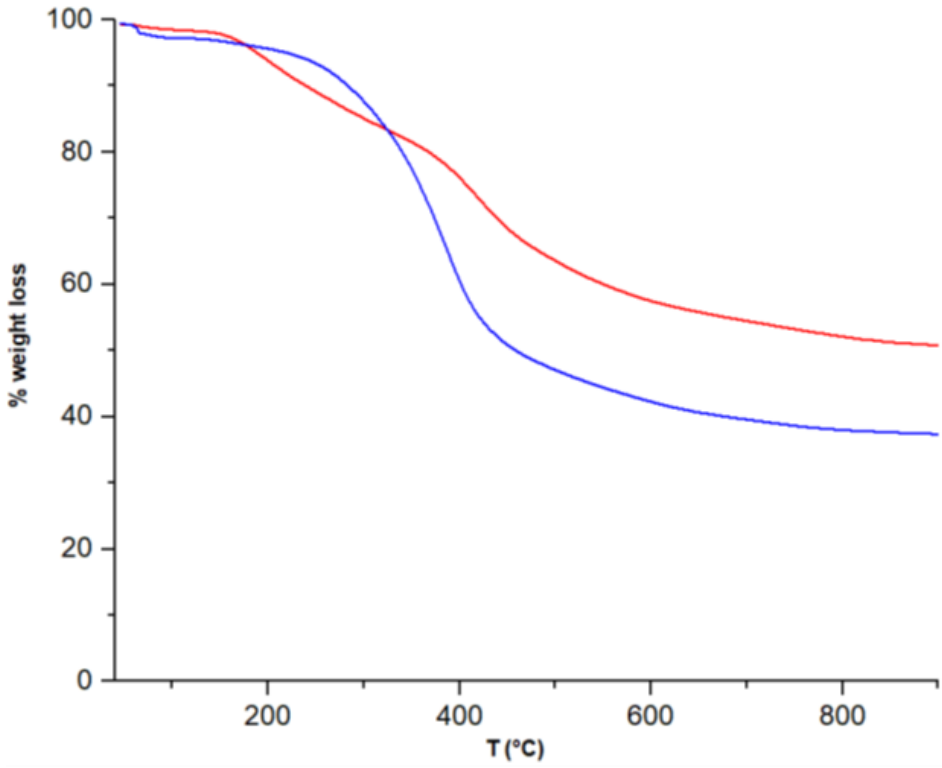

Figure S1.4. TGA profiles of HMW (blue) and P_Lig (red). [55,57]

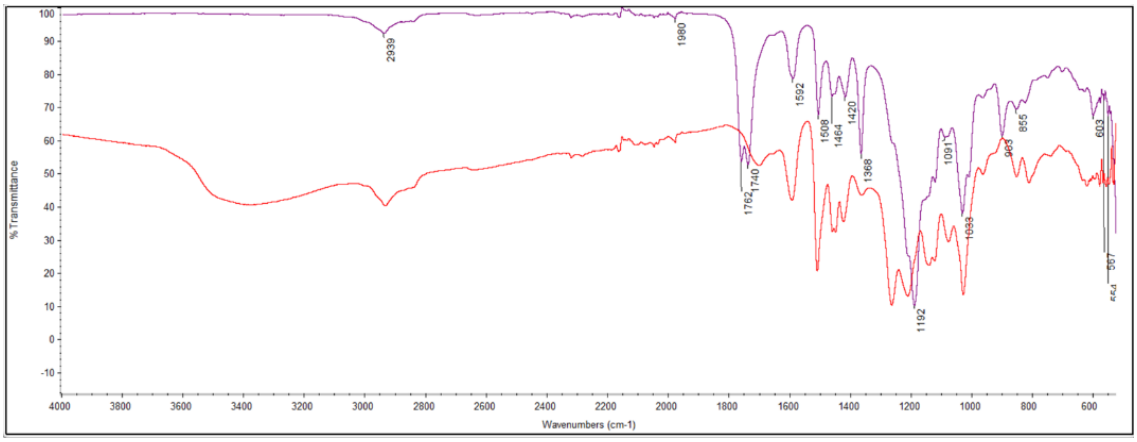

Figure S1.5. FT-IR spectra of HMW (red) and Ac_Lig (purple). [55,57]

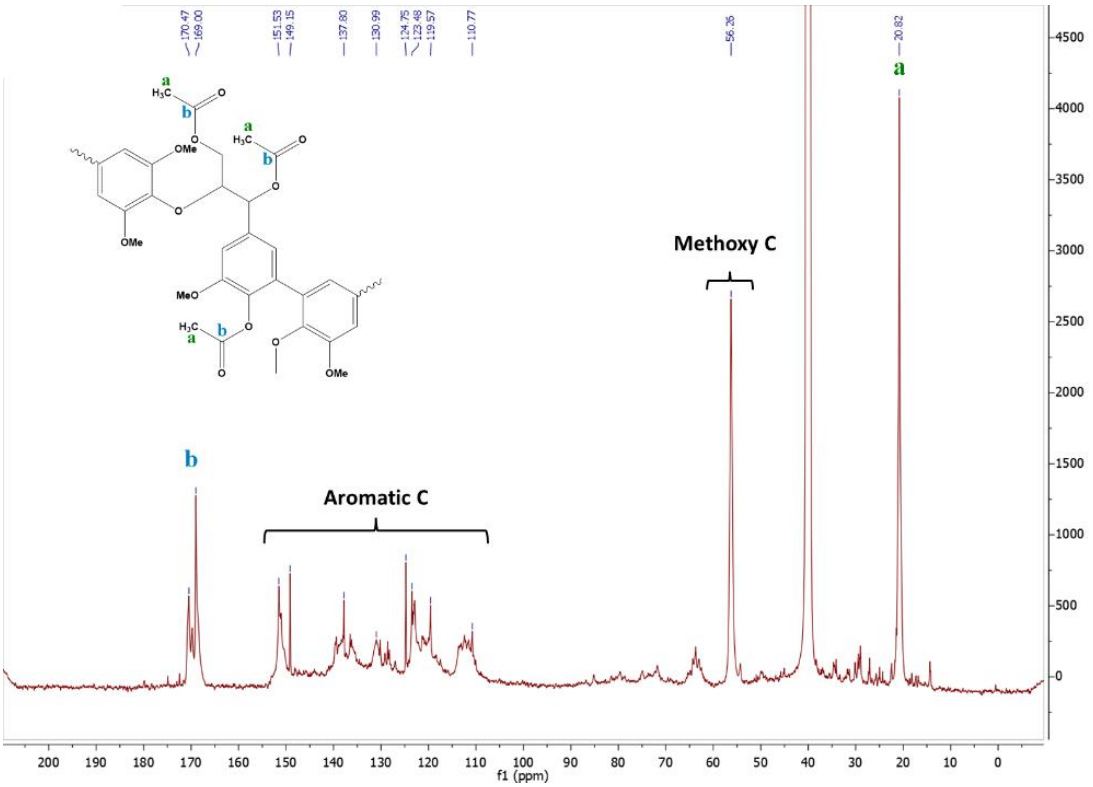

Figure S1.6. $^{13}C\{^{1}H\}$NMR spectrum of Ac_Lig in DMSO-d_6. [55,57]

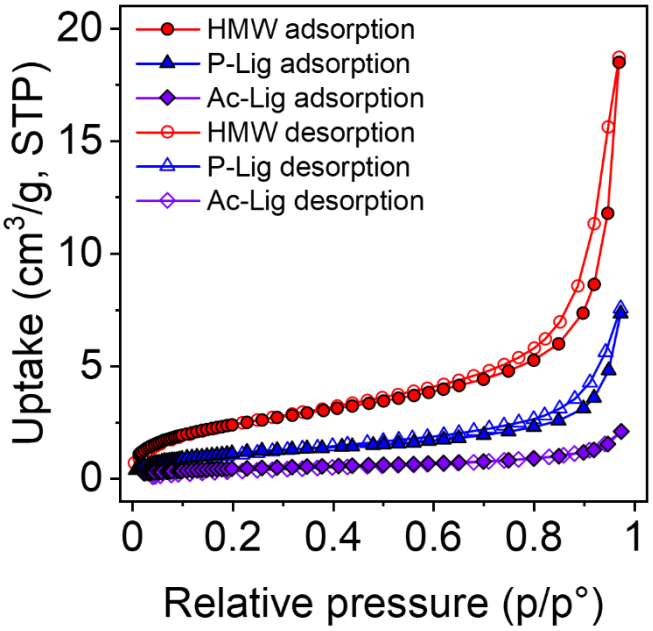

Figure S1.7. N_2 adsorption isotherms collected at 77 K up to 1 bar for sample HMW lignin (red circles), P_Lig (blue triangles) and Ac_Lig (violet diamonds). [55]

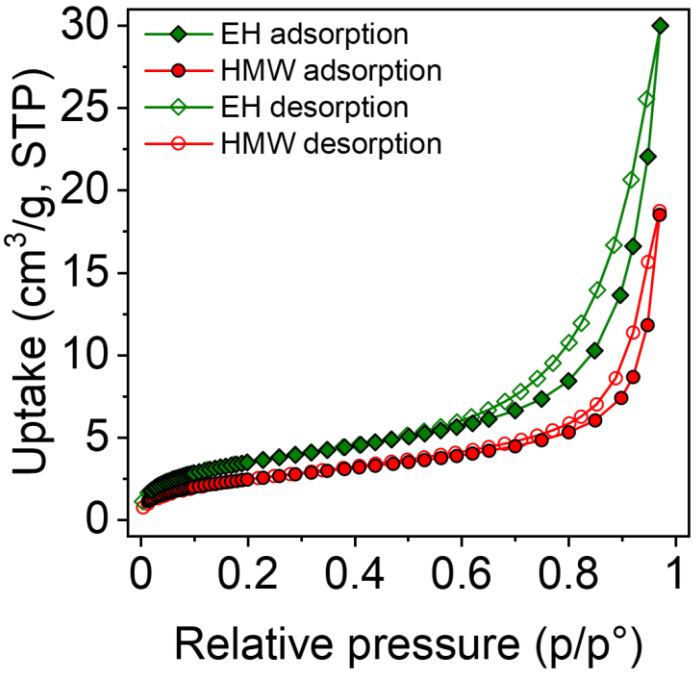

Figure S1.8. N_2 adsorption isotherms collected at 77 K up to 1 bar for sample HMW lignin (red circles), and EH (green diamonds). [55]

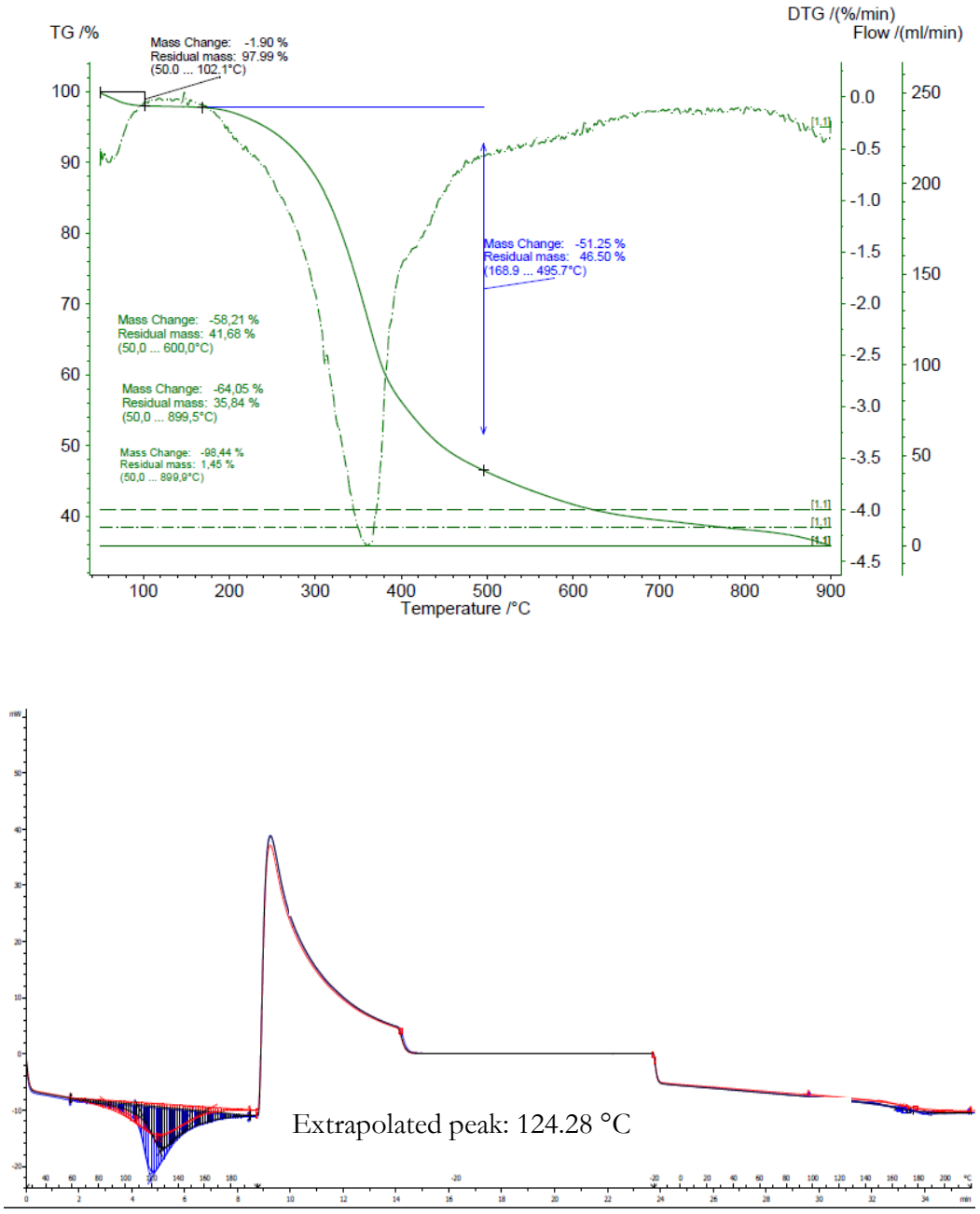

Figure S1.9. TGA and DSC profiles of EH lignin

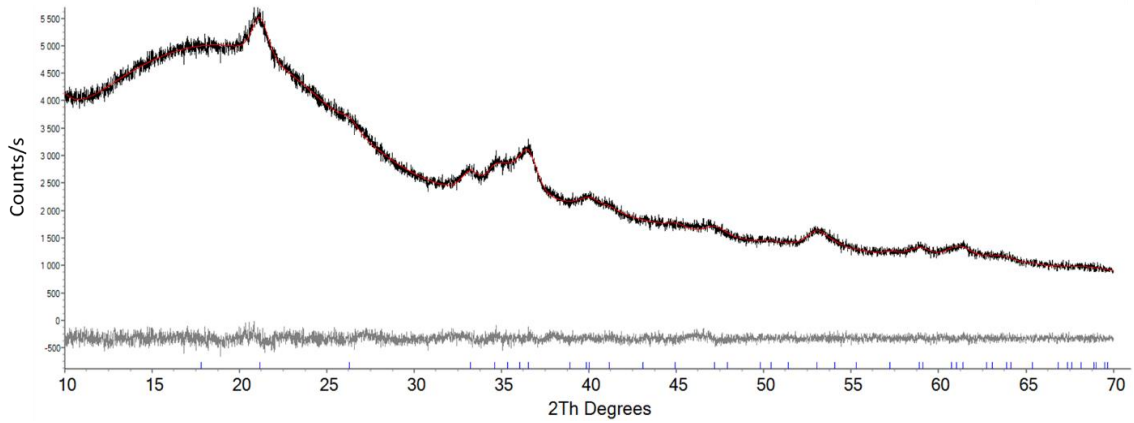

Figure S1.10. Pawley fit (red line) of the experimental PXRD pattern of HMW@goethite (black line). Blue sticks shown the refined positions of goethite Bragg peaks. Differential pattern (gray line; Yobs-Ycal) is also reported. Iron content ≈10%.[55,57]

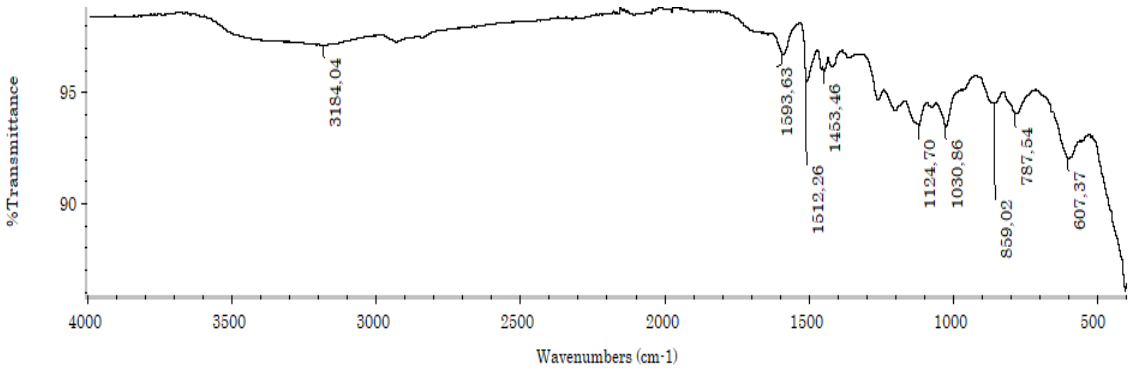

Figure S1.11. Infrared spectrum of HMW@goethite.[55,57]

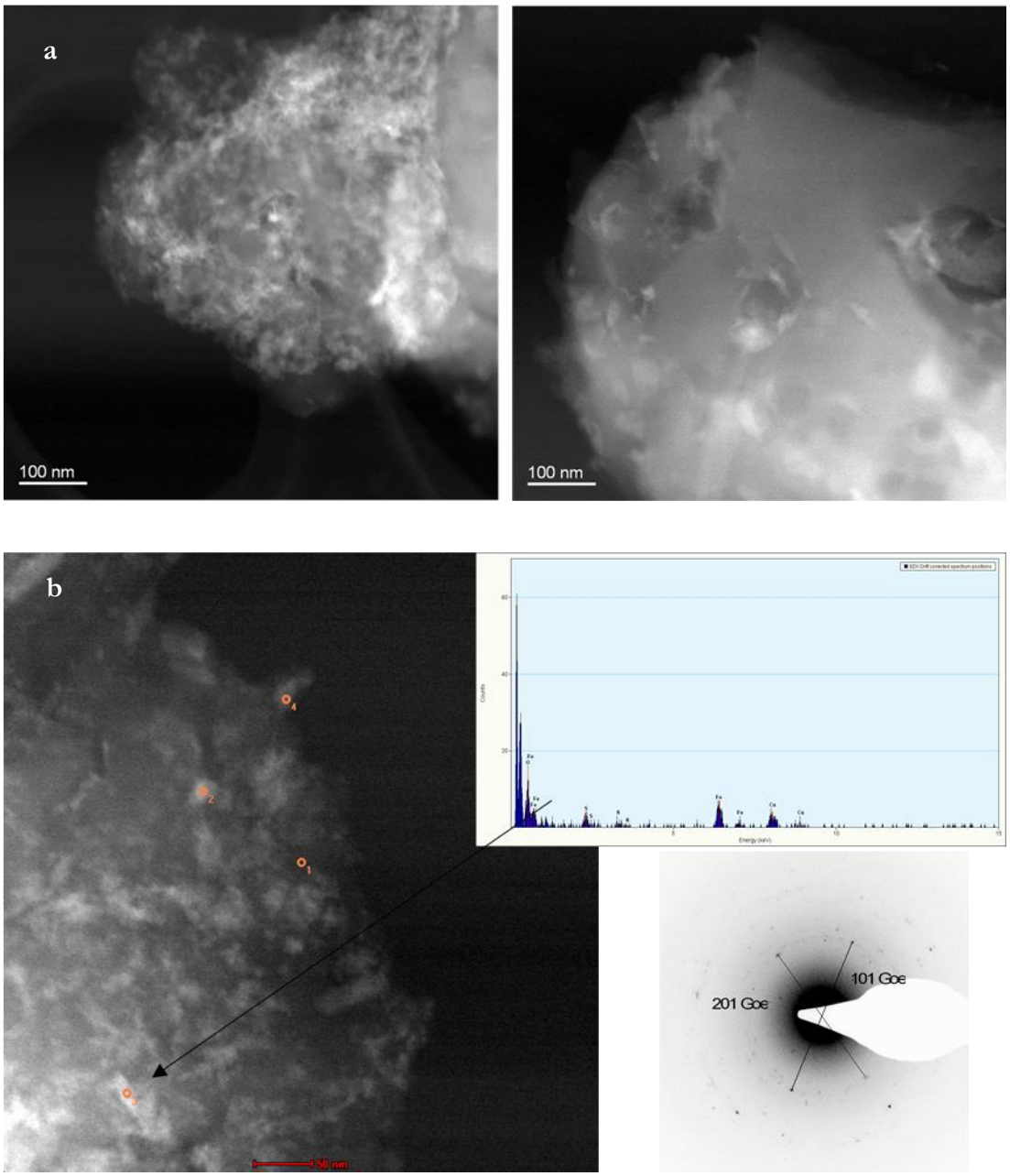

Figure S1.12. a) STEM-HAADF images of HMW@goethite hybrid material. The goethite crystals appear brighter than the lignin matrix. Crystals have elongated form with length in the range 30-80 nm and thickness in the range 10-20 nm. Rounded clusters are present, with a size between 10 and 30 nm. b) X-ray microanalysis on both elongated crystals and rounded clusters confirms the presence of iron. Electron diffraction on selected area mainly corresponds to the presence of goethite.[55,57]

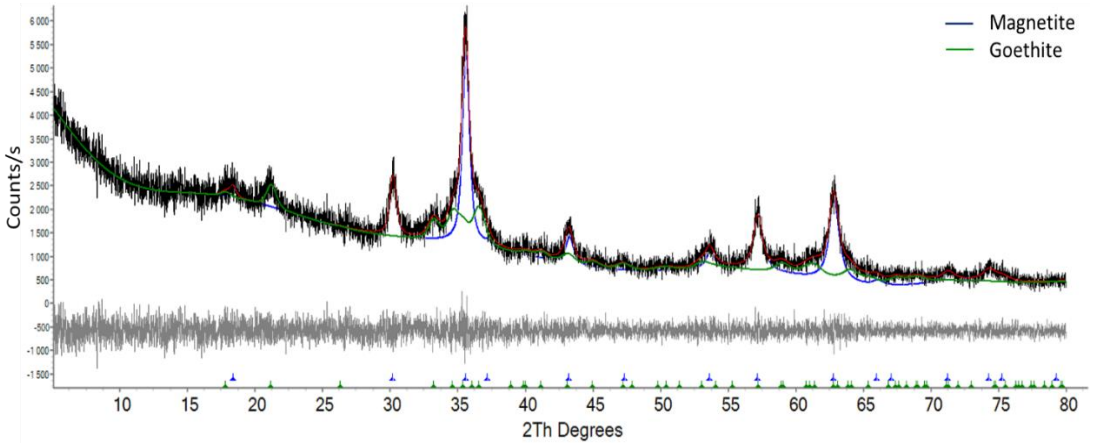

Figure S1.13. Pawley fit (red line) of the experimental PXRD pattern of HMW@Fe_3O_4 (black line). Deconvolution of magnetite (blue line) and goethite (green line) contributions is emphasized. Blue and green sticks shown the refined positions of magnetite and goethite Bragg peaks respectively. Differential pattern (gray line; Y_{obs}-Y_{cal}) is also reported.[55]

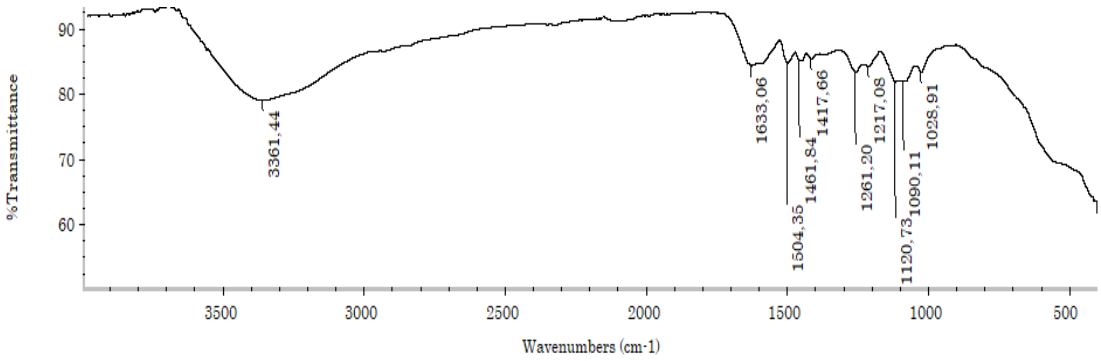

Figure S1.14. Infrared spectrum of HMW@Fe_3O_4.[55]

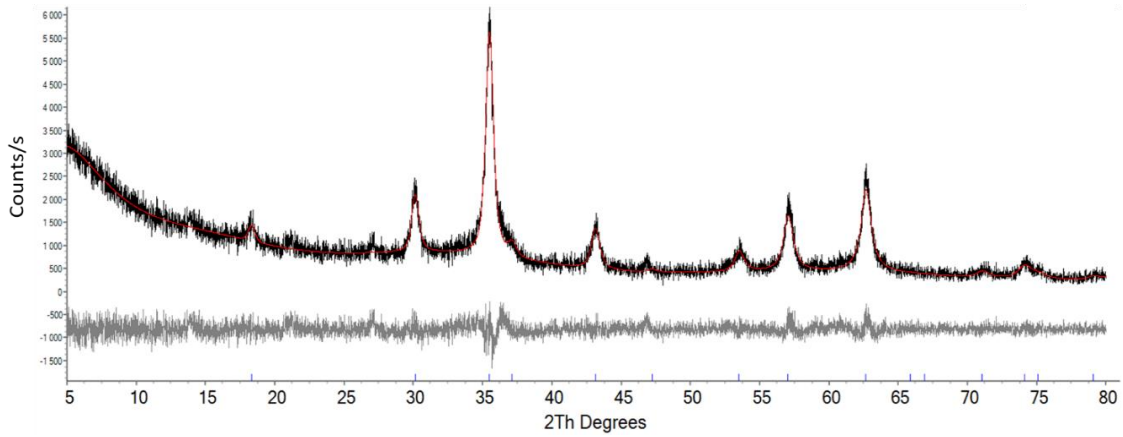

Figure S1.15. Pawley fit (red line) of the experimental PXRD pattern of magnetite (black line). Blue sticks shown the refined positions of magnetite Bragg peaks. Differential pattern (gray line; Y_{obs}-Y_{cal}) is also reported. [55]

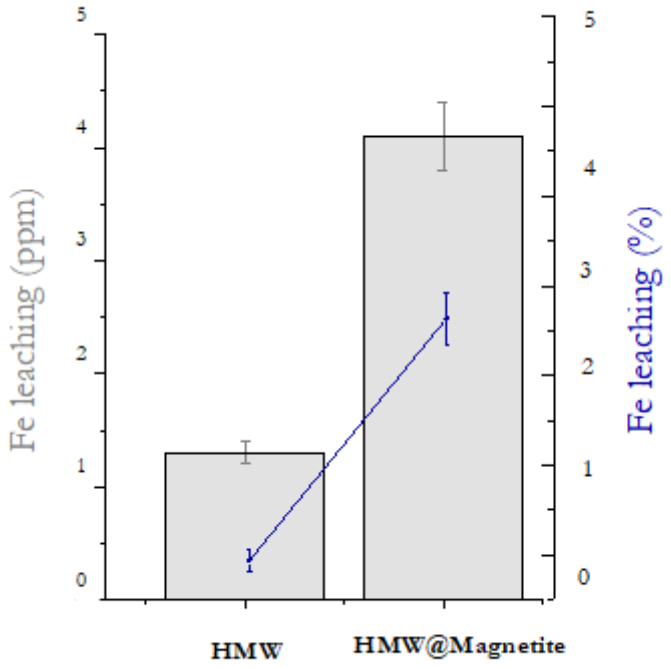

Figure S1.16. Fe leaching for the Cr(VI) removal experiments with Fe-containing adsorbents. Both the leaching in terms of final Fe concentration (grey on the left) and in terms of percentage leaching (blue on the right) are reported.[55]

References

[1] D. Božić, V. Stanković, M. Gorgievski, G. Bogdanović, R. Kovačević, Adsorption of Heavy Metal Ions by Sawdust of Deciduous Trees, *Journal of Hazardous Materials*, **171**, 1–3, 684–692, 2009, DOI: 10.1016/j.jhazmat.2009.06.055.

[2] Y. Bulut et al., Removal of Heavy Metals from Aqueous Solution by Sawdust Adsorption, *J. Environ. Sci.*, **19**, 160–167, 2007, DOI: 10.1016/S1001-0742(07)60026-6.

[3] C. Vasilachi, D. M. Asiminicesei, D. I. Fertu, M. Gavrilescu, Occurrence and Fate of Emerging Pollutants in Water Environment and Options for Their Removal, Water, **13**, 181, 2021, DOI: 10.3390/w13020181.

[4] M. Azam, S. M. Wabaidur, M. R. Khan, S. I. Al-Resayes, M. S. Islam, Heavy Metal Ions Removal from Aqueous Solutions by Treated Ajwa Date Pits: Kinetic, Isotherm, and Thermodynamic Approach, *Polymers,* **14**, 914, 2022, DOI: 10.3390/polym14050914.

[5] M. A. Khan, M. Otero, M. Kazi, A. A. Alqadami, S. M. Wabaidur, M. R. Siddiqui, Z. A. Alothman, S. Sumbul, Unary and Binary Adsorption Studies of Lead and Malachite Green onto a Nanomagnetic Copper Ferrite/Drumstick Pod Biomass Composite, *J. Hazard. Mater.*, **365**, 759–770, 2019, DOI: 10.1016/j.jhazmat.2018.11.072.

[6] A. A. Alqadami, S. M. Wabaidur, B. H. Jeon, M. A. Khan, Co-hydrothermal Valorization of Food Waste: Process Optimization, Characterization, and Water Decolorization Application, *Biomass Convers. Biorefin.*, **13**, 1–11, 2023, DOI: 10.1007/s13399-022-03711-7.

[7] M. Tumolo, V. Ancona, D. De Paola, D. Losacco, C. Campanale, C. Massarelli, V. F. Uricchio, Chromium Pollution in European Water, Sources, Health Risk, and Remediation Strategies: An Overview, *Int. J. Environ. Res. Public Health*, **17**, 5438, 2020, DOI: 10.3390/ijerph17155438.

[8] J. Johnson, L. Schewel, T. E. Graedel, The Contemporary Anthropogenic Chromium Cycle, *Environ. Sci. Technol.*, **40**, 7060, 2006, DOI: 10.1021/es060061i.

[9] S. Fendorf, B. W. Wielinga, C. M. Hansel, Chromium Transformations in Natural Environments: The Role of Biological and Abiological Processes in Chromium(VI) Reduction, *Int. Geol. Rev.,* **42**(8), 691, 2000, DOI: 10.1080/00206810009465107.

[10] J. Kotaś, Z. Stasicka, Chromium Occurrence in the Environment and Methods of its Speciation, *Environmental Pollution,* **107**, 3, 263–283, 2000, DOI: 10.1016/S0269-7491(99)00168-2.

[11] V. Gómez, M. P. Callao, Chromium Determination and Speciation since 2000, *TrAC Trends in Analytical Chemistry*, **25**, 10, 1006–1015, 2006, DOI: 10.1016/j.trac.2006.06.010.

[12] Y. Wang, H. Su, Y. Gu, X. Song, J. Zhao, Carcinogenicity of Chromium and Chemoprevention: a Brief Update, *OncoTargets Ther.*, **10**, 4065–4079, 2017, DOI: 10.2147/OTT.S139262.

[13] M. G. Medeiros, A. S. Rodrigues, M. C. Batoréu, A. Laires, J. Rueff, A. Zhitkovich, Elevated Levels of DNA–Protein Crosslinks and Micronuclei in Peripheral Lymphocytes of Tannery Workers Exposed to Trivalent Chromium, *Mutagenesis*, **18**, 1, 19–24, 2003, DOI: 10.1093/mutage/18.1.19

[14] Guidelines for Drinking-water Quality, fourth edition incorporating the first and second addenda, World Health Organization, 2022.

[15] S. A. Razzak, M. O. Faruque, Z. Alsheikh, L. Alsheikhmohamad, D. Alkuroud, A. Alfayez, S. M. Z. Hossain, M. M. Hossain, A Comprehensive Review on Conventional and Biological-driven

Heavy Metals Removal from Industrial Wastewater, *Environ. Adv.*, **7**, 100168, 2022, DOI: 10.1016/j.envadv.2022.100168.

[16] H. M. Solayman, M. Hossen, A. A. Aziz, N. Y. Yahya, K. H. Leong, L. C. Sim, M. U. Monir, K.-D. Zoh, Performance Evaluation of Dye Wastewater Treatment Technologies: A Review, *J. Environ. Chem. Eng.,* **11**, 109610, 2023, DOI: 10.1016/j.jece.2023.109610.

[17] A. S. S. Ahmed, M. M. Billah, M. M. Ali, M. K. A. Bhuiyan, L. Guo, M. Mohinuzzaman, M. B. Hossain, M. S. Rahman, M. S. Islam, M. Yan, W. Cai, Microplastics in Aquatic Environments: A Comprehensive Review of Toxicity, Removal, and Remediation Strategies, *Sci. Total Environ*., **876**, 162414, 2023, DOI: 10.1016/j.scitotenv.2023.162414.

[18] M. Owlad, M. K. Aroua, W. A. W. Daud, S. Baroutian, Removal of Hexavalent Chromium-Contaminated Water and Wastewater: A Review, *Water, Air, Soil Pollut*., **200**, 59, 2009, DOI: 10.1007/s11270-008-9893-7.

[19] P. Malaviya, A. Singh, Physicochemical Technologies for Remediation of Chromium-Containing Waters and Wastewaters, *Crit. Rev. Environ. Sci. Technol*., **41**, 1111, 2011, DOI: 10.1080/10643380903392817.

[20] P. C. Manuel, M. M. Jose, T. M. Rosa, Chromium (VI) Removal with Activated Carbons, *Water Res.,* **29**, 2174–2180, 1995, DOI: 10.1016/0043-1354(95)00035-J.

[21] N. R. Bishnoi, M. Bajaj, N. Sharma, A. Gupta, Adsorption of Cr (VI) on Activated Rice Husk Carbon and Activated Alumina, *Bioresour. Technol*., **91**, 305–307, 2004, DOI: 10.1016/j.biortech.2003.07.004.

[22] V. K. Garg, R. K. Gupta, Adsorption of Chromium from Aqueous Solution on Treated Sawdust, *Bioresour. Technol*., **92**, 79–81, 2004, DOI: 10.1016/j.biortech.2003.07.004.

[23] D. Gang, S. Hu, K. Banerji, T. E. Clevenger, Modified Poly-(4-vinylpyridine) Coated Silica Gel. Fast Kinetics of Diffusion-controlled Sorption of Chromium (VI), *Ind. Eng. Chem. Res*., **40**, 1200–1204, 2001, DOI: 10.1021/ie000771b.

[24] J. Bayuo, An Extensive Review on Chromium (VI) Removal using Natural and Agricultural Wastes Materials as Alternative Biosorbents*, J. Environ. Health Sci. Eng*., **19**, 1193, 2021, DOI: 10.1007/s40201-021-00641-w.

[25] A. Guleria, G. Kumari, E. C. Lima, D. K. Ashish, V. Thakur, K. Singh, Removal of Inorganic Toxic Contaminants from Wastewater using Sustainable Biomass: A Review, *Sci. Total Environ*., **823**, 153689, 2022, DOI: 10.1016/j.scitotenv.2022.153689.

[26] B. Saha, C. Orvig, Biosorbents for Hexavalent Chromium Elimination from Industrial and Municipal Effluents, *Coord. Chem. Rev.,* **254**, 2959, 2010, DOI: 10.1016/j.ccr.2010.06.005.

[27] Z. Zhang, Y. Chen, D. Wang, D. Yu, C. Wu, Lignin-based Adsorbents for Heavy Metals, *Industrial Crops and Products,* **158**, 113026, 2021, DOI: 10.1016/j.indcrop.2020.113026.

[28] M. F. E. Zayed, A. E. Khalil, Application of Modified Biosorbents for Removal of Toxic Heavy Metals from Aqueous Solutions, *J. Environ. Manag.,* **245**, 170–185, 2019, DOI: 10.1016/j.jenvman.2019.05.031.

[29] H. Harmita, K. G. Karthikeyan, and X. Pan, Copper and Cadmium Sorption onto Kraft and Organosolv Lignins, *Bioresour. Technol.*, **100**, 6183, 2009, DOI: 10.1016/j.biortech.2009.06.093

[30] Y. Wu, S. Zhang, X. Guo, and H. Huang, Adsorption of Chromium(III) on Lignin, *Bioresour. Technol.*, **99**, 7709, 2008, DOI: 10.1016/j.biortech.2008.01.069.

[31] A. B. Albadarin, A. H. Al-Muhtaseb, N. A. Al-laqtah, G. M. Walker, S. J. Allen, and M. N. M. Ahmad, Biosorption of Toxic Chromium from Aqueous Phase by Lignin: Mechanism, Effect of other Metal Ions and Salts, *Chem. Eng. J.*, **169**, 20, 2011, DOI: 10.1016/j.cej.2011.02.044.

[32] Y. Ge and Z. Li, Application of Lignin and Its Derivatives in Adsorption of Heavy Metal Ions in Water: a Review, *ACS Sustainable Chem. Eng.*, **6**, 7181, 2018, DOI: 10.1021/acssuschemeng.8b01345.

[33] P. Miretzky and A. F. Cirelli, Cr(VI) and Cr(III) Removal from Aqueous Solution by Raw and Modified Lignocellulosic Materials: a Review, *J. Hazard. Mater.*, **180**, 1, 2010, DOI: 10.1016/j.jhazmat.2010.04.060.

[34] M. Bansal, D. Singh and V. K. Garg, A Comparative Study for the Removal of Hexavalent Chromium from Aqueous Solution by Agriculture Wastes Carbons, *J. Hazard. Mater.*, **171**, 83, 2009, DOI: 10.1016/j.jhazmat.2009.05.124.

[35] N. Fiol, I. Villaescusa, M. Martinez, N. Miralles, J. Poch and J. Serarols, Biosorption of Cr(VI) Using Low Cost Sorbents, *Environ. Chem. Lett.*, **1**, 135, 2003, DOI: 10.1007/s10311-003-0027-6.

[36] X. Shi, Y. Qiao, X. An, Y. Tian and H. Zhou, High-capacity Adsorption of Cr(VI) by Lignin-based Composite: Characterization, Performance and Mechanism, *Int. J. Biol. Macromol.*, **159**, 839, 2020, DOI:10.1016/j.ijbiomac.2020.05.130.

[37] Y. Wu, S. Zhang, X. Guo and H. Huang, Adsorption of Chromium(III) on Lignin, *Bioresour. Technol.*, **99**, 7709–7713, 2008, DOI: 10.1016/j.biortech.2008.01.069.

[38] D. Jin, W. Dong, H. Zhang, Y. Ci, L. Hou, L. zang, F. Kong and L. Lucia, Comparison of Structural Characteristics of Straw Lignins by Alkaline and Enzymatic Hydrolysis, *BioResources,* **14**(3), 5615, 2019, DOI: 10.15376/biores.14.3.5615-5632.

[39] H. Zhang and H. Zhou, Industrial Lignins: the Potential for Efficient Removal of Cr(VI) from Wastewater, *Environ. Sci. Pollut. Res.*, 10467, 2022**,** DOI: 10.1007/s11356-021-16402-z.

[40] H. W. Kwak, H. Lee, and K. H. Lee, Surface-modified Spherical Lignin Particles with Superior Cr(VI) Removal Efficiency, *Chemosphere*, **239,** 124733, 2020, DOI: 10.1016/j.chemosphere.2019.124733.

[41] L. Tan, Y. Zhang, W. Zhang, R. Zhao, Y. Ru, and T. Liu, One-pot Method to Prepare Lignin-based Magnetic Biosorbents for Bioadsorption of Heavy Metal Ions, *Ind. Crops Prod.*, **176,** 114387, 2022**,** DOI: 10.1016/j.indcrop.2021.114387.

[42] V. Sinisi, P. Pelagatti, M. Carcelli, A. Migliori, L. Mantovani, L. Righi, G. Leonardi, S. Pietarinen, C. Hubsch, and D. Rogolino, A Green Approach to Copper-Containing Pesticides: Antimicrobial and Antifungal Activity of Brochantite Supported on Lignin for the Development of Biobased Plant Protection Products, *ACS Sustainable Chem. Eng.*, **7**, 3213, 2019**,** DOI: 10.1021/acssuschemeng.8b05135.

[43] C. Gazzurelli, A. Migliori, P. P. Mazzeo, M. Carcelli, S. Pietarinen, G. Leonardi, A. Pandolfi, D. Rogolino, P. Pelagatti, Making Agriculture More Sustainable: An Environmentally Friendly Approach to the Synthesis of Lignin@Cu Pesticides, *ACS Sust. Chem. & Eng.*, **8**, 11896-11907, 2020, DOI: 10.1021/acssuschemeng.0c04645.

[44] C. Gazzurelli, M. Carcelli, P. P. Mazzeo, C. Mucchino, A. Pandolfi, A. Migliori, S. Pietarinen, G. Leonardi, D. Rogolino, and P. Pelagatti, Exploiting the Reducing Properties of Lignin for the Development of an Effective Lignin@Cu_2O Pesticide, *Adv. Sustainable Syst.*, **6**, 2200108, 2022, DOI: 10.1002/adsu.202200108.

[45] A. N. Tavtorkin, S. A. Korchagina, P. D. Komarov, A. A. Vinogradov, A. V. Churakov, I. E. Nifant'ev, M. E. Minyaev, Chromium Complexes Bearing Disubstituted Organophosphate Ligands and their Use in Ethylene Polymerization. *Acta Crystallogr. C Struct. Chem.*, **76**(Pt 1), 93–103, 2020, DOI: 10.1107/S2053229619015699.

[46] Z. Song, Li, W. Liu, W. Yang, Y. Wang, N. Wang, H., H. Gao, Novel Magnetic Lignin Composite Sorbent for Chromium (VI) Adsorption, *RSC Adv.*, **5**, 13028, 2015. DOI: 10.1039/c4ra15546g.

[47] Reddy, D. H. K., & Lee, S. M., Application of Magnetic Chitosan Composites for the Removal of Toxic Metal and Dyes from Aqueous Solutions. *Adv. Colloid Interface Sci.*, **201**, 68, 2013. DOI: 10.1016/j.cis.2013.10.002.

[48] Y. J. Jiang, X. Y. Yu, T. Luo, Y. Jia, J. H. Liu, X. J. Huang, γFe2O3 Nanoparticles Encapsulated Millimeter-sized Magnetic Chitosan Beads for Removal of Cr(VI) from Water: Thermodynamics, Kinetics, Regeneration, and Uptake Mechanisms. *J. Chem. Eng. Data*, **58**, 3142, 2013. DOI: 10.1021/je400603p.

[49] Y. M. Hao, C. Man, Z. B. Hu, Effective Removal of Cu(II) Ions from Aqueous Solution by Amino-Functionalized Magnetic Nanoparticles. *J. Hazard. Mater.*, **184**, 392, 2010. DOI: 10.1016/j.jhazmat.2010.08.048.

[50] J. Hu, G.H. Chen, I.M.C. Lo, Selective Removal of Heavy Metals from Industrial Wastewater using Maghemite Nanoparticle: Performance and Mechanisms, *J. Environ. Eng.*, **132**(7), 709–715, 2006, DOI: 10.1061/(ASCE)0733-9372(2006)132:7(709).

[51] M. Ozmen, K. Can, G. Arslan, A. Tor, Y. Cengeloglu, M. Ersoz, Adsorption of Cu (II) from Aqueous Solution by Using Modified Fe_3O_4 Magnetic Nanoparticles, *Desalination*, **254,** 162–169, 2010, DOI: 10.1016/j.desal.2009.11.043.

[52] S. P. Schwaminger, C. Syhr and S. Berensmeier, Controlled Synthesis of Magnetic Iron Oxide Nanoparticles: Magnetite or Maghemite?, *Crystals*, **10**, 214, 2020**,** DOI: 10.3390/cryst10030214.

[53] M. S. Elovitz, W. Fish, Redox Interactions of Cr(VI) and Substituted Phenols: Products and Mechanism, *Environ. Sci. Technol.*, **29**(8), 1746-1751, 1995, DOI: 10.1007/s11356-021-16402-z.

[54] A. Santos**,** P. Yustos**,** A. Quintanilla**,** S. Rodríguez**,** F. García-Ochoa, Route of the catalytic Oxidation of Phenol in Aqueous Phase*, Appl. Catal. B Environ.*, **39**(2), 97-113, 2002**,** DOI: 10.1016/S0926-3373(02)00087-5.

[55] M. Vescovi, M. Melegari, C. Gazzurelli, M. Maffini, C. Mucchino, P. P. Mazzeo, M. Carcelli, J. Perego, A. Migliori, G. Leonardi, S. Pietarinen, P. Pelagatti and D. Rogolino, Industrial Lignins as Efficient Biosorbents for Cr(VI) Water Remediation: Transforming a Waste into an Added Value Material, *RSC Sustainability*, **1,** 1423, 2023, DOI: 10.1039/D3SU00081H

[56] G. Donmez, Z. Asku, Removal of Chromium (VI) from Saline Wastewater by Dunaliella Species, *Process Biochemistry*, **38** (7): 751–762, 2002. DOI: 10.1016/S0032-9592(02)00007-4.

[57] C. Gazzurelli, Combining Lignin with Metals for Agrochemical Applications, PhD thesis, 2021

[58] A. Karrasch, E. Wawrzyn, B. Schartel e C. Jäger, Solid-state NMR on Thermal and Fire Residues of Bisphenol A Polycarbonate/Silicone Acrylate Rubber/Bisphenol A Bis(diphenyl-phosphate)/(PC/SiR/BDP) and PC/SiR/BDP/Zinc borate (PC/SiR/BDP/ZnB) - Part I: PC Charring and the Impact of BDP and ZnB, *Polym. Degrad. Stab.*, **95**, 2525, 2010, DOI: 10.1016/j.polymdegradstab.2010.07.030.

[59] S. Y. Lin e C. W. Dence, Methods in Lignin Chemistry*, Springer Series in Wood Science: Wood Structure and Environment,* 1992

[60] B. Prieur, M. Meub, M. Wittemann, R. Klein, S. Bellayer, G. Fontainea e S. Bourbigot, Phosphorylation of Lignin: Characterization and Investigation of the Thermal Decomposition, *RSC Adv.*, **7**, 16866, 2017, DOI: 10.1039/c7ra00295e.

[61] P. Buono, A. Duval, P. Verge, L. Averous e Y. Habibi, New Insights on the Chemical Modification of Lignin: Acetylation versus Silylation, *ACS Sustainable Chem. Eng.*, **4**, 5212, 2016, DOI: 10.1021/acssuschemeng.6b00903.

[62] N. Akiba, A. T. Omori, I. Gaubeur, Kraft Lignin and its Derivatives – A Study on the Adsorption of Mono and Multielement Metals, Potential Use for Noble Metal Recycling and an Alternative Material for Solid Base Catalyst, *Chemosphere*, **308**, 136538, 2022, DOI: 10.1016/j.chemosphere.2022.136538.

[63] M. Usman, M. Abdelmoula, P. Faure, C. Ruby, K. Hanna, Transformation of Various Kinds of Goethite into Magnetite: Effect of Chemical and Surface Properties, *Geoderma*, **9**, 197, 2013, DOI:10.1016/j.geoderma.2012.12.015

Chapter 2:
Lignin@ZnO

The agricultural sector is facing numerous global challenges, including climate change, urbanization, the sustainable use of resources, and environmental issues such as pesticide and fertilizer drainage. As the world population continues to grow rapidly, food demand is surging. By 2050, the global population is expected to rise from 6 billion to 9 billion, further intensifying environmental issues.[1] Among the most urgent concerns, it is possible to find the overexploitation of soils for farming and widespread deforestation to create new agricultural land. One of the major concerns is the spread of pathogens that can drastically reduce soil fertility and even destroy large swaths of farmland, resulting in substantial economic losses and threatens food security. To address these challenges, the adoption of more efficient and sustainable agricultural techniques is essential.[2] Previous studies by our research group have demonstrated the effectiveness of an approach focused on the development of sustainable hybrid lignin-copper-based pesticides,[3,4,5] with very promising *in vivo* results. As already state in the general introduction section, lignin is a highly versatile organic matrix that can be used to synthesize hybrid organic-inorganic materials incorporating inorganic nanoparticles. The beneficial antioxidant, antibacterial and antifungal features of lignin can be further enhanced by embedding crystalline inorganic phases within the lignin matrix, resulting in improved bioactive materials. Building on this work, we have now focused on the synthesis of lignin-based materials incorporating zinc oxide nanoparticles. Pesticides are the primary solution for managing pests, and the development of safer, more efficient plant protection products remains a key focus in scientific research. Various substances have been explored for their ability to control fungi, moulds and bacteria, including organic compounds and metals like copper, iron, and zinc, which have long been recognized for their antibacterial properties.[6,7] Nanotechnology is playing a transformative role in agriculture and food production, offering significant potential to improve conventional farming practices. A major issue with agrochemicals is that much of the applied pesticides and fertilizers are lost due to leaching, drifting, hydrolysis, photolysis, and microbial degradation, meaning they often fail to reach their intended targets. The use of nanotechnology in farming is gaining importance, as it enables the efficient control and targeted release of pesticides, herbicides, and fertilizers. The synthesis of nanoparticles within a biopolymeric matrix such as lignin can promote a slow release and efficient results at low metal concentration, overcoming these issues. Nanotechnology involves the study of nanoparticles, which have sizes smaller than 100 nanometres. These nanoparticles, with their high surface area-to-volume ratio, often exhibit greater activity over their bulk counterpart. By leveraging the biological properties of transition metals—such as redox reactions, hydroxylation, and electron transport—along with the unique characteristics of nanoscale materials, metal-based nanoparticles could enhance antibacterial effectiveness. The bactericidal action of these nanoparticles is amplified through better control over the release of active ionic species and their ability to generate Reactive Oxygen Species (ROS). They may also interfere with bacterial processes at the subcellular level and, if positively charged, can disrupt the bacterial electron transport chain. Despite their proven efficacy, metal nanoparticles raise concerns due to their potential toxicity to humans. In fact, the same mechanisms that make them effective against bacteria—such as ROS generation, gene regulation alteration, membrane disruption, and metabolite binding—can also harm human cells. One of the main challenges is that the concentration needed to achieve

antimicrobial effects often exceeds the threshold at which toxicity becomes a risk. Moreover, limited research and the complexity of nanoparticle systems, combined to lack of systematic studies in the existing literature, make difficult to assess their safety and effectiveness comprehensively.[8] ZnO nanoparticles have garnered significant research interest due to their unique semiconducting, optical, and piezoelectric properties. These characteristics have spurred extensive studies into their potential use in nano-electronic and nano-optical devices. Furthermore, the optical properties of ZnO nanomaterials can be fine-tuned by doping them with specific elements, opening up a wide range of applications.[9] ZnO is commonly used as an additive in several materials and products, such as ceramics, glass, cement, rubber (e.g. car tires), lubricants, paints, ointments, adhesives, plastics, sealants, pigments, food (as a source of zinc), batteries, ferrites, and fire retardants.[10]

Zinc oxide (ZnO) is widely used as a semiconductor due to its unique properties, such as excellent transparency, a direct wide band gap of 3.3 eV in the near-UV spectrum, and a high excitonic binding energy of 60 meV at room temperature. Additionally, ZnO exhibits natural n-type electrical conductivity.[11] The wide band gap plays a critical role in determining ZnO electrical and optical properties, including its conductivity and absorption behaviour. Notably, its conductivity can be enhanced by doping with other metals. These characteristics have spurred extensive studies into their potential use in nano-electronic and nano-optical devices. Furthermore, the optical properties of ZnO nanomaterials can be fine-tuned by doping them with specific elements, opening a wide range of applications.

Zinc oxide has garnered great interest due to its environmental friendliness and biocompatibility. Given the high demand for pesticides and fertilizers, studies on the effects of zinc oxide on plants have been conducted in recent years.[12] When compared to conventional compounds, metal oxide nanoparticles are more stable under harsh conditions, exhibit antimicrobial properties at lower concentrations, and are generally considered safe for human use.[13] Among these, ZnO nanoparticles are recognized as potent antibacterial agents and the antibacterial and antifungal properties of ZnO could be exploited in agriculture to protect crops. [14] ZnO nanoparticles (ZnO NPs) exhibit diverse morphologies and significant antibacterial activity against a wide range of bacterial species, as extensively studied in the literaute.[15,16,17] At the nanometres scale, ZnO antimicrobial properties are enhanced, allowing it to interact with bacterial surfaces or even penetrate their core. Studies also highlight a correlation between the nanoparticles morphology and their antibacterial efficacy, underscoring the importance of shape in optimizing their performance. Wahab et al.[15] employed a non-hydrolytic solution process using zinc acetate dihydrate to prepare ZnO NPs. This method resulted in spherical structures that exhibited strong antibacterial activity against diverse pathogens. Similarly, spherical ZnO NPs were synthesized[16] using a soft chemical solution process and were then used to treat bacteria (*E. coli, S. aureus, P. aeruginosa, B. subtilis, and S. acidaminiphila*) and cancer cells (HepG2 and MCF-7 cell lines). In contrast, Stanković et al.[17] synthesized ZnO powder hydrothermally with different stabilizing agents, resulting in various nanostructures. The synthesized ZnO exhibited nanorods with hexagonal prismatic and pyramid-like shapes, along with some spherical and ellipsoid forms. Significant differences

in the antibacterial activity depending on the morphology, size and the specific surface area of ZnO NPs have been observed, with the nanospherical particles giving the best results. The antimicrobial mechanisms of nanomaterials could primarily be attributed to their high surface-to-volume ratio[18] leading to enhanced particles surface reactivity and unique physicochemical properties. Once inside the cell, ZnO NPs triggers distinct bactericidal mechanisms, and although the exact mechanisms are still debated, several models have been proposed. One mechanism involves the electrostatic interactions between ZnO NPs and bacterial cell walls, leading to damage of bacterial cell integrity;[13,19,20] the release of antimicrobial Zn^{2+} ions,[21,22,23] which accumulate within bacterial cells;[14,19,24] the formation of reactive oxygen species (ROS)[13,25,26] like hydrogen peroxide (H_2O_2), hydroxyl radicals (OH-), and superoxide ($O_2^{\bullet-}$). (Figure 2.1). ROS plays a key role in several mechanisms, including damage of the cell wall, increased membrane permeability, internalization of nanoparticles due to a loss of proton motive force, and the uptake of toxic dissolved zinc ions. These processes lead to mitochondrial dysfunction, intracellular leakage, and altered gene expression related to oxidative stress, ultimately resulting in cell death.

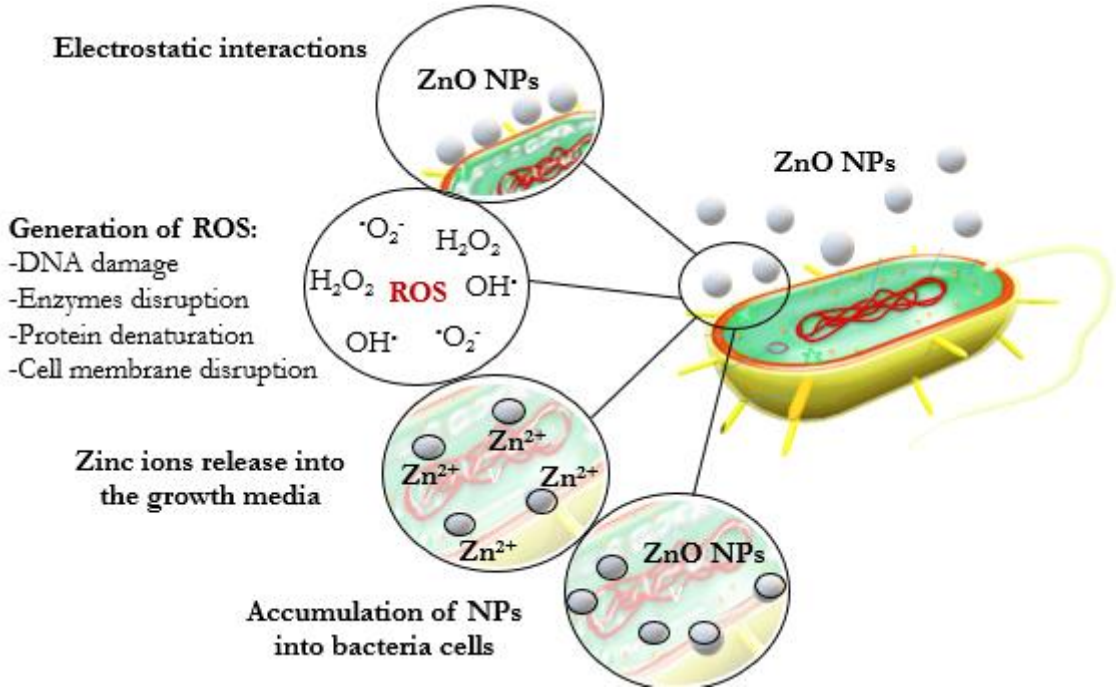

Figure 2.1. Possible mechanisms of ZnO antibacterial activity.[27]

Jones et al.[24] examined the antibacterial effects of ZnO NPs against both Gram-positive (e.g., *Staphylococcus aureus, Staphylococcus epidermidis*) and Gram-negative bacteria (e.g., *Escherichia coli*), comparing them to other metal oxide nanoparticles, such as MgO, TiO_2, and CuO. They found that ZnO NPs exhibited the most significant growth inhibition against *Staphylococcus aureus*, leading to further investigation into the role of particle size. Their results indicated that smaller nanoparticles caused over 95% growth inhibition at relatively low concentrations (1 mM), while larger particles resulted in only 50% inhibition at higher concentrations (5 mM). These findings suggest that nanoparticle size is crucial for their antimicrobial activity, likely due to the accumulation of NPs inside bacterial membranes and cytoplasm. This idea was supported by the studies performed by Brayner

et al.[19], founding that ZnO NPs accumulated intracellularly, inhibiting *E. coli* growth. Studies have confirmed that the antimicrobial properties of ZnO NPs are, at least in part, due to the release of Zn^{2+} ions into the growth medium, leading to disruptions in bacterial metabolism and cell wall integrity.[28,29,30,31] Sharma et al. synthesized ZnO nanoparticles ranging from 2 to 28 nm and found them to possess both antimicrobial and antifungal properties against *Pseudomonas* and *Fusarium* species.[32] He et al.[33] further explored the antifungal effects of ZnO NPs against *Botrytis cinerea* and *Penicillium expansum*, finding that 70 nm particles at concentrations above 3 mM significantly inhibited fungal growth. They also noted that the antifungal activity of ZnO nanoparticles was dose-dependent, with higher concentrations leading to increased effectiveness. SEM and Raman spectroscopy confirmed that ZnO nanoparticles inhibited *B. cinerea* by disrupting cellular functions and causing deformation in fungal hyphae. *P. expansum* was demonstrated to be sensitive to the nanoparticles, with ZnO preventing the development of conidiophores and causing the death of fungal hyphae. Kairyte et al.[34] investigated the antifungal activity of ZnO NPs against *Botrytis cinerea* under both dark and photoactivated conditions. The results showed that ZnO nanoparticles exhibited antifungal properties, with a significant reduction in mycelial growth. This effect was more pronounced at higher nanoparticle concentrations, with photoactivation enhancing the antifungal action. Antifungal activity is influenced by particle size, concentration, exposure to light and it is clear that zinc oxide nanoparticles can be an effective tool for combating fungal pathogens.

Zinc oxide exists in two primary forms: hexagonal wurtzite and cubic zincblende. The wurtzite structure, which features a hexagonal unit cell, is the most stable under ambient conditions and is therefore the most diffused form[35] (Figure 2.2). Each anion is surrounded by four cations positioned at the corners of a tetrahedron.

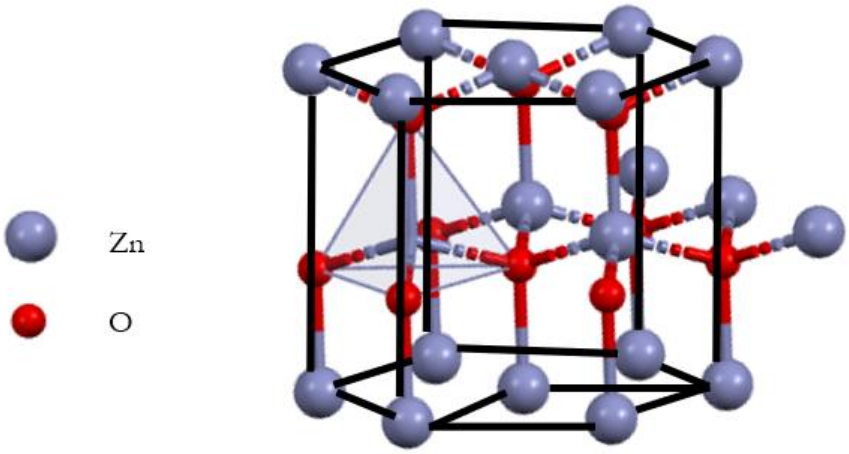

Figure 2.2. Wurtzite crystal structure of ZnO with hexagonal unit cell[36]

While zincite is the mineral form of zinc oxide found in the Earth crust, most of the zinc oxide used commercially is produced synthetically. The synthesis of zinc oxide can be performed in different ways and nanoparticles can be isolated by using chemical, physical, or biological methods, here briefly described (Figure 2.3).

Physical methods for synthesizing zinc nanomaterials include techniques such as physical vapor deposition, arc plasma, thermal evaporation, ultrasonic irradiation, and laser ablation.[37]

Chemical methods are classified based on their physical state, such as solid phase, liquid phase (wet chemical methods), or vapor phase. Among the wet-chemical methods, microemulsion,[38] sol-gel synthesis,[39] precipitation,[40] and hydrothermal and solvothermal methods [41]are commonly used.

The sol-gel process involves the preparation of a colloidal solution (sol), which is then converted into a gel and solid materials through hydrolysis, condensation, and polymerization reactions. Common precursors include metal alkoxides ($Zn(OR)_x$,) or their corresponding chlorides in an aqueous or organic medium, often alcohol. For zinc nanomaterials, zinc acetate hydrate in alcohol is commonly used as a precursor. Several factors, including the nature of the alkyl group, the solvent, the concentration of each species, the temperature, and the molar ratio of water to alkoxide, can influence the growth of ZnO NPs. [42]

The precipitation method has also been successfully employed to design various nanostructures of zinc oxide. This method involves a reaction between zinc salts (e.g., $Zn(NO_3)_2$, $Zn(CH_3COO)_2 \cdot 2H_2O$, $ZnSO_4 \cdot 7H_2O$) and basic solutions containing LiOH, NH_4OH, or NaOH.[43,44,45] The process begins with a reaction between zinc and hydroxide ions, followed by aggregation. The morphology of the resulting ZnO nanoparticles can be controlled by adjusting parameters such as concentration, pH, washing medium, or calcination temperature.[46] Kumar et al.[47] used zinc sulphate heptahydrate and sodium hydroxide to synthesize zinc oxide nanostructures, highlighting that nanoparticle morphology changed with calcination temperature. At 300°C and 500°C, the samples were nanoflakes, while at 700°C, spherical nanoparticles were obtained. Wang et al.[48] also used the precipitation method to synthesize ZnO nanoparticles with controlled morphology, achieving approximately 20 nm particles with zinc chloride as the precursor and ammonium carbamate as the precipitating agent. Thermogravimetric analysis and SEM revealed that the precipitate formation and nanoparticle morphology depended on the zinc precursor concentration. Higher zinc concentrations promoted more dominant precipitate formation, but excessive precursor led to aggregation. Furthermore, they observed that higher Zn^{2+} concentrations led to larger, aggregated particles with varied shapes. Pourrahimi et al.[49] examined the use of different zinc oxide precursors, including zinc nitrate, chloride, sulphate, and acetate, under identical reaction conditions. The most narrowly sized nanoparticles (averaging 25 nm) were obtained with the acetate precursor, while chloride and sulphate precursors produced nanoparticles ranging from 10–30 nm and 80–100 nm, respectively. Using the nitrate precursor, the particles were star-shaped, averaging around 500 nm. These findings suggest that NPs morphology could depend heavily on the selection of the appropriate zinc precursor. An additional advantage is the ability to synthesize ZnO NPs from saline precursors through methods that do not require hazardous chemicals or excessive energy, creating favourable conditions for potential scale-up productions. Wahab et al.[50] have synthesized flower-shaped ZnO nanostructures which were produced via solution process at low temperature (90°C) using the zinc acetate dihydrate and NaOH.

Biological methods foresee the use of bacteria, yeast, fungi, and plant extracts[51,52,53] to treat the metal precursor obtaining the final desired NPs. This approach implies considering several process parameters, including the selection of organisms with the most suitable enzyme activities and biochemical pathways, as well as optimizing conditions for medium, temperature, pH, and buffer. By fine-tuning these factors, it is possible to control the morphology of ZnO nanoparticles.

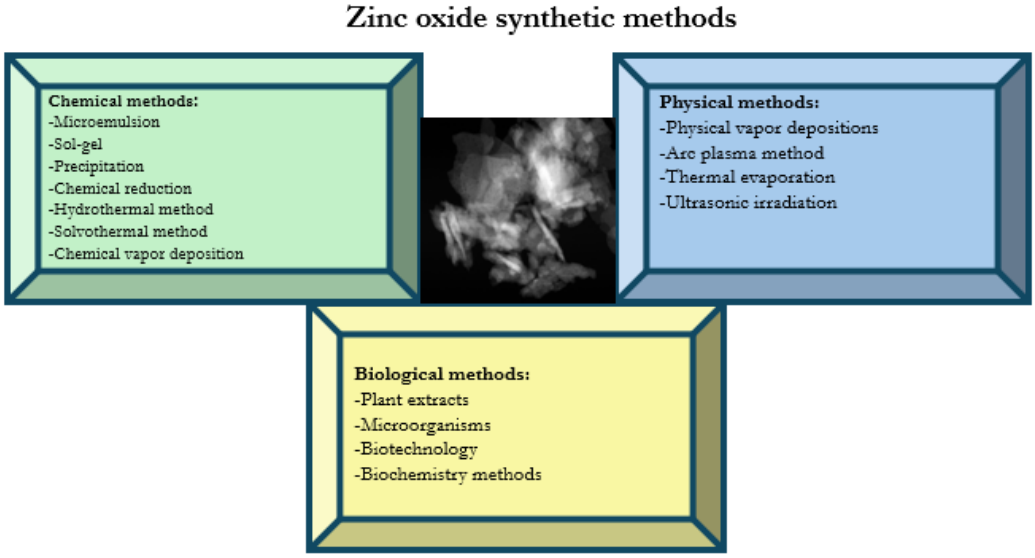

Figure 2.3. Synthetic approaches to ZnO nanoparticle.[54]

The choice of the synthetic method primarily depends on the intended application, as different techniques yield ZnO particles with varying sizes and morphologies, which are key features for activity. Consequently, factors such as solvent type, precursors, pH, and temperature are carefully considered. A variety of ZnO nanostructures, including nanorods, nanospheres, nanotubes, nanowires, nanoneedles, and nanorings, have been successfully synthesized.[55] Other shapes can also be obtained, such as ZnO spirals, drums, polyhedrons, disks, flowers, stars, boxes, and plates,[56] those are possibly grown by adjusting the growth conditions. The structure of nanomaterials, which directly influences their physicochemical properties, plays a critical role in their effectiveness.[57] Since the synthetic method directly influences the NPs morphological properties, selecting the right preparation technique is crucial when designing ZnO NPs for specific applications[58].

Some studies have proposed that zinc oxide nanoparticles combined with lignin could be effective in addressing bacterial and fungal issues in crops.[59] The natural antimicrobial properties of lignin, due to its phenolic hydroxyl groups, may further boost the antimicrobial activity of ZnO-based products, limiting the amounts of material necessary to see an effect. Hybrid systems composed of lignin and zinc oxide (ZnO) are examples of organic/inorganic nanomaterials that display unique structural and electrical properties.[60] Numerous studies have explored the integration of lignin and metal oxides into various polymeric matrices, revealing significant improvements in antibacterial, antifungal, thermal, and mechanical performance due to the presence of these hybrids.[61] Although both lignin and ZnO NPs are increasingly being used in various agricultural

applications, there is limited research exploring their potential synergy when combined in hybrid systems. Sharma et al.[59] introduce a lignin-based approach for synthesizing zinc oxide nanoparticles, utilizing lignin extracted from waste biomass as a stabilizing agent for the surface, which show antifungal activity against *F. oxysporum* and *F. proliferatum* that cause diseases in commercially important crops like garlic, onion, maize tomato, wheat, beans and cotton. Jose et al.[62] developed photoresponsive NPs incorporated in lignin matrix with optical and antifungal properties.

To note that, in addition to antifungal and antibacterial properties discussed above, zinc also plays a crucial role in various physiological processes as a vital microelement for plants and animals.[63] Zinc is primarily found intracellularly, especially in the nucleus, cytoplasm, and cell membrane.[64] This element is essential for the proper functioning of many macromolecules and enzymes, serving both catalytic (as an enzyme active centre) and structural roles. Zinc finger motifs, for instance, provide a unique framework that allows protein subdomains to interact with DNA or other proteins[65]. Additionally, zinc is crucial for the activity of metalloproteins. It affects plant metabolism by regulating the activities of enzymes such as hydrogenase and carbonic anhydrase, as well as stabilizing ribosomal fractions and promoting cytochrome synthesis. Zn-activated enzymes play a key role in glucose metabolism, maintaining cellular membrane integrity, protein synthesis, auxin production regulation, and pollen development.[66] A deficiency in zinc can lead to various symptoms in plants, including chlorosis, necrosis, spikelet sterility, increased membrane permeability, stunted growth, leaf bronzing, smaller leaves, thin stems, and even shoot dieback.[67] An interaction between two nutrients is considered significant when the application of one nutrient influences the plant response to the other, and vice versa. In plants, Zn has a positive interaction with nitrogen and potassium, but a negative one with phosphorus, calcium, iron, and copper.[68] The negative interaction with P, Ca, Fe, and Cu is attributed to their interference with Zn absorption on root surfaces and/or its translocation from roots to shoots.[69] Zn also negatively interacts with Ca due to competition for the same adsorption sites on soil particles and root surfaces.[69] Zinc helps mitigate excessive sodium uptake in saline environments by influencing the structural integrity and permeability of stem cell membranes.[70] Zinc nutrition plays a key role in reducing sodium accumulation and enhancing the potassium/sodium (K/Na) ratio in plants under saline conditions.[71] In the absence of adequate zinc content, plant cell membranes exhibit increased permeability, leading to leakage of compounds from the roots.[72] Zinc deficiency can also result in the accumulation of harmful ions like sodium and chloride. Therefore, the combined effects of salinity and zinc deficiency on plant growth are crucial and warrant further investigation.

When applied to crops at moderate concentrations, ZnO NPs has been shown to provide several benefits, including the ability to promote seed germination, enhance plant growth at different developmental stages, increased biomass production, and improved antioxidant defences, reducing disease infections with these effects influenced by the particle size and form[73]. Their beneficial role in mitigating abiotic stress factors such as drought, salinity, and high temperatures in various crops is particularly noteworthy. The characteristics in terms of morphology and size of ZnO NPs play a crucial role in determining how they are absorbed, transported, and accumulated by plants.[74] Prasad et

al. treated peanut seeds with varying concentrations of zinc oxide nanoparticles. Treatment with a 25 nm mean particle size at a concentration of 1000 ppm resulted in improved seed germination, seedling vigour, and overall plant growth. The nanoparticles also effectively stimulated stem and root development in peanuts.[75] Zinc oxide nanoparticles in colloidal form are used as nanofertilizers, which play a significant role in agriculture. Unlike traditional fertilizers, nanofertilizers not only supply essential nutrients to plants but are effective even in very small quantities. Nanopowders can also be used effectively as both fertilizers and pesticides.[76,] Furthermore, wheat plants grown from seeds treated with metal nanoparticles have shown an average yield increase of 20–25%. [77] The positive effects are summarized in Figure 2.4.

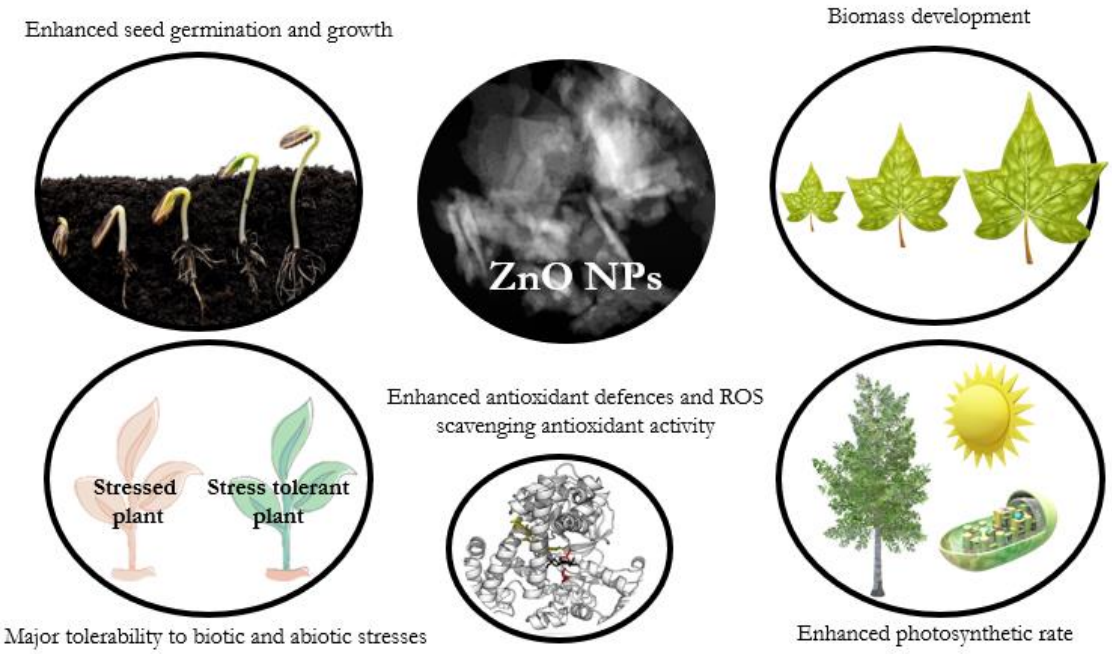

Figure 2.4. Schematic representation of ZnO NPs positive effects on plants[78]

However, some negative effects on plant growth and various metabolic processes cannot be ignored, depending on the developmental stage. The uptake and the effect of ZnO NPs depend on the type of plant, on the dose and the type of NPs employed.[79] Indeed, high concentrations of ZnO NPs have been related to several toxic effects, including growth and yield inhibition, physiological abnormalities, cytotoxicity, genotoxicity, and oxidative stress. The outcomes—whether beneficial or detrimental—are influenced by factors such as the type and dosage of nanomaterials, treatment methods, plant developmental stage, species genotype, and environmental conditions. Several studies have indicated that high doses of ZnO can be toxic due to its accumulation in plant tissues, potentially disrupting physiological and biochemical processes.[80] Until a more comprehensive understanding of the interactions between ZnO NPs and the plant genome or epigenome is achieved, it remains challenging to fully harness these materials for optimal use, replacing traditional growth-promoting or protective agents. This requires development of appropriate methods to identify plant conditions and optimize the nanomaterial treatment. Furthermore, the prolonged and indiscriminate use of zinc fertilizers in soil may result in toxic levels of accumulation. In this context, the use of

hybrid materials could provide a solution, offering more effective materials with improved toxicological profiles and enhanced sustainability. Del Buono et al.[81] synthesized a hybrid material (ZnO@LNP) consisting of lignin nanoparticles containing zinc oxide (4 wt %). ZnO@LNP exhibited positive effects during the early stages of wheat seed development, as well as on plant growth and biomass accumulation in young seedlings. Specifically, the ZnO@LNP-treated primed seeds showed increased levels of chlorophyll, carotenoids, anthocyanins, total phenols, and enhanced antioxidant activity, as evidenced by lower lipid peroxidation compared to the control samples. Both ZnO NPs and lignin have been studied as biostimulants for tomato plants and seedlings, showing promising results, although some conflicting data exist in the literature regarding dose-response effects.[82,83,84]

With all these considerations in mind, we focused on the synthesis and characterization of HMW@ZnO hybrid materials, described in this chapter, investigating their effect on tomato seed germination and seedling growth promotion, in collaboration with the research group of Professor S. Woo of the University of Naples. Uptake, translocation and accumulation of zinc by plants were determined to preliminary evaluate the role of zinc accumulation in relation to plant growth.

EXPERIMENTAL SECTION

Materials and methods

HMW (Biopiva395®, Kraft softwood lignin from *Pinus taeda*, Mw 5950-6000 g/mol, Mn 1560-1565 g/mol) is kindly provided by UPM-Kymmene Oyj (Helsinki, Finland) and Green Innovation GmbH (Innsbruck, Austria). Zinc acetate dihydrate (99%) and zinc sulphate heptahydrate (99%) are purchased by Carlo Erba; zinc chloride and zinc sulphate monohydrate are purchased by Brenntag. Sodium hydroxide is purchased by AnalaR NORMAPUR®ACS (99.5-100%); hydrochloric acid 37% is purchased by Fluka Honeywell; glacial acetic acid (≥99%) and ZnO (99.9%) are purchased by Sigma Aldrich. All the reagents are used as received with no further purification. pH is measured using a Crison pHmeter basic 20 equipped with an Ag/AgCl electrode. The phosphate buffer is prepared at pH 6, by using sodium hydroxide and sodium phosphate monobasic monohydrate.

Materials preparation

HMW@ZnO (*Procedure 1*). In a 500 mL beaker, the zinc salt ($Zn(OAc)_2 \cdot 2H_2O$, $ZnCl_2$, or $ZnSO_4 \cdot 7H_2O$) has been dissolved into distilled water under magnetic stirring. NaOH 1M aqueous solution has been added (4 equivalents with respect to the zinc salt), and the immediate precipitation of zinc hydroxide has been observed. HMW has been immediately added to the suspension by using the amount calculated for reaching the desired metal content, as reported in Table 2.1 and Table S2.1. The formation of a dark brown suspension occurs with pH varying in the range 11-13. The mixture has been then stirred for 1 hour at room temperature. After this time, the mixture has been dried inside an oven at 95 °C, until complete evaporation of the solvent. The brown materials have been then washed with 100 mL of distilled water, centrifuged, and dried again at 95°C overnight. All the experiments have been performed at least in duplicate.

Table 2.1. Stoichiometric ratios of reagents for the preparation of HMW@ZnO_X% (X= 5, 10, 20 %, 30%) by using zinc sulphate heptahydrate. 65 mL, 100 mL, 100 mL and 400 mL of water were used for X = 5, 10, 20 and 30%, respectively. Percentages refer to content of zinc.

	HMW/$Zn(SO_4) \cdot 7H_2O$ mass ratio (g/g)	NaOH (mol)	NaOH/$Zn(SO_4) \cdot 7H_2O$ molar ratio
HMW@ZnO_5%	5/1.17	0.016	4/1
HMW@ZnO_10%	5/2.5	0.035	4/1
HMW@ZnO_20%	5/5.8	0.080	4/1
HMW@ZnO_30%	5/10.4	0.145	4/1

HMW@ZnO (*Procedure 2).* In a 500 mL beaker, $ZnSO_4 \cdot 7H_2O$ has been dissolved into distilled water under magnetic stirring. HMW has been added to the solution by using the amount calculated for reaching the desired metal content, NaOH 1M aqueous solution has been added (4 equivalents with respect to the zinc salt), as reported in Table 2.2. The formation of a dark brown suspension occurs with pH varying in the range 11-13. The mixture has been then stirred for 1 hour at room temperature. After this time, the mixture has been dried inside an oven at 95 °C, until complete evaporation of the solvent. The

brown materials have been then washed with 100 mL of distilled water, centrifuged, and dried again at 95°C overnight. All the experiments have been performed at least in duplicate.

Table 2.2. Stoichiometric ratios of reagents for the preparation of HMW@ZnO_X% (X= 5, 10) by using zinc sulphate heptahydrate.

	HMW/$Zn(SO_4)\cdot 7H_2O$ mass ratio (g/g)	NaOH (mol)	NaOH/$Zn(SO_4)\cdot 7H_2O$ molar ratio
HMW@ZnO_5%	5/1.17	0.016	4/1
HMW@ZnO_10%	5/2.5	0.035	4/1

ZnO_ref. In a 100 mL beaker, $ZnSO_4\cdot 7H_2O$ (0.004 mol) has been dissolved into 15 mL of distilled water. 50 mL of NaOH 1M have been added (0.015 mol of NaOH, 4 equivalents), and the immediate precipitation of zinc hydroxide occurs. Then, the suspension has been stirred for 1 hour at room temperature. After this time, the mixture has been dried at 95 °C in an oven until complete evaporation of the solvent. The product has been then washed with 20 mL of distilled water, centrifuged, and dried again at 95°C overnight. All the experiments have been performed at least in duplicate.

Scale-up preparation of HMW@ZnO. A NaOH solution (30% w/w) was added to a $ZnSO_4\cdot H_2O$ aqueous solution and the immediate formation of a white precipitate of zinc hydroxide occurred. Then, HMW was added to the suspension in the amount calculated for reaching the desired final percentage (Table 2.3): the formation of a dark brown suspension occurred (pH 11-13), which was then stirred for 1 hour at room temperature. The mixture was dried at 95 °C, then the pH was adjusted to 8, the solid plenty washed with water and finally dried at 95°C overnight. All the experiments were performed at least in duplicate. HMW@ZnO materials are powders stable at air, at room temperature and for a prolonged time. They can be stored for at least one year without alteration signs.

Table 2.3. Reagents content for the scale-up preparation of HMW@ZnO_X% (X= 5%, 10%, 30%).

	HMW/$Zn(SO_4)\cdot H_2O$ mass ratio (g/g)	NaOH (mol)	NaOH/$Zn(SO_4)\cdot H_2O$ molar ratio
HMW@ZnO_5%	1000/147	3.5	4.4/1
HMW@ZnO_10%	1000/320	7.5	4.2/1
HMW@ZnO_30%	500/646	14.4	4/1

HMW_HCl. 1 g of HMW has been suspended into 100 mL of HCl 0.05 M solution (pH about 1.5). After 24 hours, the suspension has been centrifuged and washed with 10 mL of water twice. The brown powder has been collected and dried at 85 °C overnight.

HMW@ZnO_HCl. 1 g of HMW@ZnO 10% has been suspended into 100 mL of HCl 0.05 M solution (pH about 1.5). After 24 hours, the suspension has been centrifuged and washed with 10 mL of water twice. The brown powder has been collected and dried at 85 °C overnight.

HMW_NaOH. In a 50 mL beaker, 270 mg of NaOH dissolved in 10 mL of water have been added to 1 g of HMW (ratios among lignin and NaOH have been chosen accordingly to HMW@ZnO 10% experimental synthetic conditions), pH 13. The reaction mixture has been stirred at RT for 1 hour and then dried at 95 °C. The product is water soluble.

Stability of HMW@ZnO at pH 6. In a 50 mL vessel, about 200 mg of HMW@ZnO_10% have been suspended in 20 mL of an aqueous phosphate buffer (pH 6). The suspension has been stirred for different contact times (1, 4, 8, 24, and 48 hours), then centrifuged. The supernatants have been collected and microfiltered with Nylon syringe filters (0.45 μm). The solutions have been analysed by ICP-AES. The experiments have been conducted in duplicate.

RESULTS AND DISCUSSION

As highlighted in the introduction, our previous research on HMW@Cu materials, which contain brochantite ($Cu_4(SO_4)(OH)_6$) or cuprite (Cu_2O) as inorganic phases, have demonstrated very promising anti-phytopathogenic properties against various pathogens. The effectiveness varied depending on the size and morphology of the inorganic nanocrystals, together with copper contents, as shown in previous studies.[4,5] In this work, we aim to develop ZnO NPs embedded in a lignin matrix, combining the advantages of both components into a single material that could stimulate plant growth and demonstrate antimicrobial properties. This approach allows for a synergistic effect between the two elements, reducing the amount of metal required for effective performance. We focus on the development of a simple, sustainable, and scalable synthesis method for practical *in vivo* applications. We therefore avoid multi-step procedures, toxic chemicals and solvents, and high calcination temperatures commonly used in similar studies.[85] So, the goal is favouring a sustainable approach by using only water as solvent, low temperatures, short production times, and effectiveness in scalability. The first optimization has been carried out on a hundreds milligram-scale to meet the requirements of a simple, repeatable synthetic procedure using only water as the solvent to obtain a hybrid material with 10% of metal content (HMW@ZnO_10%). Then, the study has been proceeded by increasing the production scale of the material. First, an optimization of the synthesis has been carried out on a mg-scale. The optimized synthesis method (*Procedure 1,* detailed in the Experimental Section) involves mixing a zinc salt ($Zn(OAc)_2{\cdot}2H_2O$, $ZnCl_2$, or $ZnSO_4{\cdot}7H_2O$) with NaOH to form a zinc hydroxide precursor. Then, solid HMW has been added under vigorous stirring at room temperature. Using a stoichiometric amount of NaOH (2 equivalents to the zinc salt) results in a mixture of hexagonal wurtzite (ZnO) and a phase, which can not be definitively identified, but potentially attributable to a form of zinc oxide[86] (Figure S2.1). We have then performed the synthesis with an excess of NaOH, in order to take into account the acidic nature of the lignin matrix and favor the formation of final ZnO. By using 4 equivalents of NaOH hexagonal wurtzite zinc oxide only is produced with highly reproducible results. To evaluate the role of the lignin matrix as a stabilizing agent and to serve as a reference for *in vitro* and *in vivo* tests, pure ZnO (referred to as ZnO_ref) has been synthesized under the same conditions applied for HMW@ZnO_5%, but without lignin. The crystalline phase of the hybrid material has been determined using powder X-ray diffraction (PXRD) analysis by comparison with COD reference data bank pattern.[87] The lignin component is amorphous and contributes to broad, diffuse scattering at low 2θ values. In contrast, ZnO displays its distinctive diffraction peaks at 2θ values of 31.8°, 34.4°, 36.3°, 47.5°, 56.7°, 62.8°, 64.4°, 67.9°, and 68.3°. Figure 2.5 presents the diffractograms of materials synthesized from zinc sulfate heptahydrate with varying metal contents, where only the hexagonal wurtzite phase is observed in all samples. The presence of sharp, intense peaks indicates that lignin does not hinder the formation of highly crystalline ZnO nanoparticles. For comparison, the diffractograms of the synthesized ZnO_ref, commercial ZnO, and the reference from the COD database are also shown in Figure 2.5.

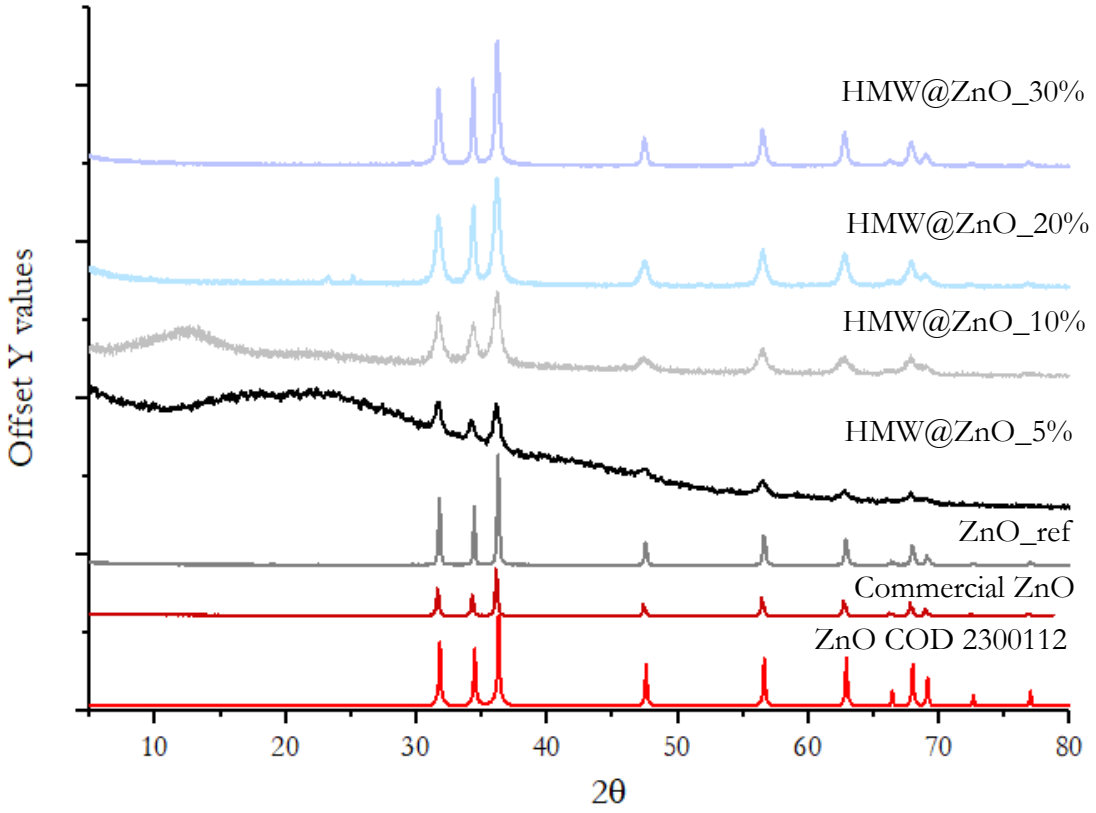

Figure 2.5. Stacked PXRD patterns of HMW@ZnO_5%, HMW@ZnO_10%, HMW@ZnO_20%, HMW@ZnO_30%, ZnO_ref and commercial ZnO. ZnO from data bank (ZnO COD 2300112) is displayed for comparison.

The FT-IR spectra of HMW, ZnO_ref, and HMW@ZnO_10% are shown in Figure 2.6. The HMW spectrum features typical Kraft lignin signals, including a broad band around 3400 cm^{-1} corresponding to hydroxyl group stretching, weaker bands at 2936-2835 cm^{-1} for aromatic and aliphatic C-H stretching, and a C=C aromatic stretching band at 1595 cm^{-1}. Bands at 1512 and 1427 cm^{-1} correspond to the aromatic ring vibrations in the lignin phenylpropanoid structure. Other signals at 1214 cm^{-1} and 1120 cm^{-1} relate to C-C, C-O, and C=O stretches, while a band at 1081 cm^{-1} confirms the presence of secondary alcohols and aliphatic ethers. The ZnO reference shows a peak at 500-400 cm^{-1} corresponding to Zn-O vibrations, which is also present in the HMW@ZnO_10% spectrum, confirming the formation of zinc oxide. The lignin-related bands remain unchanged in the hybrid material, suggesting that the embedding of ZnO nanoparticles does not affect the lignin structure. The spectra of HMW@ZnO materials with varying zinc content are similar, as shown in Figure S2.2.

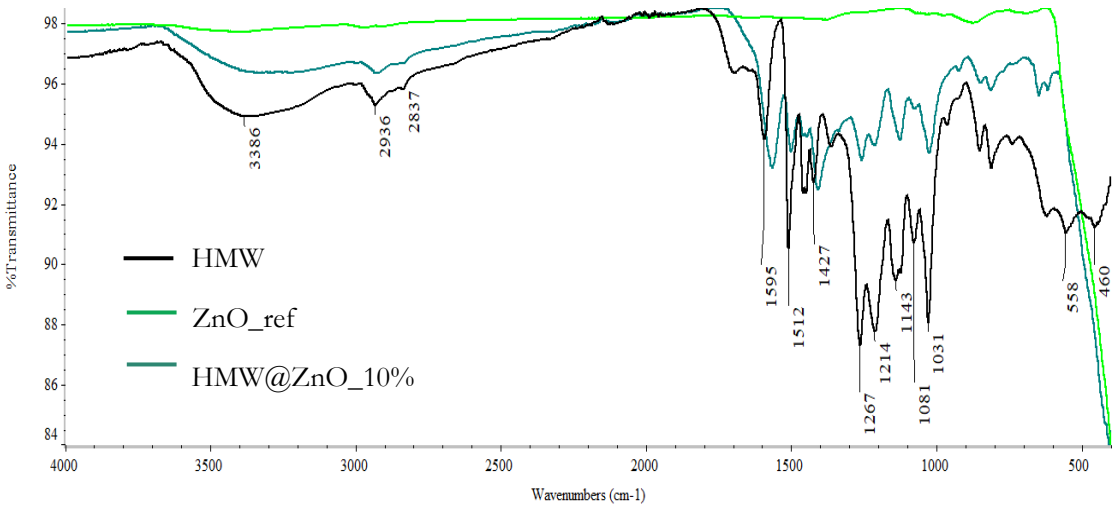

Figure 2.6. Stacked infrared spectra of HMW, ZnO_ref and HMW@ZnO_10%.

TEM studies were carried out on HMW@ZnO_X% materials (X = 5, 10, 20%, 30%), synthesized using zinc sulphate heptahydrate as reagent (Figure 2.7). HMW@ZnO_5% exhibits aggregates of NPs with sizes ranging from 20 to 300 nm, composed of crystals with dimensions of 10-20 nm. Crystallized needle-like structures are also present, with lengths ranging from 50 to 200 nm and thicknesses between 10 and 40 nm. Similar morphologies can be observed in HMW@ZnO_10%, where aggregates of 20-200 nm, made up of 10-20 nm NPs, coexist with needle structures having lengths from 50 to 200 nm and thicknesses between 10 and 50 nm. HMW@ZnO_20%, where well-crystallized needles range from 50 to 500 nm in length and 20 to 50 nm in thickness. Additionally, this sample contains aggregates spanning from 20 to 500 nm constituted by NPs with sizes ranging from 5 to 10 nm. Extremely comparable features can be found for HMW@ZnO_30%, where well-crystallized needles range from 50 to 200 nm in length and 10 to 50 nm in thickness. In addition, this sample contains aggregates of NPs with sizes ranging from 5 to 10 nm, along with larger aggregates spanning from 20 to 500 nm.

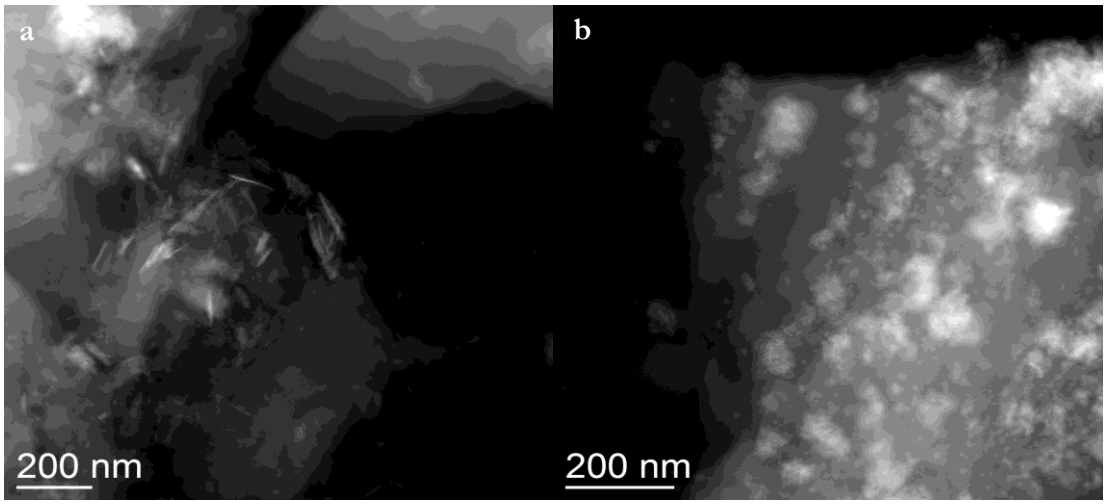

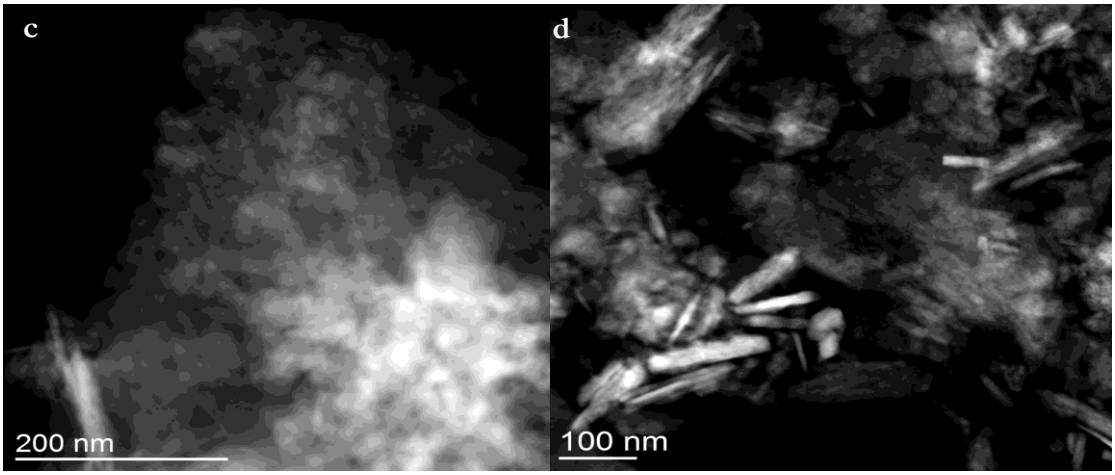

Figure 2.7. TEM images showing the different dimensions and morphologies of the nanoparticles of a) HMW@ZnO_5%, b) HMW@ZnO_10%, c) HMW@ZnO_20%, d) HMW@ZnO_30%. Zinc sulphate heptahydrate was used as metal source.

The TEM images of ZnO_ref and commercial ZnO are shown in Figure 2.8. For ZnO_ref, the crystals retain a needle-like shape, although they are larger in size (ranging from 50 to 500 nm in length and 10 to 50 nm in thickness) compared to the crystals observed in the hybrid materials. This indicates that lignin likely serves as a capping agent during nanoparticle growth. In contrast, commercial zinc oxide displays a distinctly different morphology, consisting of block-shaped crystals with larger dimensions (50 to 800 nm).

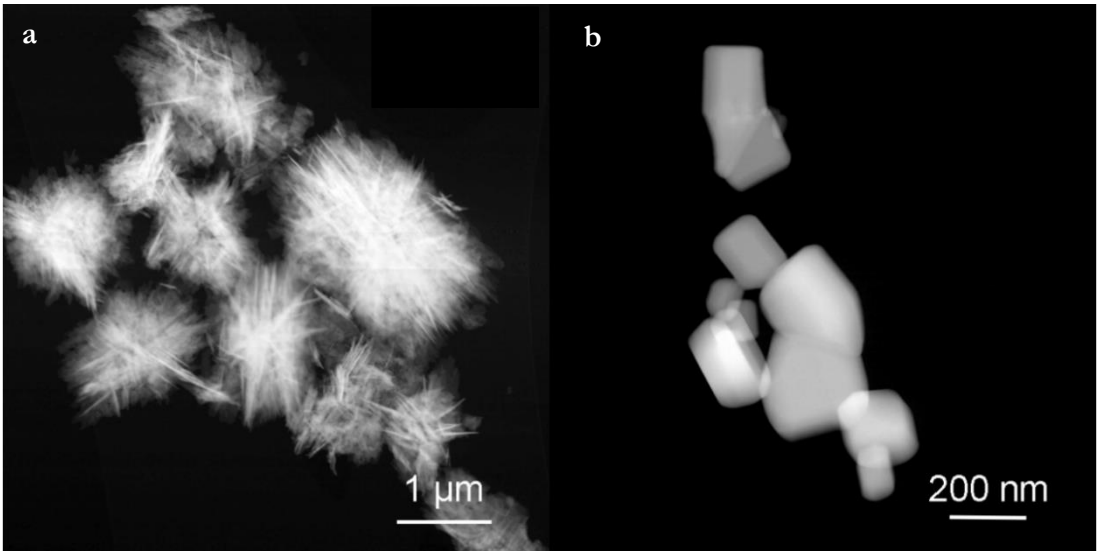

Figure 2.8. TEM images highlighting the different dimensions and morphologies obtained for a) ZnO_ref and b) commercial ZnO

The size and morphology of the samples analysed using TEM are summarized in Table 2.4, highlighting the key features.

Table 2.4. Dimension and morphology of the NPs in HMW@ZnO_X% (X = 5, 10, 20, 30) and ZnO_ref. Dimensions of commercial zinc oxide are also reported as a comparison.

	Size and shape
HMW@ZnO_5%	Aggregates of 20-300 nm constituted by NPs of 10-20 nm. Presence of some needles with length of 50-200 nm and a thickness of 10-40 nm
HMW@ZnO_10%	Aggregates of 20-200 nm constituted by 10-20 nm NPs. Presence of some needles with length of 50-200 nm and a thickness of 10-40 nm (sporadic)
HMW@ZnO_20%	Aggregates of 20-500 nm constituted by 5-10 nm NPs. Presence of some needles with length of 50-500 nm and a thickness of 20-50 nm
HMW@ZnO_30%	Aggregates of 20-500 nm constituted by 5-10 nm NPs. Presence of some needles with length of 50-200 nm and a thickness of 10-50 nm
ZnO_ref	Needle-like crystals with length 50-500 nm and thickness 10-50 nm
ZnO (commercial)	Crystalline blocks with dimensions 50-800 nm

Since the products with 20% and 30% zinc show comparable morphologies and sizes, the hybrid material with the 30% zinc content is chosen between the two for the following studies. To verify the repeatability of the synthesis concerning the metal loading, the synthesis has been independently replicated three times following the conditions for obtaining HMW@ZnO 5%. The materials were then analyzed using ICP-AES. As can be inferred from the results shown in Table 2.5, the zinc percentage in the final material is quite reproducible, with the metal loading very close to the expected value.

Table 2.5. Zinc content determined by ICP-AES analysis for HMW@ZnO_5%, obtained from independent triplicates

	Zn% mean ±SD
HMW@ZnO_5% 1	5.6 ± 0.1
HMW@ZnO_5% 2	5.9 ± 0.1
HMW@ZnO_5% 3	4.7 ± 0.1

We have also investigated whether the choice of different anions in the starting zinc salt could influence the morphology and dimensions of the crystals, as highlighted in the literature by Pourrahimi et al.,[49] using three different salts (zinc acetate dihydrate, zinc sulphate heptahydrate, and zinc chloride). The synthetic procedures are described in the supporting information (Procedure S2.1 and Table S2.2). We have analyzed HMW@ZnO_10% materials obtained from the three different salts, both on a mg and a gram-scale (obtained with Procedures S2.1 and Procedure 1, respectively), by means of PXRD and TEM. Stacked diffraction patterns of HMW@ZnO_10% (gram-scale synthesis) and ZnO_ref from different zinc sources are provided respectively, in Figure 2.9 and Figure S2.3.

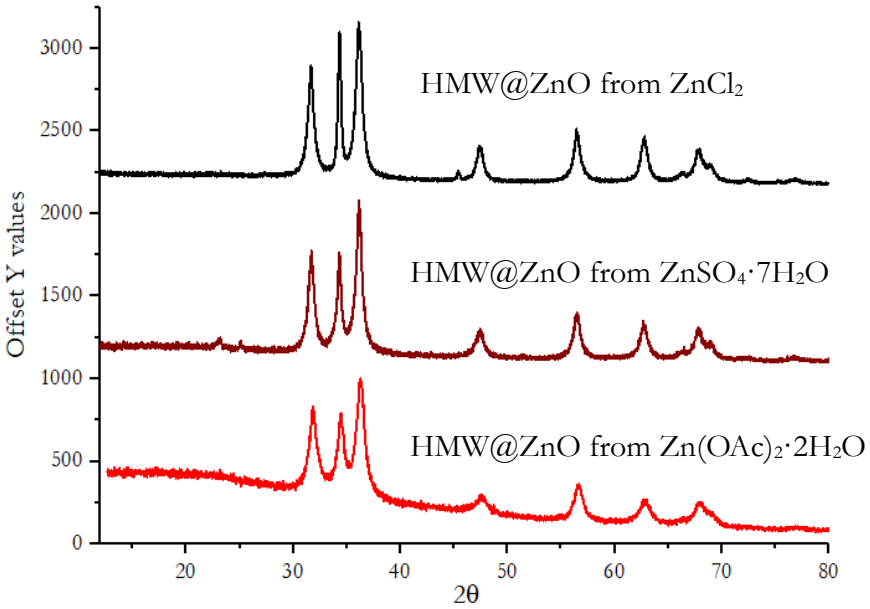

Figure 2.9. PXRD diffractograms for HMW@ZnO_10% from different zinc salts on a gram-scale synthesis

From the comparison of these diffractograms, it can be supposed that the choice of zinc salt as the starting reagent has little impact on the final diffraction patterns, and this has been further investigated by means of TEM analyses. The inorganic crystals exhibit the presence of aggregates with very comparable dimensions together with the presence of needles (Figure 2.10), indicating that the anion seems not significantly influence these characteristics. Further details regarding the features of HMW@ZnO_10% materials derived from different zinc salts are provided in Table S2.3.

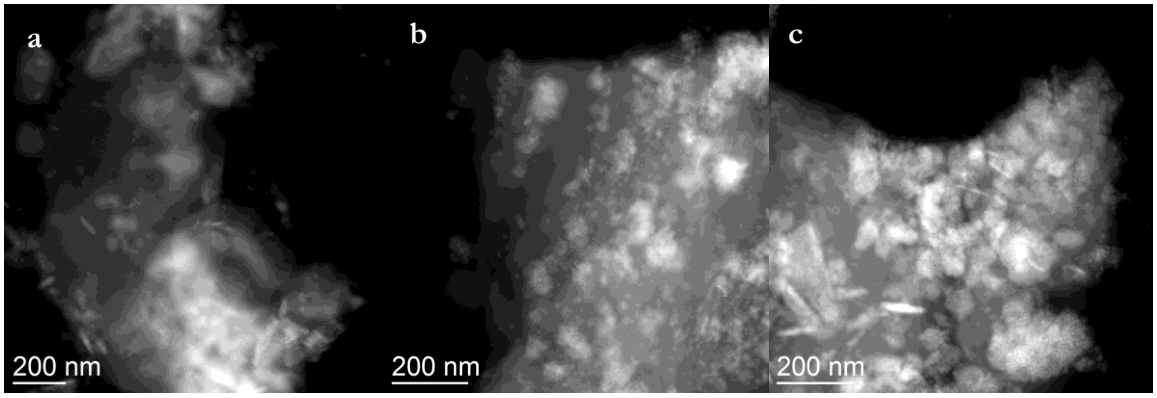

Figure 2.10. TEM images showing dimensions and morphologies of the nanoparticles of HMW@ZnO_10% synthesized from a) $Zn(OAc)_2·2H_2O$ b) $ZnSO_4·7H_2O$ and c) $ZnCl_2$.

The same results can be found on a mg-scale (Figure S2.4 and the description of the morphologies and sizes found are summarized in Table S2.4): TEM analysis revealed the presence of larger aggregates (up to 500 nm) consisting of small polycrystalline units for the product isolated from zinc acetate. For zinc sulphate and chloride, the presence of aggregates is observed (400 nm and 200 nm, respectively), also composed of small units (about 5-10 nm) along with the presence of needle-like structures. The results seem to

indicate that when choosing zinc sulphate and chloride salts, there is a stronger tendency for needle-like structures to form. However, in all samples, aggregates with similar final sizes were observed. It can be concluded that, under the experimental conditions employed, the size and morphology of the particles do not depend on the zinc salt used. The final dimensions and morphologies may result from a combination of synthetic parameters rather than solely from the choice of the starting salt. For these reasons, for further scale-up studies we have decided to use $ZnSO_4 \cdot 7H_2O$ based on its availability and cost. Different drying temperatures (ranging from 70°C to 95°C) were tested on a mg-scale to convert the hydroxide to zinc oxide (Procedure S2.2, Supporting Information). PXRD analysis confirms the formation of pure ZnO at temperatures above 70°C and TEM analyses have been conducted on these materials (Figure S2.5 and S2.6, respectively). The description of the morphologies and sizes found are summarized in Table S2.5. No significant variations have been observed in the sizes and morphologies of the nanoparticles compared to those synthesized at 95 °C and this temperature is chosen to minimize conversion time in the scale-up synthesis.

We have also evaluated the influence of the order of reagents addition: lignin has been added to the zinc solution prior to the base (*Procedure 2*) for the obtainment of HMW@ZnO_5 % and HMW@ZnO_10% from zinc sulphate heptahydrate. PXRD of HMW@ZnO_5 % is reported in Figure S2.7 a): it shows very broad peaks, likely due to the presence of very small crystals; furthermore, the low zinc percentage in the material negatively affects the peak intensity. EDX confirms the formation of ZnO phase with a Zn/O ratio close to 1, as reported in Figure S2.7 b. TEM studies conducted on HMW@ZnO_5 % obtained by *procedure 2*, shows the presence of very small NPs (Table 2.6). Images collected in STEM mode for HMW @ZnO_5% show needle like crystals with a width of 3-5 nm and a length of 40-60 nm, as can be seen in Figure 2.11.

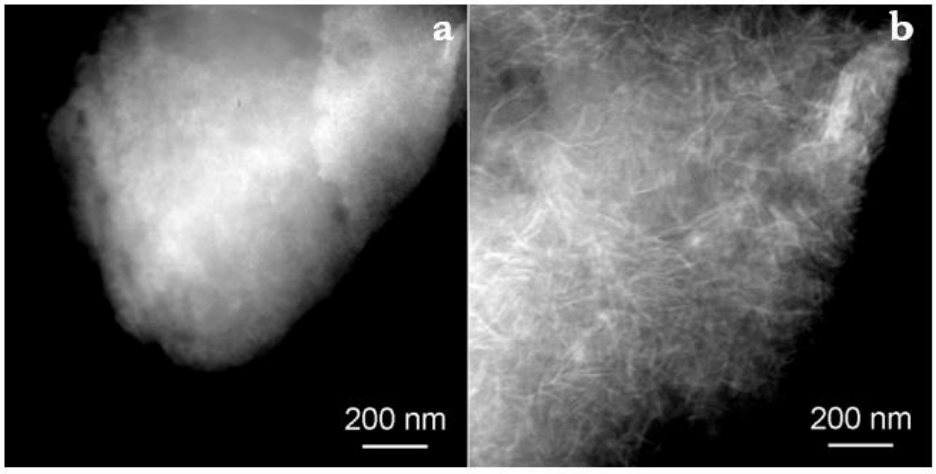

Figure 2.11. TEM images showing the small nanoparticles present in HMW@ZnO_5 % obtained by *procedure 2*.

PXRD of HMW@ZnO_10 % is reported in Figure S2.8 and comparable with the one obtained by *procedure 1*. TEM studies conducted on HMW@ZnO_10 %, obtained by *procedure 2,* showed the presence of very small NPs with 10-20 nm, forming aggregates and sporadic needles (Figure 2.12). In fact, the images obtained by microscopy do not

appear to show a significant difference between the samples obtained with the two different procedures. The descriptions of the sizes and morphologies obtained from the two procedures are compared in the Table 2.6. Lignin seems to highly affect the nanoparticle dimensions for HMW@ZnO_5% materials when added prior to the base, maybe inducing a pH effect during nucleation, while for HMW@ZnO_10% it seems that the two procedures are equivalent. For scale-up studies aimed at producing materials for subsequent *in vivo* testing, we have chosen *procedure 1*.

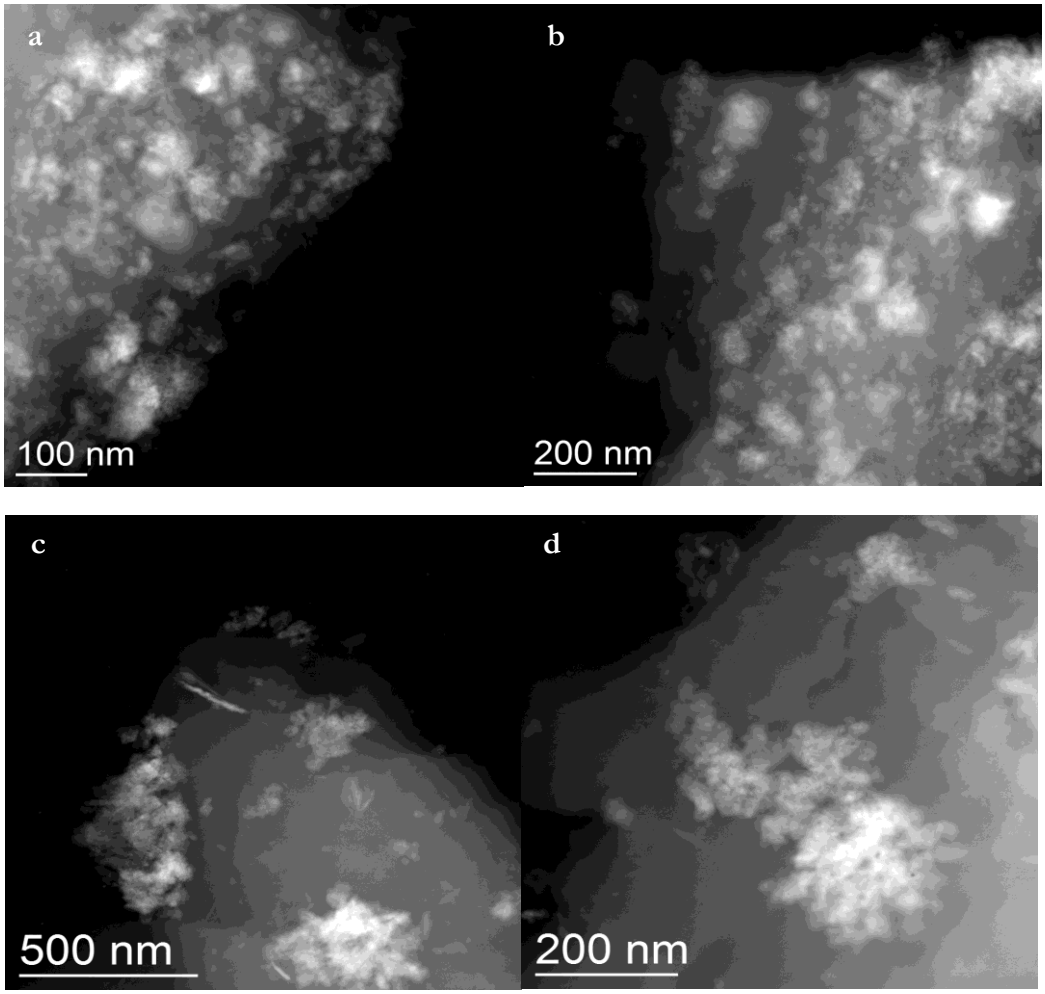

Figure 2.12. TEM images showing the small nanoparticles present in HMW@ZnO_10 % obtained by *procedure 1 (*(a) and b)) compared to those obtained by *procedure 2 (*(c) and d))

Table 2.6. Dimensions and morphologies for NPs comparing the samples HMW@ZnO_5 % obtained by *procedure 1* and *procedure 2*.

	Size	Shape
procedure 1 HMW@ZnO_5%	Aggregates with dimensions 20-300 nm constituted by 10-20 nm elements. Sporadic presence of needles with length 50-200 nm and thickness 10-40 nm	Aggregates of small nanoparticles with no clear shape together with sporadic presence of needles
procedure 2 HMW@ZnO_5%	Needles with width 3-5 nm and length 40-60 nm	Poor crystallinity, probably due to the presence of very thin needles
procedure 1 HMW@ZnO_10%	Aggregates of 20-200 nm constituted by 10-20 nm NPs. Presence of some needles with length of 50-200 nm and a thickness of 10-40 nm (sporadic)	Aggregates of small nanoparticles together with sporadic presence of needles
procedure 2 HMW@ZnO_10%	Aggregates of 10-20 nm with the sporadic presence of needles	Aggregates of 10-20 nm nanoparticles with no clear shape together with sporadic presence of needles

Energy dispersive X-ray spectroscopy (EDX) spectra have been also recorded, with one example shown in Figure S2.9 a. In all cases, an average Zn:O ratio of 40/60 is observed, which is in good agreement with the expected 1:1 ratio. The selected area electron diffraction (SAED) results are presented in Figure S2.9 b., where the patterns can be indexed as zinc oxide. Scanning electron microscopy (SEM) images are shown in Figure 2.13. The surface morphology of native HMW is comparable to that of HMW@ZnO_10%, indicating that the applied synthesis conditions do not significantly alter the biopolymer surface.

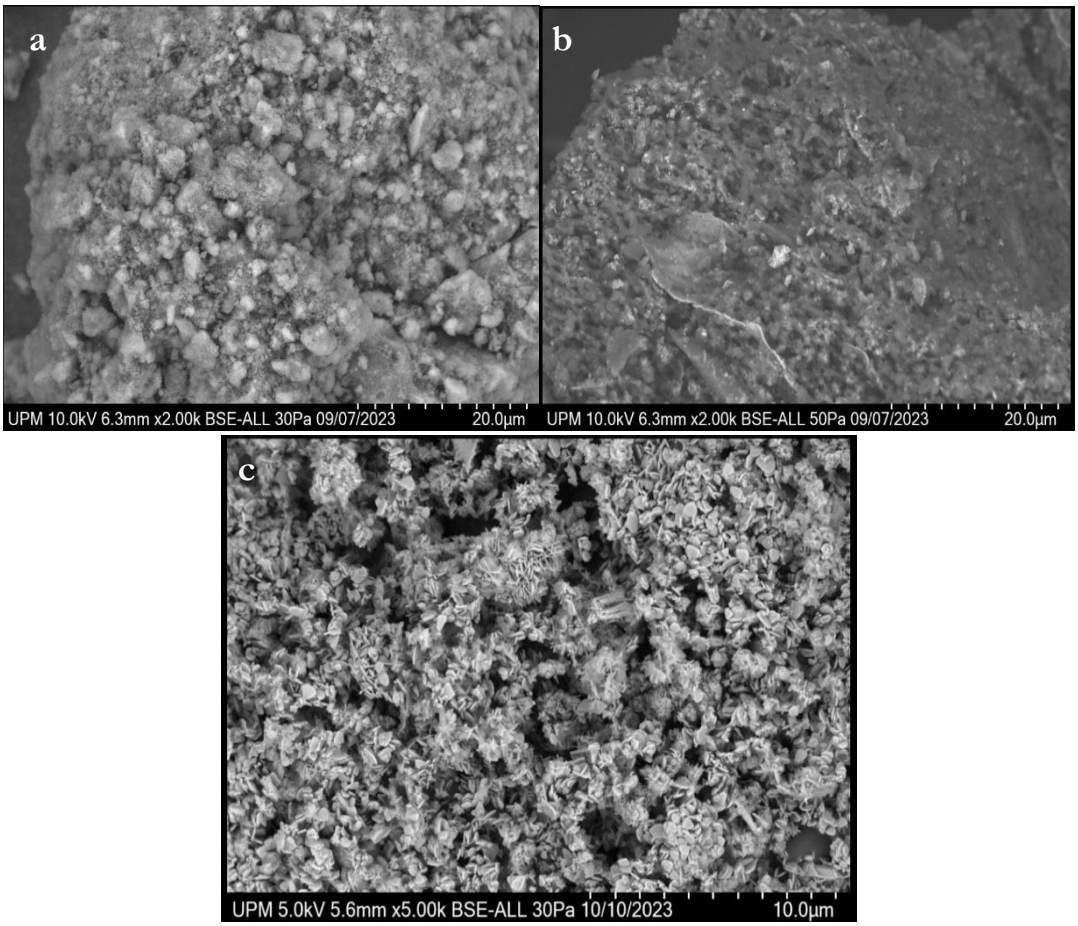

Figure 2.13. SEM images of (a) HMW compared to(b) HMW@ZnO_10% and (c) ZnO_ref.

The nanoparticles are encapsulated within the surface protrusions of the lignin macromolecular matrix and are uniformly distributed throughout the organic phase, as evidenced by EDX mapping. This mapping, which highlights zinc in red for both HMW@ZnO_10% and HMW@ZnO_30%, demonstrates that the zinc content in the final material does not impact the uniformity of its distribution (Figure 2.14).

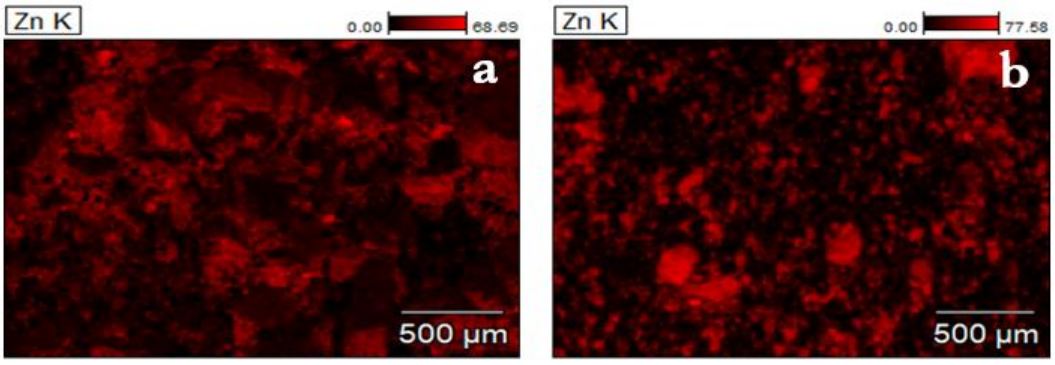

Figure 2.14. SEM-EDX analysis, reporting elemental mapping of zinc for (a) HMW@ZnO_10% and (b) HMW@ZnO_30%.

Dynamic light scattering (DLS) was used to assess the average aggregate size of the particles using a Malvern Zetasizer Nano ZS (Malvern, UK) and the results are presented

in Figure 2.15, Figure S2.10 and Table S2.6. A relatively broad size distribution of the nanoparticles is observed in all cases, with comparable polydispersity indexes (PDI) ranging from 0.184 to 0.192. In contrast, PDI for ZnO_ref is higher (0.246) (Figure S2.11). The average particle diameters are found to be 137 nm, 156 nm, and 123 nm for HMW@ZnO_5%, HMW@ZnO_10%, and HMW@ZnO_30%, respectively, while for ZnO_ref, the average diameter is 218 nm (Figure 2.15, Figure S2.10 and Table S2.6).

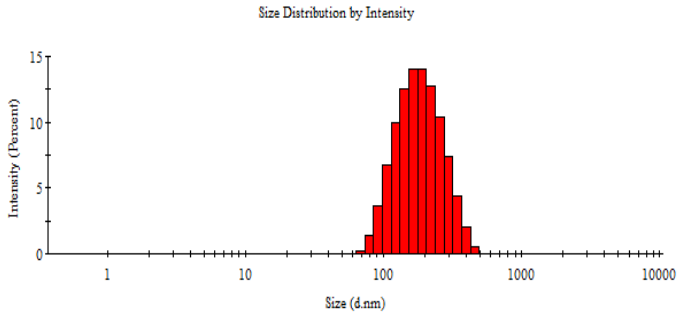

Figure 2.15. DLS size distributions for HMW@ZnO_10%

The aggregation of nanoparticles of HMW@ZnO_10% in water at room temperature over time is assessed (Figure 2.16); results for HMW@ZnO_5%, HMW@ZnO_30% and ZnO_ref are shown in Figure S2.11. HMW@ZnO_5% remain quite stable in solution up to 4 days, with slight aggregation phenomena occurring, while both ZnO_ref and HMW@ZnO_30% exhibit aggregation, likely due to a higher concentration of nanoparticles. The results are summarized in Table S2.7.

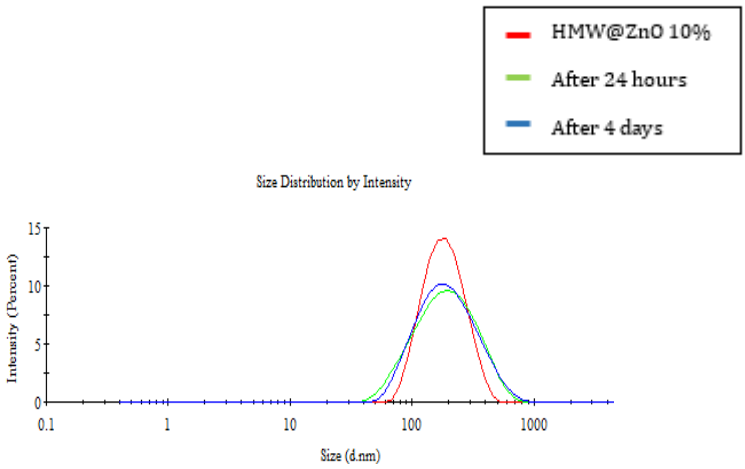

Figure 2.16. DLS size distributions investigated during a time of four days of HMW@ZnO_5% (a), HMW@ZnO_10% (b), HMW@ZnO_30% (c) and ZnO_ref (d).

We have further confirmed the scalability of the synthesis of HMW@ZnO materials, proceeding with a Kg-scale procedure (see Experimental Section for details). As already mentioned, since no significant differences in terms of size and morphology of the inorganic particles have been observed by using different metal sources, zinc sulphate heptahydrate has been employed in the synthesis. For lower metal contents, complete ZnO formation is observed with a slight excess of base (Table 2.3). PXRD of the materials

obtained by scale up procedure are reported in Figure S2.12. TEM studies have been carried out on the HMW@ZnO_X% materials (X = 5, 10, 30%) produced through a kilogram-scale process (Figure 2.17) to evaluate whether these conditions affect the size and morphology of the ZnO nanoparticles. PXRD of HMW@ZnO_5% contains aggregates ranging from 50 to 500 nm in size, made up of nanoparticles with dimensions between 10 and 20 nm, alongside larger needle-like crystals (50-500 nm in length, 20-40 nm in thickness). For HMW@ZnO_10%, the inorganic phase consists of two types of needle-like structures: one with lengths ranging from 20 to 300 nm and thicknesses of 10-20 nm, and another with lengths between 50 and 100 nm and thicknesses of 5-20 nm. HMW@ZnO_30% shows aggregates composed of nanoparticles measuring 5-10 nm, as well as larger crystals ranging from 20 to 200 nm in size and 10-20 nm in thickness. Overall, the synthetic procedure, whether on a laboratory scale or during the scale-up process, ensures very similar morphologies and sizes for the ZnO nanoparticles, with small nanoparticle aggregates alongside well-crystallized needle-like structures. However, it can be noted that during the scale-up, larger aggregates, up to 500 nm, are present in HMW@ZnO_5%.

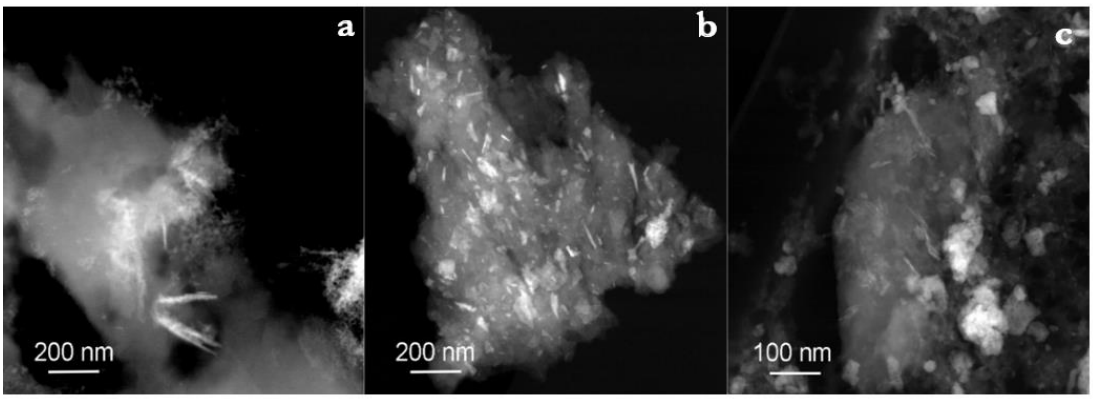

Figure 2.17. TEM images showing the different dimensions and morphologies of the nanoparticles for a) HMW@ZnO_5%, b) HMW@ZnO_10%, c) HMW@ZnO_30% obtained by scale-up procedures. $ZnSO_4 \cdot H_2O$ was used as metal source.

The key features obtained from the TEM analyses are summarized in Table 2.7.

Table 2.7. Dimensions and morphologies for NPs in HMW@ZnO_X% (X = 5, 10, 30) obtained by Kg scale up compared to the ones obtained with laboratory scale procedures (data collected also in Table 2.4).

	Size	Shape
HMW@ZnO_4% scale up	Aggregates constituted by 5-10 nm elements	Aggregates constituted of small nanoparticles
	Sporadic presence of needles with length 50-500 nm and thickness 20-40 nm	Needles
HMW@ZnO_5%	Aggregates of 20-300 nm constituted by NPs of 10-20 nm	Aggregates of small nanoparticles
	Sporadic presence of elongated crystals with a length of 50-200 nm and a thickness of 10-40 nm	Needles
HMW@ZnO_10% scale up	Aggregates with dimensions 20-200 nm constituted by 5-10 nm elements	Elongated shape
	Presence of needles with different distribution of sizes: 1) Length: 300 nm Thickness: 10-20 nm 2) Length: 50-100 nm Thickness: 5-20 nm	Needles
HMW@ZnO_10%	Aggregates of 20-200 nm constituted by 10-20 nm NPs	Aggregates of small nanoparticles
	Sporadic presence of needles with length 50-300 nm and thickness 10-50 nm	Needles
HMW@ZnO_23% scale up	Aggregates of constituted by elements with dimensions 5-10 nm	Aggregates of small nanoparticles
	Presence of needles with length: 20-200 nm and thickness: 10- 20 nm	Needles
HMW@ZnO_30%	Aggregates of 20-500 nm constituted by 5-10 nm NPs	Aggregates of small nanoparticles
	Sporadic presence of elongated crystals with length: 50-200 nm and thickness: 10- 50 nm	Needles

During the workup, the pH has been adjusted to around 8 using glacial acetic acid to ensure maximum material recovery, avoiding loss of soluble lignin. The zinc content in the final materials has been quantified using inductively coupled plasma atomic emission spectroscopy (ICP-AES), with results shown in Table 2.8. ICP-AES analyses have been conducted on the scale up obtained material to verify the metal loading. This information is particularly crucial since the materials derived from the scale-up process are those used in the *in vivo* trials, since the concentrations for the tests are calculated based on data obtained from ICP-AES analysis. For HMW@ZnO_30% it can be observed a lower metal content than expected, and this could be related to the washing step, that may result in slight material loss, especially with higher zinc contents, due to partial solubility of the materials in alkaline aqueous suspensions. In general, this issue can be overcome since many *in vivo* applications do not require the provision of washed material, as long as an appropriate cation is chosen for the final byproduct salt (potassium, for instance, in case

of agronomic applications). HMW@ZnO_10% has been selected for trials on plants, with the actual zinc concentrations confirmed by ICP-AES, as described in the *in vivo* section.

Table 2.8. Zinc content determined by ICP-AES analysis for HMW@ZnO_X% (X: 5, 10, 30%), obtained by scale up procedures. The materials were prepared in duplicate.

	Zn% mean ± SD
HMW@ZnO_5%	4.3± 0.1
HMW@ZnO_10%	9.7 ± 0.1
HMW@ZnO_30%	23.2 ± 0.2

To complete the characterization of the HMW@ZnO materials, we have examined potential changes in the lignin matrix due to the experimental conditions needed for the formation of the inorganic phase. Thermogravimetric analysis (TGA), differential scanning calorimetry (DSC), and Pyrolysis-Gas Chromatography coupled with mass spectrometry (Py/GC-MS) have been performed on both HMW and HMW@ZnO_X% materials. The TGA profile of HMW shows water release starting around 100 °C, followed by a significant weight loss of 52.6% at approximately 380 °C due to decomposition, leading to the formation of low molecular weight products and cleavage of the main lignin chain, in agreement with the literature data for Kraft lignin.[88] The TGA profile of HMW is compared to the one of HMW@ZnO_10% in Figure 2.18. The degradation of HMW@ZnO_10% starts similarly with water release, followed by a two-step decomposition: one between 250-500 °C with a slight shift to lower temperatures (around 350 °C) compared to HMW, and a third loss from 618 to 880 °C. The residual mass in the presence of the inorganic phase is higher (about 20%) than that of HMW (about 6%), reflecting the presence of approximately 14% residual zinc, consistent with ICP-AES results. TGA and DTG profile of ZnO_ref are also reported in Figure S2.13 for comparison: the TGA profile shows negligible weight loss.

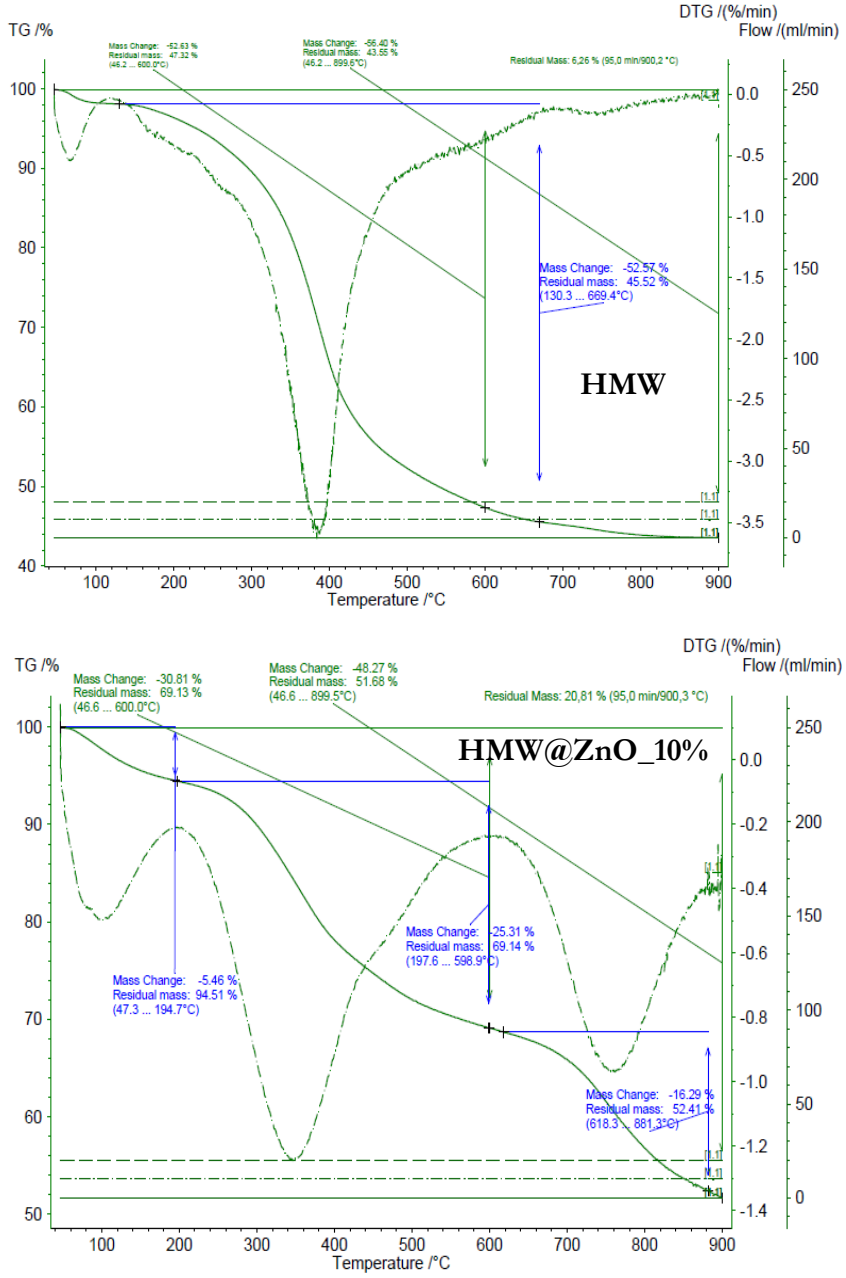

Figure 2.18. TGA/DTG curves of HMW, HMW@ZnO_10%.

Since ZnO_ref exhibits a negligible weight loss in the temperature range observed, subsequent studies were aimed at investigating the presence of the third weight loss between approximately 600 and 880 °C in HMW@ZnO. Given the alkaline conditions of the hybrid material synthesis, HMW has been treated with NaOH in an amount similar to that used for the synthesis of HMW@ZnO_5% (the procedure is described in the experimental section as HMW_NaOH) and then this salified lignin form has been analysed by TGA. In this case, a weight loss is also observed in the same temperature range as that seen for the hybrid material (Figure 2.19).

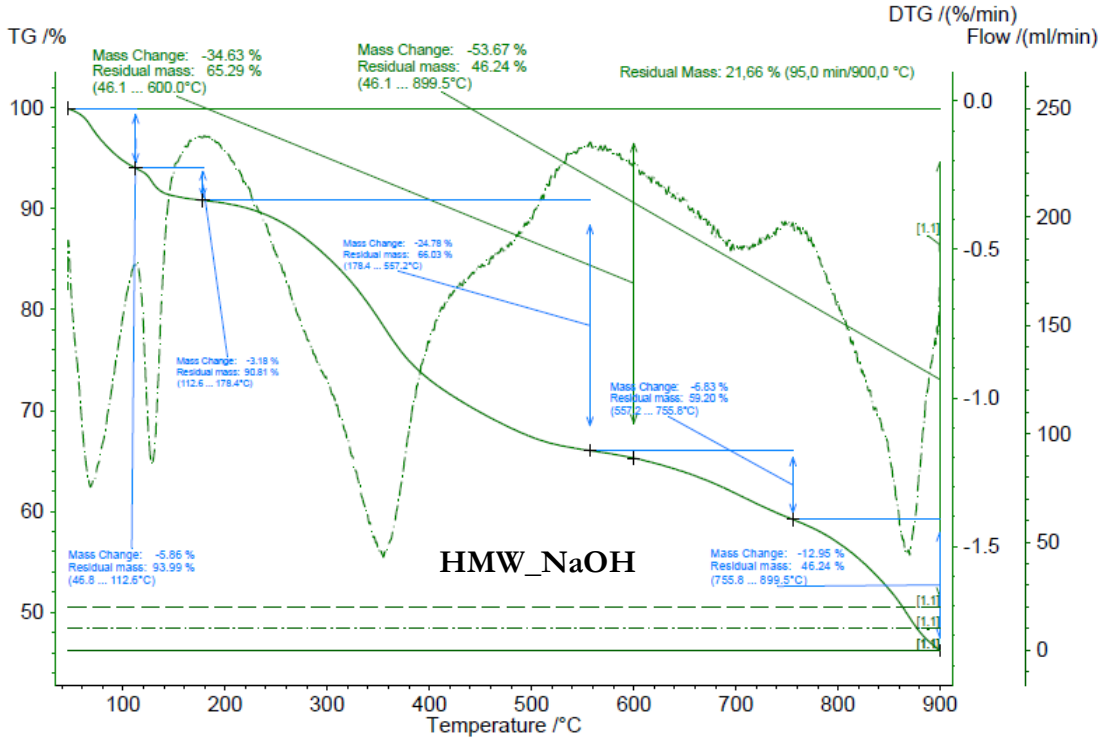

Figure 2.19. TGA/DTG curves of HMW_NaOH

DTG analysis reveals that HMW@ZnO_10% exhibits a significantly lower degradation rate compared to HMW. Differential scanning calorimetry indicates a glass transition at approximately 125 °C for HMW, which aligns with literature values for Kraft lignin (124–174 °C).[88] For HMW@ZnO_X% materials, the glass transition temperature remains similar, with only a slight increase compared to HMW. It is interesting to note that the DSC profile of HMW_NaOH does not differ from native lignin, indicating that the features of the polymeric matrix result unchanged. DSC curves of HMW, HMW_NaOH and HMW@ZnO_10% are provided in Figure 2.20, while the results for HMW@ZnO_5%, HMW@ZnO_30% and ZnO ref are reported in Figure S2.14. The extrapolated peaks are collected in Table S2.8.

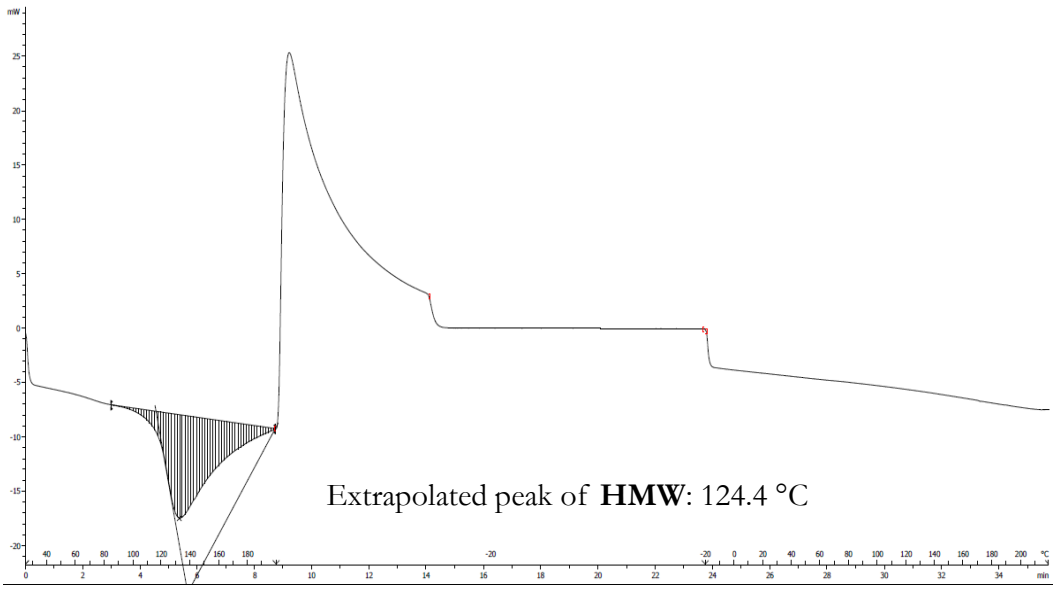

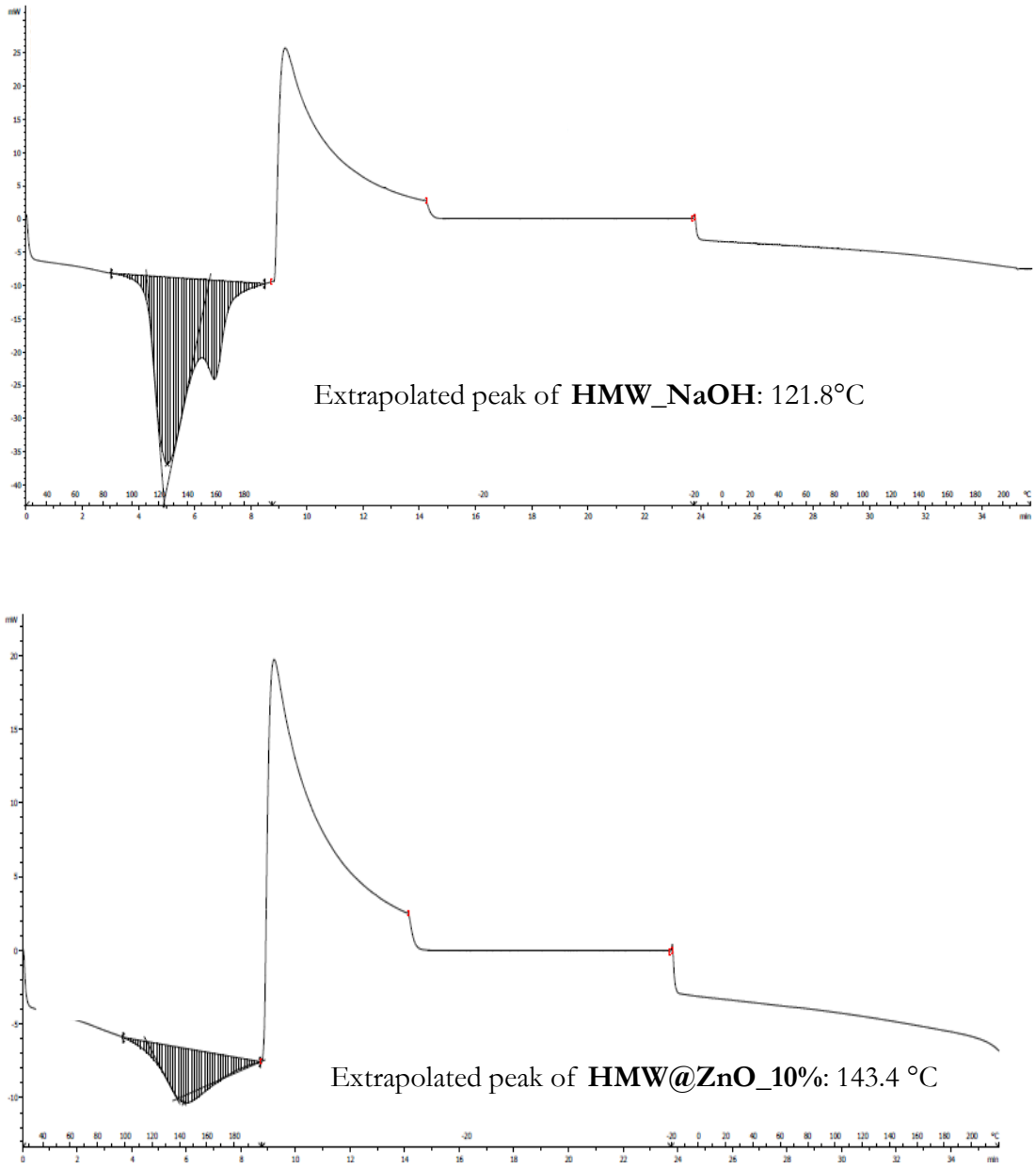

Figure 2.20. DSC analysis of HMW, with exothermic process up. The DSC profile is expressed both in the °C (above the x axes) and in minutes (below the x axes), compared to those of HMW_NaOH and HMW@ZnO_10%

Pyrolysis is a useful technique for investigating the structure of lignocellulosic materials, as it produces characteristic fragmentation patterns of the polymer. Py-GC/MS results for HMW and HMW@ZnO_X % (X: 5%, 10%, and 30%) are presented in Figure 2.21. As expected, the main fragments are phenol-derived molecules. No significant differences are observed between the fragmentation profiles of HMW and the hybrid materials, which confirms the retention of the lignin structure, except for a noticeable increase in the guaiacol fraction, as expected for the presence of Lewis acids, confirming the retention of lignin structure.[89]

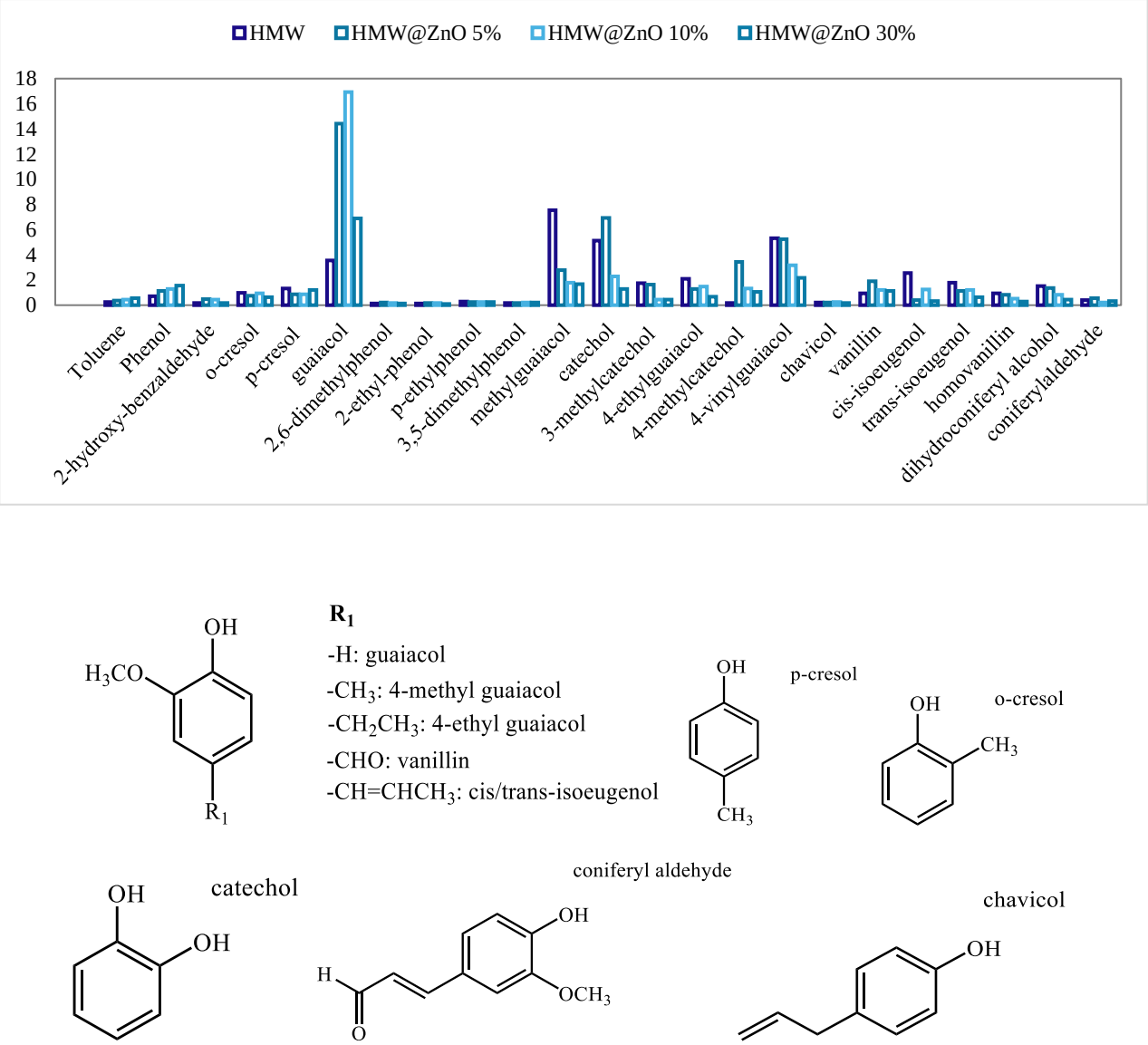

Figure 2.21. Most abundant fragments from pyrolysis-GC/MS of HMW and HMW@ZnO_X% (X = 5, 10, 30). The bars represent the relative area percentages of the analytes.

A key evaluable factor of polymers is also the distribution of molecular weight which in turn affects their properties. The hypothesis that the presence of the inorganic phase can influence the hydrodynamic radius of the lignin molecules was studied. What is observed is a significant increase in the evaluated parameters of M_n, M_W, and PD for the hybrid materials compared to the HMW, as reported in Table 2.9.

Table 2.9. SEC comparison of HMW and HMW@ZnO_X% (X: 5, 10, 30%)

	Number average (M_n)	Weight average (M_w)	Polydispersity (PD)
HMW	1551	5259	3.39
HMW@ZnO_5%	2098	15170	7.23
HMW@ZnO_10%	2353	33773	14.36
HMW@ZnO_30%	1413	8875	6.29

It can be supposed that the presence of the inorganic phase influences the hydrodynamic radius of lignin molecules, therefore, the effect of removing the zinc from the materials has been also investigated. The inorganic phase has been removed soaking the material in a strong acidic environment. The regenerating procedure of the hybrid materials (HMW@ZnO_10%) has been performed at pH 2 in HCl 0.05 M aqueous solution for 24h to remove the inorganic phase and analyse the corresponding lignin matrix. The procedure resulted to be efficient to guarantee the almost complete removal of metal, as demonstrated by means of ICP-AES (Table 2.10). The ICP analysis of the unwashed starting material detected a zinc percentage of 5.61±0.01. Therefore, the removal percentage achieved by the treatment is 90.7%.

Table 2.10. ICP-AES of HMW regenerated, obtained from soaking HMW@ZnO_10% with HCl 0.05 M for 24 hours.

	Zn% mean ± SD
HMW@ZnO_10% treated with HCl	0.52 ± 0.01

FT-IR spectrum of HMW, HMW_HCl and HMW@ZnO_HCl are compared in figure S2.15, showing no variation in the functional groups. The same treatment has been conducted also for HMW, as reference. Table 2.11 shows that the regenerated materials have lower M_n, M_w and PD values but still significantly higher than the starting materials, suggesting that the synthetic conditions of the nanoparticles inside the matrix can lead to phenomena that can be considered irreversible, also after the zinc removal.

Table 2.11. SEC comparison of HMW, HMW treated with HCl and HMW@ZnO_10%_HCl

	Number average (M_n)	Weight average (M_w)	Polydispersity (PD)
HMW	1551	5259	3.39
HMW_HCl	1614	7328	4.54
HMW@ZnO_10%	2353	33773	14.36
HMW@ZnO 10%_HCl	2083	25311	12.16

This behaviour could be explained studying HMW_NaOH material and the results are reported in Table 2.12, comparing them to those obtained for HMW and HMW@ZnO_5% (the hybrid material synthesized with comparable alkaline conditions). It can be concluded that the hybrid material and the NaOH-treated material exhibit very similar behaviour. This is probably due to the alkaline conditions of the synthesis, which lead to an irreversible swelling of the polymer, showing M_n, M_w, and PD highly increased, even after the removal of the inorganic phase.

Table 2.12. SEC comparison of HMW, HMW treated with NaOH and HMW@ZnO_5%

	Number average (M_n)	Weight average (M_w)	Polydispersity (PD)
HMW	1551	5259	3.39
HMW_NaOH	2230	10652	4.78
HMW@ZnO_5%	2098	15170	7.23

Overall, the reported investigations (TGA, DSC, Pyrolysis GC-MS and SEC) highlight that the lignin matrix maintains its structure when treated with a zinc salt with alkaline conditions.

Since the biostimulant effect is strongly influenced by the dose of active ingredient released over time, and slow release can improve performance, we have examined zinc release from HMW@ZnO_10% in a phosphate buffer at pH 6, simulating the soil pH conditions used in *in vivo* tests (see below). As shown in Figure 2.22, zinc release is minimal (about 1%) over 48 hours, suggesting that the hybrid material could provide a slow, sustained release of zinc ions into the soil.

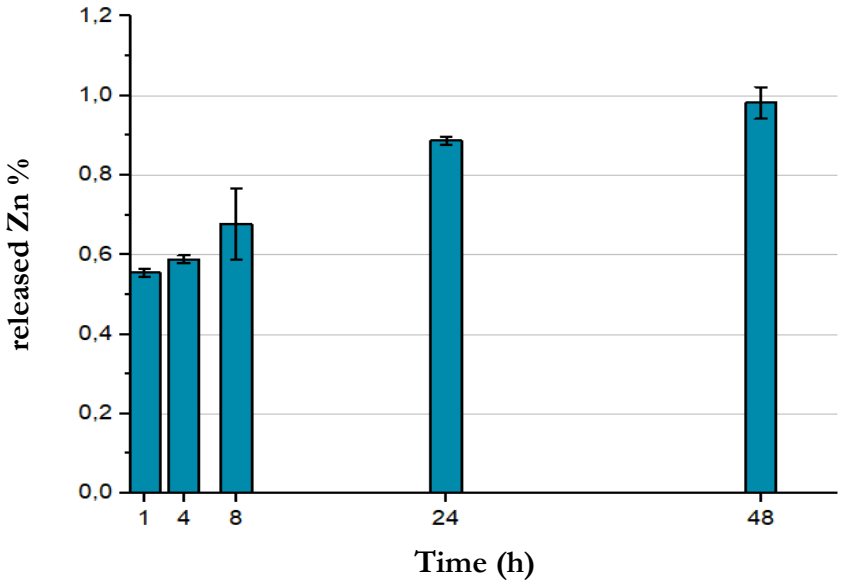

Figure 2.22. Zn^{2+} release profile in a phosphate buffer at pH 6 of HMW@ZnO_10%

Seed germination and *in vivo* preliminary studies

EXPERIMENTAL SECTION

Materials and methods

Tests have been conducted by the research group of Professor Sheridan Woo at University Federico II (Naples).

Germination tests. Tomato (*Solanum lycopersicum* cv San Marzano nano) seeds surface have been sterilized with 1% sodium hypochlorite for 5 min, then rinsed 3 times with sterile distilled water. For seed-priming, HMW@ZnO_10% have been suspended in sterile distilled water considering ZnO supply of 13.7 (C1) and 55 (C2) mg/L, corresponding to 11 mg/L and 44 mg/L of zinc, respectively. Controls have been prepared suspending HMW or ZnO_ref at the same concentrations of each HMW@ZnO formulation, as reported in Table 2.13. Seeds have been immersed in 10 mL of the above-mentioned solutions overnight under slow agitation. Then, the seeds have been sown in double sterilized soil pots (12 cm ⌀) (Ptzer erden GmbH- Orange substrate) naturally containing 220 mg/L of Zn^{2+}. Seeds have been let germinate in a growth chamber in the dark (25 ± 2 °C). Untreated control seeds have been obtained following the same procedure in distilled sterile water. Seed germination have been monitored every 24 hours for the following 16 days.

Table 2.13. Concentration of HMW@ZnO materials applied for seed priming. For each test HMW and ZnO_ref were used as controls. In parentheses the corresponding concentration of zinc for each formulation. Actual zinc content of the hybrid materials have been determined by ICP-AES analysis (see Table 2.8).

	C1 (mg/L)	C2 (mg/L)
Lignin@Zn_10%	114	465
ZnO_ref	13.7	55
(Zn)	(11)	(44)
HMW	100.3	410

***In vivo* tests.** The growth promotion assay has been carried out applying HMW@ZnO_10% with its respective controls (HMW and ZnO_ref). Soil has been twice sterilized at 121° C for 40 minutes and let to cool down for the following 48 hours in sterile plastic bags. HMW@ZnO_10% has been suspended in sterile distilled water considering ZnO supply of 13 mg/L (C1). Controls have been prepared by suspending HMW or ZnO_ref and maintaining their ratios as in the hybrid material (Table 2.13). For each condition, 8 L of soil have been drenched with the above-mentioned suspensions, manually homogenized and transferred into sterile plastic pots (12 cm ⌀). Then, seeds have been sown and let germinate in a greenhouse at 25 ± 2 °C. Each condition consisted of 15 replicates arranged in randomized block design. Seedlings grown in untreated soil, drenched only with sterile distilled water, have been used as controls. Plants have been monitored for 30 days after sowing and manual weekly irrigation was performed. One month-old plants have been collected and biometric parameters as shoot height, fresh and

dry weight of roots and shoots have been measured. Furthermore, root and shoot samples have been dried at 50° C for 72 hours, dry weights have measured and then samples have been reduced to a fine powder using conventional mortars and pestles for ICP-AES analysis in order to determine the content of zinc.

Statistical analysis. Indices related to germination have been calculated by GerminaR package in R version 4.1.2. All datasets (germination and plant biometric parameters) have been subjected to statistical analysis of variance (ANOVA) which have been performed using the software package "Agricolae" in R version 4.1.2[90] Duncan's multiple-range test has been used to analyze separated means with a cut-off for statistical significance at $p \leq 0.05$.

ICP-AES analysis (Inductively Coupled Plasma – Atomic Emission Spectroscopy). ICP-AES analysis on root and shoot samples have been performed as follows: 0.25 g of dry solid sample have been suspended in 3 mL of HNO_3 65% and 1 mL of H_2O_2 30%, then digested in a Milestone microwave MLS-1200 MEGA (digestion sequence: 1 min at 250 Watt, 1 min at 0 Watt, 5 min at 250 Watt, 5 min at 400 Watt, 5 min at 650 Watt, 5 min of cooling). The solutions have been diluted to 10 mL with bi-distilled water and analyzed by using an emission spectrometer JY 2501 with coupled plasma induction in radial configuration HORIBA Jobin Yvon (Kyoto, Japan), ULTIMA2 model. Instrumental features: monochromator Model JY 2501; focal length 1 m; resolution 5 pm; nitrogen flow 2 L/min. ICP source: nebulizer Meinhard, cyclonic spraying chamber; argon flow 12 L/min; wavelengths range 160-785 nm; optical bench temperature 32 °C. The wavelength used for quantitative analysis has been chosen by examining the emission line with greater relative intensity, ensuring that there was no spectral interference with the Argon emission lines. Acquisition parameters: wavelength Zn (nm): 213.856; Voltage (V): 630; Gain: 10. The quantitative analysis has been performed after the acquisition of a calibration line using standard solutions in HNO_3 10%, to simulate the final acidity of the samples; the concentration range of the standards varied from 0.5 mg/L to 40 mg/L. Data acquisitions and processing have been performed using the ICP JY v 5.2 software (Jobin Yvon).

RESULTS AND DISCUSSION

Germination Trials. HMW@ZnO_X% (with X = 10 %) has been utilized for plant trials, taking into account the actual metal content as determined by ICP-AES. The effect of seed priming at two different zinc concentrations has been assessed (C1 corresponding to 11 mg/L and C2 corresponding to 44 mg/L of zinc). Various key germination indices have been analysed to describe the dynamics of the germination process, such as time, rate, and synchrony. The Mean Germination Time (MGT) index calculates the average day of germination, with a lower MGT indicating faster seed germination. Seed priming with HMW@ZnO_10% at concentration C1 results in a significant reduction in MGT compared to seeds treated with HMW alone, ZnO_ref (at the same zinc concentration), and untreated seeds. This positive effect on germination may be attributed to zinc, acting as a precursor for auxin, a growth hormone that regulates growth promotion.[91] Consistent with our findings, several studies have reported enhanced seed germination in maize following zinc oxide nanoparticle priming.[92,93] Conversely, the use of the hybrid material at concentration C2 does not result in any beneficial effects on the parameters assessed (Figure 2.23), suggesting a negative dose-dependent response, as previously observed by Youssef et al.[94] in *Vicia faba* (fava bean). At concentration C1, however, a noticeable reduction in germination time can be observed in seeds primed with HMW alone at a concentration of 410 mg/L (Figure 2.24). No significant improvements have been found in seed germination percentage (rate) or synchrony 16 days after sowing (data not shown) across all tested conditions. Following this, the effect of applying HMW@ZnO_10% containing zinc at 11 mg/L was further explored to assess its potential for promoting tomato plant growth.

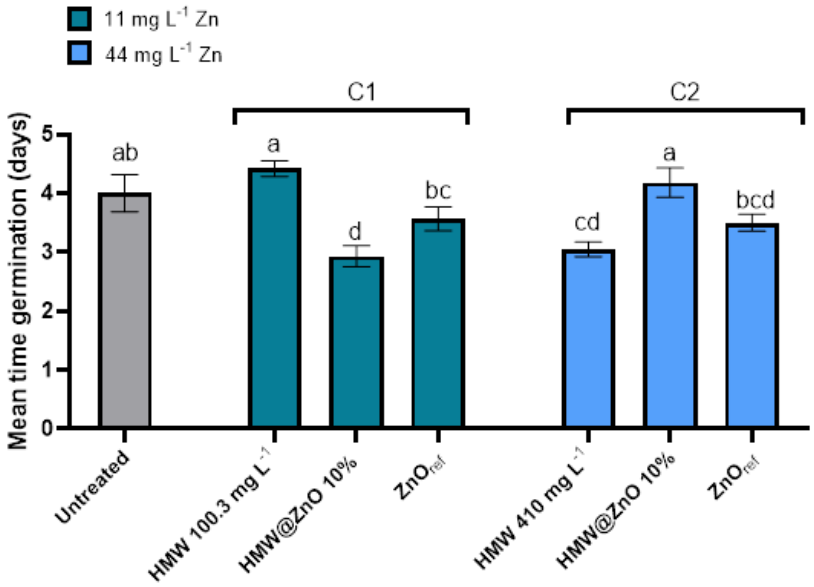

Figure 2.23. Mean germination time of tomato seeds primed with HMW@ZnO_10% containing zinc concentrations of 11 mg/L (C1) and 44 mg/L (C2), respectively. Control groups were prepared by suspending HMW or ZnO_ref, maintaining the same ratios as in the hybrid materials (Table 2.13). Data were analyzed using one-way ANOVA, and different letters denote statistically significant differences in means according to Duncan's multiple-range test (p-value ≤ 0.05).

***In vivo* experiments**. The impact of HMW@ZnO_10% has been evaluated on tomato seedlings by measuring several biometric parameters in 30-day-old plants. Treatments with lignin alone or HMW@ZnO_10% led to a positive effect on shoot dry weight, showing a 33% increase compared to untreated controls, whereas plants treated with ZnO_ref exhibit a significant reduction in this parameter (Figure 2.24 A). Conversely, a 75% increase in root dry weight can be observed in plants treated with HMW, while no notable improvements were seen in plants treated with ZnO_ref or HMW@ZnO_10% (Figure 2.24 B). No significant changes have been noted in shoot height, or the fresh weight of roots and stems for plants treated with HMW@ZnO_10% when compared to untreated controls (data not shown).

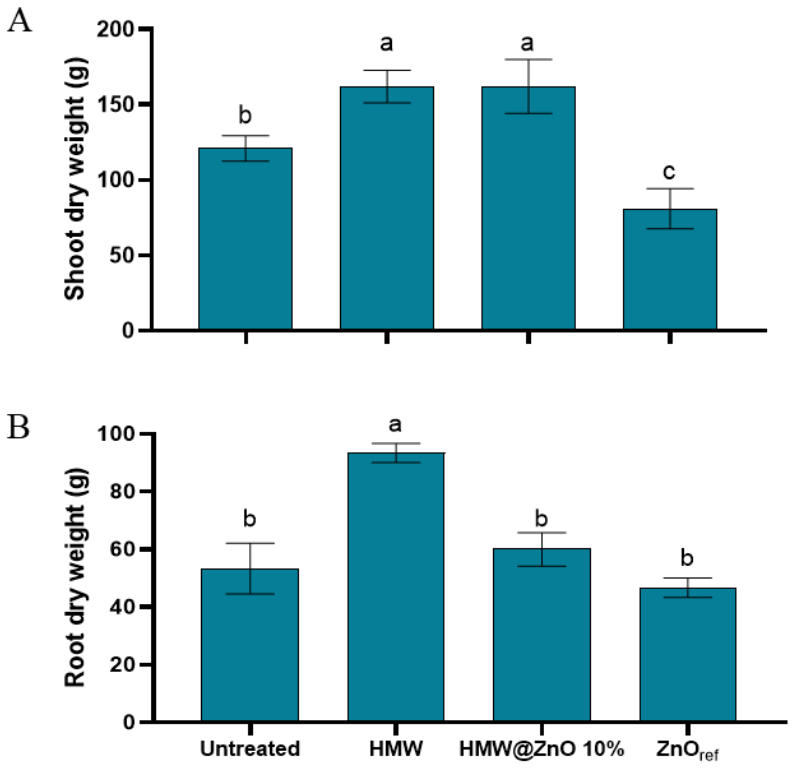

Figure 2.24. Impact of HMW@ZnO_10% on A) shoot dry weight and B) root dry weight. HMW and ZnO_ref served as control treatments. Data were analyzed using one-way ANOVA, with different letters representing statistically significant differences in means according to Duncan's multiple-range test (p-value ≤ 0.05).

ICP analysis of plant tissue. To assess the presence, potential accumulation, and translocation of Zn in plant tissues from source to sink organs, root and shoot samples from the previously described *in vivo* assay have been oven-dried at 50°C for 72 hours. The dried samples have been then ground into a fine powder using standard mortars and pestles. The samples were subsequently analysed using ICP-AES, with Zn content in plant tissues reported as mg per kg of plant dry weight (Figure 2.25). The results showed that plants treated with HMW@ZnO_10% has lower Zn accumulation in root tissues and higher levels of the metal in the shoots, compared to untreated plants (Figure 2.25 A and B, respectively). When compared to the controls, the overall Zn balance in the plants

remained unchanged (Figure 2.25 C). However, the increased Zn content in the aerial parts of the plants may explain the positive effect on biomass observed in the HMW@ZnO_10%-treated plants. This could be related to the role played by zinc in leaf tissues: it helps regulating auxin, restoring photosystem II, stabilizing CO_2 levels in the mesophyll, and contributing to carbohydrate biosynthesis.[95] Additionally, treatment with lignin alone result in lower Zn accumulation compared to ZnO_ref, suggesting possible chelation of metal ions in the soil. In contrast, HMW@ZnO_10% exhibits intermediate Zn accumulation, indicating that the embedded nanoparticles are available for controlled metal release through gradual crystal dissolution. On the other hand, plants treated with ZnO_ref showed a 40% increase in Zn content compared to untreated and HMW@ZnO_10%-treated plants. Moreover, root tissues of ZnO_ref-treated plants contained approximately 60% more Zn compared to untreated, HMW-, and HMW@ZnO_10%-treated plants (Figure 2.25). This significant accumulation in the roots may explain the negative effect of the treatment on shoot biomass. Previous studies have shown that direct application of Zn to the roots in growing plants can inhibit their growth due to the rapid release of Zn from the oxide form, which can negatively impact root physiology and function, even at low concentrations.[96] Furthermore, excess Zn can stunt plant growth and disrupt the availability of other essential nutrients by interfering with phyto-uptake and transport within the plant.[97] An excessive amount of zinc can also disrupt physiological processes by reducing photosynthetic activity, stomatal conductance, and by generating oxidative damage through the production of reactive oxygen species.[98]

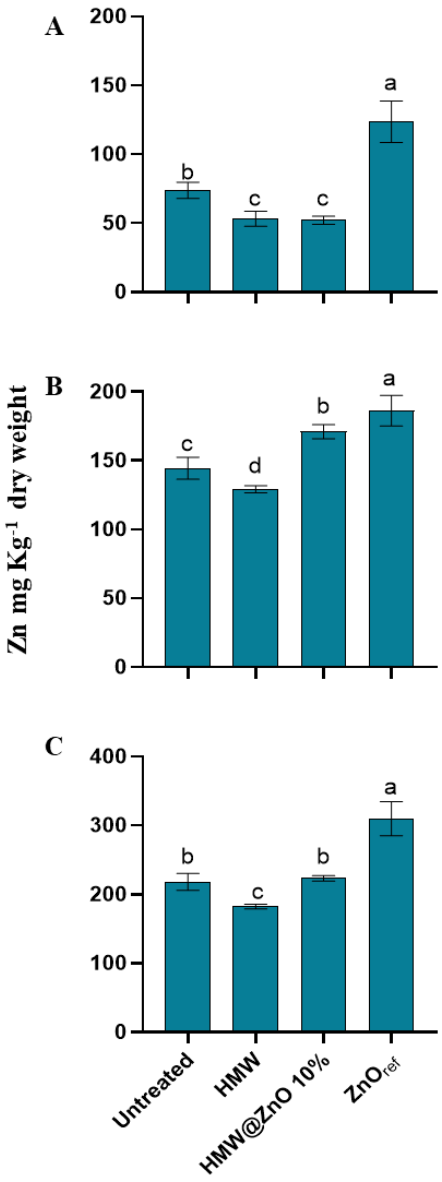

Figure 2.25. Zinc accumulation, expressed as mg per kg of plant dry weight, in A) roots, B) shoots, and C) whole plants treated with HMW@ZnO_10%, HMW, or ZnO_ref, compared to untreated controls. Data were analyzed using one-way ANOVA, with different letters indicating statistically significant differences in means according to Duncan's multiple-range test (p-value ≤ 0.05).

These preliminary results are encouraging, opening the way to further *in vivo* studies with foliar applications.

Antimicrobial activity: *in vitro* tests

EXPERIMENTAL SECTION

Materials and Methods

The tests have been conducted by BICT- Bioindustry Innovation. The aim of this study is to characterize various lignin hybrid material to evaluate their antimicrobial activity against specific microorganisms. This activity has been assessed using a liquid dilution method (CLSI protocol – Clinical and Laboratory Standards Institute) to determine the minimum inhibitory concentrations (MICs) of HMW@ZnO hybrid materials, along with related controls. Specifically, the following samples have been evaluated: HMW@ZnO_10% obtained from zinc sulphate heptahydrate. HMW mixed with ZnO_ref to reach the same zinc content of the hybrid materials, commercial zinc oxide (purchased from Sigma Aldrich, 99%), HMW and ZnO_ref alone. MIC (Minimum Inhibitory Concentration) values have been determined using the CLSI Method M07 "Methods for Dilution Antimicrobial Susceptibility Tests for Bacteria That Grow Aerobically." The experiment was performed in 96-well multiwell plates with a liquid medium. The microorganisms tested were *Listeria monocytogenes* (ATCC 13932), *Bacillus subtilis* (ATCC 9943), *Escherichia coli* (DSM 1576), *Salmonella enteriditis* (ATCC 13076), *Rhizoctonia solani* (DSM 843). Since the compounds are not fully soluble, the tests have been conducted in liquid suspension, with serial dilutions made to maintain homogeneity between each dilution. The products have been tested at varying initial concentrations (ranging from 50 to 5 g/L), ensuring that the relative concentration of zinc remained consistent across all samples, reported in Table 2.14.

Table 2.14. Range of concentrations tested

Sample	Percentage of zinc in sample	Concentration in test (g/L)	Concentration of zinc in test (g/L)
HMW	-	50-0.024	-
HMW@ZnO_10% from $ZnSO_4 \cdot H_2O$	10	40-0.020	4-0.002
HMW + ZnO_ref	10	40-0.020	4-0.002
ZnO_ref	80	5-0.002	4-0.002
Commercial ZnO	80	5-0.002	4-0.002

Specific growth conditions have been followed for each microorganism, as shown in Table 2.15.

Table 2.15. Growth conditions of each microorganism during the tests.

Microrganisms	Inoculum CFU/mL	Growth medium	Temperature	Time of incubation
L. monocytogenes	10^5	Tryptic Soy Broth (TSB)	37 °C	18 h
B. subtilis	10^5	Tryptic Soy Broth (TSB)	37 °C	18 h
E. coli	10^5	Tryptic Soy Broth (TSB)	37 °C	18 h
S. enteriditis	10^5	Tryptic Soy Broth (TSB)	37 °C	18 h
R. solani	10^4	Potato Dextrose Broth (PDB)	25 °C	24 h

The following controls were also included:

- Positive growth control: Growth medium with microorganisms, without the addition of compounds.
- Sterility control: Growth medium without inoculum or compounds.
- Compound control: Growth medium with serial dilutions of the compounds.
- Antimicrobial activity control: Growth medium with the addition of an antibiotic (ampicillin, streptomycin, or ceftriaxone) for bacteria, or an antifungal (ketoconazole) for *R. solani*.

In cases where microbial growth has not been easily detectable, wells have been analysed by plating serial dilutions of each well on TSA (Tryptic Soy Agar) or PDA (Potato Dextrose Agar). The plates have been incubated at the same temperature described above (Table 2.15) for 24 hours, and CFU/ml has been quantified for each condition. Due to the colour and solubility of the products, serial dilutions of the liquid culture have been plated on TSA or PDA. The plates have been examined after 24 hours, and the MIC (Minimum Inhibitory Concentration) or MBC (Minimum Bactericidal Concentration) has been determined.

RESULTS AND DISCUSSION

For *in vitro* tests, pathogens that negatively affect agricultural production or are water/food contaminants have been selected. *Listeria monocytogenes*[99] is a Gram-positive, widely distributed in the environment, including in soil, water, and vegetation. Its ability to grow and reproduce at a wide range of temperatures (from refrigeration temperatures up to 45°C), as well as its tolerance to salty environments and acidic pH, make it a highly resilient bacterium capable of surviving various environmental conditions, including those found in food production and processing. Under favorable conditions, *L. monocytogenes* can proliferate in contaminated food, reaching concentrations high enough to cause human infection. Gram-positive *Bacillus subtilis*[100] is a component of soil microflora, commonly found in the soil surrounding plant roots (the rhizosphere). *E. coli* is one of the main species of bacteria that live in the lower part of the intestines of warm-blooded animals (birds and mammals, including humans). They are essential for proper food digestion. Its presence in water indicates fecal contamination. Although *E. coli*[101] is a common symbiont of the intestines and plays a role in the digestive process, there are situations where it can cause diseases in humans and animals. Some strains of *E. coli* are the causative agents of both intestinal and extra-intestinal diseases, such as urinary tract infections, meningitis, peritonitis, septicemia, and pneumonia. In dairy cattle, it is known to cause acute forms of mastitis. Some strains of *E. coli* are toxigenic, meaning they produce toxins that can cause diarrhea. *Salmonella enteriditis*[102] is a Gram-negative bacterium and is the most commonly isolated bacterial agent in cases of foodborne infections, both sporadic and epidemic. In particular, it has been linked to several egg-related outbreaks of salmonellosis in humans. *R. solani*[103] is the most common disease in lawns during late spring and summer. It causes unsightly brown patches that eventually merge into larger areas, turn yellow, and, if left untreated, lead to the death of the grass. This fungus remains dormant in dead plant material in the soil (usually in the lawn thatch) but, under certain conditions, it becomes active and develops hyphae that attack the living parts of plants, particularly the grass leaves. The plates have been examined after 24 hours, and the MIC (Minimum Inhibitory Concentration) or MBC (Minimum Bactericidal Concentration) is determined. Our data indicate that sterility controls have not shown contamination, and the microorganisms exhibited differential sensitivity to the antibiotics used.

Specifically:

-*E. coli* had an MIC value of 100 μg/mL for ampicillin.

-*B. subtilis* had an MIC value of 0.5 μg/mL for ceftriaxone.

-*S. enteriditis* had an MIC value of 100 μg/mL for streptomycin.

-*L. monocytogenes* had an MIC value of 100 μg/mL for ampicillin.

-*R. solani* was not susceptible to the antifungal ketoconazole up to the tested concentration of 100 μg/mL

Table 2.16 presents the MIC values of the compounds against different microorganisms. The data provided report both the product concentration and the corresponding zinc content. The conditions where the MIC value also corresponds to the MBC value are

highlighted in green, indicating that the product concentration exhibits both growth-inhibiting and bactericidal effects. In these tests, *E. coli* and *S. enteriditis* have been not found to be susceptible to zinc oxide and HMW controls, as they have not shown growth inhibition at the concentrations tested. On the contrary, both are susceptible to the hybrid materials and the mixed preparation of HMW+ZnO_ref, which contains 4 g/L of zinc. *R. solani*, the only fungus tested, has been susceptible to HMW (50 g/L) and the mixed product (HMW+ZnO_ref), suggesting that the growth-inhibiting action is primarily due to lignin. *B. subtilis* and *L. monocytogenes* were more susceptible (compared to the other microorganisms) to the action of both ZnO controls and HMW. Furthermore, for these microorganisms, both the hybrid materials are more effective than the product where ZnO_ref is simply mixed with HMW. This demonstrates that synthesizing the particles in the presence of lignin can lead to crystal sizes and morphologies that are more active than those obtained by simply mixing the commercial product with lignin.

These preliminary results are encouraging, opening the way to further applications as potential pesticides for crop protection.

Table 2.16. Summary table of MIC values of the product and corresponding concentration of zinc.

	Escherichia coli		*Salmonella enteriditis*		*Bacillus subtilis*	
Material	**Product (g/L)**	**Zinc (g/L)**	**Product (g/L)**	**Zinc (g/L)**	**Product (g/L)**	**Zinc (g/L)**
HMW	no MIC		no MIC		25	/
HMW@ZnO_10% from $ZnSO_4 \cdot H_2O$	40	4	40	4	5	0.5
HMW + ZnO_ref	40	4	40	4	20	2
ZnO_ref	no MIC		no MIC		5	4
Commercial ZnO	no MIC		no MIC		5	4

	Listeria monocytogenes		*Risoctonia solani*	
Material	**Product (g/L)**	**Zinc (g/L)**	**Product (g/L)**	**Zinc (g/L)**
HMW	25	/	50	/
HMW@ZnO_10% from $ZnSO_4 \cdot H_2O$	5	0.5	no MIC	
HMW + ZnO_ref	20	2	40	4
ZnO_ref	5	4	no MIC	
Commercial ZnO	5	4	no MIC	

Solargo@ZnO

This section is dedicated to the use of a pre-formulated lignin, Solargo™, supplied by UPM-Kymmene and Green innovation, which is a commercial product. In Solargo™, lignin is suspended with propylene glycol, KOH and water, obtaining a liquid formulate. The use of Solargo™ as source of lignin is a very interesting task, since this liquid formulate is already used by itself for sprayable applications on plants. The idea of using Solargo™ for *in situ* preparation of lignin and metal NPs hybrid materials has already been explored with copper-based materials,[5] with the aim of developing procedures easy to use in practical applications. The perspective is in fact the possibility to obtain the final material directly in field, with an easy and quick synthetic procedure. However, it must be taken into account that the use of Solargo™ could influence NPs formation, due to the presence of surfactants, such as polypropylene glycol, and considering the highly basic character (pH about 12) of the formulation. We have therefore investigated if the mixing of the liquid formulates in presence of zinc salt, using different lignin: metal salts ratios, can lead to the isolation of the same crystalline phases ZnO discussed in the previous section. All the materials, named as Solargo@ZnO_X% (X: 5, 10 or 20%) have been characterized by FT-IR, PXRD, ICP-AES, DLS, TEM.

EXPERIMENTAL SECTION

Materials and Methods

Solargo™, kindly provided by UPM-Kymmene Oij and Green Innovation GmbH, is a formulation containing lignin (100 g), water (325 g), potassium hydroxide 50% (75 g) and propylene glycol (500 g) for 1 L of Solargo100. Zinc chloride is purchased by Brenntag. All the reagents have been used as received with no further purification. pH is measured using a Crison pHmeter basic 20 equipped with an Ag/AgCl electrode.

Materials preparation

Solargo@ZnO_X% (with X= 5, 10, 20 %). In a 500 mL beaker, 1 mL of Solargo™ (100 mg HMW, 75 mg KOH) has been diluted with water to a final volume of 50 or 100 mL. $ZnCl_2$ has been dissolved into distilled water (10 mL) and this solution has been added dropwise to the suspension by using the amount calculated for reaching the desired metal content, as reported in Table 2.17. The formation of a dark brown suspension occurs with pH varying in the range 11-13. The mixture has been then stirred for 10 minutes at room temperature. After this time, the mixture has been dried inside an oven at 130 °C, until complete evaporation of the solvent. The brown materials have been then washed with 10 mL of distilled water, centrifuged, and dried again at 85°C overnight. All the experiments are performed at least in duplicate.

Table 2.17. Stoichiometric ratios of reagents for the preparation of Solargo@ZnO_X%_Y (X= 5, 10, 20%, where Y is the final volume) by using zinc chloride.

	Solargo (HMW)/$ZnCl_2$ mass ratio (mg/mg)	Volume of water (mL)	KOH/$ZnCl_2$ molar ratio
Solargo@ZnO_5%_110	1 mL (100 mg)/12 mg	109	15/1
Solargo@ZnO_10%_60	1 mL (100 mg)/24 mg	59	8/1
Solargo@ZnO_10%_110	1 mL (100 mg)/24 mg	109	8/1
Solargo@ZnO_20%_60	1 mL (100 mg)/49 mg	59	4/1
Solargo@ZnO_20%_110	1 mL (100 mg)/49 mg	109	4/1

RESULTS AND DISCUSSION

The effect of dilution on the synthesis has been studied, as the lignin formulation must be diluted for field applications. In this case, a higher drying temperature compared to wet synthesis described in previous section has been chosen, in order to achieve complete dryness. HMW@ZnO_10% has been synthesized using 59 mL and 109 mL of water respectively, to test dilution conditions of approximately 1:50 and 1:100 of Solargo™: water. The PXRD results are presented in Figure 2.26, displaying similar patterns with the different experimental conditions adopted.

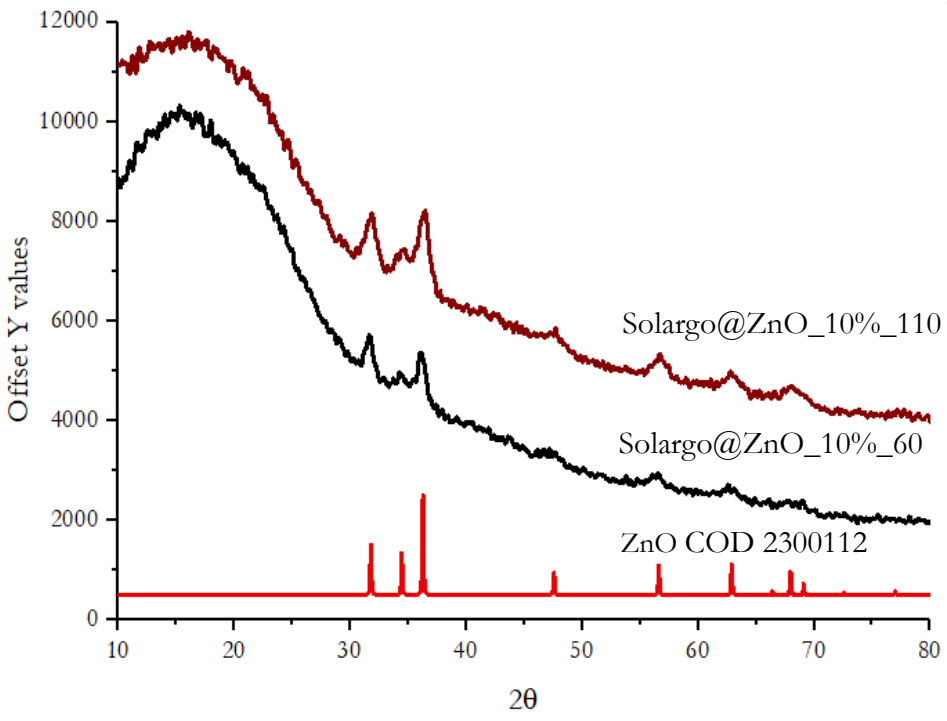

Figure 2.26. PXRD of Solargo@ZnO_10% synthesized with two different dilution conditions compared to ZnO (COD 2300112).

ICP-AES analyses show an experimental metal percentage close to the calculated value (Table 2.18).

Table 2.18. ICP-AES of HMW@ZnO_10% synthesized with two different dilution conditions

	ICP-AES Zn% mean ± SD
HMW@ZnO_10%_60	8.6 ± 0.1
HMW@ZnO_10%_110	10.3 ±0.3

The ability to control the metal content within the material has been studied, as in the wet synthesis, and PXRD analyses have demonstrated the formation of pure ZnO under the various tested conditions (Figure 2.27).

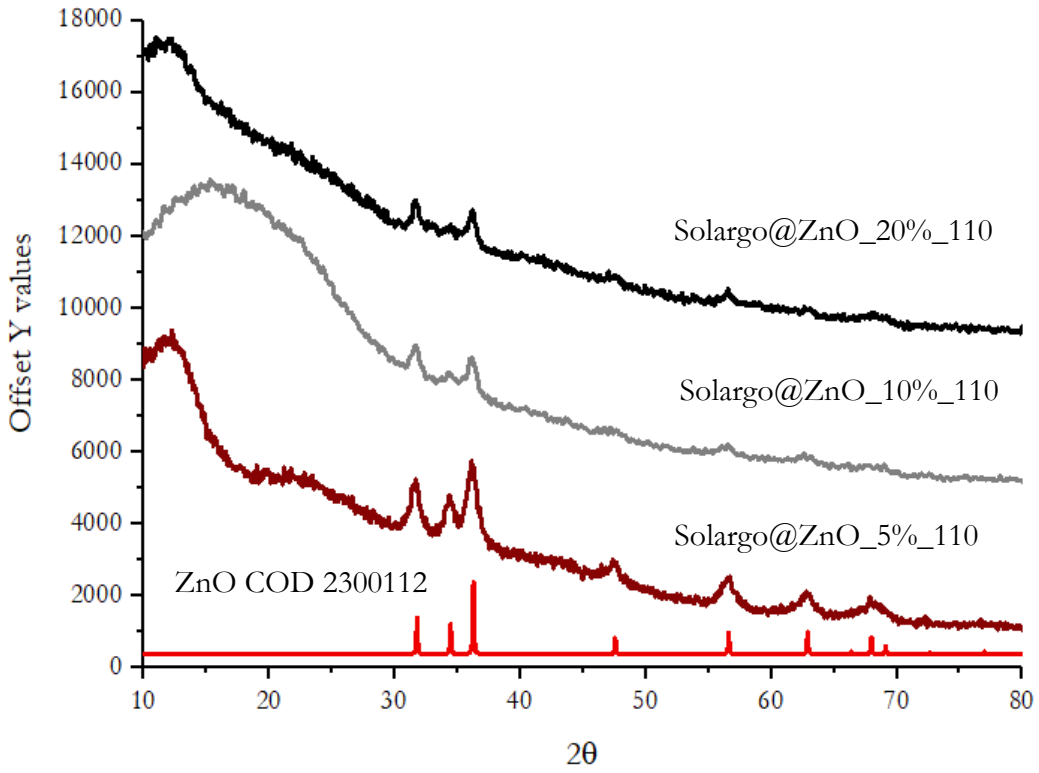

Figure 2.27. PXRD of Solargo@ZnO_X% (with X: 5, 10 and 20%) compared to ZnO (COD 230011).

ICP-AES analyses have been conducted on these samples to determine whether the different metal content can be loaded with equal effectiveness and results are reported in Table 2.19. The results show an experimental metal percentage close to the calculated value with respect to lignin, with the exception for Solargo@ZnO_20% at both dilutions studied. This result can be explained by the fact that, in the lignin formulation, the ratio between lignin and base is fixed. In contrast, under the synthetic conditions described in the previous section, the base is added in a specific molar ratio to zinc. In this case, the amount of zinc relative to lignin has been varied to achieve desired percentages. The ICP-AES data suggest that for zinc concentrations of 5% and 10%, the base content in

Solargo™ is sufficient to fully convert zinc salts into zinc oxide. However, at higher concentrations, only about 10% of the zinc is successfully incorporated into the material.

Table 2.19. ICP-AES of HMW@ZnO_10% synthesized with two different dilution conditions

	ICP-AES Zn% mean ± SD
HMW@ZnO_5%_110	5.47 ± 0.05
HMW@ZnO_20%_110	10.8 ±0.1
HMW@ZnO_20%_60	8.79±0.04

TEM analyses have been carried out on Solargo@ZnO_5% (Figure 2.28 a). Selected Area Electron Diffraction (SAED) is presented, collected from a 200 nm area, along with the corresponding radial average. The peaks observed are all identifiable as reflections from zincite. The crystals are very small, and the intensity of the peaks relative to the background generated by the matrix is quite low. EDX spectra have been collected at various points of the matrix on the crystals. Quantitative analysis of the larger crystals shows an average Zn:O ratio of 40/60, which is consistent with the nominal composition of zincite, considering that the beam does reach the matrix. SAED and EDX spectra are reported in Figure S2.16. Scanning Transmission Electron Microscopy (STEM) images have been recorded using a high-angle annular detector. The intensity of the image in this mode is proportional to the atomic number $Z^{1.7}$ and the sample thickness t. In the lignin matrix, we observe zincite crystals with sizes ranging from 10 to 30 nm, exhibiting an irregular shape. No lanceolate-shaped crystals are present. Solargo@ZnO_10% show the presence of aggregates of zincite crystals with irregular shapes and sizes ranging from 100 to 200 nm (Figure 2.28 b). The zincite crystals have sizes between 10 and 20 nm and exhibit a spherical shape: it must be taken into account that the use of Solargo™ could influence NPs formation, due to the presence of surfactants, such as polypropylene glycol. Results are collected in Table S2.9.

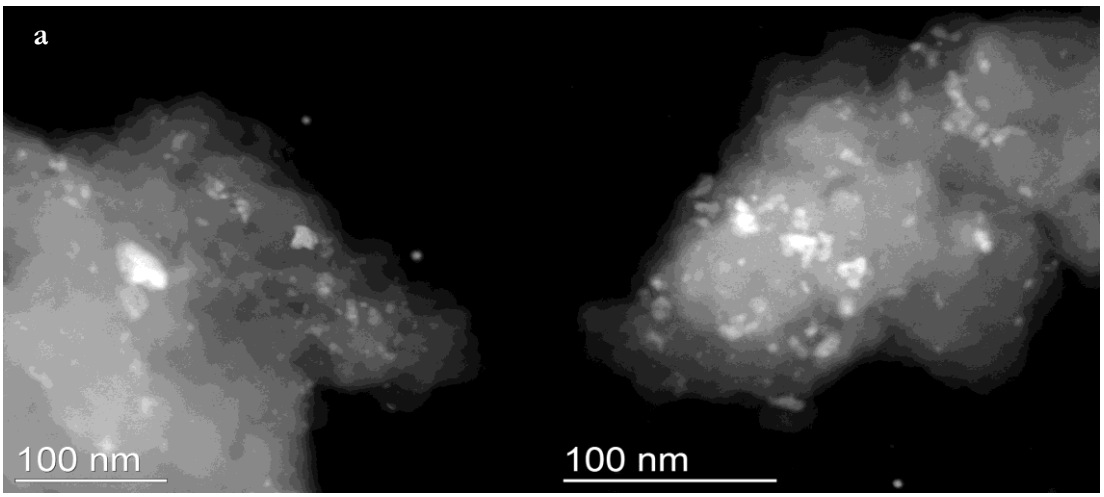

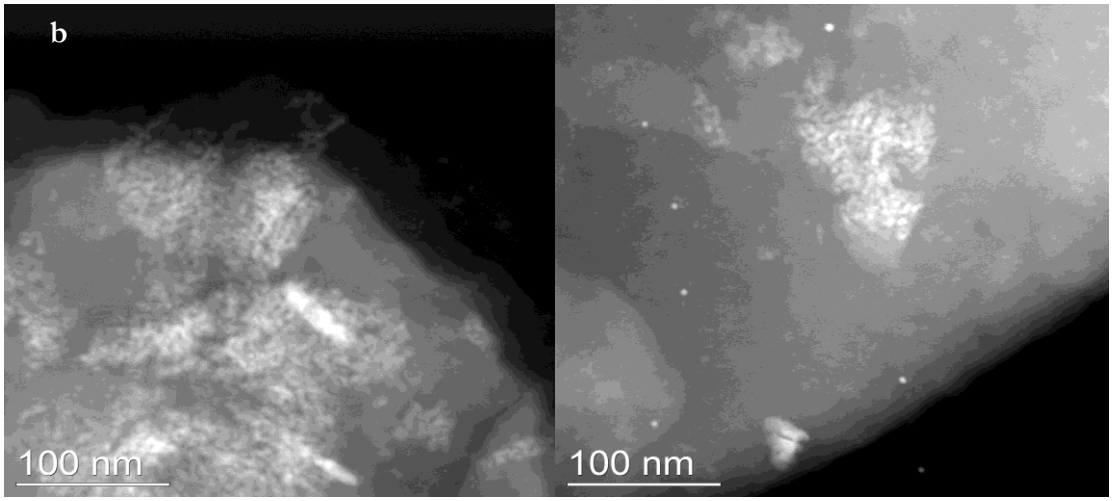

Figure 2.28. TEM of Solargo@ZnO_X% (with X: 5, 10%, respectively figures a and b);

DLS studies have been carried out both on the isolated powders and on the *in situ* prepared liquid material. The suspensions have been prepared following the experimental conditions reported in the Experimental Section with the amount reported in Table 2.17, stirred for 10 minutes and then analysed. The DLS results of Solargo@ZnO_5%, (Figure 2.29) showed that the *in situ* suspension has a distribution with two peaks and a high polydispersity index. Probably, when prepared *in situ,* the crystals tend to aggregate less compared to the isolated powder material. The sizes and PDI are collected in Table S2.10. A similar behaviour was also found for Solargo@ZnO_10%, showed in Figure S2.17.

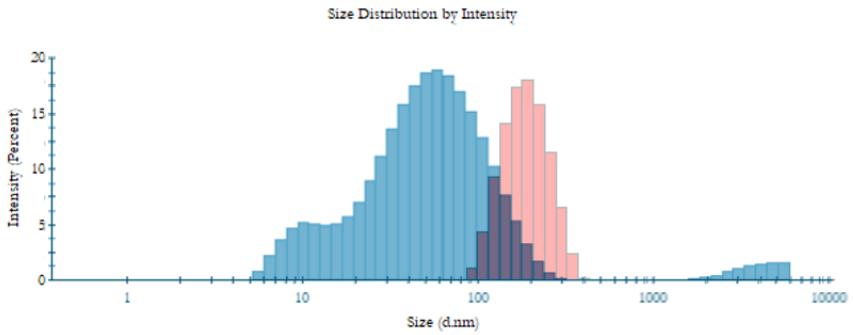

Figure 2.29. DLS of liquid suspension prepared with in situ Solargo@ZnO_5% (blue) and isolated powder (red)

DLS measurements of in situ suspensions prepared according to the conditions for the synthesis of Solargo@ZnO_10% were compared at two different dilutions (60 and 110 mL of water). The results suggest that under higher concentration conditions a major tendency to particle aggregation can be observed. Distributions are stacked in Figure 2.30 and results are reported in Table S2.11.

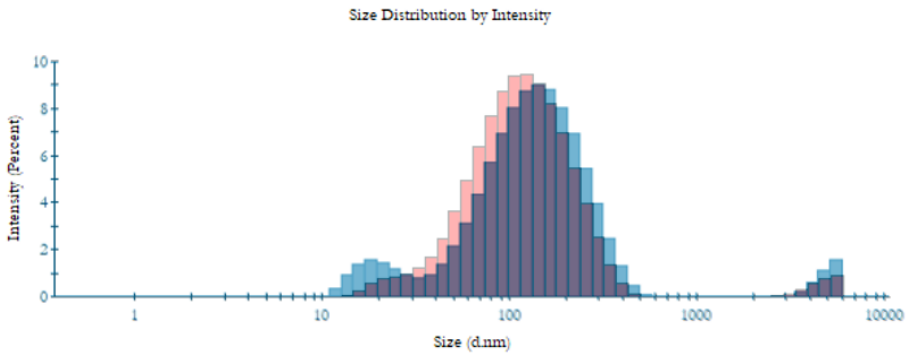

Figure 2.30. DLS of liquid suspension prepared with Solargo@ZnO_10% experimental conditions, prepared respectively with 60 mL total volume (blue) and 110 mL (red).

Conclusions

In conclusion, we have successfully synthesized hybrid materials containing zinc oxide, demonstrating the versatility of these materials for various applications in the agrochemical field. As highlighted in the introduction, these materials hold promise for improving plant health through two main mechanisms. First, they can provide essential micronutrients that support well-being and plant growth. In particular, we have demonstrated the obtainment of reduced germination times by treatment with HMW@ZnO_10% on tomato seedlings. The incorporation of lignin in the matrix plays a critical role in enabling a slow-release mechanism for these nutrients, ensuring a gradual supply over time. This slow-release function is particularly important, as without it, heavy metals could accumulate in the plant, potentially leading to toxicity and negative environmental consequences. *In vivo* trials have been performed on tomato plants, assessing several plant parameters. Results highlight a beneficial effect of HMW@ZnO_10% on dry weight. ICP-AES analysis of plant sections demonstrate zinc accumulation when using ZnO_ref, in particular in the roots, with no beneficial effects observed. In contrast, with the hybrid material, zinc accumulated in the shoots, where a positive effect was observed. This preliminary finding is significant because it lays the basis for further studies of these materials in the agrochemical sector as fertilizers. A second promising application lies in the use of HMW@ZnO materials as pesticides for crop protection. *In vitro* studies demonstrated better results of the hybrid materials when compared to the controls and to the combination of HMW+ZnO_ref against *Bacillus subtilis*, that is a Gram-positive, a component of soil microflora, commonly found in the soil surrounding plant roots (the rhizosphere). Therefore, it is possible to consider the use of these materials not only to enhance plant health, but also to protect crops from various pathogens, potentially reducing the reliance on harmful chemicals in agriculture. The inorganic phases have been synthesized using a sustainable and easy procedure that is scalable, making it suitable for in-field applications. This method ensures that the materials are not only effective but also environmentally friendly, in line with the increasing demand for "green" chemistry in industrial applications. The materials have been studied from both inorganic and organic perspectives, ensuring a comprehensive understanding of their properties and behaviours. A liquid lignin formulation Solargo™ has been used in the synthesis and this approach can be particularly advantageous for foliar applications. To compare the different synthetic strategies, TEM (Transmission Electron Microscopy) studies were conducted to analyse the crystalline structures formed and assess the quality of the materials produced by each method. The comparison of these methods is crucial for optimizing the synthetic process and ensuring the reproducibility and scalability of the materials. Furthermore, future perspectives could be related to the fact that ZnO is currently recognized as "generally recognized as safe (GRAS)" by the Food and Drug Administration and is also used as a food additive. Given their antimicrobial properties and micronutrient content, the potential to apply these in the livestock sector is an intriguing area of research. For this reason, studies have currently being conducted on pigs in collaboration with the research group of Professor A. Maggiolino (University of Bari).

Supporting information

Procedures

Procedure S2.1. HMW@ZnO_10% small laboratory-scale production: In a 50 mL flask, a zinc salt ($Zn(OAc)_2 \cdot 2H_2O$, $ZnSO_4 \cdot 7H_2O$ or $ZnCl_2$) has been dissolved into distilled water under magnetic stirring. HMW has been added to the solution by using the amount calculated for reaching the desired metal content, NaOH 1 M aqueous solution has been added (4,5 equivalents respect to the zinc salt), as reported in Tables S2.1. The formation of a dark brown suspension occurs with pH about 11.5-12. The mixture has been then stirred for 4 hours at room temperature. After this time, the mixture has been dried inside an oven at 95 °C, until complete evaporation of the solvent. The brown materials have been then washed with 10 mL of distilled water, centrifuged, and dried again at 85°C overnight. All the experiments are performed at least in duplicate.

Procedure S2.2. HMW@ZnO_10% small laboratory-scale production with different drying temperatures: In a 50 mL flask, a zinc salt ($Zn(OAc)_2 \cdot 2H_2O$, $ZnSO_4 \cdot 7H_2O$ or $ZnCl_2$) has been dissolved into distilled water under magnetic stirring. HMW has been added to the solution by using the amount calculated for reaching the desired metal content, NaOH 1 M aqueous solution has been added (4,5 equivalents respect to the zinc salt), with the same amounts reported in Table S2.1. The formation of a dark brown suspension occurs with pH about 11.5-12. The mixture has been then stirred for 1 hour at room temperature. After this time, the mixture has been dried inside an oven at 70 °C, until complete evaporation of the solvent. The brown materials have been then washed with 10 mL of distilled water, centrifuged, and dried again at 85°C overnight. All the experiments have been performed at least in duplicate.

Tables

Table S2.1. Stoichiometric ratios of reagents for the preparation of HMW@ZnO_X% (X= 5, 10, 20 %, 30%) by using zinc acetate dihydrate and zinc chloride. 65 mL, 100 mL, 100 mL and 400 mL mL of water were used for X = 5, 10, 20 and 30%, respectively.

	HMW/$Zn(OAc)_2 \cdot 2H_2O$ mass ratio (g/g)	NaOH (mol)	NaOH/ $Zn(OAc)_2 \cdot 2H_2O$ molar ratio
HMW@ZnO_5%	5/0.878	0.016	4/1
HMW@ZnO_10%	5/1.9	0.035	4/1
HMW@ZnO_20%	5/4.39	0.08	4/1
HMW@ZnO_30%	5/7.9	0.144	4/1
	HMW/$ZnCl_2$ mass ratio (g/g)	NaOH (mol)	NaOH/ $ZnCl_2$ molar ratio
HMW@ZnO_5%	5/0.557	0.016	4/1
HMW@ZnO_10%	5/1.2	0.035	4/1
HMW@ZnO_20%	5/2.8	0.08	4/1
HMW@ZnO_30%	5/5	0.146	4/1

Table S2.2. Stoichiometric ratios of reagents for the preparation of HMW@ZnO_10% by using different zinc salts with procedure S2.1 with 10 mL of water.

	HMW/$Zn(OAc)_2 \cdot 2H_2O$ mass ratio (mg/mg)	NaOH (mol)	NaOH/ $Zn(OAc)_2 \cdot 2H_2O$ molar ratio
HMW@ZnO_10%	500/190	0.004	4.5/1
	HMW/ $ZnSO_4 \cdot 7H_2O$ mass ratio (g/g)	NaOH (mol)	NaOH/ $ZnSO_4 \cdot 7H_2O$ molar ratio
HMW@ZnO_10%	500/255	0.004	4.5/1
	HMW/ $ZnCl_2$ mass ratio (g/g)	NaOH (mol)	NaOH/ $ZnCl_2$ molar ratio
HMW@ZnO_10%	500/118	0.004	4.5/1

Table S2.3. Dimension and morphologies for NPs in HMW@ZnO_10% obtained from different zinc salt reagents analyzed by TEM.

	Size	Shape
HMW@ZnO_10% from $Zn(OAc)_2 \cdot 2H_2O$	Aggregates with dimensions: 20 e 200 nm constituted by 10-20 nm NPs	Aggregates of small nanoparticles with
	Sporadic presence of needles with length 50-200 nm and thickness 10-50 nm	Needles
HMW@ZnO_10% from $ZnSO_4 \cdot 7H_2O$	Aggregates with dimensions: 20 e 200 nm constituted by 10-20 nm elements	Aggregates of small nanoparticles
	Sporadic presence of needles with length 50-300 nm and thickness 10-50 nm	Needles
HMW@ZnO_10% from $ZnCl_2$	Aggregates with dimensions: 30 e 300 nm constituted by 10-20 nm elements.	Aggregates of small nanoparticles with simultaneous presence of some crystals with elongated shape
	Sporadic presence of needles with length 50-100 nm and thickness 10-30 nm	Needles

Table S2.4. Dimensions and morphologies for crystals of HMW@ZnO_10% obtained on a laboratory milligrams scale from different zinc salts (zinc acetate dihydrate, zinc sulphate heptahydrate and zinc chloride), drying at 95 °C.

	Size	Shape
HMW@ZnO_10% from $Zn(OAc)_2 \cdot 2H_2O$	Size ranging from 20 to 500 nm. The width of zincite crystals is between 10 and 50 nm. the larger crystals are polycrystalline structures made up of elements of approximately 5-10 nm	Aggregates with not defined shape
HMW@ZnO_10% from $ZnSO_4 \cdot 7H_2O$	There are needles together with larger crystals of 50-400 nm that are polycrystalline structures made up of elements of approximately 5-10 nm.	Aggregates with not defined shape together with needles
HMW@ZnO_10% from $ZnCl_2$	Sizes between 20 and 200 nm. Small crystals tend to agglomerate forming polycrystalline elements. There are elongated and well crystallized zincite crystals	Aggregates with not defined shape together with needles

Table S2.5. Dimensions and morphologies for crystals of HMW@ZnO_10% obtained on a laboratory milligrams scale with Procedure S2.2 from different zinc salts (zinc acetate dihydrate, zinc sulphate heptahydrate and zinc chloride), drying at 70 °C;

	Size	Shape
HMW@ZnO_10% from $Zn(OAc)_2 \cdot 2H_2O$	Size ranging from 20 to 300 nm. The width of zincite crystals is between 10 and 50 nm. The larger crystals have polycrystalline structures made up of elements of approximately 5-10 nm	Aggregates with not defined shape
HMW@ZnO_10% from $ZnSO_4 \cdot 7H_2O$	Needles of 50-400 nm length and width of 10-30 nm	Needles
HMW@ZnO_10% from $ZnCl_2$	Sizes between 20 and 200 nm. Small crystals tend to agglomerate forming polycrystalline elements. There are also elongated and well crystallized zincite crystals	Aggregates with not defined shape together with needles

Table S2.6. Z-averages and PDI results collected with DLS technique on HMW@ZnO materials and ZnO_ref

	Z-Average (d. nm)	PDI
HMW@ZnO_5%	137.1	0.187
HMW@ZnO_10%	156.1	0.192
HMW@ZnO_30%	123.4	0.184
ZnO_ref	218.4	0.246

Table S2.7. Size distribution by intensity results collected with DLS technique on HMW@ZnO materials over 24 hours and 4 days.

	Z-Average (d. nm)	PDI	Z-Average (d. nm) after 24 hours	PDI after 24 hours	Z-Average (d. nm) after 4 days	PDI after 4 days
HMW@ZnO_ 5%	137.1	0.187	132.9	0.211	141.4	0.243
HMW@ZnO_ 10%	156.1	0.192	161.8	0.244	163.4	0.247
HMW@ZnO_30%	123.4	0.184	1003	0.675	1173	0.535
ZnO_ref	218.4	0.246	583.1	0.545	605.3	0.533

Table S2.8. Extrapolated peaks from DSC results.

	Extrapolated peak from DSC
HMW	124.4 °C
HMW@ZnO_5%	137.5 °C
HMW@ZnO_10%	143.4 °C
HMW@ZnO_30%	137.9 °C
ZnO_ref	81.8 °C

Table S2.9. Dimensions and morphologies for crystals of Solargo@ZnO_X% (with X: 5 and 10 %).

	Size	Shape
Solargo@ZnO_5%	Zincite crystals of dimensions 10-30 nm	Irregular shape
Solargo@ZnO_10%	Aggregates 100-200 nm, constituted by 10-20 nm spheres	Aggregates of irregular shape, constituted by spherical elements

Table S2.10. Sizes and PDI results collected with DLS technique on Solargo@ZnO materials with 110 mL final volume.

	Size (d. nm)	PDI
Solargo@ZnO_5%	212.6	0.236
Solargo@ZnO_5% liquid suspension	Peak 1: 10.01	0.417
	Peak 2: 66.25	
Solargo@ZnO_10%	174.0	0.315
Solargo@ZnO_10% liquid suspension	Peak 1: 27.50	0.246
	Peak 2: 124.5	

Table S2.11. Sizes and PDI results collected with DLS technique on Solargo@ZnO_10%_Y materials with different dilution conditions, with Y related to the final reaction volume

	Size (d. nm)	PDI
Solargo@ZnO_10%_60	182.0	0.276
Solargo@ZnO_10%_60 liquid suspension	Peak 1: 20.81	0.436
	Peak 2: 154.1	
Solargo@ZnO_10%_110	174.0	0.315
Solargo@ZnO_10%_110 liquid suspension	Peak 1: 27.50	0.246
	Peak 2: 124.5	

Figures

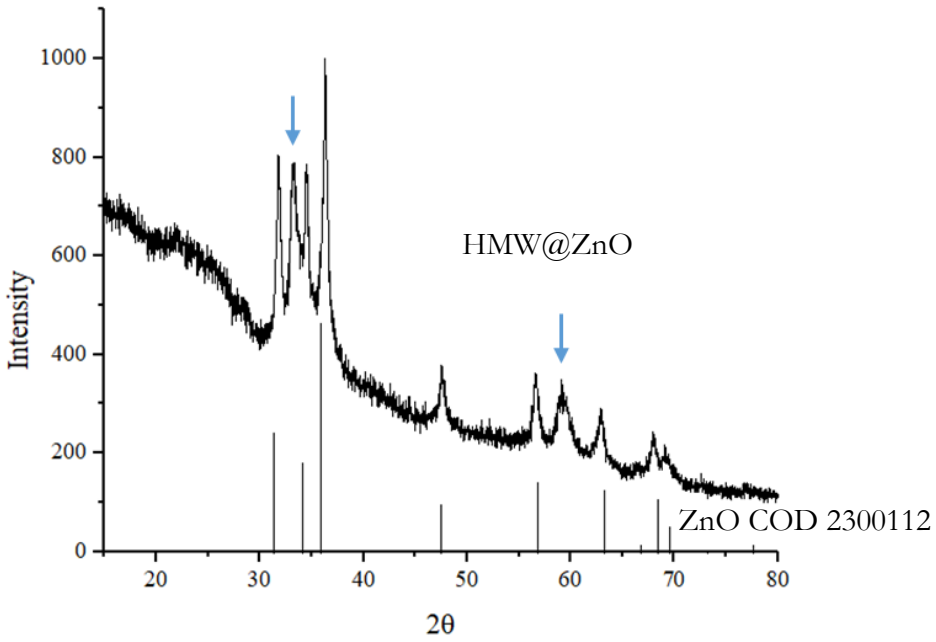

Figure S2.1. PXRD analysis for HMW@ZnO obtained with the use of 2 equivalents of NaOH: together with ZnO, an unidentified crystalline phase is formed (blue arrows).

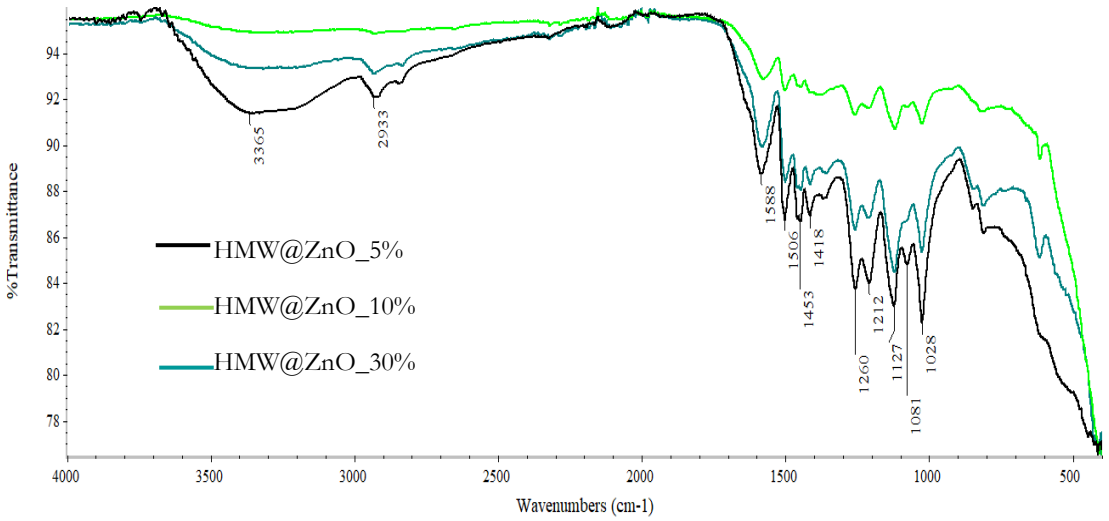

Figure S2.2. Superimposed infrared spectra of HMW@ZnO_5%, HMW@ZnO_10%, and HMW@ZnO_30%.

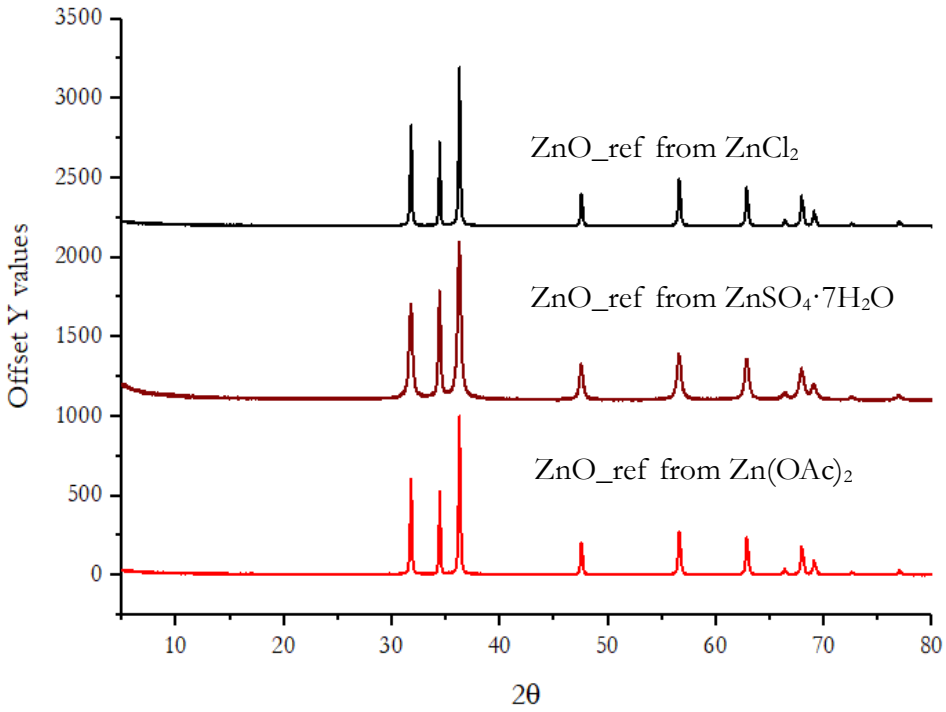

Figure S2.3. PXRD diffractograms for ZnO_ref obtained from different zinc salts;

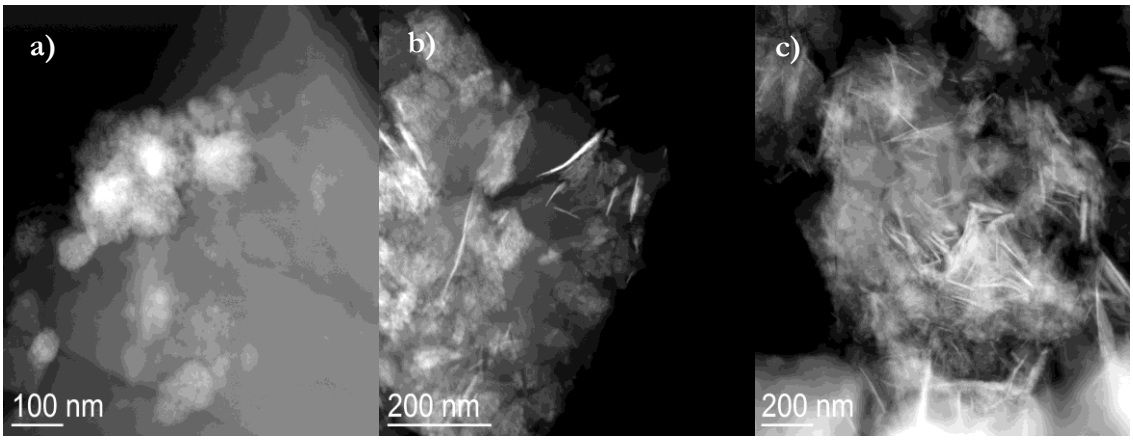

Figure S2.4. TEM images highlighting the different dimensions and morphologies obtained on mg scale for HMW@ZnO_10% from a) zinc acetate dihydrate, b) zinc sulphate heptahydrate and c) zinc chloride.

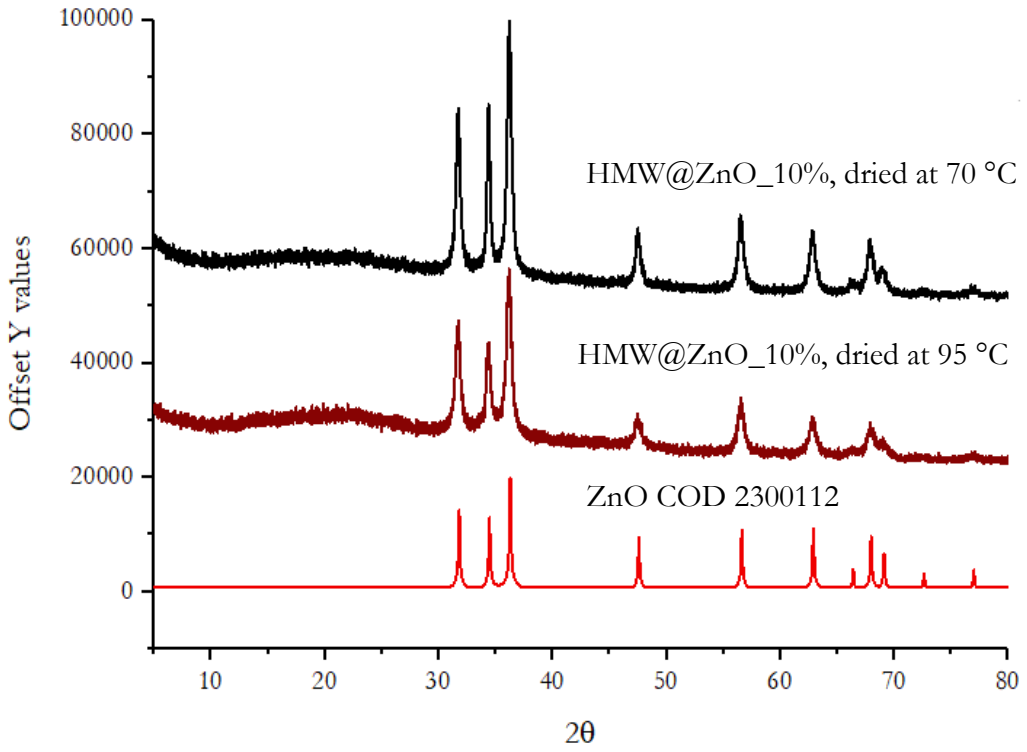

Figure S2.5: Stacked PXRD of HMW@ZnO 10% obtained at different drying temperatures (95 and 70 °C) compared to ZnO from data bank (COD 2300112)

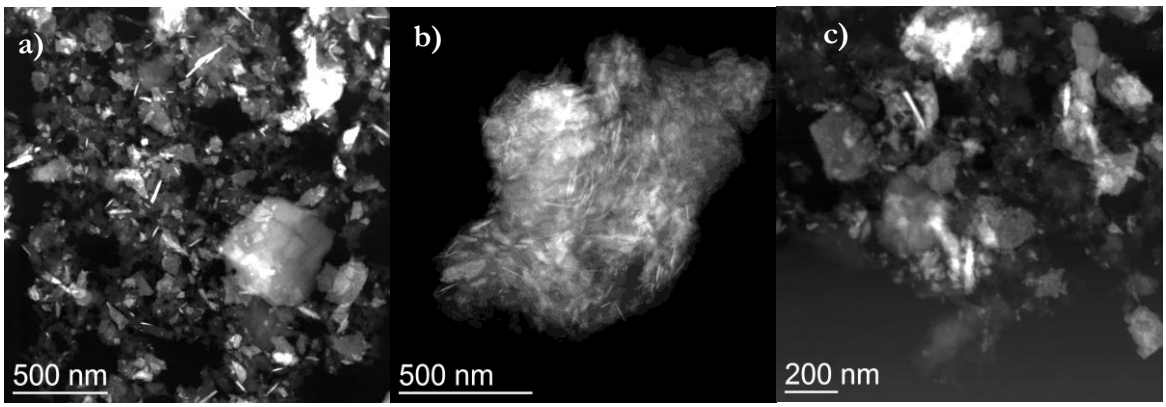

Figure S2.6. TEM images showing the dimensions and morphologies obtained on mg scale drying at 70 °C for HMW@ZnO_10% from a) zinc acetate dihydrate, b) zinc sulphate heptahydrate and c) zinc chloride

a)

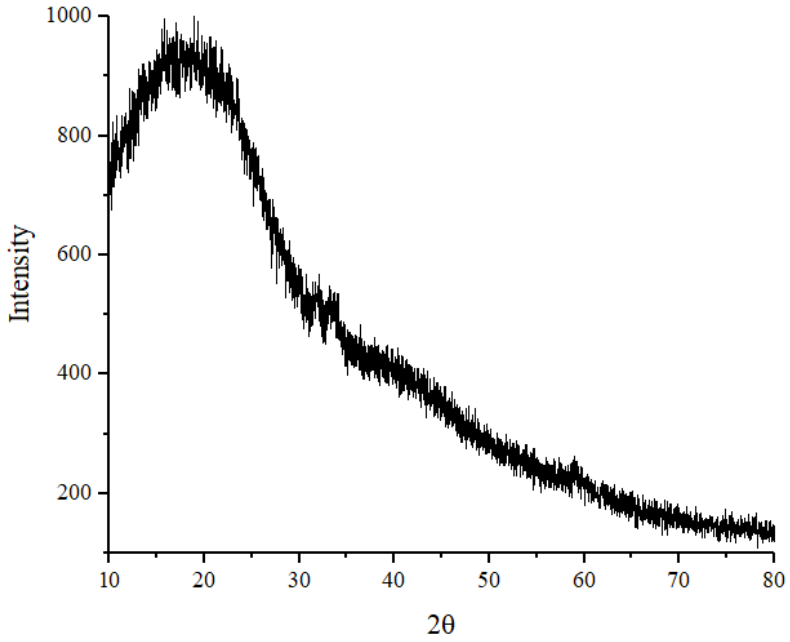

b)

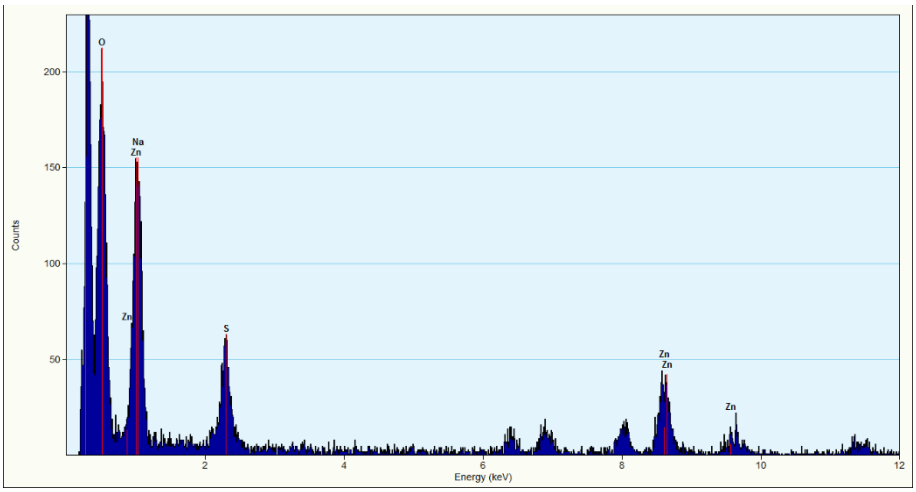

Figure S2.7. a) PXRD diffractograms of HMW@ZnO_5 % obtained by *procedure 2*, b) EDX confirming the presence of ZnO with a Zn/O ratio close to 1.

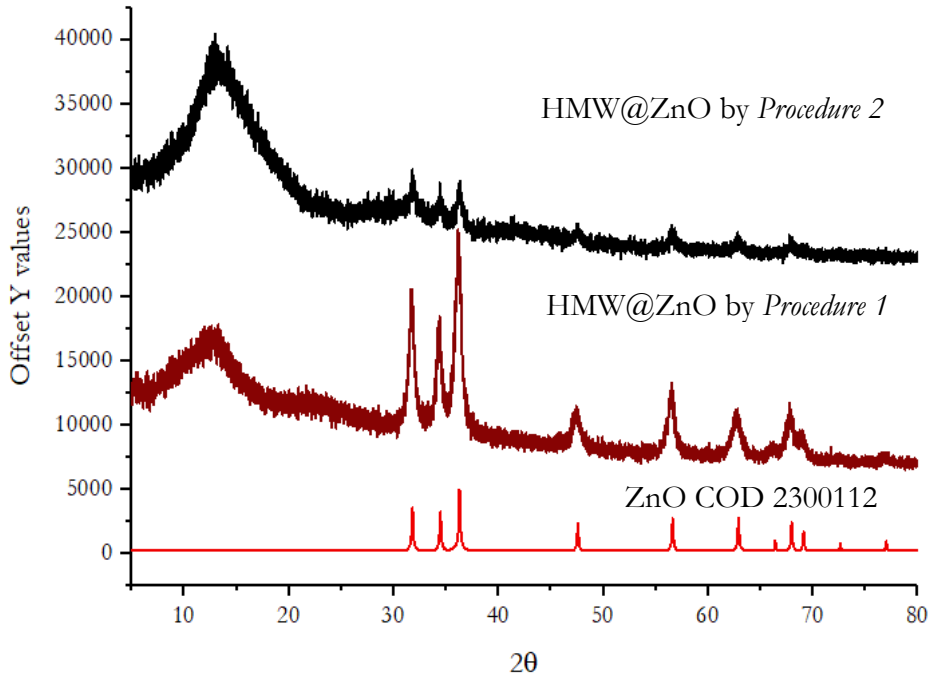

Figure S2.8. PXRD diffractograms of HMW@ZnO_10% obtained by *procedure 2* compared to the one obtained by *procedure 1* and ZnO (COD 2300112).

a)

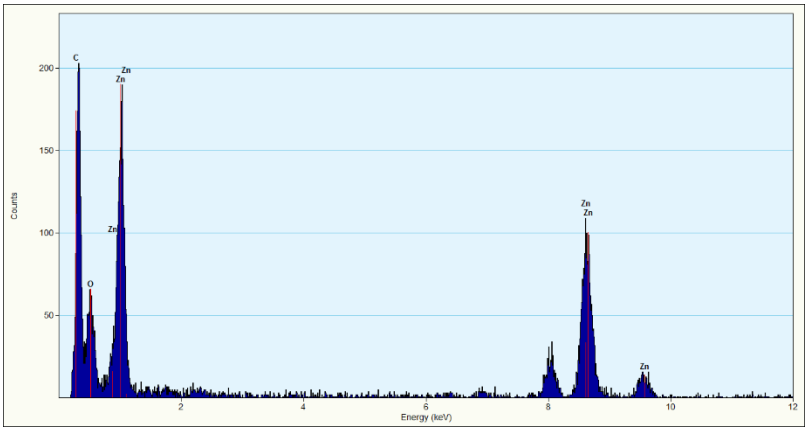

b)

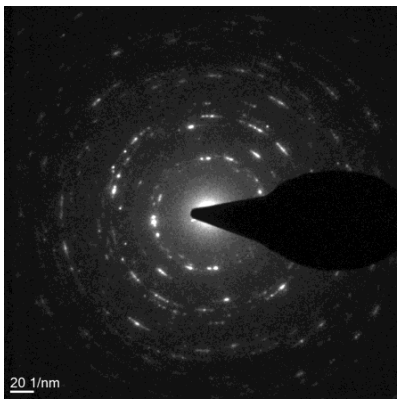

d^{-1} (nm^{-1})	d (nm)	Reflections
3.91	0.255	(002)+(101)
5.10	0.195	(102)
6.22	0.161	(110)
6.82	0.146	(103)

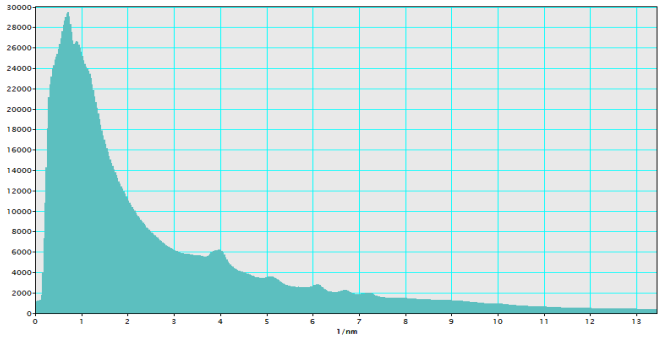

Figure S2.9. a) The EDX analysis displays the composition of the zinc oxide nanoparticles synthesized in HMW@ZnO materials. The reported EDX corresponds to HMW@ZnO_10% obtained from zinc sulphate, taken as an example. b) Electron diffraction from a selected area (SAED) was collected over a 200 nm region, accompanied by the corresponding radial average. The observed peaks are clearly identifiable as reflections corresponding to zincite. These peaks are sharp and intense, indicating the presence of large crystals with high crystalline quality. The reported SAED corresponds to the HMW@ZnO_10% sample, which was obtained from zinc sulphate as a representative example.

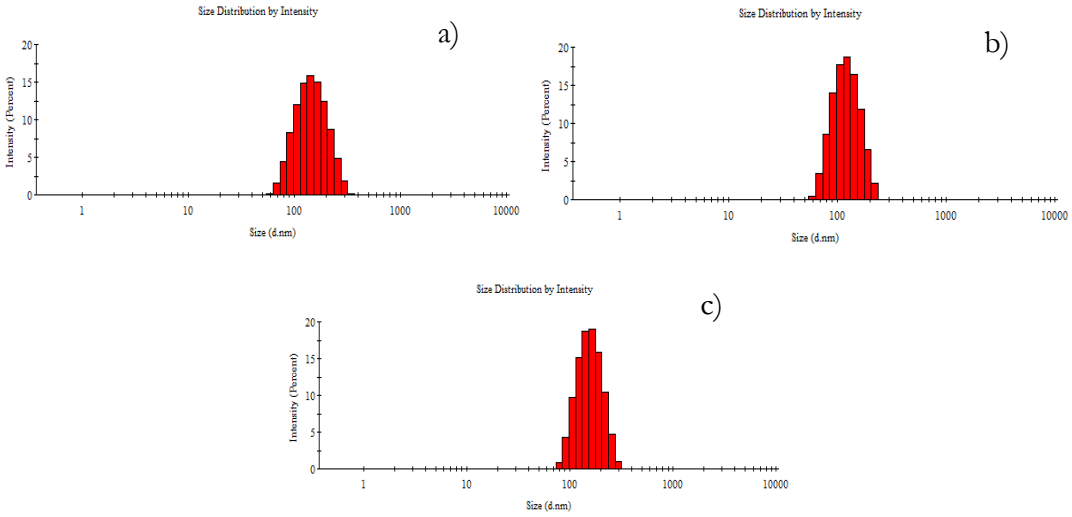

Figure S2.10. DLS size distributions for a) HMW@ZnO_5%, b) HMW@ZnO_30% and c) ZnO_ref.

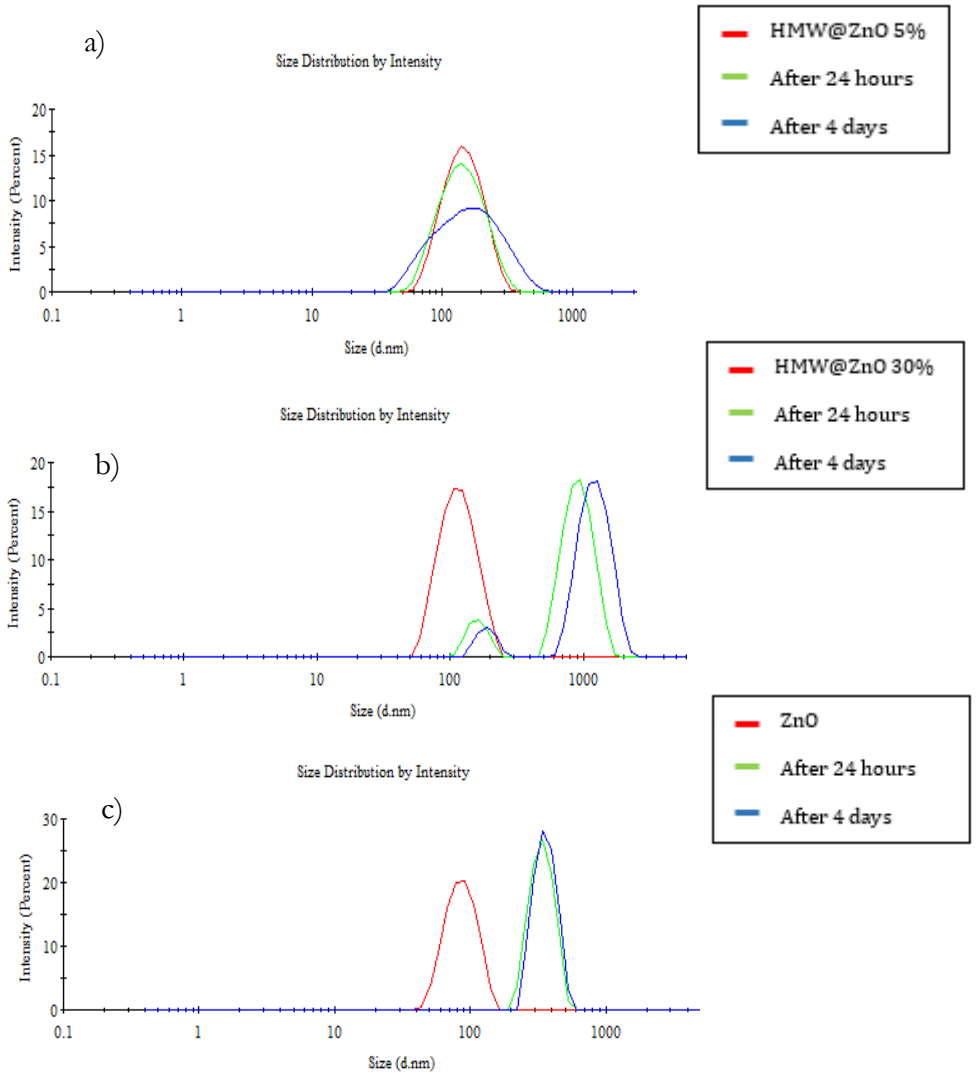

Figure S2.11. DLS size distributions investigated during a time of four days of a) HMW@ZnO_5%, b) HMW@ZnO_30% and c) ZnO_ref.

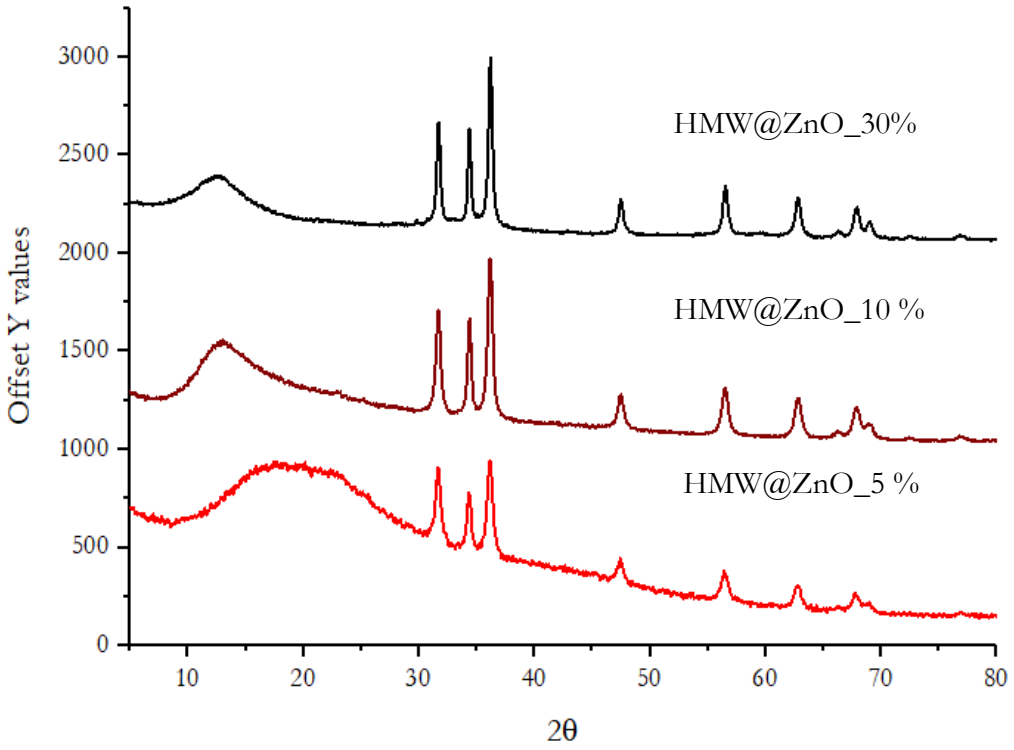

Figure S2.12. PXRD diffractograms of HMW@ZnO_5%, HMW@ZnO_10% and HMW@ZnO_30% of products obtained by scale up procedures.

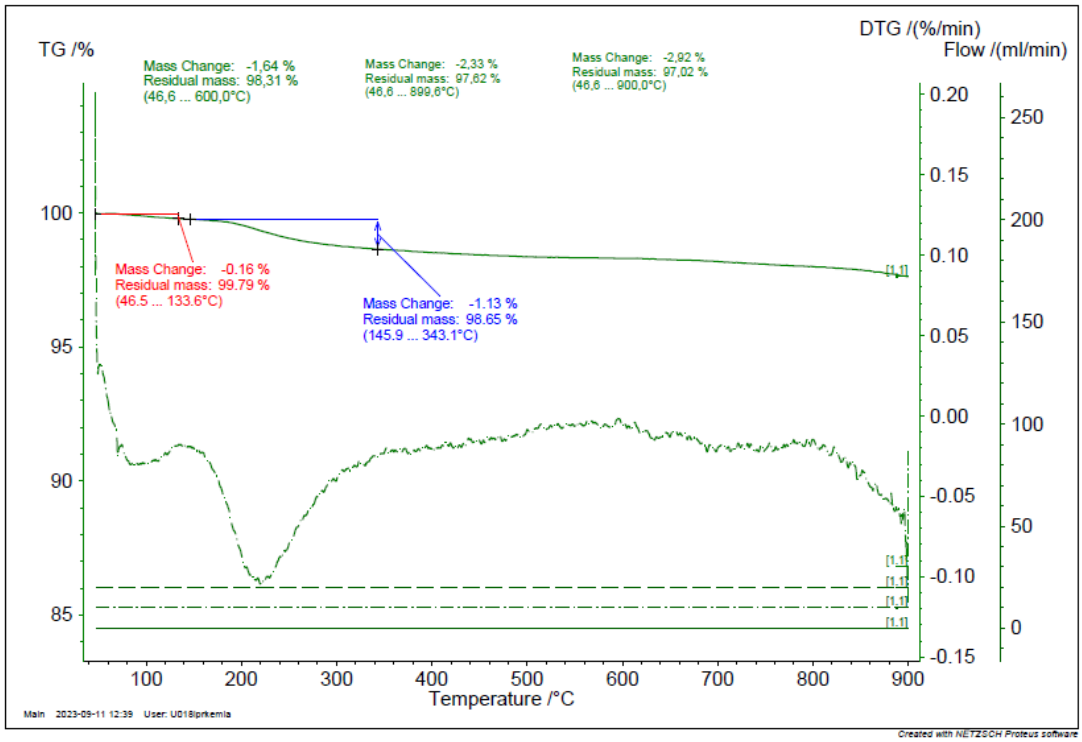

Figure S2.13. TGA/DTG curves of ZnO_ref.

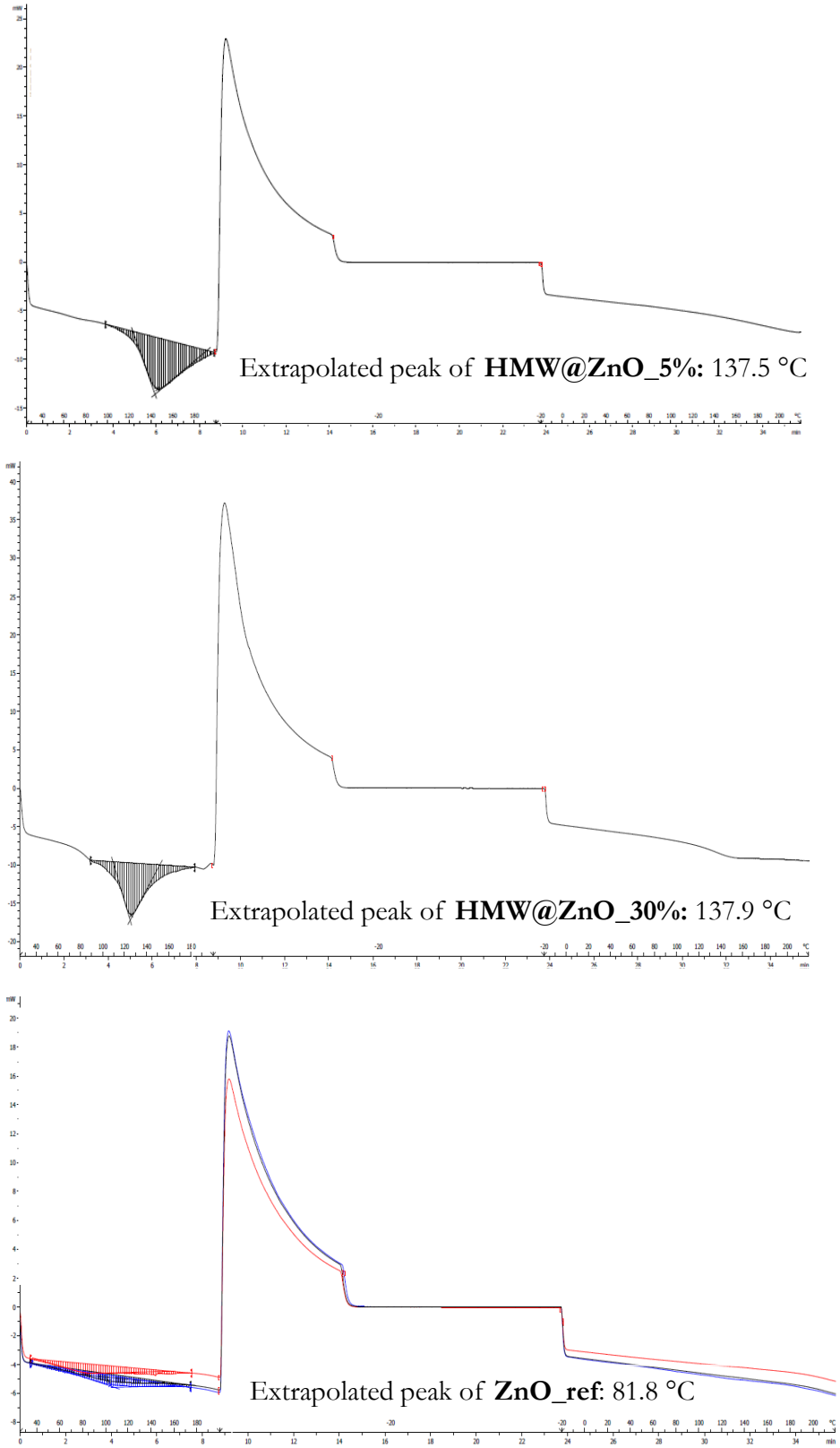

Figure S2.14. DSC analysis with exothermic process up. The DSC profile is expressed both in the °C (above the x axes) and in minutes (below the x axes). HMW@ZnO_5% HMW@ZnO_30% and ZnO_ref are also reported for comparison.

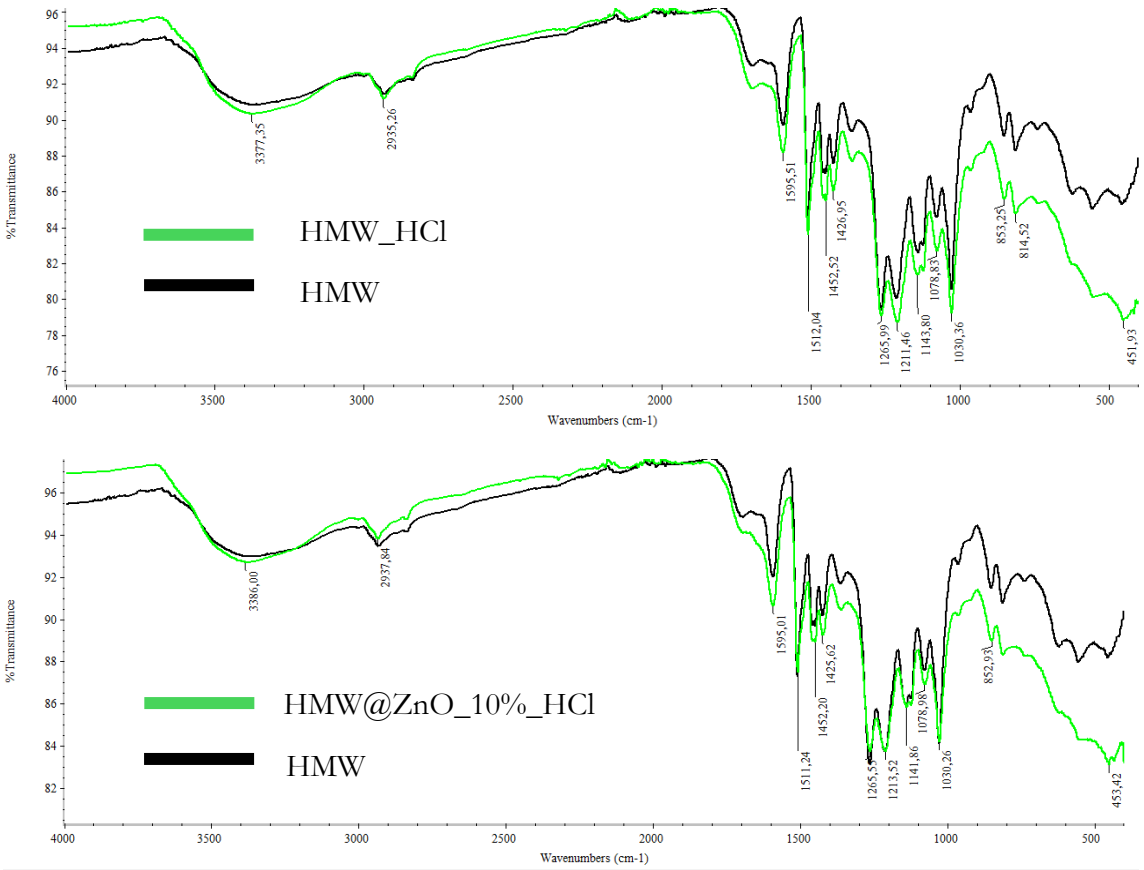

Figure S2.15. Superimposed infrared spectra of a) HMW and HMW_HCl and b) HMW and HMW@ZnO_10%_HCl.

a)

d^{-1} (nm^{-1})	d (nm)	Reflections
3.54	0.282	(100)
4.03	0.247	(101)
5.22	0.191	(102)
6.13	0.163	(110)

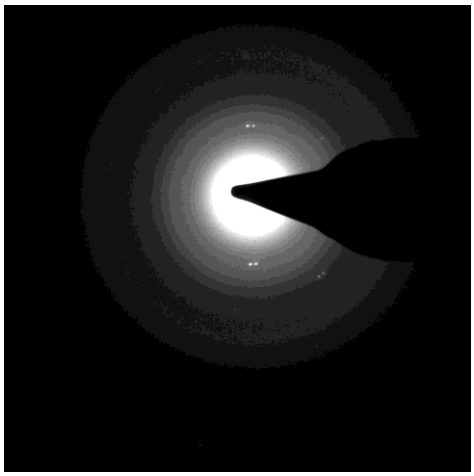

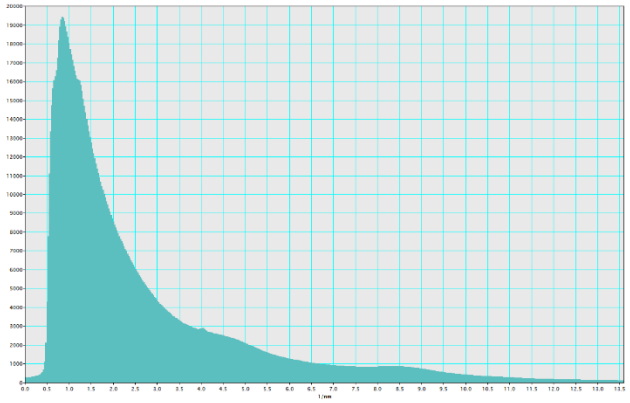

b)

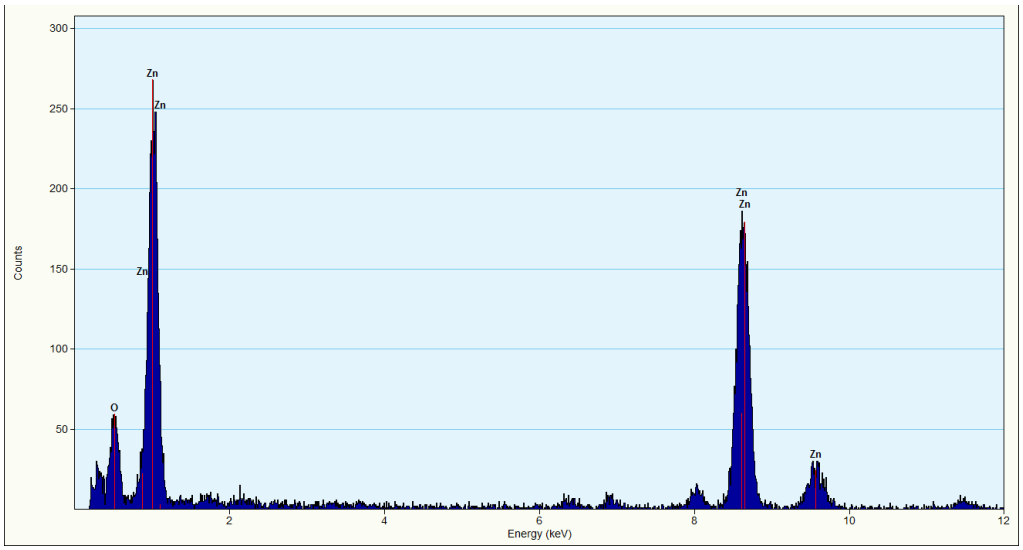

Figure S2.16. SAED (a) and EDX (b) of Solargo@ZnO materials.

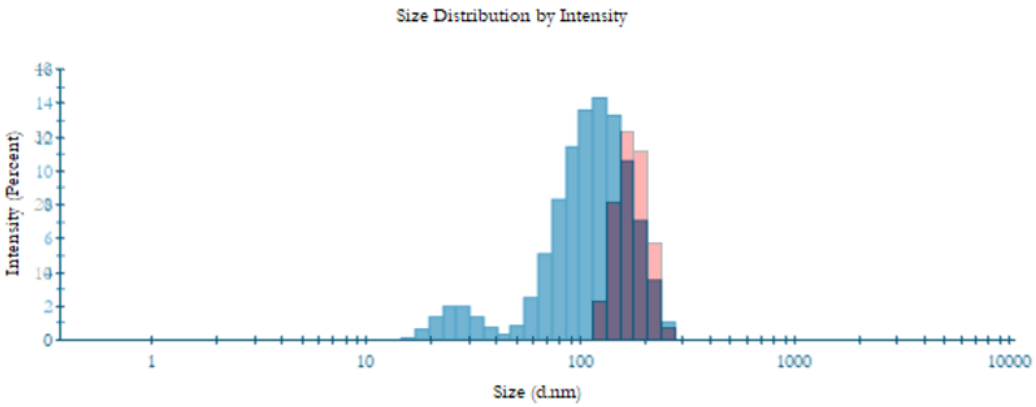

Figure S2.17. DLS of liquid suspension prepared with Solargo@ZnO_10% experimental conditions (blue) and isolated powder (red)

References

[1] S. M. F. Islam, Z. Karim, World's Demand for Food and Water: The Consequences of Climate Change, *Desalination: Challenges and opportunities,* 2019. DOI:10.5772/intechopen.85919.

[2] H. Chen, & R. Yada, Nanotechnologies in Agriculture: New Tools for Sustainable Development, *Trends in Food Science & Technology*, **22**(11), 585–594, 2011. DOI: 10.1016/j.tifs.2011.07.004.

[3] V. Sinisi, P. Pelagatti, M. Carcelli, A. Migliori, L. Mantovani, L. Righi, G. Leonardi, S. Pietarinen, C. Hubsch and D. Rogolino, A Green Approach to Copper-Containing Pesticides: Antimicrobial and Antifungal Activity of Brochantite Supported on Lignin for the Development of Biobased Plant Protection Products, *ACS Sustainable Chem. Eng.,* **7**, 3213, 2019. DOI: 10.1021/acssuschemeng.8b05135.

[4] C. Gazzurelli, A. Migliori, P. P. Mazzeo, M. Carcelli, S. Pietarinen, G. Leonardi, A. Pandolfi, D. Rogolino and P. Pelagatti, Making Agriculture More Sustainable: An Environmentally Friendly Approach to the Synthesis of Lignin@Cu Pesticides, *ACS Sustainable Chem. Eng*., **8**, 14886, 2020, DOI: 10.1021/acssuschemeng.0c04645.

[5] C. Gazzurelli, M. Carcelli, P. P. Mazzeo, C. Mucchino, A. Pandolfi, A. Migliori, S. Pietarinen, G. Leonardi, D. Rogolino and P. Pelagatti, Exploiting the Reducing Properties of Lignin for the Development of an Effective Lignin@Cu_2O Pesticide, *Adv. Sustainable Syst.,* **6**, 2200108, 2022, DOI: 10.1002/adsu.202200108.

[6] Q. Ding, H. L. Wu, Y. Xu, L. J. Guo, K. Liu, H. M. Gao, H. Yang, Impact of Low Molecular Weight Organic Acids and Dissolved Organic Matter on Sorption and Mobility of Isoproturon in two Soils, *J Hazard Mater.*, **190**(1-3):823-32, 2011. DOI: 10.1016/j.jhazmat.2011.04.003.

[7] H. Chhipa, Applications of Nanotechnology in Agriculture, *Methods in Microbiology*, **46**, 115–142, 2019. DOI:10.1016/bs.mim.2019.01.002.

[8] G. Oberdörster, A. Maynard, K. Donaldson, V. Castranova, K. Peterson, Principles for Characterizing the Potential Human Health Effects from Exposure to Nanomaterials: Elements of a Screening Strategy*, Particle and Fibre Toxicology*, **6**(1), 1-35, 2009. DOI:10.1186/1743-8977-6-8

[9] R. Bhargava, A. Varma, A. Srivastava, A. Sharma, A. Jain, ZnO nanostructures: Doping and Applications. *Journal of Materials Science: Materials in Electronics*, **27**(1), 1–10, 2016. DOI:10.1007/s10854-015-3644-9

[10] S. Rathod, P. K. Yadav, R. Sharma, P. R. Waghmare, Zinc Oxide Nanoparticles: Synthesis, Properties, and Applications in Various Fields. *Materials Science and Engineering: B*, **251**, 99–118, 2019. DOI:10.1016/j.mseb.2019.03.001.

[11] Z. L. Wang, Z. J. Yu, J. Zhai, Zinc Oxide Nanostructures: Growth, Properties, and Applications. *Journal of Materials Science*, **44**(6), 1600–1612, 2009. DOI: 10.1007/s10853-008-3152-5.

[12] S. Sabir, M. Arshad, S. K. Chaudhari, Zinc Oxide Nanoparticles for Revolutionizing Agriculture: Synthesis and Applications. *ScientificWorldJournal.,* 925494, 2014. DOI: 10.1155/2014/925494.

[13] L. Zhang, Y. Jiang, Y. Ding, M. Povey, D. York, Preparation, Characterization, and Antibacterial Properties of ZnO Nanoparticles. *Journal of Nanoparticle Research*, **9**(4), 479–489, 2007. DOI: 10.1007/s11041-006-0084-3.

[14] A. Sirelkhatim, S. Mahmud, A. Seeni, N. H. M. Kaus, L. C. Ann, S. K. M. Bakhori, et al., Review on Zinc Oxide Nanoparticles: Antibacterial Activity and Toxicity Mechanism. *Nano-Micro Letters*, **7**(4), 219–242, 2015. DOI:10.1007/s40820-015-0040-x.

[15] R. Wahab, A. Mishra, S.-I. Yun, Y.-S. Kim, H.-S. Shin, Antibacterial Activity of ZnO Nanoparticles Prepared *via* non-hydrolytic Solution Route, *Appl. Microbiol. Biotechnol.* **87**(5), 1917–1925, 2010. DOI:10.1007/s00253-010-2692-2.

[16] R. Wahab, M.A. Siddiqui, Q. Saquib, S. Dwivedi, J. Ahmad, J. Musarrat, A.A. Al-Khedhairy, H.-S. Shin, ZnO Nanoparticles Induced Oxidative Stress and Apoptosis in HepG2 and MCF-7 Cancer Cells and their Antibacterial Activity. *Colloids Surf. B.,* **117**, 267–276 2014. DOI:10.1016/j.colsurfb.2014.02.038.

[17] S. Stankovic´, D. Dimitrijevic´, D. Uskokovic´, Influence of Size Scale and Morphology on Antibacterial Properties of ZnO Powders Hydrothermally Synthesized Using Different Surface Stabilizing Agents. *Colloids Surf. B*, **102**, 21–28, 2013. DOI:10.1016/j. colsurfb.2012.07.033.

[18] J. T. Eil, E. N. Taylor, T. J. Webster, Reduced Activity of *Staphylococcus epidermidis* in the Presence of Sonicated Piezoelectric Zinc Oxide Nanoparticles. In *Proceedings of the IEEE 35th Annual Northeast Bioengineering Conference* (pp. 1–2). Boston, MA, USA, 2009. DOI:10.1109/NEBC.2009.5077739.

[19] R. Brayner, R. Ferrari-Iliou, N. Brivois, S. Djediat, M. F. Benedetti, F. Fiévet, Toxicological Impact Studies Based on ZnO Nanoparticles. *Nano Letters*, **6**(4), 866–870, 2006. DOI: 10.1021/nl060135v.

[20] L. K. Adams, D. Y. Lyon, P. J. Alvarez, Nano and Micro-scale Technologies for the Environmental Applications of Zinc Oxide Nanoparticles. *Nano-Micro Letters*, **7**(4), 219–242, 2015. DOI:10.1007/s40820-015-0040-x.

[21] K. Kasemets, A. Ivask, H. C. Dubourguier, A. Kahru, Toxicity of Nanoparticles and Nanomaterials: from *in Vitro* Studies to *in Vivo* Monitoring. *Toxicology in Vitro*, **23**(5), 1116–1122, 2009. DOI: 10.1016/j.tiv.2009.06.017.

[22] T. J. Brunner, P. Wick, P. Manser, P. Spohn, R. N. Grass, L. K. Limbach, et al., *In Vitro* Cytotoxicity of Nanoparticles in Human Lung Cells. *Environmental Science & Technology*, **40**(14), 4374–4381, 2006. DOI: 10.1021/es060290u.

[23] M. Li, L. Zhu, D. Lin, Toxicity of Nanoparticles in the Environment: A Review. *Environmental Science & Technology*, **45**(5), 1977–1983, 2011. DOI:10.1021/es103582w.

[24] N. Jones, B. Ray, K. T. Ranjit, A. C. Manna, Antibacterial activity of ZnO Nanoparticle Suspensions on a Broad Spectrum of Microorganisms. *FEMS Microbiology Letters*, **279**(1), 71–76, 2008. DOI:10.1111/j.1574-6968.2007.01069.x.

[25] J. Sawai, S. Shoji, H. Igarashi, A. Hashimoto, T. Kokugan, M. Shimizu, et al., Antibacterial Activity of Zinc Oxide Particles. *Journal of Bioscience and Bioengineering*, **86**(5), 521–522, 1998. DOI: 10.1016/S1389-1723(98)80113-6.

[26] A. Lipovsky, Y. Nitzan, A. Gedanken, R. Lubart, Antibacterial Activity of ZnO Nanoparticles—The Role of ROS and the Effect of UV Irradiation. *Nanotechnology*, **22**(10), 105101, 2011. DOI:10.1088/0957-4484/22/10/105101.

[27] C.R. Mendes, G. Dilarri, C. F. Forsan, V de M.R. Sapata, P. R.M. Lopes, P. B. de Moraes, R. N. Montagnolli, H. Ferreira, E. D. BiDOIa, Antibacterial Action and Target Mechanisms of Zinc Oxide Nanoparticles against Bacterial Pathogens. *Scientific Reports*, **12**, 2658, 2022. DOI: 10.1038/s41598-022-06498-w.

[28] B. A. Sevinc, L. Hanley, Toxicity of ZnO Nanoparticles: Effects on Cell Viability, Proliferation, and Apoptosis. *Journal of Biomedical Materials Research Part B: Applied Biomaterials*, **94**(1), 22–31, 2010. DOI:10.1002/jbm.b.31437.

[29] A. Kahru, H. C. Dubourguier, I. Blinova, A. Ivask, K. Kasemets, Ecotoxicity of Nanoparticles: Assessment of Different Test Strategies. *Sensors*, **8**(8), 5153–5170, 2008. DOI:10.3390/s8085153.

[30] M. Heinlaan, A. Ivask, I. Blinova, H. C. Dubourguier, A. Kahru, Toxicity of Nanoparticles: Assessment of the Ecotoxicity of Nanoparticles. *Chemosphere*, **71**(7), 1308–1316, 2008. DOI: 10.1016/j.chemosphere.2007.10.084.

[31] O. Yamamoto, J. Sawai, T. Sasamoto, Antibacterial Activities of Zinc Oxide Powders and the Effect of Particle Size. *Materials Transactions*, **43**(5), 1069–1073, 2002. DOI:10.2320/matertrans.43.1069.

[32] D. Sharma, J. Rajput, B.S. Kaith, M. Kaur, S. Sharma, Structural and Optical Properties of Zinc Oxide Thin Films Prepared by Spray Pyrolysis Technique. *Thin Solid Films*, **519**(4), 1224–1229, 2010. DOI:10.1016/j.tsf.2010.09.050.

[33] L. He, Y. Liu, A. Mustapha, M. Lin, Antibacterial Activity of Zinc Oxide Nanoparticles against *Escherichia coli* and *Salmonella in vitro*. *Microbiological Research*, **166**(3), 207–215, 2011. DOI:10.1016/j.micres.2010.03.005.

[34] K. Kairyte, A. Kadys, Z. Luksiene, Photocatalytic Properties of Zinc Oxide Nanoparticles under UV and Visible Light Irradiation. *Journal of Photochemistry and Photobiology B: Biology*, **128**, 78–84, 2013. DOI:10.1016/j.jphotobiol.2013.09.014.

[35] J. L. G. Fierro, Metal oxides: Chemistry and applications (1st ed.), 2005. DOI: 10.1201/9781420028126.

[36] A. Kumar, R. Yadav, Design and Tailoring of One-dimensional ZnO Nanomaterials for Photocatalytic Degradation of Organic Dyes: A Review. *Research on Chemical Intermediates*, **45**(4), 1153–1177, 2019. DOI:10.1007/s11164-018-03729-5.

[37] C. Zou, F. Liang, S. Xue, Photocatalytic Degradation of Organic Pollutants using ZnO-based Nanomaterials: A Review. *Research on Chemical Intermediates*, **41**(6), 5167–5176, 2015. DOI: 10.1007/s11164-015-1853-9.

[38] K. Elen, A. Kelchtermans, H. Van den Rul, R. Peeters, J. Mullens, A. Hardy, et al., Surface Functionalization of Zinc Oxide Nanoparticles for Biological Applications. *Journal of Nanomaterials*, **18**, 2011. DOI: 10.1155/2011/616404.

[39] M. Ristić, S. Mušić, M. Ivanda, S. Popović, Structural and Optical Properties of ZnO Thin Films Grown by Sol-gel Method. *Journal of Alloys and Compounds*, **397**(1–4), 1–4, 2005. DOI: 10.1016/j.jallcom.2005.02.036.

[40] S. Sepúlveda-Guzmán, B. Reeja-Jayan, E. de La Rosa, A. Torres-Castro, V. González-González, M. José-Yacamán, Optical Properties of Zinc Oxide Nanorods: Influence of Shape and Size. *Materials Chemistry and Physics*, **115**(1), 172–178,2009. DOI:10.1016/j.matchemphys.2008.12.048.

[41] Y. Zhou, W. Wu, G. Hu, H. Wu, S. Cui, Synthesis and Photocatalytic Properties of ZnO Nanorods Prepared by a Low-temperature Hydrothermal Method. *Materials Research Bulletin*, **43**(8), 2113–2118, 2008. DOI: 10.1016/j.materresbull.2007.10.010.

[42] L. L. Hench, J. K. West, J. K. The Sol-gel Process. *Chemical Reviews*, **90**(1), 33–72, 1990. DOI: 10.1021/cr00099a003.

[43] S. D. Škapin, G. Dražič, Z. C. Orel, Structural and Electrical Properties of ZnO-based Thin Films for Gas Sensing Applications. *Materials Letters*, **61**(14), 2783–2788, 2007. DOI:10.1016/j.matlet.2006.10.048.

[44] S. Musić, S. Popović, M. Maljković, D. Dragčević, Structural and Optical Properties of ZnO Films Prepared by Sol-gel Method. *Journal of Alloys and Compounds*, **347**(1–2), 324–332, 2002. DOI:10.1016/S0925-8388(02)00812-2.

[45] C. Pacholski, A. Kornowski, H. Weller, Synthesis of Monodisperse ZnO Nanocrystals and their Use in Nanostructured Solar Cells. *Angewandte Chemie International Edition*, **41**(6), 1188–1191, 2002. DOI: 10.1002/1521-3773(20020402)41:7<1188::aid-anie1188>3.0.co;2-5.

[46] J. E.Rodríguez-Páez, A. C. Caballero, M. Villegas, C. Moure, P. Durán, J. F. Fernández, Synthesis and Characterization of ZnO-based Powders for Ceramics Applications. *Journal of the European Ceramic Society*, **21**(6), 925–930, 2001. DOI:10.1016/S0955-2219(00)00310-3.

[47] S. S. Kumar, P. Venkateswarlu, V. R. Rao, G. N. Rao, Synthesis and Characterization of ZnO Nanoparticles and their Application in Photocatalysis. *International Nano Letters*, **3**(1), 1–6, 2013. DOI:10.1186/2228-5326-3-1.

[48] L. Wang, M. Muhammed, Preparation and Characterization of Nanosized Zinc Oxide Powders and their Application in Photocatalysis. *Journal of Materials Chemistry*, **9**(12), 2871–2878, 1999. DOI:10.1039/a904359c.

[49] A. M. Pourrahimi, D. Liu, L. K. Pallon, R. L. Andersson, A. M. Abad, J. M. Lagarón, et al., Water-based Synthesis and Cleaning Methods for High Purity ZnO Nanoparticles – Comparing Acetate, Chloride, Sulphate, and Nitrate Zinc Salt Precursors. *RSC Advances*, **4**(66), 35568–35577, 2014. DOI:10.1039/C4RA07056A.

[50] R. Wahab, S. Ansari, Y. Kim, H. Seo, G. Kim, G. Khang, H.-S. Shin, Low Temperature Solution Synthesis and Characterization of ZnO Nano-flowers. *Mater. Res. Bull.,* **42**(9), 1640–1648, 2007. DOI:10.1016/j.materresbull.2006.11.035.

[51] K. Prasad, A. K. Jha, Effect of ZnO Nanoparticles on the Properties of Soil and Plants. *Nature Science*, **1**, 129, 2009. DOI:10.4236/ns.2009.13019.

[52] J. Qu, X. Yuan, X. Wang, P. Shao, The effect of ZnO Nanoparticles on the Growth and Biological Properties of Plants. *Environmental Pollution*, **159**, 1783–1789, 2011. DOI:10.1016/j.envpol.2011.02.021.

[53] J. Qu, C. Luo, J. Hou, Preparation and Photocatalytic Properties of ZnO Nanorods. *Micro & Nano Letters*, **6**, 174–176, 2011. DOI:10.1049/mnl.2010.0446.

[54] A. Król, P. Pomastowski, K. Rafińska, V. Railean-Plugaru, B.Buszewski, Zinc Oxide Nanoparticles: Synthesis, Antiseptic Activity and Toxicity Mechanism. *Science of the Total Environment*, **711**, 134581, 2020. DOI:10.1016/j.scitotenv.2019.134581.

[55] N. Yahya, H. Daud, N. A. Tajuddin, H. M. Daud, A. Shafie, P. Puspitasari, Application of ZnO Nanoparticles EM Wave Detector Prepared by Sol–gel and Self-combustion Techniques. *Journal of Nano Research*, **11**, 25–34, 2010. DOI:10.4028/www.scientific.net/JNanoR.11.25.

[56] S. Mahmud, One-dimensional Growth of Zinc Oxide Nanostructures from Large Micro-Particles in a Highly Rapid Synthesis. *Journal of Alloys and Compounds*, **509**(9), 4035–4040, 2011. DOI:10.1016/j.jallcom.2010.11.144.

[57] Y. Wang, Y. Xia, One-dimensional Nanostructures: Synthesis, Characterization, and Applications. *Nano Letters*, **4**(11), 2047–2050, 2004. DOI:10.1021/nl048575f.

[58] H. Van den Rul, D. Mondelaers, M. K. Van Bael, J. Mullens, Synthesis and Characterization of Sol–gel-Derived Zinc Oxide Thin Films. *Journal of Sol-Gel Science and Technology*, **39**(1), 41–47, 2006. DOI:10.1007/s10971-006-0955-9.

[59] P. Sharma, N. Sharma, Y. S. Parmar, Lignin Derived from Forestry Biomass as Capping Reagent in the Biosynthesis and Characterization of Zinc Oxide Nanoparticles and their *in Vitro* Efficacy as a Strong Antifungal Biocontrolling Agent for Commercial Crops. *BioNanoScience*, **13**(6), 2037–2047, 2022. DOI:10.1007/s12668-022-01052-3.

[60] F. Luzi, I. Tortorella, A. Di Michele, F. Dominici, C. Argentati, F. Morena, L. Torre, D. Puglia, S. Martino, Novel Nanocomposite PLA Films with Lignin/Zinc Oxide Hybrids: Design, Characterization, Interaction with Mesenchymal Stem Cells, *Nanomaterials*, **10**, 2176, 2020. DOI: 10.3390/nano10112176.

[61] I. Klapiszewska, A. Parus, Ł. Ławniczak, T. Jesionowski, Ł. Klapiszewski, A. Slosarczyk, Production of Antibacterial Cement Composites Containing ZnO/Lignin and ZnO–SiO_2/Lignin Hybrid Admixtures. *Cement and Concrete Composites*, **124**, 104250, 2021. DOI:10.1016/j.cemconcomp.2021.104250.

[62] M. L. Josè, S. Kuriakose, S. Thomas, Fabrication, Characterization and *in Vitro* Antifungal Property Evaluation of Biocompatible Lignin-stabilized Zinc Oxide Nanoparticles against Selected Pathogenic Fungal Strains. *Nanomaterials*, **10**, 583–596, 2020. DOI:10.3390/nano10030583.

[63] W. Maret, The Metals in the Biological Sciences: Role of Zinc in Gene Expression and Enzyme Function. *Biometals*, **24**(3), 411–418, 2011. DOI:10.1007/s10534-011-9435-3.

[64] H. Tapiero, K. D Tew,. Trace Elements in Human Biology and Medicine. *Biomedicine & Pharmacotherapy*, **57**(9), 399–411, 2003. DOI:10.1016/S0753-3322(03)00077-X.

[65] A. Klug, D. Rhodes, Zinc fingers: A Novel Class of a Zinc-Binding Structural Motif. *Cold Spring Harbor Symposia on Quantitative Biology*, **52**, 473–482, 1987. DOI:10.1101/SQB.1987.052.01.059.

[66] J. C. Stangoulis, M. Knez, Biofortification of Major Crop Plants with Iron and Zinc—Achievements and Future Directions. *Plant and Soil*, 1–20, 2022. DOI:10.1007/s11104-022-05577-7.

[67] S. Zafar, M. Y. Ashraf, M. Saleem, Shift in Physiological and Biochemical Processes in Wheat Supplied with Zinc and Potassium under Saline Conditions. *Journal of Plant Nutrition*, **41**, 19–28, 2018. DOI:10.1080/01904167.2017.1346602.

[68] W. T. Li, M. He, J. Wang, Y. P. Wang, Zinc Finger Protein (ZFP) in Plants—A Review. *Plant Omics*, **6**, 474–480, 2013.

[69] A. Ullah, M. Farooq, A. Rehman, M. Hussain, K. H. Siddique, Zinc Nutrition in Chickpea (*Cicer arietinum*): A Review. *Crop and Pasture Science*, **71**, 199–218, 2020. DOI:10.1071/CP19040.

[70] H. Aktaş, K. Abak, L. Öztürk, I. Çakmak, The Effect of Zinc on Growth and Shoot Concentrations of Sodium and Potassium in Pepper Plants under Salinity Stress. *Turkish Journal of Agriculture and Forestry*, **30**, 407–412, 2006. DOI:10.3906/tar-0609-2.

[71] J. Saleh, M. Maftoun, S. Safarzadeh, A. Gholami, Growth, Mineral Composition and Biochemical Changes of Broad Bean as Affected by Sodium Chloride and Zinc Levels and Sources. *Communications in Soil Science and Plant Analysis*, **40**, 3046–3060, 2009. DOI:10.1080/00103620903261619.

[72] I. Cakmak, Role of Zinc in Protecting Plant Cells from Reactive Oxygen Species. *New Phytologist*, **146**(2), 185-205, 2000. DOI:10.1046/j.1469-8137.2000.00639.x.

[73] L. Sun, Y. Wang, R. Wang, R. Wang, P. Zhang, Q. Ju, J. Xu, Physiological, Transcriptomic, and Metabolomic Analyses Reveal Zinc Oxide Nanoparticles Modulate Plant Growth in Tomato. *Environmental Science: Nano*, **7**, 3587–3604, 2020. DOI:10.1039/D0EN00729C.

[74] M. Ali, X. Wang, U. Haroon, H. J. Chaudhary, A. Kamal, Q. Ali, M. H. Saleem, K. Usman, A. Alatawi, S. Ali, et al., Antifungal Activity of Zinc Nitrate Derived Nano ZnO Fungicide Synthesized from *Trachyspermum ammi* to Control Fruit Rot Disease of Grapefruit. *Ecotoxicology and Environmental Safety*, **233**, 113311, 2022. DOI:10.1016/j.ecoenv.2022.113311.

[75] T. N. V. K. V. Prasad, P. Sudhakar, Y. Sreenivasulu, et al., Effect of Nanoscale Zinc Oxide Particles on the Germination, Growth and Yield of Peanut. *Journal of Plant Nutrition*, **35**(6), 905–927, 2012. DOI:10.1080/01904167.2012.672587.

[76] V. N. Selivanov, E. V. Zorin, Sustained Action of Ultrafine Metal Powders on Seeds of Grain Crops. *Perspektivnye Materialy*, **4**, 66–69, 2001.

[77] L. M. Batsmanova, L. M. Gonchar, N. Y. Taran, A. A. Okanenko, Using a Colloidal Solution of Metal Nanoparticles as Micronutrient Fertiliser for Cereals. *Proceedings of the International Conference Nanomaterials*, **2**(4), 2 pages, 2013.

[78] A. Kumar, I. K. Singh, R. Mishra, A. Singh, N. Ramawat, A. Singh, The Role of Zinc Oxide Nanoparticles in Plants: A Critical Appraisal. In *Nanomaterial Biointeractions at the Cellular, Organismal and System Levels*, 249–267, 2021. DOI:10.1007/978-3-030-64094-4_16.

[79] P. Almendros, D. Gonzàlez, M. D. Fernàndez, C. Garcìa-Gomez, A. Obrador, Both Zn Biofortification and Nutrient Distribution Pattern in Cherry Tomato Plants are Influenced by the Application of ZnO Nanofertilizer, *Heliyon*, **8,** 3, 2022. DOI:10.1016/j.heliyon.2022.e09130.

[80] Rajput, V. Minkina, T. Behal, A. Sushkova, S. Mandzhieva, S. Singh, R. Gorovtsov, A. Tsitsuashvili, V. Purvis, O. Ghazaryan, K. Movsesyan, Hasmik; Effects of Zinc-oxide Nanoparticles on Soil, Plants, Animals and Soil Organisms: A Review.; *Environmental Nanotechnology Monitoring & Management*, **9**, 76–84, 2018. DOI:10.1016/j.enmm.2017.12.006.

[81] D. Del Buono, F. Luzi, C. Tolisano, D. Puglia, A. Di Michele, Synthesis of a Lignin/Zinc Oxide Hybrid Nanoparticles System and its Application by Nano-Priming in Maize. *Nanomaterials*, **11**(6), 1446, 2021. DOI:10.3390/nano11061446

[82] M. Faizan, A. Faraz, M. Yusuf, S. T. Khan, S. Hayat, Zinc Oxide Nanoparticle-Mediated Changes in Photosynthetic Efficiency and Antioxidant System of Tomato Plants. *Photosynthetica*, **56**, 678–686, 2018. DOI:10.1007/s11099-018-0783-1.

[83] H. Khan, B.A. Vaishnavi, A. G. Shankar, Rise of Nano-Fertilizer Era: Effect of Nano Scale Zinc Oxide Particles on the Germination, Growth, and Yield of Tomato (*Solanum lycopersicum*). *International Journal of Current Microbiology and Applied Sciences*, **7**(5), 1861–1871, 2018. DOI:10.20546/ijcmas.2018.705.221.

[84] C. Tolisano, D. Priolo, M. Brienza, D. Puglia, D. Del Buono, Do Lignin Nanoparticles Pave the Way for a Sustainable Nanocircular Economy? Biostimulant Effect of Nanoscaled Lignin in Tomato Plants. *Plants*, **13**, 1839, 2024. DOI:10.3390/plants13101839.

[85] H. Wang, W. Lin, X. Qiu, F. Fu, R. Zhong, W. Liu, D. Yang, In-Situ Synthesis of Flower-like Lignin/ZnO Composites with Excellent UV-Absorption Property and Its Application in Polyurethane*, ACS Sustain. Chem. Eng.*, **6** (3), 3696–3705, 2018. DOI: 10.1021/acssuschemeng.7b03990.

[86] S. S. Alias, A. B. Ismail, A.A. Mohamad, Effect of pH on ZnO Nanoparticle Properties Synthesized by Sol–Gel Centrifugation. *Journal of Alloys and Compounds,* **499**(2), 231-237, 2010. DOI: 10.1016/j.jallcom.2010.03.174.

[87] https://www.crystallography.net/cod/

[88] W. G. Glasser, Classification of Lignin According to Chemical and Molecular Structure. In *Lignin: Properties and Applications*; American Chemical Society (ACS): Washington, DC, USA, 1999; Vol. 742, pp. 216–238.

[89] X. Shen, Q. Meng, Q. Mei, H. Liu, J. Yan, J. Canzone, D. Abbronzatura, B. Chen, Z. Zhang, G. Yang, B. Han, Selective Catalytic Transformation of Lignin with Guaiacol as the Only Liquid Product. *Nature Communications*, **10**, 4756, 2019. DOI:10.1039/C9SC05892C.

[90] DOI:10.32614/CRAN.package.agricolae

[91] X. Zhao, J. Song, Q. Zeng, Y. Ma, H. Fang, L. Yang, B. Deng, J. Liu, J. Fang, L. Zuo, J. Yue, Auxin and Cytokinin Mediated Regulation Involved in *In Vitro* Organogenesis of Papaya, *Journal of Plant Physiology,* **260,** 153405, 2021. DOI:10.1016/j.jplph.2021.153405.

[92] T. Adhikari, S. Kundu,A.Subba Rao, Zinc Delivery to Plants through Seed Coating with Nano Zinc Oxide Particles. *Journal of Plant Nutrition,* **39**(1), 2015. DOI:10.1080/01904167.2015.1087562.

[93] J. Estrada-Urbina, A. Cruz-Alonso, M. Santander-González, A. Méndez-Albores, A. Vázquez-Durán, Nanoscale Zinc Oxide Particles for Improving the Physiological and Sanitary Quality of a Mexican Landrace of Red Maize, *Nanomaterials***, 8** (4): 247, 2018. DOI:10.3390/nano8040247.

[94] M. S. Youssef, R. M. Elamawi, Evaluation of Phytotoxicity, Cytotoxicity, and Genotoxicity of ZnO Nanoparticles in *Vicia faba. Environmental Science and Pollution Research*, **25**(16), 18972-18984, 2018. DOI:10.1007/s11356-018-3250-1.

[95] M. Hamzah Saleem, K. Usman, M. Rizwan,H. Al Jabri, M. Alsafran, Functions and Strategies for Enhancing Zinc Availability in Plants for Sustainable Agriculture, *Front Plant Sci.*, **7**, 13:1033092, 2022. DOI: 10.3389/fpls.2022.1033092.

[96] R. Castiglione, M. S. Bottega, C. Sorce, C. Spanò, Effects of Zinc Oxide Particles with Different Sizes on Root Development in *Oryza sativa. Rice Science,* **30** (5): 449–458, 2023. DOI:10.1016/j.rsci.2023.03.016.

[97] I., R. M. Bankaji, I. Pérez-Clemente, Caçador, N. Sleimi. Accumulation Potential of *Atriplex halimus* to Zinc and Lead Combined with NaCl: Effects on Physiological Parameters and Antioxidant Enzymes Activities. *South African Journal of Botany,* **123,** 51–61, 2019. DOI:10.1016/j.sajb.2019.02.011

[98] R. S. Sagardoy, I. D. Vázquez, A. Florez-Sarasa, M. Albacete, J. Ribas-Carbó, Flexas, J. Abadía, F. Morales, Stomatal and Mesophyll Conductances to CO_2 Are the Main Limitations to Photosynthesis in Sugar Beet (*Beta vulgaris*) Plants Grown with Excess Zinc, *New Phytologist*, **187** (1): 145–158, 2010. DOI:10.1111/j.1469-8137.2010.03241.x.

[99] J. M. Farber, P. I. Peterkin., *Listeria Monocytogenes*, a Food-Borne Pathogen, *Microbiological Reviews,* **55** (3): 476–511, 1991. DOI: 10.1128/mr.55.3.476-511.1991.

[100] P. Cash, Characterisation of Bacterial Proteomes by Two-Dimensional Electrophoresis. *Analytica Chimica Acta,* **371** (1-2): 3–15, 1998. DOI:10.1016/S0003-2670(98)00355-9.

[101] B. Vânia Santos, K. Melchior, C. Gallina Moreira, *Escherichia coli* as a Multifaceted Pathogenic and Versatile Bacterium. *Frontiers in Cellular and Infection Microbiology,* **10**, 548492, 2020. DOI:10.3389/fcimb.2020.548492.

[102] Steven C. Ricke, Gastrointestinal Ecology of *Salmonella Enteritidis* in Laying Hens and Intervention by Prebiotic and Nondigestible Carbohydrate Dietary Supplementation, *Microbial Ecology of Salmonella*, *Producing Safe Eggs*, 323–345, 2017. DOI:10.1016/B978-0-12-802582-6.00016-1.

[103] O. O. Ajayi-Oyetunde, C. A. Bradley, Rhizoctonia Solani: Taxonomy, Population Biology and Management of Rhizoctonia Seedling Disease of Soybean, *Plant Pathology,* 2017. DOI:10.1111/ppa.12733.

Chapter 3
Lignin@metal oxides: mechanochemical synthesis

Mechanochemistry is experiencing a revival as a sustainable approach for large-scale production, building upon its centuries-old tradition of use.[1,2] It consists in a chemical synthesis where the physicochemical transformations are triggered by mechanical impacts. Repeated application of mechanical energy causes atoms or molecules to shift from their stable equilibrium positions, resulting in changes to bond lengths and angles. In some cases, this also leads to electron promotion.[3] The application of mechanical energy to solids initiates a series of physical processes known as mechanical activation. While these processes do not directly cause chemical changes, they alter the chemical system in ways that increase the likelihood of reactions occurring. Key processes involved in mechanical activation include particle size reduction (comminution), which increases the surface area, and the formation of lattice defects[4], which enhance reactivity by weakening the attractive forces holding the solid together, often leading to amorphization. Beyond the physical effects, many substances undergo chemical reactions during or after mechanical activation. These can include the breaking and forming of covalent bonds, acid-base reactions, hydrogen bonding rearrangements, redox reactions, polymerization, and decomposition, among others. New phases containing the reaction products often crystallize during the milling process, typically as powders, exhibiting varying degrees of crystallinity, particle sizes, and morphologies. At the beginning, mechanochemistry has been intensively applied in metallurgy: mechanochemical synthesis of alloying represent a consistent field of study.[5] The major inspiration behind the rediscovery of mechanochemistry is related to its sustainability: the need of pharmaceutical and chemical industries for cleaner, safer, and more efficient transformations,[6,7] paved the way for investigating synthetic approaches alternative to classical wet procedures.[8] Growing awareness of the environmental impact of chemical research and manufacturing has in fact spurred the advancement of cleaner, safer, and more sustainable methods for chemical and material synthesis. Mechanochemistry not only aligns with key green chemistry principles,[9] such as waste reduction and energy-efficient processes, but also promotes the use of simplified reaction set-up, reducing risks and human exposure to hazardous chemicals. Often, mechanochemical reactions enable "one-pot" syntheses, eliminating the need for intermediate product purification and isolation. Furthermore, these reactions frequently involve high atom economy, ensuring that virtually all the atoms from the reactants are incorporated into the final products. Typically, reduced reaction times,[10,11] good stoichiometry control, and enhanced product selectivity are advantageous features, in addition to larger yields than the analogous reactions in solution. Another notable advantage of mechanochemical reactions is their ease of scalability. Additionally, they often yield products that differ from those obtained through other synthetic methods, in terms of structure, stereochemistry, stoichiometry, or mixture composition. This is likely due to the distinct chemical mechanisms unique to mechanochemistry. Another benefit of mechanochemical techniques is their ability to produce nanoparticles with minimal agglomeration: this could be achieved inserting a solid inert matrix that serves as a physical barrier between particles during the particle-growth phase.[12] It is therefore not surprising that mechanochemistry has been applied in many different areas, including organic, organometallic, inorganic chemistry and material engineering.[13]

Over the past two decades, it became clear that solvents are not strictly required in mechanochemical processes: many well-known inorganic, organic, and organometallic reactions can in fact readily be conducted in the absence of a bulk solvent under mechanochemical conditions. This is an issue of the upmost importance, since solvents represent a significant hazard and a major contribution to the creation of toxic chemical waste. Additionally, reactants must be soluble in solvents, which can limit the choice of starting materials and increase costs. Separating and purifying the products can also be complicated, and residual solvents may represent a risk in term of toxicity. Furthermore, solvents often require preliminary treatments such as degassing and distillation: these steps increase costs, consume energy, and generate waste and pollution. Many processes also consume large quantities of water for washing, cooling, or using it as solvent. In contrast, mechanochemical reactions typically involve simpler workup procedures, improved safety, and often minimal purification steps for the products and this results in lower costs, reduced energy consumption, and less waste production. However, it must be pointed out that small amounts of solvents can also find applications in mechanochemistry. One of the most significant advancements in mechanochemistry is the so-called liquid-assisted grinding (LAG), that involves the mechanical treatment of powdered reactants combined with a small amount of liquid additive. The liquid-to-solid ratio typically ranges from 0 to about 2 μL per mg of solid, which generally leads to enhanced reaction rates and, in some cases, enables previously inaccessible mechanochemical reactions.[13,14] The amount of liquid additive relative to the mass of the reactants is denoted as η, representing the ratio of the liquid volume (in μL) to the total mass of the reactants (in mg). A schematic representation of the range of η values is reported in Figure 3.1, from neat grinding at 0 μL/mg to $\eta \geq$ 12 μL/ mg in case of solution chemistry.[15]

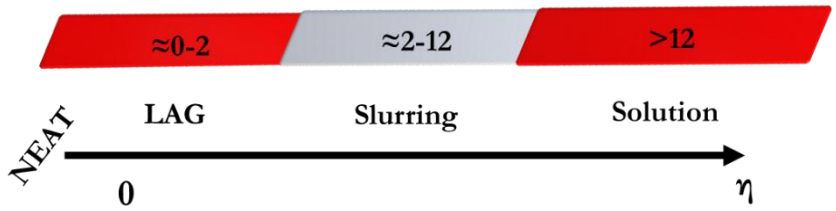

Figure 3.1. Schematic representation of the range of η values, from neat grinding to solution chemistry.[15]

Notably, LAG offers a unique advantage by promoting chemical transformations that might not occur readily in either solution or traditional neat milling, regardless of the solubility of the reactants: for this reason, LAG is crucial for expanding mechanochemistry as a viable alternative to solution-based synthesis. This technique allows for the optimization of reactions, enabling the achievement of quantitative conversions. Mechanochemical reactions in LAG conditions can offer advantages similar to those of reaction solvents in solution chemistry, such as stabilizing ionic species energetically.[16] Examples of how LAG can help control product selectivity, topology, and polymorphism can be found in the literature.[17] The success of LAG in facilitating a broad range of reactions has led to the development of further innovations, such as ion- and liquid-assisted grinding (ILAG), which uses both liquid additives and catalytic amounts of ionic salts to enhance reactions. Additionally, polymer-assisted grinding (POLAG[18]) employs

organic polymer additives to improve co-crystallization reactions and control the polymorphic forms of organic solids, especially in pharmaceutical applications.

Mechanochemical reactions can be carried out using a variety of tools, ranging from the basic mortar and pestle, where reactions are achieved through manual grinding,[19] to more sophisticated and automated electrical mills. Each type of device offers its own set of advantages and drawbacks. The mortar and pestle, while being the simplest and most accessible option, have limitations in terms of reproducibility and control over grinding force or reaction environment. Additionally, as the mechanical agitation relies heavily on the operator, it is challenging to perform reactions that require prolonged or sustained grinding. The development of modern technology has led to the creation of various types of high-energy ball mills, with mechanical energy outputs (energy densities) sufficient to trigger numerous chemical reactions. Ball mills are frequently used as chemical reactors, which is why this process is also referred to as "reactive milling".[20] Common types of mills include attrition mills, planetary mills, and horizontally or vertically shaker ones. The first two types are commonly used for the large-scale commercial production of metal-oxide nanoparticles, which integrate a milling vessel with robust milling media, typically balls made by durable materials. Different mills present different mechanical energy per unit of time and can be used under different experimental conditions, further influencing the total mechanical energy input. As a result, the chemical reactivity of substances, the rates of mechanochemical reactions, and the properties of the resulting products can vary, leading to a wide range of possible outcomes.

Ball mills are equipped with a jar, partially filled with balls, which act as the grinding media. Both the spheres and the internal part of the jar can be made of abrasion-resistant materials such as stainless steel, ceramic, or agate. The ball milling process involves several steps: first, the jar is loaded with the spheres (milling media) and the reactants. Next, the grinding jar is secured within the mill using clamps, and the appropriate grinding times and frequencies are selected. Finally, the milled material is removed from the jar, and optional steps may be performed to remove any by-products. Currently, there are various types of ball mills available, ranging from laboratory-scale models (1-500 mL) to industrial-scale versions with vessels that can hold several hundred litres or more.[21] In a planetary mill, jars are mounted on a rotating disk, where a mechanism causes them to rotate around their own axes while simultaneously rotating around a central point. As the jars and disk rotate in opposite directions, centrifugal forces alternate in opposing directions (Figure 3.2) allowing the milling media to gain and maintain kinetic energy throughout the milling process. This dual rotation in opposite directions generates very high centrifugal forces, which promote high-energy grinding. Ball mills are typically equipped with timers to control the operation time, and generally it is possible to define the frequency.

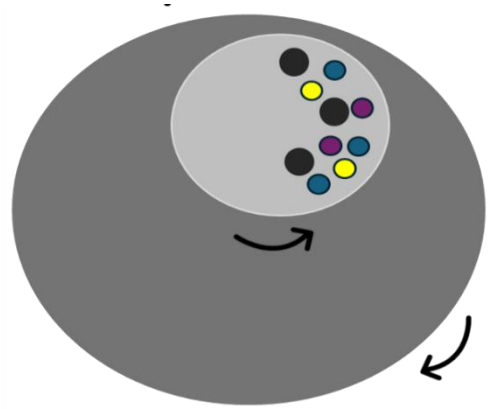

Figure 3.2. Schematic representation of motions inside a planetary ball mill[22]

The balls repeatedly collide each other and with the container walls, involving the reactants in inelastic collisions, where kinetic energy is transferred to the reactants through repeated impacts. In planetary mills, the rotations cause the grinding balls to roll along the inner walls of the jars, generating friction. Subsequently, the balls are propelled and collide with the opposite wall, producing impact forces. Therefore, a combination of friction, shear, and impacts[23] is generated (Figure 3.3). In this way, mechanical energy is delivered to the reactants, synergizing with the internal energy of the chemical system and increasing the chemical reactivity by raising temperature. The combination of impact and shear forces between the balls, as well as the interaction with the powder reagents, generates the mechanical stress required to trigger the reaction. Most of the mechanical energy provided to the reactants is dissipated as frictional heat.

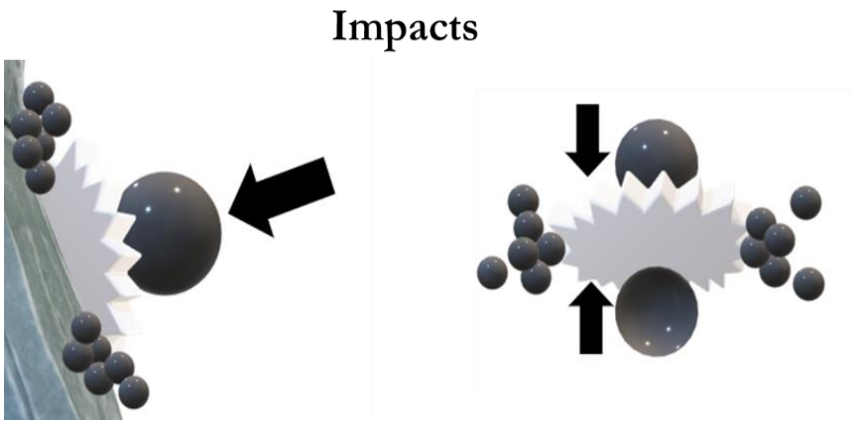

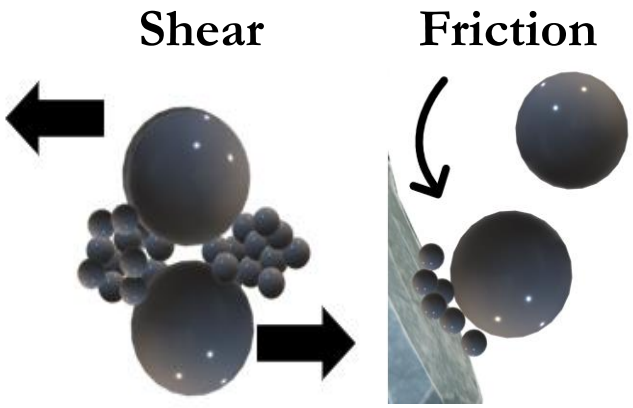

Figure 3.3. Schematic representation of combinations of impacts, shear and friction generated in a planetary ball mill.[23]

During our studies, we have focused on the use of a planetary ball mill (Retsch® PM100) and on a horizontal mixer mill (Retsch® MM400), whose use is described in Chapter 4. Pictures of the instrumentations are reported in Figure 3.4. Retsch® PM 100 is extensively used in various industries that require strict standards of purity, speed, fineness, and reproducibility in their quality control processes. This mill is particularly well-suited for research in mechanochemistry (such as co-crystal screening, mechanosynthesis and mechanical alloying), as well as for ultrafine colloidal grinding at the nanometres scale. It is also ideal for routine tasks like mixing and homogenizing soft, hard, brittle, or fibrous materials. The mill generates exceptionally high centrifugal forces, delivering significant pulverization energy and ensuring very short grinding times. Retsch® MM 400 achieves mixing and homogenization of powders and suspensions at a frequency of 30 Hz, offering unmatched speed and ease of use, furnish an excellent choice for research applications, particularly in mechanochemistry.

Figure 3.4. Picture of the milling systems adopted during the PhD studies. Left: A Retsch® GmbH (Haan, Germany) mixer-type mill model MM 400, endowed with horizontally oscillatory movements of the reaction jars. Right: A Retsch® GmbH (Haan, Germany) planetary ball mill model PM 100, endowed with 80 mL agate jar and spheres (ø 15 mm). Pictures taken from Retsch® website (https://www.retsch.com).

Despite the lack of a fully comprehensive understanding of the mechanochemical process, which has largely been approached through trial and error, the extensive literature now allows for some general guidelines to be established.[21] Selecting the appropriate material for the grinding jar and media is of paramount importance. Commonly used materials include various types of steel, tungsten carbide, sintered corundum, yttria-stabilized zirconia, agate, and silicon nitride (Si_3N_4). Transparent poly(methyl)methacrylate jars are also employed to enable *in situ* monitoring.[24] The choice of materials for both the jar and the grinding media can result in contamination, due to abrasion during milling. The degree of abrasion depends on several factors, including the relative hardness of the milled material, the wear resistance of the technical materials, the ball-to-powder weight ratio, and the milling energy regime. Steel is the most commonly used material, but prolonged milling can lead to metal contamination. Elements such as iron from steel may alloy with other metals commonly present in milled powders, including titanium, chromium, manganese, nickel, copper, and molybdenum. To minimize such contaminations, zirconia is often preferred, as it has a similar density as steel and provides comparable impact performance without the risk of introducing metal impurities. The number and size of the grinding balls are also critical factors in the milling process. The selection of these parameters is typically driven by the goal of achieving optimal productivity in the shortest time. To maximize efficiency, higher ball-to-powder weight ratios are often preferred, as this increases the frequency of collisions per unit time and transfers more energy to the powder particles. However, this must be balanced with the need to avoid overfilling of the jar, as this could restrict the free movement of the grinding balls.[25] Larger and denser grinding media contribute to more energetic collisions, while smaller, lighter balls generate intense frictional forces. In planetary ball mills, it has been observed that the balls tend to follow well-defined trajectories, rather than randomly colliding with the surfaces. The

duration and intensity of the milling treatment are of course other crucial variables. The time required to complete the process depends on the specific combination of experimental conditions, including temperature and the amount of mechanical energy applied. While the effect of temperature has been well studied,[26,27] the influence of pressure, especially in reactions involving gases, remains less explored. Despite its growing interest, significant limitations remain in our fundamental understanding of mechanochemical processes, particularly in terms of how they relate to thermodynamics and kinetics. One major challenge is that, in most commercially available ball mills, key thermodynamic variables such as temperature and pressure, critical for studying and controlling chemical reactions, are not routinely measured or controlled.

Furthermore, key factors in mechanochemical reactions—such as how energy is transferred to the reactants, the influence of temperature and mechanical treatment on energy distribution within the chemical system, and the mechanisms driving product selectivity—remain poorly understood. Investigating mechanochemical activation during ball milling is particularly challenging due to the short duration of each collision and the highly localized heat and pressure generated during these events. However, *in situ* measurements, thermodynamic analyses, and kinetic modeling have been conducted to better understand the underlying reaction processes. Additionally, computational methods show promise in providing the insights and data needed to address these issues.

As mentioned earlier, mechanochemical synthesis is now widely applied across various fields. Multistep organic and organometallic reactions can be conveniently carried out as "one-pot" mechanochemical syntheses,[28] eliminating the need for isolation and purification of intermediate products. Research has also explored mechanochemical rearrangements in organic compounds, further expanding the scope of mechanochemistry in organic synthesis.[29] Beyond traditional organic chemistry, mechanochemistry is also used in the preparation of peptides and polymers, demonstrating its versatility.[30,31] Mechanochemical techniques can be applied to enhance the extraction of chemicals from plants,[32] contributing to more efficient use of renewable resources. Furthermore, mechanochemical processing has been shown to be effective in producing complex structures, such as hybrid materials that feature an inorganic core and an organic shell. The potential of mechanochemical processing for the creation of nanostructured materials was also acknowledged early in the development of nanotechnology.[33,34] In addition, the synthesis of metal oxides is an area of active research. Metal-oxide nanoparticles, in particular, find applications across a vast array of industries, including the production of integrated circuits, biomedical applications and cancer treatment, pharmaceuticals, personal care products, surface coatings, plastics, textiles, food processing, construction materials, electronics, and automotive industries.[35] Numerous synthetic techniques are now employed in laboratories around the globe and among these, mechanochemical processing has gained recognition as a distinctive method for producing metal oxide nanoparticles.[36] As already described in Chapter 2, zinc oxide (ZnO) is a versatile material with potential applications in various fields, including gas sensors, short-wavelength light-emitting devices, blue lasers, transparent conductive coatings for flat panels, solar cells, and surface acoustic wave devices.[37,38] In addition to its unique physical properties, ZnO is part of a group of metal oxides known for their photocatalytic and photo-oxidizing capabilities

against both chemical and biological substances.[39] As a result, ZnO is widely recognized for its effectiveness in biological applications, particularly as an antibacterial material.[40,41] Some studies are available about the mechanochemical synthesis of ZnO nanoparticles (NPs). The strategy proposed by Salah et al.[42] consists of milling with a high-energy ball mill the commercial microcrystalline powder. They have obtained the formation of nearly spherical, very fine ZnO NPs with almost uniform sizes, lattice relaxation along the z-axis, deep-level defects resulting from oxygen loss, and the appearance of a new photoluminescence band at 365 nm, possibly indicating the formation of a new phase. These structural and optical changes suggest that ZnO NPs could have promising potential as an effective antibacterial material, since the increase in c value of the lattice induced by milling change in the crystal structure of ZnO could have a great effect on the amount of reactive oxygen species generated from the surface of ZnO crystals, which in turn is effective for the inhibition of bacterial growth.[40] Tòthovà et al. have chosen a two steps synthetic approach: they start with the mechanochemical synthesis of phase-pure nanocrystalline hydrozincite, $Zn_5(CO_3)_2(OH)_6$ (ZnHC), by milling a mixture of either $Zn(NO_3)_2 \cdot 6H_2O$ or $ZnCl_2$ and Na_2CO_3 for 10 minutes. Zinc oxide NPs with a specific surface area exceeding 70 m^2/g were then obtained by heating ZnHC to 300°C.[43] Ao et al. successfully synthesized pure nanocrystalline zinc oxide (ZnO) by using the mechanochemical method, followed by heat treatment, with $ZnCl_2$ and Na_2CO_3 as reagents and NaCl as a diluent. This study examined the effects of milling time and heat-treatment temperature on the size of ZnO nanocrystals. Experimental results indicate that increasing the milling time effectively reduces the size of the ZnO nanocrystals. After calcining the milled powder at 600°C in air and washing off NaCl, the average crystal size was approximately 20 nm. Additionally, the crystal size increased with higher heat-treatment temperatures.[44]

Taking in mind all these considerations, we have therefore decided to investigate the possibility of obtaining lignin@ZnO hybrid materials *via* mechanochemical synthesis, in order to develop a green synthetic method, feasible for a scale up production for *in vivo* applications, with reduced amounts of solvent involved. During our research, we have decided to take an approach that avoid the use of surfactants or high calcination temperatures. We have used lignin as a capping agent for the formation of zinc oxide nanoparticles, performing a mechanochemical one-pot synthesis within a jar using zinc salts and sodium hydroxide as reagents. In this synthetic approach, lignin can also work as a diluent as well, preventing the aggregation of nanoparticles and regulating their size and morphology.

Copper compounds have been utilized as plant protection agents for over 50 different diseases on crops. The precise mechanisms behind the antimicrobial action of copper compounds remain poorly understood. With an effort to shed light on these mechanisms, Meghana et al.[45] have investigated the radical species generated by copper (II) oxide (cupric oxide) and copper (I) oxide (cuprous oxide) and their effects on microorganisms. Their research has demonstrated that cupric oxide produces superoxide radical ions, while cuprous oxide leads to an increase in hydroxyl radicals. The generation of hydroxyl radicals is believed to be related to Fenton reactions, where Cu(I) is oxidized to Cu(II) by hydrogen peroxide, resulting in the formation of hydroxyl ions and highly reactive hydroxyl radical

ions. These radicals then attack various cellular molecules indiscriminately, causing cellular damage. Further studies have shown that Cu(I) can damage enzymes, such as fumarase, and its main mechanism of action appears to be related to its ability to bind to thiol groups in amino acids of intracellular proteins.[46] This interaction disrupts protein function, contributing to the antibacterial effects of copper oxide. However, the reduction of copper usage in agriculture has become a critical concern due to its harmful environmental effects. Our research group has studied the use of hybrid organic-inorganic materials, which result from combining lignin with brochantite, $Cu_4(OH)_6SO_4$. or cuprite (Cu_2O).[47,48] Greenhouse trials on strawberry and tomato plants have demonstrated the significant effectiveness of the hybrid materials against various pathogens, with copper content much lower than that found in copper-based commercial pesticides. By optimizing the synthetic process, we have been able to isolate lignin-based materials with varying copper content, where the NPs exhibit different morphologies and sizes. Additionally, a more environmentally friendly synthesis has been explored through mechanochemistry, which reduces water usage and facilitates the isolation of the final products.[47] However, while it has been possible to isolate brochantite by mechanochemistry,[47] preliminary attempts to use the same approach to isolate HMW@Cu_2O hybrid materials necessitate further improvements.[49] At present, mechanochemical synthetic strategies for the formation of cuprite are scarce in the literature, despite the promising properties of this material. The goal of this study is to investigate a mechanochemical approach to produce cuprite, given that previous research has demonstrated its excellent *in vitro* and *in vivo* tests conducted on tomato against *Listeria monocytogenes* and *Rhizoctonia solani* at low copper dosage.[48] The reduction of copper (II) to copper (I) can be achieved by high-molecular-weight (HMW) lignin under basic conditions, exploiting lignin reducing properties. The reduction process occurs *via* the phenolic groups of lignin, as described by Fiss et al.[50] In our research, studies have been conducted on the synthesis of materials that, in combination with lignin, contain zincite, cuprite or both inorganic phases. It is important to emphasize that, in addition to their antimicrobial and antifungal properties, these materials also contain metals that can be considered micronutrients, providing a supplement for plants or animals. Overall, the synthesis of the hybrid materials has been optimized and they have been fully characterized by several techniques, ranging from PXRD to TEM, DLS and ICP-AES analysis, highlighting also the possible modification of the lignin matrix by SEC, FT-IR, Pyrolysis GC-MS, TGA and DSC. *In vitro* studies to assess the antibacterial and antifungal features of the isolated materials are ongoing at University of Naples in the research group of Prof. S. Woo.

EXPERIMENTAL SECTION

Materials and Methods

HMW (Biopiva395®, Kraft softwood lignin from *Pinus taeda*, M_w 5950-6000 g/mol, M_n 1560-1565 g/mol) is kindly provided by UPM-Kymmene Oyj (Helsinki, Finland) and Green Innovation GmbH (Innsbruck, Austria). Zinc acetate dihydrate (99%) and zinc sulphate heptahydrate (99%) are purchased by Carlo Erba; zinc acetate is provided by Thermoscientific (99%), zinc chloride is purchased by Brenntag; copper sulphate pentahydrate (98%) is purchased by Fluorochem; sodium hydroxide is purchased by AnalaR NORMAPUR®ACS (99.5%). All the reagents are used as received with no further purification. The mechanochemical syntheses described in this chapter are conducted with a planetary ball mill Retsch® PM100 using a 80 mL agate jar or a 500 mL zirconia jar.

Materials preparation

HMW@ZnO_X%_m (X=5, 10, 20, 30% of Zn). In a 80 mL agate jar, HMW, zinc salt ($Zn(OAc)_2 \cdot 2H_2O$, $ZnCl_2$, or $ZnSO_4 \cdot 7H_2O$) and 5 agate spheres (15 mm ø) have been loaded according to the mass ratio reported in Table 3.1 and Table S3.1. A pre-mixing of the reagents has been performed for 1 minute at 200 rpm. Then, NaOH solution (4 or 5 equivalents of NaOH with the respect to the zinc salt) has been added. The concentration of the solution have been varied accordingly to the amount of reagent to reach LAG conditions, with η (mL/g) values ranging from 0.75 to 1.7. The mixture has been ground at 300 rpm for 30 minutes. The brown product obtained has been dried in a heating chamber at 95 °C overnight. The obtained powder has been washed with distilled water, centrifuged and dried again at 95°C overnight. All the experiments have been performed at least in duplicate.

Table 3.1. Stoichiometric ratios of reagents for the preparation of HMW@ZnO_X%_m (X= 5, 10, 20%, 30%) by using $ZnSO_4 \cdot 7H_2O$. Concentration of NaOH solution is reported in parenthesis.

	HMW/$Zn(SO_4) \cdot 7H_2O$ mass ratio (g/g)	NaOH (mol)	NaOH/$Zn(SO_4) \cdot 7H_2O$ molar ratio
HMW@ZnO_5%_m	7.5/1.8	0.032 (2 M)	5/1
HMW@ZnO_10%_m	6.7/3.4	0.047 (5 M)	4/1
HMW@ZnO_20%_m	6/6.9	0.097 (10 M)	4/1
HMW@ZnO_30%_m	4/8.6	0.116 (10 M)	4/1

HMW@ZnO_X%_m scale up (X=5, 10, 20, 30% of Zn). In a 500 mL zirconia jar, HMW), $ZnSO_4 \cdot 7H_2O$ (0.082 mol) and 4 zirconia spheres (20 mm ø) have been loaded, according to the mass ratio reported in Table 3.2 and Table S3.2. A pre-mixing of the reagents has been performed for 5 minutes at 300 rpm. Then, NaOH 5 M solution (4 or 5 equivalents of NaOH with the respect to the zinc salt) has been added. The concentration of the solution has been varied accordingly to the amount of reagent to reach LAG conditions, with η (mL/g) values ranging from 0.5 to 1.3. The mixture has been ground at 300 rpm for 30 minutes. The brown product obtained has been dried in the heating chamber at 95 °C overnight. The obtained powder has been washed with

distilled water, centrifuged and dried again at 95°C overnight. All the experiments have been performed at least in duplicate. HMW@ZnO_10%_m has been synthesized also by using zinc acetate and zinc chloride as starting reagent: the experimental conditions are reported in Table S3.2.

Table 3.2. Stoichiometric ratios of reagents for the preparation of HMW@ZnO_X%_m (X= 5, 10, 20, 30%) by using $ZnSO_4 \cdot 7H_2O$. Concentration of NaOH solution is reported in parenthesis.

	HMW/$Zn(SO_4) \cdot 7H_2O$ mass ratio (g/g)	NaOH (mol)	NaOH/$Zn(SO_4) \cdot 7H_2O$ molar ratio
HMW@ZnO_5%_m	48/11.3	0.196 (2 M)	5/1
HMW@ZnO_10%_m	60.3/30.8	0.421 (10 M)	4/1
HMW@ZnO_20%_m	33.6/39.7	0.548 (10 M)	4/1
HMW@ZnO_30%_m	26.8/55.6	0.764 (20 M)	4/1

HMW@Cu_2O_X%_m (X=5, 10, 15, 20% of Cu). In a 80 mL agate jar, HMW (the amount has been calculated to reach the desired metal content, as reported in Table 3.3), $CuSO_4 \cdot 5H_2O$ and 5 agate spheres (15 mm ø) have been loaded. A pre-mixing of the reagents has been performed for 1 minute at 200 rpm. Then, NaOH aqueous solution (4 equivalents of NaOH with the respect to the zinc salt) has been added. The concentration of the solution has been accordingly to the amount of reagent to reach LAG conditions, with η (mL/g) values ranging from 0.7 to 1.4. The mixture has been ground at 300 rpm for 30 minutes. The brown product obtained has been dried in the heating chamber at 95 °C overnight. The obtained powder has been washed with distilled water, centrifuged and dried again at 95°C overnight. All the experiments have been performed at least in duplicate.

Table 3.3. Stoichiometric ratios of reagents for the preparation of HMW@Cu_2O_X% (X= 5, 10, 15%, 20%) by using $CuSO_4 \cdot 5H_2O$. Concentration of NaOH solution is reported in parenthesis.

	HMW/$Cu(SO_4) \cdot 5H_2O$ mass ratio (g/g)	NaOH (mol)	NaOH/$Cu(SO_4) \cdot 5H_2O$ molar ratio
HMW@Cu_2O_5%_m	8.5/1.88	0.030 (2 M)	4/1
HMW@Cu_2O_10%_m	6.9/3.5	0.056 (4 M)	4/1
HMW@Cu_2O_15%_m	6.4/5.6	0.089 (8M)	4/1
HMW@Cu_2O_20%_m	4.7/6.7	0.109 (10 M)	4/1

HMW@ZnO_X%_Cu_2O_Y%_m (X=4, 8, 12 % of Zn; Y= 4, 8, 12 % of Cu). In a 80 mL agate jar, HMW (the amount has been calculated to reach the desired metal content, as reported in Table 3.4), $ZnSO_4 \cdot 5H_2O$, $CuSO_4 \cdot 5H_2O$ and 5 agate spheres (15 mm ø) have been loaded. A pre-mixing of the reagents has been performed for 1 minute at 200 rpm. Then, a NaOH aqueous solution has been added (Table 3.4). The concentration of the solution has been chosen to reach LAG conditions, with η (mL/g) values ranging from 0.8 to 0.9. The mixture has been ground at 300 rpm for 30 minutes. The brown product

obtained has been dried in the heating chamber at 95 °C overnight. The obtained powder has been washed with distilled water, centrifuged and dried again at 95°C overnight. All the experiments have been performed at least in duplicate.

Table 3.4. Stoichiometric ratios of reagents for the preparation of HMW@Zn_X%_Cu_Y%_m (X,Y= 4, 8%, 12%) by using $ZnSO_4 \cdot 5H_2O$ and $CuSO_4 \cdot 5H_2O$. Concentration of NaOH solution is reported in parenthesis.

	HMW/ $Zn(SO_4) \cdot 7H_2O$ /$Cu(SO_4) \cdot 5H_2O$ mass ratio (g/g)	NaOH (mol)	NaOH/ $Zn(SO_4) \cdot 7H_2O$ /$Cu(SO_4) \cdot 5H_2O$/ molar ratio
HMW@Zn_8%_Cu_8%_m	6.8/3.4/2.9	0.070 (7 M)	6/1/1
HMW@Zn_8%_Cu_4%_m	6.8/3.4/1.5	0.070 (7 M)	6/1/0.5
HMW@Zn_4%_Cu_8%_m	6.8/1.5/2.9	0.070 (7 M)	6/0.5/1
HMW@Zn_12%_Cu_12%_m	4.5/4.2/3.7	0.074 (7 M)	6/1/1

RESULTS AND DISCUSSION

As outlined in the Introduction, hybrid materials containing zinc oxide are of great interest due to their potential applications. Mechanochemical synthesis is an environmentally friendly and scalable approach, offering several advantages over traditional wet methods. With the goal of scaling up the synthesis of HMW@ZnO hybrid materials for *in vivo* applications, we have explored the feasibility of using a mechanochemical approach. An interesting aspect is that mechanochemistry requires a little amount of solvent, which accelerates the drying step and this is beneficial in terms of preparation costs of the material. We have operated by using a planetary ball mill and a 80 mL agate or a 500 mL zirconia jar. The jars have been loaded with the reagents for about 1/3 of the volume and the number and dimensions of the spheres has been changed accordingly to the amount of material and volume of the jar. We have varied the molar ratio of the reagents to define the best synthetic approach to isolate the final materials. The optimized procedure consists in a quick pre-mixing of a zinc salt ($Zn(OAc)_2 \cdot 2H_2O$, $ZnCl_2$ or $ZnSO_4 \cdot 7H_2O$) with HMW and 5 agate spheres (15 mm ø) for 1 minute at 200 rpm in a 80 mL agate jar. Then, a sodium hydroxide aqueous solution has been added, and the concentration of the solution has been varied accordingly to the amounts of reagent to reach LAG conditions, that guarantee a homogeneous mixing and a complete conversion of the precursors. 4 equivalents of base are required with the respect to the zinc salt, with the exception of the preparation of HMW@ZnO_5%_grind, where 5 equivalents of base are necessary. This is related to the high amount of lignin and, consequently, of acidic sites present, with respect to the metal, which requires more base to reach the complete conversion of the zinc precursor. In case of syntheses performed with 4 equivalents of NaOH instead of 5 with the respect to the zinc salt, the presence of an unidentified phase together with zinc oxide has been outlined (Figure S3.1). The mixing is performed for 30 minutes at 300 rpm, then the product is dried at 95 °C. The isolated powder has been washed with water and dried again at the same temperature. To note that the recovery of the material is about 30% respect the expected final powder, due to the loss of compound during the washing step, considering the high solubility in the basic environment required for the synthesis.

The hybrid materials obtained have been characterized by FT-IR, PXRD, ICP-AES, DLS, TEM, EDX and SAED. We first isolate HMW@ZnO_m materials, identified as HMW@ZnO_X%_m (X=5, 10, 20, 30 %) and the attempts have been focused on finding the simplest, most sustainable and scalable synthetic approach. The schematic representation of the synthesis is reported in Figure 3.5.

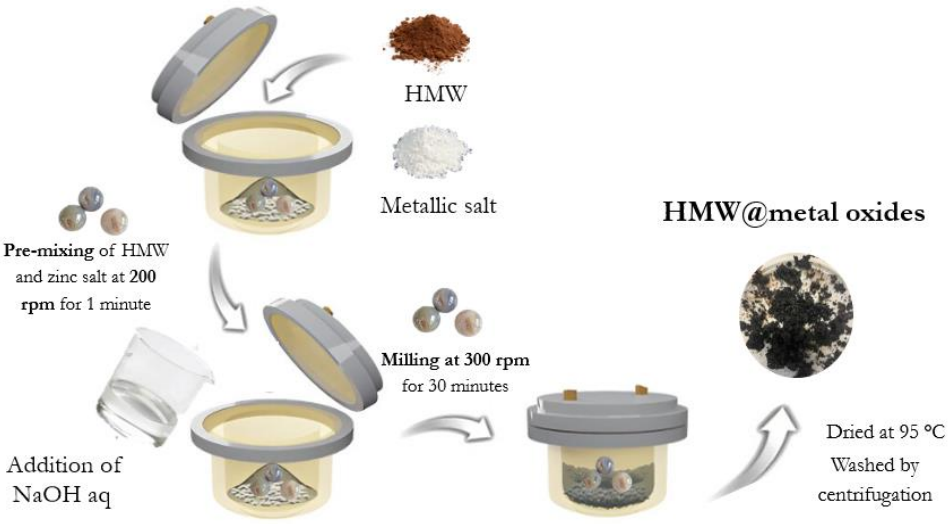

Figure 3.5. Schematic representation of the mechanochemical synthesis

The nature of the crystalline phase in the hybrid material and its purity have been verified by means of powder X-ray diffraction analysis (PXRD). As expected, the lignin matrix is amorphous and is responsible for a broad diffuse scattering at low 2θ, while ZnO exhibits the characteristic diffraction peaks at 2θ 31.8 °, 34.4 °, 36.3 °, 47.5 °, 56.7°, 62.8°, 64.4°, 67.9°, 68.3°. Figure 3.6 shows the stacked diffractograms collected for the materials obtained from zinc sulphate heptahydrate with different metal contents: in all cases, only hexagonal wurtzite is found. For comparison, the diffractogram of the ZnO COD data bank reference is reported in Figure 3.6.

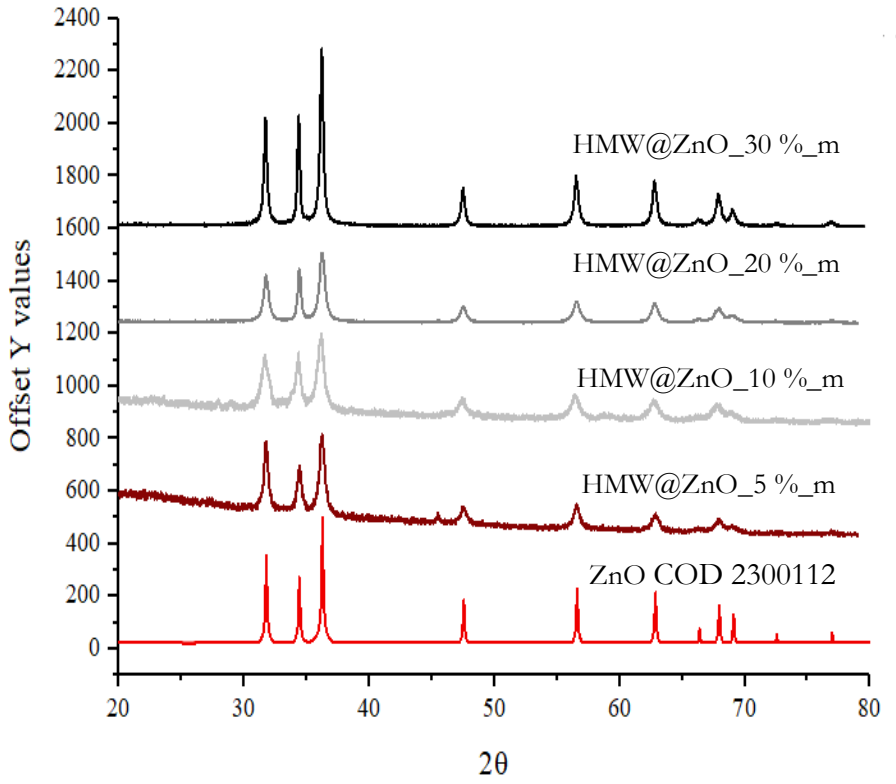

Figure 3.6. Stacked PXRD patterns of HMW@ZnO_5%_m, HMW@ZnO_10%_m, HMW@ZnO_20%_m, HMW@ZnO_30%_m and ZnO from data bank ZnO (COD 2300112), synthesized from $ZnSO_4 \cdot 7H_2O$.

Stacked diffraction patterns of HMW@ZnO_10%_m obtained from different zinc sources are reported in Figure S3.2, showing that the intensities and widths of the PXRD peaks do not change significantly accordingly to the zinc salt chosen. The same behaviour has been evidenced under wet conditions, where TEM studies indicated that the metal source has not any influence on the morphology and dimensions of the crystals (see Chapter 2). It can be assumed that this holds true also under mechanochemical conditions, opening the possibility to choose the most suitable and disposable metal source. Zinc chloride is then chosen as metal source, since the PXRD trace of NaCl contains few peaks that do not interfere with those of ZnO. Analysing the whole reaction mixture prior to washing (Figure S3.3), it is possible to verify the exclusive presence of ZnO and NaCl phases, with no trace of other species. FT-IR spectrum of HMW@ZnO_m is comparable to the one of HMW@ZnO_wet, as shown in Figure S3.4. HMW@ZnO_10%_wet and HMW@ZnO_10%_m materials have been also investigated by DLS and results are collected in Figure 3.7 and Table 3.5. A quite similar size distribution of the nanoparticles can be observed in all cases, with comparable polydispersity indexes (PDI). A slightly higher aggregation for the product obtained by wet conditions can be observed.

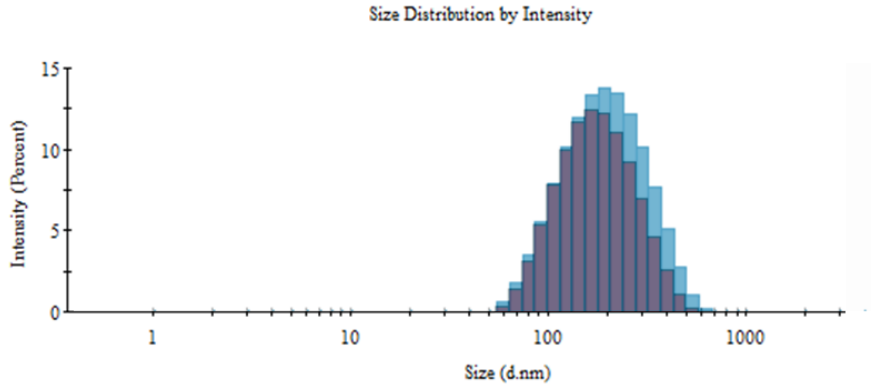

Figure 3.7. DLS size distributions for HMW@ZnO_10%_m (red) and HMW@ZnO_10%_wet (blue).

Table 3.5 Z-averages and PDI results collected by DLS technique on HMW@ZnO materials obtained by wet conditions or mechanochemistry.

	Z-Average (d. nm)	PDI
HMW@ZnO_10%_m	139.0	0.253
HMW@ZnO_10%_wet	167.1	0.265

The different approaches, wet and mechanochemical, for the preparation of HMW@ZnO_10%_m are compared analysing the final materials by TEM microscopy (Figure 3.8). Analysis of HMW@ZnO_10%__wet procedure has been already disclosed in Chapter 2. The analysis of HMW@ZnO_10%_m reveals the presence of crystals with dimensions of 20-100 nm and the presence of well-defined needles with length of 50 nm and thickness of 5-20 nm. HMW@ZnO_10%_wet shows aggregates with slightly increased dimensions (20-200 nm), constituted by nanocrystals of 10-20 nm. The presence of well-defined needles can also in this case be detected, with length 50-300 nm and

thickness of 10-50 nm. It can be inferred that the mechanochemical approach doesn't affect significantly the morphologies and dimensions of NPs, apart from preventing a bit their aggregation. In both cases, the presence of aggregates with not clear morphology and needles can be observed, with slightly bigger crystals obtained with wet conditions. Sizes and morphologies of the crystals obtained with the two methodologies are reported in Table S3.3.

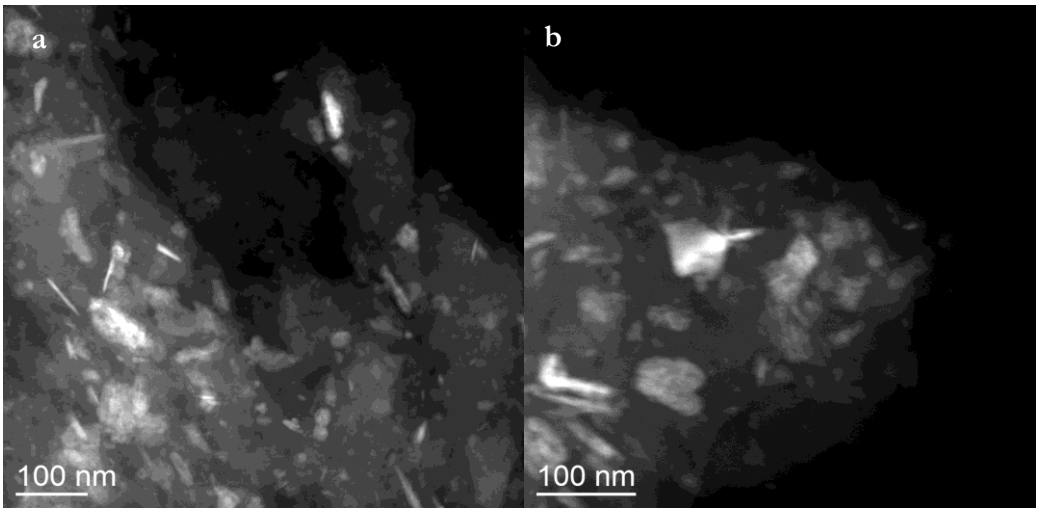

Figure 3.8. TEM images showing the different dimensions and morphologies of the nanoparticles of a) HMW@ZnO_10%_wet and b) HMW@ZnO_10%_m, using zinc sulphate heptahydrate as metal source

We have further isolated HMW@ZnO_m materials with different metal content (HMW@ZnO_X%_m, with X = 5, 20, 30% of Zn), to evaluate the influence of different reagent ratios on the size and morphology of the metal NPs, investigated by means of TEM microscopy (Figure 3.9). The analysis of HMW@ZnO_5%__m shows the presence of crystals with dimensions of 20-200 nm constituted by elements of 10-50 nm with the simultaneous sporadic presence of well-defined needles with length of 50-100 nm and thickness of 20-50 nm. HMW@ZnO_20%_m has crystals with sizes between 10 and 200 nm, with aggregates of 10-20 nm. The largest crystals are needle-shaped, with thickness of 10-20 nm and length 50-100 nm. HMW@ZnO_30%_m shows aggregates with increased dimensions (20-500 nm), constituted by elements of 5-10 nm and bigger crystals have needle shape, with length 50-200 nm and thickness 10-50 nm. It can be noticed that increasing the loading of the metal, the presence of well-defined needles increases and the crystals have bigger dimensions. Sizes and morphologies of the crystals obtained with different metal loadings are reported in Table S3.4.

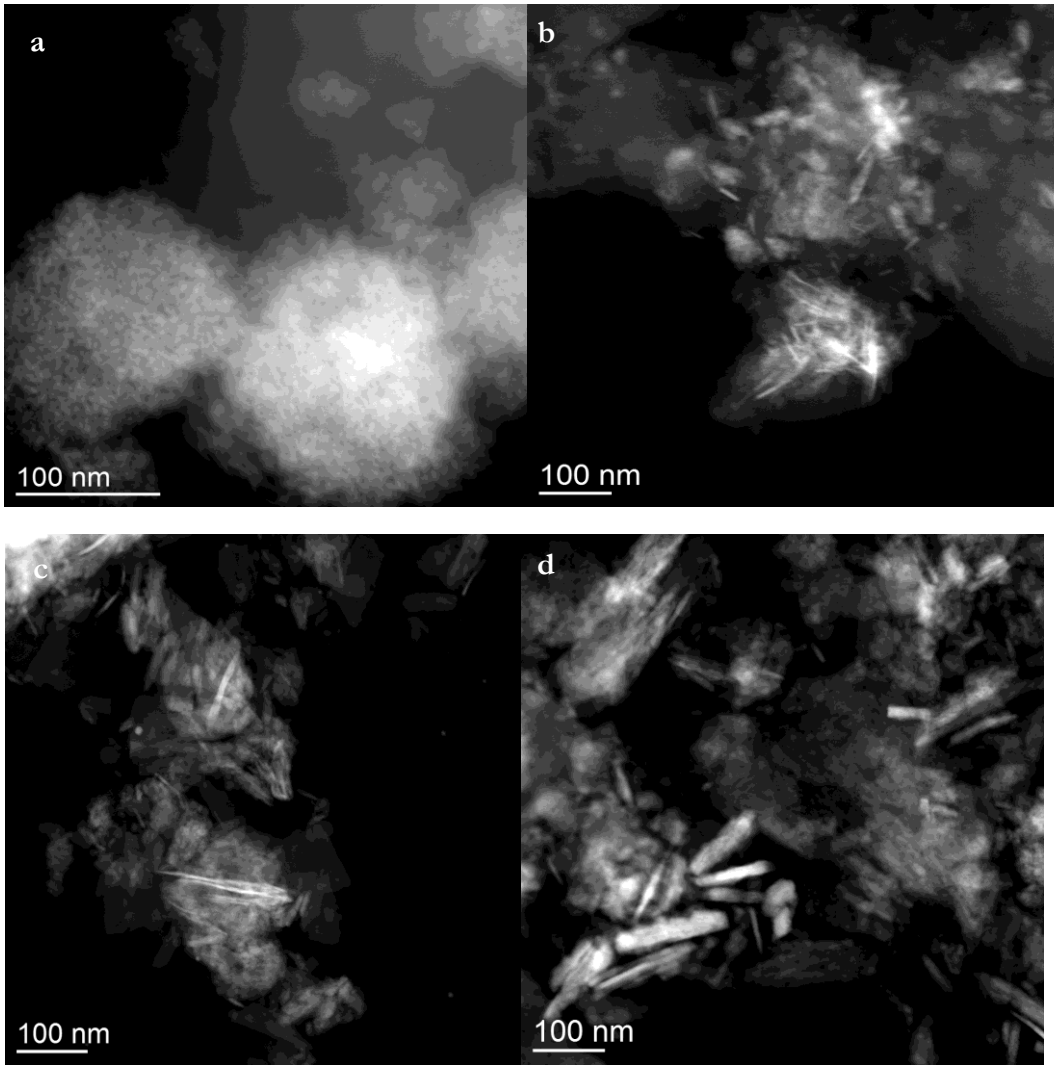

Figure 3.9. TEM images showing the different dimensions and morphologies of the nanoparticles of a) HMW@ZnO_5%_m, b) HMW@ZnO_10%_m, c) HMW@ZnO_20%_m, d) HMW@ZnO_30%_m.

Energy dispersive X-ray spectroscopy (EDX) spectra have been also collected, and one example is reported in Figure S3.5. SAED results are reported in Figure S3.6, where the reflections obtained can be indexed as zinc oxide**.**

The amount of zinc uploaded for HMW@ZnO_10%_m is determined by inductively coupled plasma atomic emission spectroscopy analysis (ICP-AES) and the results are reported in Table 3.6.

Table 3.6. Zinc content determined by ICP-AES analysis for HMW@ZnO_10%_m, obtained by mechanochemical procedure.

	ICP-AES
	Zn% mean ± SD
HMW@ZnO_10%_m	7.6 ± 0.2

As already discussed for the wet products in Chapter 2, during washing there is a partial loss of product due to its solubility in water at basic pH, which results in an experimental

ICP value slightly lower than expected. However, it must be considered that for *in vivo* applications the washing step could not be required.

Analyses have been conducted on lignin to confirm that the grinding conditions used for the synthesis do not affect the polymeric structure of the matrix. Therefore, HMW (14.7 g), 10 mL of water and 5 agate spheres (15 mm ø) have been loaded into a 80 mL agate jar for about 1/3 of the volume. The mixture has been ground at 300 rpm for 30 minutes. Then, the material has been dried at 95 °C. The treated lignin (HMW_ground) has been studied by means of FT-IR, TG, DSC, SEC and Pyrolysis-GC/MS, to verify possible different features if compared to the starting material. Stacked FT-IR spectra of HMW and HMW_ground in Figure 3.10 show the presence of the same bands, typical of Kraft Lignin (as described in Chapter 2).

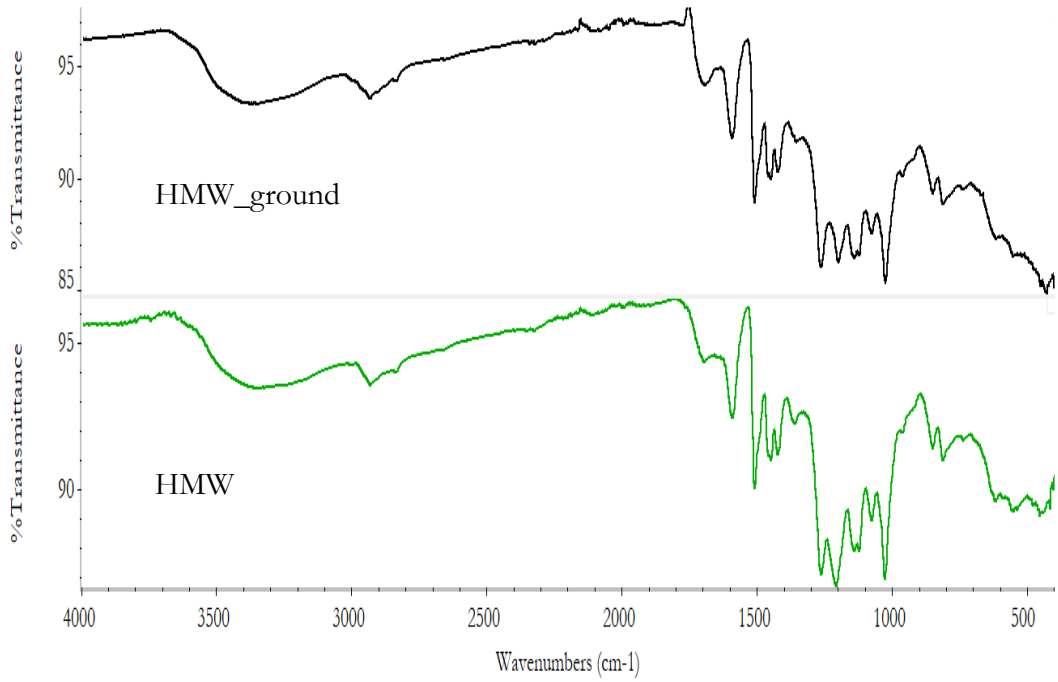

Figure 3.10. Stacked FT-IR of HMW_groung (black line) and HMW (green line)

TGA profile of HMW and HMW_ground indicate water release at about 100 °C, followed by a maximum weight loss (about 50%) at approximately 380 °C, due to decomposition, leading to the formation of low molecular weight products, with the cleavage of the main lignin chains. TGA and DTG profile of the two materials are comparable and are reported in Figure S3.7. The differential scanning calorimetry indicates a glass transition occurring at about 122 °C for HMW, in agreement with the literature data for Kraft lignin (124–174 °C).[51] For HMW_ground the glass transition temperature remains similar, with a slight increase of about 10 °C with respect to the one of HMW. DSC curves are reported in Figure S3.8. By Py-GC/MS analysis, it is possible to infer the presence of phenol-derived molecules, constituting the polymer, and it is possible to ascertain the good agreement between the pyrolysis profiles of HMW and HMW_ground, thus confirming the retention of lignin structure (Figure 3.11).

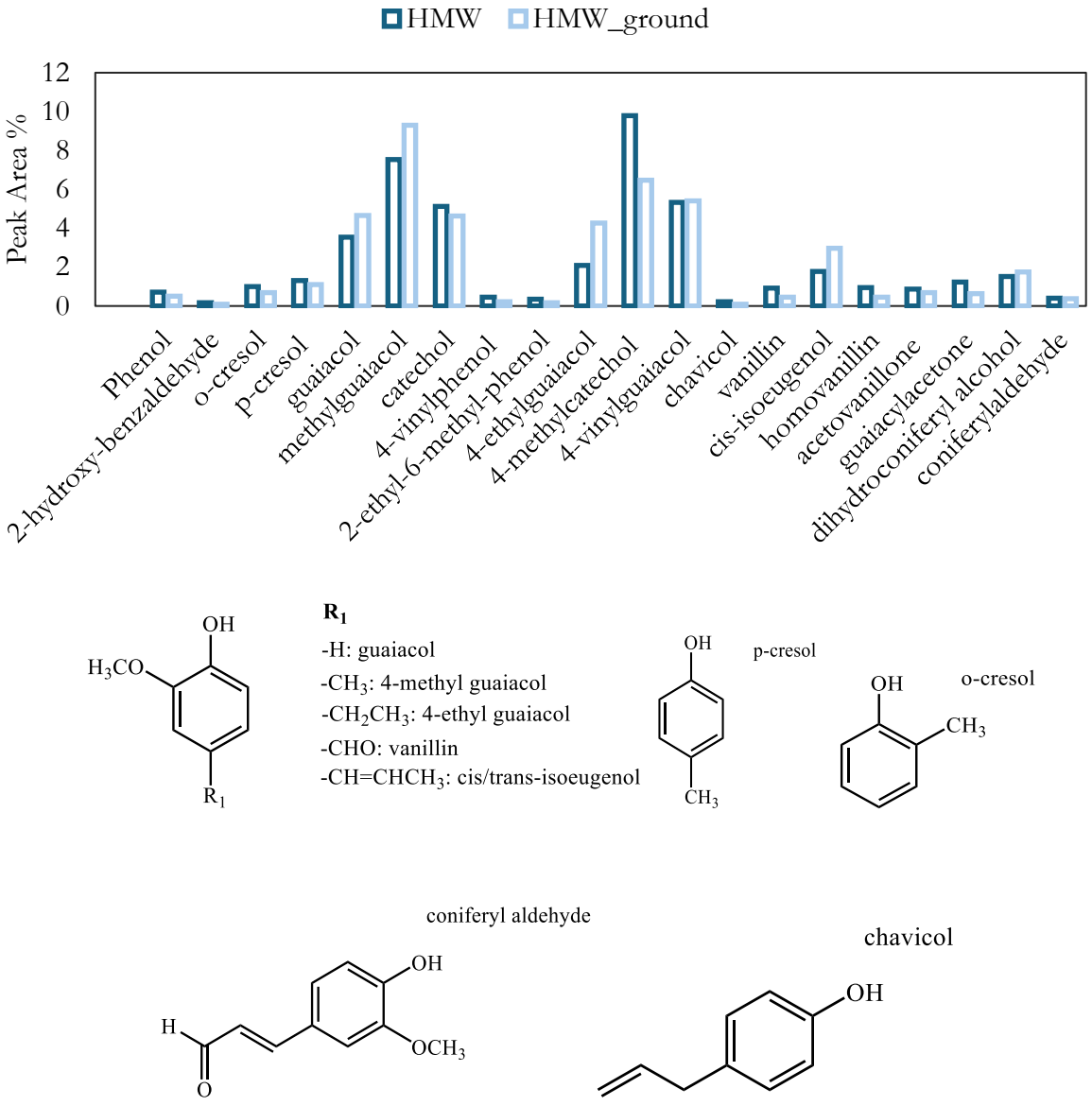

Figure 3.11. Main fragments from pyrolysis GC/MS of HMW and HMW_ground. The bars represent the percentage of the total area of each peak.

Size exclusion chromatography profiles for HMW and HMW_ground are comparable, and the parameters are reported in Table 3.7, demonstrating that grinding does not affect the molecular weight distribution of the polymer.

Table 3.7. SEC results for HMW and HMW_ground

Parameters	HMW	HMW_ground
Number average, M_n (Da)	1551	1552
Weight Average, M_w (Da)	5259	5837
Peak maximum, (Da)	2135	2142
Polydispersity, PD	3.39	3.76

A mechanochemical scale up has been further performed, using a 500 mL zirconia jar, which allows a material loading of about 70 g of reagents. The amount of solvent has been chosen to perform the synthesis in LAG condition, to guarantee a proper homogenization of the mixture and a complete conversion of the precursors. HMW@ZnO_X%_m (with X: 5, 10, 20, 30 % of Zn) have been synthesized with this scale up approach by using zinc sulphate heptahydrate as a metal source. PXRD traces of the materials are shown in Figure 3.12, highlighting the presence of ZnO. HMW@ZnO_10%_m has been also synthesized from different zinc salts (zinc acetate, zinc sulphate heptahydrate and zinc chloride and even in this case the PXRD are comparable (Figure S3.9).

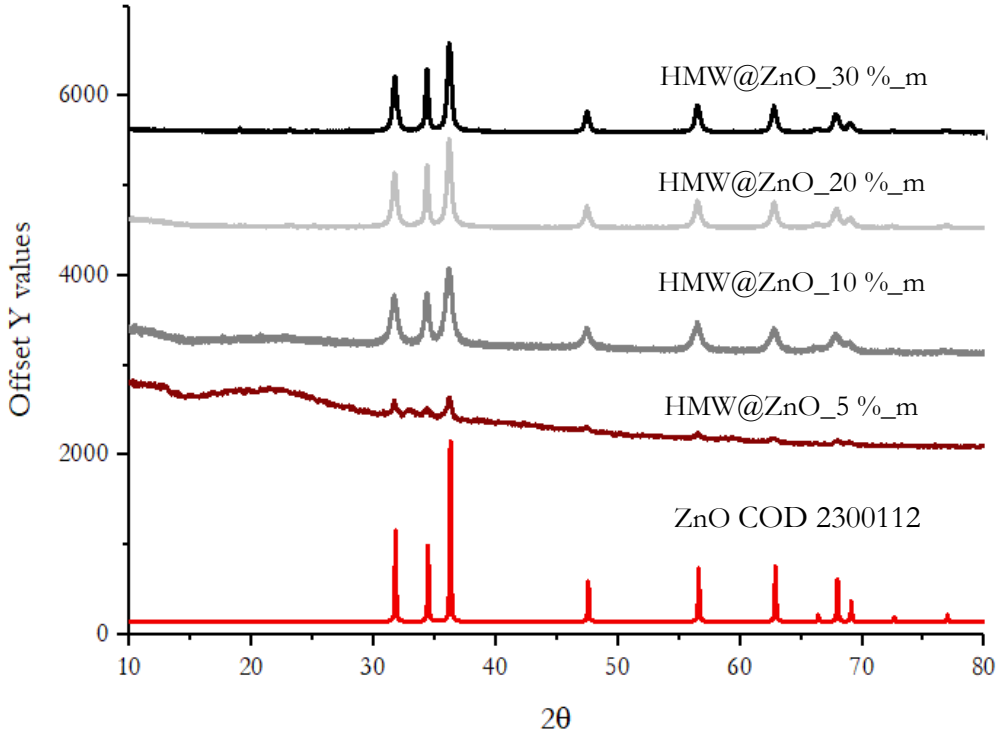

Figure 3.12. Stacked PXRD patterns of HMW@ZnO_5%_m, HMW@ZnO_10%_m, HMW@ZnO_20%_m, HMW@ZnO_30%_m and ZnO from data bank ZnO (COD 2300112), synthesized from zinc sulphate heptahydrate with mechanochemical scale up.

TGA and DTG profiles of HMW@ZnO_10%_m obtained in the scale-up mechanical synthesis has been reported in Figure S3.10, together with the differential scanning calorimetry analysis. A glass transition occurs at about 122 °C for HMW, very similar to that of the hybrid material (119 °C). DSC curves are reported in Figure S3.11. By Py-GC/MS analysis, it is possible to determine the good agreement between the pyrolysis profiles of HMW and HMW@ZnO_10%_m, thus confirming the retention of lignin

structure during the reaction (Figure S3.12). Attempts to synthetize HMW@ZnO_10%_m by neat grinding have been also carried out, but the removal of the material from the jar has been very difficult and a lot of water has been necessary to isolate the material. The product obtained has been analysed without washing and the PXRD pattern demonstrated the presence of mainly sodium sulphate and zinc oxide, together with traces of an unidentified phase (Figure S3.13), LAG conditions, therefore, have been confirmed to be the best option to form the ZnO crystals within the lignin matrix, simplifying the removal of the product and the drying step.

HMW@Cu_2O mechanochemical synthesis

As outlined in the introduction, our previous studies about HMW@Cu materials, containing brochantite, $Cu_4(SO_4)(OH)_6$, or cuprite, Cu_2O, as inorganic phases, have highlighted promising activity against several pathogens, with different *in vivo* performances according to the different dimension and morphology of the inorganic nanocrystals.[47,48,49] Bigger crystals, in fact, ensure prolonged release of the metal over time, and a better pathogen control. HMW@$Cu_4(SO_4)(OH)_6$ has been successfully obtained by mechanochemical procedures, while an optimization for the mechanochemical preparation of HMW@Cu_2O needed further investigations.[48] In this section, efforts devoted to the mechanochemical obtainment of HMW@Cu_2O_m materials are described. The starting metal salt used is copper(II) sulphate, since it is possible to exploit the capability of lignin to reduce Cu(II) to Cu(I). We have therefore investigated if, by using mechanochemistry, it was possible to obtain copper reduction, in analogy with what seen under wet conditions. The synthetic approach is analogous to the one used for the formation of zinc oxide, explained in the previous paragraph. Also in this case, we have operated using a planetary ball mill Retsch® PM 100 and 80 mL agate jar, that allowed the production of about 2 g of material. The jar has been loaded with the solid reagents for about 1/3 of the volume and with 5 spheres (15 mm ø). The amount of solvent has been chosen as to perform the synthesis under LAG condition, the operating frequencies was set to 300 rpm, and the working times to 30 minutes.

The optimized procedure for the preparation of HMW@Cu_2O_5%_m consists in a quick pre-mixing of $CuSO_4 \cdot 5H_2O$ with HMW and 5 agate spheres (15 mm ø) for 1 minute at 200 rpm in a 80 mL agate jar. Then, a 2 M sodium hydroxide aqueous solution has been added: the concentration of the solution has been chosen accordingly to the amounts of reagents to reach LAG conditions, that guarantee a homogeneous mixing of the precursors. 4 equivalents of base are tested with respect to the copper salt to obtain cuprite. The mixing has been performed for 30 minutes at 300 rpm, then the product has been dried at 95 °C. The isolated powder has been washed with 50 mL of water and dried again at the same temperature. The complete conversion of the whole reaction mixture is demonstrated by analysing the product without washing by PXRD: no other phases than cuprite and the expected sodium sulphate are detected (Figure S3.14). The materials have been characterized by FT-IR, PXRD, ICP-AES, DLS, TEM and EDX. We have isolated HMW@Cu_2O_m materials, identified as HMW@ Cu_2O_X%_m (X=5, 10). PXRD on

HMW@Cu_2O_X%_m (X = 5, 10%) after washing with water, evidencing the presence of cuprite as unique crystalline phase.

The nature of the crystalline phase in the HMW@Cu_2O_5%_m hybrid material and its purity have been verified by means of powder X-ray diffraction analysis (PXRD). The lignin matrix is amorphous and is responsible for a broad diffuse scattering at low 2θ, while Cu_2O exhibits the characteristic diffraction peaks at 2θ 29.5°, 36.42°, 42.3°, 61.36 °, 73.5°, 77.3°. Figure 3.13 shows the experimental pattern of HMW@Cu_2O_5%_m, matching with cuprite phase.

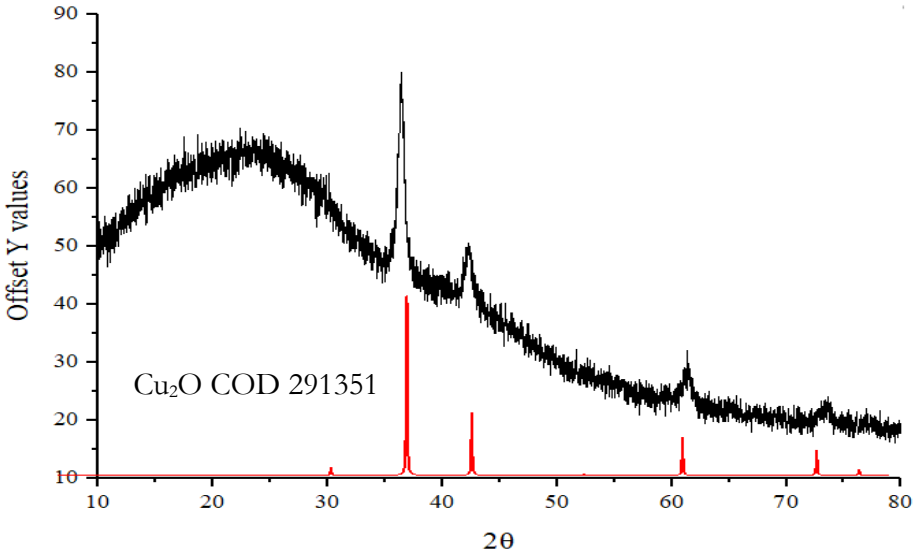

Figure 3.13. Matching of experimental PXRD patterns of HMW@Cu_2O_5%_m with cuprite.

Figure 3.14 reports stacked FT-IR spectra of HMW@Cu_2O _5%_m and HMW. The main difference is related to the appearance, in the spectrum of the hybrid material, of the Cu-O stretching band at about 400-500 cm^{-1}.

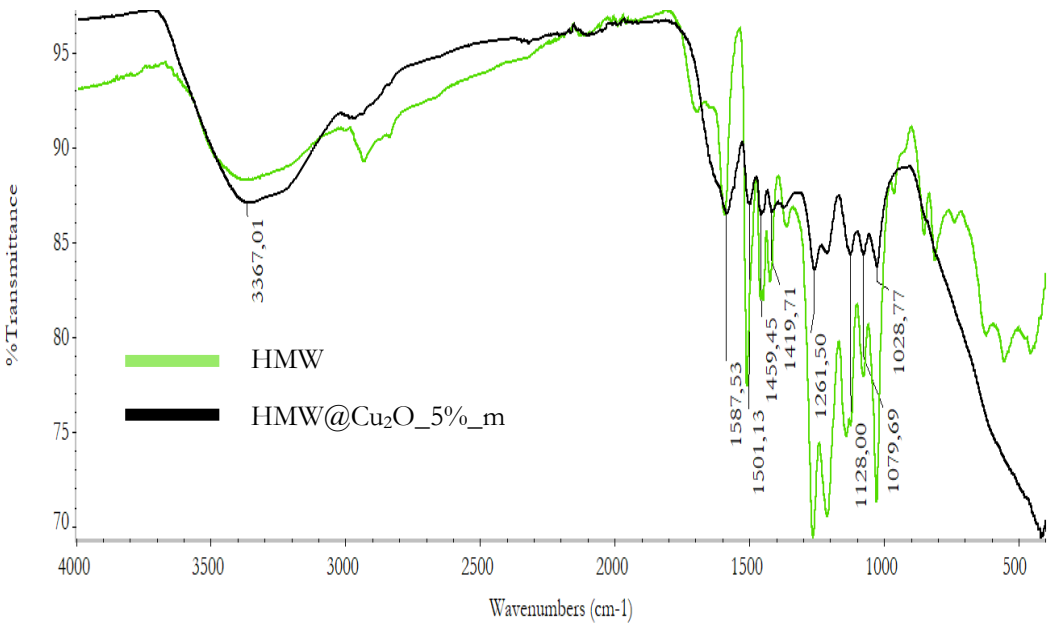

Figure 3.14. FT-IR of HMW@Cu_2O_5%_m (black line) and HMW (green line).

HMW@Cu_2O_5%_m has been investigated by TEM microscopy (Figure 3.15). The analysis reveals the presence of crystals with dimensions of 10-50 nm and of spheres with diameter of 5-20 nm. There are some aggregates of about 100 nm constituted by 10-20 nm elements. The corresponding hybrid material obtained by wet conditions of previous work[48] has showed aggregates with slightly increased dimensions (20-200 nm), constituted by elements of 10-20 nm (HMW@Cu_2O_5%_wet, see Supporting Information for details: Procedure S1 and Table S3.5). The presence of well-defined needles can also in this case be detected, with 50-300 nm length and thickness 10-50 nm. If we compare the dimension and morphology of the NPs obtained by wet and mechanochemical procedure, we can observe that with the wet procedure the crystals have bigger dimension (up to 300 nm), while by using mechanochemistry NPs are generally smaller (up to 50 nm): it seems therefore that by mechanochemistry it is possible to prevent aggregation of the crystals. Sizes and morphologies of the crystals obtained by the two different methodologies are reported in Table S3.6. Energy dispersive X-ray spectroscopy (EDX) spectra are also collected, revealing the presence of copper and oxygen with a ratio close to 2: one example is reported in Figure S3.15. HMW@Cu_2O_5%_m has been also investigated by DLS in aqueous suspension and the size distribution by intensity is reported in Figure 3.16 and Table S3.7. A quite broad size distribution of the nanoparticles can be observed, with polydispersity indexes (PDI) of 0.160. The average diameters of the particles indicated by DLS are 194.2 nm, probably because of slight aggregation phenomena in aqueous suspension.

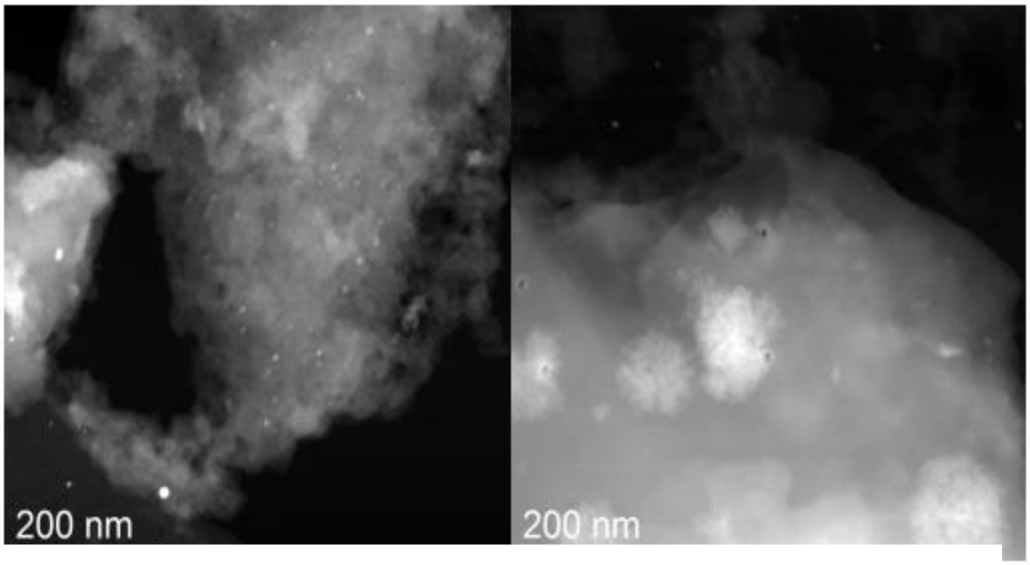

Figure 3.15. TEM images showing the different dimensions and morphologies of the nanoparticles of HMW@Cu_2O_5%_m.

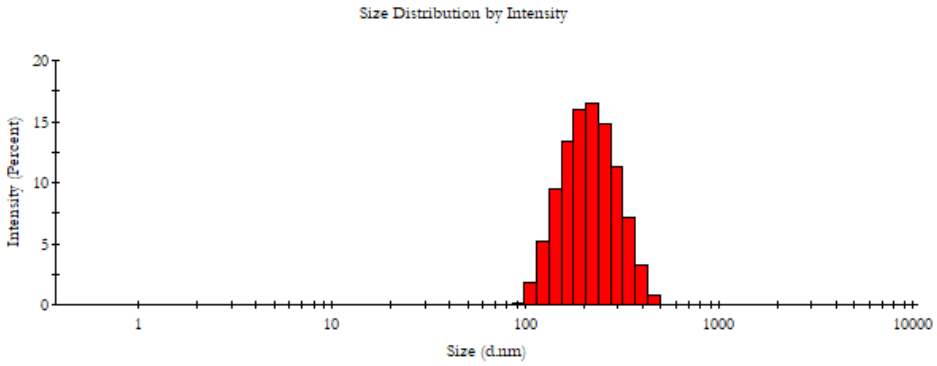

Figure 3.16. DLS size distributions for HMW@Cu_2O_5%_m.

Keeping the same experimental milling conditions described above, but varying lignin/copper salt ratio, it is possible to isolate HMW@Cu_2O_10%_m. In this case, 6.9 g/3.5 g ratio of HMW/copper sulphate pentahydrate are used, and a NaOH 4 M solution is added (4 equivalents of base with the respect to copper salt). Figure 3.17 shows the stacked diffractograms collected for the materials obtained from copper sulphate pentahydrate with copper percentages of 5 and 10% in the final material, respectively. For comparison, the diffractogram of Cu_2O (COD data bank reference) is also reported.

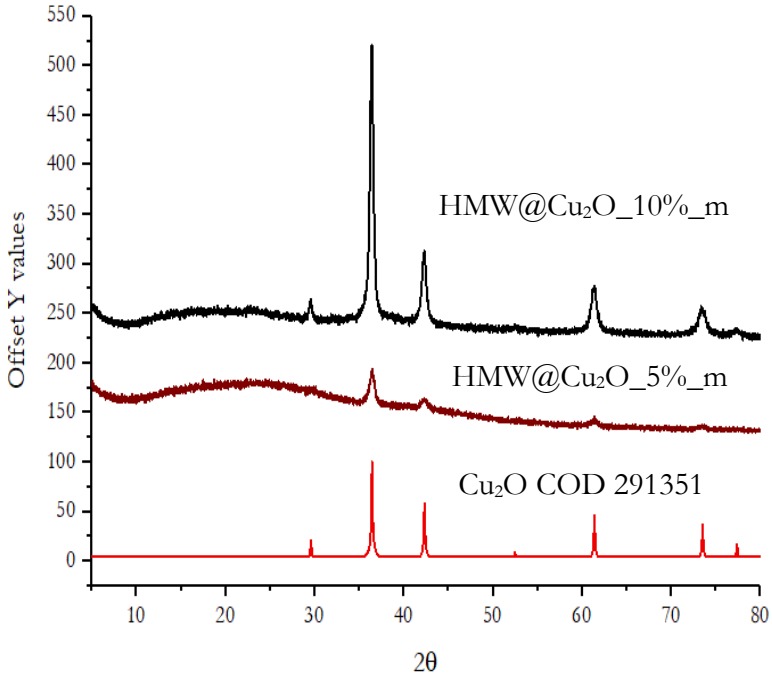

Figure 3.17. Stacked PXRD patterns of HMW@Cu_2O_5%_m, HMW@Cu_2O_10%_m and Cu_2O from data bank (COD 291351)

The amount of copper uploaded in the final materials has been determined by inductively coupled plasma atomic emission spectroscopy analysis (ICP-AES) and the results are reported in Table 3.8.

Table 3.8. Copper content determined by ICP-AES analysis for HMW@Cu_2O_m, obtained by mechanochemical procedure

	ICP-AES Cu% mean ± SD
HMW@Cu_2O_5%_m	3.9± 0.1
HMW@Cu_2O_10%_m	11.99 ± 0.04

Size distribution by intensity obtained by DLS analysis of HMW@Cu_2O_10%_m in water is reported in Figure S3.16 and compared to HMW@Cu_2O_5%_m in Table S3.7. A quite broad size distribution of the nanoparticles can be observed in comparison to HMW@Cu_2O_5%_m, with increased PDI (0.302). The average diameters of the particles are also increased (245.9 nm), suggesting probable aggregation phenomena due to the higher metal content.

It is important to note that cuprite has been successfully isolated as the crystalline phase instead of posnjakite for HMW@Cu_2O_10%_m using the mechanochemical method, contrarily to what observed for the wet procedure (see supporting information and Table S3.5 for details). Typically, with this copper concentration and under these pH conditions, posnjakite forms instead of cuprite.[52] This highlights the crucial role of pH in determining the final crystalline phase during the synthesis of these materials. In the mechanochemical procedure, we have operated under alkaline conditions. It is well known that at room temperature and with a pH ≤ 10, posnjakite is the favored phase, whereas at higher pH

values, cuprite or tenorite (CuO) form. Tenorite has been isolated together with cuprite at higher contents of copper, like in HMW@Cu_15%_m and HMW@Cu_20%_m. However, tenorite (CuO) and cuprite (Cu_2O) are present in the two materials at a different extent, with the first being apparently the most abundant phase, as can be inferred form Figure 3.18, corresponding to the material with 20% copper.

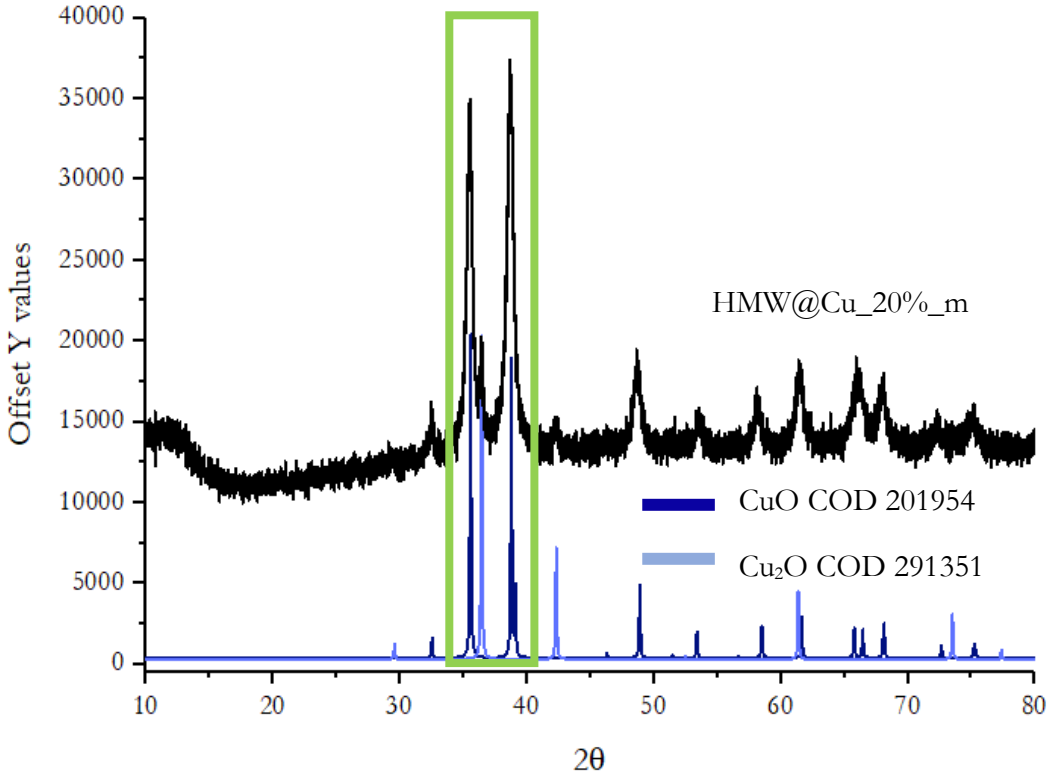

Figure 3.18. Stacked PXRD patterns of HMW@Cu_20%_m, CuO (dark blue, COD 201954) and Cu_2O from data bank (light blue, COD 291351). The most diagnostic area for discrimination of the two phases has been highlighted with a green box.

HMW@Cu_2O_15 %_m (Figure 3.19) shows the presence of a mixture of tenorite and cuprite as well.

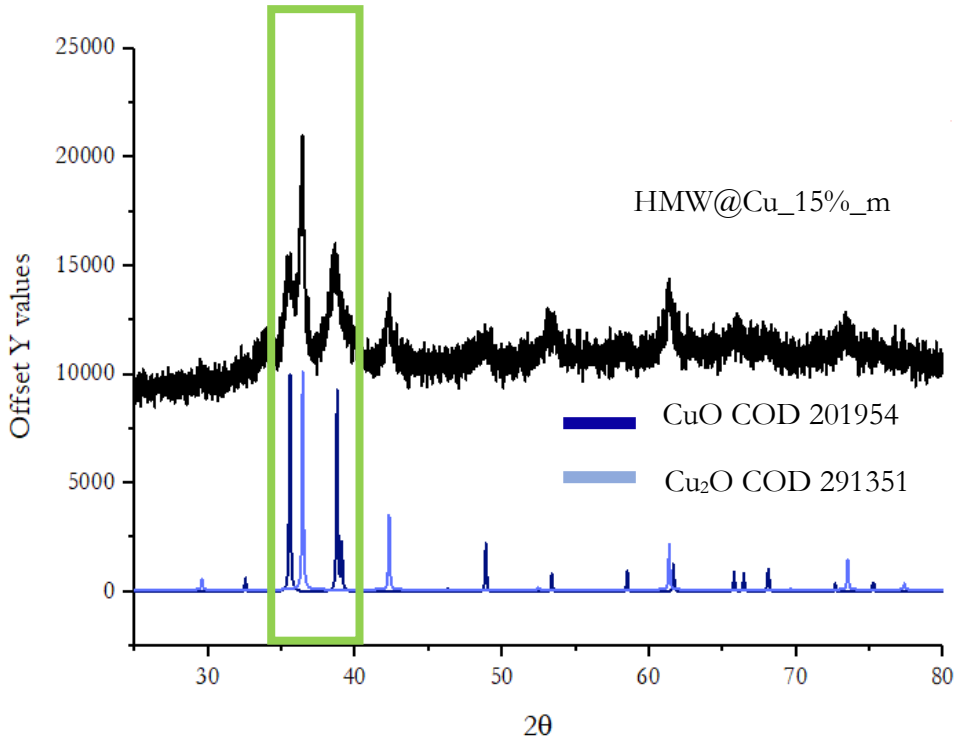

Figure 3.19. Stacked PXRD patterns of HMW@Cu_15%, CuO (COD 201954) and Cu_2O from data bank (COD 291351). The most diagnostic area for discrimination of the two phases has been highlighted with a green box.

HMW@ZnO_Cu_2O mechanochemical synthesis

The advantages of hybrid materials containing zinc oxide or cuprite have been already described in previous paragraphs; in this section we have reported the possibility of combining both phases, embedded in the same matrix. It has also been investigated the possibility of tuning the different amounts of metals, obtaining hybrid materials with different metal contents. As in the case of HMW@Cu_2O_m materials, the reducing properties of HMW have been exploited to reduce copper under mild conditions and with a scalable approach, at the same time obtaining zinc oxide in a one pot synthesis. Before studying the mechanochemical synthetic optimization, the synthesis has been performed *via* wet conditions, in order to find the proper amount of base necessary for the conversion of both metallic salts. At first, lignin copper sulphate pentahydrate, and zinc sulphate heptahydrate (1:1 molar ratio) have been suspended in 50 mL of water and a NaOH 3.5 M solution has been added (5 equivalents with the respect to the metallic salt, conditions reported in the Supporting Information as Procedure S2); after 3 hours of stirring at R.T. the product has been dried at 95°C. After washing, the product has been analysed by means of PXRD and the analysis has revealed that with these synthetic conditions the conversion of both metals is not complete, since the presence of zinc oxide and spertiniite ($Cu(OH)_2$), can be observed, as reported in Figure S3.17. Adopting the same experimental conditions, but increasing the amount of NaOH (6 equivalents with the respect to the two metallic salts) the conversion has been completed, as demonstrated by PXRD analysis (Figure S3.18). ICP-AES analysis confirms the expected loading of both metals inside the material (Table S3.8). After finding the proper reagent ratio, the optimization of the mechanochemical synthetic approach has been performed. We operated using a planetary ball mill PM 100 Retsch® equipped with a 80 mL agate jar. The jar has been loaded with the reagents for about 1/3 of the volume and with 5 spheres of the same materials (15 mm ø). The amount of solvent has been chosen to perform the synthesis in LAG condition, to guarantee a proper homogenization of the mixture and a complete conversion of the precursors. The operating frequencies has been set to 300 rpm, and the working times to about 30 minutes. The materials have been characterized by FT-IR, PXRD, ICP-AES, DLS, TEM, EDX, TG and DSC. At first, We have isolated HMW@ZnO_Cu_2O materials, identified as HMW@ZnO X%_Cu_2O Y%_m (X=4, 8; Y= 4%, 8%, the percentages refer to copper and zinc, respectively) and the attempts have been focused on finding the simplest and most sustainable synthetic approach. The optimized procedure for the preparation of HMW@ZnO_8%_Cu_2O_8%_m consists in a quick pre-mixing of $CuSO_4 \cdot 5H_2O$ (2.9 g), with $ZnSO_4 \cdot 7H_2O$ (3.4 g), HMW (6.8 g) and 5 agate spheres (15 mm ø) for 1 minute at 200 rpm in a 80 mL agate jar. Then, a 7 M sodium hydroxide aqueous solution has been added (6 equivalents with respect to the two salts), and the concentration of the solution has been chosen accordingly to the amounts of reagent to reach the desired LAG conditions. The mixing has been performed for 30 minutes at 300 rpm, then the product has been recovered and dried at 95 °C. The isolated powder has been washed with 50 mL of water and dried again at the same temperature. The exclusive formation of zinc oxide and cuprite from the whole reaction mixture is demonstrated by analysing the product, without washing, by PXRD (Figure S3.19 and Figure S3.20). The PXRD analyses on the final material HMW@ZnO _8%_Cu_2O_8%_m is reported in Figure 3.20. The lignin matrix is amorphous and is responsible for a broad

diffuse scattering at low 2θ, while Cu_2O and ZnO exhibit the characteristic diffraction peaks as reported in Figure 3.20, where the reference patterns of the crystalline phases (cuprite and zincite) are also indicated.

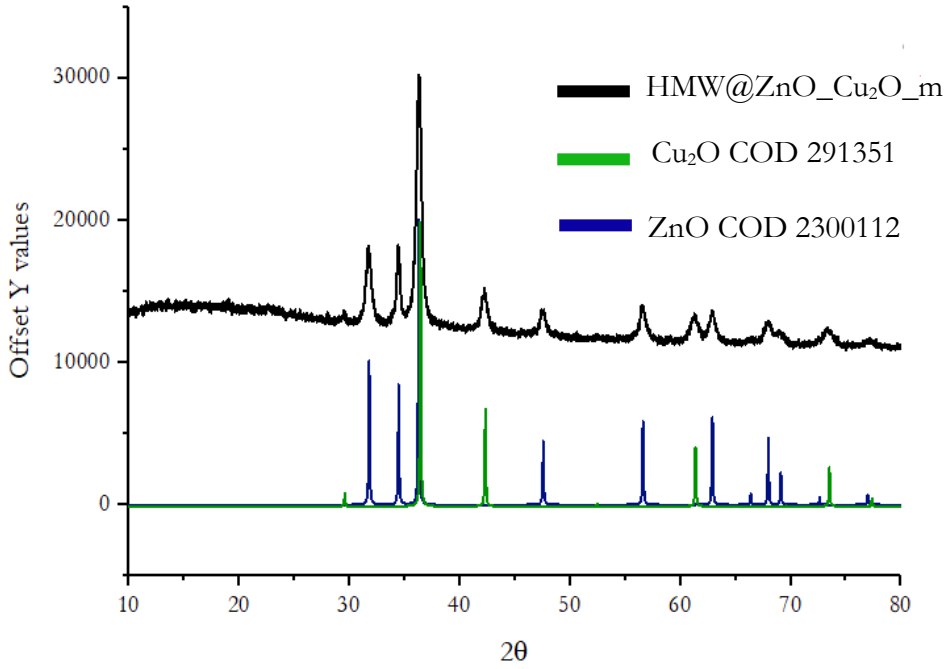

Figure 3.20. Matching of the experimental PXRD patterns of HMW@ZnO_ 8%_Cu_2O_8%_m with cuprite (COD 291351) and zincite (COD 2300112)

Figure S3.21 reports FT-IR spectra of HMW@ZnO_Cu_2O%_m, compared to those of HMW@Cu_2O_m and HMW@ZnO_m, showing that they are superimposable, and no significant differences could be noticed.

The morphological and dimensional analysis of the obtained NPs has been performed by TEM microscopy (Figure 3.21), comparing the results obtained by mechanochemical and wet synthesis.

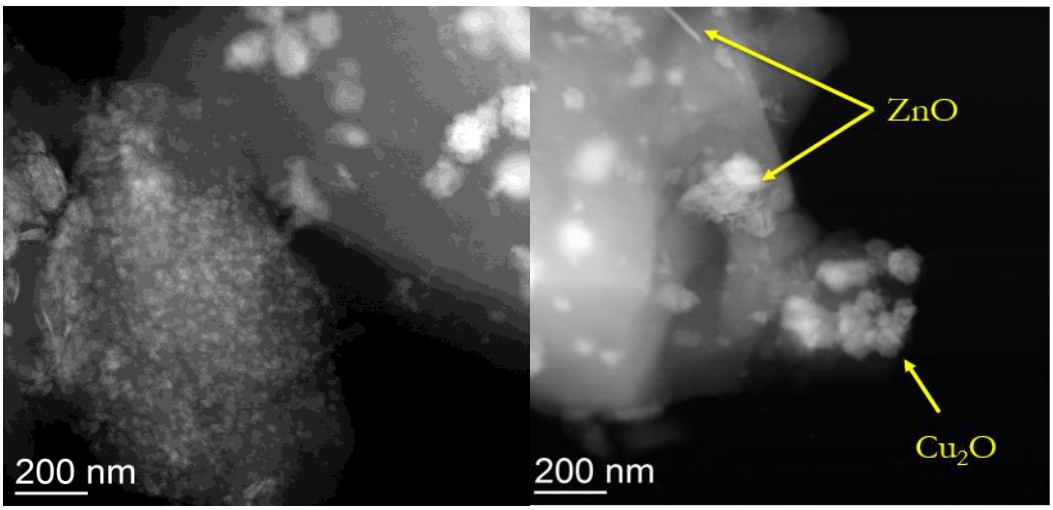

Figure 3.21. TEM images showing the different dimensions and morphologies of the nanoparticles of HMW@ZnO_8%_Cu_2O_ 8%_m, obtained via mechanochemical synthesis.

The analysis reveals the presence of crystals with dimensions 10-50 nm and presence of spheres with diameter of 5-20 nm. There are some aggregates of 100 nm dimensions constituted by 10-20 nm elements of cuprite, as revealed by EDX analysis. NPs dimensions of HMW@ZnO_Cu_2O_m obtained by wet conditions (Procedure S3, Supporting Information paragraph) are highly comparable to the ones observed with the mechanochemical synthesis: in this case, TEM images (Figure 3.22) reveal the presence of aggregates of 100 nm dimensions constituted by 10-20 nm elements.

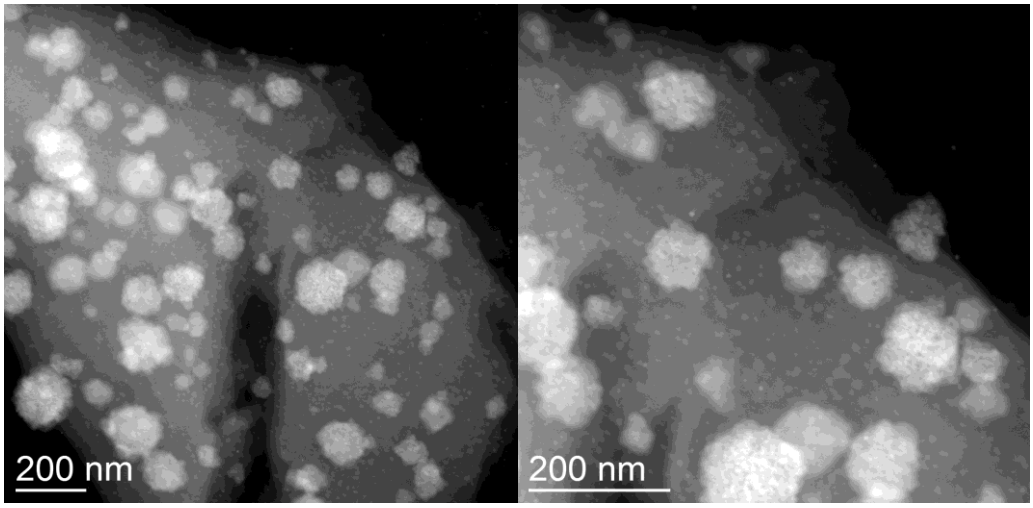

Figure 3.22. TEM images showing the dimensions and morphologies of the nanoparticles for HMW@ZnO_Cu_2O_m, obtained via wet synthesis.

The amount of copper and zinc uploaded in the final materials has been determined by inductively coupled plasma atomic emission spectroscopy analysis (ICP-AES) and the results are reported in Table 3.9.

Table 3.9. Copper and zinc content determined by ICP-AES analysis for HMW@ZnO _X%_Cu_2O_Y%_m (with X referring to the percentage of zinc and Y to the percentage of copper), obtained by mechanochemical procedure

	ICP-AES Zn% mean ± SD	ICP-AES Cu% mean ± SD
HMW@ZnO_8%_Cu_2O_8%_m	9.3 ± 0.2	8.5 ± 0.1

Size and morphology of the crystals obtained by the two methodologies are reported in Table S3.9. Energy dispersive X-ray spectroscopy (EDX) analysis has been also conducted, and one example is reported in Figure 3.23 a., revealing the presence of both copper and zinc. The distribution of the two metals embedded in the biopolymeric matrix has been evaluated by means of EDX mapping (Figure 3.23 b), revealing the presence of both phases homogeneously dispersed. Sulphur in minor amount is also detected, probably due to some residual sulphate. EDX mapping of single elements with the relative colour intensity are reported in Figure S3.22 and EDX with ZAF corrections are reported, showing percentages of zinc and copper very close to the expected values.

a)

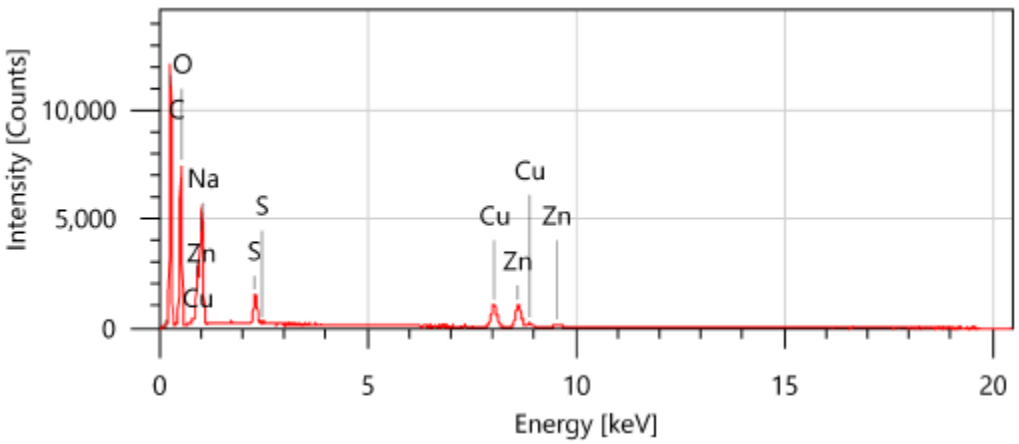

b)

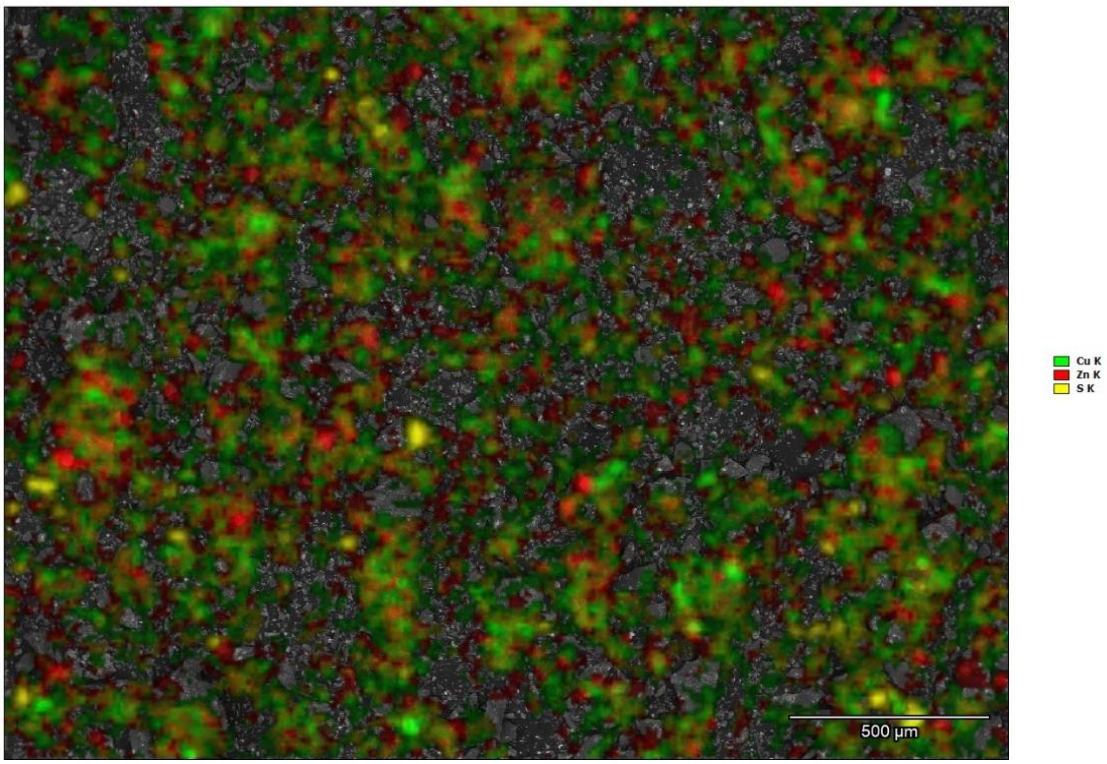

Figure 3.23. a) EDX analysis shows the presence of both copper and zinc; b) EDX mapping shows the metal distribution inside the hybrid material (copper coloured in green, zinc in red).

SAED analysis has not been possible, owing to the small dimensions of the nanoparticles; only the most intense reflection of Cu_2O (111) are detectable, but partly superimposed with the (101) line of ZnO (Figure S3.23). HMW@ZnO_ 8%_Cu_2O 8 %_m has been also investigated by DLS and the size distribution by intensity is reported in Figure 3.24 and Table S3.10. A quite broad size distribution of the nanoparticles can be observed, with a polydispersity index (PDI) of 0.278: this can be probably related to aggregation phenomena in aqueous medium.

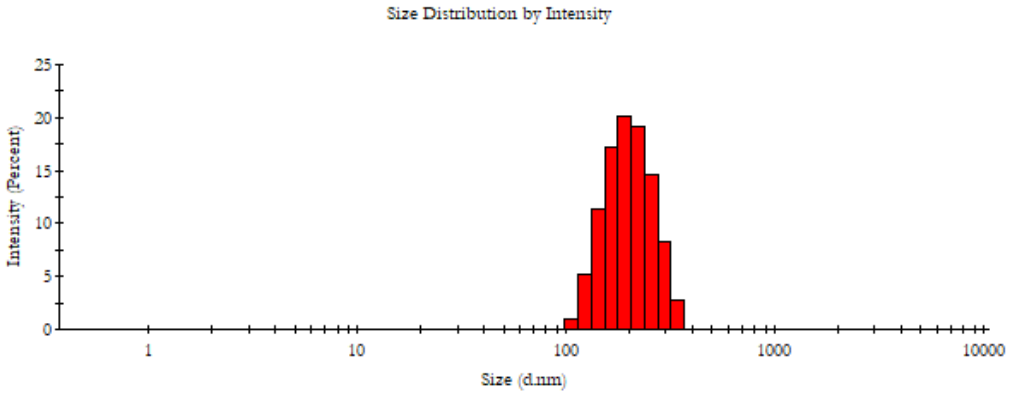

Figure 3.24. DLS size distributions for HMW@ZnO_8%_Cu_2O_8%_m.

This hybrid material has been also studied from thermal point of view, by means of TGA and DSC profile. TGA indicates water release at about 100 °C, followed by a maximum weight loss of about 30 % in the range 200-400 °C, due to lignin decomposition step which leads to the formation of low molecular weight products, with the cleavage of the main chains. A third weight loss occurs at about 750 °C, already discussed in Chapter 2. The profile is comparable to those of HMW@ZnO_m (already described in Figure S3.10) and HMW@Cu_2O_m[48] (reported in Figure S3.24[48,49]). TGA and DTG profiles of the two materials are comparable and reported in Figure S3.25. The differential scanning calorimetry (DSC) analysis of the hybrid material reveals a glass transition at 148.9 °C. For comparison, high-molecular-weight (HMW) lignin alone exhibits a glass transition at 122 °C (Figure S3.8), consistent with literature values for Kraft lignin (124–174 °C).[51] A higher glass transition temperature of the hybrid material has been found—approximately 26 °C above that of HMW lignin. Keeping the experimental milling conditions of the synthesis unchanged, but increasing the metal salt/ lignin ratio, it has been possible to isolate HMW@Zn_12%_Cu_12_%_m. Figure 3.25 shows the experimental pattern obtained, which indicates the formation of a mixture of zincite (ZnO) and cuprite (Cu_2O), together with traces of tenorite (CuO). This is in line with what previously observed during the synthesis of HMW@Cu_2O_m: high copper content inhibits the reducing ability of lignin decrease. For comparison, the diffractogram of Cu_2O, ZnO and CuO COD data bank reference is reported in Figure 3.25.

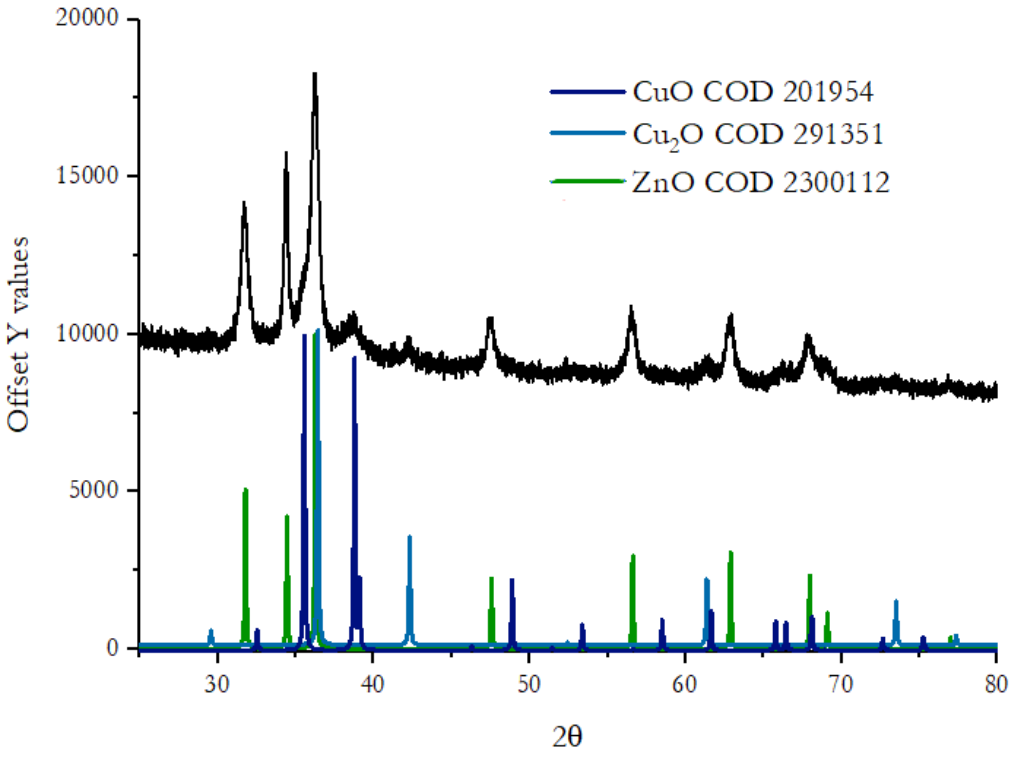

Figure 3.25. Matching of experimental PXRD patterns of HMW@ZnO_12%_Cu_2O_12%_m with cuprite (COD 291351), zincite (COD 2300112) and traces of tenorite (COD 291351)

The possibility to load different percentages of copper and zinc in the same material has been also evaluated, in view of *in vivo* applications, where the tuning of metal content could be useful. The experimental milling conditions of the synthesis have been kept unchanged, but metal ratio has been varied to obtain HMW@ZnO_4%_Cu_2O_8%_m and HMW@ZnO_8%_Cu_2O_4%_m (see Table 3.4 in the experimental section). Figure 3.26 shows the stacked diffractograms collected for the materials obtained with 4-8 %. For comparison, the diffractogram of Cu_2O and ZnO COD data bank reference.

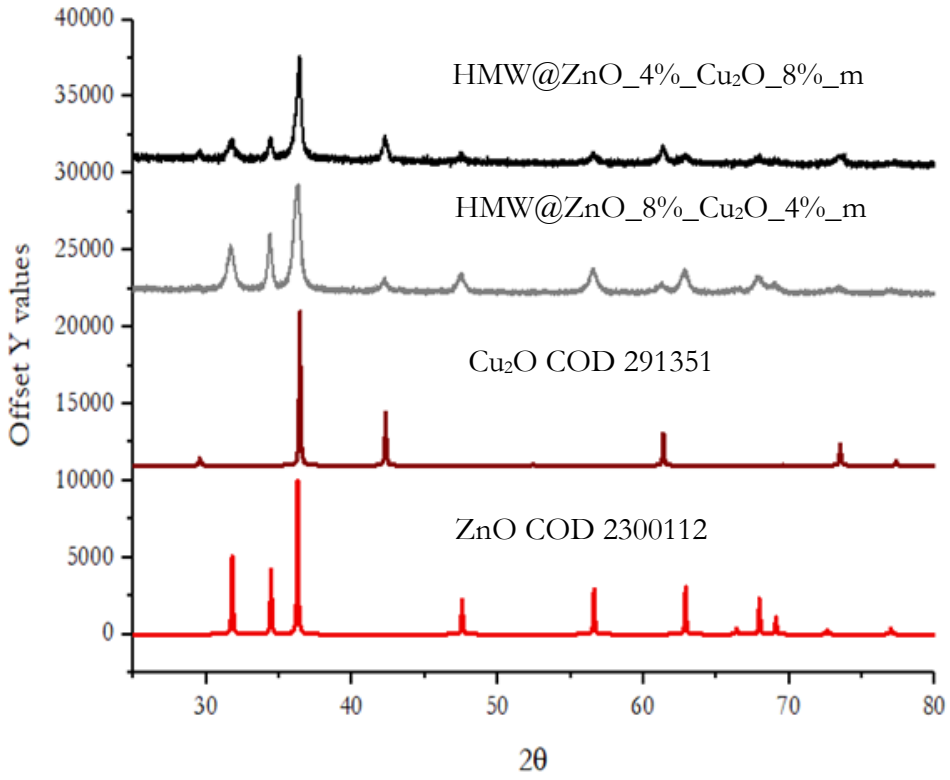

Figure 3.26. Matching of experimental PXRD patterns of HMW@ZnO_ 4%_Cu_2O_8%_m and HMW@ZnO_ 8%_Cu_2O_4%_m with cuprite (COD 291351) and zincite (COD 2300112)

The amount of copper uploaded in the final materials obtained has been determined by inductively coupled plasma atomic emission spectroscopy analysis (ICP-AES) and the results are reported in Table S3.11. HMW@ZnO_8%_Cu_2O_4 %_m and HMW@ZnO_8%_Cu_2O_4 %_m have been also investigated by DLS in aqueous suspension and the size distribution by intensity is reported in Figure S3.26 and Table S3.10, comparing the results to those already described for the material HMW@ZnO_8%_Cu_2O_%_m. A very similar broad size distribution of the nanoparticles can be observed, with a PDI of 0.288 and the Z-Average is similar, giving the hint that the behaviour in aqueous suspension remain similar for the hybrid material containing both the phases.

Conclusions

This chapter demonstrates the feasibility of obtaining hybrid materials through mechanochemistry. This approach offers several advantages, including the synthesis of compounds and materials without the need for solvents or requiring minimal solvent quantities, thereby reducing environmental impact and health risks. Mechanochemistry also enables faster and more controllable chemical reactions with enhanced energy efficiency. Moreover, it is a versatile technique, applicable to a wide range of chemical reactions and materials and facilitates easy scale-up. In our case, it has also streamlined the drying step necessary to obtain the final product. The mechanochemical synthesis of HMW@ZnO_m has been initially investigated, with results compared to those obtained *via* wet synthesis, discussed in Chapter 2. The materials have been synthesized with varying zinc percentages, and a mechanochemical scale-up was successfully performed. Similarly, HMW@Cu_2O_m has been synthesized, driven by previous studies that highlights its promising properties in agrochemical applications,[48,49] making it valuable to explore the mechanochemical reduction of Cu(II) to Cu(I). Finally, a material containing both cuprite and zincite crystals within the same biopolymeric matrix has been synthesized under sustainable and simple conditions, aiming for potential scale-up. The formation of both inorganic phases has been confirmed, and EDX-Mapping analysis revealed a homogeneous distribution of the two metals within the matrix. Additionally, biopolymer analyses have been conducted for all hybrid materials to ensure that the synthesis conditions cannot adversely affect the organic component of the product.

Future perspectives can be related to the potential of mechanochemistry to enable continuous manufacturing with minimal solvent waste, short reaction times, and the ability to achieve novel reactivity, which is clearly demonstrated by twin-screw extrusion (TSE). TSE is a scalable, continuous processing technique that exemplifies the advantages of mechanochemical methods. In fact, IUPAC has recently recognized reactive extrusion—a type of mechanochemistry conducted in flow reactors—as one of the ten most significant technological innovations for advancing sustainability.[53] Future developments of the project could focus on the development of synthetic strategies for extruding the hybrid materials successfully studied in this chapter through mechanochemistry.

Supporting information

Procedures

Procedure S1 **for preparation of HMW@Cu_2O_m and posnjakite_wet:**[48,49] 100 mg of HMW have been suspended in 5 mL of oxygen-free deionized water in a 50 mL two necked round bottom flask. Under vigorous stirring 350 μl of a 1M NaOH solution have been added in such a way to reach pH 11. After the complete dissolution of lignin, 10mL of a solution containing 20 mg of $CuSO_4 \cdot 5H_2O$ has been added dropwise. After the addition the pH drops at 10.2. The reaction has been conducted under nitrogen atmosphere to avoid the formation of carbonates which hinder its characterization. After 5 minutes from the complete addition of copper sulphate, water has been removed under stirring at 50°C by a gentle flux of nitrogen. When a brown dried powder formed, the material has been washed twice with distilled water by centrifugation and dried again at 50°C. The same procedure has been followed using 50 mg of copper salt in such a way to increase the metal content; after the addition of copper sulphate solution, the pH of the system dropped from 11 to 5.8.

Procedure S2 **for preparation of HMW@ZnO_10%_Cu_2O 10%_wet (5 equivalents of NaOH)** 2.1 g of HMW have been suspended in 50 mL of water in a 100 mL round bottom flask, together with $CuSO_4 \cdot 5H_2O$ (874 mg) and $ZnSO_4 \cdot 7H_2O$ (1 g). Under vigorous stirring, 10 mL of a 1,7 M NaOH solution (5 equivalents with the respect to the metallic salts) have been added dropwise. The reaction has been conducted at RT for 3 hours then the product has been dried overnight at 95 °C. Then, the obtained powder has been washed with 15 mL, isolated by centrifugation and dried at 85 °C overnight.

Procedure S3 **for preparation of HMW@ZnO_10%_Cu_2O 10%_wet (6 equivalents of NaOH)** 2.1 g of HMW has been suspended in 50 mL of water in a 100 mL round bottom flask, together with $CuSO_4 \cdot 5H_2O$ (874 mg) and $ZnSO_4 \cdot 7H_2O$ (1 g). Under vigorous stirring, 10 mL of a 2 M NaOH solution (6 equivalents with the respect to the metallic salts) have been added dropwise. The reaction has been conducted at RT for 3 hours then the product has been dried overnight at 95 °C. Then, the obtained powder has been washed with 15 mL, isolated by centrifugation and dried at 85 °C overnight.

Tables

Table S3.1. Stoichiometric ratios of reagents for the preparation of HMW@ZnO_X%_m (X= 5, 10, 20%, 30%) with 80 mL Agate jar by using $Zn(OAc)_2 \cdot 2H_2O$ or $ZnCl_2$. Concentration of NaOH is given in parenthesis.

	$HMW/Zn(OAc)_2 \cdot 2H_2O$ mass ratio (g/g)	NaOH (mol)	NaOH/ $Zn(OAc)_2 \cdot 2H_2O$ molar ratio
HMW@ZnO_5%_m	7.85/1.4	0.032 (2 M)	5/1
HMW@ZnO_10%_m	6.8/2.6	0.047 (5M)	4/1
HMW@ZnO_20%_m	6.5/5.8	0.104 (10 M)	4/1
HMW@ZnO_30%_m	4.1/6.4	0.116 (10 M)	4/1
	$HMW/ZnCl_2$ mass ratio (g/g)	NaOH (mol)	NaOH/ $ZnCl_2$ molar ratio
HMW@ZnO_5%_m	8.1/0.893	0.033 (2 M)	5/1
HMW@ZnO_10%_m	6.8/1.6	0.047 (5M)	4/1
HMW@ZnO_20%_m	6.5/3	0.088 (10 M)	4/1
HMW@ZnO_30%_m	4.4/4.35	0.125 (10 M)	4/1

Table S3.2. Stoichiometric ratios of reagents for the preparation of HMW@ZnO_10%_m with 500 mL Zirconia jar, by using $Zn(OAc)_2$ or $ZnCl_2$. Concentration of NaOH is given in parenthesis.

	$HMW/Zn(OAc)_2$ mass ratio (g/g)	NaOH (mol)	NaOH/ $Zn(OAc)_2$ molar ratio
HMW@ZnO_10%_m	50/16.1	0.45 (5M)	5/1
	$HMW/ZnCl_2$ mass ratio (g/g)	NaOH (mol)	NaOH/ $ZnCl_2$ molar ratio
HMW@ZnO_10%_m	51/12.3	0.45 (5M)	5/1

Table S3.3. Dimension and morphology of the NPs in HMW@ZnO_10% synthesized by wet or mechanochemical procedure.

	Size	Shape
HMW@ZnO_10%_wet	Aggregates of 20-200 nm constituted by 10-20 nm NPs	Aggregates with no clear morphologies constituted by small NPs
	Sporadic presence of needles with length 50-300 nm and thickness 10-50 nm	Needles
HMW@ZnO_10%_m	Aggregates of 20-100 nm	no clear morphologies
	Sporadic presence of needles with length 50 nm and thickness 5-20nm	Needles

Table S3.4. Dimension and morphology of the NPs in HMW@ZnO_5%_m, HMW@ZnO_10%_m, HMW@ZnO_20%_m, HMW@ZnO_30%_m

	Size	Shape
HMW@ZnO_5%_m	Aggregates of 20-200 nm constituted by 10-50 nm NPs	Aggregates with no clear morphologies constituted by small NPs
	Sporadic presence of needles with length 50-100 nm and thickness 20-50 nm	Needles
HMW@ZnO_10%_m	Aggregates of 20-100 nm	Aggregates with no clear morphologies constituted by small NPs
	Sporadic presence of needles with length 50 nm and thickness 5-20nm	Needles
HMW@ZnO_20%_m	Aggregates of 10-200 nm constituted by 10-20 nm NPs	Aggregates with no clear morphologies constituted by small NPs
	Significant presence of needles with length 50-100 nm and thickness 10-20 nm	Needles
HMW@ZnO_30%_m	Aggregates of 20-500 nm constituted by 5-10 nm NPs	Aggregates with no clear morphologies constituted by small NPs
	Significant presence of needles with length 50-200 nm and thickness 10-50 nm	Needles

Table S3.5. Percentage of Cu calculated with respect to the mass of lignin in the final material and the percentage of Cu determined by ICP analysis, as well as the inorganic phase detected by PXRD analysis for the preparation of HMW@Cu_2O_wet.[48,49]

% Cu respect to the lignin mass	% Cu (from ICP-AES)	PXRD
5%	3.64±0.05	cuprite
13%	-----	posnjakite

Table S3.6. Dimension and morphology of the NPs in HMW@Cu_2O_5% synthesized by mechanochemical procedure and by wet conditions.

	Size	Shape
HMW@Cu_2O_5%_m	10-50 nm NPs, spheres with 5-20 nm diameter	Spheres
	Aggregates of 100 nm constituted by 5-20 nm NPs	Aggregates with no clear morphologies constituted by small NPs
HMW@Cu_2O_5%_wet from previous work[48,49]	Dimensions of 50-200 nm	Spheres
	Statistical analysis on 70 individuals highlighted the presence of two populations	Particles with diameter 100±10 nm
		Particles with diameter 200±10 nm

Table S3.7. Z-averages and PDI results collected with DLS technique on HMW@Cu_2O_m materials

	Z-Average (d. nm)	PDI
HMW@Cu_2O_5%_m	194.2	0.160
HMW@Cu_2O_10%_m	245.9	0.302

Table S3.8. Copper and zinc content determined by ICP-AES analysis for HMW@ZnO_ 10%_Cu_2O 10%_wet, obtained by wet procedure S3. The percentages refer to metal content.

	ICP-AES Zn % mean ± SD	ICP-AES Cu% mean ± SD
HMW@ZnO_10%_Cu_2O_10%_wet	10.4± 0.2	10.6 ± 0.3

Table S3.9. Dimension and morphology of the NPs in HMW@ZnO_Cu_2O synthesized by mechanochemical procedure and HMW@ZnO_Cu_2O by wet conditions.

	Size	Shape
HMW@ZnO_Cu_2O_m	10-50 nm NPs, spheres with 5-20 nm diameter	Spheres
	Aggregates of 100 nm constituted by 5-20 nm NPs	Aggregates with no clear morphologies constituted by small NPs
HMW@ZnO_Cu_2O_wet	Aggregates of 100 nm constituted by 5-20 nm NPs	Aggregates with no clear morphologies constituted by small NPs

Table S3.10. Z-averages and PDI collected by DLS technique on HMW@ZnO_m 8%_Cu_2O 8% material.

	Z-Average (d. nm)	PDI
HMW@ZnO_8%_Cu_2O_8%_m	222	0.278
HMW@ZnO_8%_Cu_2O_4%_m	224.8	0.288
HMW@ZnO_4%_Cu_2O_8%_m	275.9	0.288

Table S3.11. Copper and zinc content determined by ICP-AES analysis for HMW@ZnO_4%_Cu_2O_8%_m and HMW@ZnO_8%_Cu_2O_4%_m of metal's loadings, obtained by mechanochemical procedures

	ICP-AES Zn% mean ± SD	ICP-AES Cu% mean ± SD
HMW@ZnO_8%_Cu_2O_4%_m	12.3± 0.3	4.64± 0.09
HMW@ZnO_4%_Cu_2O_8%_m	6.6± 0.1	6.2± 0.1

Figures

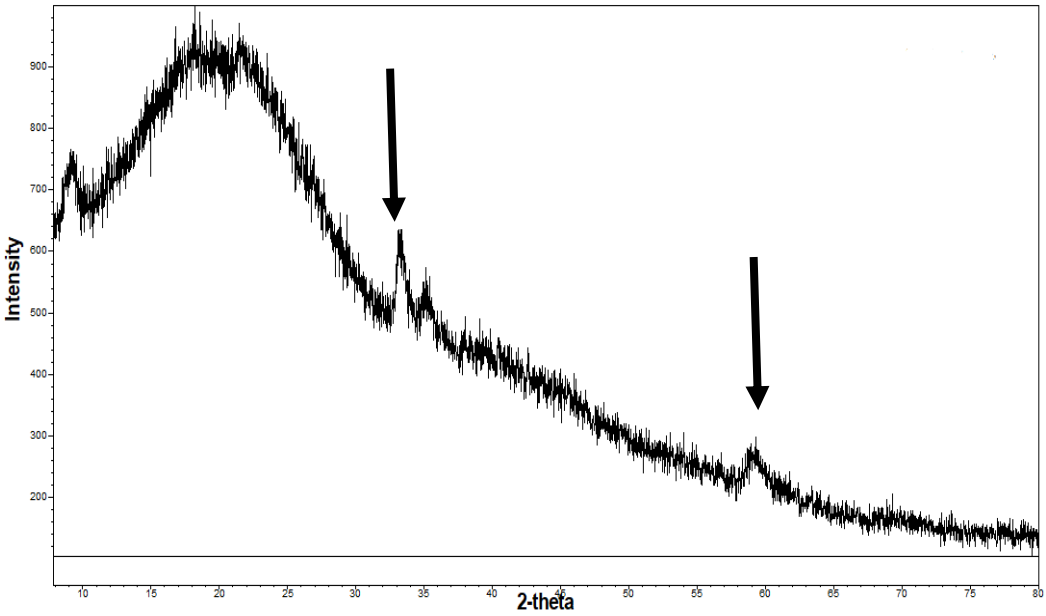

Figure S3.1. Experimental PXRD pattern obtained with 4 equivalents of NaOH with the respect to zinc sulphate heptahydrate (8.9 g lignin/ 2.1 g $ZnSO_4 \cdot 7H_2O$, 4 equivalents NaOH 2 M). Unknown phase indicated by the arrows.

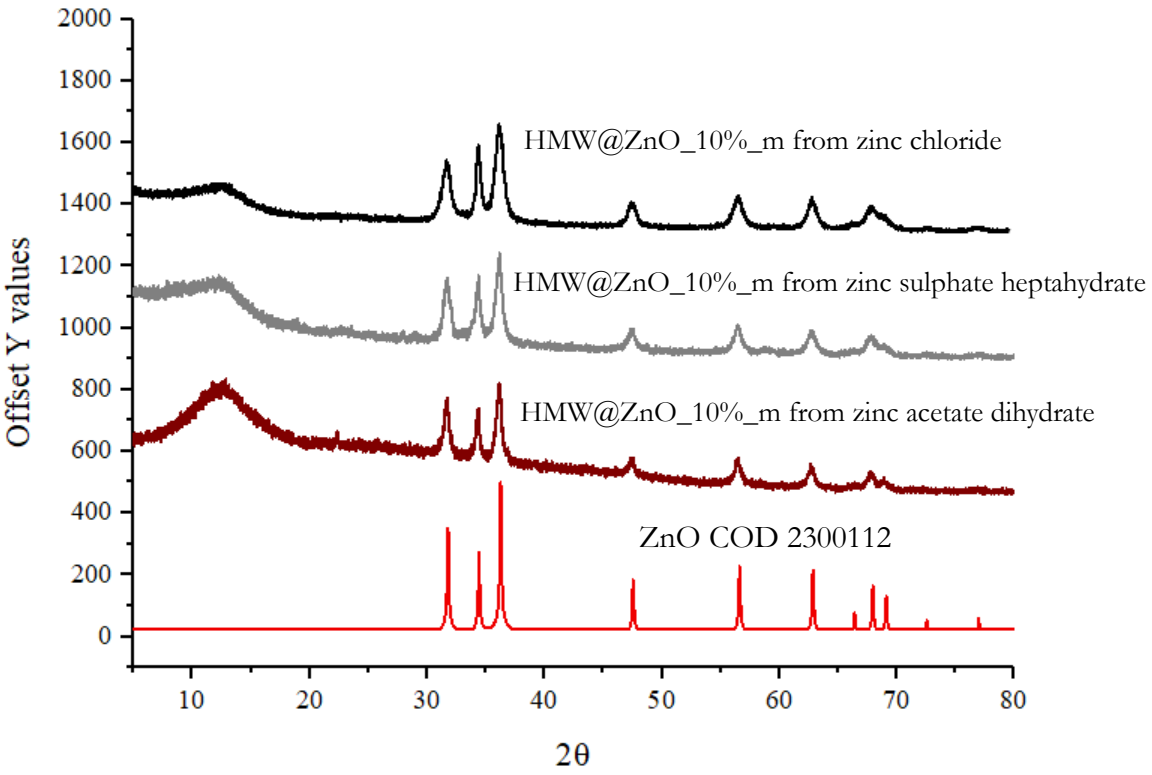

Figure S3.2. Stacked PXRD patterns of HMW@ZnO_10%_m obtained from different zinc salts, compared to ZnO pattern (COD 2300112).

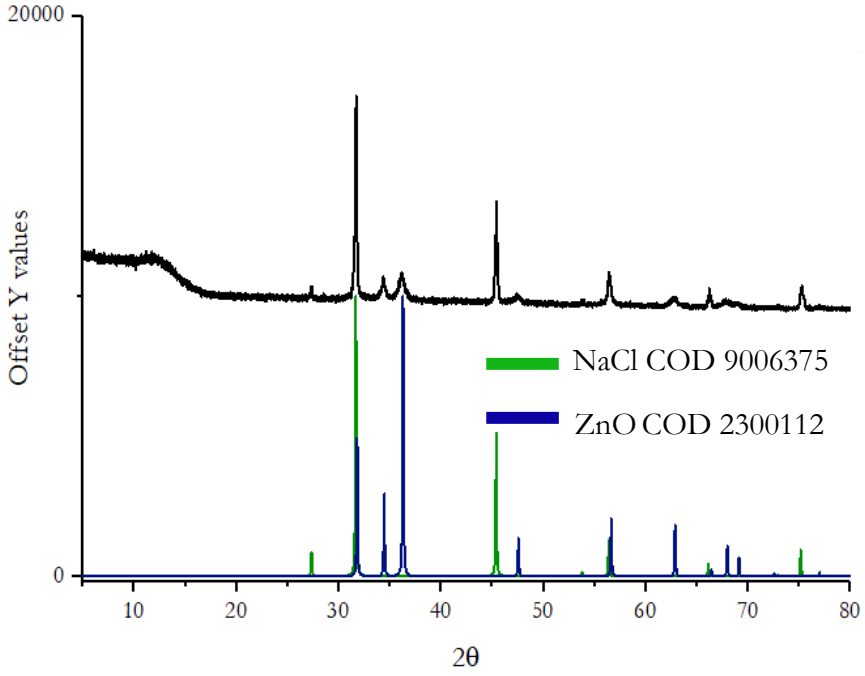

Figure S3.3. Experimental PXRD pattern obtained isolating the mixture of reaction without washing it, by using 4 equivalents of NaOH with the respect to zinc chloride (6.8 g lignin/ 1.6 g $ZnCl_2$, 4 equivalents NaOH 5 M), the only presence of sodium chloride (green, COD 9006375) and zinc oxide (blue, COD 2300112) was demonstrated by means of PXRD.

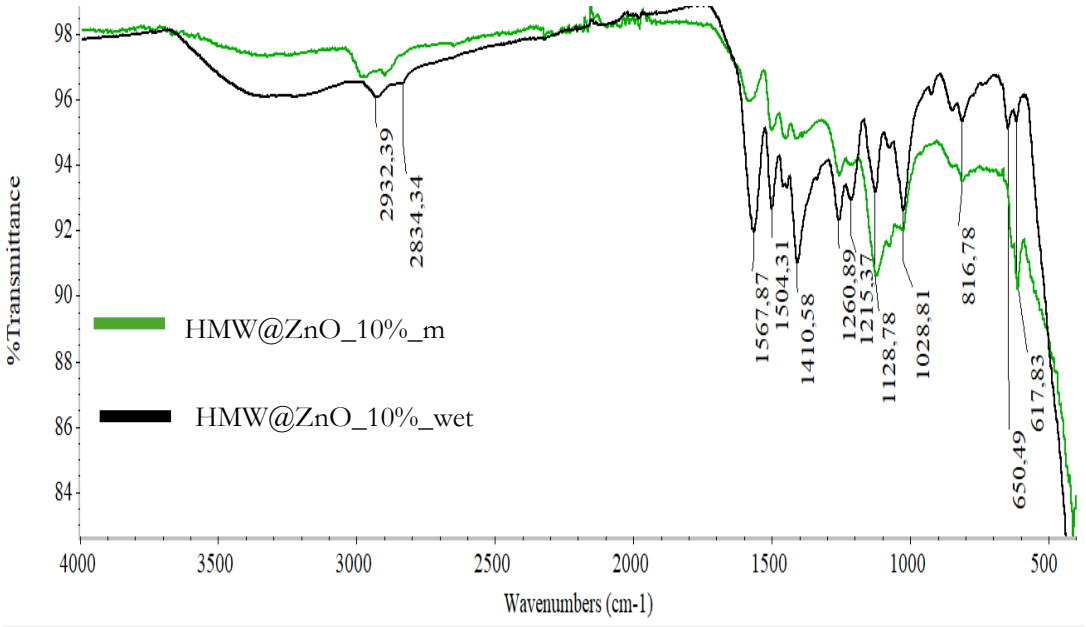

Figure S3.4. Superimposed FT-IR spectra of HMW@ZnO _10%_m and HMW@ZnO _10%_wet.

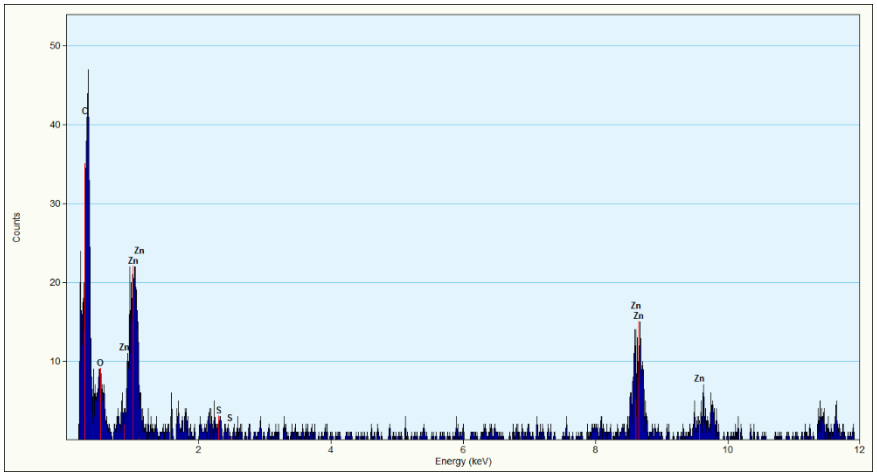

Figure S3.5. EDX analysis shows the composition of the zinc oxide nanoparticles synthesized in HMW@ZnO_m materials. The EDX reported is related to HMW@ZnO_m obtained from zinc sulphate, taken as an example.

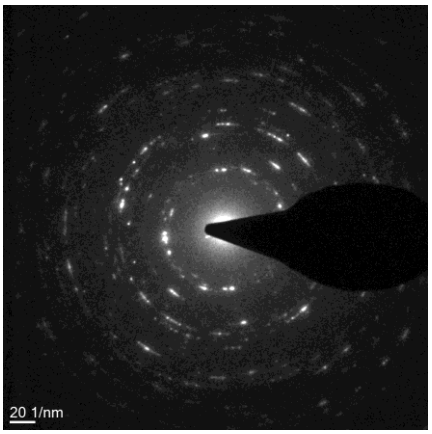

d^{-1} (nm^{-1})	d (nm)	Reflections
3.91	0.255	(002)+(101)
5.10	0.195	(102)
6.22	0.161	(110)
6.82	0.146	(103)

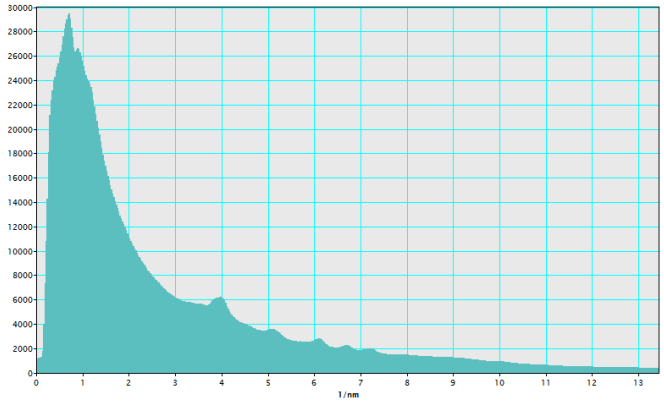

Figure S3.6. Selected area electron diffraction (SAED) collected over an area of 200 nm accompanied by the relative radial average. The peaks present are all identifiable as reflections of the zincite. The peaks are intense and well defined: the crystals are quite large and of good crystalline quality. The SAED reported is related to HMW@ZnO_10%_m obtained from zinc sulphate taken as an example.

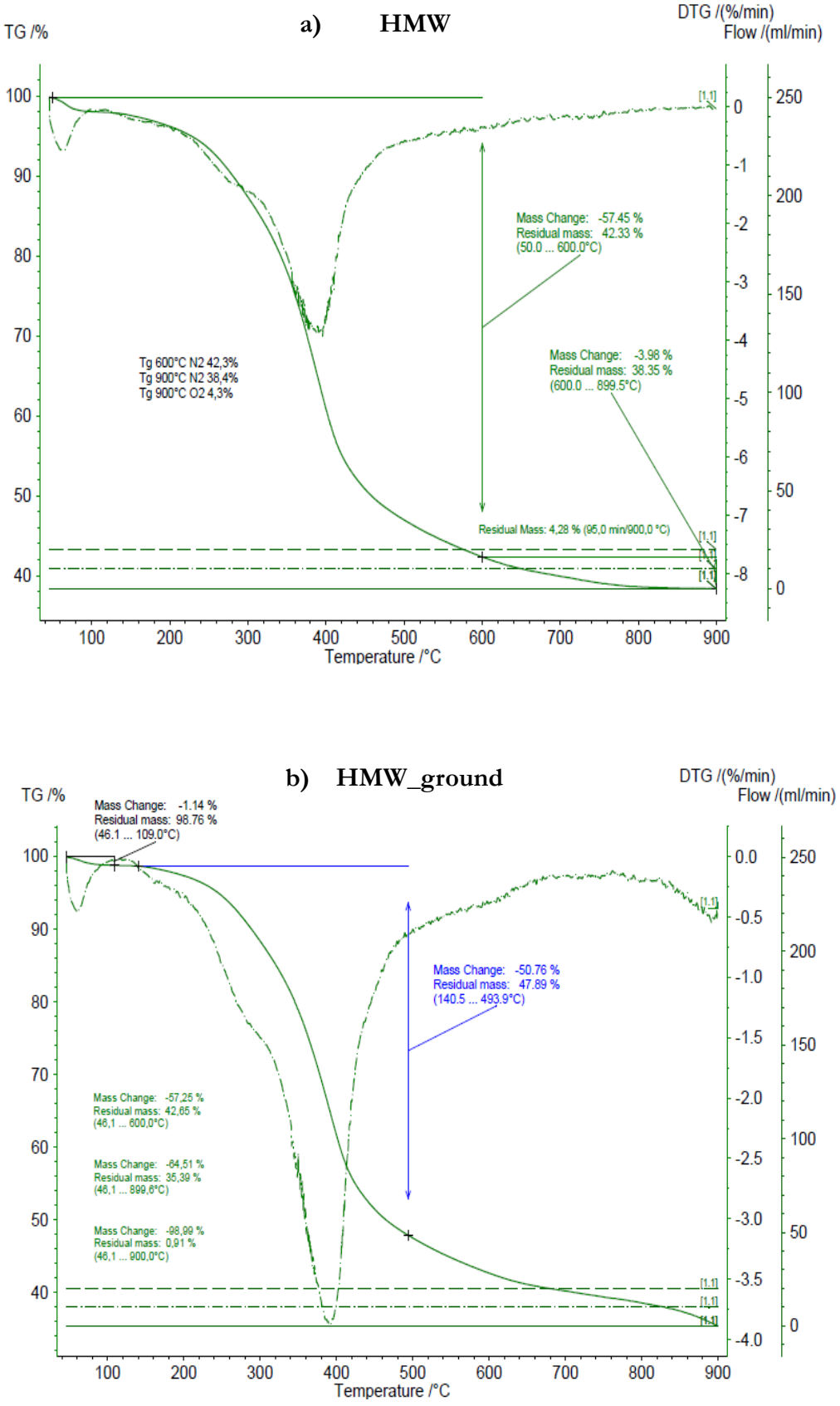

Figure S3.7. TGA/DTG curves of HMW (a), HMW_ground (b)

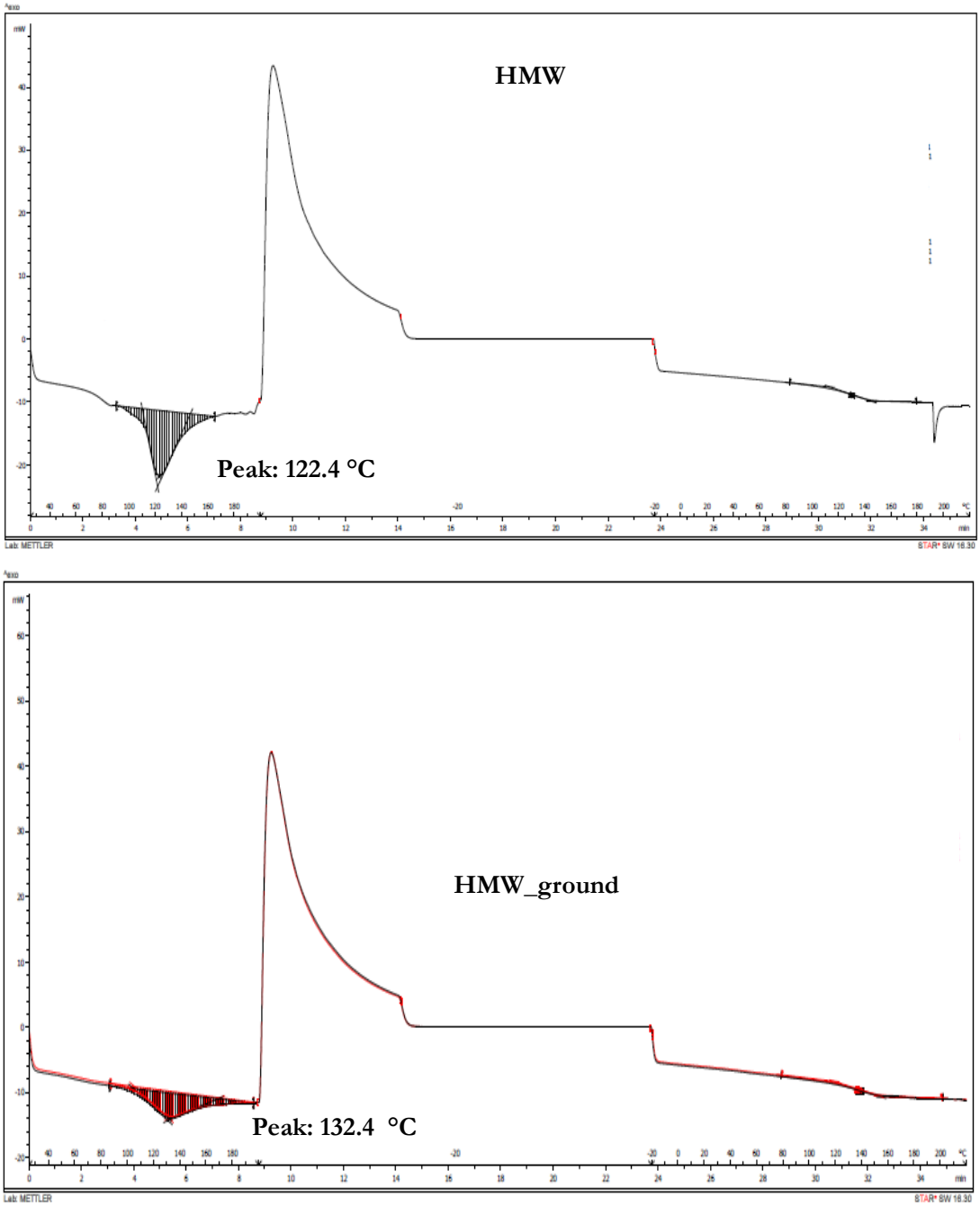

Figure S3.8. DSC analysis of HMW (a) and HMW_ground (b) with exothermic process up. The DSC profile is expressed both in the °C (above the x axes) and in minutes (below the x axes)

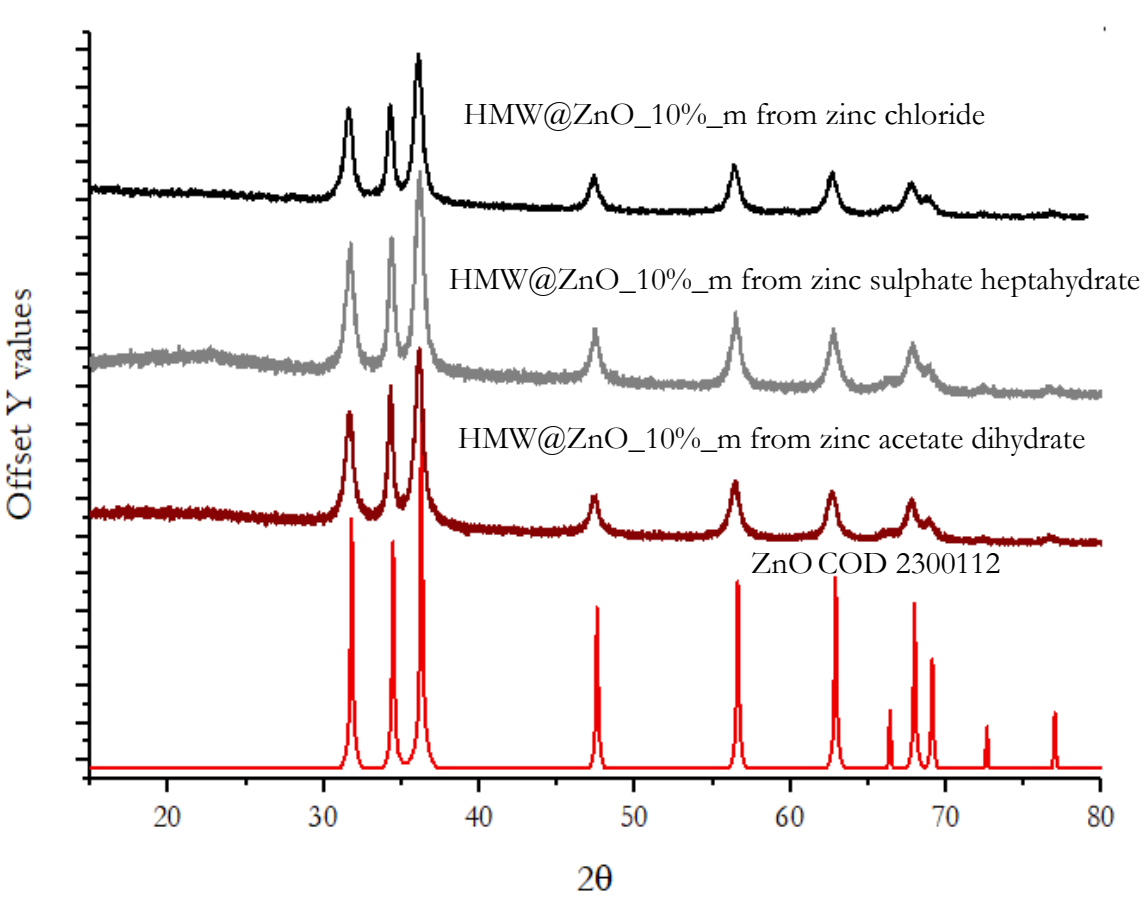

Figure S3.9. Stacked PXRD patterns of HMW@ZnO_10%_m from different zinc salts obtained by mechanochemical scale up.

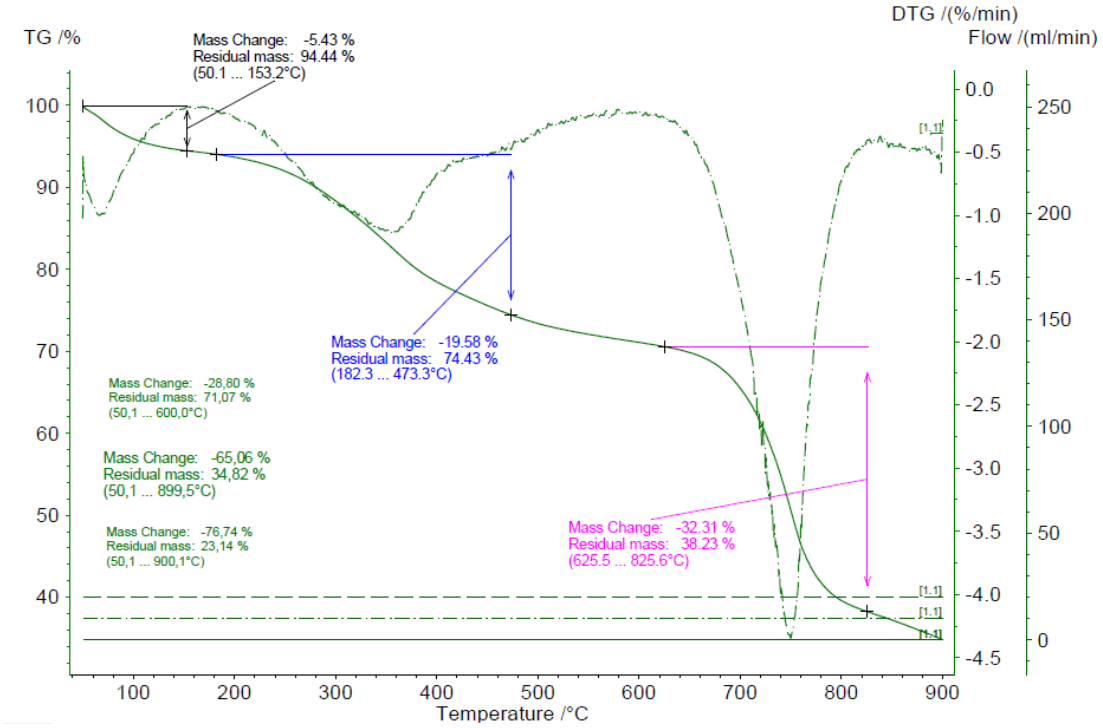

Figure S3.10. TGA/DTG curves of HMW@ZnO _10%_m mechanochemical scale up

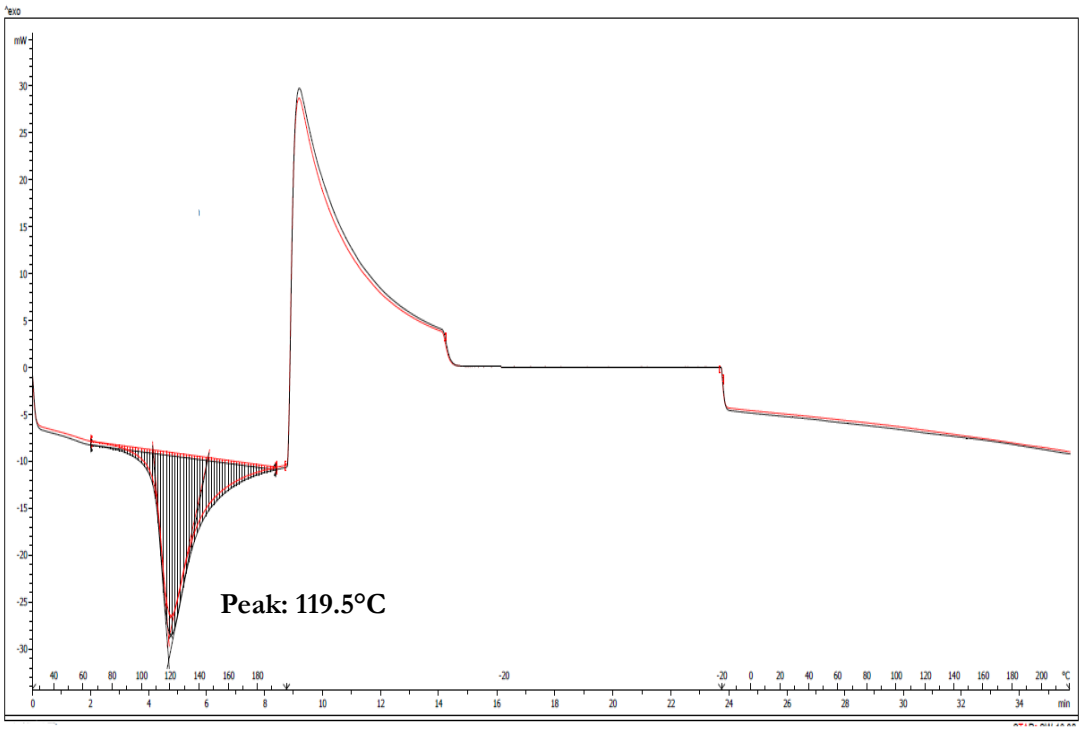

Figure S3.11. DSC analysis of HMW@ZnO_10%_m mechanochemical scale up(a), with exothermic process up. The DSC profile is expressed both in the °C (above the x axes) and in minutes (below the x axes)

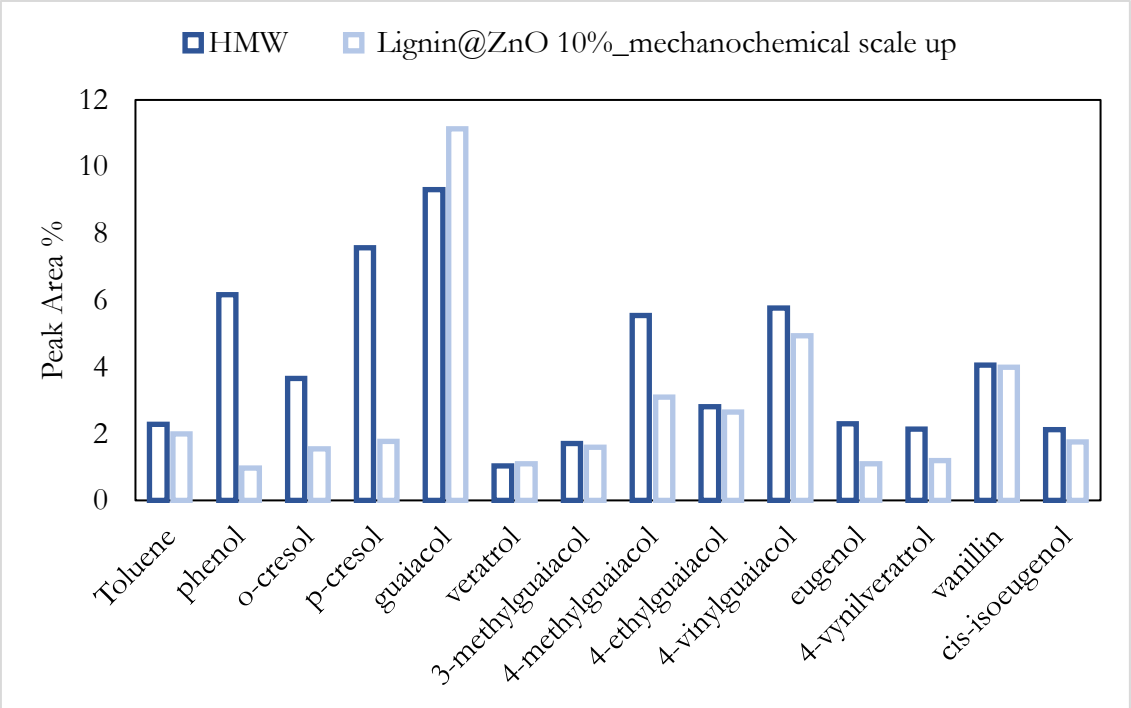

Figure S3.12. Main fragments studied by pyrolysis GC/MS of HMW@ZnO_10%_m mechanochemical scale up. The bars represent the peak area percentages of the analysis.

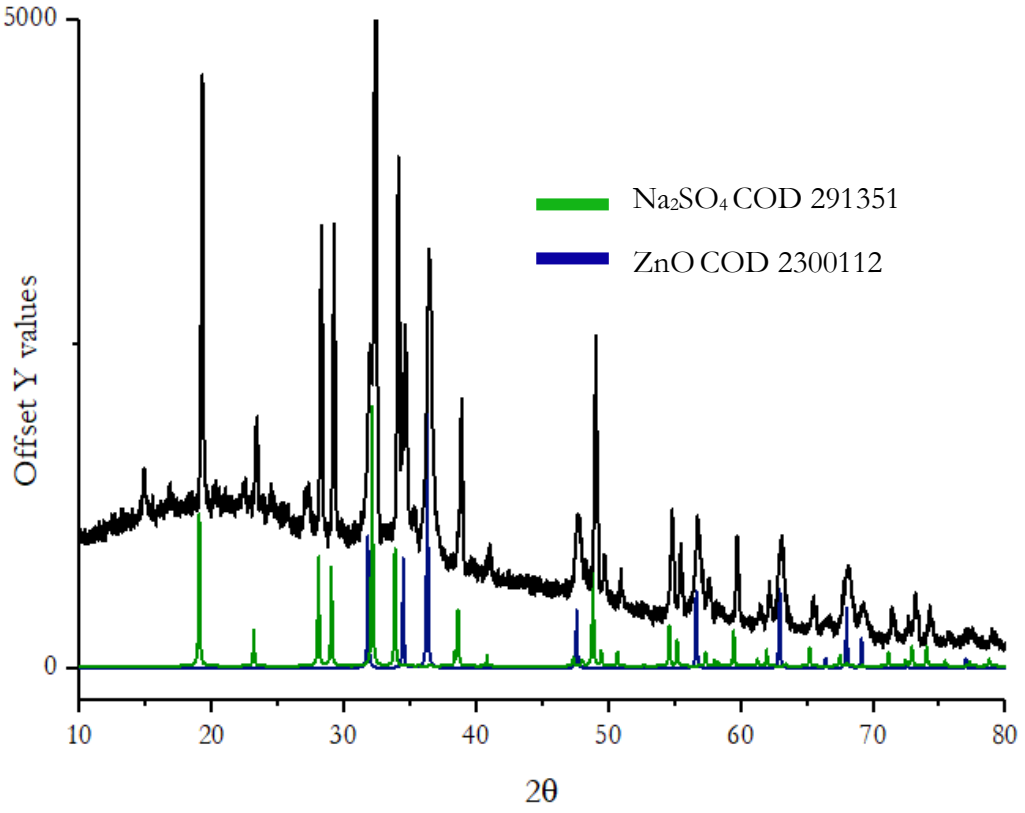

Figure S3.13. PXRD pattern of HMW@ZnO_10%_m, showing the presence of mainly sodium sulphate and zinc oxide, with traces of an unidentified phase.

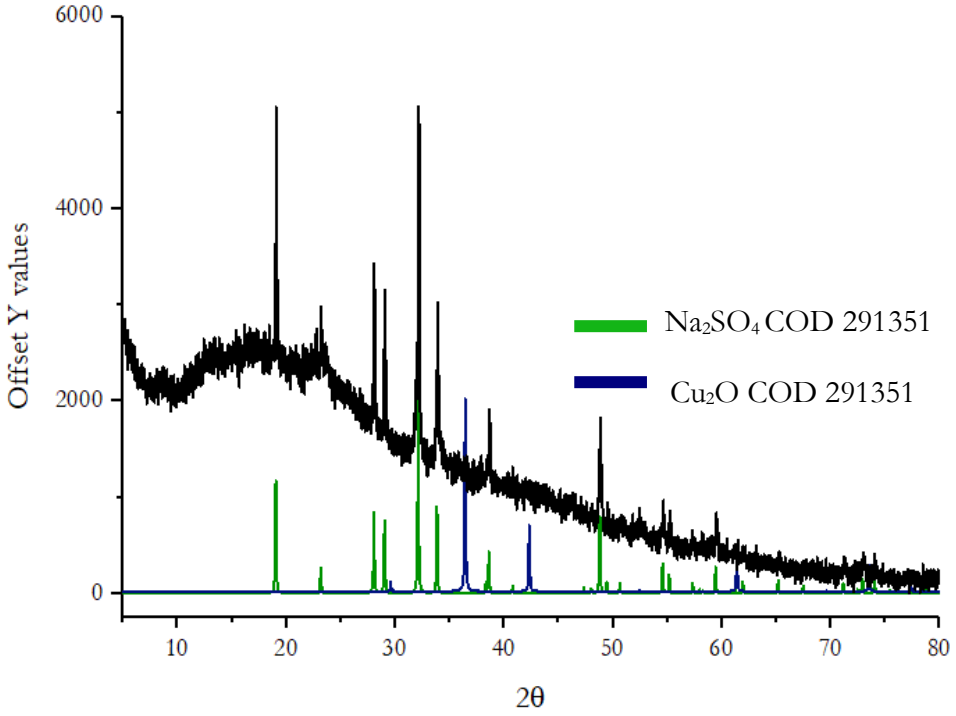

Figure S3.14. PXRD pattern of unwashed HMW@Cu_2O_5%_m, demonstrating the presence of only sodium sulphate and cuprite (low intensity due to low percentage of copper).

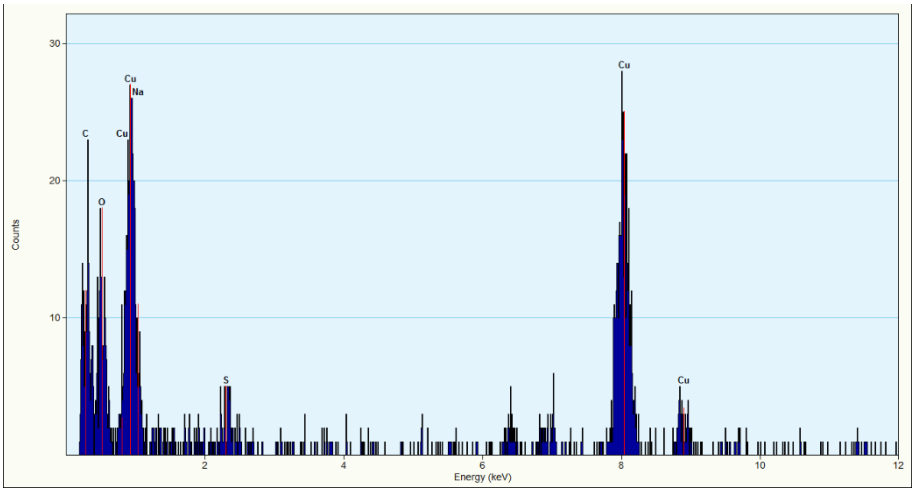

Figure S3.15. EDX analysis shows the composition of the cuprite nanoparticles synthesized in HMW@Cu_2O_5%_m material.

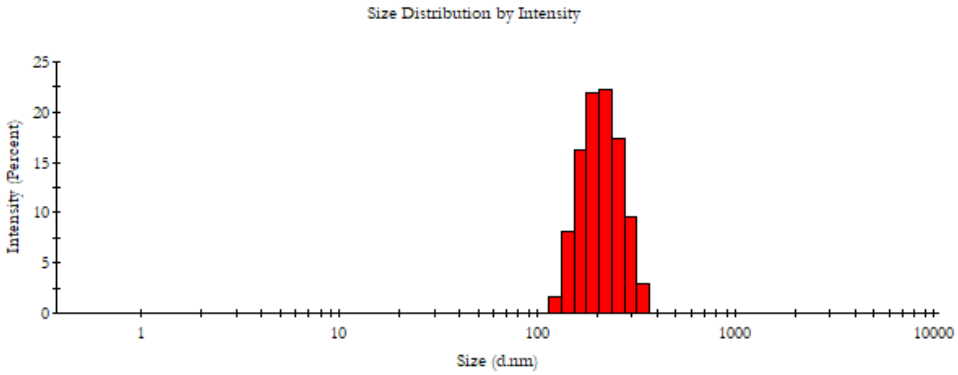

Figure S3.16. DLS size distributions for HMW@Cu_2O_10%_m.

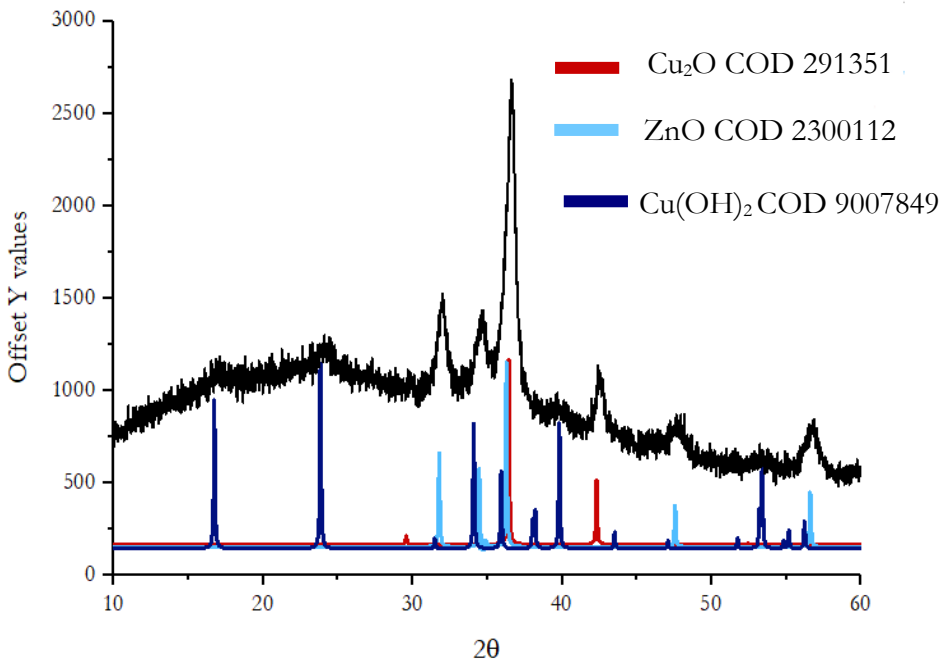

Figure S3.17. PXRD experimental pattern of HMW@ZnO_10%_Cu_2O_10%_wet, highlighting the presence of zinc oxide (COD 2300112), cuprite (COD 291351) and traces of spertiniite ($Cu(OH)_2$) (COD 9007849)

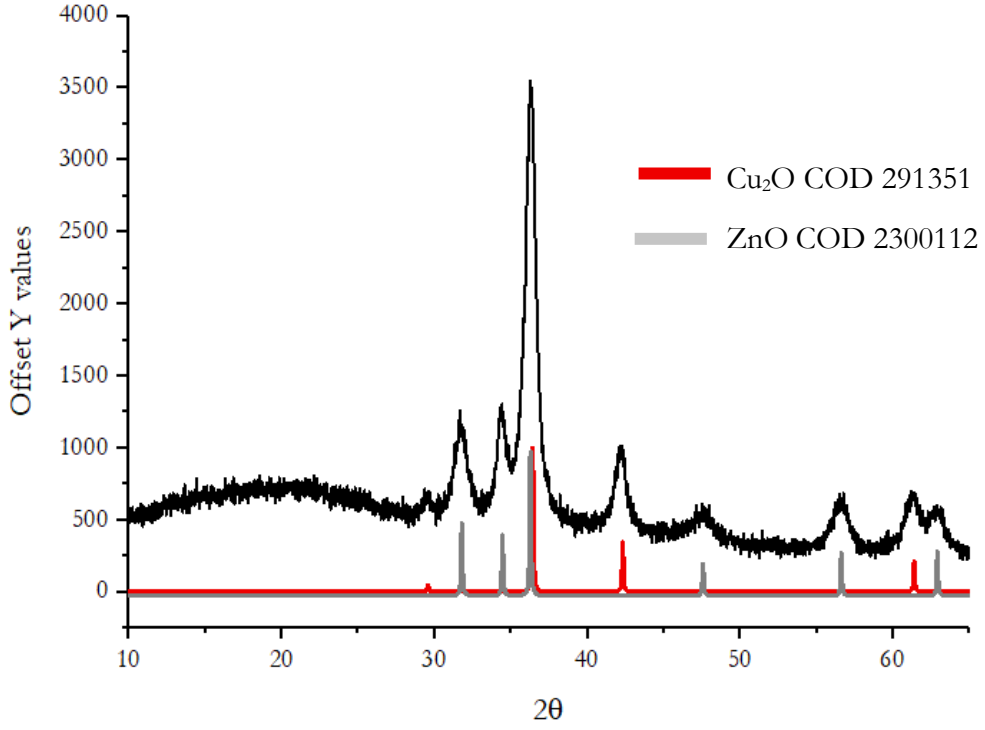

Figure S3.18. PXRD experimental pattern of HMW@ZnO_10%_Cu_2O_10%_wet, indicating the presence of zincite (COD 2300112) and cuprite (COD 291351).

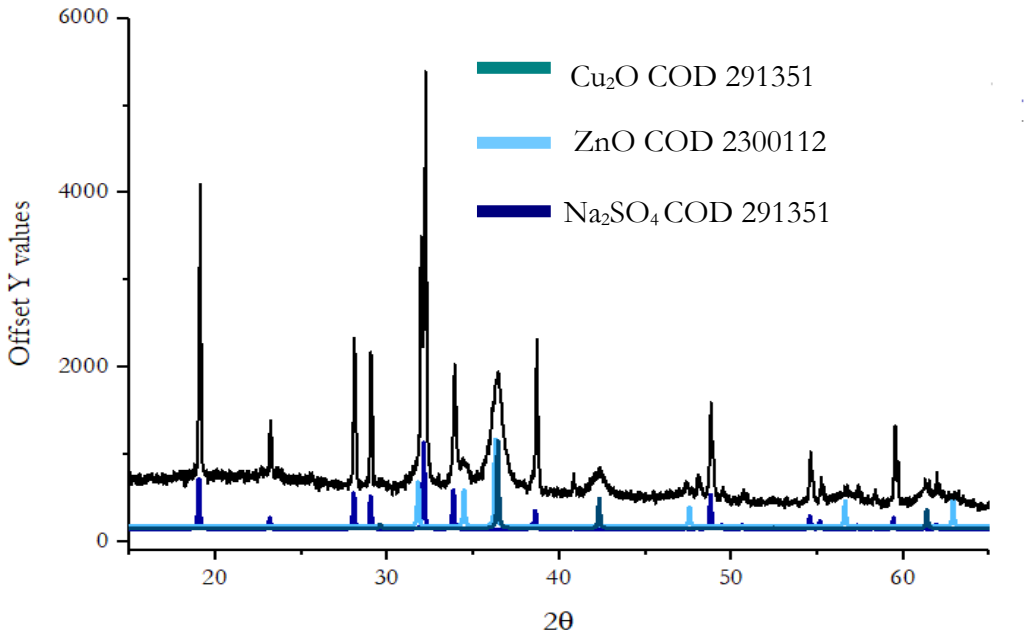

Figure S3.19. PXRD experimental pattern of unwashed HMW@ZnO_10%_Cu_2O_10%_wet indicating only the presence of sodium sulphate (COD 291351), cuprite (COD 291351) and zincite (COD 2300112)

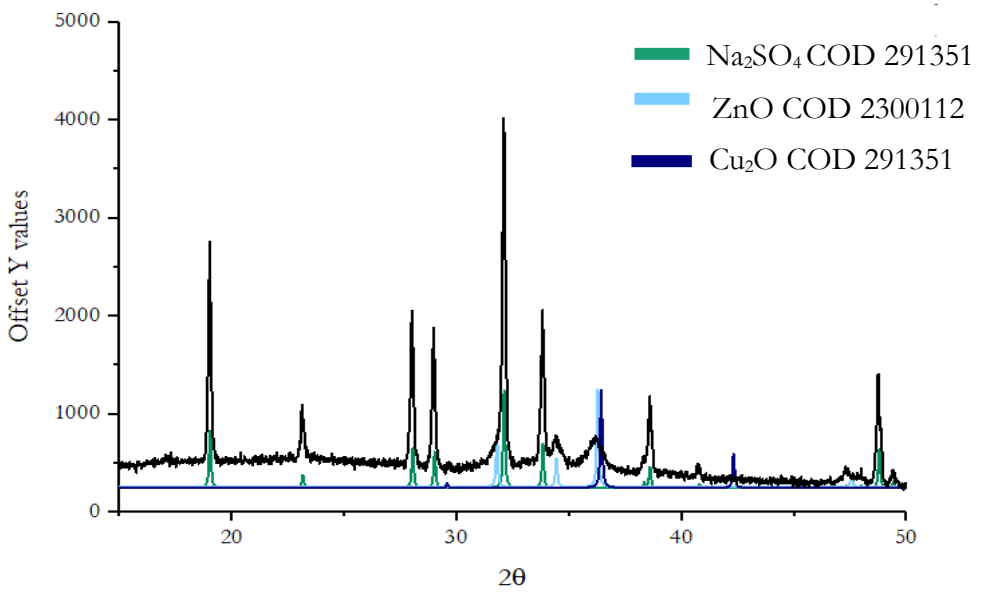

Figure S3.20. PXRD experimental pattern of unwashed HMW@ZnO_8%_Cu_2O_8%_m by mechanochemical synthesis, demonstrating the presence of only sodium sulphate (COD 291351), zinc oxide and cuprite.

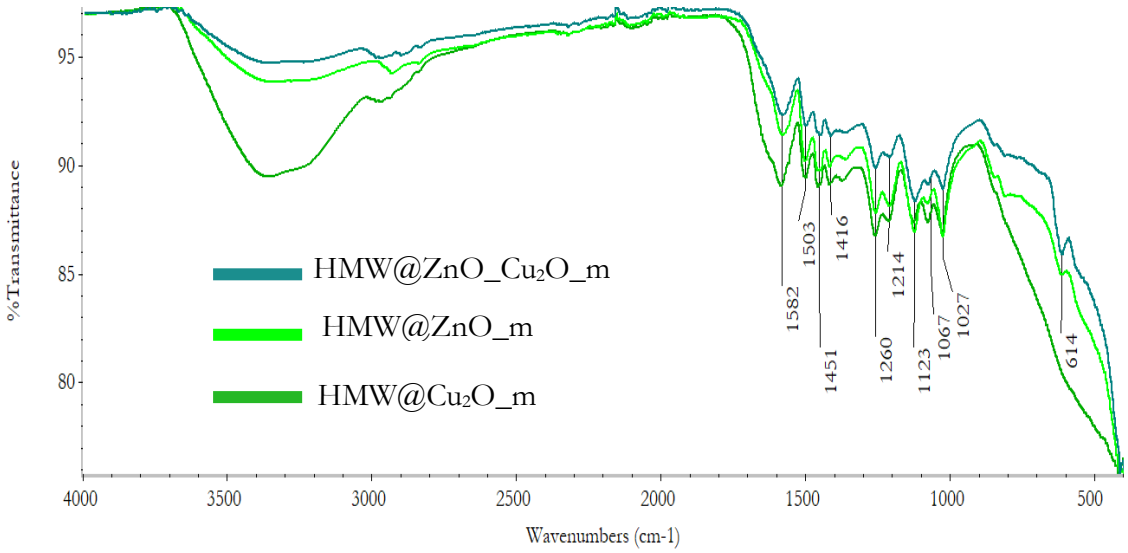

Figure S3.21. Superimposed FT-IR spectra of HMW@ZnO_Cu_2O_m, HMW@ZnO_m and HMW@Cu_2O_m

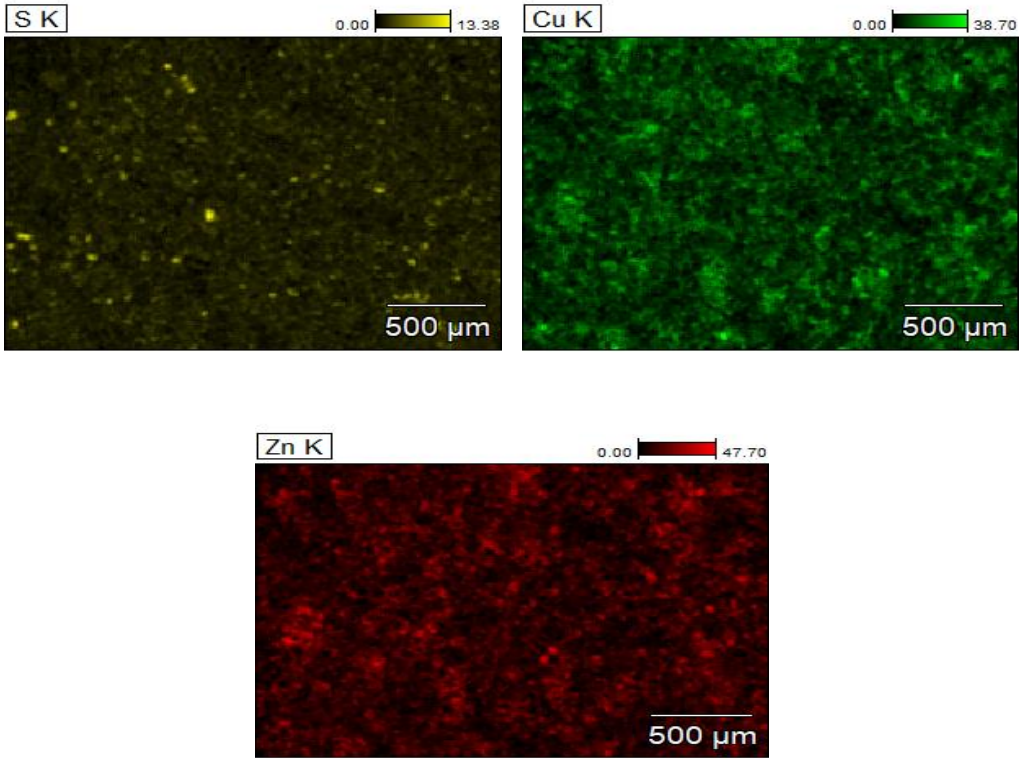

Display name	Standard data	Quantification method	Result Type
Spc_001	Standardless	ZAF	Metal

Element	Line	Mass%	Atom%
C	K	48.12	64.10
O	K	27.27	27.26
Na	K	4.77	3.32
S	K	1.59	0.79
Cu	K	8.66	2.18
Zn	K	9.59	2.35
Total		100.00	100.00
Spc_001			Fitting ratio 0.0071

Figure S3.22. EDX mapping shows the metal distribution inside the hybrid material HMW@ZnO_Cu_2O_m (copper coloured in green, zinc in red) and their relative colour scale.

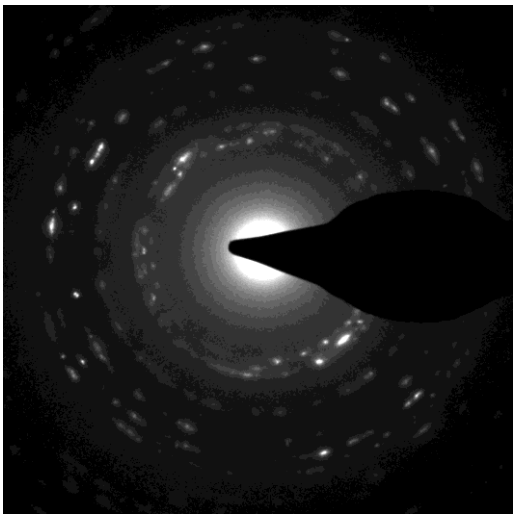

d^{-1} (nm^{-1})	d (nm)	
3.52	0.283	(100)
3.84	0.261	(002)
4.07	0.246	(101) (111 Cu_2O)
5.24	0.191	(102)
6.13	0.163	(110)
6.76	0.148	(103)

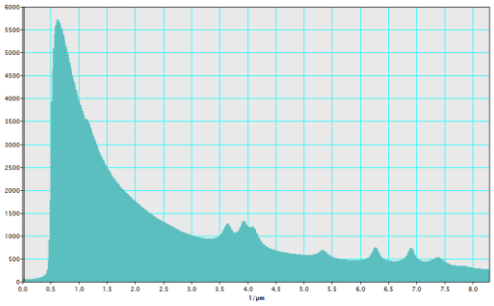

Figure S3.23. Selected area electron diffraction (SAED) collected over an area of 200 nm accompanied by the relative radial average. The peaks clearly identifiable are reflections of the zincite. The most intense line (d=0.247 nm) of cuprite (1 1 1). The SAED reported is related to HMW@ZnO_Cu_2O_m obtained via mechanochemistry.

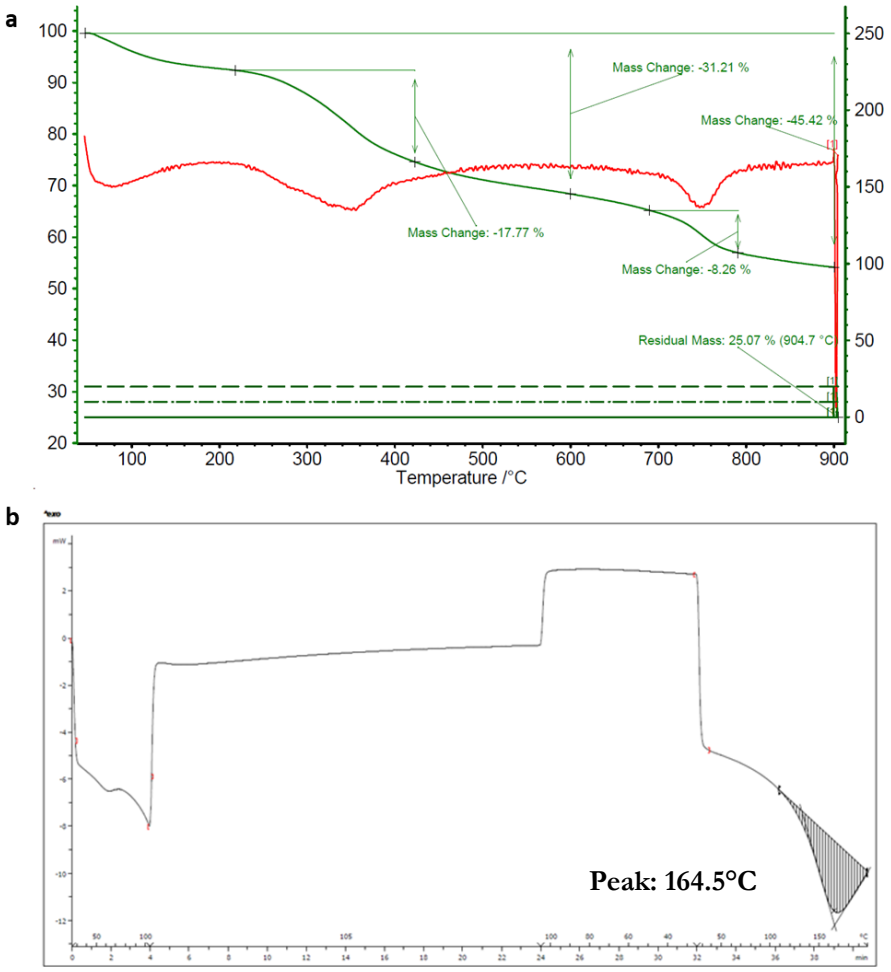

Figure S3.24. TGA/DTG curves of HMW@Cu_2O_5%_m studied in previous work of our research group[48,49]. a) TGA and b) DSC. The DSC profile is expressed both in °C (above the x axis) and in minutes (below the x axis). The peak at 164.5 °C is likely a combination of the glass transition temperature of the polymer with a process related to the inorganic phase.

a)

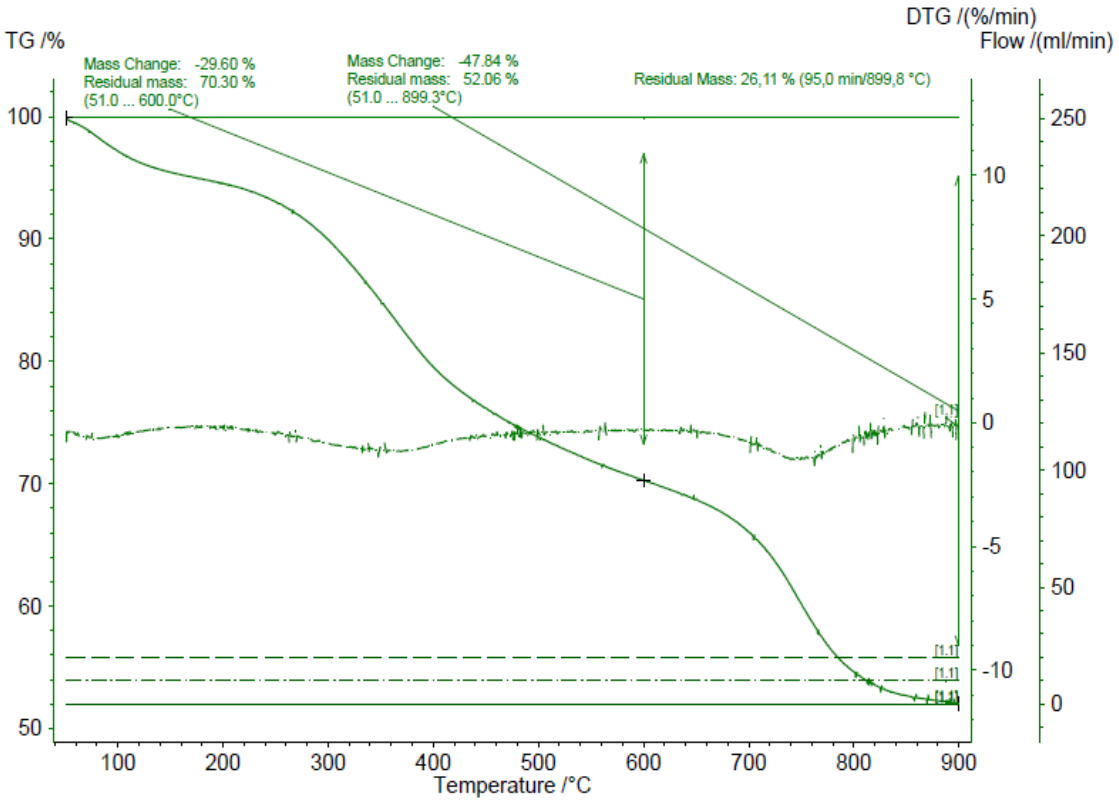

b)

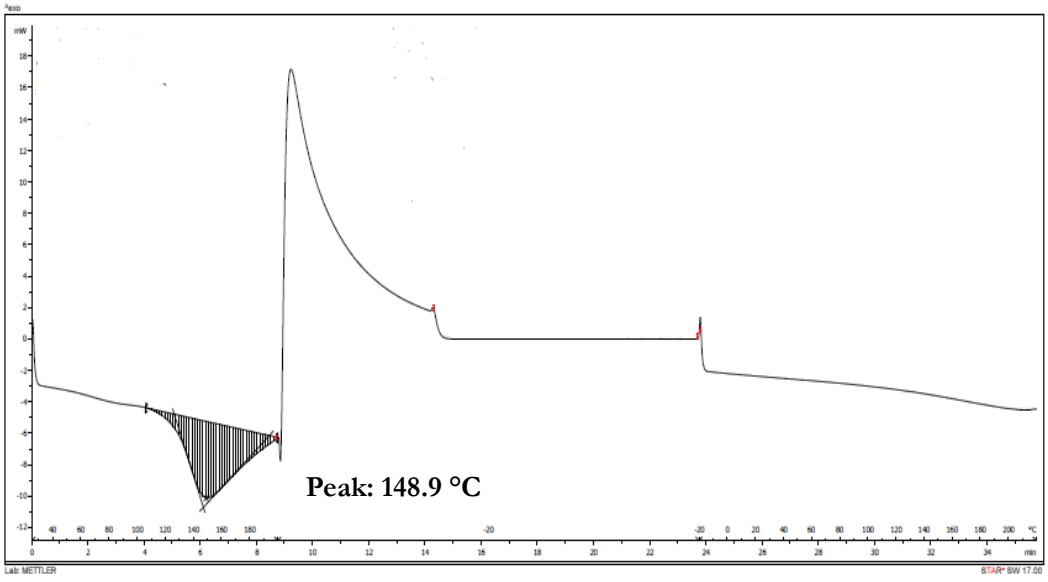

Figure S3.25. TGA/DTG curves of HMW@ZnO_8%_Cu_2O_8%_m obtained via mechanochemistry. a) TGA and b) DSC. The DSC profile is expressed both in °C (above the x axis) and in minutes (below the x axis). The peak at 148.9 °C could be a combination of the glass transition temperature of the polymer with a process related to the inorganic phase.

a)

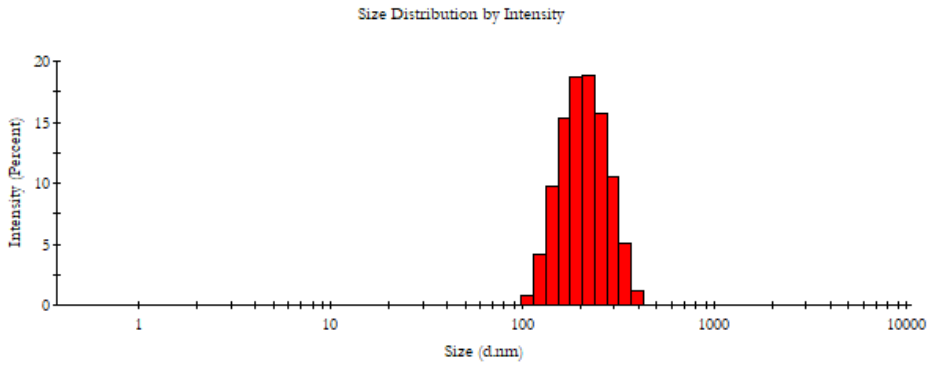

b)

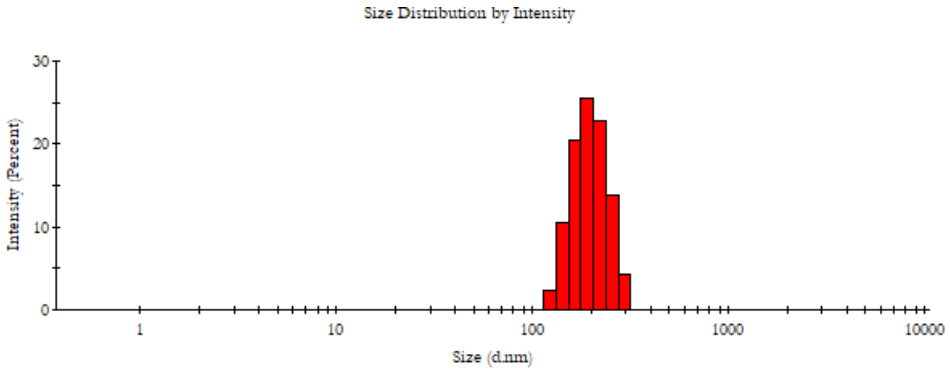

Figure S3.26. DLS size distributions for HMW@ZnO_8%_Cu_2O_4%_m and HMW@ZnO_4%_Cu_2O_8%_m.

References

[1] V.V. Boldyrev, K. Tkáčová, Mechanochemistry of Solids: Past, Present, and Prospects. *Journal of Materials Synthesis and Processing*, **8**, 121–132,2000. DOI: 10.1023/A:1011347706721

[2] P. Baláž, Mechanochemistry in Nanoscience and Minerals Engineering. (Springer-Verlag, 2008). DOI: 10.1007/978-3-540-74855-7

[3] K. Tkáčová, H. Heegn, N. Števulová, Energy Transfer and Conversion During Comminution and Mechanical Activation. *Int. J. Miner. Process.*, **40**, 17–31, 1993. DOI: 10.1016/0301-7516(93)90004-I

[4] P. Baláž, M. Achimovičová, M. Baláž, P. Billik, Z. Cherkezova-Zheleva, J. M. Criado, F. Delogu, E. Dutková, E. Gaffet, F. J. Gotoret al., Hallmarks of Mechanochemistry: From Nanoparticles to Technology. *Chem. Soc. Rev.*, **42**, 7571–7637, 2013. DOI: 10.1039/C3CS60087J

[5] C. Suryanarayana, Mechanical Alloying and Milling. *Progress in Materials Science*, **46**, 1–184,2001. DOI: 10.1016/S0079-6425(99)00010-9

[6] C. Jiménez-González, D. J. C. ConsTable, C. S. Ponder, Green Chemistry: a Perspective. *Chem. Soc. Rev.*, **41**, 1485–1498,2012. DOI: 10.1039/C2CS15342A

[7] A. Czaja, E. Leung, N. Trukhan, U. Müller, Industrial MOF Synthesis. In Metal-Organic Frameworks: Applications from Catalysis to Gas Storage, Farrusseng, D. (Ed.); Wiley-VCH Verlag GmbH: Weinheim, 2011. DOI: 10.1002/9783527635856.ch14

[8] X. Liu, Y. Li, L. Zeng, X. Li, N. Chen, S. Bai, H. He, Q. Wang, C. Zhang, A Review on Mechanochemistry: Approaching Advanced Energy Materials with Greener Force. *Adv. Mater.*, **34**, 2108327, 2022. DOI:10.1002/adma.202108327

[9] K. J. Ardila-Fierro, J. G. Hernández, Sustainability Assessment of Mechanochemistry by Using the Twelve Principles of Green Chemistry. *ChemSusChem*, **14**, 2145–2162. 2021. DOI: 10.1002/cssc.202100252

[10] D. Margetić, V. Štrukil, Mechanochemical Organic Synthesis, 1st ed.; Elsevier: Amsterdam, The Netherlands, 2016.

[11] J. L. Howard, Q. Cao, D. L. Browne, Mechanochemistry as an Emerging Tool for Molecular Synthesis: What Can It Offer? *Chem. Sci.*, **9**, 3080–3094. 2018. DOI: 10.1039/C8SC00956A

[12] T. Tsuzuki, F. Schaffel, M. Muroi, P. G. McCormick, α-Fe_2O_3 Nanoplatelets Prepared by Mechanochemical/Thermal Processing. *Powder Technol.*, **210**, 198–202. 2011. DOI: 10.1016/j.powtec.2010.12.003

[13] S. L. James, J. Adams, Green Chemistry: From Molecule to Manufacturing. *Chem. Soc. Rev.*, **41**, 413–447. 2012. DOI: 10.1039/C1CS15166E

[14] T. Friščić, New Opportunities for Materials Synthesis Using Mechanochemistry. *J. Mater. Chem.*, **20**, 7599–7605. 2010. DOI: 10.1039/C0JM00959A

[15] B. G. Fiss, A. J. Richard, G. Douglas, M. Kojic, T. Friščić, A. Moores, Mechanochemical Methods for the Transfer of Electrons and Exchange of Ions: Inorganic Reactivity from Nanoparticles to Organometallics. *Nat. Rev. Chem.*, **5**, 232–247, 2021. DOI: 10.1038/s41570-021-00231-3

[16] R. Chen, M. K. Gokus, S. Pagola, Tetrathiafulvalene: A Gate to the Mechanochemical Mechanisms of Electron Transfer Reactions. *Crystals*, **10**, 482, 2020. DOI: 10.3390/cryst10060482

[17] B. Karadeniz, D. Žilić, I. Huskić, L.S. Germann, A. M. Fidelli, S. Muratović, I. Lončarić, M. Etter, R. E. Dinnebier, D. Barišić, D., Controlling the Polymorphism and Topology Transformation in Porphyrinic Zirconium Metal-Organic Frameworks via Mechanochemistry. *J. Am. Chem. Soc.*, **141**, 19214–19220,2019. DOI: 10.1021/jacs.9b10889

[18] D. Hasa, E. Carlino, W. Jones, Mechanochemistry of Metal-Organic Frameworks: Insights into the Growth and Formation of Porous Crystals. *Cryst. Growth Des.*, **16**, 1772–1779, 2016. DOI: 10.1021/acs.cgd.5b01559

[19] D. Braga, F. Grepioni, Mechanochemistry: From Functional Materials to Synthetic Strategies. *Angew. Chem., Int. Ed.*, **43**, 4002–4011, 2004. DOI: 10.1002/anie.200300618

[20] P. G. McCormick, F. H. Froes, The Fundamentals of Mechanochemical Processing. *J. Miner., Met. Mater. Soc.*, **50**, 61–65,1998. DOI: 10.1007/s11837-998-0290-x

[21] A. P. Amrute, Catalytic Reactions in Ball Mill, *Catalysis*, **33,** 2020. DOI: 10.1039/9781839163128-00307

[22] C. Burmeister, A. Kwade, Process Engineering with Planetary Ball Mills. *Chemical Society reviews,* **42**, 18 (2013): 7660-7. DOI: 10.1039/c3cs35455e

[23] Amrute, A. P., De Bellis, J., Felderhoff, M., & Scheth, F. Mechanochemical Synthesis of Catalytic Materials. *Chem. Eur. J.,* **26**, 5616–5634, 2020. DOI: 10.1002/chem.202004583

[24] S. T. Emmerling, L. S. Germann, P. A. Julien, I. Moudrakovski, M. Etter, T. Friščić, R. E. Dinnebier, B. V. Lotsch, *In situ* monitoring of Mechanochemical Covalent Organic Framework Formation Reveals Templating Effect of Liquid Additive. *Chem.*, **7**, 1–12, 2021. DOI: 10.1016/j.chempr.2021.04.012

[25] K. Tamura, T. Tanaka, Studies on the Mechanochemistry of Organic and Inorganic Compounds. *Ind. Eng. Chem. Process. Des. Dev.*, **9**, 165–173, 1970.

[26] N. Cindro, M. Tireli, B. Karadeniz, T. Mrla, K. Užarević, Investigations of Thermally Controlled Mechanochemical Milling Reactions. *ACS Sustain. Chem. Eng.*, **7**, 16301–16309, 2019. DOI: 10.1021/acssuschemeng.9b03721

[27] J. Andersen, J. Mack, Insights into Mechanochemical Reactions at Targetable and Stable, Sub-Ambient Temperatures. *Angew. Chem. Int. Ed.*, **57**, 13062–13065, 2018. DOI: 10.1002/anie.201806355

[28] R. Li, X. Ren, H. Ma, X. Feng, Z. Lin, X. Li, C. Hu, B. Wang, Nickel-Substituted Zeolitic Imidazolate Frameworks for Time-Resolved Alcohol Sensing and Photocatalysis under Visible Light. *J. Mater. Chem. A*, **2**, 5724–5729, 2014. DOI: 10.1039/C4TA00798J

[29] D. Virieux, F. Delogu, A. Porcheddu, F. García, E. Colacino, Mechanochemical Rearrangements. *J. Org. Chem.*, **86**, 13885–13894, 2021. DOI: 10.1021/acs.joc.1c01618

[30] L. Hu, S. Xu, Z. Zhao, Y. Yang, Z. Peng, M. Yang, C. Wang, J. Zhao, Ynamides as Racemization-Free Coupling Reagents for Amide and Peptide Synthesis. *J. Am. Chem. Soc.*, **138**, 13135–13138, 2016. DOI: 10.1021/jacs.6b08767

[31] P. Ying, J. B. Yu, W. K. Su, Liquid-Assisted Grinding Mechanochemistry in the Synthesis of Pharmaceuticals. *Adv. Synth. Catal.*, **363**, 1246–1271, 2021. DOI: 10.1002/adsc.202000725

[32] O. I. Lomovsky, I. O., Lomovskiy, D. V. Orlov, Mechanochemical Solid Acid/Base Reactions for Obtaining Biologically Active Preparations and Extracting Plant Materials. *Green Chem. Lett. Rev.*, **10**, 171–185, 2017. DOI: 10.1080/17518253.2017.1378487

[33] T. P. Shakhtshneider, S. A. Myz, E. V. Boldyreva, A. I. Nizovskii, R. Kumar, Core-shell Mechanocomposites of Drugs with Inorganic Oxides and Hydroxides. *Acta Phys. Polonica A*, **126**, 1019–1024, 2014. DOI: 10.12693/APhysPolA.126.1019

[34] P. Matteazzi, D. Basset, F. Miani, Mechanosynthesis of Nanophase Materials. *Nanostruct. Mater.*, **2**, 217–229, 1993. DOI: 10.1016/0965-9773(93)90149-6

[35] T. Tsuzuki, Commercial Scale Production of Inorganic Nanoparticles. *Int. J. Nanotechnol.*, **6**, 567–578, 2009. DOI: 10.1504/IJNT.2009.027457

[36] T. Tsuzuki, Mechanochemical Synthesis of Metal Oxide Nanoparticles. *Nanotechnology*, **19**, 435602, 2008. DOI: 10.1088/0957-4484/19/43/435602

[37] J. Wu, C. S. Xie, Z. K. Bai, et al. Preparation of ZnO-glass Varistor from Tetrapod ZnO Nanopowders. *Mater. Sci. Eng. B*, **95**, 157–161,2002. DOI: 10.1016/S0921-5107(02)00029-1

[38] J. Q. Xu, Q. Y. Pan, Y. A Shun, Z. Z. Tian, Grain Size Control and Gas Sensing Properties of ZnO Gas Sensor. *Sens. Actuators B Chem.*, **66**, 277–279, 2000. DOI: 10.1016/S0925-4005(00)00320-5

[39] T. Szabo, J. Nemeth, I. Dekany, Zinc Oxide Nanoparticles Incorporated in Ultrathin Layer Silicate Films and Their Photocatalytic Properties. *Colloids Surf. A Physicochem. Eng. Aspects*, **230**, 23–35, 2003. DOI: 10.1016/S0927-7757(02)00417-3

[40] O. Yamamoto, M. Komatsu, J. Sawai, et al. Effect of Lattice Constant of Zinc Oxide on Antibacterial Characteristics. *J. Mater. Sci. Mater. Med.*, **15**, 847–851, 2004. DOI: 10.1023/B:JMSM.0000023065.39409.23

[41] X. Y., Ma, W. D. Zhang, Effects of Flower-like ZnO Nanowhiskers on the Mechanical,Thermal and Antibacterial Properties of Waterborne Polyurethane. *Polym. Degrad. Stabil.*, **94**(7), 1103–1109, 2009. DOI: 10.1016/j.polymdegradstab.2009.03.009

[42] N. Salah, S. S. Habib, Z. H. Khan, A. Memic, A. Azam, E. Alarfaj, N. Zahed, S. Al-Hamedi, High-Energy Ball Milling Technique for ZnO Nanoparticles as Antibacterial Material. *Journal of Nanomaterials*, 1–7, 2017. DOI: 10.1155/2017/1637362

[43] E. Tothova, M. Senna, A. Yermakov, J. Kovac, E. Dutkova, M. Hegedüs, M. Kanuchova, M. Baláz, M. Lukacova Z. Bujnakova, J. Briancin, P. Makreski, Zn Source-Dependent Magnetic Properties of Undoped ZnO Nanoparticles from Mechanochemically Derived Hydrozincite. *J. Mater. Chem. C*, **8**, 9075–9085, 2020. DOI: 10.1039/D0TC02045E

[44] W. Ao, J. Li, H. Yang, X. Zeng, X. Ma, Mechanochemical Synthesis of Zinc Oxide Nanocrystalline. *J. Mater. Sci.*, **40**, 2677–2680,2005. DOI: 10.1007/s10853-005-0023-6

[45] S. Meghana, P Kabra, S. Chakraborty, N. Padmavathy, Understanding the Pathway of Antibacterial Activity of Copper Oxide Nanoparticles. *RSC Adv.*, **5**, 12293–12299, 2015. DOI: 10.1039/C5RA01312G

[46] M. Cho, J. Kim, J. Y. Kim, J. Yoon, J. H. Kim, Mechanisms of *Escherichia coli* Inactivation by Several Disinfectants. *Water Res.*, **44**, 3410–3418, 2010. DOI: 10.1016/j.watres.2010.03.033

[47] C. Gazzurelli, A. Migliori, P. P. Mazzeo, M. Carcelli, S. Pietarinen, G. Leonardi, A. Pandolfi, D. Rogolino and P. Pelagatti, Making Agriculture More Sustainable: An Environmentally Friendly

Approach to the Synthesis of Lignin@Cu Pesticides, *ACS Sustainable Chem. Eng*., **8**, 14886, 2020. DOI: 10.1021/acssuschemeng.0c04645.

[48] C. Gazzurelli, M. Carcelli, P. P. Mazzeo, C. Mucchino, A. Pandolfi, A. Migliori, S. Pietarinen, G. Leonardi, D. Rogolino and P. Pelagatti, Exploiting the Reducing Properties of Lignin for the Development of an Effective Lignin@Cu_2O Pesticide, *Adv. Sustainable Syst.,* **6**, 2200108, 2022. DOI: 10.1002/adsu.202200108

[49] C. Gazzurelli, Combining Lignin with Metals for Agrochemical Applications, 2022

[50] B. G. Fiss, A. J. Richard, G. Douglas, M. Kojic, T. Friščić, A. Moores, Mechanochemical Methods for the Transfer of Electrons and Exchange of Ions: Inorganic Reactivity from Nanoparticles to Organometallics. *Chem. Soc. Rev.*, **50**, 8279–8318. 2021. DOI: 10.1039/D1CS00281D

[51] W. G. Glasser, Classification of Lignin According to Chemical and Molecular Structure. In *Lignin: Properties and Applications*; American Chemical Society (ACS): Washington, DC, USA, **742**, 216–238, 1999.

[52] A. H. Zittlau, Q. Shi, J. Boerio-Goates, B. F. Woodfield, J. Majzlan, A Study of the Thermodynamic Properties of Minerals and their Applications in Earth Sciences, *Chem. Erde***, *73***, 39–47, 2013. DOI: 10.1016/j.chemer.2012.12.002

[53] F. Gomollón-Bel, Ten Chemical Innovations That Will Change Our World. *Chem. Int.,* **42**, 3–9, 2020. DOI: 10.1515/ci-2020-0402.

Chapter 4: Lignin@molybdate hybrid materials

Molybdenum is a trace element found in the soil, and it is required for the growth of most biological organisms, including plants and animals. Molybdenum has several oxidation states, from 0 to VI, which is the most common in agricultural soils. It is naturally present in mineral forms in rocks such as molybdenite (MoS_2), wulfenite ($PbMoO_4$) and ferrimolybdite ($Fe_2(MoO_4)_3$;[1] the release of metal from the solid minerals occurs from weathering and processes involving continuous redox reactions. Apart from copper, it is the least abundant essential micronutrient found in the tissue of most plants (ranging from 0.5-0.6 ppm to 1 ppm) and it is often set as the base from which all the other nutrients are compared and measured.[2,3] Currently, there is little information on how plants access molybdate from soil and redistribute it within the tissues. Usually, the roots present higher contents of molybdenum than leaves, stems and seeds. This element has a crucial role in many biological pathways, and its deficiency could negatively affect plant growth.[4] Despite the very low requirement of Mo for plant health (up to 1 ppm), there is great concern about the problematics caused by molybdenum deficiency: these have been investigated in different studies, assessing that this deficiency can negatively affect plant metabolisms at many different levels, associated with the reduced activity of molybdenum enzymes.

Molybdenum is in fact utilized to carry out redox reactions by selected enzymes, which include nitrate reductase, xanthine dehydrogenase, aldehyde oxidase and sulfite oxidase. It serves as a pterin cofactor (Moco) within most of these enzymes, enabling key reactions in nitrogen, carbon, and sulfur metabolism. In addition, legume plants need Mo for symbiotic nitrogen fixation, which depends on the Mo-based enzyme nitrogenase produced by bacteria.[5] Molybdenum deficiency is related to its availability in the soil, particularly influenced by soil pH, the concentration of some oxides (such as iron oxides), the degree of water drainage, and the presence of organic colloids.[2] Soil pH has the strongest effect on adsorption and release processes of MnO_4^{2-} ions from soil. In acidic soils, molybdate anions are adsorbed onto positively charged oxides of iron, manganese, and aluminium, as well as onto clay minerals and organic colloids. As soil pH increases, still within acidic values, the availability of molybdenum to plants also improves. The maximum adsorption of molybdenum onto positively charged metal oxides occurs between pH 4 and 5.[6] Furthermore, its availability can be influenced by the presence of other metals, clays and organic colloids, since it can form ionic complexes with various soil cations (calcium, sodium, potassium, magnesium) or it can be complexed by organic ligands, such as humic and fulvic acid. Large amounts of phosphates influence the adsorption of molybdenum while an excess of sulphates can reduce its uptake. In Australia, Riley et al. have reported that molybdenum deficiency has been identified as the second most common micronutrient deficiency, affecting large areas of croplands with acidic soils.[7] In China molybdenum deficiency affects nearly half of all agricultural soils and has been identified as limiting yields factor of winter and soya beans.[8] Plants grown in nutrient solution without molybdenum developed characteristic phenotypes, including mottling lesions on the leaves and altered leaves morphologies, where the lamellae have become involuted (a phenomenon commonly referred as "whiptail").[9] A work on cauliflower by Mitchell et al. have demonstrated that the whiptail could be overcome with the addition of molybdenum to the soil; in tomato plants grown in molybdenum deficient soils it can be rapidly recovered by sodium molybdate soil or foliar application.[10] A study

on mandarin tree considering foliar spraying of sodium molybdate in Egypt demonstrated an increase of fruit yield by 37%.[11]

The symptoms of molybdenum deficiency are always correlated to nitrogen metabolism: when molybdenum catalytic role is not sufficiently fulfilled, accumulation of nitrate in the leaves can be observed and enzyme production necessary for normal growth is impaired, with consequent weakening of green leaves coloration.[12] Usually, molybdenum deficiency is misdiagnosed as nitrogen one, and this often leads to inefficient overuse of nitrogen fertilizer, with serious drawbacks for the environment. Therefore, a careful micronutrient management, with a particular focus on molybdenum, is an issue of particular importance in agriculture, with different implications for the economy, plant health, and the environment. The extensive use of nitrogen fertilizers has led to the leaching of significant amounts of nitrate into groundwater, which has been linked to methemoglobinemia in infants and ruminants, as well as to conditions such as goitre, congenital defects, heart disease, and even cancer.[13] The EU transition to safe, sustainable agricultural and food production systems aims to reduce the use of fertilizers by 20% without compromising soil fertility or crop yields; to reach this goal the efficiency of agro-products must be significantly enhanced.[14] As the global population grows, food demand increases accordingly, which is estimated to double in the next 50 years as the global population approaches nine billion.[15] In this context, optimizing the existing production by acting on the micronutrient deficiencies gains importance. Nowadays, molybdenum is typically delivered in the form of ammonium heptamolybdate, ammonium dimolybdate, ammonium molybdate, sodium molybdate, calcium molybdate or molybdenum trioxide. Due to the inefficiency in the utilization of several plant nutrients, considerable efforts have been made to develop innovative materials for the controlled release of conventional fertilizers. This approach aims to slow the rate of nutrient solubilization and optimize plant uptake. An excess of nutrients, often resulting from the use of conventional soluble fertilizers, can lead to high concentrations of soluble salts in the root zone.[16] This can cause osmotic stress and trigger specific damage to plants at various growth stages, as well as undesirable effects such as lodging.[17] One common method to achieve a delayed release is to coat the fertilizers with compounds that either slow down their dissolution in the soil solution or prevent their fixation on clay mineral surfaces. Another strategy involves encapsulating fertilizers in micro- or nano-capsules. A range of materials, such as synthetic and natural polymers, have been proposed as coatings or scaffolds for controlled release of fertilizers. However, these materials are often expensive, raise environmental concerns, exhibit poor stability in soil, or suffer from low mechanical strength. Additionally, some have been associated with negative effects on plant growth and human health.[18,19] In contrast, using lignin to coat or encapsulate fertilizers offers a cost-effective alternative, as lignin is inexpensive, has interesting mechanical properties, is safe for human health and has beneficial effects on plant growth.[20,21] Despite these advantages, research into lignin-based slow-release fertilizers is still in its early stages, and only a few studies have investigated its potential. For this reason, I focused on the development of hybrid materials containing lignin during my research project, which, as explained, can provide a controlled release and a beneficial impact on plant wellness. Previous studies of our research group[22,23,24] have already demonstrated the effectiveness of this approach with copper-based hybrid materials, used as pesticides. The combination of the organic matrix

with the synthesized crystalline phases (brochantite and cuprite) have led to products with higher effectiveness compared to commercially used copper sulphate, allowing for the use of lower quantities of heavy metal while achieving high-performance results. In this Chapter, we have concentrated on studying heterometallic materials containing molybdenum and other metals, like zinc or copper (Figure 4.1). Zinc plays a crucial role in the growth of both humans and animals.[25] As outlined in the previous Chapters, it is also an essential nutrient for plants, participating in a variety of enzymatic processes, as well as metabolic and redox reactions. Zinc is involved in energy transfer, protein synthesis, and nitrogen metabolism, among other vital functions.[26] Copper is a vital micronutrient that plays a key role in the health of both animals and plants, enhancing reproductive health in livestock. In grazing animals, copper is essential for bone development, immune system function, and the proper functioning of the nervous system. For plants, copper is crucial for processes such as photosynthesis, transpiration, and nitrogen fixation.[27]

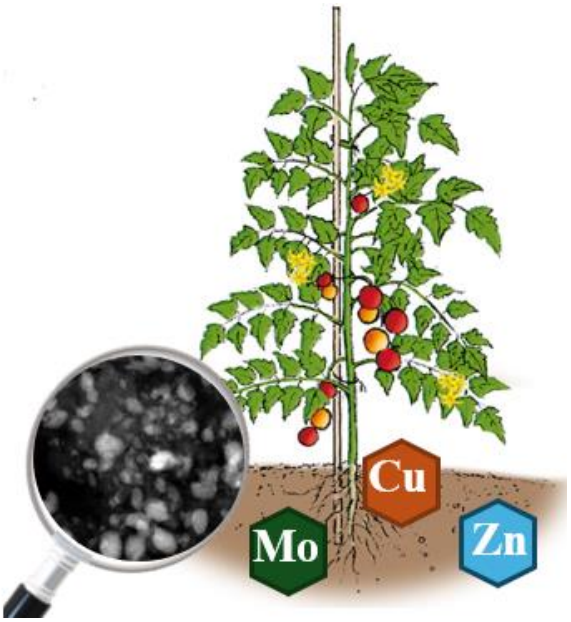

Figure 4.1. Image showing the action of hybrid lignin-based organic-inorganic materials, whose slow release provides essential micronutrients for plant health.

The use of bimetallic phases containing both copper and molybdenum could also be of interest considering some negative drawbacks related to Mo accumulation in plants. It has been in fact demonstrated that high molybdenum levels in plants can be associated with the occurrence of molybdenosis[28] in rumens, a disorder that induces copper deficiency. This can be controlled maintaining adequate Mo/Cu ratios in the diet and, in this context, the use of inorganic phases containing both metals could represent a potential solution.

Crop production is severely affected, besides lack of nutrients, also by another crucial factor: bacterial and fungal diseases and the related phytopathogen control is then a key issue in modern agriculture. Pesticides are widely used to protect plants and crops from pathogenic microorganisms, such as bacteria and fungi, but this poses important drawbacks, due to large amount of harmful residues, dangerous for human, animal and the environment. Commercial pesticides exhibit in fact a high level of toxicity, so there is the need to prevent environment pollution and human exposure by developing antifungal

and antibacterial substances safe for the human health and for the environment.[29,30] In addition, due to resistance phenomena[31], the treatment of some diseases is not always effective. For decades, pest control has been pursued by using copper-based pesticides.[32] However, there are important concerns about their long-term sustainability, due to phytotoxicity, food and groundwater contamination, accumulation in the soil and its use is indeed strictly regulated.[33] In this scenario, its use in combination with an organic matrix, such as lignin, can be considered a good attempt to develop novel materials with good antibacterial activity and reduced metal content with respect to traditional copper-based pesticides.[22,23,24] As pointed out in previous Chapters, in fact, lignin itself is endowed of antimicrobial and antifungal activity.[34] The idea, in line with previous studies, is to combine the micronutrient role with the antibacterial one of the two metals, contributing to plant wellness in a synergic action. Some molybdate systems have in fact been studied for their antimicrobial properties.[35,36,37] Interestingly, copper molybdate ($CuMoO_4$) and its thermally converted form $Cu_3Mo_2O_9$ have shown promising inhibitory effect against *E. coli,*[38,39] but minerals containing MoO_4^{2-} anions are mainly studied because of their catalytic properties.[40] $Cu_3(MoO_4)_2(OH)_2$ is a mineral, named lindgrenite, which is usually found in Chile and has received great attention due to its excellent ferrimagnetic, photocatalytic and electrochemical properties.[41] The disadvantage related to the use of natural lindgrenite is the presence of impurities making the material unfeasible to use for specific applications. Lindgrenite has shown interesting antifungal properties: due to its structural characteristics and the presence of copper in its composition, lindgrenite is a promising candidate as an antifungal agent. Feitosa de Carvalho et al.[41] have proposed ultrasonic irradiation as synthetic strategy to obtain $Cu_3(MoO_4)_2(OH)_2$ microcrystals and they have demonstrated antifungal activity of this material against *T. rubrum* and *C. albicans* strains. In this study, a rationalization of the mechanism of action has been tried. In the crystalline structure there is the presence of $[CuO_6]$ clusters with terminal hydroxyl groups and $[MoO_4]$ clusters, displaying crystalline defects, among which there are oxygen vacancies. Water molecules and air oxygen can be adsorbed on lindgrenite surface, giving raise to oxidative processes which result in ROS (reactive oxygen species) at the basis of the antibacterial and antifungal activity, since they can interfere with the biological pathways of the microorganisms, interrupting cell activity and replication and resulting in cell lysis, as shown in Figure 4.2.

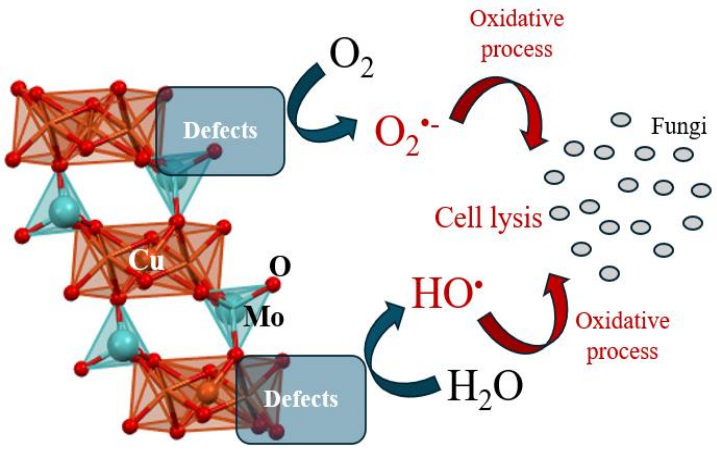

Figure 4.2. Proposed mechanism for the antifungal action of lindgrenite [41]

Xu et al.[42] have conducted studies on oil seed rapes with outdoor planting trials by foliar application which have shown enhanced immunity of rapeseed against *S. sclerotium* infections. In this work, the synthetic procedure requires an ultrasound equipment. Nowadays, the synthetic reports about lingrenite are limited and the majority refer to multi-steps synthesis,[43] with the use of costly and not eco-friendly procedures. The reported hydrothermal route may be a simple approach,[44] but it could be interesting in a scale up perspective to operate by an aqueous chemical precipitation performed at room temperature, without the use of any surfactants, template, expensive chemicals, complex instrumentation and multi-step processes, as the one performed by Swain et al.[45] In their work, Swain et al. have hypothesized a possible chemical mechanism that could explain the chemistry involved in the aqueous precipitation through speciation diagrams. Considering an experimental pH about 5, molybdenum mostly exists as MoO_4^{2-}, while the precursor of Cu^{2+} either exists as $Cu_2(OH)^{3+}$ or $Cu(OH)^{+}$. Then, the chemical reaction for the synthesis of lindgrenite can be represented by equation (1):

$$2MoO_4^{2-} + Cu_2(OH)^{3+} + Cu(OH)^{+} \rightarrow Cu_3(MoO)_4(OH)_2 \quad (1)$$

The crystallization process and the structure of lindgrenite have been reported in the literature.[46] Xu et al.[44] have described the architecture of crystals obtained by hydrothermal route. The asymmetrical unit contains two symmetrically distinct Cu^{2+} positions, one Mo^{6+} position and five O^{2-} positions (Figure 4.3a). Each Cu^{2+} ion coordinates two OH^{-} groups and four O^{2-} in a $CuO_4(OH)_2$ octahedral arrangement. Due to Cu^{2+} d^9 configuration the octahedron suffers the Jahn Teller effect and becomes distorted. These octahedrons are bonded together to form strips along the c-axis that are cross-linked by MoO_4^{2-} tetrahedra that share corners with $CuO_4(OH)_2$ octahedra. Each tetrahedron connects to three octahedron strips and the fourth binding occurs along the strips, resulting in a three dimensional tetrahedral-octahedral framework, as shown in Figure 4.3b.

a)

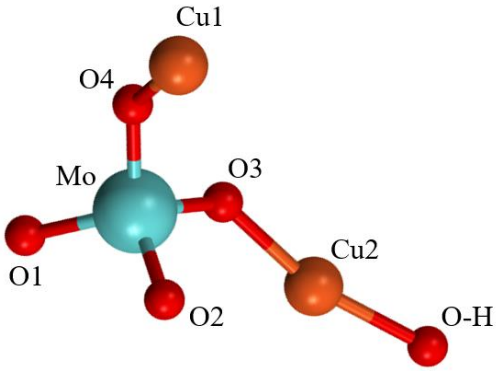

b)

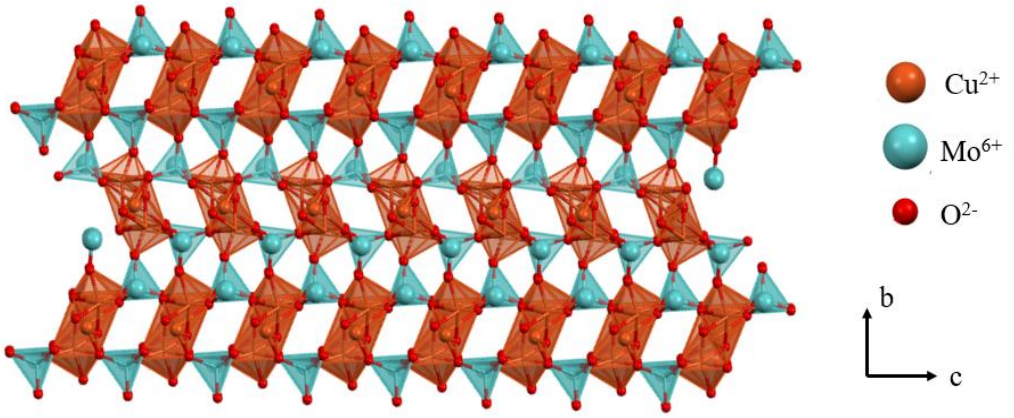

Figure 4.3. Lindgrenite crystallographic structure. a) the asymmetrical unit is shown, b) strips of edge-sharing $CuO_4(OH)_2$ octahedra (orange) running parallel to the c-axis. tetrahedra of MoO_4^{2-} are represented in light blue.[46]

Besides lindgrenite, other bimetallic phases containing both copper and molybdenum are known in the literature: $NH_4Cu_2(MoO_4)_2(OH)(H_2O)$, for instance, has been studied by Sajò et. Al as active photocatalyst in the decomposition of Congo Red when irradiated by UV or visible light, which is prepared by subjecting $[Cu(NH_3)_4]MoO_4$ to moisture at RT.[47] It is worth to notice the presence, in this crystalline phase, of ammonium ions, used in most fertilizers. However, when urea and ammonium-based fertilizers are applied in excessive amounts, they can be toxic to soil microorganisms. This toxicity arises from the release of ammonia, which increases soil pH and elevates ionic strength, all of which negatively affect microbial activity.[48,49] The use of urea and ammonium fertilizers can cause ammoniacal nitrogen (NH_3 and NH_4^+) concentrations to spike dramatically in localized areas. For instance, near a urea granule, concentrations can exceed 3000 mg/g of soil, [50]while ammonia injection can lead to levels of 500 ppm.[48] Such elevated concentrations can be detrimental, significantly inhibiting or even killing fungal and bacterial populations.[48,49] It would be interesting to evaluate the application of these materials containing ammonium with the aim of achieving fertilizing effects, but without reaching harmful quantities, thanks to the combination with other metals. In this context, an analogous phase containing zinc $NH_4Zn_2(MoO_4)_2(OH)(H_2O)$ can be interesting to be evaluated for these applications.[51] Levin et al.[51] have studied the obtainment of this material by a room-temperature synthesis from a metastable mixed oxide prepared by calcination of a layered double hydroxide (LDH) and the crystallographic features have been investigated. Furthermore, some studies on bimetallic phases containing zinc and molybdenum with antibacterial activity[52,53] have been conducted, paving the way for future research on phases different from those already studied.

With all these considerations in mind, we have thought that a good candidate in the design of the hybrid material for the inorganic part constituent can contain both molybdenum and copper or zinc, meeting the requirements of micronutrient supply, together with antibacterial and antifungal activity.

The aim of our work is the implementation of a green and scalable synthetic approach for the obtainment of hybrid materials, consisting of bimetallic phases containing copper or zinc and molybdenum, embedded in a lignin matrix for agrochemical applications. The possibility to obtain these materials by means of a simple aqueous chemical precipitation at low temperatures has been studied, in view to implement a large-scale synthetic procedure for applications on crops. The synthetic approach provides a combination of ammonium molybdate or sodium molybdate with different metallic salts containing copper or zinc. The loading of molybdenum has been varied to verify the formation of the desired phase, changing the ratio between lignin and the starting salts. The procedure has been optimized to obtain the final product with a simple and scalable approach, considering also the role of pH in the synthesis of the final material. We have used a classical wet procedure, but we have also investigated the possibility to obtain the materials *via* mechanochemical approach. Advantages of this synthetic route are explained in Chapter 3. Moreover, we have also used Solargo™ (introduced in Chapter 2) with the aim to investigate the use of a liquid formulation as alternative source of lignin.

Characterization of the materials has been performed by using different spectroscopic techniques. The inorganic phase has been characterized by means of PXRD, to identify the formed phase and to verify its purity. Studies have been conducted to reduce reaction times as much as possible, with a view to possible direct applications in field. The upload of the metals (from 4 to 20%) has been assessed by using ICP-AES analysis. The morphologies of the synthesized nanoparticles have been studied by TEM; EDS mapping has allowed to verify the homogeneous distribution of the metals. DLS has been used to study the size distribution of the NPs. The thermal behaviour of the hybrid materials has been studied via DSC and TGA analyses. *In vitro* studies to assess the antibacterial and antifungal features of the materials are ongoing at University of Naples in the research group of Prof. S. Woo.

Wet synthesis of HMW@molybdate materials

EXPERIMENTAL SECTION

Materials and methods

HMW (Biopiva395®, Kraft softwood lignin from *Pinus taeda*, M_w:5950-6000 g/mol, M_n:1560-1565 g/mol) is kindly provided by UPM-Kymmene Oyj (Helsinki, Finland) and Green Innovation GmbH (Innsbruck, Austria). Zinc acetate dihydrate, zinc sulphate heptahydrate (99%) are purchased by Carlo Erba; zinc chloride is purchased by Brenntag. Ammonium molybdate dihydrate (99%) is purchased by ThermoScientific and abcr GmbH; Sodium molybdate dihydrate is purchased by Bluestone (Mo content: 39.5%); copper acetate monohydrate is purchased by Aldrich (99%), copper chloride dihydrate is purchased by Carlo Erba (99%), copper sulphate pentahydrate (98%) is purchased by Fluorochem, sodium hydroxide is purchased by AnalaR NORMAPUR®ACS (99.5-100%); ammonium hydroxide (30-33% NH_3 in H_2O) is purchased by Fluka, KOH is purchased by ACS (85 %). All the reagents are used as received with no further purification. pH has been measured using a Crison pHmeter basic 20 equipped with an Ag/AgCl electrode.

A schematic overview of the wet syntheses conducted for the hybrid materials is reported in Scheme 4.1.

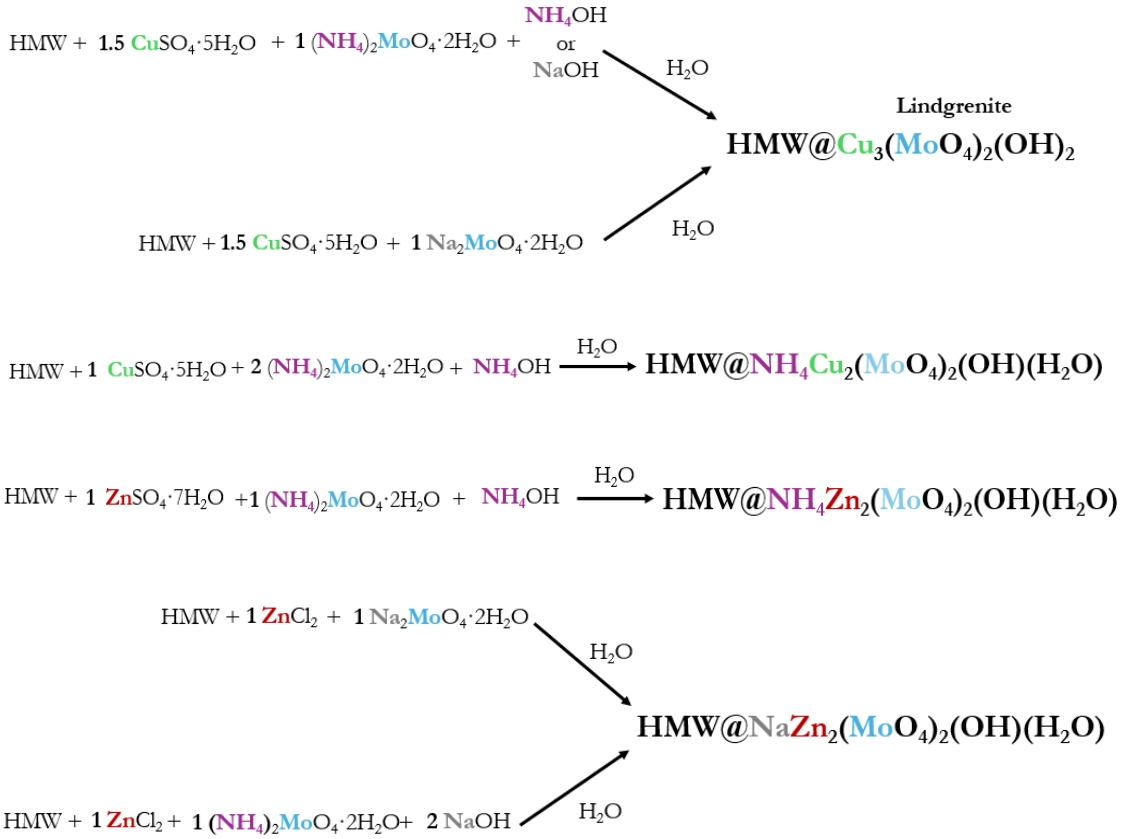

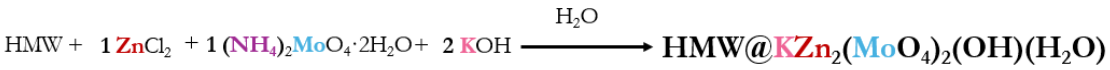

Scheme 4.1. Schematic overview of the wet synthesis of the hybrid materials described in this paragraph

Preparation of HMW@$Cu_3(MoO_4)_2(OH)_2$ (HMW@lindgrenite)

HMW@$Cu_3(MoO_4)_2(OH)_2$ by using $(NH_4)_2MoO_4·2H_2O$ as molybdenum source. The reaction has been conducted suspending HMW at room temperature in water, together with $(NH_4)_2MoO_4·2H_2O$ (140 mg), then a solution of copper salt has been added ($Cu(CH_3COO)_2·H_2O$, $CuSO_4·5H_2O$ or $CuCl_2·2H_2O$, 1.5 equivalents of Cu with respect to Mo). A solution of NaOH 0.15 M (1 equivalent with the respect to Mo) or 1 drop of NH_4OH 33% w/w solution has been added, in both cases setting the pH to about 5.5-6 (20 mL total volume of water). The formation of an aquamarine-coloured colloid immediately occurs, followed by formation of a green precipitate after a few hours. The mixture has been kept stirring for 5 hours, centrifuged and the recovered solid fraction has been dried at 85 °C overnight. The different lignin and molybdenum salts ratio are reported in Table 4.1, where X% (X: 4%, 10%, 13%, 20%) refers to the % of Mo. The experiments have been performed at least twice.

HMW@$Cu_3(MoO_4)_2(OH)_2$ by using $Na_2MoO_4·2H_2O$ as molybdenum source. The reaction has been conducted suspending HMW at room temperature in water, together with $Na_2MoO_4·2H_2O$ (139 mg), then a solution of copper salt ($CuSO_4·5H_2O$, 1.5 equivalents of Cu with the respect to Mo, 15 mL total volume of water) has been added. The pH of reaction is about 5 and the formation of an aquamarine-coloured colloid immediately occurs, followed by formation of a green precipitate after a few hours. The mixture has been kept stirring for 4 hours, centrifuged and the recovered solid fraction has beendried at 85 °C overnight. The lignin and metal salt ratio is reported in Table 4.2, where X% (X: 13%) refers to the % of Mo. The experiments have been performed at least twice.

Preparation of HMW@ $NH_4Cu_2(MoO_4)_2(OH)_2(H_2O)$

HMW@$NH_4Cu_2(MoO_4)_2(OH)(H_2O)$ with $(NH_4)_2MoO_4·2H_2O$ as molybdenum source. The reaction has been conducted suspending lignin HMW at room temperature in aqueous environment, together with a solution of $(NH_4)_2MoO_4·2H_2O$ (140 mg, 2 equivalents of Mo with the respect to Cu, 20 mL total volume of water) and $CuSO_4·5H_2O$. Then NH_4OH solution has been added to the mixture while stirring, setting the pH to about 6.5 and the formation of a green precipitate immediately occurs. The mixture has been kept stirring for 24 hours, then centrifuged and the recovered solid fraction has been dried at 85 °C overnight. The different lignin and metal salts ratio are reported in Table 4.1, where X% (X: 6 or 12) refers to the % of Mo. The experiments have been performed at least twice.

Preparation of HMW@$XZn_2(MoO_4)_2(OH)_2(H_2O)$ (with X: NH_4, Na, or K)

HMW@$NH_4Zn_2(MoO_4)_2(OH)(H_2O)$ by using $(NH_4)_2MoO_4 \cdot 2H_2O$ as molybdenum source. The reaction has been conducted suspending lignin HMW at room temperature in water, together with a solution of a zinc salt ($Zn(OAc)_2 \cdot 2H_2O$, $ZnSO_4 \cdot 7H_2O$ or $ZnCl_2$, 1 equivalent of Zn with the respect to Mo) and $(NH_4)_2MoO_4 \cdot 2H_2O$ (140 mg, 20 mL total volume of water). Then, two drops of NH_4OH 33% w/w solution have been added to the mixture while stirring, setting the pH to about 6.5 and the formation of a white precipitate immediately occurs. The mixture has been kept stirring for 24 hours, then centrifuged and the recovered solid fraction has been dried at 85 °C overnight. The different lignin and metal salts ratio are reported in Table 4.1 where X% (X: 4%, 10%, 14%, 20%) refers to the percentage of Mo. The experiments have been performed at least twice.

HMW@$NaZn_2(MoO_4)_2(OH)(H_2O)$ by using $Na_2MoO_4 \cdot 2H_2O$ as molybdenum source. The reaction has been conducted suspending HMW at room temperature in water, together with a solution of zinc salt ($ZnCl_2$, 1 equivalent of Zn with the respect to Mo) and $Na_2MoO_4 \cdot 2H_2O$, with 15 mL total volume of water. The pH of reaction is about 6.5 and the formation of a white precipitate immediately occurs. The mixture has been kept stirring for 4 hours, centrifuged and the recovered solid fraction has been dried at 85 °C overnight. The experiments have been performed at least twice. The lignin and metal salt ratio are reported in Table 4.2 and with X% (X 13%) refers to the percentage of Mo. The experiments have been performed at least twice.

HMW@$NaZn_2(MoO_4)_2(OH)(H_2O)$ or HMW@$KZn_2(MoO_4)_2(OH)(H_2O)$ by using $(NH_4)_2MoO_4 \cdot 2H_2O$ as molybdenum source. The reaction has been conducted suspending lignin HMW at room temperature in aqueous environment, together with $(NH_4)_2MoO_4 \cdot 2H_2O$; then a solution of $ZnCl_2$ has been added (1 equivalent of Zn with the respect to Mo, 20 mL H_2O as total volume). NaOH aq 0.15 M solution or KOH aq 0.15 M solution (2 equivalents with the respect to Mo) have been added to the mixture while stirring. The pH is set to about 6.5 and the formation of a white precipitate immediately occurs. The mixture has been kept stirring for 24 hours, then centrifuged and the recovered solid fraction has been dried at 85 °C overnight. The lignin and metal salts ratio used are reported in Table 4.1 and named as HMW@$NaZn_2(MoO_4)_2(OH)(H_2O)$_14% and HMW@$KZn_2(MoO_4)_2(OH)(H_2O)$_14%. The percentage refers to Mo. The experiments were performed at least twice.

Table 4.1: different lignin/molybdate salt g/g ratio according to the synthetic procedure; the percentage reported in the code refers to the theorical loading of molybdenum with $(NH_4)_2MoO_4 \cdot 2H_2O$ as molybdenum source.

Sample	Lignin/$(NH_4)_2MoO_4 \cdot 2H_2O$ g/g
HMW@$Cu_3(MoO_4)_2(OH)_2$_4%	0.255/0.042
HMW@$Cu_3(MoO_4)_2(OH)_2$_10%	0.255/0.140
HMW@$Cu_3(MoO_4)_2(OH)_2$_13%	0.125/0.140
HMW@$Cu_3(MoO_4)_2(OH)_2$_20%	0.095/0.107
HMW@$NH_4Cu_2(MoO_4)_2(OH)(H_2O)$_6%	0.400/0.140
HMW@$NH_4Cu_2(MoO_4)_2(OH)(H_2O)$_12%	0.125/0.140
HMW@$NH_4Zn_2(MoO_4)_2(OH)(H_2O)$_4%	0.255/0.043
HMW@$NH_4Zn_2(MoO_4)_2(OH)(H_2O)$_10%	0.255/0.140
HMW@$NH_4Zn_2(MoO_4)_2(OH)(H_2O)$_14%	0.125/0.140
HMW@$NaZn_2(MoO_4)_2(OH)(H_2O)$_14%	0.125/0.140
HMW@$KZn_2(MoO_4)_2(OH)(H_2O)$_14%	0.125/0.140
HMW@ $NH_4Zn_2(MoO_4)_2(OH)(H_2O)$_20%	0.095/0.107

Table 4.2: different lignin/molybdate salt g/g ratio according to the synthetic procedure; the percentage reported in the code refers to the theorical loading of molybdenum by using $Na_2MoO_4 \cdot 2H_2O$ as molybdenum source:

Sample	Lignin/$Na_2MoO_4 \cdot 2H_2O$ g/g
HMW@$Cu_3(MoO_4)_2(OH)_2$_13%	0.122/0.139
HMW@$NaZn_2(MoO_4)_2(OH)(H_2O)$_13 %	0.122/0.137

$Cu_3(MoO_4)_2(OH)_2$_ref by using $(NH_4)_2MoO_4 \cdot 2H_2O$ as molybdenum source. To a solution of $CuSO_4 \cdot 5H_2O$ (265 mg, 1.5 equivalents of Cu with the respect to Mo) and $(NH_4)_2MoO_4 \cdot 2H_2O$ (140 mg) in 20 mL H_2O, NaOH 0.14 M (1 equivalent of NaOH with the respect to Mo) has been added under stirring, setting the pH to about 5. The formation of an aquamarine-coloured colloid immediately occurs and is followed by the formation of a green precipitate after a few hours. The mixture has been kept stirring for 5 hours, then it has been centrifuged and the recovered solid fraction has been dried at 85 °C overnight. The experiments have been performed at least twice.

$Cu_3(MoO_4)_2(OH)_2$_ref by using $Na_2MoO_4 \cdot 2H_2O$ as molybdenum source. To To a solution of $Na_2MoO_4 \cdot 2H_2O$ (140 mg), a solution of $CuSO_4 \cdot 5H_2O$ (217 mg, 1.5 equivalents of Cu with the respect to Mo, 15 mL total volume of water) has been added under stirring, setting the pH to about 5. The formation of an aquamarine-coloured colloid immediately occurs and followed by the formation of a green precipitate after a few hours. The mixture has been kept stirring for 4 hours, then it has been centrifuged and the recovered solid fraction was dried at 85 °C overnight. The experiments have been performed at least twice.

$NH_4Cu_2(MoO_4)_2(OH)(H_2O)$_ref by using $(NH_4)_2MoO_4 \cdot 2H_2O$ as molybdenum source. To a solution of $CuSO_4 \cdot 5H_2O$ (90 mg) and $(NH_4)_2MoO_4 \cdot 2H_2O$ (140 mg, 2equivalents of Mo with the respect to Cu), 2 drops of NH_4OH aq 33% have been added under stirring, setting the pH to about 7 in 20 mL H_2O. The formation of an aquamarine colloid immediately occurs and followed by the formation of a green precipitate after a few hours. The mixture has been kept stirring for 4 hours, then it has been centrifuged, and the recovered solid fraction has been dried at 85 °C overnight. The experiments have been performed at least twice.

$NH_4Zn_2(MoO_4)_2(OH)(H_2O)$_ref by using $(NH_4)_2MoO_4 \cdot 2H_2O$ as molybdenum source.· To a mixture of $ZnCl_2$ (95 mg, 1 equivalent with the respect to Mo) and $(NH_4)_2MoO_4 \cdot 2H_2O$ (140 mg) in 15 mL H_2O, two drops of NH_4OH (33%) aqueous solution have been added under stirring, setting the pH to about 6 and the formation of a white precipitate immediately occurs. The mixture has been kept stirring for 24 hours, then it has been centrifuged, and the recovered solid fraction has been dried at 85 °C overnight. The experiments have been performed at least twice.

$NaZn_2(MoO_4)_2(OH)(H_2O)$_ref by using $Na_2MoO_4 \cdot 2H_2O$ as molybdenum source. To a solution of $Na_2MoO_4 \cdot 2H_2O$ (140 mg), a solution of $ZnCl_2$ (79 mg, 1 equivalent of Zn with the respect to Mo, 15 mL total volume of water) has been added under stirring, setting the pH to about 6.5. The formation of white suspension immediately occurs and followed by the formation of a green precipitate after a few hours. The mixture has been kept stirring for 4 hours, then it has been centrifuged and the recovered solid fraction has been dried at 85 °C overnight. The experiments have been performed at least twice.

RESULTS AND DISCUSSION

As already mentioned in the introduction, bimetallic phases containing molybdenum, such as $NH_4Zn_2(MoO_4)_2(OH)(H_2O)$[47] and $NH_4Cu_2(MoO_4)_2(OH)(H_2O)$ or lindgrenite ($Cu_3(MoO_4)_2(OH)_2$), can be studied as promising plant micronutrients and also for possible antibacterial and antifungal properties.[42] The reports about the synthesis of these kind of materials are limited, and the majority are multi-stage synthesis[43] with disadvantages related to low purity and tedious procedures, calcination,[51] the involvement of toxic organic chemicals[42] or complex instrumentations, such as the use of electrochemically assisted laser ablation or ultrasound equipments.[42] The hydrothermal route that has been reported by Xu et al.[44] may be a simpler approach, but it is still unfeasible for scale-up applications and in presence of thermally degradable biopolymers like lignin. We have therefore investigated the possibility to operate with an aqueous chemical precipitation method performed at room temperature, without the use of any surfactants, expensive chemicals, complex instrumentation and multi-step processes. This kind of synthetic approach has the advantage of being extremely simple and sustainable, easy scalable, suitable for future *in vivo* applications. The wet synthetic procedure which we have developed consists of a heterogeneous mixing, where lignin is suspended in water together with two metallic salts (ammonium molybdate or sodium molybdate in combination with a zinc or copper salt) at room temperature. The synthetic approach used by Swain et al.[45] for lindgrenite involves the use of $Na_2MoO_4 \cdot 2H_2O$ as reagent; we have also investigated the possibility to use $(NH_4)_2MoO_4 \cdot 2H_2O$ as starting material: in this case, the addition of a base is necessary to reach the proper pH for the precipitation of the lindgrenite phase within the lignin matrix. The role of the base is crucial for the obtainment of an insoluble crystalline phase, since for all the metal combinations investigated (Cu/Mo, Zn/Mo) a pH of about 5-6 is required for precipitation.

We have tried to identify the soluble product formed without base addition: in Figure S4.1 are reported the results obtained suspending HMW (200 mg) in 15 mL of water with $ZnCl_2$ (65 mg) and $(NH_4)_2MoO_4 \cdot 2H_2O$ (91.5 mg, 1 equivalent with respect to Zn) are reported as an example. Since no precipitation occurred, a powder has been isolated via thermal drying step at 150 °C, then the dark blue powder isolated has been washed with water and centrifuged. During centrifugation, it has bene possible to notice a good separation (see Figure S4.1 a), with the presence of a solid fraction and a dark blue supernatant. The phase isolated from the solid fraction has been studied by means of PXRD (the pattern is shown in Figure S4.1 b), which could correspond to diammonium catena tetramolybdate, $(NH_4)_2(Mo_4O_{13})$. However, ICP-AES analysis has showed the presence of both zinc (4.83 ± 0.01) and Mo (12.7 ± 0.2), suggesting that the identification proposed by the database might not be fully accurate. The powder obtained by drying at 150 °C the blue supernatant has been also studied by means of PXRD (Figure S4.1 c.), which could match the phase $(NH_4)_6(Mo_7O_{24}) \cdot (H_2O)$. The same reaction has been repeated in the absence of lignin: in this case, a light blue powder has been isolated (see Figure S4.2 a.) and the PXRD analysis seems to indicate the formation of $(NH_4)_2(Mo_4O_{13})$ phase (Figure S4.2 b). When suspending HMW (200 mg) in 15 mL of water with $CuSO_4 \cdot 5H_2O$ (117 mg) and $(NH_4)_2MoO_4 \cdot 2H_2O$ (92 mg, 1 equivalent with the respect to Cu) PXRD (Figure S4.3) has indicated the possible correspondence to the lingrenite

$Cu_3(MoO_4)_2(OH)_2$ phase. This is in agreement with data obtained by ICP-AES analysis that showed the presence of both copper (7.7±0.1) and Mo (8.0±0.1). This synthetic approach therefore requires further investigations; since the identification of the obtained phases has been uncertain with this procedure, the following studies have been focused on promoting inorganic phase precipitation by adding a base.

With the addition of the base, adjusting the pH at about 5.5-6, it has been possible to isolate bimetallic crystalline phases embedded in the lignin matrix. We have investigated different metal ratios, highlighting that depending on the molar ratio employed, the isolated crystalline phase is different. By using a 1:1:1.5 Mo^{6+}:OH^-:Cu^{2+} molar ratio the material HMW@$Cu_3(MoO_4)_2(OH)_2$ has been isolated, while with 1:1:0.5 Mo^{6+}:OH^-:Cu^{2+} ratio HMW@$NH_4Cu_2(MoO_4)_2(OH)(H_2O)$ has been obtained. The materials $Cu_3(MoO_4)_2(OH)_2$ and $NH_4Cu_2(MoO_4)_2(OH)(H_2O)$ (named respectively as $Cu_3(MoO_4)_2(OH)_2$_ref, $NH_4Cu_2(MoO_4)_2(OH)(H_2O)$_ref) have been prepared in the absence of lignin, to verify whether the biopolymer can have an influence during the formation of the crystal nanoparticles, leading to different dimensions or morphologies.
The powder X-Ray diffraction analysis and the COD reference data bank pattern[54] have been used to determine both the crystalline phase and purity of the synthesized samples. As shown in Figure 4.4, by using 1:1:1.5 Mo^{6+}:OH^-:Cu^{2+} ratio and setting pH to 5.5, the diffractogram of the isolated material agrees with the reference diffraction pattern of lindgrenite [$Cu_3(MoO_4)_2(OH)_2$] (COD 9004056).[45] The lignin matrix is amorphous and is responsible for a broad diffuse scattering at low 2θ. The patterns of HMW@$Cu_3(MoO_4)_2(OH)_2$ and $Cu_3(MoO_4)_2(OH)_2$_ref show slightly different relative intensities among the peaks and different peaks width, which can be indicative of different morphologies and dimensions of the nanoparticles, when synthesized in presence or absence of lignin. It could be noticed also the presence of an amorphous band in $Cu_3(MoO_4)_2(OH)_2$_ref, probably indicating that not the whole sample has crystalline nature when synthesized in absence of lignin.

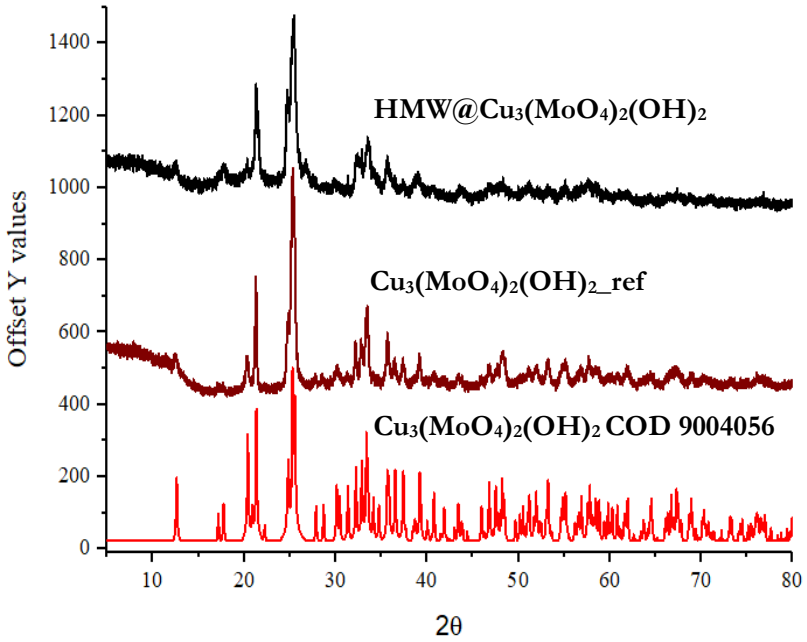

Figure 4.4. Experimental PXRD patterns of HMW@$Cu_3(MoO_4)_2(OH)_2$ (black line) and $Cu_3(MoO_4)_2(OH)_2$_ref (dark red line) compared to the one of lindgrenite COD 9004056 (red line)

The FT-IR spectra of HMW@$Cu_3(MoO_4)_2(OH)_2$ compared to the ones of HMW and $Cu_3(MoO_4)_2(OH)_2$_ref are shown in Figure 4.5 and are indicative of the presence of the molybdate phase within the lignin matrix. HMW infrared spectrum shows the typical signals that feature Kraft lignin.[55] The broad band at about 3400 cm^{-1} corresponds to the stretching of the hydroxyl groups of phenolic and carboxylic acid moieties. The weak bands at 2936-2835 cm^{-1} can be associated with the aromatic and aliphatic C-H stretching, respectively, while the band at 1595 cm^{-1} refers to the C=C aromatic stretching. Signals at 1512 and 1427 cm^{-1} can be attributed to the aromatic ring vibrations of phenylpropanoid (C9) skeleton of lignin. At 1215 cm^{-1} it is visible a band related to the presence of C-C, C-O and C=O stretching, while the band at 1143 cm^{-1} confirms the presence of the condensed aromatic units and the band at 1034 cm^{-1} is related to the C-O stretching of secondary alcohols and aliphatic ethers. The infrared spectrum of HMW@$Cu_3(MoO_4)_2(OH)_2$ shows the signals relative to the lignin matrix, but also some bands that could be ascribed to the presence of the molybdate anion, as can be inferred by the comparison with the spectrum of $Cu_3(MoO_4)_2(OH)_2$_ref (Figure 4.5).[45] In the range 400-500 cm^{-1}, the O-Mo-O symmetric and anti-symmetric bending vibrations can be observed, together with the Cu-OH stretching. The bands between 600-700 cm^{-1} are attributable to the (Cu-Mo-O) stretching and Cu-OH bending. Furthermore, the bands visible from 700 to 1000 cm^{-1} correspond to the Mo-O symmetric and anti-symmetric stretching vibrations within the MoO_4 tetrahedra. The bands at 966 and 917 cm^{-1} represent the symmetric stretching vibration peaks of the Mo=O bond, while the strong band visible at 814 cm^{-1} is due to the anti-symmetric stretching vibration, slightly shifted at higher frequencies with the respect to $Cu_3(MoO_4)_2(OH)_2$_ref (780 cm^{-1}). The band at 1034 cm^{-1} is due to the bending of the Cu(OH)Cu (bridge).

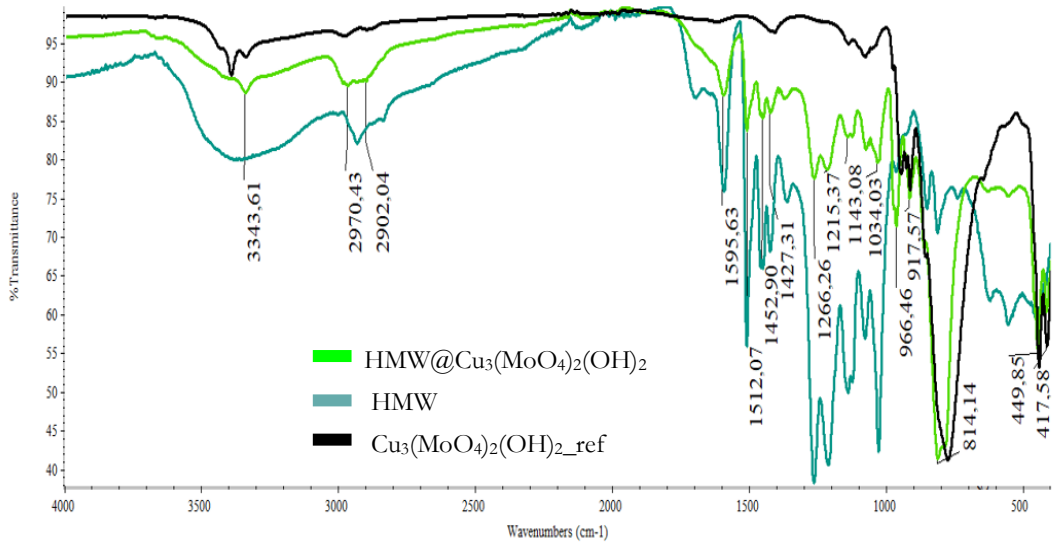

Figure 4.5. Stacked FT-IR spectra of HMW@$Cu_3(MoO_4)_2(OH)_2$ (light green), compared to the one of HMW (dark green) and $Cu_3(MoO_4)_2(OH)_2$_ref (black).

The size and morphology of the crystals embedded in the lignin matrix have been investigated by TEM analysis. The crystals have a size between 50 and 200 nm. There are some lanceolate crystals that have a length of 100-600 nm and width 40-80 nm (Figure 4.6 a). Figure 4.6 b shows the results of the energy dispersive X-Ray spectroscopy (EDX) analysis, demonstrating the presence of both Mo and Cu, with a copper to molybdenum ratio of about 60 to 40.

a)

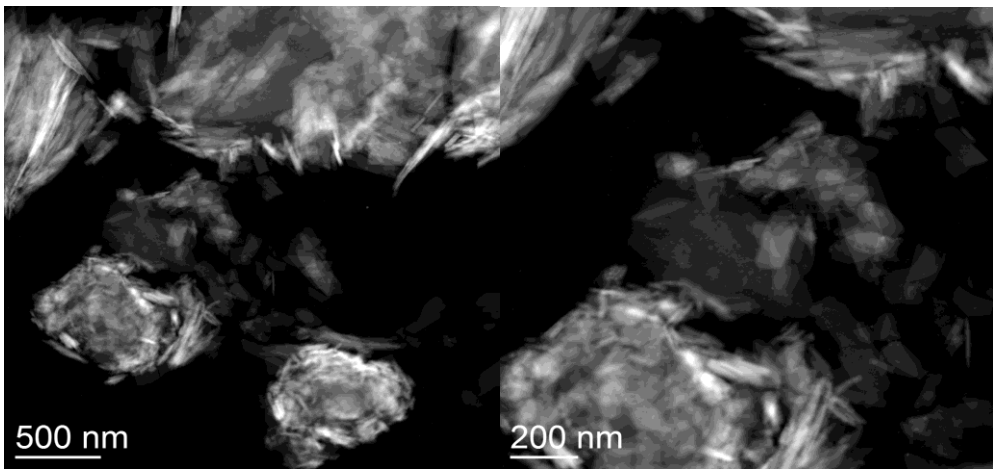

b)

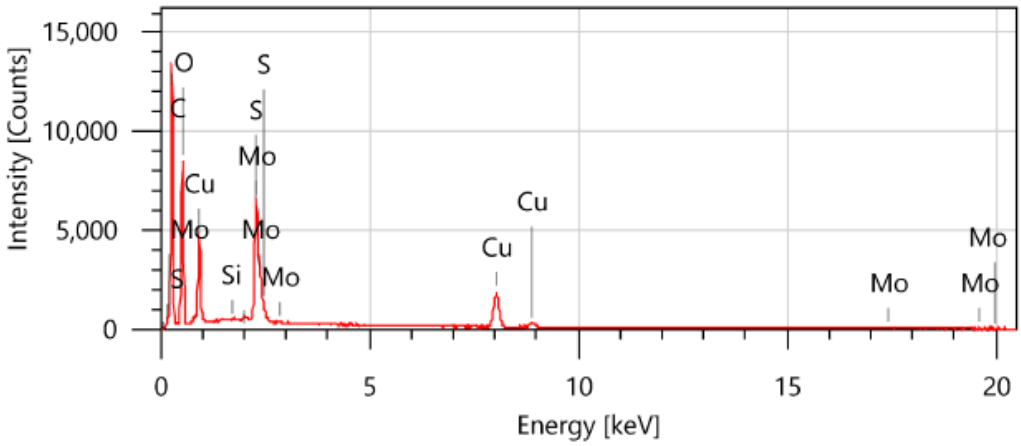

Figure 4.6: a) TEM images of HMW@$Cu_3(MoO_4)_2(OH)_2$; b) EDX analysis of the sample.

EDX with ZAF correction results are reported in Figure S4.4, showing percentages of molybdenum and copper very close to the expected values and that are comparable with ICP-AES data reported for HMW@$Cu_3(MoO_4)_2(OH)_2$_13% (Table 4.5). The distribution of the two metals embedded in the biopolymeric matrix has been evaluated by means of EDX mapping (Figure 4.7), revealing a homogenous distribution of the crystals.

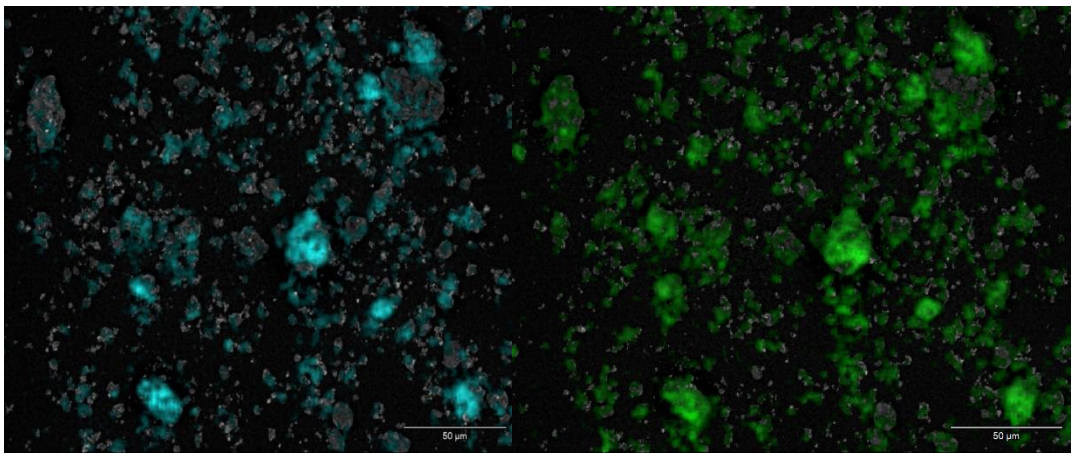

Figure 4.7. EDX mapping shows the metal's distribution inside lignin matrix (molybdenum inlight blue, copper in green).

HMW@$Cu_3(MoO_4)_2(OH)_2$ material has been also studied by dynamic light scattering in aqueous suspension (Figure 4.8). A quite broad size distribution of the nanoparticles can be observed (from 70 to 300 nm), with PDI of 0.250.

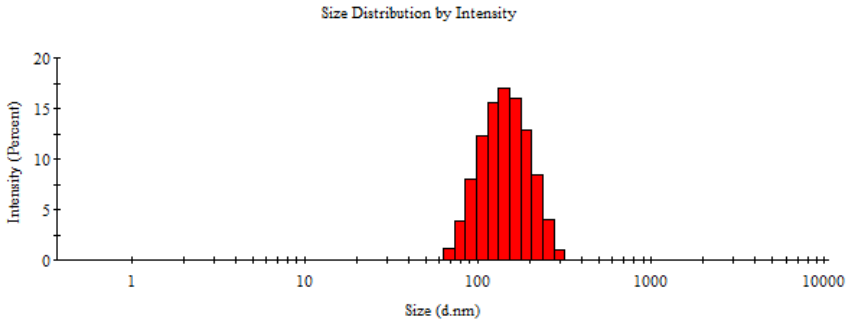

Figure 4.8. Size distribution of HMW@$Cu_3(MoO_4)_2(OH)_2$ in aqueous medium.

TG analysis has been performed, comparing the profile of HMW@$Cu_3(MoO_4)_2(OH)_2$ and of the corresponding lindgrente reference ($Cu_3(MoO_4)_2(OH)_2$_ref) and results are shown in Figure 4.9. For $Cu_3(MoO_4)_2(OH)_2$_ref the total weight loss is 11.8%. Thermal analyses have been performed on both the inorganic phase alone and on the hybrid material, allowing to highlight some interesting behaviour for HMW@$Cu_3(MoO_4)_2(OH)_2$. The TG curve of $Cu_3(MoO_4)_2(OH)_2$_ref aligns with data from the literature and indicates that weight loss increases relatively quickly from room temperature to 300 °C during a first stage. This stage, accounting for a 4.73% mass loss, could correspond to the dehydration of lindgrenite, resulting in the formation of $Cu_3Mo_2O_9$. In the second stage, the weight loss proceeds more gradually until 656 °C, amounting to a 4.71% loss. This phase could be associated with the thermal decomposition of $Cu_3Mo_2O_9$ into CuO and MoO_3. In contrast, HMW@$Cu_3(MoO_4)_2(OH)_2$ exhibits a distinct TG profile, as shown in Figure 4.9b, with a total weight loss of 40.01%. The TG curve reveals a rapid weight loss (8.63%) from room temperature to 290 °C during a first stage, likely due to the presence of water and lindgrenite dehydration, which also results in the formation of $Cu_3Mo_2O_9$. This is followed by a second stage of mass loss (2.7%) from 290 °C to 325 °C, potentially linked to the presence of HMW (see Chapter 2). Additionally, a third transition, absent in both pure lignin and lindgrenite, may result from the interaction of these two components. The weight loss associated with the thermal decomposition of $Cu_3Mo_2O_9$ into CuO and MoO_3 appears to occur at higher temperatures, between 850 and 900 °C.

The DSC (differential scanning calorimetry) profile of HMW@$Cu_3(MoO_4)_2(OH)_2$ shows a peak at 164.47 °C, likely representing a combination of the polymer glass transition temperature and an endothermic process related to the inorganic phase (Figure 4.10). The DSC analysis of the hybrid material also indicates a glass transition at 131.4 °C, consistent with literature values for Kraft lignin (124–174 °C)[56]. This transition occurs approximately 10 °C higher than that observed for HMW alone (122 °C, as discussed in Chapter 2). The DSC profile of $Cu_3(MoO_4)_2(OH)_2$_ref is provided in Figure S4.5 for reference.

a)

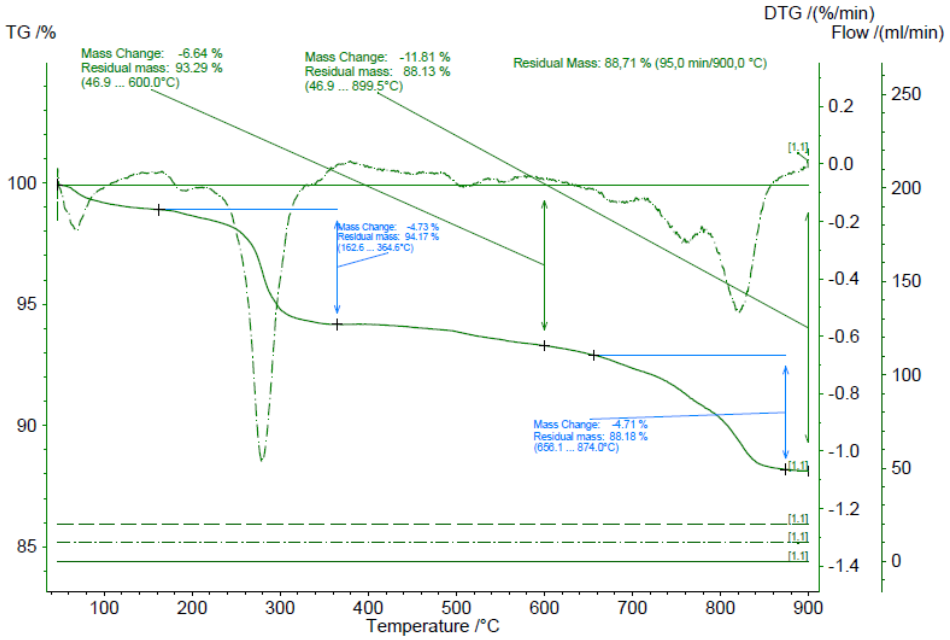

b)

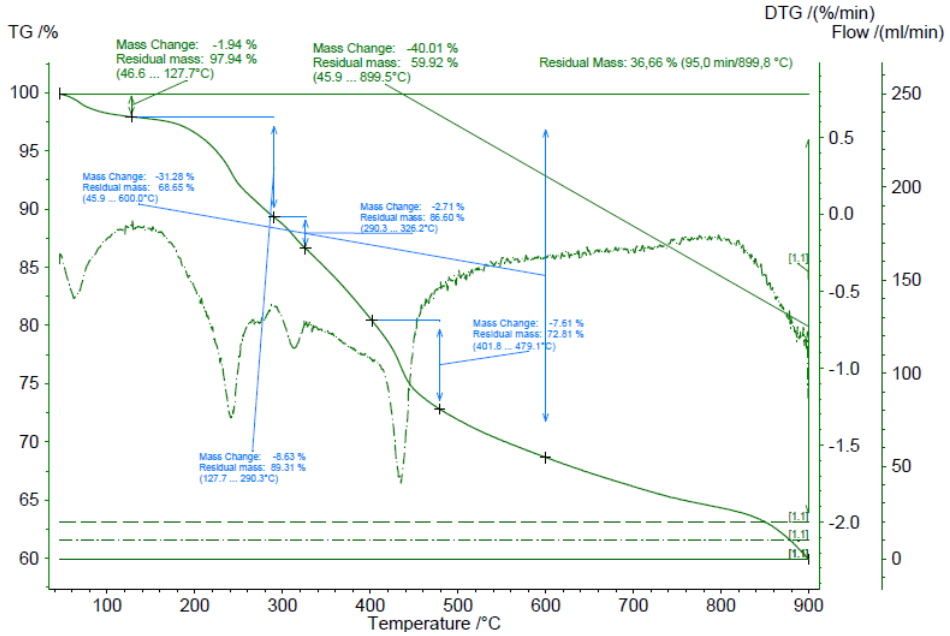

Figure 4.9. a) TGA/DTG curves of $Cu_3(MoO_4)_2(OH)_2$_ref. and b) of HMW@$Cu_3(MoO_4)_2(OH)_2$.

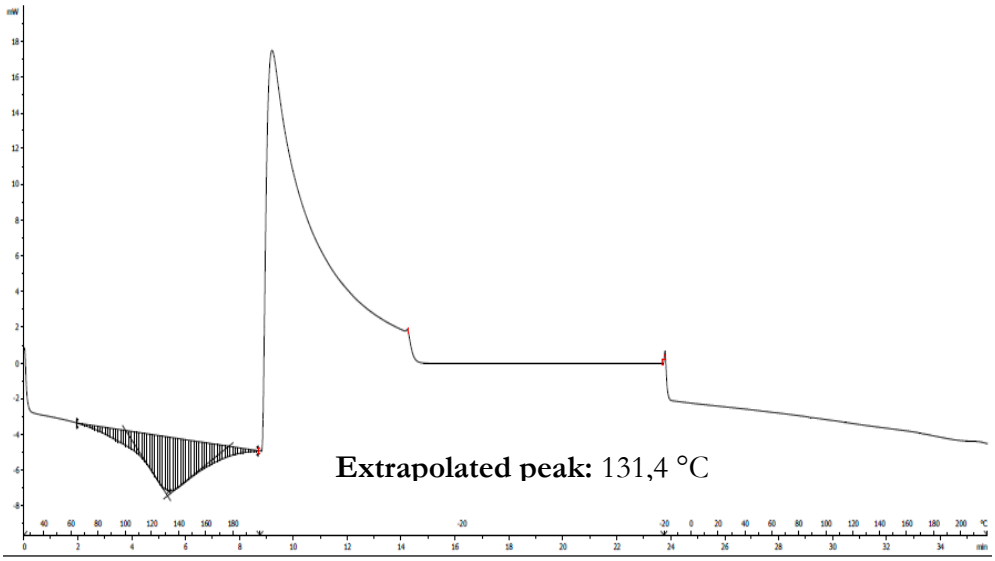

Figure 4.10. DSC profile of HMW@$Cu_3(MoO_4)_2(OH)_2$ expressed both in °C (above the x axis) and in minutes (below the x axis).

SEC analysis has revealed a very comparable trend of M_n, M_w and PD with the respect to those obtained for HMW. We can observe that the absence of a strong alkaline environment during the synthesis prevents the polymer from swelling, unlike the results obtained with HMW@ZnO (Chapter 2), and HMW@ZnO_Cu_2O (Chapter 3); in this case M_n, M_w, and PD values are similar to those of HMW. The chromatogram is reported in Figure S4.6: measurements are performed twice and the mean results are reported in Table 4.3.

Table 4.3. SEC data for HMW and HMW@$Cu_3(MoO_4)_2(OH)_2$

Parameters	HMW	HMW@$Cu_3(MoO_4)_2(OH)_2$
Number average, M_n (Da)	1551	1318
Weight Average, M_w (Da)	5259	4289
Peak maximum, (Da)	2135	2142
Polydispersity, PD	3.39	3.76

After assessing the main characteristics of the hybrid material obtained, we have decided to vary the copper salt reagent used for the reaction to infer whether the choice of different anions can influence the obtainment of the final material. As shown in Figure 4.11, the diffractograms of materials obtained from different metal sources ($CuCl_2 \cdot 2H_2O$, $CuSO_4 \cdot 5H_2O$ or $Cu(CH_3COO)_2 \cdot H_2O$) are quite superimposable: the relative intensities of the peaks in the diffraction pattern and the peak width do not change significantly.

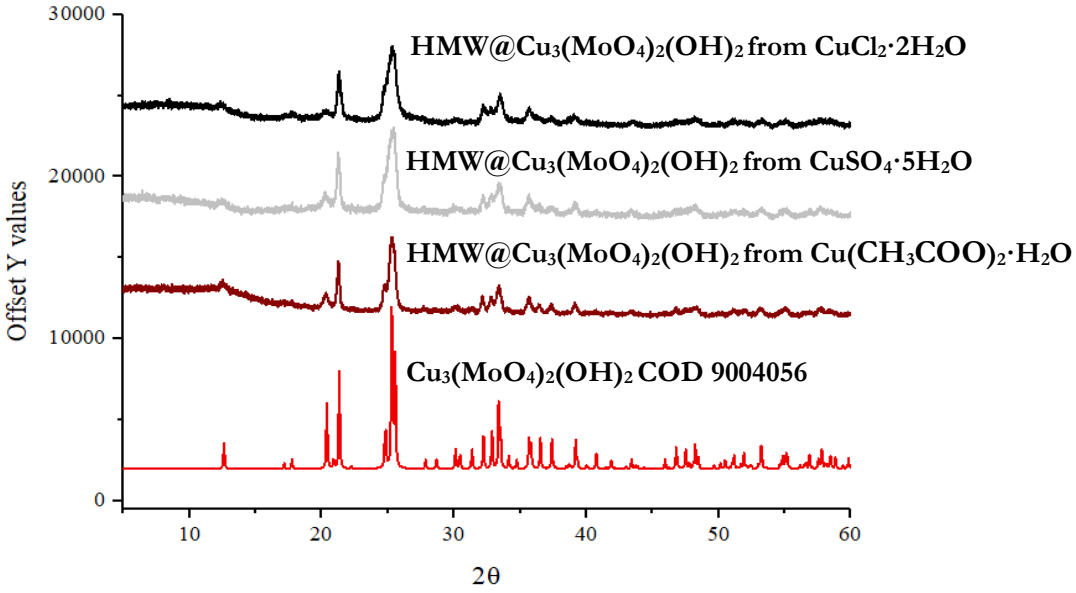

Figure 4.11. The experimental PXRD pattern of HMW@$Cu_3(MoO_4)_2(OH)_2$ obtained from $CuCl_2 \cdot 2H_2O$ salt (black line), from $CuSO_4 \cdot 5H_2O$ salt (light grey line), from $Cu(CH_3COO)_2 \cdot H_2O$ salt (dark red line), compared to the one of lindgrenite COD 9004056 (red line).

It is possible to conclude that the choice of the starting material can be set exclusively on the cheapest one, taking into account the scale up perspective. We have further investigated the possibility of changing the Mo^{6+}:Cu^{2+} ratio (1 eq Mo^{6+}: 1 eq OH^-: 0.5 eq Cu^{2+}) using NH_4OH as base: it has been possible to isolate a different crystalline phase embedded in the lignin matrix, corresponding to $NH_4Cu_2(MoO_4)_2(OH)(H_2O)$. All the peaks present in the pattern of the synthesized HMW@$NH_4Cu_2(MoO_4)_2(OH)(H_2O)$ and of the $NH_4Cu_2(MoO_4)_2(OH)(H_2O)$_ref are in fact in accordance with the reference diffraction pattern of $NH_4Cu_2(MoO_4)_2(OH)(H_2O)$ (COD 1538471) (Figure 4.12). Differently, using the same operating conditions but with a molar ratio 1:1 Mo^{6+}:Cu^{2+}, a mixture of $NH_4Cu_2(MoO_4)_2(OH)(H_2O)$ and lindgrenite has been obtained, as reported in Figure S4.7. It is therefore necessary an excess of molybdenum to ensure the isolation of a unique crystalline bimetallic phase.

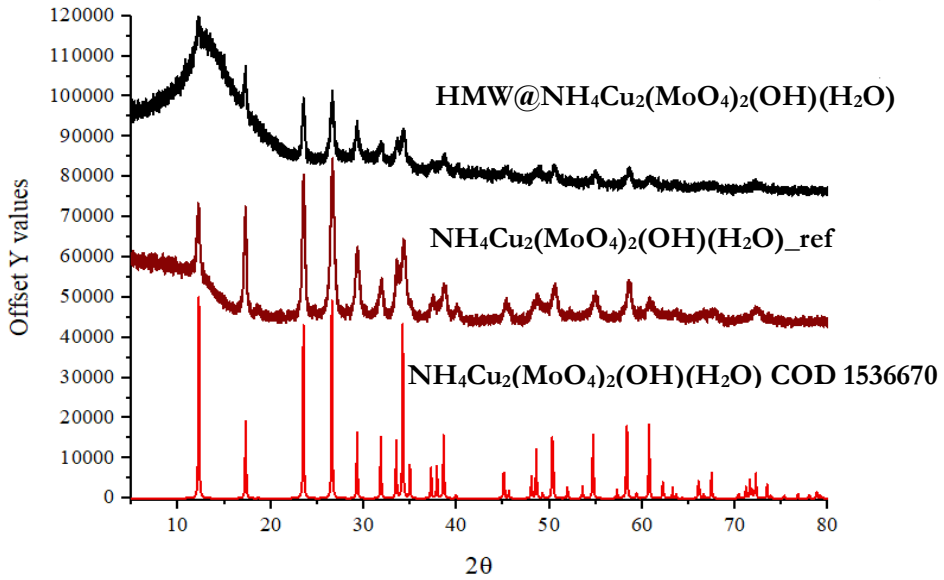

Figure 4.12. The experimental PXRD pattern of HMW@$NH_4Cu_2(MoO_4)_2(OH)(H_2O)$ (black line) compared to the one of $NH_4Cu_2(MoO_4)_2(OH)(H_2O)$_ref (dark red line) and $NH_4Cu_2(MoO_4)_2(OH)(H_2O)$ COD 1536670 (red line).

The stacked FT-IR spectra of HMW@$NH_4Cu_2(MoO_4)_2(OH)(H_2O)$ compared to the ones of HMW and $NH_4Cu_2(MoO_4)_2(OH)(H_2O)$_ref are shown in Figure S4.8, confirming the correspondence with the reference phase. Figure 4.13 shows the FT-IR spectrum of HMW@$NH_4Cu_2(MoO_4)_2(OH)(H_2O)$ compared to the one of HMW@$Cu_3(MoO_4)_2(OH)_2$. HMW infrared spectrum shows the typical signals that feature Kraft lignin, as described before. The spectra are quite similar apart from some aspects: in HMW@$NH_4Cu_2(MoO_4)_2(OH)(H_2O)$ there is a band at 503 cm^{-1} due to the symmetric stretching of (CuOMo).[47] It is also possible to notice the presence of the band at 1416 cm^{-1} in the HMW@$NH_4Cu_2(MoO_4)_2(OH)(H_2O)$ spectrum, which could be related to the asymmetric bending of NH_4^+ and an enlargement of the band at 1600 cm^{-1} ascribable to the symmetric bending of this group. Furthermore, a significant difference can be noticed in the range 2800-3400 cm^{-1}, due to the bending and stretching of the N-H group.

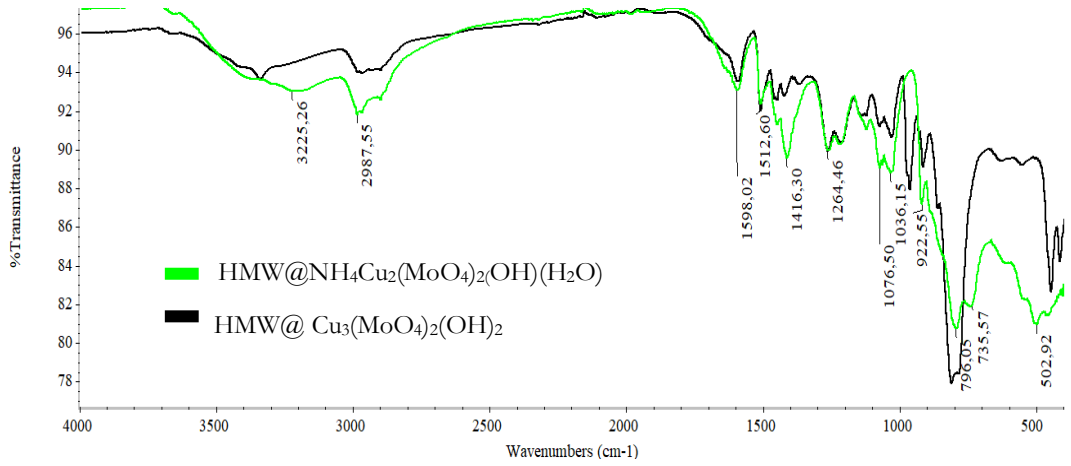

Figure 4.13. Stacked FT-IR spectra of HMW@$NH_4Cu_2(MoO_4)_2(OH)(H_2O)$ (light green), compared to the one of HMW@$Cu_3(MoO_4)_2(OH)_2$ (black).

The size distribution of the HMW@$NH_4Cu_2(MoO_4)_2(OH)(H_2O)$ material has been studied in aqueous suspension by DLS analysis. A quite broad size distribution of the nanoparticles can be observed (from 60 to 255 nm), with a polydispersity index (PDI) of 0.300 (Figure 4.14).

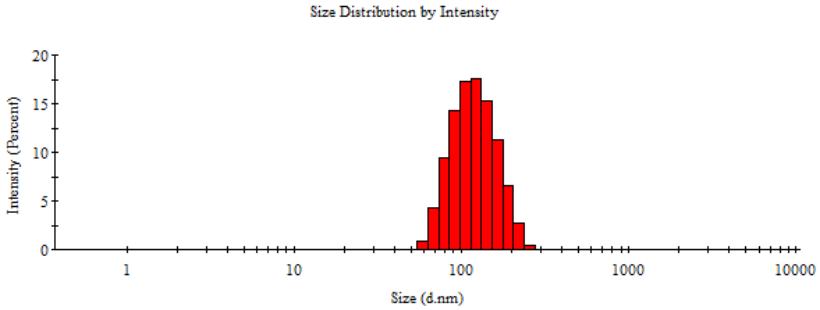

Figure 4.14. Size distribution of HMW@$NH_4Cu_2(MoO_4)_2(OH)(H_2O)$ in aqueous medium.

We have also investigated the possibility to employ $Na_2MoO_4 \cdot 2H_2O$ as alternative reagent in the synthesis of HMW@ $Cu_3(MoO_4)_2(OH)_2$ and of $Cu_3(MoO_4)_2(OH)_2$_ref, by using the same molar ratios and conditions described before, but without the addition of a base, since in this case the pH of the slurry is already around 5-6. The experimental PXRD pattern of HMW@Mo_Cu material agrees with the reference diffraction pattern of lindgrenite [$Cu_3(MoO_4)_2(OH)_2$] and in Figure 4.15 the experimental pattern is compared to the one obtained by using ammonium molybdate and the one obtained for $Cu_3(MoO_4)_2(OH)_2$_ref.

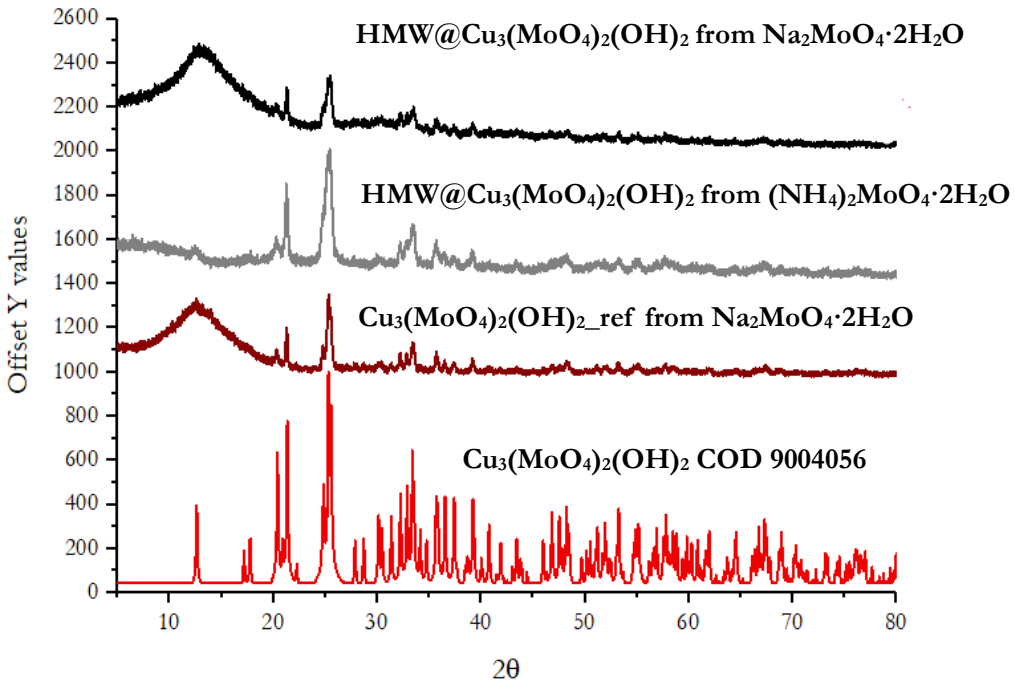

Figure 4.15. Experimental PXRD pattern of HMW@$Cu_3(MoO_4)_2(OH)_2$ obtained from sodium molybdate as reagent (black line), and from ammonium molybdate (grey line), $Cu_3(MoO_4)_2(OH)_2$_ref from $Na_2MoO_4 \cdot 2H_2O$ (dark red line), compared to the one of lindgrenite COD 9004056 (red line).

The size and morphology of the crystals embedded in the lignin matrix of HMW@$Cu_3(MoO_4)_2(OH)_2$ from $Na_2MoO_4 \cdot 2H_2O$ have been investigated by TEM analysis. The crystals have sizes between 50 and 500 nm. Small crystals with a size of 10-20 nm are also present (Figure 4.16 a). Aside from the presence of small NPs, there are not significant differences in terms of morphology and crystal size compared with the phase synthesized from ammonium molybdate. Results are compared in Table S4.1. Figure S4.9 shows the results of the energy dispersive X-Ray spectroscopy (EDX) analysis, demonstrating the presence of both Mo and Cu, with a copper to molybdenum ratio of about 60 to 40. Selected Area Electron Diffraction (SAED) have been collected from an area of 200 nm along with the corresponding radial average. The table shows the most intense reflections, that can all be indexed as lindgrenite (AMCSD 005073), Figure S4.10. $Cu_3(MoO_4)_2(OH)_2$_ref from $Na_2MoO_4 \cdot 2H_2O$ have been also studied by TEM, which evidences crystals having sizes ranging from 50 to 500 nm (Figure 4.16 b.). For the crystals synthesized in the absence of lignin the presence of small NPs has not been detected, and it seems that the crystals synthesized in the absence of lignin have a larger thickness (Table S4.1).

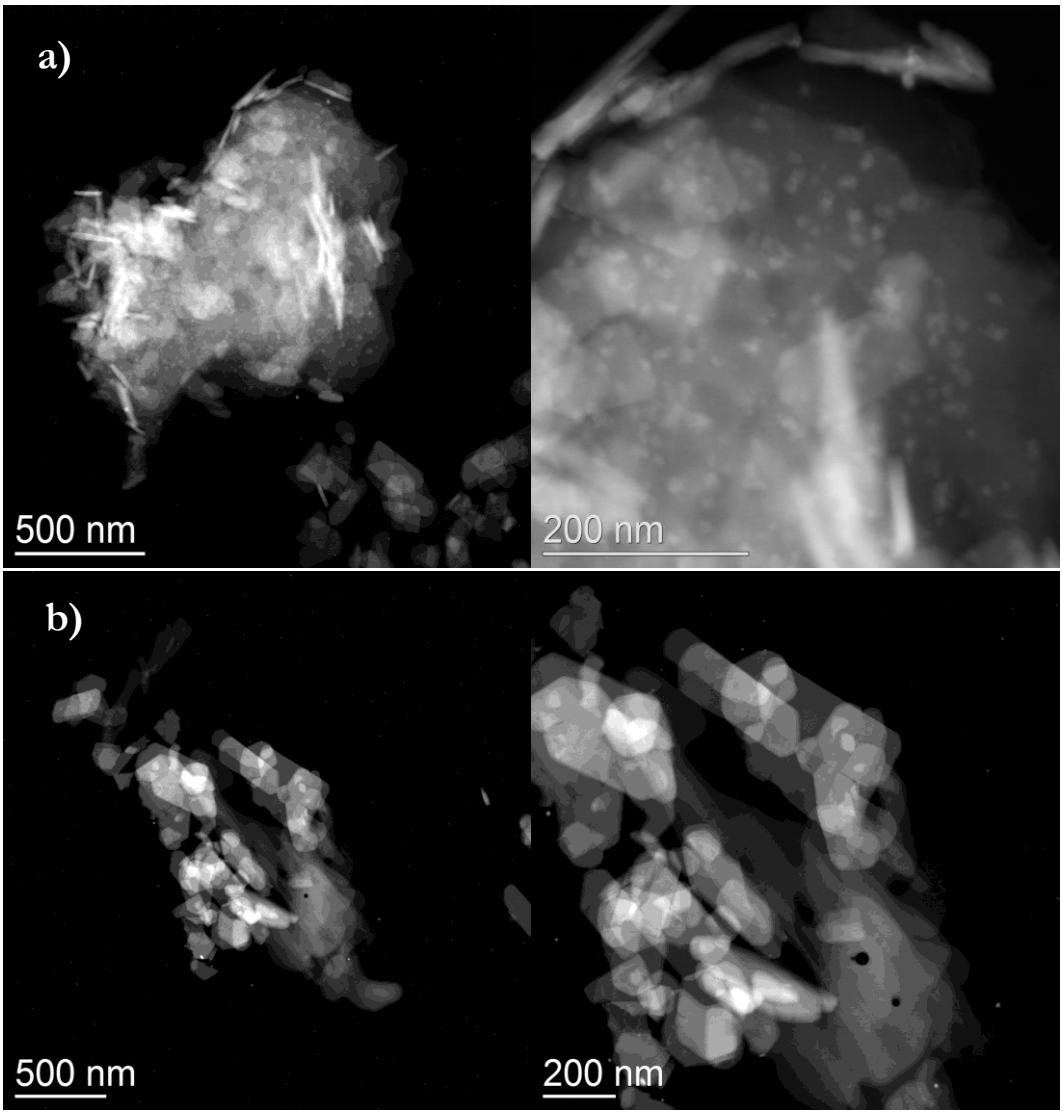

Figure 4.16: a) TEM images of HMW@$Cu_3(MoO_4)_2(OH)_2$ from $Na_2MoO_4 \cdot 2H_2O$; b) TEM images of $Cu_3(MoO_4)_2(OH)_2$_ref from $Na_2MoO_4 \cdot 2H_2O$.

We have also investigated the possibility to obtain Zn/Mo crystalline phases within the lignin matrix. Differently from the case of copper, it has not been possible with zinc to completely substitute the cation present in the starting molybdate reagent: the phases isolated have been identified by PXRD as $NH_4Zn_2(MoO_4)_2(OH)(H_2O)$, $NaZn_2(MoO_4)_2(OH)(H_2O)$ or $KZn_2(MoO_4)_2(OH)(H_2O)$, depending on the base employed. It is in fact possible to select the cation by changing the base (NH_4OH, NaOH or KOH) during the synthesis. $Zn_3(OH)_2(MoO_4)_2$ the phase corresponding to lindgrenite with zinc in place of copper, has been isolated and described in the literature, but with synthetic conditions[57] very different with respect to the ones here employed. $NH_4Zn_2(MoO_4)_2(OH)(H_2O)$ has been also prepared in the absence of lignin (named $NH_4Zn_2(MoO_4)_2(OH)(H_2O)$_ref) to verify the influence of the matrix on dimensions or morphologies of the crystalline nanoparticles. In Figure 4.17, all the peaks in the diffraction pattern of the synthesized HMW@$NH_4Zn_2(MoO_4)_2(OH)(H_2O)$ match those in the reference pattern for $NH_4Zn_2(MoO_4)_2(OH)(H_2O)$ (COD 1538471). Similarly, the pattern for $NH_4Zn_2(MoO_4)_2(OH)(H_2O)$_ref also aligns with the reference. However, an amorphous band is observed in the $NH_4Zn_2(MoO_4)_2(OH)(H_2O)$_ref sample.

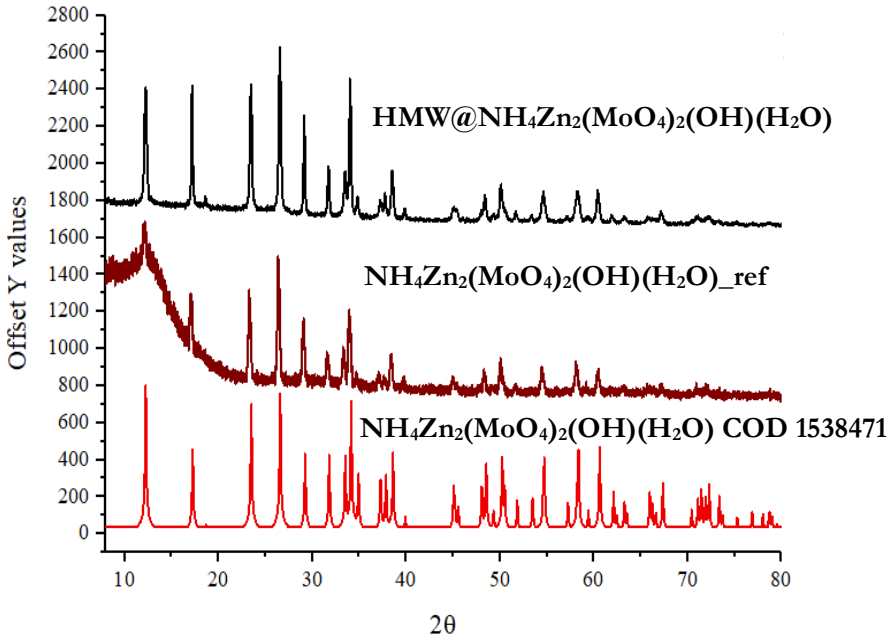

Figure 4.17. Experimental PXRD pattern of HMW@$NH_4Zn_2(MoO_4)_2(OH)(H_2O)$ (black) in comparison with $NH_4Zn_2(MoO_4)_2(OH)(H_2O)$_ref (dark red) and $NH_4Zn_2(MoO_4)_2(OH)(H_2O)$ data bank reference COD 1538471 (red)

The FT-IR spectra of HMW@$NH_4Zn_2(MoO_4)_2(OH)(H_2O)$ is, as expected, quite similar to the one of HMW@$NH_4Cu_2(MoO_4)_2(OH)(H_2O)$: the comparison with the spectra of HMW and $NH_4Zn_2(MoO_4)_2(OH)(H_2O)$_ref is shown in Figure 4.18. The infrared spectrum of $NH_4Zn_2(MoO_4)_2(OH)(H_2O)$_ref shows a band at 481 cm^{-1}, which is relatable to the Zn-Mo-O symmetric stretching vibrations. Furthermore, the band visible at 925 cm^{-1} is related to the symmetric stretching vibration peaks of the Mo-O bond. The strong band visible at 735 cm^{-1} of $NH_4Zn_2(MoO_4)_2(OH)(H_2O)$_ref is due to the anti-symmetric stretching vibration of Mo-O, that for HMW@$NH_4Zn_2(MoO_4)_2(OH)(H_2O)$ is shifted to

higher frequencies (809 cm^{-1}). The band at 1413 cm^{-1} is ascribable to the asymmetric bending of NH_4^+, while the one at 1633 cm^{-1} is related with the symmetric one. The broad band centred at 3200 cm^{-1} could be associated with the stretching of N-H and O-H bonds.

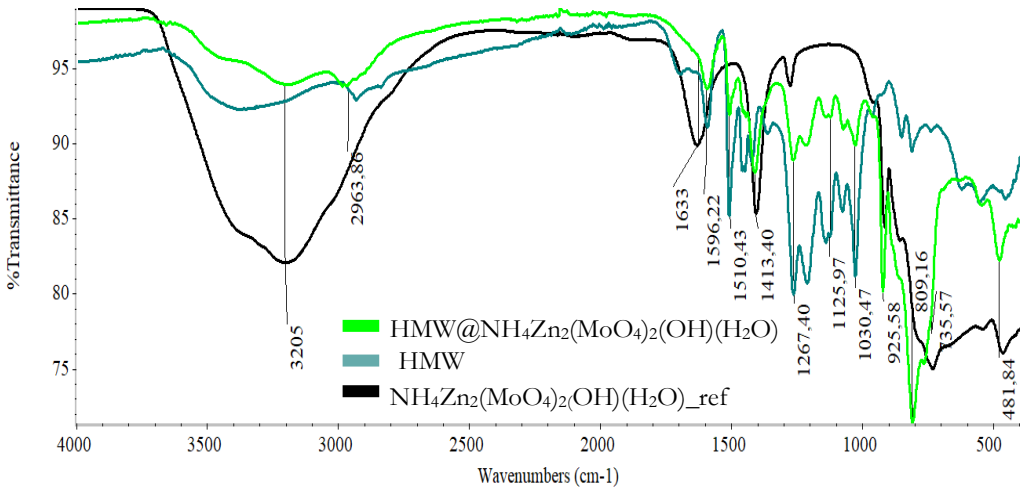

Figure 4.18. Stacked FT-IR spectra of HMW@$NH_4Zn_2(MoO_4)_2(OH)(H_2O)$ (light green), compared to the one of HMW (dark green) e $NH_4Zn_2(MoO_4)_2(OH)(H_2O)$_ref (black).

The size and morphology of the HMW@$NH_4Zn_2(MoO_4)_2(OH)(H_2O)$ crystals have been investigated by TEM analysis. The crystals have a size between 50 and 200 nm (Figure 4.19 a); Figure 4.19 b shows the results of the energy dispersive X-Ray spectroscopy (EDX) analysis, demonstrating the presence of both Mo and Zn, with a ratio among zinc and molybdenum of 1 to 1. The dimensions of the crystals are comparable to those found in HMW@$Cu_3(MoO_4)_2(OH)_2$. EDX with ZAF correction results are reported in Figure S4.11, showing percentages of molybdenum and zinc very close to the expected values, comparable to ICP-AES data obtained for HMW@$NH_4Zn_2(MoO_4)_2(OH)(H_2O)$_14% (reported in Table 4.5).

a)

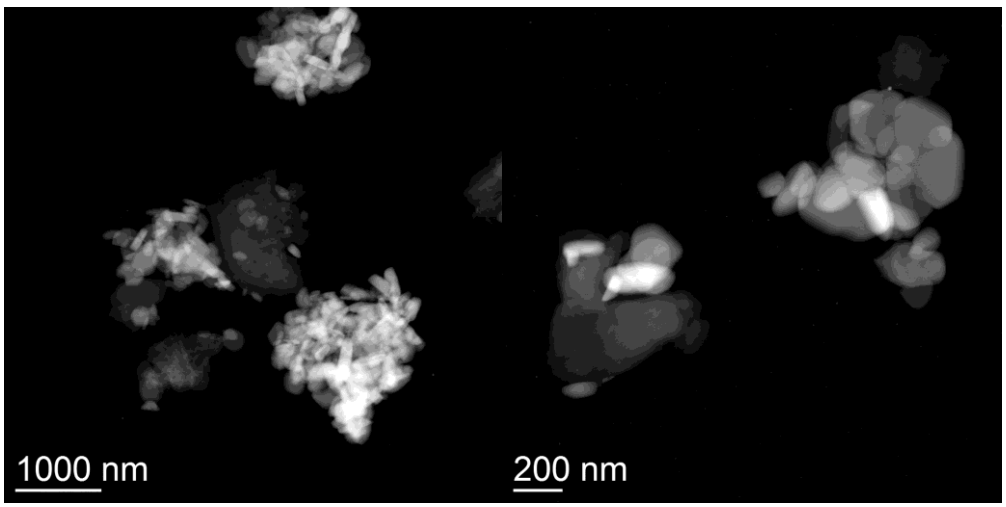

b)

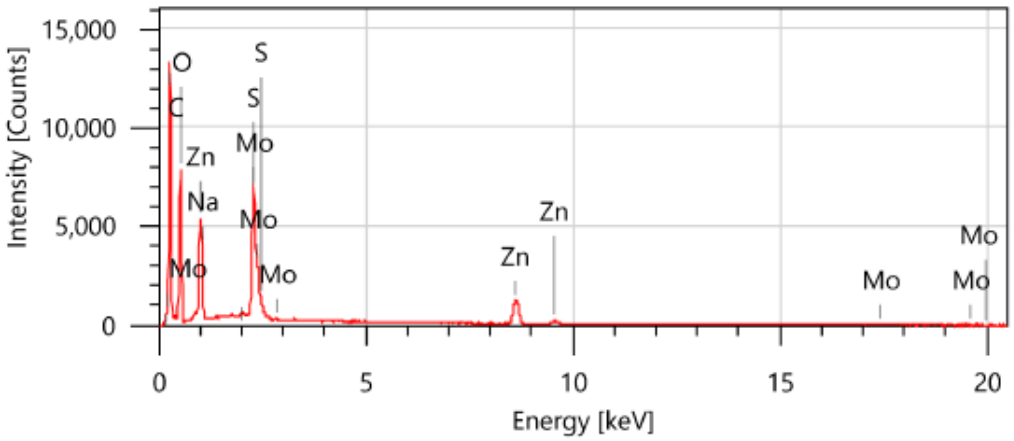

Figure 4.19. a) TEM images of HMW@$NH_4Zn_2(MoO_4)_2(OH)(H_2O)$; b) EDX analysis of the sample.

The distribution of the two metals embedded in the biopolymeric matrix has been evaluated by means of EDX mapping (Figure 4.20), revealing a homogenous dispersion of the two metals in the final material.

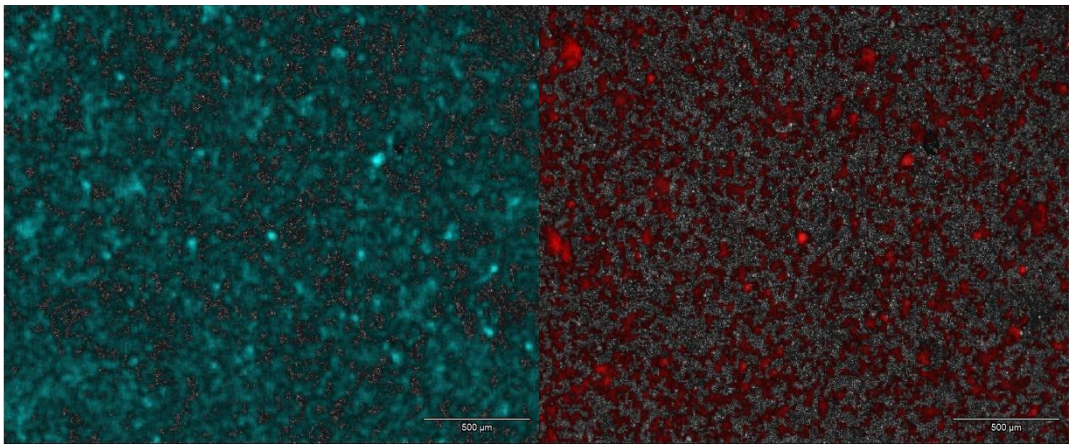

Figure 4.20. EDX mapping shows the metal's distribution within lignin matrix (molybdenum coloured in light blue, zinc in red).

The size distribution of HMW@$NH_4Zn_2(MoO_4)_2(OH)(H_2O)$ material has been studied in aqueous suspension by DLS analysis. A quite broad size distribution of the nanoparticles can be observed (70-200 nm), with a polydispersity index (PDI) of 0.200 (Figure 4.21).

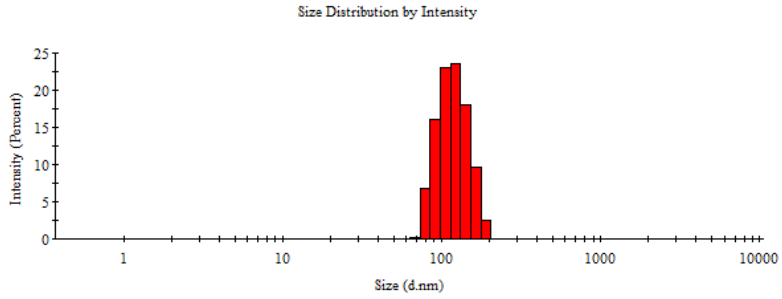

Figure 4.21. Size distribution of HMW@$NH_4Zn_2(MoO_4)_2(OH)(H_2O)$ in aqueous medium.

Thermogravimetric analysis (TG) has been performed in a nitrogen atmosphere at a heating rate of 10 °C/min, from 47 to 900 °C. As shown in Figure 4.22a, the $NH_4Zn_2(MoO_4)_2(OH)(H_2O)$_ref sample exhibits a mass loss of 10.5%, likely due to the release of NH_3 and H_2O. The TG curve is similar to that reported in the literature for $NH_4Cu_2(MoO_4)_2(OH)(H_2O)$ and indicates that weight loss occurs around 260 °C. The TG profile for HMW@$NH_4Zn_2(MoO_4)_2(OH)(H_2O)$, shown in Figure 4.22 b, appears to reflect the combined thermal behaviour of its two components. Two weight losses can be observed: the first occurs around 270 °C, resembling the behaviour of $NH_4Zn_2(MoO_4)_2(OH)(H_2O)$_ref, while the second, occurring between 300 °C and 400 °C, may be attributed to the presence of HMW (see Chapter 2).

a)

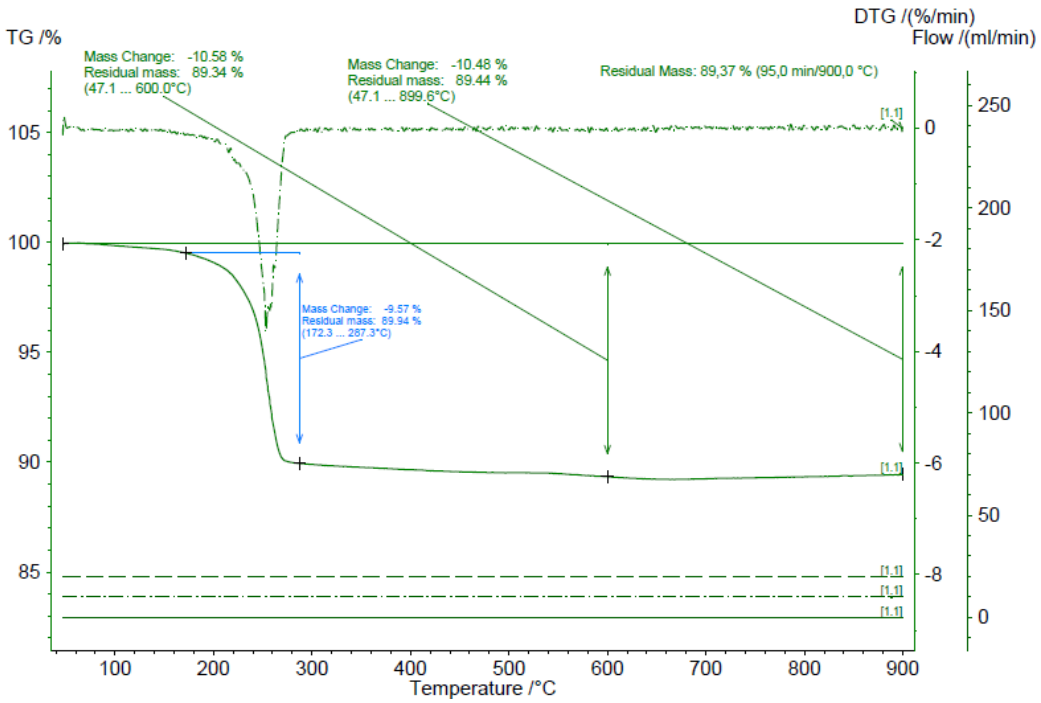

b)

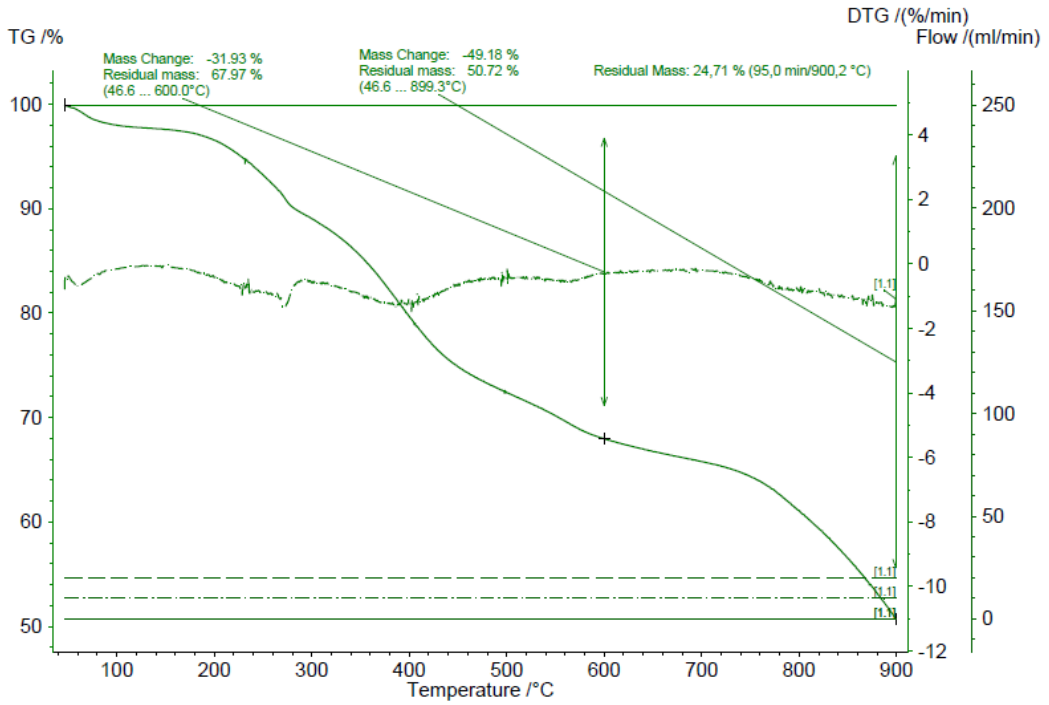

Figure 4.22. a) TGA/DTG curves of $NH_4Zn_2(MoO_4)_2(OH)(H_2O)$_ref. b) TGA/DTG curves of HMW@$NH_4Zn_2(MoO_4)_2(OH)(H_2O)$

DSC profile of $NH_4Zn_2(MoO_4)_2(OH)(H_2O)$_ref shows no peak from 20 to 200 °C (Figure S4.12 a), while a glass transition at 129.7 °C related to the polymer, can be observed for the hybrid material $NH_4Zn_2(MoO_4)_2(OH)(H_2O)$ in agreement with the literature data for Kraft lignin (124–174 °C) (Figure S4.12 b).[56]

SEC analysis has revealed a very comparable trend of M_n, M_w and PD for the hybrid material with the respect to HMW alone. We can observe that the absence of a strong alkaline environment during the synthesis prevents the polymer from swelling, unlike the results obtained with HMW@ZnO (Chapter 2) and HMW@ZnO_Cu_2O (Chapter 3), giving M_n, M_w, and PD values similar to those of HMW. The chromatogram is reported in Figure S4.13: measurements are performed twice and the mean results are reported in Table 4.4.

Table 4.4. SEC results of HMW and HMW@$NH_4Zn_2(MoO_4)_2(OH)(H_2O)$

Parameters	HMW	HMW@ $NH_4Zn_2(MoO_4)_2(OH)(H_2O)$
Number average, M_n (Da)	1551	1428
Weight Average, M_w (Da)	5259	4976
Peak maximum, (Da)	2135	2325
Polydispersity, PD	3.39	3.49

We have also investigated in this case the possibility to use different zinc salts (zinc acetate dihydrate, zinc sulphate heptahydrate and zinc chloride) and, similarly to what have been observed for copper salts, the metal source does not affect the final outcome (Figure S4.14).

We have further investigated the role of reaction time for both hybrid materials, HMW@$Cu_3(MoO_4)_2(OH)_2$ and HMW@$NH_4Zn_2(MoO_4)_2(OH)(H_2O)$. During the synthesis of HMW@$Cu_3(MoO_4)_2(OH)_2$, the precipitation of an aquamarine colloid has been observed immediately after the addition of the base, which turns to a green powder after a few times. The initial reaction time adopted for the isolation of the lindgrenite phase has been set to 24 hours. We have therefore investigated the possibility to have the complete conversion to lindgrenite at shorter reaction times. The study was performed using PXRD. After stirring for 10 minutes at room temperature (RT), the reaction mixture has been centrifuged. The solid fraction has been separated, dried overnight at 85°C, and analysed by PXRD (Figure S4.15a), which revealed the presence of lindgrenite along with some peaks attributed to impurities. The aquamarine-coloured supernatant was also collected and dried at 85°C. PXRD analysis (Figure S4.15b) indicated that the reaction was not yet complete after 10 minutes, as traces of the reagents $NH_4MoO_4{\cdot}2H_2O$ and $(NH_4)_2Cu(SO_4)_2(H_2O)_6$ were still detectable. The reaction has been then tested at various time intervals. The only presence of lindgrenite phase has been achieved after 5 hours of reaction, as confirmed by PXRD, which showed a pattern comparable to that obtained after 24 hours (Figure 4.23). But to assess whether the conversion is completed after 5 hours ICP-AES studies will be conducted.

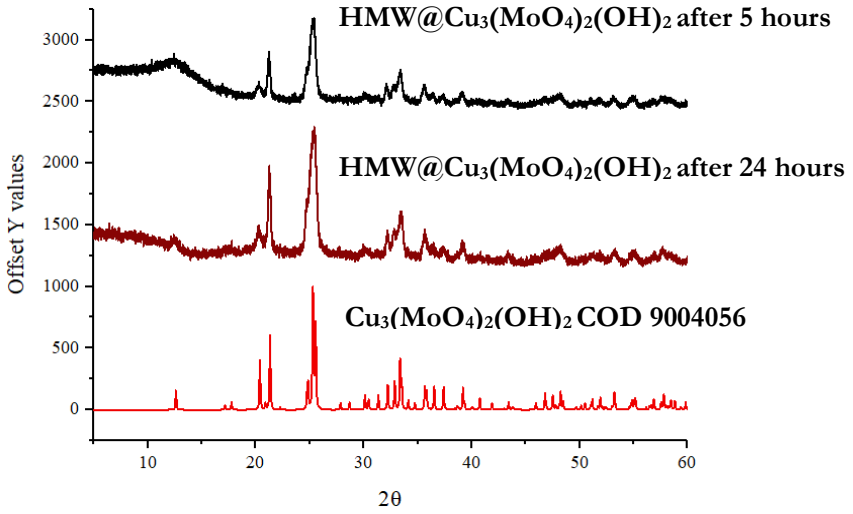

Figure 4.23. The experimental PXRD pattern of HMW@$Cu_3(MoO_4)_2(OH)_2$ obtained after 5 hours (black pattern), after 24 hours of stirring (dark red line), compared to the one of lingrenite COD 9004056

A similar study has been conducted on HMW@$NH_4Zn_2(MoO_4)_2(OH)(H_2O)$. After 10 minutes of reaction the pattern results also in this case comparable to the one obtained after 24 hours (Figure 4.24), demonstrating the possibility to reduce the reaction time and opening perspectives for *in situ* preparations for practical applications.

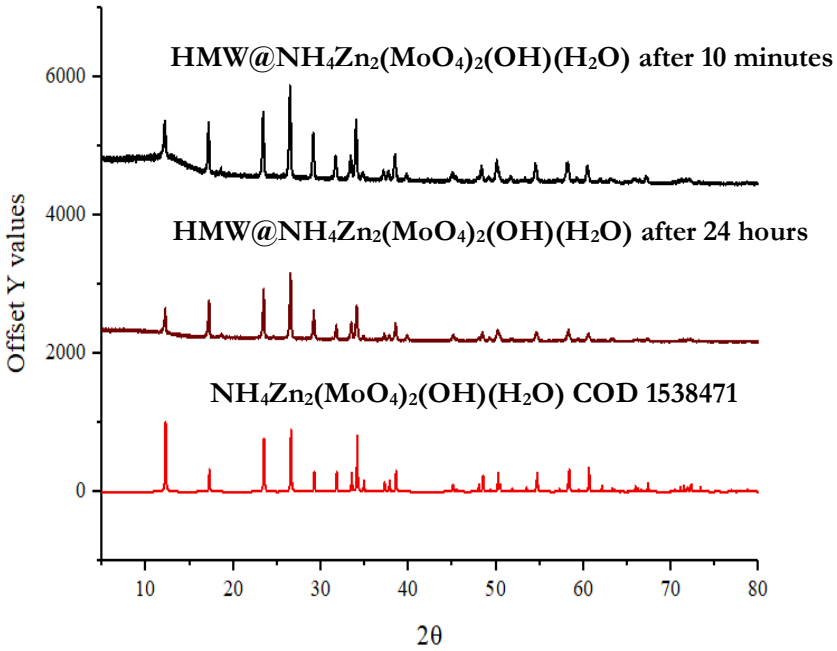

Figure 4.24. The experimental PXRD pattern of HMW@$NH_4Zn_2(MoO_4)_2(OH)(H_2O)$ obtained isolating the product after 10 minutes of reaction (black) compared to the one of HMW@$NH_4Zn_2(MoO_4)_2(OH)(H_2O)$ obtained isolating the product after 24 hours of stirring at RT (dark red) and $NH_4Zn_2(MoO_4)_2(OH)(H_2O)$ COD 1538471 (red).

The possibility to tune the loading of the metals inside the materials has been also studied, knowing that have different lignin:metal ratios could give interesting and diversified features for biological applications. The materials have been prepared in order to obtain 4%, 10%, 14% and 20% Mo loading, by changing the lignin/metals salts/OH^- ratio, for both HMW@$Cu_3(MoO_4)_2(OH)_2$ and HMW@$NH_4Zn_2(MoO_4)_2(OH)(H_2O)$ materials. The obtainment of the desired phase has been confirmed by PXRD (Figure 4.25 and Figure S4.16, respectively). The loading of the metals has been confirmed by ICP-AES as reported in Table 4.5. From the obtained results, it can be concluded that the best loading results have been achieved for intermediate percentages.

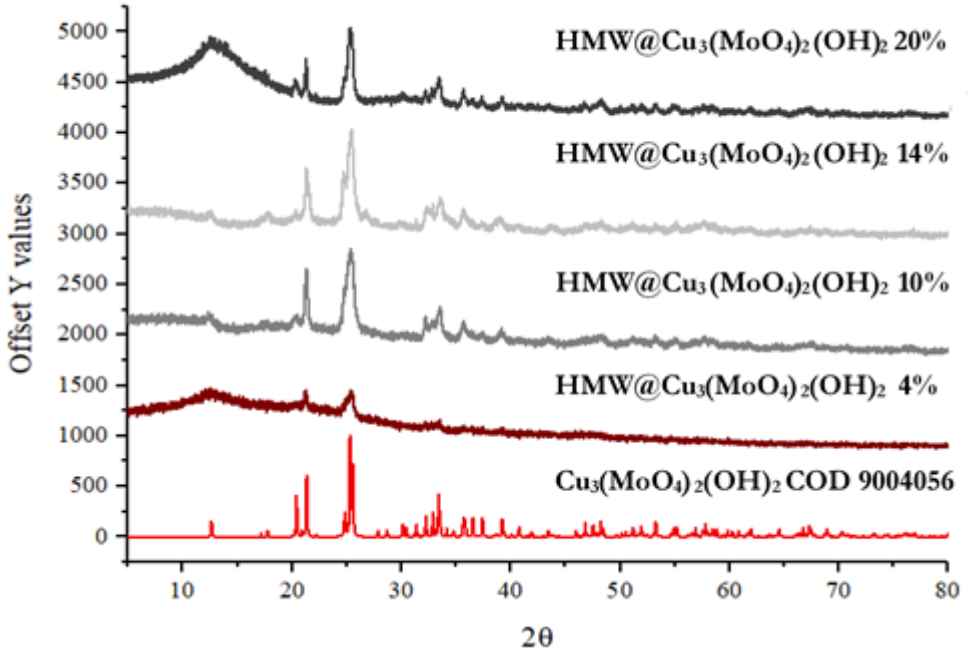

Figure 4.25. The experimental PXRD pattern of HMW@ $Cu_3(MoO_4)_2(OH)_2$_4%(dark red), 10% (dark grey), 14% (light grey), 20% (black) compared to the one of lindgrenite COD 9004056 (red).

Table 4.5. ICP-AES analysis of HMW@$NH_4Zn_2(MoO_4)_2(OH)(H_2O)$ and HMW@ $Cu_3(MoO_4)_2(OH)_2$ samples with different loading of molybdenum (4-20%). For HMW@$Cu_3(MoO_4)_2(OH)_2$ materials the % refer to both molybdenum and copper calculated amounts. In HMW@$NH_4Zn_2(MoO_4)_2(OH)(H_2O)$ materials the calculated percentages refer to molybdenum and zinc, respectively. After mineralization, the presence of some white floccules could be observed in certain samples, whose origin must be verified in future studies.

Sample	% Mo ± SD	% Cu ± SD
HMW@$Cu_3(MoO_4)_2(OH)_2$_4%	2.74±0.05	4.02±0.06
HMW@$Cu_3(MoO_4)_2(OH)_2$_10%	9.1±0.1	11.0±0.1
HMW@$Cu_3(MoO_4)_2(OH)_2$_13%	11.6±0.1	14.69±0.03
HMW@$Cu_3(MoO_4)_2(OH)_2$_20%	22.5±0.3	15.2±0.3
Sample	% Mo ± SD	% Zn ± SD
HMW@$NH_4Zn_2(MoO_4)_2(OH)(H_2O)$_4%_3%	1.02±0.03	4.39±0.04
HMW@$NH_4Zn_2(MoO_4)_2(OH)(H_2O)$_10%_8%	10.35±0.04	10.8 ±0.1
HMW@$NH_4Zn_2(MoO_4)_2(OH)(H_2O)$_14%_10%	14.3±0.2	13.1±0.3
HMW@$NH_4Zn_2(MoO_4)_2(OH)(H_2O)$_20%_18%	13.5±0.2	16.4±0.2

Another interesting aspect is related to the possibility of changing the cation in the bimetallic Mo/Zn materials, substituting ammonium with other monovalent cations that could be of interest. Therefore, the use of different alkaline sources (KOH and NaOH) has been evaluated in addition to NH_4OH. PXRD analyses confirmed the possibility to modulate the final phase, obtaining HMW@$NaZn_2(MoO_4)_2(OH)(H_2O)$ or HMW@$KZn_2(MoO_4)_2(OH)(H_2O)$ (Figure 4.26). An excess of a base is necessary (at least 2 equivalents), in order to ensure complete cation substitution: otherwise, a mixture of phases has been isolated, with the simultaneous presence of $NaZn_2(MoO_4)_2(OH)(H_2O)$ and $NH_4Zn_2(MoO_4)_2(OH)(H_2O)$, as shown in Figure S4.17. $KZn_2(MoO_4)_2(OH)(H_2O)$ has

not a corresponding data bank reference, but the pattern is similar to the one of $NaZn_2(MoO_4)_2(OH)(H_2O)$ and the presence of potassium has been confirmed by ICP-AES in Table 4.6.

Table 4.6. ICP-AES analysis of $HMW@KZn_2(MoO_4)_2(OH)(H_2O)$. After mineralization, the presence of some white floccules could be observed, whose origin must be verified in future studies.

Sample	Calculated % K	% K ± SD
$HMW@KZn_2(MoO_4)_2(OH)(H_2O)$	5%	4.67 ±0.03
	Calculated % Mo	% Mo ± SD
	13%	12.7 ±0.2
	Calculated % Zn	% Zn ± SD
	10 %	16.7 ± 0.2

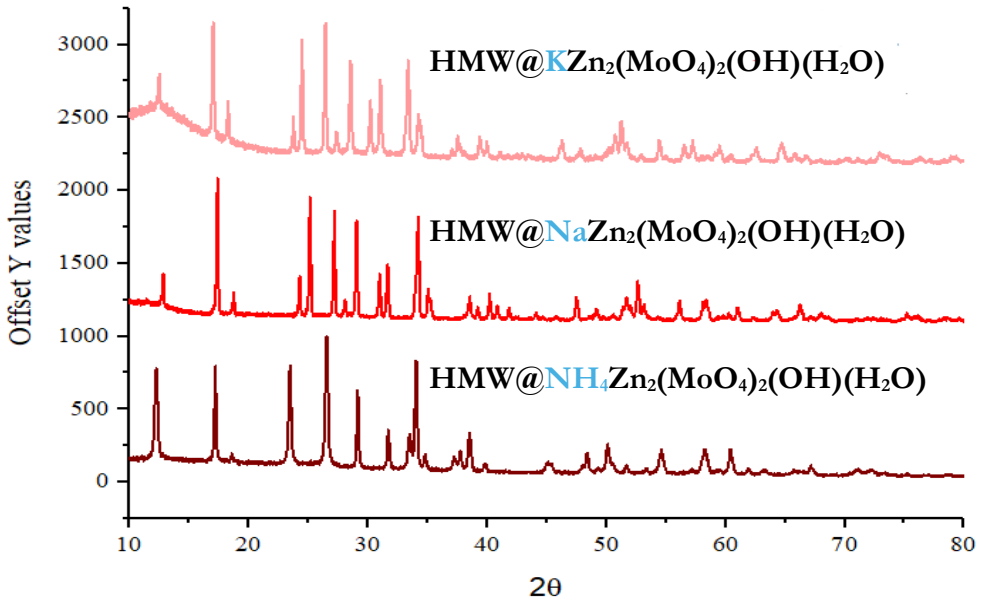

Figure 4.26. Experimental PXRD pattern of $HMW@NH_4Zn_2(MoO_4)_2(OH)(H_2O)$, $HMW@NaZn_2(MoO_4)_2(OH)(H_2O)$ and $HMW@KZn_2(MoO_4)_2(OH)(H_2O)$, obtained with different bases (NH_4OH, KOH, NaOH, respectively).

The matching of the synthesized $HMW@NaZn_2(MoO_4)_2(OH)(H_2O)$ and the $NaZn_2(MoO_4)_2(OH)(H_2O)$ data bank reference pattern are reported in Figure S4.18.

The FT-IR spectra of $HMW@NH_4Zn_2(MoO_4)_2(OH)(H_2O)$ are compared to those of $HMW@NaZn_2(MoO_4)_2(OH)(H_2O)$, and $HMW@KZn_2(MoO_4)_2(OH)(H_2O)$ shows the disappearance of the bands related to the stretching of N-H at 2987, 2901 cm^{-1} (Figure S4.19).

Also in this case, we have investigated the possibility to use $Na_2MoO_4 \cdot 2H_2O$ as alternative reagent in the synthesis of $NaZn_2(MoO_4)_2(OH)(H_2O)$, by using the same molar ratios and conditions described before (Mo:Zn 1:1), but without the addition of a base, since in this case the pH of the reaction slurry already is around 6.5. The experimental PXRD pattern of the material is in agreement with the reference diffraction pattern of $NaZn_2(MoO_4)_2(OH)(H_2O)$ and in Figure 4.27 the experimental pattern is compared to the one obtained using the same experimental conditions in absence of lignin ($NaZn_2(MoO_4)_2(OH)(H_2O)$_ref).

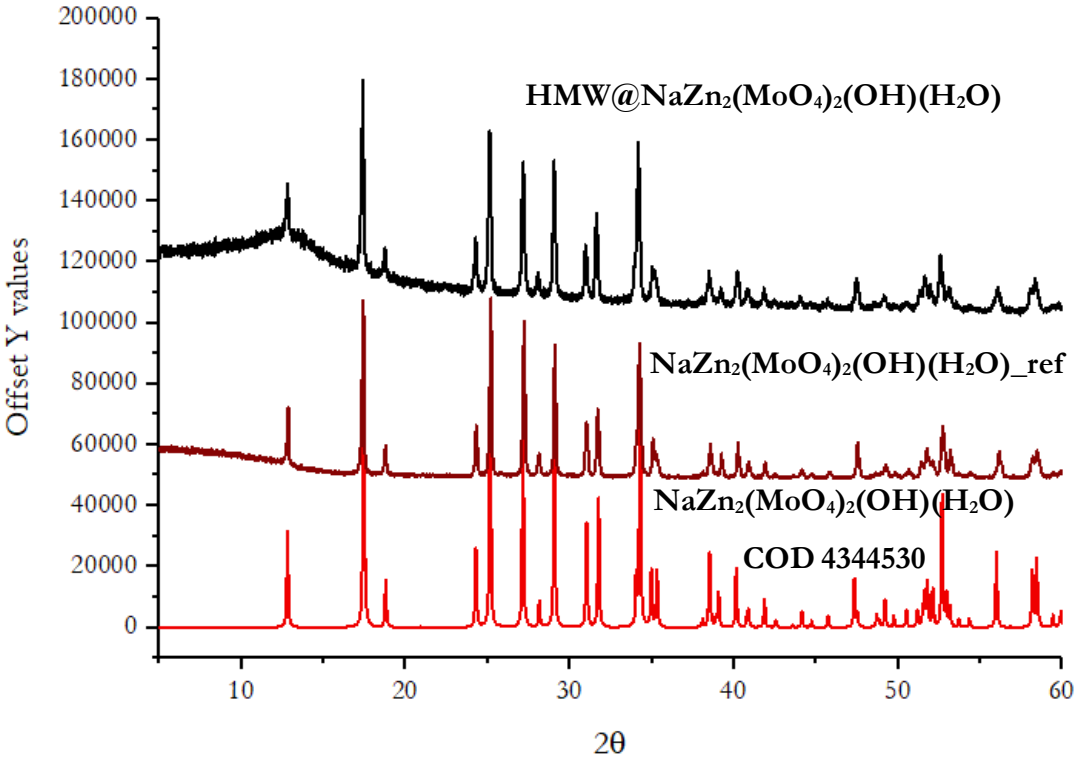

Figure 4.27. Experimental PXRD pattern of HMW@$NaZn_2(MoO_4)_2(OH)(H_2O)$, $NaZn_2(MoO_4)_2(OH)(H_2O)$_ref synthesized from sodium molybdate dihydrate and $NaZn_2(MoO_4)_2(OH)(H_2O)$ COD 4344530 from data bank.

Solargo@molybdate

This section is dedicated to the use of a commercial pre-formulated lignin, Solargo™, supplied by UPM-Kymmene and Green innovation. In Solargo™, lignin is suspended in propylene glycol, KOH and water, obtaining a liquid formulate. The use of Solargo™ as source of lignin is a very interesting issue, since this liquid formulate is already used by itself for sprayable applications on plants. The idea of using Solargo™ for *in situ* preparation of lignin and metal NPs hybrid materials has already been explored with copper-based materials,[25] with the aim of developing procedures easy to use in practical applications. The perspective is in fact the possibility to obtain the final material directly in the field, with an easy and quick synthetic procedure. However, it has to take into account that the use of Solargo™ could influence inorganic crystals formation, due to the presence of surfactants, such as polypropylene glycol, and considering the highly basic character (pH about 12) of the formulation. We have therefore investigated whether the mixing of ammonium molybdate with the liquid formulate in presence of copper or zinc salt, using different lignin:metal salts ratios, could lead to the isolation of the same crystalline phases ($Cu_3(MoO_4)_2(OH)_2$ or $KZn_2(MoO_4)_2(H_2O)$) discussed in the previous section. All the materials have been characterized by FT-IR, PXRD, ICP-AES, TEM.

EXPERIMENTAL SECTION

Materials and methods

Solargo™, kindly provided by UPM-Kymmene Oij and Green Innovation GmbH, is a formulation containing lignin (100 g), water (325 g), potassium hydroxide 50% (75 g) and propylene glycol (500 g) for 1 L of Solargo™. Zinc chloride is purchased by Brenntag. Ammonium molybdate (99%) is purchased by ThermoScientific and abcr GmbH; copper sulphate pentahydrate (98%) is purchased by Fluorochem. Ammonium hydroxide (30-33% NH_3 in H_2O) is purchased by Fluka, KOH is purchased by ACS (85 %). All the reagents are used as received with no further purification. pH is measured using a Crison pHmeter basic 20 equipped with an Ag/AgCl electrode.

Materials preparation

Solargo@$Cu_3(MoO_4)_2(OH)_2$. 5 mL of $(NH_4)_2MoO_4 \cdot 2H_2O$ aqueous solution (0.0178 mmol) have been added to 1 mL Solargo™ diluted with 10 mL H_2O (containing 100 mg lignin, 75 mg KOH, 7.6 equivalents with the respect to Mo). Then, a solution of $CuSO_4 \cdot 5H_2O$ (5 mL, 1.5 equivalents of Cu with the respect to Mo) has been added dropwise to the mixture under stirring: the pH is about 6. The mixture has been kept stirring for 4 hours, then it has been centrifuged and the recovered solid fraction has been dried at 85 °C overnight. The experiments have been performed at least twice.

Solargo@$KZn_2(MoO_4)_2(OH)(H_2O)$. 5 mL of $(NH_4)_2MoO_4 \cdot 2H_2O$ aqueous solution (0.017 mmol) has been added to 1 mL Solargo™ (containing 100 mg lignin, 75 mg KOH, 7.6 equivalents with the respect to Mo). Then, a solution of $ZnCl_2$ (5 mL, 1 equivalents of Zn with the respect to Mo) has been added dropwise to the mixture under stirring: the pH is about 6 (dilution of 1 mL Solargo™ in 20 mL water). The mixture has been kept stirring

for 4 hours, then it has been centrifuged, and the recovered solid fraction has been dried at 85 °C overnight. The experiments have been performed at least twice.

RESULTS and DISCUSSION

Preliminary attempts have been conducted in order to obtain lindgrenite when using Solargo™ as a lignin source. As initial experimental conditions, the lignin/molybdenum salt ratio has been the same applied with HMW, as described in the previous section. However, it must be considered that in the case of Solargo™, the lignin/KOH ratio is fixed at 1.33 g/g. By using these conditions (lignin/molybdenum salt 0.9 g/g and Mo^{6+}:Cu^{2+}:OH^- 1:1.5:2.25 ratio, pH = 4.4), the PXRD diffractogram shows the formation of a mixture of phases in addition to lindgrenite (Figure S4.20). By adding NH_4OH to adjust the pH to 6, the same operating pH used with HMW in the previous section, the formation of pure lindgrenite has been observed, as demonstrated by PXRD in Figure 4.28.

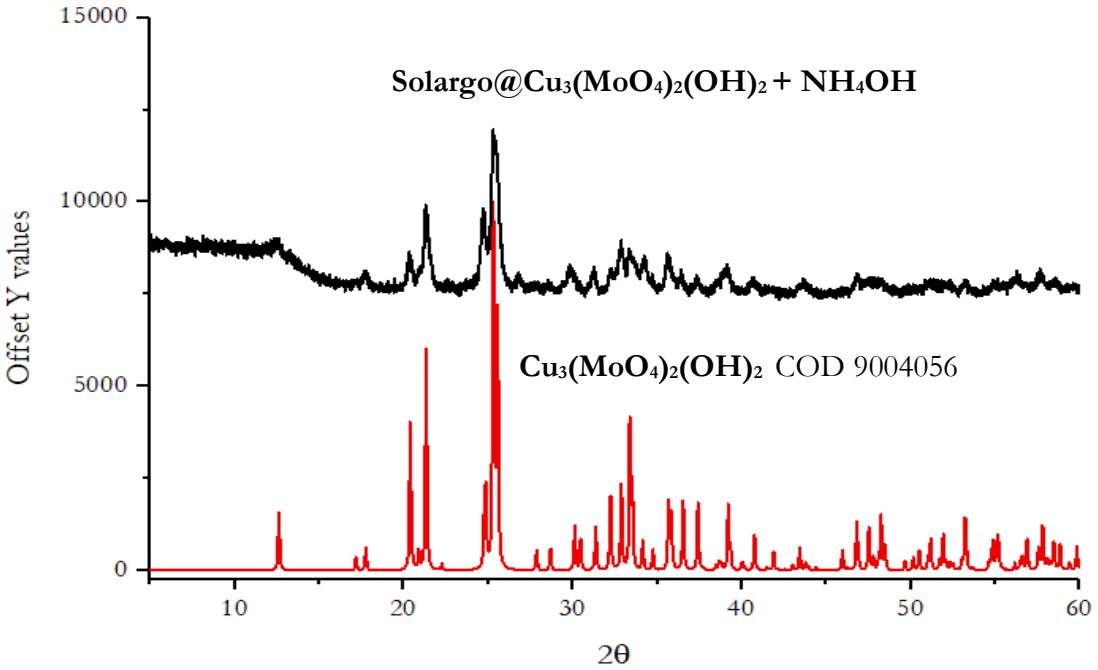

Figure 4.28. The experimental PXRD pattern of Solargo@$Cu_3(MoO_4)_2(OH)_2$ (black), obtained with lignin/molybdenum salt 0.9 g/g, adjusting the pH to 5.5, compared to the one of lindgrenite COD 9004056 (red);

Different operating conditions have been tested, in order to develop an optimized procedure, but only the one performed using 7.6 equivalents of KOH in Solargo™ with the respect to 1 equivalent of $(NH_4)_2MoO4{\cdot}2H_2O$ and 1.5 equivalents of $CuSO_4{\cdot}5H_2O$ has been found to be successful, probably because these experimental conditions reach the optimum pH for lindgrenite precipitation (pH about 6). The use of lower quantities of base leads in any case to the isolation of a mixture of unidentified crystalline phases. Moreover, two different dilution conditions have been investigated by keeping the ratio among the reagents constant, using 4 mL or 1 mL of Solargo™, diluting the mixture respectively with 15 mL and 20 mL of water. PXRD analysis of the powder obtained in more concentrated conditions seem to evidence the presence of a mixture of lindgrenite

and its triclinic polymorphic, named poly[bis-(μ-3-hydroxido)-bis-molybdate(VI) tricopper(II)]) (COD 4341497), as shown in Figure 4.29.

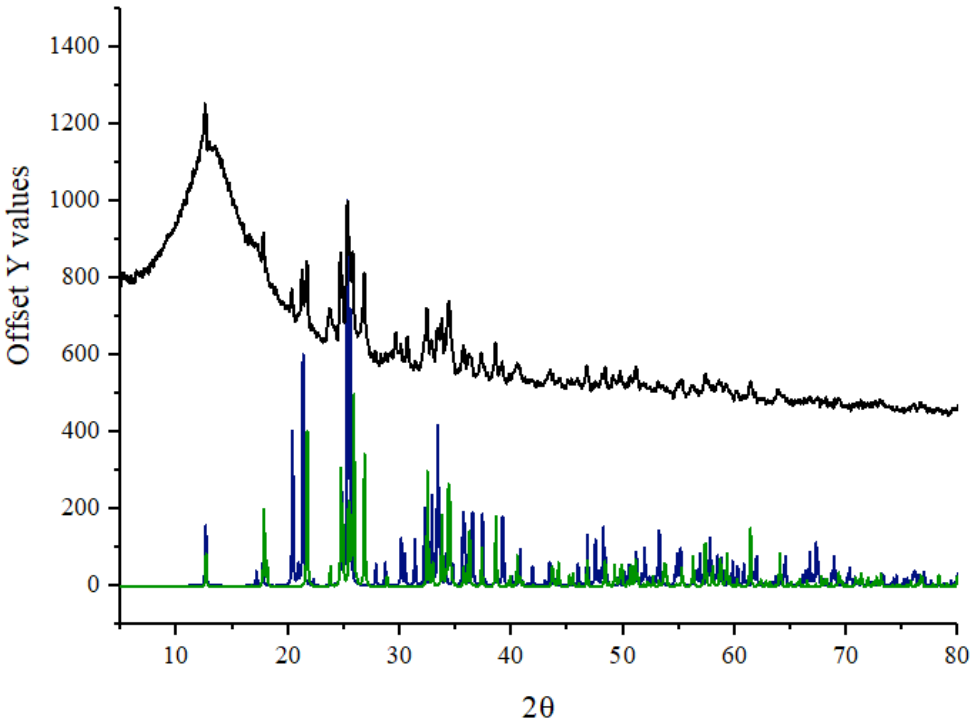

Figure 4.29. Experimental PXRD pattern of Solargo@$Cu_3(MoO_4)_2(OH)_2$ (black, obtained diluting 1 mL of Solargo™ with 20 mL of water), compared to the one of $Cu_3(MoO_4)_2(OH)_2$ triclinic polymorph of lindgrenite (Poly[bis-(μ3-hydroxido)-bis-molybdate(VI) tricopper(II)) data bank reference COD 4341497 (green) and lindgrenite COD 9004056 (blue); as can be inferred the product is a mixture of the two phases

Only one polymorph has been instead obtained by diluting 1 mL of Solargo™ with 20 mL of water in presence of 7.6 equivalents of base with the respect to Mo. PXRD analysis of the powder demonstrates the presence of pure lindgrenite $Cu_3(MoO_4)_2(OH)_2$ (Figure 4.30). These data evidence the crucial role of concentration of Solargo™ in determining the final crystalline phase embedded in the matrix. ICP-AES results are reported in Table 4.7.

Table 4.7. ICP-AES analysis of Solargo@$Cu_3(MoO_4)_2(OH)_2$_X%, with X as percentage of both copper and molybdenum. After mineralization, the presence of some white floccules could be observed, whose origin must be verified in future studies.

Sample	% Mo ± SD	% Cu ± SD
Solargo@$Cu_3(MoO_4)_2(OH)_2$_ 9% with 1 mL of Solargo™	6,35 ± 0,08	8.6 ± 0.1

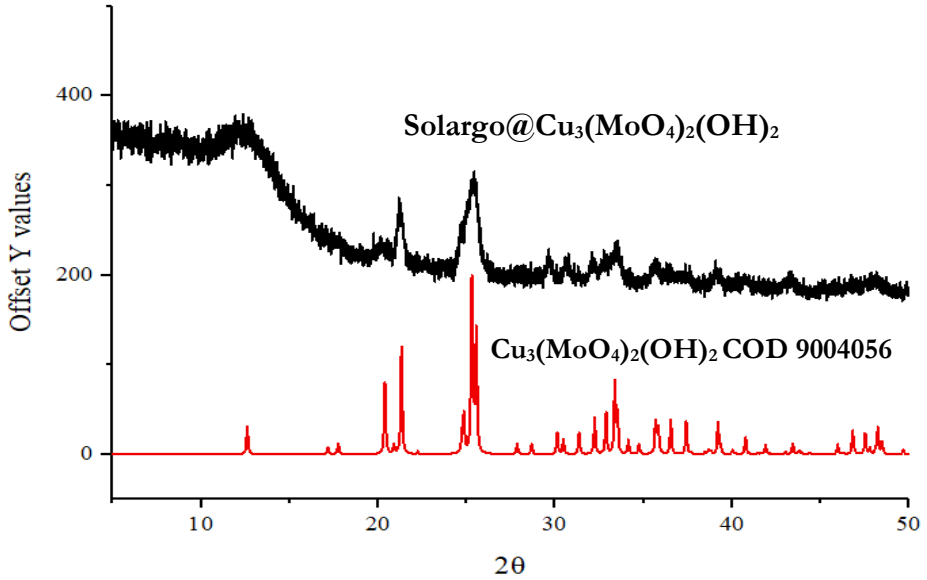

Figure 4.30. Experimental PXRD pattern of Solargo@$Cu_3(MoO_4)_2(OH)_2$ (black, obtained diluting 1 mL of Solargo™ with 20 mL of water) compared to the one of lindgrenite COD 9004056 (red).

The product has been analysed by TEM (Figure 4.31 a). Embedded in the matrix, there are crystals containing copper and molybdenum that appear lighter compared to the Solargo™ matrix and have sizes ranging from 50 to 300 nm. Small crystals with sizes between 10 and 50 nm as well as needle-shaped crystals with a length of 200-300 nm and a thickness of 50 nm are observed. EDX confirmed the presence of Mo and Cu (Figure 4.31 b.). It does not seem that the crystals differ significantly in terms of size and morphology from those studied in the previous section, with the results compared in Table S4.1 This suggests that Solargo™ can be used together with HMW as alternative lignin source. In Figure 4.32 the FT-IR spectra of lindgrenite obtained by using Solargo™ or by using HMW as lignin are superimposed: no significant variations of the bands can be observed, confirming the possibility to directly use a formulated lignin for the synthesis of the hybrid materials.

a)

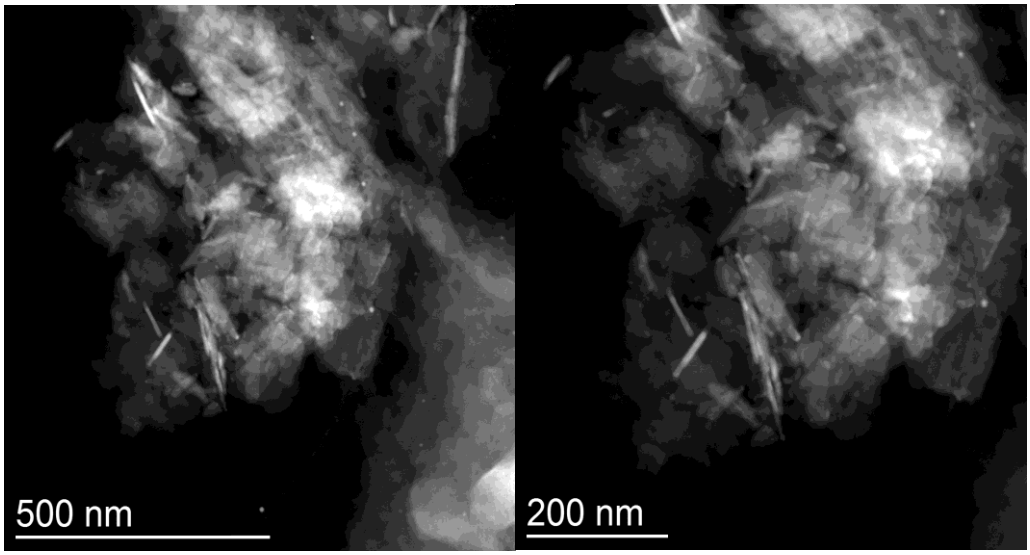

b)

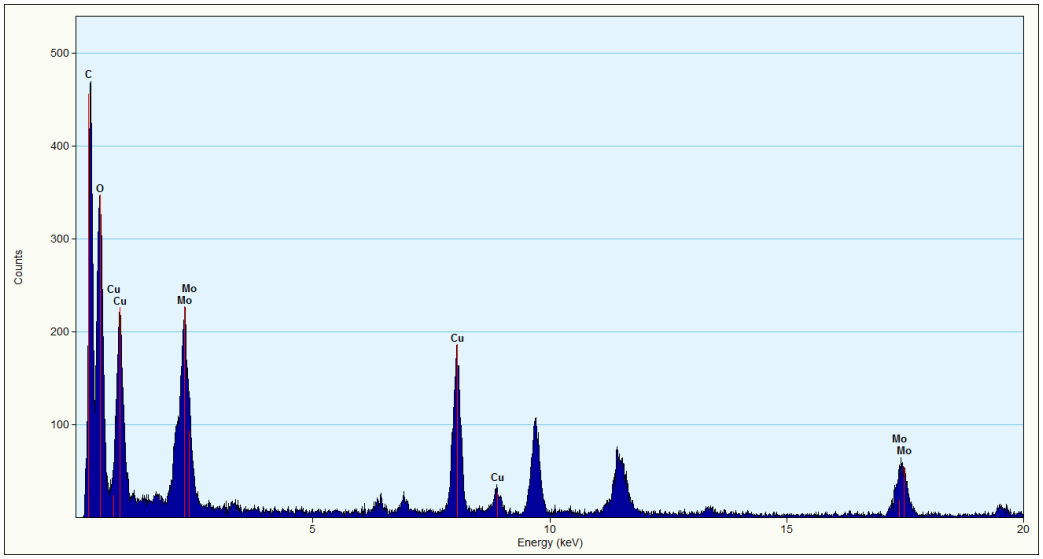

Figure 4.31. a) TEM of Solargo@$Cu_3(MoO_4)_2(OH)_2$, obtained diluting 1 mL of Solargo™ with 20 mL of water. b) EDX revealed the presence of Mo and Cu.

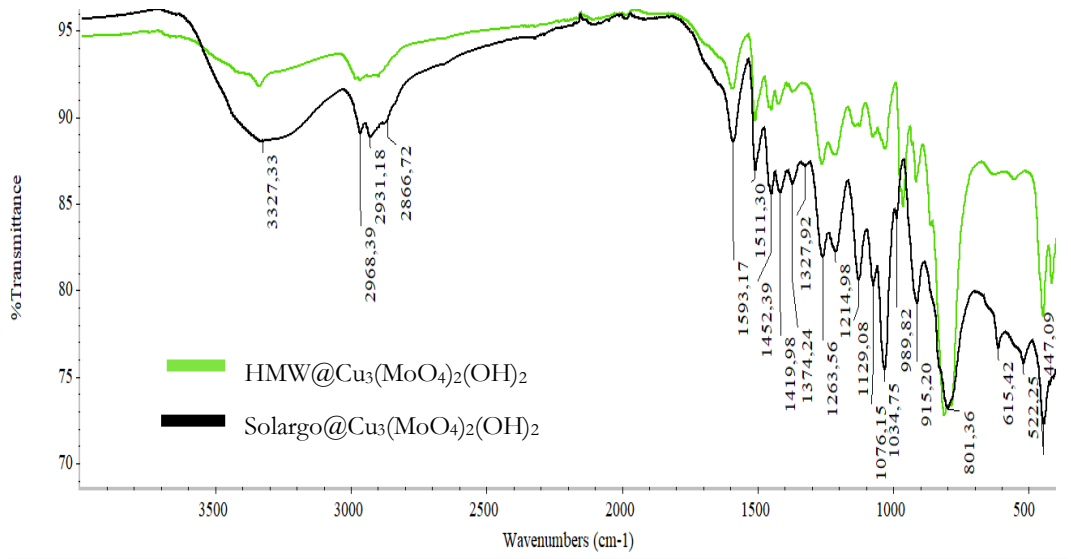

Figure 4.32. Stacked FT-IR spectra of HMW@ $Cu_3(MoO_4)_2(OH)_2$ (light green), compared to the one of Solargo@$Cu_3(MoO_4)_2(OH)_2$ (black).

A different result can be obtained by changing Mo^{6+}:Cu^{2+} ratio: using a 1:1 ratio instead of 1:1.5 the obtained phase is different. By mixing at RT for 4 hours, 4 mL of Solargo™ (containing 400 mg lignin, 300 mg KOH, 7.6 equivalents with the respect to Mo), 0.07 mol of $(NH_4)_2MoO_4$ and 0.07 mol of $CuSO_4 \cdot 5H_2O$, a material has been isolated by centrifugation after drying at 85 °C. PXRD analysis of the powder obtained has evidenced the presence of a phase that has no data bank matching (Figure 4.33). Since the pattern is very similar to the one of HMW@$KZn_2(MoO_4)_2(OH)(H_2O)$, the formation of Solargo@$KCu_2(MoO_4)_2(OH)(H_2O)$ can be supposed. ICP-AES analysis has been used to confirm the presence of potassium, copper and molybdenum (Table 4.8).

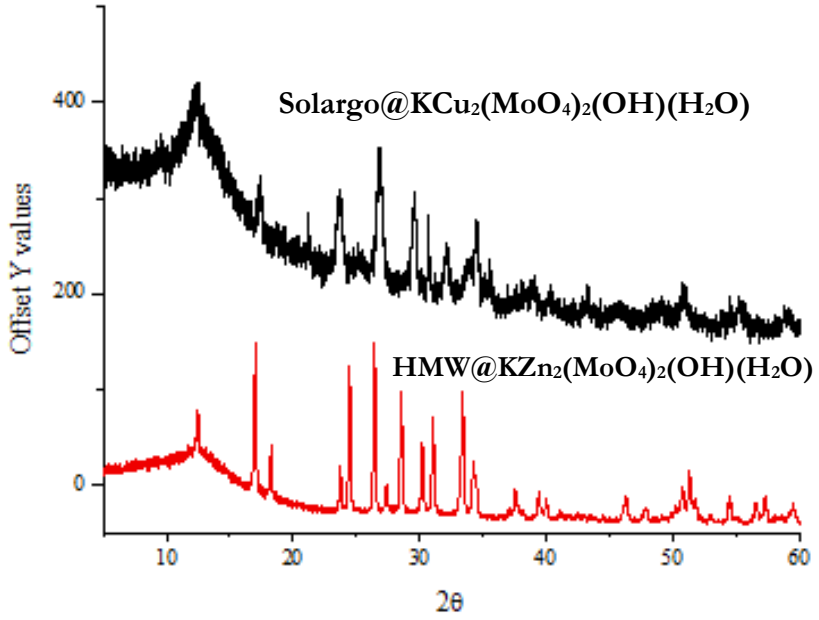

Figure 4.33. The experimental PXRD pattern of Solargo@$KCu_2(MoO_4)_2(OH)(H_2O)$ (black, obtained with 1:1 Mo:Cu ratio) compared to the one of HMW@$KZn_2(MoO_4)_2(OH)(H_2O)$ (red).

Table 4.8. ICP-AES analysis of Solargo@$KCu_2(MoO_4)_2(OH)(H_2O)$. After mineralization, the presence of some white floccules could be observed, whose origin must be verified in future studies.

Sample	Calculated % K	% K ± SD
Solargo@$KCu_2(MoO_4)_2(OH)(H_2O)$	4 %	4.4 ±0.3
	Calculated % Mo	% Mo ± SD
	9 %	8.28 ±0.08
	Calculated % Cu	% Cu ± SD
	6 %	7.77 ± 0.06

Similar conclusions can be drawn for the synthesis of Solargo@Mo_Zn materials. As initial studied conditions, the same lignin/molybdenum salt ratio has been kept constant with the respect to the conditions already studied with HMW of the previous section, considering that with Solargo™ the ratio lignin/KOH is fixed. With a lignin/molybdenum salt 0.9 g/g and Mo^{6+}:Zn^{2+}:OH^- 1:1:2.25 ratio, the PXRD study shows the formation of the phase $KZn_2(MoO_4)_2(OH)(H_2O)$. The experimental diffraction pattern obtained keeping the same operating conditions but adjusting pH with KOH to about 6.5 shows an increased intensity of the peaks. These patterns are compared to the one synthesized using HMW in Figure 4.34.

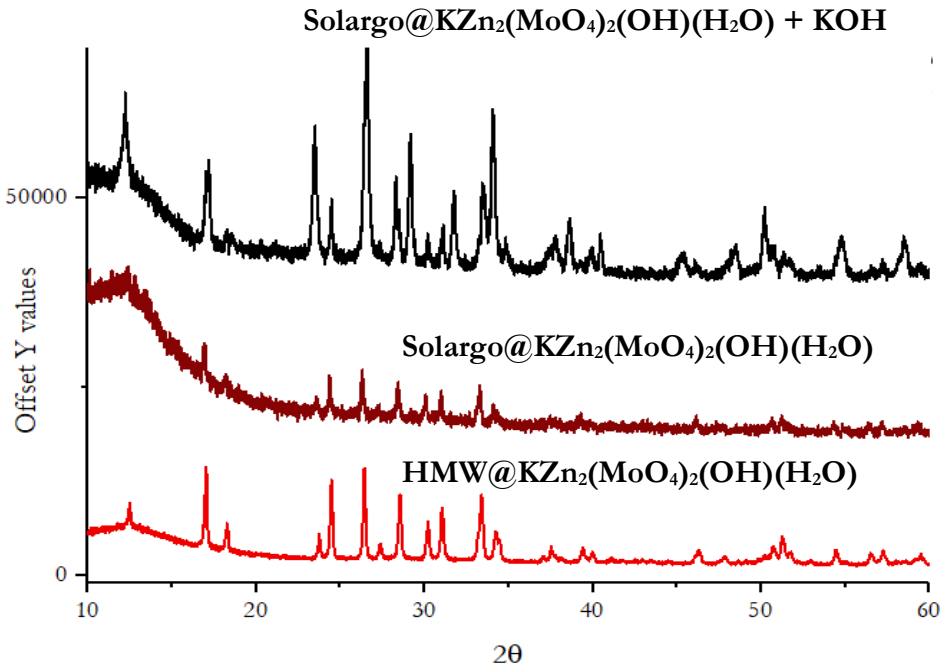

Figure 4.34. The experimental PXRD pattern of Solargo@$KZn_2(MoO_4)_2(OH)(H_2O)$ (dark red), obtained with lignin/molybdenum salt 0.9 g/g, and Mo:Zn.OH^- 1:1:2.25 ratio, compared to the one of Solargo@$KZn_2(MoO_4)_2(OH)(H_2O)$ (black), obtained with lignin/molybdenum salt 0.9 g/g and adjusting the pH to 6.5 and the experimental pattern of HMW@$KZn_2(MoO_4)_2(OH)(H_2O)$.

A similar approach to the one explained in previous section has been conducted for the obtainment of Solargo@$KZn_2(MoO_4)_2(OH)(H_2O)$ and also in this case 7.6 equivalents of KOH is the amount of base that can give the best results. Using 1 mL of Solargo™ and diluting the mixture respectively with 20 mL of water, $KZn_2(MoO_4)_2(OH)(H_2O)$ phase has been found in analogy with what we have found by using HMW, as demonstrated by PXRD (Figure 4.35).

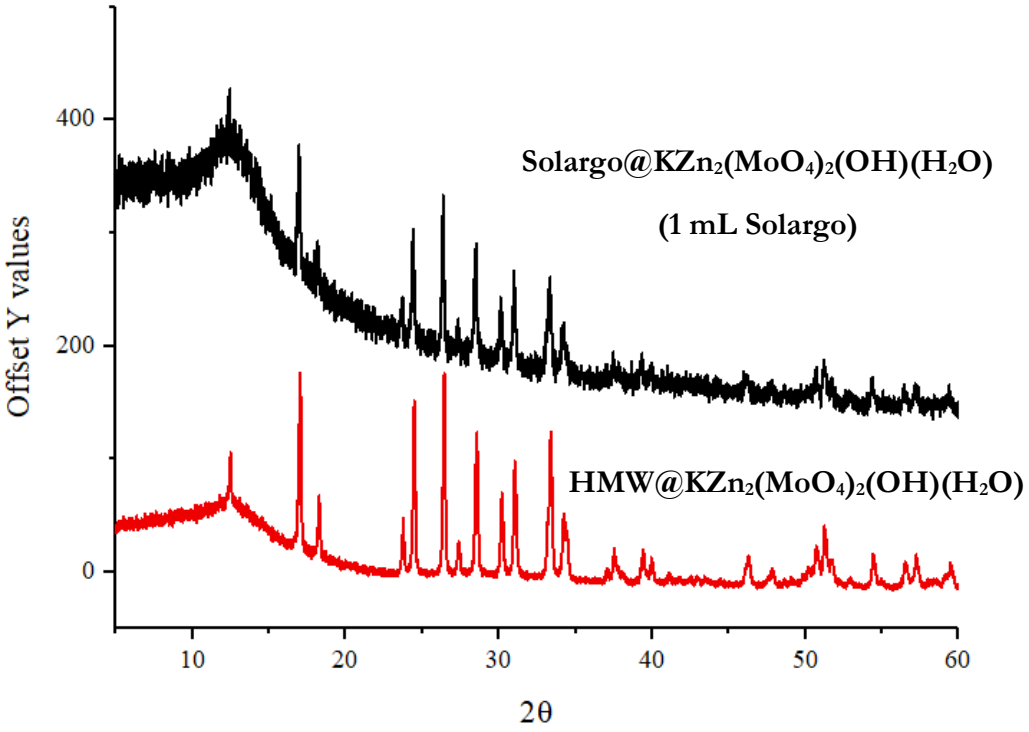

Figure 4.35. The experimental PXRD pattern of Solargo@$KZn_2(MoO_4)_2(OH)(H_2O)$ (black, obtained diluting 1 mL of Solargo™ with 20 mL of water), the experimental PXRD pattern of Solargo@$KZn_2(MoO_4)_2(OH)(H_2O)$ (dark red, obtained diluting 4 mL of Solargo™ with 15 mL of water), compared to the experimental pattern of HMW@$KZn_2(MoO_4)_2(H_2O)$ (red).

In Figure S4.21 it is reported the FT-IR spectrum of Solargo@$KZn_2(MoO_4)_2(OH)(H_2O)$. ICP-AES analysis has been used to confirm the presence of potassium, zinc and molybdenum (Table 4.9). This product has been analysed by TEM (Figure 4.36 a). Embedded in the matrix, there are crystals containing zinc and molybdenum that appear lighter compared to the Solargo™ matrix and have sizes ranging from 50 to 200 nm. EDX confirm the presence of K, Mo and Zn (Figure 4.36 b.). Comparable results have been found using HMW (Table S4.1).

Table 4.9. ICP-AES analysis of Solargo@$KZn_2(MoO_4)_2(OH)(H_2O)$. After mineralization, the presence of some white floccules could be observed, whose origin must be verified in future studies.

Sample	Calculated % K	% K ± SD
Solargo@$KZn_2(MoO_4)_2(OH)(H_2O)$	3.5 %	2.6 ± 0.1
	Calculated % Mo	% Mo ± SD
	8 %	4.65 ±0.04
	Calculated % Zn	% Zn ± SD
	6 %	4.09 ± 0.1

a)

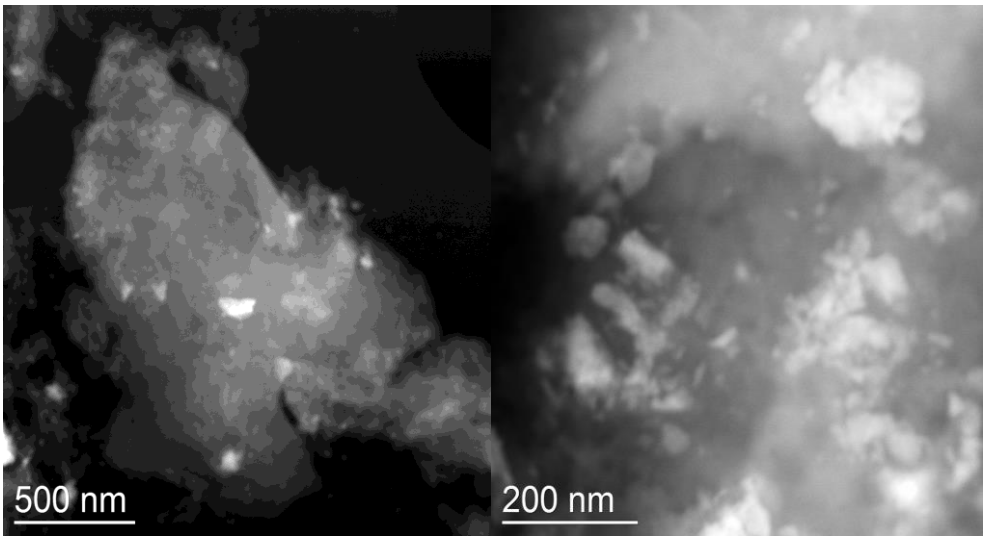

b)

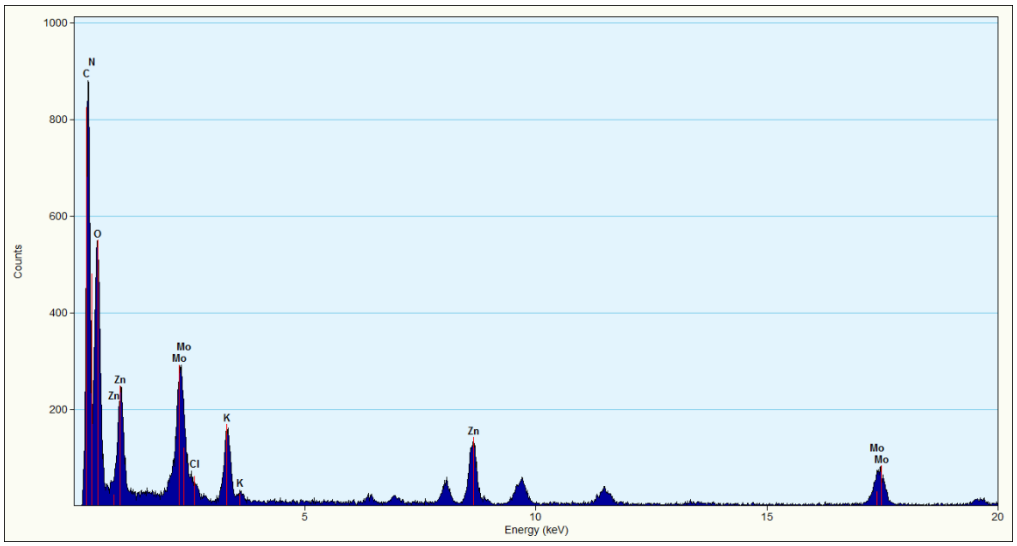

Figure 4.36. a) TEM of Solargo@$KZn_2(MoO_4)_2(OH)(H_2O)$, obtained diluting 1 mL of Solargo™ with 20 mL of water (7.6 equivalents of base with the respect to Mo); b) EDX revealed the presence of Mo, Zn and K.

HMW@molybdate mechanochemical synthesis

This section is dedicated to the use of mechanochemistry as an alternative synthetic methodology to obtain the HMW@molybdate hybrid materials, described in the previous sections. This kind of approach has been discussed in detail in Chapter 3, highlighting the advantages in term of scalability and sustainability for practical applications. The jars have been loaded for 1/3 of the volume and the number of spheres has been changed accordingly to the amount of material and the volume of the jar. The amount of solvent has been chosen to perform the synthesis in LAG conditions (liquid assisted grinding, see Chapter 3), which are conditions allowing homogenous mixing and easy removal of the product from the jar. Two different types of mills have been used, as follows.

Retsch® mixer mill MM400, endowed with horizontal oscillation and a 5 mL steel, loaded with 1 sphere (10 mm ø) and with about 0.5 g of material and 300 μL of liquid. The operating frequencies are 30 Hz. Retsch® planetary ball PM100 has been equipped with a 80 mL agate jar, with 5 spheres (15 mm ø). The jar has been loaded with about 10 g of material. The operating frequency is 300 rpm. It is important to notice the different frequencies applied with the two synthetic methodologies: 1 Hz= 1 oscillation for second= 60 turns for minute=60 rpm. With MM400 the working frequency is 30 Hz, corresponding to 1800 rpm. But, the main difference lies in the type of mechanochemical event: impact predominates in mixers, while shear and friction prevail in planetary mixers. The working times for both the procedures are about 30 minutes. All the materials have been characterized by FT-IR, PXRD, DLS, TEM.

EXPERIMENTAL SECTION

Materials and methods

HMW (Biopiva395®, Kraft softwood lignin from *Pinus taeda*, M_w 5950-6000 g/mol, M_n 1560-1565 g/mol) is kindly provided by UPM-Kymmene Oyj (Helsinki, Finland) and Green Innovation GmbH (Innsbruck, Austria). Zinc chloride is purchased by Brenntag. Ammonium molybdate (99%) is purchased by ThermoScientific and abcr GmbH; copper sulphate pentahydrate (98%) is purchased by Fluorochem. Ammonium hydroxide (30-33% NH_3 in H_2O) is purchased by Fluka, sodium hydroxide is purchased by AnalaR NORMAPUR®ACS. All the reagents are used as received with no further purification. The mechanochemical syntheses are conducted with a planetary ball mill Retsch® PM100 or a mixer mill Retsch® MM400, respectively using a 80 mL agate jar and 5 mL steel jar.

Materials preparation

Mechanochemical procedure for HMW@$Cu_3(MoO_4)_2(OH)_2$_PM100. In a 80 mL agate jar, 1.9 g of HMW, 2.63 g of $Na_2MoO_4 \cdot 2H_2O$, $CuSO_4 \cdot 5H_2O$ (2.72 g, 1 equivalent with the respect to Mo) and 3 mL water have been loaded. The milling has been performed for 30 minutes at 300 rpm. Then, the brown mixture has been washed with 50 mL water and isolated by centrifugation. It was then dried at 85°C overnight.

Mechanochemical procedure for HMW@$NH_4Cu_2(MoO_4)_2(OH)(H_2O)$_MM400. In a 5 mL steel jar, 72 mg of HMW, 82 mg of $(NH_4)_2MoO4 \cdot 2H_2O$, 2 drops of NH_4OH

(33%), 1 drop H_2O and 1 sphere (10 mm ø) have been put together and pre-mixed for 1 minute at 30 Hz. $CuCl_2 \cdot 2H_2O$ (108 mg, 1,5 equivalent respect to Mo) has been added to the mixture and the reaction has been performed for 15 minutes at 30 Hz. The brown mixture collected has been washed with water and isolated by centrifugation. It has been dried at 85°C overnight.

Mechanochemical procedure for HMW@$NH_4Cu_2(MoO_4)_2(OH)(H_2O)$_PM100. In a 80 mL agate jar, 1.9 g of HMW, 2.10 g of $(NH_4)_2MoO4 \cdot 2H_2O$, $CuSO_4 \cdot 5H_2O$ (1.3 g, 0.5 equivalent with the respect to Mo) have been pre-mixed at 200 rpm for 1 minute. 3 mL of NH_4OH (33%) have been added to the mixture and the reaction has been performed for 30 minutes at 300 rpm. Then, the brown mixture has been washed with 50 mL water and isolated by centrifugation. It has been then dried at 85°C overnight.

Mechanochemical procedure for HMW@$NH_4Zn_2(MoO_4)_2(OH)(H_2O)$_MM400. In a 5 mL steel jar, 78 mg of HMW, 95 mg of $(NH_4)_2MoO4 \cdot 2H_2O$, $ZnCl_2$ (67 mg, 1 equivalent with the respect to Mo), 2 drops of NH_4OH (33%), 1 drop H_2O and 1 sphere (10 mm ø) have been put together and mixed for 30 minutes at 30 Hz. Then, the brown mixture collected has been washed with water and isolated by centrifugation. It has been dried at 85°C overnight.

Mechanochemical procedure for HMW@$NH_4Zn_2(MoO_4)_2(OH)(H_2O)$ PM100. In a 80 mL agate jar, 1.9 g HMW, 2.13 g $(NH_4)_2MoO4 \cdot 2H_2O$, $ZnCl_2$ (1.5 g, 1 equivalent with the respect to Mo), 3 mL of NH_4OH (33%) and 5 spheres (15 mm ø) have been put together and pre-mixed for 30 minutes at 30 Hz. Then, the brown mixture collected has been washed with water and isolated by centrifugation. It has been dried at 85°C overnight.

RESULTS AND DISCUSSION

Preliminary attempts to obtain HMW@molybdate hybrid materials have been focused on the use of Retsch® mixer mill MM400: this kind of mill has the advantage of reaching high operating frequencies (30 Hz) which corresponds to high energetics of the impacts. The oscillations are horizontally directed and impact phenomena prevail in mixers. In this case, 5 mL steel jar has been chosen, loaded with 1 sphere (10 mm ø) and with about 0.5 g of reagents which is usually a good filling for reaching complete and homogeneous grindings, even though is less than 1/3 of the volume. At first, we have used the same reagents ratios employed for the obtainment of HMW@$Cu_3(MoO_4)_2(OH)_2$ *via* wet synthesis, but for a 0.5 g of total reagent mass: the synthesis has been performed loading the jar with 82 mg of $(NH_4)_2MoO_4 \cdot 2H_2O$, 72 mg of HMW, 2 drops of NH_4OH aq solution (33% w/w) and 1 drop H_2O (about 300 µL of liquid). These reagents have been quickly pre-mixed for 1 minute at 30 Hz and then $CuCl_2 \cdot 2H_2O$ (108 mg, 1.5 equivalents with the respect to Mo) have been loaded inside the jar. The synthesis has been performed in LAG condition (η<2): $\eta = \frac{liquid\ (\mu L)}{reactants\ weight\ (mg)} = 1.14$. The mixing has been performed for 15 minutes at 30 Hz. Unfortunately, side reactions on the jar walls have occurred: the copper salt has reacted with the steel, forming dark red spots on the walls, probably related to reduction processes of copper. The solid recovered from the milling has been washed with water, isolated by centrifugation and dried at 80 °C overnight. The powder obtained has been analysed by means of PXRD, as shown in Figure 4.37. The phase formed can be identified as HMW@$NH_4Cu_2(MoO_4)_2(OH)(H_2O)$. ICP-AES (data not shown) indicates an excess of molybdenum over copper, maybe due to the presence of some amorphous unreacted molybdenum phase, suggesting that not all the molybdenum could react due to the copper subtraction by side reactions with the jar. The procedure is described in the experimental section and named HMW@$NH_4Cu_2(MoO_4)_2(OH)(H_2O)$_MM400.

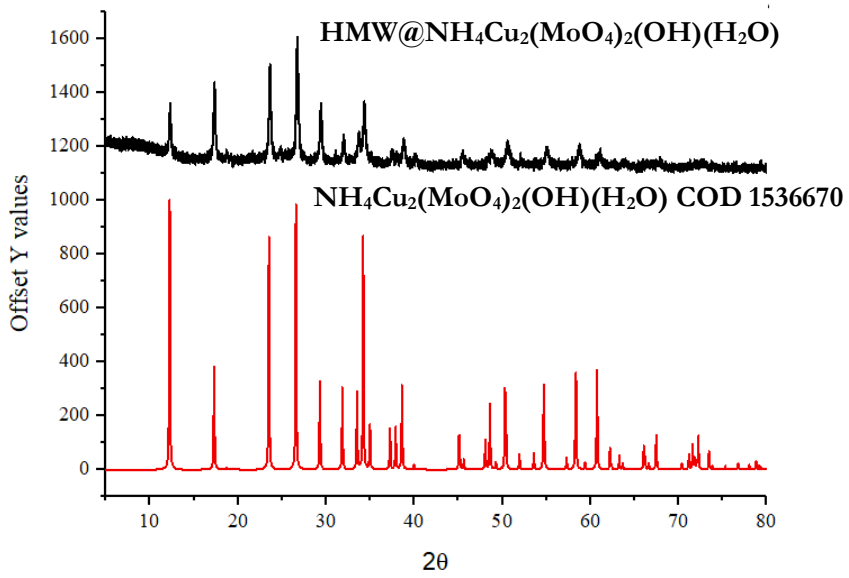

Figure 4.37. Experimental PXRD pattern of HMW@$NH_4Cu_2(MoO_4)_2(OH)(H_2O)$ (black pattern) obtained by mechanochemical procedure with steel jar compared to the data bank reference $NH_4Cu_2(MoO_4)_2(OH)(H_2O)$ COD 1536670 (red).

A further trial has been conducted with a 80 mL agate jar and with a planetary ball mill PM 100, endowed with a rotating system. Using a jar with major volume, a scale up procedure could be optimized and the ratios that have been observed to work well under wet conditions have been kept constant, but the weight of the reagents has been rescaled to ensure an appropriate filling of the jar for homogeneous grinding. The jar has been loaded with 5 spheres (15 mm ø), 4.2 g $(NH_4)_2MoO_4 \cdot 2H_2O$, 1.9 g HMW and $CuSO_4 \cdot 5H_2O$ (1.33 g, 0.5 equivalent with the respect to Mo) inside the jar and pre-mixed for 1 minute at 200 rpm. 3 mL NH_4OH have been then added to the powders and the mixing has been performed for 30 minutes at 300 rpm. Then, the brown mixture has been washed with 50 mL H_2O, isolated by centrifugation and it has been again dried at 85°C overnight. The synthesis has been performed in LAG conditions (η<2): $\eta = \frac{liquid\ (\mu L)}{reactants\ weight\ (mg)} = 0.56$. The PXRD analysis conducted on the obtained powder has demonstrated the formation of $NH_4Cu_2(MoO_4)_2(OH)(H_2O)$ phase (Figure 4.38).

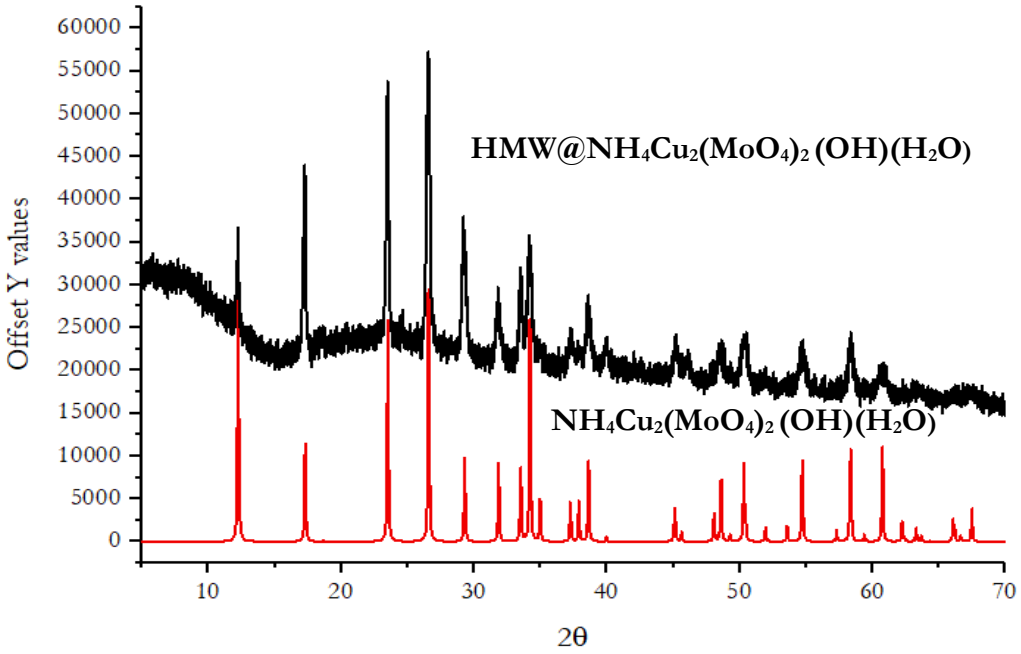

Figure 4.38. Experimental PXRD pattern of HMW@$NH_4Cu_2(MoO_4)_2(OH)(H_2O)$ (black pattern) obtained by mechanochemical procedure with agate jar compared to the data bank reference $NH_4Cu_2(MoO_4)_2(OH)(H_2O)$ COD 1536670 (red).

Attempts of using ammonium molybdate as a reagent, therefore, has not resulted in the formation of lindgrenite. However, this phase has been successfully obtained when sodium molybdate has been used. The experiments have been conducted under similar conditions: by using a planetary ball mill PM 100, a 80 mL agate jar has been loaded with 5 spheres (15 mm ø), 2.63 g $Na_2MoO_4 \cdot 2H_2O$, 1.9 g HMW, 3 mL H_2O and $CuSO_4 \cdot 5H_2O$ (1 equivalent with the respect to Mo). The milling has been performed for 30 minutes at 300 rpm. Then, the brown mixture washed with 50 mL H_2O, isolated by centrifugation and it has been again dried at 85°C overnight. The synthesis is performed in LAG condition (η<2): $\eta = \frac{liquid\ (\mu L)}{reactants\ weight\ (mg)} = 0.35$. The PXRD analysis conducted on the obtained powder demonstrated the formation of $Cu_3(MoO_4)_2(OH)_2$ phase (Figure 4.39).

ICP-AES analyses are ongoing to verify the complete conversion of the reagents and to verify if these conditions require further optimization. .

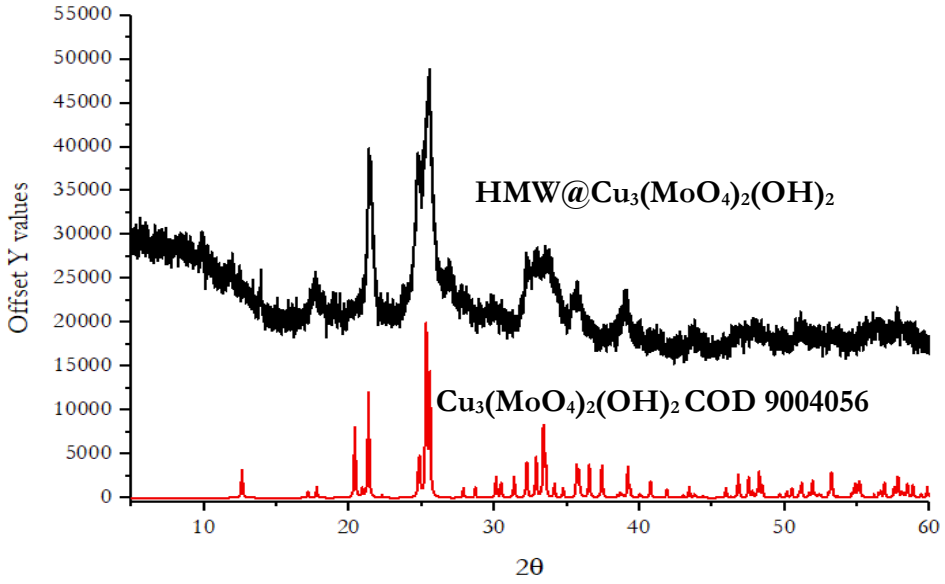

Figure 4.39. The experimental PXRD pattern of HMW@$Cu_3(MoO_4)_2(OH)_2$ (black, obtained with sodium molybdate and performing the reaction in a 80 mL agate jar, compared to the one of $Cu_3(MoO_4)_2(OH)_2$ COD 9004056 (red).

The stacked FT-IR spectra of HMW@$Cu_3(MoO_4)_2(OH)_2$_mechanochemistry compared to the ones of HMW@$Cu_3(MoO_4)_2(OH)_2$_wet are shown in Figure S4.22. The product has been analysed by TEM (Figure 4.40). Embedded in the matrix, there are crystals containing copper and molybdenum have sizes ranging from 50 to 200 nm, with the presence of NPs having dimensions of 10-50 nm. Descriptions are collected in Table S4.1.

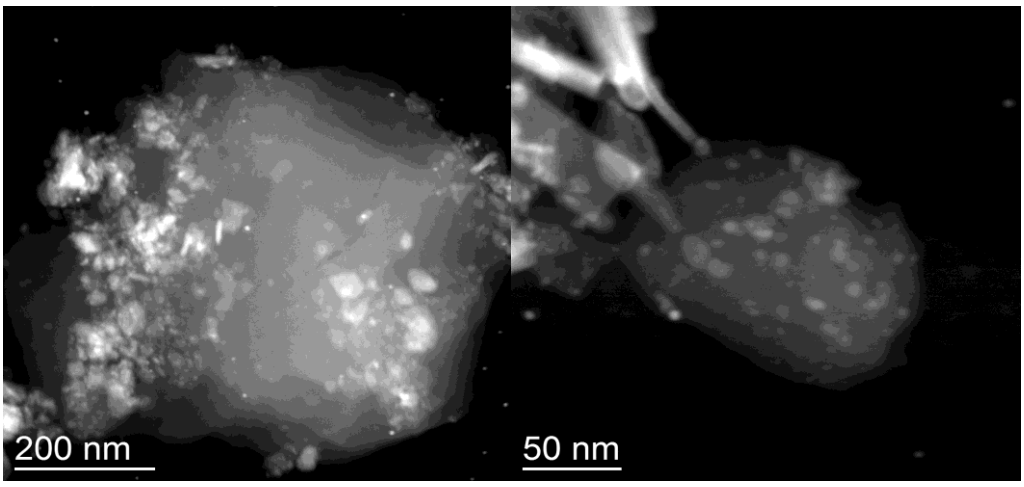

Figure 4.40. TEM of HMW@$Cu_3(MoO_4)_2(OH)_2$ from sodium molybdate by mechanochemistry.

A very similar approach with Retsch® mixer mill MM400 and 5 mL steel jar has been also tried for the obtainment of HMW@$NH_4Zn_2(MoO_4)_2(H_2O)$, as reported in the experimental section (named as HMW@$NH_4Zn_2(MoO_4)_2(H_2O)$_MM400). The reaction

has been performed in a 5 mL steel jar, with 1 equivalent of Zn with the respect to Mo), and 1 sphere (10 mm ø) and mixed for 30 minutes at 30 Hz. Then, the brown mixture collected has been washed with water, isolated by centrifugation and dried at 85°C overnight. The synthesis is performed in LAG condition close to slurry (η<2): $\eta = \frac{liquid\ (\mu L)}{reactants\ weight\ (mg)} = 1.7$. A scale up mechanochemical procedure has been conducted with a 80 mL agate jar and with a planetary ball mill PM 100, endowed with a rotating system. The jar has been loaded with 5 spheres (15 mm ø), $(NH_4)_2MoO_4 \cdot 2H_2O$, HMW, $ZnCl_2$ (1 equivalent with the respect to Mo), 3 mL NH_4OH 33%. Then, the brown mixture has been washed with 50 mL H_2O, isolated by centrifugation and it has been again dried at 85°C overnight. The synthesis is performed in LAG condition (η<2): $\eta = \frac{liquid\ (\mu L)}{reactants\ weight\ (mg)} = 0.54$. The experimental pattern of the two mechanochemical synthesis are reported in Figure 4.41 and the PXRD analysis demonstrated the formation of a pure $NH_4Zn_2(MoO_4)_2(OH)(H_2O)$ phase, by comparison with the bank reference.

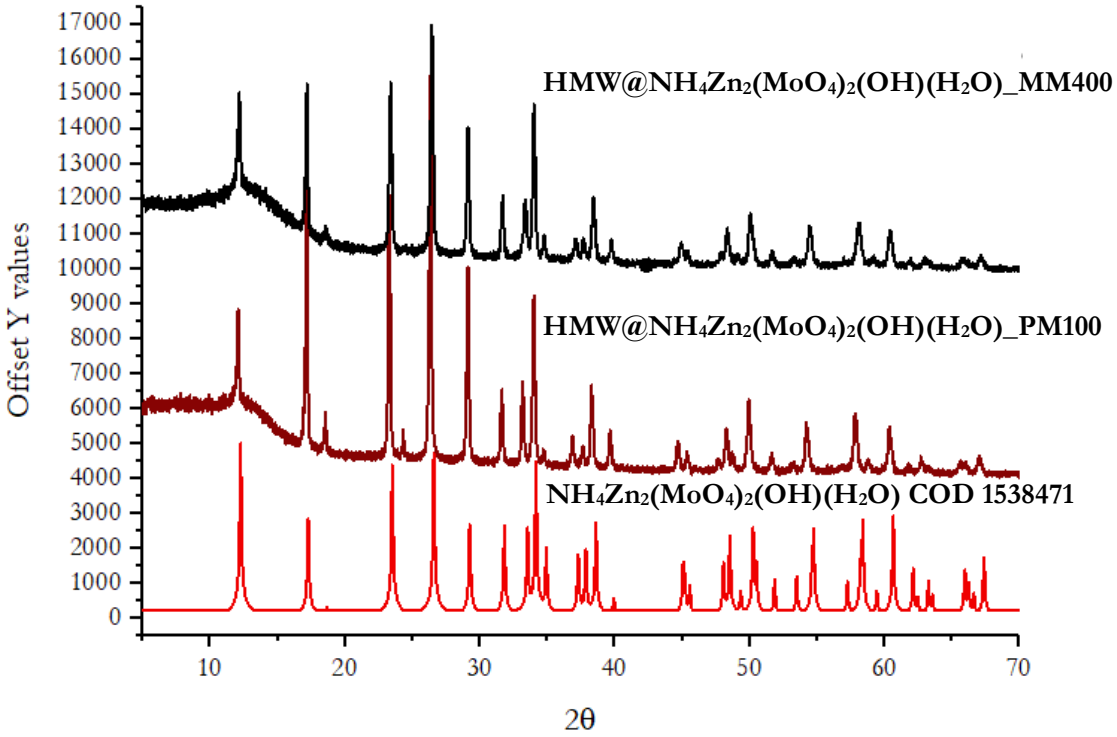

Figure 4.41. The experimental PXRD pattern of HMW@$NH_4Zn_2(MoO_4)_2(OH)(H_2O)$ (black pattern) obtained by mechanochemical procedure with MM440, HMW@$NH_4Zn_2(MoO_4)_2(OH)(H_2O)$_PM100 (dark red) compared to the data bank reference $NH_4Zn_2(MoO_4)_2(OH)(H_2O)$ COD 1538471 (red).

ICP-AES analysis has been used to confirm the presence of zinc and molybdenum with both procedures (Table 4.10).

Table 4.10. ICP-AES analysis of HMW@$NH_4Zn_2(MoO_4)_2(OH)(H_2O)$_PM100 X_Y% and HMW@$NH_4Zn_2(MoO_4)_2(OH)(H_2O)$_MM400 X_Y%, where X refers to the expected Mo% and Y to Zn %.

Sample	% Mo ± SD	% Zn ± SD
HMW@$NH_4Zn_2(MoO_4)_2(OH)(H_2O)$_PM100 14_10%	12.4 ± 0.3	14.9 ± 0.1
HMW@$NH_4Zn_2(MoO_4)_2(OH)(H_2O)$_MM400 14_10%	10.6 ± 0.2	14.9 ± 0.3

HMW@$NH_4Zn_2(MoO_4)_2(OH)(H_2O)$_MM400 has been analysed by TEM (Figure 4.42). There are crystals containing copper and molybdenum with sizes ranging from 50 to 200 nm, with the presence of needle-like crystals with length of 200-400 nm. Descriptions are collected in Table S4.1.

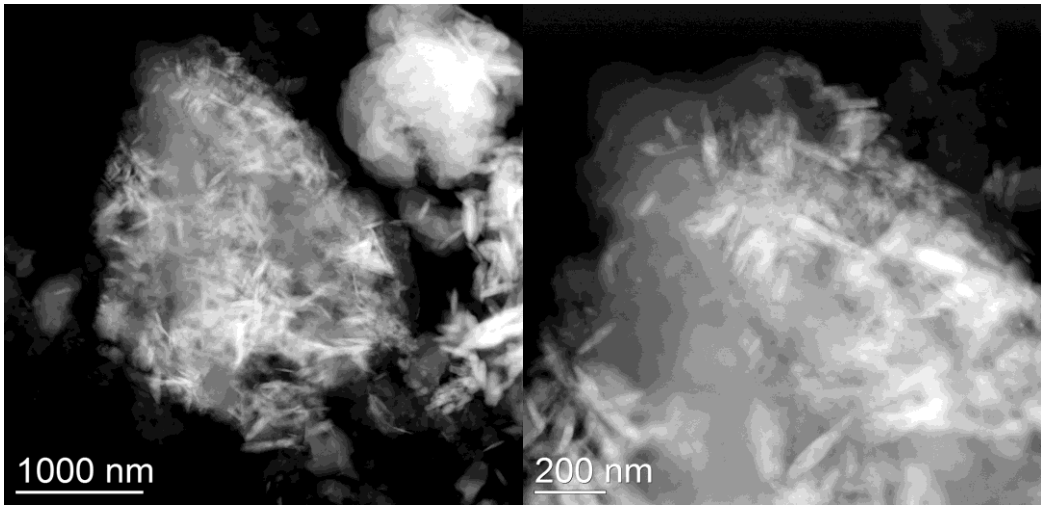

Figure 4.42. TEM of HMW@$NH_4Zn_2(MoO_4)_2(OH)(H_2O)$_MM400

Conclusions

In this section, we have described the successful synthesis of hybrid materials containing molybdenum phases combined with zinc or copper. As highlighted in the introduction, these materials hold promise for improving plant health through two main pathways. First, they can provide essential micronutrients that support plant growth and well-being. The incorporation of lignin in the matrix plays a critical role in enabling a slow-release mechanism for these nutrients, ensuring a gradual supply over time. This slow-release function is particularly important, as without it heavy metals could accumulate in the plant, potentially leading to toxicity and negative environmental consequences. A second promising application of these hybrid materials lies in their use as pesticides for crop protection. Studies exploring the antifungal properties of lindgrenite have shown encouraging results, indicating the potential for these materials to offer an environmentally friendly alternative to traditional chemical pesticides. This opens new avenues for the use of these materials not only to enhance plant health, but also to protect crops from various pathogens, potentially reducing the reliance on harmful chemicals in agriculture. The inorganic phases have been synthesized using a sustainable and easy procedure that is scalable, making it suitable for in-field applications. This method ensures that the materials are not only effective but also environmentally friendly, in line with the increasing demand for "green" chemistry in industrial applications. The materials have been studied from both inorganic and organic perspectives, ensuring a comprehensive understanding of their properties and behaviours. Furthermore, a liquid lignin formulation, Solargo™, has been used in the synthesis, offering the potential for *in vivo* applications through liquid formulations and his approach could be particularly advantageous for foliar applications. Furthermore, the study explores the use of a mechanochemical approach to provide an alternative synthetic route. This approach, as discussed in Chapter 3, offers several benefits, including potentially lower energy consumption and fewer chemical reagents, which could further enhance the sustainability of the material synthetic process. To compare the different synthetic strategies, TEM (Transmission Electron Microscopy) studies have been conducted to analyse the crystalline structures formed and assess similarity of the materials produced by each method. The comparison of these methods is crucial for optimizing the synthesis process and ensuring the reproducibility and scalability of the materials. This research demonstrates that it is indeed possible to obtain crystalline molybdate phases within the lignin matrix under mild and environmentally friendly conditions. The ability to integrate these phases into a lignin-based matrix not only enhances their functionality, but also adds value by utilizing lignin, a renewable and abundant biopolymer. Ultimately, this study opens up new opportunities for developing sustainable, efficient, and cost-effective materials for agricultural applications, which could contribute to the future of sustainable farming practices.

Supporting information

Tables

Table S4.1. Dimension and morphology of the crystals in HMW@molybdate materials.

	Size	Shape
HMW@$Cu_3(MoO_4)_2(OH)_2$	50-200 nm crystals	Not defined morphology
	Needles 10-600 nm Thickness 40-80 nm	Needles
HMW@$Cu_3(MoO_4)_2(OH)_2$ from sodium molybdate	50-200 nm crystals	Not defined morphology
	NPs of 10-20 nm	
$Cu_3(MoO_4)_2(OH)_2$ _ref from sodium molybdate	50-500 nm crystals	Not defined morphology
Solargo@$Cu_3(MoO_4)_2(OH)_2$	50 e 500 nm NPs of 10-20 nm	Not defined morphology
	Needles 20-300 nm Thickness 50 nm	Needles
HMW@$Cu_3(MoO_4)_2(OH)_2$_PM100	50-200 nm crystals	Not defined morphology
	NPs of 10-20 nm	
HMW@$NH_4Zn_2(MoO_4)_2(OH)(H_2O)$	50-200 nm crystals	Not defined morphology
Solargo@$NH_4Zn_2(MoO_4)_2(OH)(H_2O)$	50-200 nm crystals	Not defined morphology
HMW@$NH_4Zn_2(MoO_4)_2(OH)(H_2O)$_MM400	50-200 nm crystals	Not defined morphology
	Needles 50-400 nm	Needles

Figures

a)

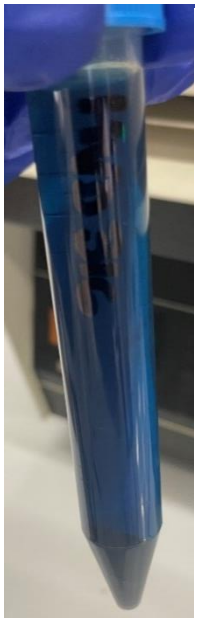

b)

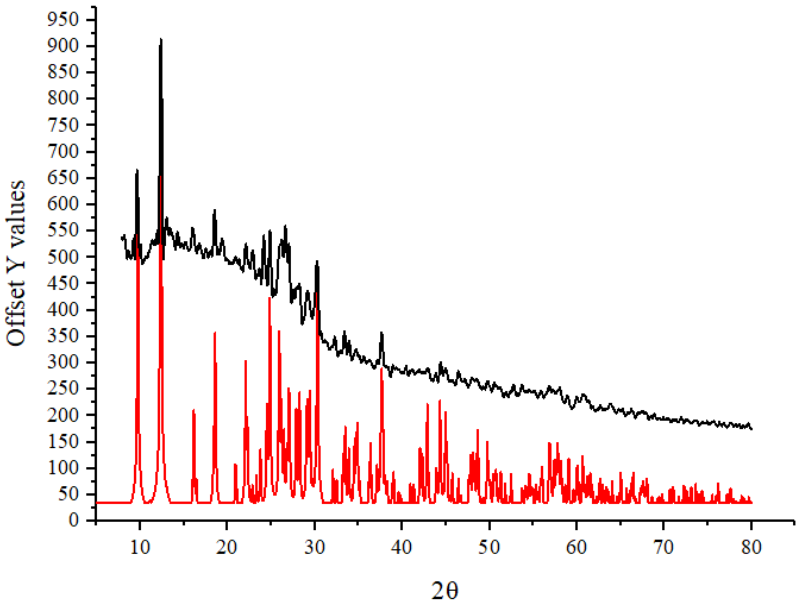

c)

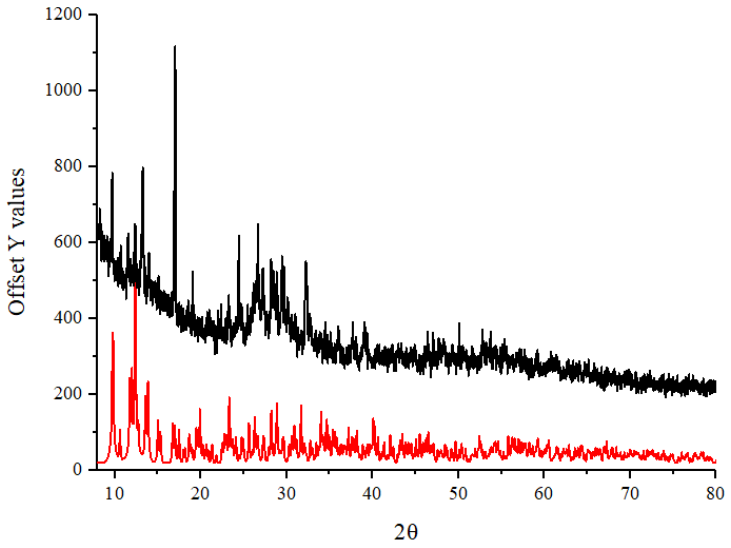

Figure S4.1: a) picture of the product after the centrifugation step; b) experimental PXRD pattern of the solid fraction (black), compared to the data bank reference of diammonium catena tetramolybdate $(NH_4)_2(Mo_4O_{13})$ COD 1000283 (red); c) experimental PXRD pattern of the dried supernatant (black), compared to the data bank reference of diammonium catena tetramolybdate $(NH_4)_6(Mo_7O_{24})(H_2O)$ COD 1539088 (red); the experimental pattern presents several peaks probably related to a mixture of polyoxomolybdate phases.

a) b)

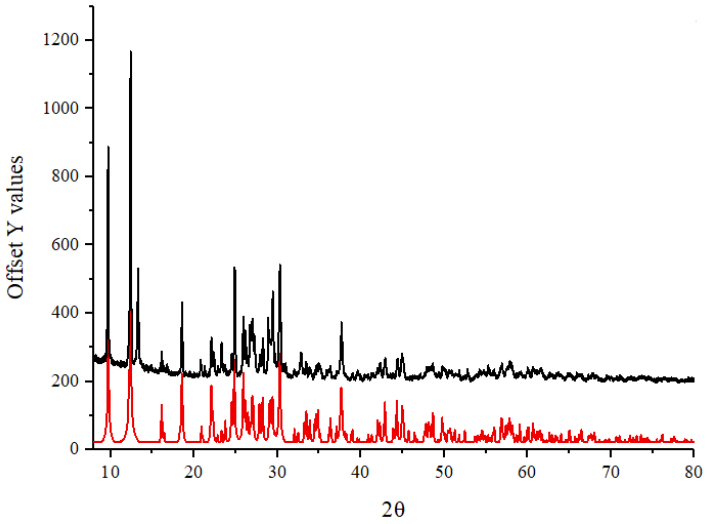

Figure S4.2: a) picture of the product, isolated as a light blue powder, after the centrifugation step b) experimental PXRD pattern of the solid fraction (black), compared to the data bank reference of diammonium catena tetramolybdate $(NH_4)_2(Mo_4O_{13})$ COD 1000283 (red).

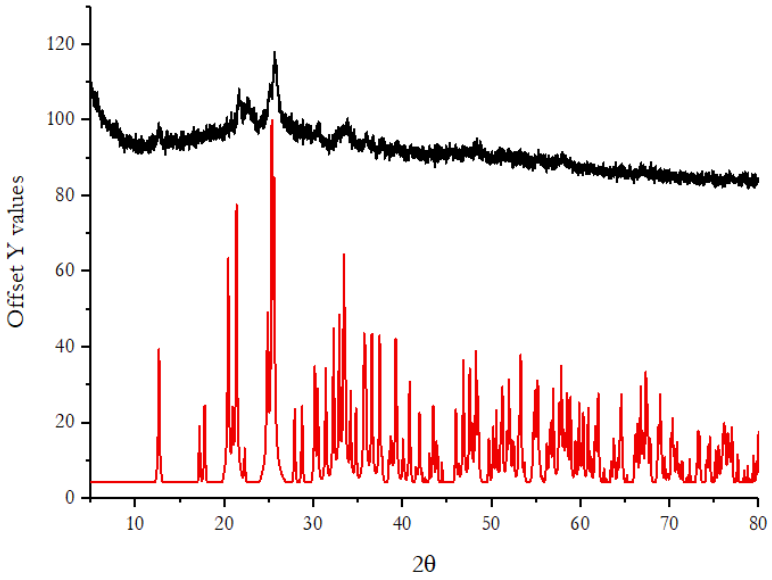

Figure S4.3: Experimental PXRD pattern of HMW@Mo_Cu (black) compared to the one of lindgrenite COD 9004056 (red).

Display name	Standard data	Quantification method	Result Type
Spc_001	Standardless	ZAF	Metal

Element	Line	Mass%	Atom%
C	K	43.77	61.27
O	K	31.37	32.97
Si	K	0.03	0.02
S	K	1.02	0.53
Cu	K	11.59	3.07
Mo	L	12.22	2.14
Total		100.00	100.00
Spc_001			Fitting ratio 0.0122

Figure S4.4. EDX with ZAF corrections is reported, showing percentages of copper and molybdenum.

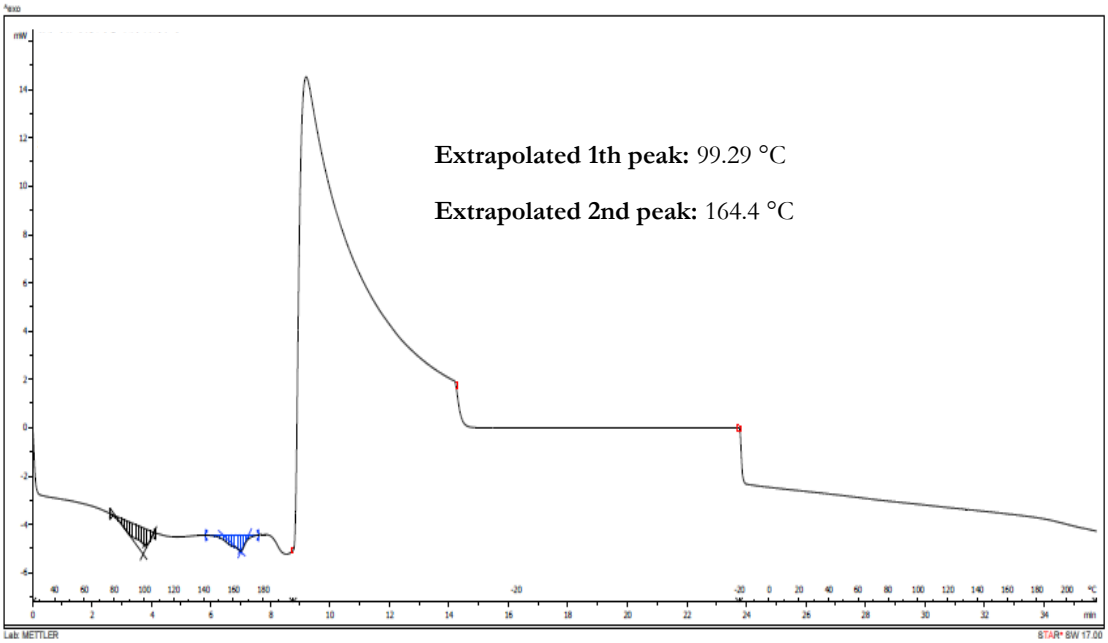

Figure S4.5. DSC profile of $Cu_3(MoO_4)_2(OH)_2$ _ref expressed both in °C (above the x axis) and in minutes (below the x axis).

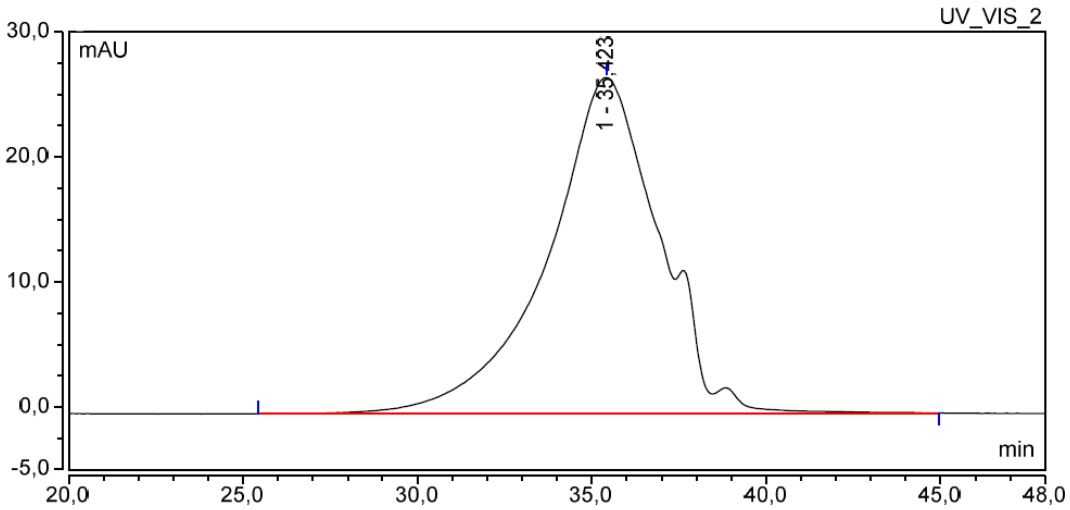

Figure S4.6. SEC Chromatogram of HMW@$Cu_3(MoO_4)_2(OH)_2$. Measurements are performed in duplicate and mediated.

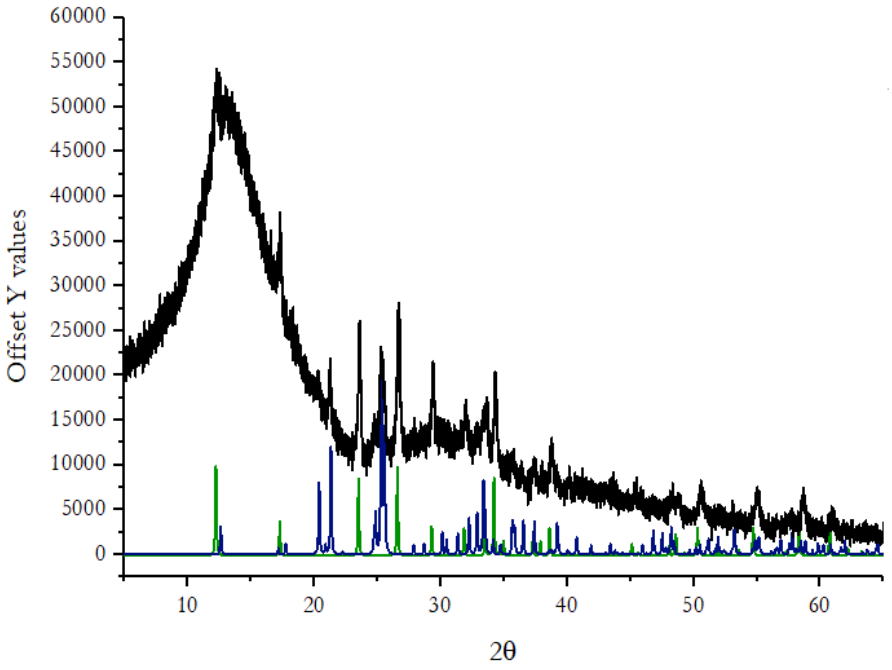

Figure S4.7: Experimental PXRD pattern of HMW@Mo_Cu (black) compared to the one of lindgrenite COD 9004056 (blue) and of $NH_4Cu_2(MoO_4)_2(OH)(H_2O)$ COD 1536670 (green), evidencing the presence of both phases in the material.

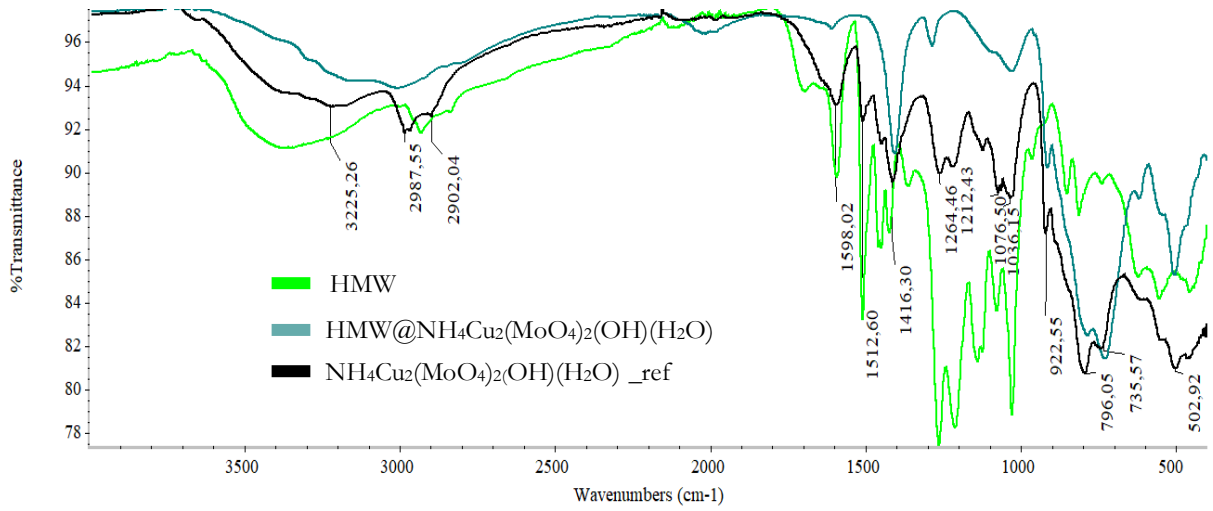

Figure S4.8. Stacked FT-IR spectra of HMW@$NH_4Cu_2(MoO_4)_2(OH)(H_2O)$ (dark green), compared to the one of HMW (light green) and $NH_4Cu_2(MoO_4)_2(OH)(H_2O$_ref (black).

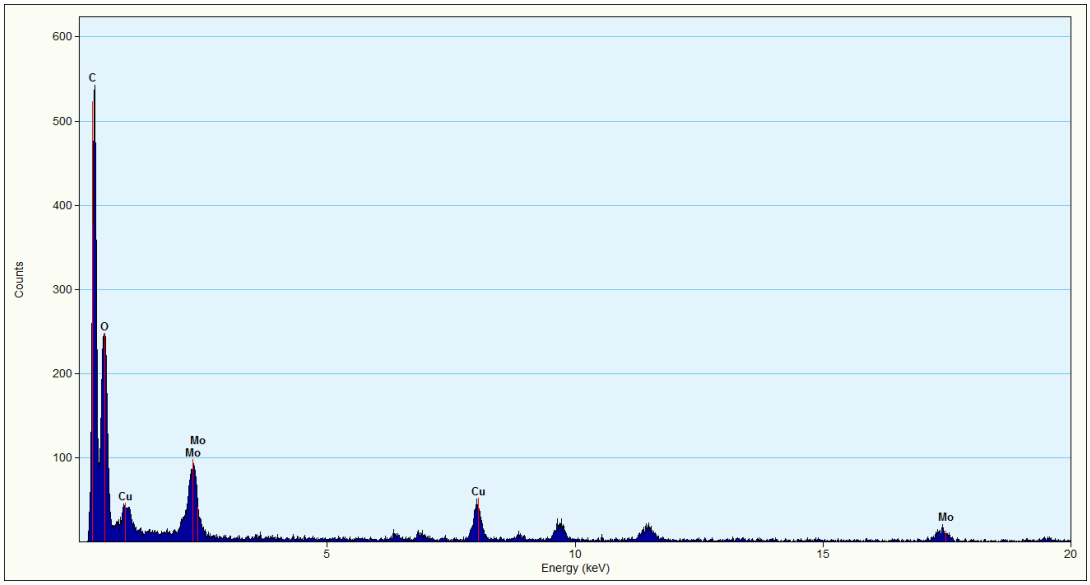

Figure S4.9. EDX analysis shows the composition of the lindgrenite crystals synthesized from sodium molybdate.

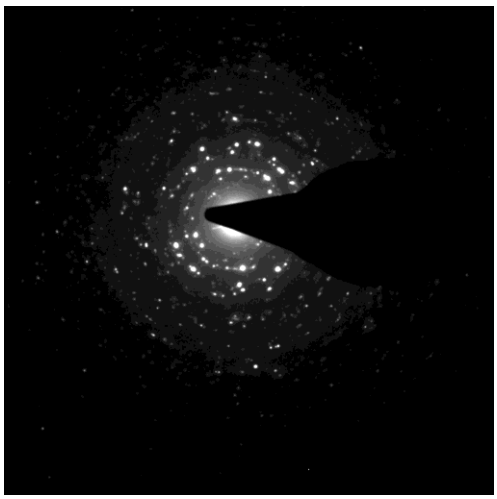

d^{-1} (nm^{-1})	d (nm)	
2.42	0.413	(-101)
2.983	0.353	(031)
3.69	0.271	(210)
4.03	0.248	(-221)
4.32	0.231	(211)
4.84	0.206	(-142) (-202)

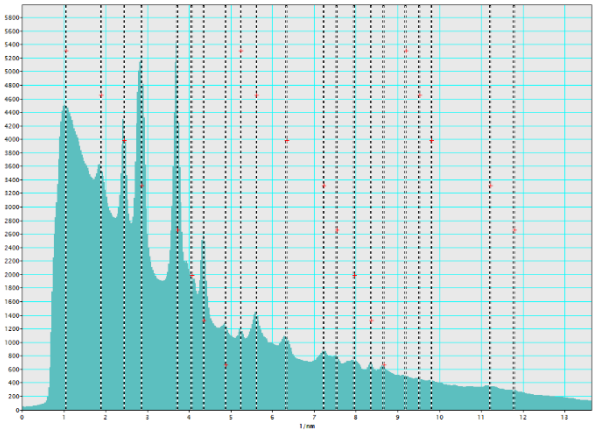

Figure S4.10. Selected Area Electron Diffraction (SAED) collected from an area of 200 nm along with the corresponding radial average. The table shows the most intense reflections, all indexed as lindgrenite (AMCSD 005073).

Display name	Standard data	Quantification method	Result Type
Spc_002	Standardless	ZAF	Metal

Element	Line	Mass%	Atom%
C	K	44.87	62.83
O	K	29.54	31.05
Na	K	0.97	0.71
S	K	0.72	0.38
Zn	K	10.34	2.66
Mo	L	13.56	2.38
Total		100.00	100.00
Spc_002			Fitting ratio 0.0103

Figure S4.11. EDX with ZAF correction results are reported, showing percentages of zinc and molybdenum.

a)

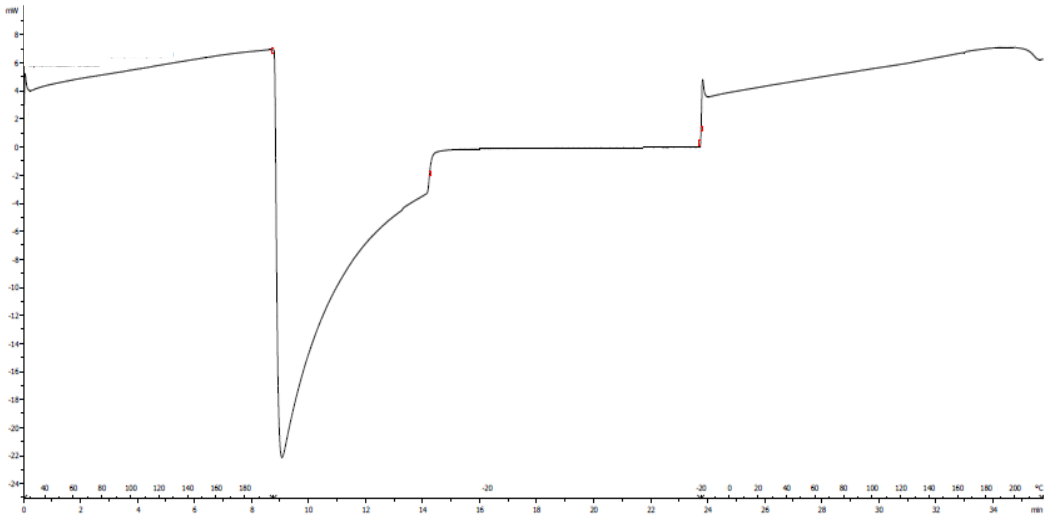

b)

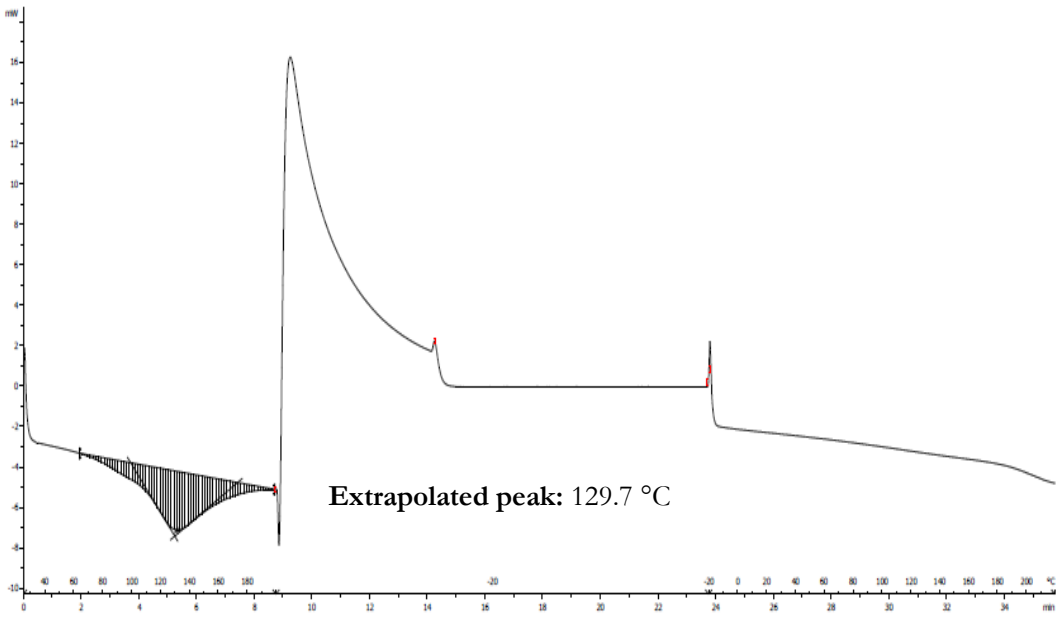

Figure S4.12. DSC profile of a) $NH_4Zn_2(MoO_4)_2(OH)(H_2O)$_ref and b) HMW@$NH_4Zn_2(MoO_4)_2(OH)(H_2O)$expressed both in °C (above the x axis) and in minutes (below the x axis).

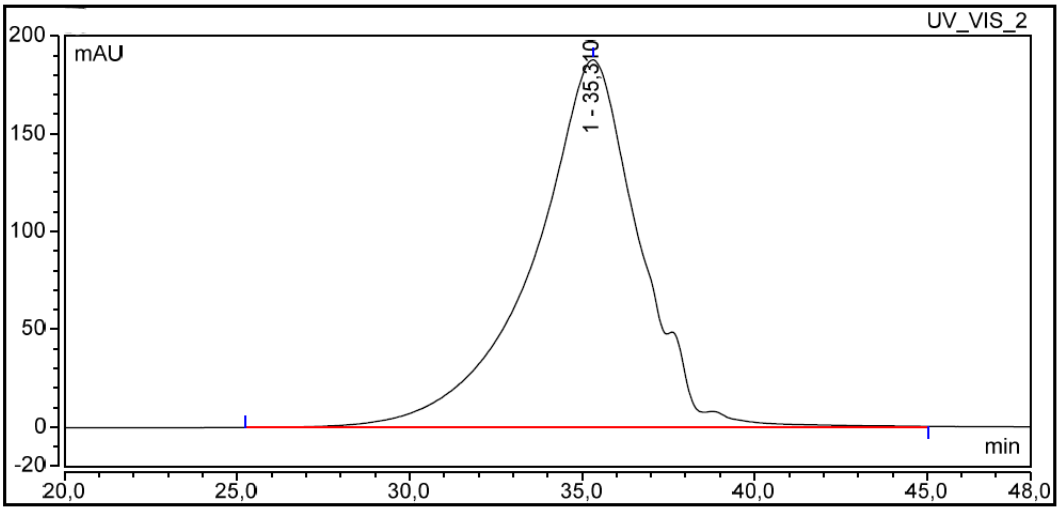

Figure S4.13. SEC chromatogram of HMW@ $NH_4Zn_2(MoO_4)_2(OH)(H_2O)$.Measurements are performed in duplicate and mediated.

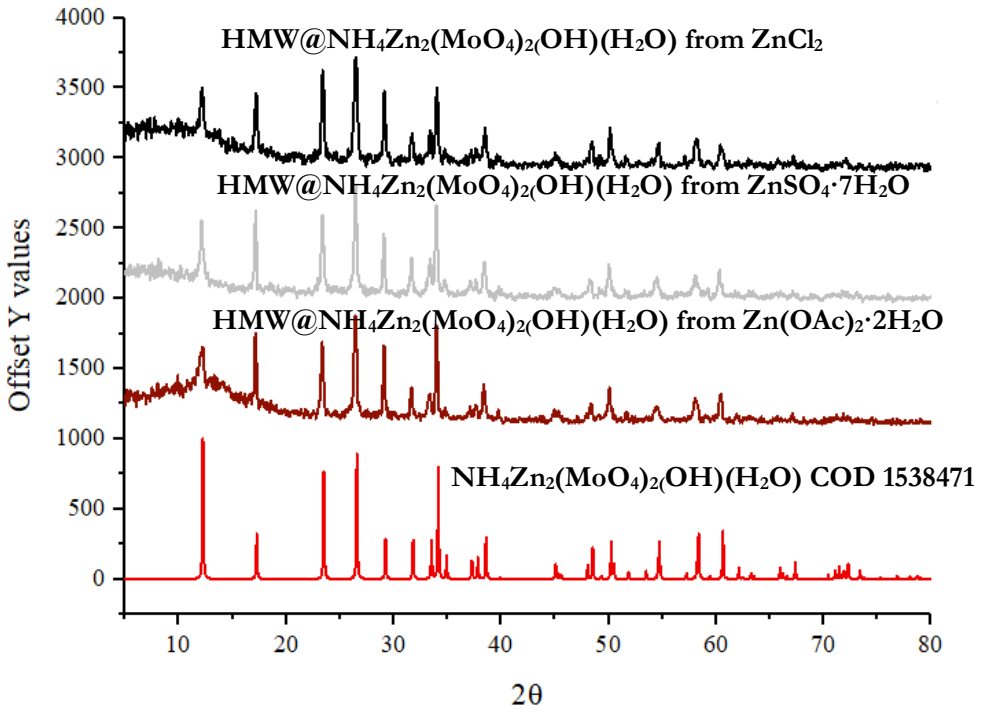

Figure S4.14. Experimental PXRD pattern of HMW@$NH_4Zn_2(MoO_4)_2(OH)(H_2O)$ obtained from $ZnCl_2$ (black), HMW@$NH_4Zn_2(MoO_4)_2(OH)(H_2O)$ obtained from $ZnSO_4·5H_2O$ (light grey), HMW@$NH_4Zn_2(MoO_4)_2(OH)(H_2O)$ obtained from $Zn(OAc)_2·2H_2O$ (dark red) compared to the one of $NH_4Zn_2(MoO_4)_2(OH)(H_2O)$_ref COD 1538471 (red).

a)

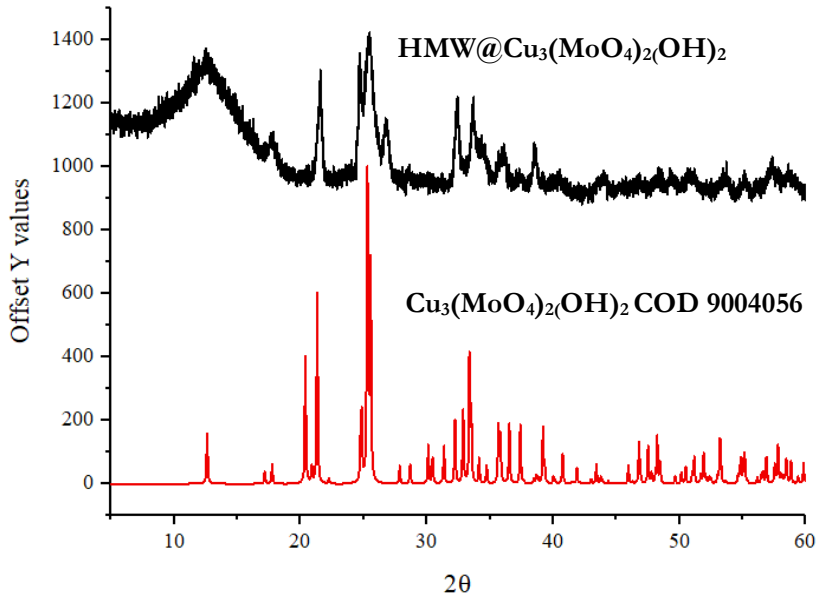

b)

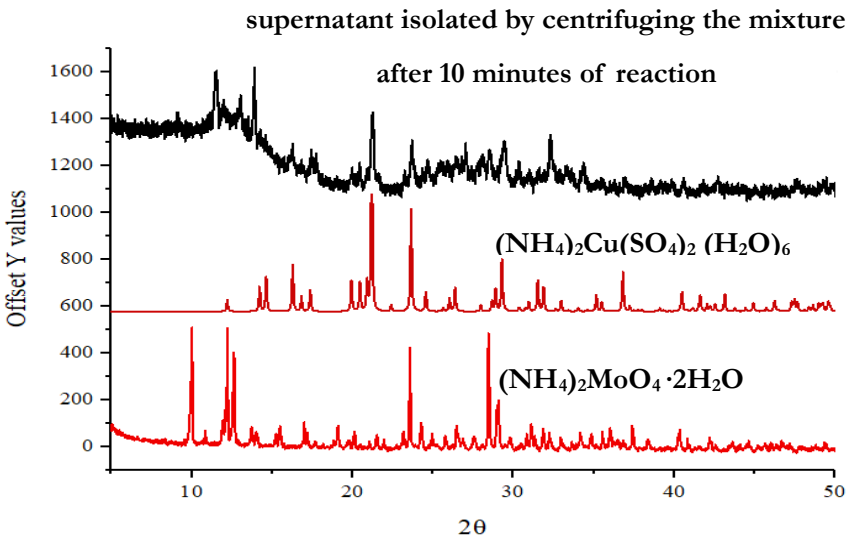

Figure S4.15. Experimental PXRD pattern of a) the solid fraction isolated by centrifuging the whole mixture of reaction after 10 minutes of reaction stirring, compared to the one of lindgrenite COD 9004056. b) the aquamarine supernatant isolated centrifuging the mixture of reaction after 10 minutes, dried at 85 °C (black) compared to those of $(NH_4)_2Cu(SO_4)_2{\cdot}(H_2O)_6$ (dark red line) and $(NH_4)_2MoO_4 \cdot 2H_2O$ (red).

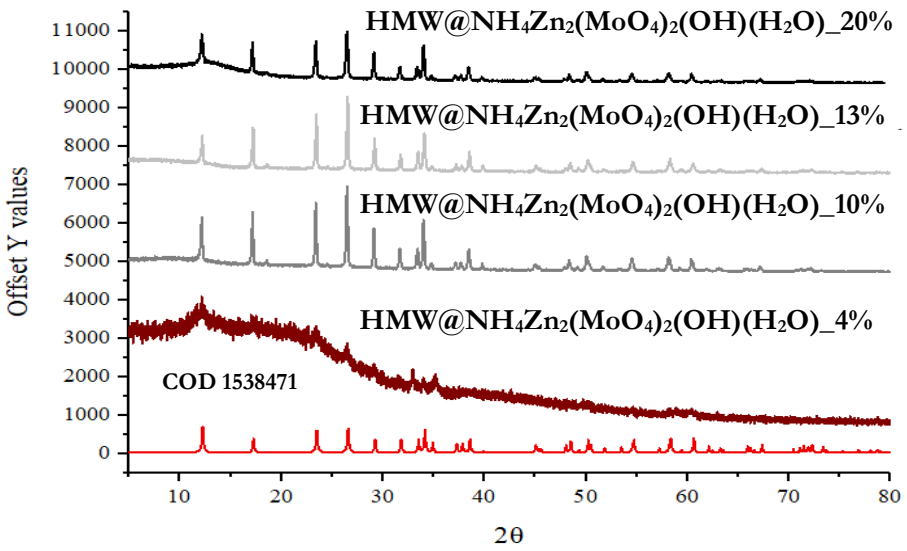

Figure S4.16. The experimental PXRD pattern of HMW@$NH_4Zn_2(MoO_4)_2(OH)(H_2O)$_4%(dark red), 10% (dark grey line), 13% (light grey), 20% (black) compared to the one of $NH_4Zn_2(MoO_4)_2(OH)(H_2O)$ COD 1538471 (red).

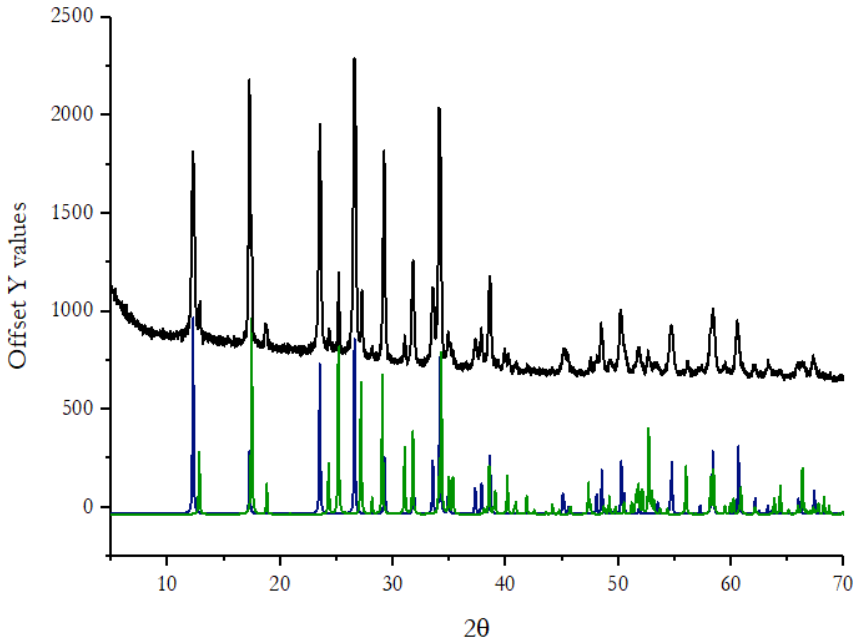

Figure S4.17. Experimental PXRD pattern of the material obtained with stoichiometric amount of base (black pattern) is a mixture of the two phases, $NaZn_2(MoO_4)_2(OH)(H_2O)$ (green) COD 4344530, and of $NH_4Zn_2(MoO_4)_2(OH)(H_2O)$ COD 1538471 (blue).

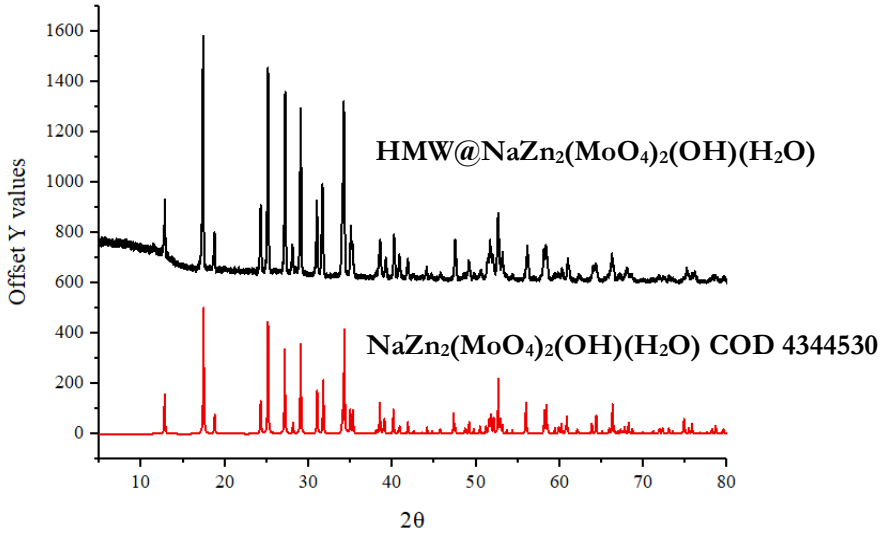

Figure S4.18. Experimental PXRD pattern of HMW@$NaZn_2(MoO_4)_2(OH)(H_2O)$ (black pattern) compared to those of $NaZn_2(MoO_4)_2(OH)(H_2O)$ (red) COD 4344530.

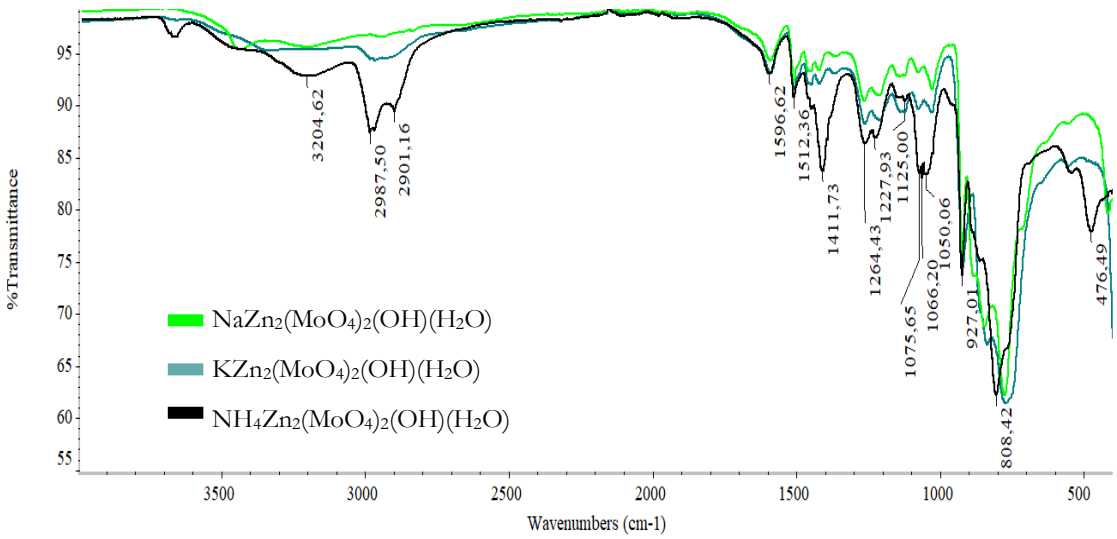

Figure S4.19. Stacked FT-IR spectra of HMW@$NH_4Cu_2(MoO_4)_2(OH)(H_2O)$ (black), compared to the one of $NaZn_2(MoO_4)_2(OH)(H_2O)$ (light green) and $KZn_2(MoO_4)_2(OH)(H_2O)$ (dark green).

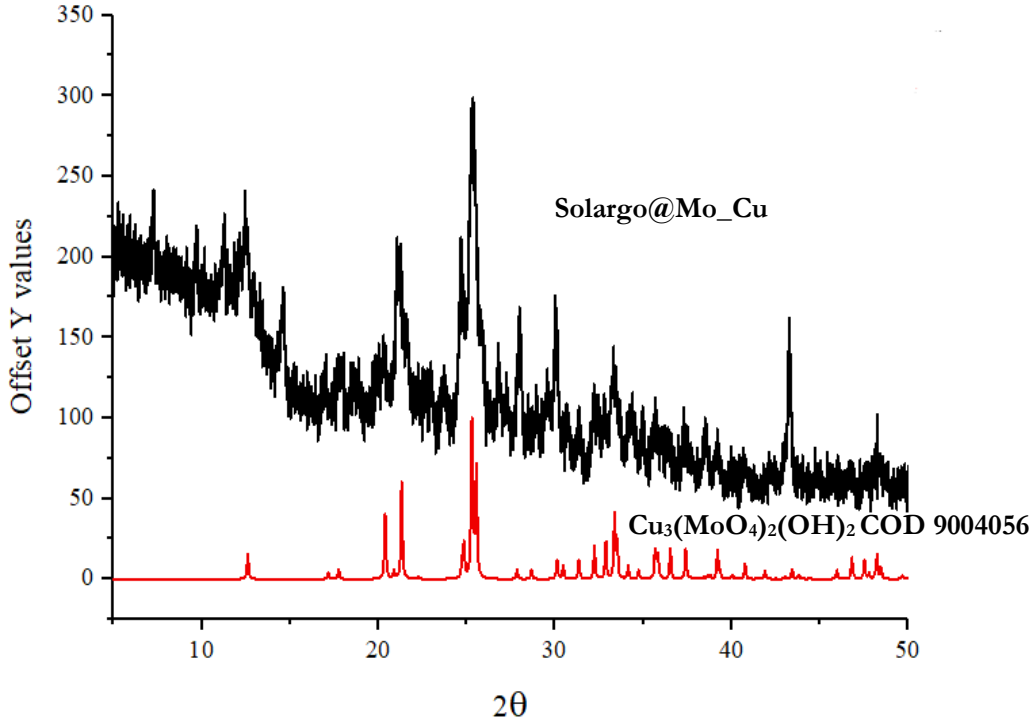

Figure S4.20. Experimental PXRD pattern of Solargo@Mo_Cu isolated from lignin/molybdenum salt 0.9 g/g ratio and Mo:Cu:OH^- 1:1.5:2.3 equivalents, compared to the one of lindgrenite COD 9004056, showing the presence of other unidentified phases.

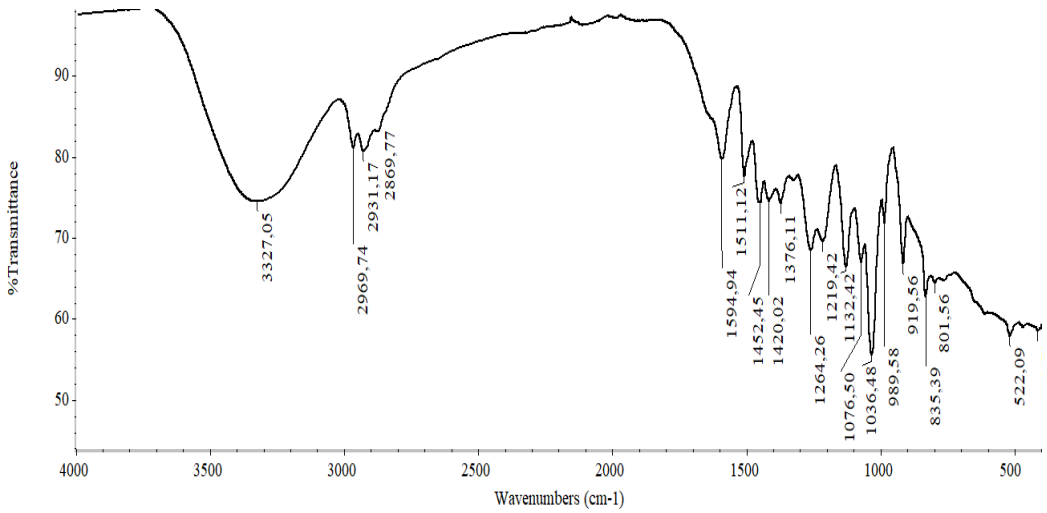

Figure S4.21. The FT-IR spectrum of Solargo@$KZn_2(MoO_4)_2(OH)(H_2O)$ (black).

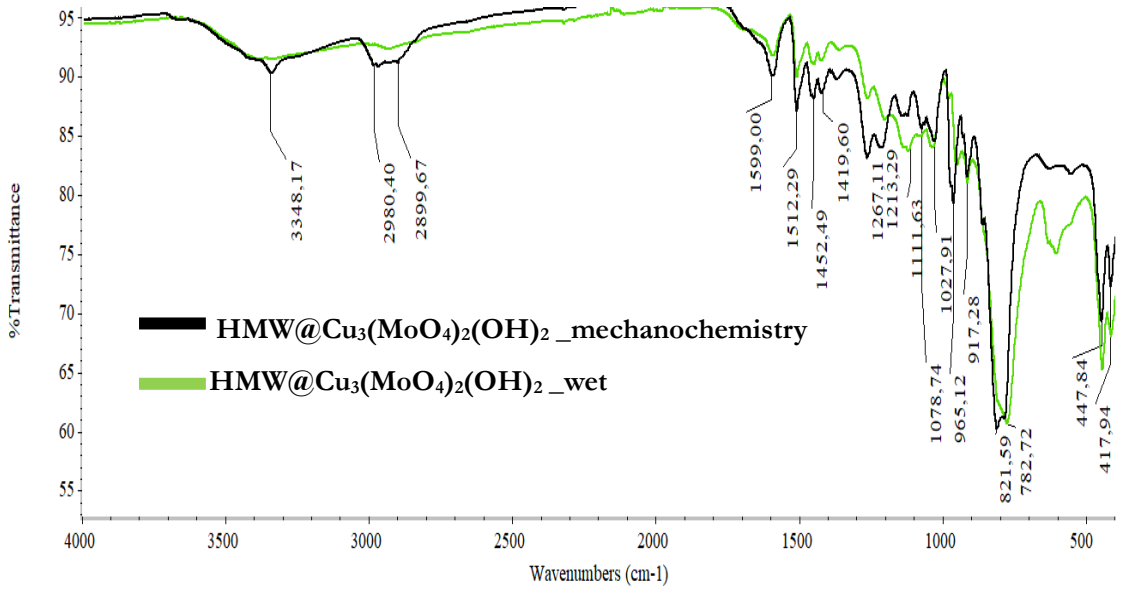

Figure S4.22. Stacked FT-IR spectra of HMW@$Cu_3(MoO_4)_2(OH)_2$_mechanochemistry (light green), compared to the one of HMW@$Cu_3(MoO_4)_2(OH)_2$ _wet (black).

References

[1] K. J. Redd, L. C. Munn, L. Wang, Chemistry and Mineralogy of Molybdenum in Soils. *Communications in Soil Science and Plant Analysis*, **28**(13-14), 1193-1211,1997

[2] B.N. Kaiser, K.L. Gridley, J. Ngaire, T. Brady Phillips, S. D. Tyerman The Role of Molybdenum in Agricultural Plant Production. *Ann Bot.,* **96**(5):745-54, 2005. DOI: 10.1093/aob/mci226

[3] P. R. Stout, W. R. Meagher, G. A. Pearson, C. M. Johnson, Molybdenum Nutrition of Crop Plants. The Influence of Phosphate and Sulfate on the Absorption of Molybdenum from Soils and Solution Cultures. *Plant and Soil*, **3**(1), 51-87, 1951. DOI: 10.1007/BF01348559

[4] S. M.Zahedi, M. Marjani, H. Rostami Ahmadvandi, M. Alemian, M. Ikram, R. Gholami, S. Sarikhani, A. Ludwików, P. Carillo, Molybdenum Amelioration of Drought Stress in Agricultural Crops: A Detailed Overview of Mechanistic Actions and Future Perspectives. *South African Journal of Botany*, 2024, DOI: 10.1016/j.sajb.2024.09.030

[5] M. A. Hossain, T. Kamiya, T. Fujiwara, Molecular and Genomic Perspectives in Crop Plants. *Plant Micronutrient Use Efficiency*, 137-159, 2018

[6] U. C. Gupta, Soil and Plant Factors Affecting Molybdenum Uptake in Plants. *Communication in Soil Science and Plant Analysis*, **9**(1), 1-9, 1978

[7] M. M. Riley, A.D. Robson, J.W. Gartrell, R.C. Jeffery, The Absence of Leaching of Molybdenum in Acidic Soil from Western Australia. *Australian Journal of Soil Research*, **25**(4), 435-445, 1987

[8] C. Zou, X Gao, R. Shi, X. Fan, F. Zhang, Micronutrient Deficiencies in Global Crop Production. *Micronutrients in Soils, Crops and Fertilizers*, 3825, 2018. DOI: 10.1007/978-1-4020-6860-7

[9] D.I. Arnon, P.R. Stout, The Essentiality of Certain Elements in Minute Quantity for Plants with Special Reference to Copper. *Plant Physiology*, **14**, 371-375, 1939. DOI: 10.1104/pp.14.2.371

[10] K. J. Mitchell, Preliminary Note on the Use of Ammonium Molybdate to Control Whiptail in Cauliflower and Broccoli Crops. *New Zealand Journal of Science and Technology, Section A: Agricultural Research*, **27**(4), 287-293, 1945

[11] T. M. Ezz, A. M. Kobbia, Effects of Molybdenum Nutrition on Growth, Nitrate Reductase Activity, Yield, and Fruit Quality on Balady Mandarin Trees Under Low and High Nitrogen Levels. *Alexandria Journal of Agricultural Research*, **44**(1), 227-238, 1999

[12] E. G. Mulder, Importance of Molybdenum in the Nitrogen Metabolism of Microorganisms and Higher Plants. *Plant and Soil*, **1**(1), 94-119, 1948. DOI: 10.1007/BF01348613

[13] A. Cockburn, G. Brambilla, M. L.Fernández, D. Arcella, L. R. Bordajandi, B. Cottrill, C. van Peteghem, J. L. Dorne, Nitrite in Feed: From Animal Health to Human Health. *Toxicology and Applied Pharmacology*, **270**, 209-217, 2013

[14] C. O. Dimkpa, J. Andrews, J. Sanabria, P. S. Bindraban, U. Singh, W. H. Elmer, J. L. Gardea-Torresdey, J.C. White, Interactive Effects of Drought, Organic Fertilizer, and Zinc Oxide Nanoscale and Bulk Particles on Wheat Performance and Grain Nutrient Accumulation. *Sci Total Environ*, **722**, 137808, 2020. DOI: 10.1016/j.scitotenv.2020.137808

[15] D. Tilman, C. Balzer, J. Hill, B. L. Befort, Global Food Demand and the Sustainable Intensification of Agriculture. *Proceedings of the National Academy of Sciences of the United States of America*, **108**(50), 20260-20264, 2011. DOI:10.1073/pnas.1116437108

[16] M. E. Trenkel, Slow- and Controlled Release and Stabilized Fertilizers in Agriculture: An Option for Enhancing Nutrient Use Efficiency in Agriculture, 2nd ed.; *International Fertilizer Industry Association* (IFA): 2010

[17] Goyal, S.; Huffaker, R. Nitrogen Toxicity in Plants. In Nitrogen in Crop Production; 1990. DOI: 10.2134/1990.nitrogenincropproduction.c6

[18] M. Y. Naz, S. Sulaiman, Slow-Release Coating Remedy for Nitrogen Loss from Conventional Urea: A review. *Journal of Controlled Release*, **238**, 108-116, 2016. DOI: 10.1016/j.jconrel.2016.01.037

[19] R. Kumar, M.A. Laskar, I.F. Hewaidy, Modified Adsorbents for Removal of Heavy Metals from Aqueous Environment: A Review. *Earth Systems and Environment*, **3**, 83-93, 2019. DOI: 10.1007/s41748-018-0085-3

[20] S. Fertahi, M. Berrada, A. El Ghzaoui, M. Alami, M. Filali, M. Belmokhtar, S. Amzazi, The Effect of Bio-based Nanomaterials on the Controlled Release of Fertilizers. *International Journal of Biological Macromolecules*, **139**, 805-818, 2019. DOI: 10.1016/j.ijbiomac.2019.12.005

[21] S. Iravani, R. S. Varma, Plants and Plant-Based Polymers as Scaffolds for Tissue Engineering. *Green Chemistry*, **21**, 4839-4867, 2019. DOI: 10.1039/C9GC02391G

[22] V. Sinisi, P. Pelagatti, M. Carcelli, A. Migliori, L. Mantovani, L. Righi, G. Leonardi, S. Pietarinen, C. Hubsch and D. Rogolino, A Green Approach to Copper-Containing Pesticides: Antimicrobial and Antifungal Activity of Brochantite Supported on Lignin for the Development of Biobased Plant Protection Products. *ACS Sustainable Chem. Eng.,* **7**, 3213, 2019, DOI: 10.1021/acssuschemeng.8b05135

[23] C. Gazzurelli, A. Migliori, P. P. Mazzeo, M. Carcelli, S. Pietarinen, G. Leonardi, A. Pandolfi, D. Rogolino and P. Pelagatti, Making Agriculture More Sustainable: An Environmentally Friendly Approach to the Synthesis of Lignin@Cu Pesticides. *ACS Sustainable Chem. Eng.,* **8**, 14886, 2020 DOI:10.1021/acssuschemeng.0c04645

[24] C. Gazzurelli, M. Carcelli, P. P. Mazzeo, C. Mucchino, A. Pandolfi, A. Migliori, S. Pietarinen, G. Leonardi, D. Rogolino and P. Pelagatti, Exploiting the Reducing Properties of Lignin for the Development of an Effective Lignin@Cu_2O Pesticide. *Adv. Sustainable Syst.,* **6,** 2200108, 2022, DOI:10.1002/adsu.202200108

[25] M. Basta, H. A. Yassin, R. G. Aly, N. S. El Sayed, Possible Protective Effect of Zinc Administration on Renal and Cognitive Changes Occurring in Uninephrectomized Adult Male Wistar Rats. *Experimental Physiology*, **107**(3), 367-376, 2022. DOI:10.1113/EP090735

[26] B. Chen, P. Yu, W. N. Chan, F. Xie, Y. Zhang, L. Liang, K. T. Leung, K. W. Lo, J. Yu, G. M. K. Tse, W. Kang, K. F. To, Cellular Zinc Metabolism and Zinc Signalling: from Biological Functions to Diseases and Therapeutic Targets. *Signal Transduction and Targeted Therapy*, **9**, 2024. DOI:10.1038/s41392-024-00850-0

[27] G. Chen, J. Li, H. Han, R. Du, X. Wang, Physiological and Molecular Mechanisms of Plant Responses to Copper Stress. *Environmental and Experimental Botany*, **185**, 104471, 2024. DOI:10.1016/j.envexpbot.2024.104471

[28] Scott, M.L. Trace Elements in Animal Nutrition. In: Mortveldt, J.J.; Giordano, P.M.; Lindsay, W.L., eds. *Micronutrients in Agriculture*. Soil Science Society of America, 1972, Madison, WI.

[29] J.P. Zubrod, M. Bundschuh, G. Arts, C.A. Brühl, G. Imfeld, A. Knäbel, S. Payraudeau, J.J. Rasmussen, J. Rohr, A. Scharmüller, K. Smalling, S. Stehle, R. Schulz, R.B. Schäfer, Fungicides: An Overlooked Pesticide Class? *Environ. Sci. Technol.* **53** (7), 3347–3365, 2019. DOI:10.1021/acs.est.8b04392.

[30] H. Tao, Z. Bao, C. Jin, W. Miao, Z. Fu, Y. Jin, Toxic Effects and Mechanisms of Three Commonly Used Fungicides on the Human Colon Adenocarcinoma Cell Line Caco-2. *Environ. Pollut.,* **267**, 114660, 2020. DOI:10.1016/j.envpol.2020.114660

[31] M. A. Ghannoum, L. B. Rice, Antifungal Agents: Mode of Action, Mechanisms of Resistance, and Correlation of These Mechanisms with Bacterial Resistance. *Clin. Microbiol. Rev.,* **12** (4), 501–517, 1999. DOI:10.1128/cmr.12.4.501.

[32] V. V. Husak, Copper and Copper-Containing Pesticides: Metabolism, Toxicity, and Oxidative Stress. *Journal of Vasyl Stefanyk Precarpathian National University*, **2**(1), 38-50, 2015. DOI: 10.15330/jpnu.2.1.38-50

[33] F. M. Fishel, Pesticide Toxicity Profile: Copper-Based Pesticides: *PI-66/PI103*, 2005. DOI:10.32473/edis-pi103-2005.

[34] D. C. Reyes, Z. Ma, J. J. Romero, The Antimicrobial Properties of Technical Lignins and Their Derivatives—A Review. *Polymers*, **16**(15), 2181, 2024. DOI: 10.3390/polym16152181

[35] C. C. De Foggi, R. C. De Oliveira, M. Assis, M. T. Fabbro, V. R. Mastelaro, C. E. Vergani, L. Gracia, J. Andrés J, E. Longo, A. L. Machado, Unveiling the role of β-Ag_2MoO_4 Microcrystals to the Improvement of Antibacterial Activity, *Mater. Sci. Eng. C.*, **111**, 110765, 2020. DOI: 10.1016/j.msec.2020.110765

[36] B. Lavakusa, D. R. Devi, N. Belachew, K. Basavaish, Selective Synthesis of Visible Light Active γ-Bismuth Molybdate Nanoparticles for Efficient Photocatalytic Degradation of Methylene Blue, Reduction of 4-Nitrophenol, and Antimicrobial Activity. *RSC Adv.,* **10**, 36636–36643, 2020. DOI: 10.1039/D0RA07459D

[37] A. Mobeen, C. Maria Magdalane, S. K. Jasmine Shahina, D. Lakshmi, R. Sundaram, G. Ramalingam, A. Raja, J. Madhavan, D. Letsholathebe, A. K. H. Bashir, M. Maaza, K. Kaviyarasu, Investigation on Antibacterial and Photocatalytic Degradation of Rhodamine-B Dye under Visible Light Irradiation by Titanium Molybdate Nanoparticles Prepared *via* Microwave Method. *Surf. Interfaces.*, **17**, 100381, 2017. DOI: 10.1016/j.surfin.2019.100381

[38] D. Tanasic, A. Rathner, J. P. Kollender, P. Rathner, N. Muller, K. C. Zelenka, A. W. Hassel, C. C. Mardare, Silver-, Calcium-, and Copper Molybdate Compounds: Preparation, Antibacterial Activity, and Mechanisms. *Biointerphases*, **12**, 05G607, 2017. DOI:10.1116/1.4996434

[39] F. Karkeh-Abadi, F. Soofivand, H. Safardoust-Hojaghan, Q. A. Yousif, M. Saavati-Niasari, Sonochimical Synthesis, Characterization and Physicochemical Properties of $Cu_3Mo_2O_9$ Graphene-Based Nanocomposites for Antibacterial Therapeutic Agent with Enhanced Activity, *J. Mater. Res. Technol*, **18**, 4413–4426, 2022. DOI: 10.1016/j.jmrt.2022.04.089

[40] A. Gaur, M. Stehle, K. V. Raun, J. Thrane, A. D. Jensen, J. D. Grunwaldt, M. Høj, Structural Dynamics of an Iron Molybdate Catalyst under Redox Cycling Conditions Studied with *in Situ* Multi-Edge XAS and XRD. *Phys. Chem. Chem. Phys.*, **22**, 11713-11723, 2020. DOI:10.1039/D0CP01506G

[41] T. A. F. Carvalho, F. X., Nobre, A. Barros, A. Ghosh, A. Lima, A. Silva, R. O. Fontenelle, RM. C. Santos, J. M. E. Matos, Investigation of Optical, Structural, and Antifungal Properties of Lindgrenite Obtained by Conventional Coprecipitation and Ultrasound-Assisted Coprecipitation Methods. *Journal of Solid State Chemistry,* ***300,*** 121957, 2021. DOI: 10.1016/j.jssc.2021.121957.

[42] Z. Xu, X. Lisha X, L. Yi, M. Yunjun, C. Luocheng, Z. Anqi, Y. Kuibo, X. Xiaolu, L. Shaozhen, S. Xuecheng, Z. Yifu, Highly Stable and Antifungal Properties on the Oilseed Rape of $Cu_3(MoO_4)_2(OH)_2$ Nanoflakes Prepared by Simple Aqueous Precipitation. *Sci Rep.*, **14**(1),5235, 2024. DOI: 10.1038/s41598-024-53612-0.

[43] J. Xia, L.X. Song, W. Liu, Y. Teng, Q.S. Wang, L. Zhao, M.M. Ruan, Highly Monodisperse $Cu_3Mo_2O_9$ Micropompons with Excellent Performance in Photocatalysis, Photocurrent Response and Lithium Storage, *RSC Adv.*, **5**, 12015-12024, 2015. DOI: 10.1039/C4RA15725G

[44] J. Xu, J., D. Xue, Hydrothermal Synthesis of Lindgrenite with a Hollow and Prickly Sphere-like Architecture. *Journal of Solid State Chemistry*, **179**(12), 3771-3777, 2006. DOI: 10.1016/j.jssc.2006.09.030

[45] B. Swain, D. H. Lee, J.R. Park, C.G. Lee, K. J. Lee, D. W. Kim, K.S. Park, Synthesis of $Cu_3(MoO_4)_2(OH)_2$ Nanostructures by Simple Aqueous Precipitation: Understanding the Fundamental Chemistry and Growth Mechanism. *CrystEngComm*, **18**(37), 6941-6949, 2016. DOI: 10.1039/C6CE02344D

[46] R. L. Bao, Z. Kong, M. Gu, B. Yue, L. Weng, H. He, Hydrothermal Synthesis and Thermal Stability of Natural Mineral Lindgrenite. *Journal of Rare Earths*, **24**(4), 468-472, 2006. DOI: 10.1016/S1005-9040(06)60189-X

[47] I. Sajó, L. Bakos, I. M. Szilágyi, G.Lendvay, J. Magyari, M. Mohai, Á.Szegedi, A. Farkas, A. Jánosity, S. Klébert, L. Kótai, Unexpected Sequential NH_3/H_2O Solid/Gas Phase Ligand Exchange and Quasi-Intramolecular Self-Protonation Yield $[NH_4Cu(OH)MoO_4]$, a Photocatalyst Misidentified Before as $(NH_4)_2Cu(MoO_4)_2$. *Inorganic Chemistry*, **57**(24), 15474-15484, 2018. DOI: 10.1021/acs.inorgchem.8b02261

[48] C. F. Eno, W. G. Blue, J. M. Jr. Good, The Effect of Anhydrous Ammonia on Nematodes, Fungi, Bacteria, and Nitrification in some Florida Soils. *Soil Science Society of America Journal*, **19**(1), 13-17, 1955. DOI: 10.2136/sssaj1955.03615995001900010013x

[49] S. A. Omar, M.A. Ismail, Microbial Populations, Ammonification and Nitrification in Soil Treated with Urea and Inorganic Salts. *Folia Microbiol (Praha)*. **44**(2), 205-12, 1999. DOI: 10.1007/BF02816244.

[50] Y. Singh, E. G. Beauchamp, Nitrogen Transformations near Urea in Soil with Different Water Potentials. *Canadian Journal of Soil Science*, **68**(3), 517-525, 1988. DOI: 10.4141/cjss88-055

[51] D. Levin, S. L. Soled, J. Y. Ying, Synthesis of a Layered Ammonium Zinc Molybdate. *Chemistry of Materials*, **8**(4), 926-930, 1996. DOI: 10.1021/cm960087y

[52] S. M. Reddy, S.B. Karmankar, H. A. Alzahrani, A. Hadap, A.Iqbal, R. Alenazy, M. M. Salem-Bekhit, B. Jain, Bioinspired Synthesis of Zinc Molybdate Nanoparticles: An Efficient Material for Growth Inhibition of *Escherichia coli*, *Staphylococcus aureus*, and Dye Remediation. *Bioinorg Chem Appl.*, 1287325, 2023. DOI: 10.1155/2023/1287325.

[53] A. S.Naeini, M. S. Seyed Dorraji, M. Rastgar, F. Daei, The Role of Zinc Molybdate in the Anticorrosion and Antibacterial Characteristics of Sustainable Polyurethane Coating Derived from

Epoxidized Soybean Oil, *Industrial Crops and Products,* **216**, 123, 2024. DOI: 10.1016/j.indcrop.2024.118771

[54] https://www.crystallography.net/cod/

[55] N. M. Stark, D. J. Yelle, U. P. Agarwal, Techniques for Characterizing Lignin. *Lignin Chemistry and Applications*, 65–86, Elsevier, 2016. DOI:10.1016/B978-0-323-35565-0.00004-7

[56] W. G. Glasser, Classification of Lignin According to Chemical and Molecular Structure. *Lignin: Historical, Biological, and Materials Perspectives*, **742**, 216–238, 1999. Washington, DC: American Chemical Society. DOI: 10.1021/bk-1999-0742.ch014

[57] A. Roy, L. Girardi, D. Mosconi, M. Tahar Sougrati, D. Jones, S. Agnoli, F. Jaouen, Bifunctional Zinc-Molybdate or Zinc Molybdenum Oxide/Metal-Nitrogen-Carbon Catalytic Layers with Improved Four-Electron Selectivity for Oxygen Reduction in Acidic Medium, *Electrochimica Acta,* **273**, 61–70, 2018. DOI: 10.1016/j.electacta.2018.03.169

Characterization techniques

This section summarizes the characterization techniques employed in this thesis to analyse various samples, including synthesized materials and starting lignin. Samples preparations are also described. The comprehensive characterization techniques have been applied to study the obtained hybrid materials and to evaluate the Cr(VI) removal properties of the materials in this thesis, providing valuable insights into their possible applications in agronomical field and in water remediation processes.

Powder X-ray Diffraction (PXRD)

The PXRD (Powder X-ray Diffraction) patterns have been recorded with a Rigaku diffractometer Smartlab XE in a theta-theta Bragg-Brentano geometry, using a Cu Kα radiation and a solid-state HyPix3000 2D detector. Data have bene collected in the 5-80 (2θ) (deg) range with a step size 0.019 with time for step 0.1. Data have been collected with 5° Soller slits. The software QualX has been used to identify the inorganic phase. Pawley refinements have been used to evaluate the content of the materials based on cell parameters from the literature.

Inductively Coupled Plasma - Atomic Emission Spectroscopy (ICP-AES)

ICP-AES analyses performed to determine the percentages of metals in the hybrid materials. 10 mg of solid sample have been suspended in 5 mL of HNO_3 65% (w/w) and 1 mL of H_2O_2 30% (w/w), then digested in a *Milestone* microwave MLS-1200 MEGA (digestion sequence: 1 min at 250 W, 1 min at 0 W, 5 min at 250 W, 5 min at 400 W, 5 min at 650 W, 5 min of cooling). Acid solutions have been diluted to 50 mL with ultrapure water and analyzed by a HORIBA Jobin Yvon - ULTIMA 2 (Kyoto, Japan) inductively coupled plasma spectrometer in radial configuration. The emission intensity measurements have been acquired under the conditions shown in Table 5.1. Data acquisition and processing have been performed using the ICP JY v 5.2 software (Jobin Yvon). Measurements have been performed in triplicate.

ICP-AES analysis on root and shoot samples after *in vivo* studies conducted on tomato plants: 0.25 g of dry solid sample have been suspended in 3 mL of HNO_3 65% and 1 mL of H_2O_2 30%, then digested in a Milestone microwave MLS-1200 MEGA, according to the digestion sequence previously reported. The solutions have been diluted to 10 mL with ultrapure water and analyzed by using the HORIBA Jobin Yvon - ULTIMA 2 (Kyoto, Japan) inductively coupled plasma spectrometer in radial configuration. Quantitative analysis has been performed after the acquisition of a calibration curve using standard solutions in HNO_3 10%, to simulate the final acidity of the samples; the concentration range of the standards varied from 0.5 mgL^{-1} to 40 mgL^{-1}. Data acquisitions and processing were performed using the ICP JY v 5.2 software (Jobin Yvon). Measurements have been performed in triplicate.

Table 5.1. Operating parameters for the inductively coupled plasma spectrometer

Incident output power	1000 W
Reflected power	< 2 W
Nebulizer	Glass, Meinhard
Plasma gas flow rate	12 l min^{-1}
Auxiliary gas flow rate	0.8 l min^{-1}
Solution uptake rate	1 ml min^{-1}
Wavelength	213.856 nm
Signal integration time	1 s
Integration for determination	3
Voltage	630
Gain	10

For **ICP-AES of liquid samples containing chromium**, the solutions have been either analysed as they were or diluted 1:2 with bi-distilled water and 1:100 with 10% HNO_3, then analysed using an emission spectrometer JY 2501 with coupled plasma induction in radial configuration HORIBA Jobin Yvon (Kyoto, Japan), ULTIMA2 model. Instrumental features: monochromator Model JY 2501; focal length 1 m; resolution 5 pm; nitrogen flow 2 L/min. ICP source: nebulizer Meinhard, cyclonic spraying chamber; argon flow 12 L/min; wavelengths range 160-785 nm; optical bench temperature 32 °C. The wavelength used for quantitative analysis has been chosen by examining the emission line with greater relative intensity, ensuring that there was no spectral interference with the Argon emission lines. Acquisition parameters: wavelength Fe(nm); Cr (nm): 267.716. Voltage (V): 580; gain: 100. The quantitative analysis has been performed after the acquisition of a calibration line using standard solutions in HNO_3 10% for the solid samples and water for solutions to simulate the final acidity of the samples. The concentration range of the standards has been varied from 0.05 mg/L to 50 mg/L of Fe and 0.05 mg/L to 70 mg/L of Cr. Data acquisitions and processing have been performed using the ICP JY v 5.2 software (Jobin Yvon). Measurements have been performed in triplicate

UV-Visible measurements

UV–visible spectra have been collected with a Lambda 465 (PerkinElmer) Diode Array spectrophotometer equipped with a Peltier Control (PerkinElmer) using the 8-position cell changer as sample holder. 1 cm path length quartz cuvettes have been used in all experiments. The analyzed solutions have been prepared by dilution of the Cr(VI) containing supernatants of the lignin reduction tests. The 1,5-diphenyl carbazide (DPC, minimum purity 98 %) solution has been prepared as follows: 20 mg of 1,5-diphhenylcarbazide have been dissolved in 20 ml of ethanol (95 %) (solution A). In a 250 ml flask, 75 mL of 85% H_3PO_4 have been added, and the volume has been brought to 250 mL with distilled water (solution B). The final solution (C) has been obtained by slow addition of 20 mL of the DPC solution to 80 mL of the H_3PO_4 solution. This solution stored at 4°C should be used within 3-4 days. The spectra have been collected in the 200–

800 nm range and the calculations for the Cr(VI) concentrations have been performed taking in consideration the absorption at λ = 540 nm (maximum absorption of the Cr(VI)-DPC adduct). To prepare the solutions for the analysis, 1:10 of the total volume of the final solution has been constituted by solution C. The rest has been constituted by the diluted Cr(VI) solution (dilution factors 1:2.5, 1:20 and 1:100) to reach a final concentration of Cr(VI) in the range of 0.02 and 0.4 ppm (linearity interval of the technique). Calibration lines have been prepared each time the sample solutions have been analyzed. Those solutions have been obtained in the same way as the samples but using a 5-ppm stock solution of $K_2Cr_2O_7$ obtaining final samples with concentrations of 0.02, 0.05, 0.10, 0.20, 0.30 and 0.40 ppm. Linear regressions of the point of the calibration lines have been performed using the Origin program.

Transmission Electron Microscopy (TEM) and Energy Dispersive X-ray Spectrometry (EDX)

TEM characterizations have been performed by using a FEI TECNAI F20ST microscope operating at 200 kV and equipped with an EDAX PV9761-SUTW energy dispersive X-Ray spectrometer (EDX). The images have been collected in scanning electron transmission STEM mode using a high-angle Annular Dark Field Detector (HAADF). The intensity I of the image in this mode is proportional to the atomic number Z and the thickness t of the sample (Z1.7t). Several Selected Area Diffractions (SAED) have been recorded, and Energy Dispersive X-ray Spectroscopy (EDX) spectra collected. The powder has been dispersed in isopropyl alcohol and sonicated for 90 minutes. The dispersion has been deposited on a perforated carbon film supported by a copper grid and dried at 60 °C.

Scanning Electron Microscopy (SEM) and Energy Dispersive X-ray Spectrometry (EDX)

SEM (scanning electron microscopy) analyses have been performed on a field emission scanning electron microscope Hitachi FE-SEM (model SU5000) equipped with EDX for microanalysis. EDX has been carried out using Thermo Scientific NORAN System 7 with an energy resolution (HWHM) ≤ 126eV (Mn-Kα @ 10 000 count per second) and using PathFinder X-ray Microanalysis Software. Images have been collected in high vacuum mode. Morphological analyses and image Z-contrast analyses have been performed detecting the signal of secondary electrons (SE) or of backscattered electron (BSE), respectively, operating with an acceleration voltage of 2.0kV. Spectra have been acquired at 15kV.

Dynamic Light Scattering (DLS)

The particles size of the synthesized materials has been studied by DLS using a Zetasizer Nano ZSP (Malvern). The measures have been performed at an angle of 175°. The hybrid materials (2 mg) have been suspended in water (3 mL) and sonicated for 5 min prior to the analysis with Ultrasonik NEY 57X. ZnO_ref (0.7 mg) has been suspended in water (3 mL) and sonicated for 5 min prior to the analysis with Ultrasonik NEY 57X. The suspension has been filtered using Nylon syringe filters with 0.45 μm pore size. For liquid suspensions with Solargo™ as HMW, 1 drop of the product has been diluted with 3 mL of distilled water, following the experimental synthetic conditions reported in Chapter 2.

Infrared Spectroscopy (IR)

FT-IR spectra have been recorded using a Perkin Elmer FT-IR Spectrum Two in the 4000-400 cm^{-1} range in ATR (attenuated total reflection) mode.

Size exclusion chromatography (SEC)

SEC has been performed with a Dionex Ultimate 3000 autosampler, column oven and pump, with Refractomax 520 ERC RI detector (deuterium UV lamp) and PCC MCX columns; pre-columns and analytical columns with dimensions ranging from 1000 Å to 100000 Å, with divinyl benzene sulphonate copolymer matrix as column material, with flow 0,5 mL/min. About 1 mg of sample has been weighted in a graduated flask and diluted with a NaOH 0.1 M solution). The injection volume is 20 µL, with analysis time of 50 minutes, pressure of about 20 bar; analysis temperature 30 °C. Molar mass number (M_n), weight average molar mass (M_w) and polydispersity (PD) are reported.

Pyrolysis-GC/MS (Py-GC/MS)

Pyrolysis-GC/MS has been performed using Pyrolysator EGA/PY-3030D Frontier Lab (Fukushima, Japan), coupled with Agilent 7890B GC and Agilent 5977A MSD (CA, USA). Identifications have been performed with MassHunter and EGA/Py 3030-program. GC separation has been performed using the HP-5ms capillary column (30 m, 0.25 i.d., film thickness 0.25µm), operating under these conditions: injector temperature 250 °C, split ratio 1:20, oven set at 70 °C for 4 minutes then 10 °C min^{-1} until 300°C, final T hold constant for 21 min. MS has been equipped with an electron ionization (EI) ion source operating with the ionizing voltage 70 eV; the transfer line temperature has been 300 °C, scan range m/z 40-550.

Thermogravimetric Analysis (TGA)

TGA has been performed using Netzsch TG 209 Fi libra equipped with Julabo FB50 cooler. About 7 mg of sample have been weighted on an 85 µL Al_2O_3 open crucible. The sample has been subjected to N_2 flow from 50 to 900 °C with a ramp rate of 10°C/min, then the sample has been kept under oxygen atmosphere for 10 minutes at 900 °C.

Differential Scanning Calorimetry (DSC)

DSC analyses have been performed using Mettler Toledo DSC 3+, with power unit 200 W, DSC sensor FRS 6+, a Huber TC 100 cooler. About 8 mg of sample have been pressed on an aluminum sample pan. The heat cycles have been the following: first step, from 25 °C to 200 °C, heating rate of 20 C° min^{-1}, N_2 flow of 50 mL min^{-1}; second step, -20 °C for 15 minutes, N_2 flow of 50 mL min^{-1}; third step from -20 °C to 220 °C, heating rate of 20°C min^{-1}, N_2 flow of 50 mL min^{-1}.

Company Partners

UPM-Kymmene Oyj

UPM-Kymmene Oyj is a Finnish forest industry company established through the merger of Kymmene Corporation with Repola Oy and its subsidiary United Paper Mills Ltd in 1996. Its logo, a griffin (Figure I), was designed by Hugo Simberg in 1899 and symbolizes the griffin as a guardian of the northern forests.

Figure I. UPM-Kymmene Oyj logo

With annual sales of approximately 8.6 billion euros and a global sales network covering all six continents, UPM employs around 17,000 people across 11 countries, including Finland, Austria, China, Estonia, France, Germany, Malaysia, Poland, the United Kingdom, Uruguay, and the United States. UPM business areas include: UPM Biorefining, comprising Pulp, Timber, and Biofuels; UPM Energy: Finland second-largest energy provider, sourcing energy from wood-based biomass, hydropower, and nuclear power; UPM Raflatac: focused on labelling materials for various commercial products; UPM Specialty Papers: producing high-quality papers using sustainable methods; UPM Communication Papers: a leading global producer of graphic papers for the publishing and advertising sectors; UPM Plywood: specializing in plywood for construction, vehicle flooring, and LNG shipbuilding, with flagship products like WISA plywood. UPM also produces biocomposite, innovative sustainable materials combining plastic modularity with wood strength. Their UPM Biochemicals division in Germany produces biomolecules from wood, such as lignin-based fillers that replace carbon black in rubber, offering benefits like higher purity and lightness. Additionally, UPM Biomedicals focuses on healthcare applications, including skin injury care and tissue engineering using nanofibrillar cellulose-based hydrogels. UPM commitment to sustainability is evident in its forest management practices. The company manages approximately 570,000 hectares of forests in Finland and the United States, and 255,000 hectares of plantations in Uruguay. They promote sustainable forest management, aiming to preserve biodiversity and combat deforestation. During my PhD, I spent six months at UPM North European Research Centre (NERC) in Lappeenranta, Finland, under the supervision of Dr. Suvi Pietarinen, Manager of Business Development, Biochemicals. During this time, I worked on the charchterization of lignin@ZnO hybrid materials, focusing on the lignin matrix to assess potential modifications after synthesis and I performed the optimization of a mechanochemical synthetic scale up of this material.

Green Innovation GmbH

Green Innovation GmbH is an Austrian company founded in 2015, headquartered in Innsbruck (Figure II). The company focuses on sustainable practices in animal husbandry, placing animal welfare at the core of its work.

Figure II. Green Innovation logo

Their flagship product is Oxilem™, derived from the same lignin used in my PhD. In addition to its work in the animal sector, Green Innovation has expanded into the agronomic field, developing products based on polyphenols and microorganisms, supported by advanced microbiology research. Green Innovation prioritizes the development of products that are not only green but also derived from sustainable and renewable resources. The company invests significantly in research, with 20 research projects and several collaborations across Europe. In 2020, research-related investments exceeded 20% of their revenues. Green Innovation collaborates with UPM-Kymmene (since 2015), Garant GmbH (Austria), and Zoogamma S.p.A. (Italy) to manage the entire process from product ideation to commercialization. Green Innovation is active in international markets, including Europe, Asia, Australia, Canada, Mexico, and China. The company economy continues to grow, with a turnover exceeding 2.2 million euros in 2020, reflecting the increasing demand for sustainable solutions that maximize the potential of natural products.

Acknowledgments

My PhD was made possible through the collaboration and support of many professionals.

I would like to express my deep gratitude to Green Innovation (Giuliano Leonardi, Vito Macchia) and UPM-Kymmene Oyj (Suvi Pietarinen) for her significant contributions to my research.

I am particularly thankful to UPM-Kymmene Oyj for welcoming me at the North Europe Research Center (UPM-NERC) in Lappeenranta, where I had the opportunity of working under the guidance of Suvi Pietarinen. I had the chance to work in a company environment, surrounded by helpful people who supported me and taught me a lot. In addition, I would like to express my gratitude to all the technicians who performed the SEM-EDS, TGA, DSC, Pyrolysis GC-MS, and SEC analyses.

Many thanks go to Green Innovation (Giuliano Leonardi) for the Kg scale up production of HMW@ZnO used in this research and for the support.

Special thanks to Monica Maffini for all the ICP-AES and data analyses, as well as for her continuous support, infinite availability, and kindness.

In vivo tests were conducted by Professor Sheridan Woo's research group from Federico II University (Naples), particularly thanks to Stefania Lanzuise and Gelsomina Manganiello for their *in field* tests and data analysis. *In vitro* tests were carried out by BICT SRL (Simone Stasi). TEM/EDS analyses were made possible thanks to the work of Andrea Migliori at the CNR, Bologna (Consiglio Nazionale delle Ricerche Area Territoriale di Ricerca di Bologna).

I would like to thank Paolo Pelagatti for his valuable scientific advice throughout these years, as well as for his continuous support.

Finally, I would like to express my heartfelt gratitude to my supervisor, Dominga Rogolino, from whom I have learned so much over the years. Her support and encouragement have been crucial to my professional growth, and I am truly thankful for her guidance throughout this journey.

UNIONE EUROPEA
Fondo Sociale Europeo
Ministero dell'Università e della Ricerca
PON RICERCA E INNOVAZIONE 2014 - 2020
REACT EU
UNIVERSITÀ DI PARMA

La borsa di dottorato è stata cofinanziata con risorse del
Programma Operativo Nazionale Ricerca e Innovazione 2014-2020, risorse FSE REACT-EU
Azione IV.4 "Dottorati e contratti di ricerca su tematiche dell'innovazione"
e Azione IV.5 "Dottorati su tematiche Green"